CRANFIELD INSTITUTE OF TECHNOLOGY

SCHOOL OF MECHANICAL ENGINEERING

DEPARTMENT OF FLUID ENGINEERING AND INSTRUMENTATION

PhD THESIS

Academic year 1991-2

M. J. WHITTON

GAS LIQUID MIXING IN TALL VESSELS FITTED WITH MULTIPLE IMPELLERS

Supervisor: Prof. M. Sanderson

October 1992

This thesis is submitted in partial fulfilment for the degree of Doctor of Philosophy

© Michael J. Whitton 1992

ProQuest Number: 10820925

All rights reserved

INFORMATION TO ALL USERS
The quality of this reproduction is dependent upon the quality of the copy submitted.

In the unlikely event that the author did not send a complete manuscript
and there are missing pages, these will be noted. Also, if material had to be removed,
a note will indicate the deletion.



ProQuest 10820925

Published by ProQuest LLC (2019). Copyright of the Dissertation is held by Cranfield University.

All rights reserved.
This work is protected against unauthorized copying under Title 17, United States Code
Microform Edition © ProQuest LLC.

ProQuest LLC.
789 East Eisenhower Parkway
P.O. Box 1346
Ann Arbor, MI 48106 – 1346

ABSTRACT

The dispersion of air into water was studied in a tall agitated vessel (ungassed liquid depth = 2.4 × vessel diameter) fitted with four different triple impeller combinations:

1. Three identical Rushton turbines
2. One Rushton turbine + 2 pitched blade turbines (both pumping down)
3. One Rushton turbine + 2 pitched blade turbines (both pumping up)
4. One Rushton turbine + 2 LE20 impellers (both pumping down)

Two vessel scales, of identical geometry, were studied:

1. 0.61 m diameter, 0.420 m^3 liquid volume
2. 0.95 m diameter, 1.570 m^3 liquid volume.

For a range of impeller speeds and gas flow rates, measurements were made of the power draw for each impeller, gas holdup, liquid mixing rates and mass transfer rates. The impeller combinations were compared on the basis of these parameters. The performance of the individual impellers in each combination were also compared with single impellers mounted in standard geometry vessels.

In terms of power draw and gas holdup many of the trends observed in standard geometry vessels can be directly applied to tall vessel, multiple impeller geometries. A method of estimating the gassed power draw of multiple Rushton turbines is presented.

All impeller combinations studied, produced compartmentalised flow patterns. Aeration was found to have a significant effect on liquid mixing rates, and the magnitude of this effect was a function of the impeller combination used. Liquid mixing with multiple impellers was found to be very complex and geometry specific. Simple staged models, used previously in the literature, were found not to apply to the impeller combinations tested in this thesis.

An economic comparison is presented, of the options available for improving mass transfer rates in an existing reactor. For the range of conditions considered, increasing the back pressure in the vessel was generally found to be a cheaper option than increasing the power input from the impellers, increasing the gas flow rate, or enriching the inlet gas.

ACKNOWLEDGEMENTS

I would like to thank Professor Mike Sanderson, of Cranfield Institute of Technology, and Professor Alvin Nienow, of the University of Birmingham. Their support and guidance on this project was a great help and very much appreciated.

I would also like to thank the members of the Fluid Mixing Processes consortium, who funded this research work, for giving this project the benefit of their industrial perspective.

I would also like to thank all of my friends and colleagues at British Hydromechanics Research Group Ltd who have been a constant source of help and encouragement. I would particularly like to thank Andrew Green and Steve Ruszkowski, for giving me the time and facilities to complete this thesis, and Bob Burnapp for his help in gathering the experimental data.

I am also grateful to Dr. Richard Grenville, Dr. Andrew Mak and Susan Cook. Without their friendship and support over the last few years this thesis would never have been completed. Thanks also to Dr. Nick Fawcett for his help with the mathematics in this thesis.

CONTENTS

Page number

ABSTRACT
ACKNOWLEDGEMENTS
CONTENTS
LIST OF TABLES
LIST OF FIGURES
NOTATION

GENERAL INTRODUCTION AND OBJECTIVES 1

CHAPTER 1: LITERATURE REVIEW 2

1.1 INTRODUCTION 2
1.2 FLOW PATTERNS AND POWER DRAW 3
1.2.1 Single impellers 3
1.2.1.1 Rushton turbines 3
1.2.1.2 Downward pumping pitched blade turbines 9
1.2.1.3 Upward pumping pitched blade turbines 13
1.2.1.4 LE20 impellers 15
1.2.2 Multiple impellers 15
1.2.2.1 Comparison of impeller combinations 16
1.2.2.2 Multiple Rushton turbines 17
1.2.2.3 Mixed impeller combinations 22
1.2.2.4 Prediction of gassed power draw 25
1.3 GAS HOLDUP 29
1.3.1 Single impellers 30
1.3.2 Multiple impellers 35
1.4 LIQUID MIXING 39
1.4.1 Single impellers 39
1.4.2 Multiple impellers 40
1.4.2.1 Liquid mixing times 40
1.4.2.2 Structured liquid mixing models 41
1.5 MASS TRANSFER 45
1.5.1 Single impellers 45
1.5.2 Multiple impellers 46
1.5.3 Gas phase mixing with multiple impellers 47
1.6 CONCLUSIONS 48
1.7 STRUCTURE OF THIS THESIS 50

CHAPTER 2: EXPERIMENTAL DETAILS 51

2.1 INTRODUCTION 51
2.2 EXPERIMENTAL FACILITIES 51
2.2.1 Vessels 51
2.2.2 Impellers 51
2.2.3 Spargers 52
2.2.4 Test fluids 52

2.3 INSTRUMENTATION AND EXPERIMENTAL TECHNIQUES 53
2.3.1 Flow patterns 53
2.3.2 Impeller power draw 53
2.3.3 Gas holdup 55
2.3.4 Liquid mixing 56
2.3.5 Mass transfer 57

CHAPTER 3: FLOW PATTERNS AND POWER DRAW 58

3.1 INTRODUCTION 58
3.2 RESULTS FROM THE 0.61 m DIAMETER VESSEL 59
3.2.1 Ungassed power numbers 59
3.2.1.1 Single impellers 59
3.2.1.2 Multiple impellers 60
3.2.2 Gas liquid flow patterns and power draw 61
3.2.2.1 Single impellers 61
3.2.2.2 Comparison of multiple impeller combinations 63
3.2.2.3 Triple Rushton turbines 63
3.2.2.4 RT + 2 LE20 combination 65
3.2.2.5 RT + 2 PBT (pumping down) combination 67
3.2.2.6 RT + 2 PBT (pumping down) combination 67
3.3 RESULTS FROM THE 0.95 m DIAMETER VESSEL 68
3.3.1 Ungassed power numbers 68
3.3.1.1 Single impellers 68
3.3.1.2 Multiple impellers 69
3.3.2 Gassed power draw 69
3.3.2.1 Triple Rushton turbines 69
3.3.2.4 RT + 2 LE20 combination 70
3.4 EFFECT OF SCALE 70
3.5 DISCUSSION OF RESULTS 70
3.5.1 Ungassed flow patterns and power draw 70
3.5.2 Gassed flow patterns and power draw 71
3.6 PREDICTION OF GASSED POWER DRAW FOR MULTIPLE RUSHTON TURBINES 73
3.7 CONCLUSIONS 74

CHAPTER 4: GAS HOLDUP 77

4.1 INTRODUCTION 77
4.2 RESULTS FROM THE 0.61 m DIAMETER VESSEL 77
4.3 RESULTS FROM THE 0.95 m DIAMETER VESSEL 79
4.4 SCALE UP 80
4.5 COMPARISON OF STANDARD AND TALL VESSEL GEOMETRIES 81
4.6 DISCUSSION 81
4.7 CONCLUSIONS 83

CHAPTER 5: LIQUID MIXING 85

5.1 INTRODUCTION 85
5.2 LIQUID MIXING IN THE 0.95 m DIAMETER VESSEL 85
5.2.1 Assumed liquid mixing model 85
5.2.2 Exchange flows 87
5.2.2.1 Ungassed 87
5.2.2.2 3RT combination with gas 89
5.2.2.3 RT+2×LE20 combination with gas 90
5.2.2.4 Comparison of impeller combinations with gas 90
5.3 EXPERIMENTS TO DETERMINE VALIDITY OF THREE CELL LIQUID MIXING MODEL 90
5.3.1 Effect of tracer addition point 92
5.3.2 Exchange flows (3RT combination) 93
5.3.3 Exchange flows (RT+2×LE20 combination) 94
5.3.4 Choice of liquid mixing model 94
5.4 LIQUID MIXING TIMES 94
5.4.1 Ungassed 97
5.4.2 Effect of aeration 98
5.4.3 Effect of scale 99
5.5 DISCUSSION 100
5.6 CONCLUSIONS 104

CHAPTER 6: MASS TRANSFER 109

6.1 INTRODUCTION 109
6.2 LIQUID AND GAS PHASE MIXING MODELS 109
6.2.1 Liquid mixing model 109
6.2.2 Gas mixing model 111
6.3 ANALYSIS OF DISSOLVED OXYGEN TRANSIENTS 112
6.4 RESULTS 113
6.5 DISCUSSION 115
6.6 CONCLUSIONS 116

CHAPTER 7: ECONOMIC ANALYSIS 117

7.1 INTRODUCTION 117
7.2 OPTIONS AVAILABLE FOR IMPROVING MASS TRANSFER 117
7.3 ECONOMIC BACKGROUND 118
7.4 COSTS ASSOCIATED WITH EACH RETROFIT OPTION 119
7.4.1 Increase the power input to the dispersion 119
7.4.2 Increase the gas flow rate 121
7.4.3 Increase the pressure in the process vessel 122
7.4.4 Use enriched gas 123
7.5 RESULTS 124
7.6 DISCUSSION 126
7.7 CONCLUSIONS 127

CHAPTER 8: OVERALL CONCLUSIONS AND SUGGESTIONS FOR FUTURE WORK 128

REFERENCES

APPENDIX 1: CALCULATION OF EXCHANGE FLOWS
APPENDIX 2: SOLUTION OF DIFFERENTIAL EQUATIONS
APPENDIX 3: TK SOLVER MODEL EQUATIONS FOR ECONOMIC ANALYSIS
APPENDIX 4: SIMPLE MODELS FOR k_La ESTIMATION
APPENDIX 5: MASS TRANSFER METHOD FOR VISCOUS LIQUIDS

TABLES

FIGURES

LIST OF TABLES

Table number	Title
2.1	Dimensions of disc turbines.
2.2	Dimensions of pitched blade turbines.
2.3	Dimensions of LE20 impellers.
3.1	Impeller ungassed power numbers in standard geometry vessel, T = 0.61 m.
3.2	Ungassed power numbers for triple impeller combinations (T = 0.61 m).
3.3	Loading to flooding transition for a single Rushton turbine and the lowest Rushton turbine in the tall vessel.
3.4	Fraction of sparge gas recirculated into upper impellers, estimated from power data, (3RT combination, T = 0.61 m).
3.5	Ungassed power numbers for triple impeller combinations (T = 0.95 m).
3.6	Fraction of sparge gas recirculated into upper impellers, estimated from flow maps, (3RT combination, T = 0.61 m).
4.1	Holdup data for 3RT combination (T = 0.61 m).
4.2	Holdup data for RT+2×LE20 combination (T = 0.61 m).
4.3	Holdup data for RT+2×PBT combination (pumping down), (T = 0.61 m).
4.4	Holdup data for RT+2×LE20 combination (pumping up), (T = 0.61 m).
4.5 & 4.6	Holdup correlations for different impeller combinations in the 0.61 m diameter vessel.
4.7 & 4.8	Effect of cavity regimes on 3RT holdup correlations (T = 0.61 m).
4.9	Holdup data for 3RT combination (T = 0.95 m).
4.10	Holdup data for RT+2×LE20 combination (T = 0.95 m).
4.11 & 4.12	Holdup correlations for different impeller combinations in the 0.95 m diameter vessel.
4.13 & 4.14	Effect of cavity regimes on 3RT holdup correlations (T = 0.95 m).
4.15	Correlation of holdup data including gas expansion energy.
4.16 to 4.18	Scale up correlations for the 3RT and RT+2×LE20 combinations (T = 0.61 m and 0.95 m).
5.1	Liquid mixing data, 3RT combination, T = 0.95 m.
5.2	Liquid mixing data, RT+2×LE20 combination, T = 0.95 m.
5.3	Unaerated exchange flows correlated versus impeller speed.
5.4	Unaerated exchange flows correlated versus power input.

5.5 Effect of tracer addition point on ungassed liquid mixing time (T = 0.61 m, 3RT combination).
5.6 Effect of tracer addition point on ungassed liquid mixing time and exchange flows (T = 0.61 m, 3RT combination).
5.7 Liquid mixing data, 3RT combination, T = 0.61 m.
5.8 Liquid mixing data, RT+2×LE20 combination, T = 0.61 m.
5.9 Effect of scale on liquid mixing times.

6.1 k_La values for the 3RT combination, T = 0.95 m.
6.2 k_La values for the RT+2×LE20 combination, T = 0.95 m.

7.1 Vessel scales considered for economic analysis

LIST OF FIGURES

Figure number	Title
Literature review	
1.1	Gas liquid flow patterns for a single Rushton turbine.
1.2	Effect of Reynolds number on Rushton turbine ungassed power number.
1.3	Gas cavities observed on the blades of a Rushton turbine.
1.4	Gas cavity regimes for a six blade Rushton turbine.
1.5	Relation between impeller cavity structure and power consumption.
1.6	Flow map for a standard Rushton turbine in a standard Rushton turbine in a standard geometry vessel.
1.7	Measured gassed power curves for a standard Rushton turbine and comparison with the straight line approximations of Warmoeskerken.
1.8	Comparison of Smith's power predictions with experimental data.
1.9	Gas loading regimes for a downward pumping impeller.
1.10	Region of up flow observed below a downward pumping impeller.
1.11	Ungassed flow profiles measured by laser doppler anemometry.
1.12	Change of flow pattern and gas cavity structure for a downward pumping pitched blade turbine.
1.13	Gas cavity structures observed on the blades of downward pumping pitched blade turbines.
1.14	Decrease in Pg/Pu with increasing aeration rate, at constant impeller speed, for different impeller designs.
1.15	Change of flow pattern and gas cavity structure for an upward pumping pitched blade turbine.
1.16	Gas liquid flow patterns observed with different dual impeller combinations.
1.17	Ungassed flow patterns observed with dual Rushton turbines as a function of impeller spacing.
1.18	Effect of impeller spacing on the ungassed power draw of dual Rushton turbines.
1.19	Flow produced by two touching Rushton turbines and comparison with a single Rushton turbine of the same total blade width.
1.20	Effect of impeller separation on the ungassed power draw of dual Rushton turbines.
1.21	Ungassed power number as a function of liquid level above the top turbine for various numbers of turbines.
1.22	Gas liquid flow pattern for triple Rushton turbines with the lowest impeller flooded.
1.23	Generalised flow map for triple Rushton turbines.
1.24	Plot of P_g/P_u versus $V_{sg}/(gT)^{0.5}$ for dual Rushton turbines.

1.25 Evolution of gas holdup with increasing impeller speed at constant gas flow rate.
1.26 Evolution of gas holdup with multiple Rushton turbines.
1.27 Comparison of gas holdup for a single Rushton turbine and dual Rushton turbines.
1.28 Comparison of gas holdup for dual and triple Rushton turbines.
1.29 Three cell model used to describe liquid mixing for dual Rushton turbines.
1.30 Four cell model used to describe liquid mixing for four Rushton turbines.

Experimental facilities

2.1 Standard geometry vessel fitted with a single impeller.
2.2 Tall vessel geometry fitted with three impellers.
2.3 Impeller designs tested.
2.4 Sparger geometry.
2.5 Instrumentation chain for strain gauge telemetry system.
2.6 Instrumentation chain for strain gauge slip ring system.
2.7 Position of ultrasonic level detector.
2.8 Conductivity probe designs tested.
2.9 Comparison of conductivity probe responses in a gas liquid dispersion.
2.10 Schematic of EDT conductivity probe fitted with mesh.
2.11 Instrumentation chain for conductivity measurement.
2.12 Effect of salt concentration on coalescence behaviour of gas bubbles.
2.13 Gas supply system for dynamic mass transfer experiments.
2.14 Electrosense fast response dissolved oxygen probe.

Flow patterns and power draw

3.1 Ungassed power numbers of single impellers (T = 0.61 m).
3.2 Gassed power draw of single impellers (T = 0.61 m).
3.3 Comparison of total power draw of multiple impeller combinations (T = 0.61 m).
3.4 Comparison of total P_g/P_u ratio for multiple impeller combinations (T = 0.61 m).
3.5 Gas liquid flow patterns observed with triple Rushton turbines.
3.6 Gassed power draw for triple Rushton turbine combination (T = 0.61 m).
3.7 Flow map for triple Rushton turbines (T = 0.61 m).
3.8 Gas liquid flow patterns observed with the RT+2×LE20 combination.

3.9 Gassed power draw for the RT+2×LE20 combination (T = 0.61 m).
3.10 Comparison of gassed power draw for LE20 impellers in the tall tank and a standard tank.
3.11 Gas liquid flow patterns observed with the RT+2×PBT (pumping down) combination.
3.12 Gassed power draw of the RT+2×PBT (pumping down) combination, (T = 0.61 m)
3.13 Comparison of gassed power draw for downward pumping PBT impellers in the tall and standard tanks, (T = 0.61 m).
3.14 Gas liquid flow patterns observed with the RT+2×PBT (pumping up) combination.
3.15 Gassed power draw of the RT+2×PBT (pumping up) combination, (T = 0.61 m).
3.16 Comparison of gassed power draw for upward pumping PBT impellers in the tall and standard tanks, (T = 0.61 m).
3.17 Flow map for triple Rushton turbines (T = 0.95 m).
3.18 Gassed power draw of triple Rushton turbine combination (T = 0.95 m)
3.19 Gassed power draw of the RT+2×LE20 combination (T = 0.95 m)
3.20 Total gassed power draw: Comparison of impeller combinations at given impeller speed, T = 0.95 m.
3.21 Comparison of power draw at different scales (3RT combination)
3.22 Comparison of power draw at different scales (RT+2×LE20 combination)
3.23 Prediction of gassed power draw for triple Rushton turbines.

Gas holdup

4.1 Comparison of gas holdup for different impeller combinations (constant N and Q_G), T = 0.61 m.
4.2 Comparison of gas holdup for different impeller combinations (constant ε_m and V_{sg}), T = 0.61 m.
4.3 Comparison of gas holdup for different impeller combinations (constant N and Q_G), T = 0.95 m.
4.4 Comparison of gas holdup for different impeller combinations (constant ε_m and V_{sg}), T = 0.95 m.
4.5 Scale up or 3RT combination
4.6 Scale up of RT+2×LE20 combination
4.7 Holdup correlation for tall and standard geometry vessels.
4.8 Local energy dissipation rates in stirred vessels.

Liquid mixing

5.1 Tracer injection and conductivity probe positions, T = 0.95 m.
5.2 Three cell model for liquid phase mixing.

5.3 Example of conductivity responses from tall vessels (3RT combination), T = 0.95 m.
5.4 Example of conductivity responses from tall vessels (RT+2×LE20 combination), T = 0.95 m.
5.5 Example of how exchange flows are determined from conductivity response curves.
5.6 Ungassed exchange flows versus power input.
5.7 Effect of gas flow rate on exchange flows for the triple Rushton turbine combination, T = 0.95 m.
5.8 Effect of power input on exchange flows for the triple Rushton turbine combination, T = 0.95 m.
5.9 Effect of gas flow rate on exchange flows for the RT+2×LE20 combination, T = 0.95 m.
5.10 Effect of power input on exchange flows for the RT+2×LE20 combination, T = 0.95 m.
5.11 Comparison of liquid exchange flows when gassed, T = 0.95 m.

5.12 Tracer injection and conductivity probe positions, T = 0.61 m.
5.13 Example of conductivity responses from tall vessels (3RT combination), T = 0.61 m.
5.14 Example of conductivity responses from tall vessels (RT+2×LE20 combination), T = 0.61 m.
5.15 Six cell model for liquid phase mixing .
5.16 Flow pattern observations and main axial mixing boundaries.
5.17 Four cell model for liquid phase mixing.
5.18 Effect of power input on liquid mixing time.
5.19 Effect of gas flow rate on liquid mixing times for the triple Rushton turbine combination, T = 0.95 m.
5.20 Effect of gas flow rate on liquid mixing times for the RT+2×LE20 combination, T = 0.95 m.
5.21 Effect of aeration and power draw on liquid mixing time, T = 0.95 m.
5.22 Comparison of impeller combinations, T = 0.95 m.
5.23 Effect of aeration and power draw on liquid mixing time, T = 0.61 m.
5.24 Effect of scale on liquid mixing time (3RT combination).
5.25 Correlation of liquid mixing time from two scales, (3RT combination).
5.26 Effect of scale on liquid mixing time (RT+2×LE20 combination).
5.27 Correlation of liquid mixing time from two scales, (RT+2×LE20 combination).

Mass transfer

6.1	Oxygen probe positions (T = 0.95 m).
6.2	Simple mass transfer model. Three separate perfectly mixed liquid cells with gas in plug flow.
6.3	Local k_La from simple model.
6.4	Mass transfer model including liquid exchange flows.
6.5	Effect of exchange flows on calculated k_La values.
6.6	Sensitivity of k_La values to exchange flows.
6.7	Local k_La from exchange flow model (bottom cell only).
6.8	Local k_La from exchange flow model.

Economics

7.1	Effect of vessel scale on process options
7.2	Effect of power input on cost of process options at large scale (low gas flow rate, low back pressure).
7.3	Effect of power input on cost of process options at large scale (low gas flow rate, high back pressure).
7.4	Effect of power input on cost of process options at large scale (high gas flow rate, low back pressure).
7.5	Effect of power input on cost of process options at large scale (high gas flow rate, high back pressure).
7.6	Effect of power input on cost of process options at small scale (low gas flow rate, low back pressure).
7.7	Effect of power input on cost of process options at small scale (low gas flow rate, high back pressure).
7.8	Effect of power input on cost of process options at small scale (high gas flow rate, low back pressure).
7.9	Effect of power input on cost of process options at small scale (high gas flow rate, high back pressure).
7.10	Sensitivity of costs to project life.
7.11	Sensitivity of costs to interest rate.

Appendix 1

A1.1	Tracer mass balances for six cell liquid mixing model
A1.2	Relationship between exchange flow values and area between conductivity response curves.

NOTATION

SYMBOL	MEANING	UNITS
A	Empirical constant	-
a	Gas liquid interfacial area per unit volume of liquid	m^2/m^3
B	Empirical constant	-
c_l	Impeller clearance (distance from impeller centre line to lowest point of vessel base)	m
c_S	Sparger clearance (distance from sparge holes to lower edge of impeller blades)	m
C	Concentration	mol/m^3
$\overline{C}$	Laplace transform of C	-
ΔC	Concentration driving force between gas and liquid	mol/m^3
C_C	Capital costs	£
C_R	Running costs	£
C_{pow}	Cost of electrical power	£/kW hr
C_T	Total costs	£
d_b	Bubble diameter	m
D	Impeller swept diameter	m
D_d	Impeller disc diameter	m
D_{RT}	Diameter of Rushton turbine (bottom impeller in all multiple impeller combinations)	m
D_F	Minimum impeller diameter required to avoid flooding	m
D_S	Pitch circle diameter of sparge ring holes	m
E_C	Isothermal efficiency of gas compressor	-
E_M	Motor efficiency	-
F	Liquid exchange flow	m^3/s
Fl_G	Gas flow number (Q_G/ND^3)	-
$Fl_{G,CD}$	Gas flow number at which complete gas dispersion is achieved	-
$Fl_{G,F}$	Gas flow number at the flooding / loading transition	-
$Fl_{G,R}$	Gas flow number at which gas recirculation is significant	-
$Fl_{G,3\text{-}3}$	Gas flow number at which the 3-3 cavity structure forms	-
Fl_m	Gas flow number corrected for surface aeration	-
Fr	Impeller Froude number (N^2D/g)	-
g	Gravitational constant (= 9.81)	m/s^2
H	Ungassed liquid depth	m
i	Annual interest rate	%
I_0	Initial investment	£
J	Mass transfer rate between gas and liquid	mol/m^3s
K	Equilibrium constant (= C_{Li}/C_G)	-
k_G	Gas film mass transfer coefficient	s/m
k_L	Liquid film mass transfer coefficient	m/s

L	Blade length	m
L_A	Liquid level above impeller	m
M	Molecular weight of air	kmol/kg
M_{O2}	Mass of oxygen	kg
N	Impeller rotational speed	revs/s
N_c	Impeller speed at which direct / indirect gas loading transition occurs	revs/s
N_Q	Impeller pumping number	-
p	Pressure	N/m^2
P_A	Additional power	W
P_g	Gassed impeller power input	W
P_{lim}	Value of P_g/P_u ratio just before impeller floods	-
P_u	Ungassed impeller power input	W
P_1	Power draw of a single impeller	W
P_2	Total power draw of dual impellers	W
Po	Ungassed impeller power number	-
Po_g	Gassed impeller power number	-
Q_G	Gas volumetric flow rate at sparger	m^3/s
Q_R	Gas volumetric flow rate recirculated to the impeller	m^3/s
Q_I	Impeller pumping capacity	m^3/s
q	Mass of tracer added to vessel	kg
R^2	Regression coefficient	-
R	Gas constant	J/mol K
Re	Impeller Reynolds number	-
S	Separation distance between impeller centre lines	m
s	Laplace transform argument	-
t	Time	s
t_{op}	Production time per year	hr
$T_{subscript}$	Liquid temperature	Kelvin
T	Vessel diameter	m
V	Volume	m^3
V_G	Total volume of the gas bubbles held up in dispersion	m^3
V_L	Volume of liquid	m^3
V_{sg}	Superficial gas velocity (= 4 Q_G / πT^2)	m/s
v_{tip}	Impeller tip speed	m/s
W	Blade width	m
We	Impeller Weber number	-
Y	Project life	Years
α	Regression exponent	-
β	Regression exponent	-
γ	Regression exponent	-
$\delta(t)$	Dirac delta function	-
ε	Energy dissipation rate	W/kg
ε_{gas}	Isothermal expansion energy of gas	W/kg
ε_G	Gas hold up (= V_G / (V_L + V_G))	-
ε_m	Impeller specific power input	W/kg

μ	Dynamic viscosity	Ns/m^2
θ	Blade angle to horizontal	degrees
$\theta_{80\%}$	80% liquid mixing time	s
$\theta_{95\%}$	95% liquid mixing time	s
ρ	Density	kg/m^3
σ_{GL}	Interfacial tension	N/m
τ	Liquid circulation time	s
τ_L	First order response time of dissolved oxygen probes	s
Λ	Torque	Nm

SUBSCRIPTS

A	at ambient conditions
b	at the bottom
B	at the bottom
F	at the flooding/loading transition
CD	at the loading/complete dispersion transition
G	of the gas phase
g	gassed
L	of the liquid phase
Li	at the liquid interface with the gas
LS	at large scale
MAX	Maximum value of
MIN	Minimum value of
m	in the middle
M	in the middle
P	of the process
R	conditions at which gas recirculation is significant
S	of the sparger
SS	at small scale
t	at the top
T	at the top
u	ungassed
3-3	at the transition from 6 clinging cavities to 3-3 cavities (Rushton turbine)

ABBREVIATIONS

rsd	Relative standard deviation
RT	Rushton turbine
LE20	Three blade axial flow impeller manufactured by APV Ltd
PBT	Pitched blade (45°) turbine
4PBT	Four blade pitched blade turbine
6PBT	Six blade pitched blade turbine

MFT	Mixed flow turbine (a Rushton turbine with blades at 45° to the horizontal)
4MFT	Four blade mixed flow turbine
6MFT	Six blade mixed flow turbine
3RT	Triple disc turbine combination
RT+2×LE20	Single Rushton turbine + dual LE20 combination (RT at bottom of vessel)
RT+2×4PBT	Single Rushton turbine + dual four blade PBT combination (RT at bottom of vessel)
vvm	Vessel volumes per minute

DIMENSIONLESS GROUPS

Fl_G	Gas flow number	=	$Q_G / N D^3$
Fr	Impeller Froude number	=	$N^2 D / g$
Po	Impeller power number	=	$P / \rho_L N^3 D^5$
Re	Impeller Reynolds number	=	$\rho_L N D^2 / \mu_L$
We	Impeller Weber number	=	$\rho_L N^2 D^3 / \sigma_{GL}$

GENERAL INTRODUCTION AND OBJECTIVES

Tall vessels (vessel height > > vessel diameter), fitted with multiple impellers, are often used for large scale gas dispersion processes. At large scale it is usually cheaper to manufacture a tall thin vessel rather than a large diameter standard vessel (vessel depth = vessel diameter). Tall thin vessels also have higher surface to volume ratios than standard vessels, and are therefore useful for processes in which heat transfer rates are critical.

For standard vessels fitted with a single impeller, the Rushton turbine has become established as the standard impeller for gas dispersion into low viscosity liquids. In tall vessels multiple Rushton turbines are therefore commonly used. However, in a tall vessel multiple radial flow impellers, such as Rushton turbines, produce very poor top to bottom mixing. This can cause problems for processes which require good liquid mixing, e.g. fermentations in which the micro organisms require a uniform environment with minimal concentration gradients. A lot of interest has been shown by the industrial members of the Fluid Mixing Processes consortium, at BHR Group Ltd, in studying alternative impeller combinations to multiple Rushton turbines.

To improve confidence in the design of multiple impeller agitators there is a need for a better understanding of the complex two phase hydrodynamics, and how they affect impeller power draw, gas holdup, liquid mixing, and interphase mass transfer rates. A full scale multiple impeller agitator is often the final step in a scale up process starting from a small scale standard vessel, so it is also important to be able to relate the hydrodynamics of single impellers to multiple impeller combinations.

When this research work started in 1987 there were very few published works on multiple impellers for gas dispersion. More interest has been shown in these geometries over the last two to three years but there are still few reliable design rules available.

The objectives of this thesis are:

1. To investigate how different impeller designs behave in tall vessel geometries and how they compare with single impellers in standard geometry vessels.

2. To identify how standard geometry design correlations can be applied to tall vessels.

3. To study how liquid mixing rates in tall vessels are affected by impeller selection and operating conditions.

4. To study the validity of various models for liquid phase mixing in tall vessels.

5. To determine local mass transfer coefficients for multiple impeller combinations.

CHAPTER 1

LITERATURE REVIEW

1.1 INTRODUCTION

Hundreds of references can be found on the subject of gas liquid contacting in agitated vessels. The majority of this literature relates to single impellers in standard vessels, i.e. liquid depth equal to the vessel diameter. Several reviews of the single impeller literature have been published, e.g. Van't Riet (1975), Mann (1983), Midoux and Charpentier (1984), Muskett and Turley (1984), Middleton (1985), Warmoeskerken (1986), Muskett (1987b), Nienow (1987 & 1990), and Tatterson (1991).

This literature review concentrates on gas dispersion with multiple impellers. This is an area in which relatively few papers have been published, and one which has not previously been reviewed in detail. The review is presented in several sections:

1. Flow patterns and power draw
2. Gas holdup
3. Liquid mixing
4. Mass transfer

Each section begins with a summary of the current level of understanding of single impeller hydrodynamics. This provides essential background information, as many aspects of single impeller hydrodynamics are directly applicable to, and can therefore help to improve understanding of, multiple impeller systems.

This review is limited to the impeller designs studied in this thesis: Rushton turbines, 45° pitched blade turbines and the LE20 impeller (a proprietary design from APV Ltd). These impellers are described in chapter 2.

1.2 FLOW PATTERNS AND POWER DRAW

1.2.1 Single impellers

This section presents the current level of knowledge, with respect to gas liquid flow patterns and power draw, for single impellers mounted in standard geometry vessels, refer to figure 2.1. The three impeller designs studied in this thesis: Rushton turbines, pitched blade turbines, and LE20 impellers, will be reviewed separately.

1.2.1.1 Rushton turbines

Flow patterns

The Rushton turbine produces predominantly radial flow. The bulk gas-liquid flow patterns observed with a single Rushton turbine in a standard geometry vessel are shown in figure 1.1, from Nienow et al (1977).

At low impeller speeds and high gas flow rates the impeller is overwhelmed by gas, figure 1.1(a), and the impeller is said to be "flooded". Under these conditions the gas flow dominates the impeller hydrodynamics and large slugs of gas rise rapidly through the impeller region to the liquid surface. The gas-liquid interfacial area and contact time are both very low, and so is the mass transfer rate.

As impeller speed is increased, at a given gas flow rate, the impeller pumping action begins to dominate the impeller hydrodynamics and bubbles are thrown out radially from the impeller blades, figure 1.1(b). Under these conditions the impeller is said to be "loaded" with gas. This is a better operating condition than the flooding regime because more interfacial area is produced, gas-liquid contact times are longer (bubbles are smaller and bubble rise velocities are lower) and therefore mass transfer rates are higher.

The following equation was defined by Nienow et al (1985b) for estimating the operating conditions at which the transition from flooding to loading occurs for a standard 6 blade Rushton turbine (as shown in figure 2.3):

$$Fl_{G,F} = 30\ Fr \left(\frac{D}{T}\right)^{3.5} \qquad \text{...Eqn (1.1)}$$

Where:
- $Fl_{G,F}$ = Gas flow number at the loading / flooding transition
- Fr = Impeller Froude number
- D = Impeller swept diameter
- T = Vessel diameter

This equation was developed using data from vessels up to 0.61 m diameter. Nienow et al (1985) concluded that equation 1.1 works well for D/T ratios from 0.22 to 0.50, impeller clearances (c_l) from 0.25T to 0.4T, and both coalescing and non coalescing low viscosity media. Muskett (1987b) showed that equation 1.1 worked well for standard Rushton turbines of $T/3$ diameter, in vessels up 2.67 m diameter. Cronin (1988) showed that this equation worked well for standard Rushton turbines of $T/3$ and $T/2$ diameter, in a 0.72 m diameter vessel.

Equation 1.1 cannot be used if the impeller geometry differs significantly from that shown in figure 2.3, and the effect on the loading / flooding transition of using a non standard design cannot be accurately quantified. Equation 1.1 only applies for point or small ring spargers ($D_S < D$) mounted centrally below the impeller disc. These sparger geometries ensure that all of the sparge gas flows through the impeller blades. For a standard Rushton turbine $Fl_{G,F}$ can be increased by up to 40% if a large ring sparger ($D_S > D$) is mounted below the impeller. With this sparger geometry the sparge gas bypasses the impeller and only flows into the impeller blades by recirculation, Nienow and Allsford (1985), Nienow et al (1986), and Nienow et al (1988). Only one design of ring sparger ($D_S = 0.8D_{RT}$) has been studied in this thesis, see chapter 2.

Machon et al (1991b) reported hysteresis around the loading / flooding transition for a single Rushton turbine ($D = T/3$). Within the hysteresis limits the flow pattern was unstable with flooding, loading or a mixture of both flow regimes existing at the same time. Nienow et al (1985c) observed hysteresis with single Rushton turbines, but only for small diameter impellers ($D = 0.22T$).

Complete dispersion is defined as the condition under which gas bubbles are swept into the region below the impeller, see figure 1.1(c). The gas flow number at which the transition to complete gas dispersion ($FL_{G,CD}$) occurs, without recirculation of gas bubbles back into the impeller region, can be estimated for a standard six blade Rushton turbine using:

$$Fl_{G,CD} = 0.2 \left(\frac{D}{T}\right)^{0.5} Fr^{0.5} \qquad \text{...Eqn (1.2)}$$

See Nienow et al (1985b). This correlation is limited to the same range of geometries as equation 1.1, except that it only applies to one impeller clearance, i.e. $c_l = 0.25T$.

As impeller speed is increased the degree of gas recirculation gradually increases. The gas flow number where gas recirculation becomes very high and effectively the gas phase becomes well mixed ($Fl_{G,R}$), is correlated by:

$$Fl_{G,R} = 13\, Fr^{2} \left(\frac{D}{T}\right)^{5} \qquad \text{...Eqn (1.3)}$$

See Nienow et al (1985c). Equation 1.3 is limited to the same range of geometries as equation 1.1, and applies only to low viscosity, freely coalescing media such as clean

water. The degree of gas recirculation will be affected by the bubble sizes present in the dispersion. A small bubble has less buoyancy than a large bubble and will therefore be carried along more readily by the liquid flow. Thus the degree of gas recirculation will increase as bubble size decreases, as a result of coalescence inhibition for example.

The total gas entering the impeller region = $Q_G + Q_R$, where Q_G is the sparger gas flow rate. Q_R consists of recirculated sparger gas and some gas entrained from the surface of the dispersion. Chapman et al (1980) showed that surface entrainment of gas is negligible over a wide range of sparged operating conditions so Q_R will mainly consist of recirculated sparger gas. At small scale Nienow (1979a) found that under some conditions $Q_R > Q_G$, so gas recirculation can have a significant effect on the impeller and vessel hydrodynamics. However, there are currently no reliable correlations available for accurately quantifying Q_R, Middleton (1985) and Tatterson (1991).

Power draw

The ungassed power draw of an impeller (P_u) is calculated from:

$$P_u = Po\ \rho_L\ N^3\ D^5 \qquad \text{...Eqn (1.4)}$$

where:
- Po = Impeller power number (dimensionless)
- ρ_L = Liquid density
- N = Impeller rotational speed

The value of Po is a function of impeller design, vessel internal geometry, scale of operation and Reynolds number. Figure 1.2 shows a plot of power number versus Reynolds number for a Rushton turbine in a standard geometry vessel. All of the work in this thesis was conducted under fully turbulent conditions, i.e. $Re > 10^4$, where for a given turbine design Po is a constant, independent of impeller speed.

As a Rushton turbine rotates in liquid, roll vortices develop behind each blade. When the impeller is gassed these vortices fill with gas bubbles, forming vortex cavities, see figure 1.3(a). As the gas flow rate is increased the gas cavities change shape and grow larger, first forming clinging cavities, figure 1.3(b), and then large cavities, figure 1.3(c), Van't Riet (1975).

The size and shape of the gas cavities is not always the same on each blade of a Rushton turbine. For a six blade Rushton turbine, at constant impeller speed, the cavity structure develops with increasing gas flow rate, in the following sequence, see figure 1.4:

a) 6 vortex cavities
b) 6 clinging cavities
c) 3 clinging cavities and 3 large cavities on alternate blades
d) 6 large cavities of two different sizes (large 3-3 structure)

e) 6 ragged cavities (flooded impeller)

Gas cavities reduce the drag force on the impeller blades and hence the power draw of the impeller falls from its ungassed value. Bruijn et al (1974) concluded that the only parameters that affect cavity shape and size are liquid viscosity and liquid density. Changes in surface tension and dissolved solutes do not affect the size and shape of the cavities. However, some electrolytes cause a reduction in bubble size (by repressing coalescence) resulting in more gas recirculation into the impeller blades. As gas recirculation into the impeller region increases, the gas cavities grow larger and the power draw of the impeller falls.

The effect of gas cavity regime on the power draw of a Rushton turbine, at constant impeller speed, is shown in figure 1.5, Warmoeskerken and Smith (1982). Vortex and clinging cavities have little effect on power draw. The power draw falls off steeply as the 3-3 cavity structure forms, and then levels out as these cavities gradually grow in size. The power curve has a concave shape at low gas flow rates and a convex shape at higher gas flow rates. The inflection point between these two curves marks the initial development of 3-3 cavities. When ragged cavities form, the impeller is flooded and the power draw rises slightly, Nienow et al (1985c).

Warmoeskerken (1986) conducted experiments at a range of scales and D/T ratios and found that the gas flow number at which the transition from vortex/clinging to small 3-3 cavities occurs ($Fl_{G,3\text{-}3}$), is correlated by:

$$Fl_{G,3\text{-}3} = 0.028\ D^{0.2} \left(\frac{T}{D}\right)^{0.5}$$

or in dimensionless form:

$$Fl_{G,3\text{-}3} = 0.0038 \left(\frac{Re^2}{Fr}\right)^{0.067} \left(\frac{T}{D}\right)^{0.5} \qquad \text{...Eqn (1.5)}$$

where: Re = Impeller Reynolds number

Warmoeskerken did not study the effect of viscosity on this cavity transition and Reynolds number only appears in equation 1.5 to make it dimensionless. The transition from 3-3 cavities to ragged cavities (same as the loading / flooding transition) is correlated by equation 1.1.

Smith and Warmoeskerken (1985) presented equations 1.1, 1.2, 1.3 and 1.5 in the form of a flow map, see figure 1.6. Each region of the map corresponds to a particular flow regime as described in the figure. Thus for a given impeller Froude number and gas flow number this type of map can be used to determine the bulk gas-liquid flow pattern and the impeller gas cavity regime.

Prediction of power draw

A large number of empirical correlations can be found in the literature for predicting the gassed power draw of a single Rushton turbine (typical gassed power curve is shown in figure 1.5). For example:

Calderbank (1958) fitted a straight line to each of the concave and convex sections of the gassed power curve:

$$\left(\frac{P_g}{P_u}\right) = 1 - 12.6\ Fl_G \qquad \text{for } Fl_G < 0.035 \qquad \text{...Eqn (1.6)}$$

$$\left(\frac{P_g}{P_u}\right) = 0.62 - 1.85\ Fl_G \qquad \text{for } Fl_G > 0.035 \qquad \text{...Eqn (1.7)}$$

where: P_u = Ungassed power draw of the impeller
P_g = Gassed power draw of the impeller

Michel and Miller (1962) fitted one curve to their data:

$$P_g = C\left(\frac{Po^2\ N\ D^3}{Q_G^{0.56}}\right)^{0.45} \qquad \text{...Eqn (1.8)}$$

where: C = Correlation constant

Kurdna (1965) also fitted one curve to his data:

$$\frac{1}{1 - \left(\frac{P_g}{P_u}\right)} = K + \frac{K'}{Fl_G}\left(\frac{P_g}{P_u}\right)^{0.5} \qquad \text{...Eqn (1.9)}$$

where K and K' are constants for a given geometry and impeller combination. (this correlation only applies for $0.015 < Fl_G < Fl_{GF}$)

Refer to Warmoeskerken (1986), Muskett (1987b), or Tatterson (1991) for a review of these and other single Rushton turbine power correlations. (The three correlations above are singled out from the literature because they have been applied to multiple impeller systems and will be discussed later).

Correlations of this type are basically curve fits to experimental data and are therefore geometry and scale specific. None of the above correlations take account of the changes in cavity regime on the impeller blades. The inability of this type of correlation to accurately predict gassed power draw at large scale is due to the complexity of the gas-liquid hydrodynamics at the impeller blades and the difficulty in defining Q_R, the amount of gas recirculation to the impeller. One correlation or curve fit cannot be expected to describe the gassed power draw of an impeller from $Q_G = 0$ to $Q_G = Q_{GF}$ because of the substantial flow regime changes involved, Tatterson (1991).

Muskett (1987b) concluded that the best approach to the correlation of gassed power data was taken by Warmoeskerken (1986) who separated his power data into the different impeller cavity regimes and then fitted straight lines to the data from each regime, see figure 1.7. However, Warmoeskerken's correlations predict that, for constant Froude number, P_g/P_u falls more rapidly as scale is increased, (when plotted against gas flow number). Muskett (1987b) measured power over a wide range of scales (T = 0.61, 1.83, and 2.67 m diameter) and observed the opposite trend, which agreed with the earlier results of Nienow et al (1977).

Smith (1989) modified Warmoeskerken's correlations by fitting curves to the data from each cavity regime. Smith developed his power correlations using Warmoeskerken's data and large scale data from Chapman (1981) (T up to 1.83 m) and Muskett (1987b) (T up to 2.73 m). The resulting curve fits are as follows:

For vortex and clinging cavities, $0 < Fl < Fl_{3\text{-}3}$

$$\frac{P_g}{P_u} = (1 - A\ Fl_m^2) \qquad \text{...Eqn (1.10)}$$

For 3-3 cavities, $Fl_{3\text{-}3} < Fl < Fl_F$

$$\frac{P_g}{P_u} = \left(\frac{B}{Fl_m^2} + P_{\text{lim}}\right) \qquad \text{...Eqn (1.11)}$$

where:

$$P_{\text{lim}} = \frac{0.24}{Fr^{0.3}} \qquad \text{...Eqn (1.12)}$$

P_{lim} = Value of P_g/P_u ratio just before impeller floods

$$A = \frac{(1 - P_{\text{lim}})^2}{4B}$$

$$B = \frac{(1 - P_{\text{lim}})\ Fl_{3\text{-}3}^2}{2}$$

$$Fl_m = Fl_G + 0.012\ Fr$$

Fl_m = Gas flow number corrected for surface aeration

These curve fits predict the correct trend for scale up at constant Froude number, see figure 1.8, where they are compared with data from Muskett (1987b).

In the use of any empirical correlation it is hazardous to extrapolate beyond the range of experimental conditions covered in developing that correlation. Many literature correlations were developed from small scale data and so cannot be confidently applied to large scale vessels. The advantage of Smith's correlations is that they are based on a very wide range of scales. It should be remembered, however, that these correlations only apply to standard geometry vessels, figure 2.1, and standard geometry Rushton turbines, figure 2.3.

The use of Smith's correlations for predicting the gassed power draw of an impeller is obviously still an empirical approach, but at least some thought has gone into what is actually happening at the impeller.

1.2.1.2 Downward pumping pitched blade turbines

Flow patterns

Warmoeskerken et al (1984) defined the two flow regimes of direct gas loading and indirect gas loading for downward pumping impellers, see figure 1.9. With direct gas loading, the buoyancy of the gas bubbles overcomes the liquid down flow from the impeller and gas bubbles rise directly into the impeller blades. With indirect gas loading, the liquid down flow from the impeller overcomes the buoyancy of the gas bubbles rising from the sparger, and the bubbles are swept away from the impeller only to be recirculated into the impeller region by the liquid flow. In the direct loading regime Muskett (1987b) observed large pockets of gas escaping from the dispersion at irregular intervals showing the instability of the dispersion. It was concluded that this behaviour is analogous to the flooded condition of a disc turbine.

Figure 1.11 shows the discharge flow produced by a pitched blade turbine and an LE20 impeller, when pumping down in an ungassed standard geometry vessel. It can be seen that both impellers produce predominantly axial flow but with a significant radial flow component. This discharge flow tends to produce a small region of up flow below the impeller, see Figure 1.10, Frijlink et al (1984) and Warmoeskerken et al (1984). As a result the dimensions and the position of the gas sparger have a significant effect on the gas dispersion performance of these impellers, see Warmoeskerken et al (1984), Frijlink et al (1984), Nienow et al (1985b) and Bujalski (1987). With a centrally mounted point sparger, the up flow below the impeller draws the gas directly into the centre of the impeller and the impeller becomes directly loaded with gas even at very low gas flow

rates. With a large ring sparger the gas is introduced into the down flow from the impeller and direct or indirect loading can occur.

Nienow et al (1985b) and Bujalski (1987) studied the effect of sparger design on the gas dispersion performance of 45° pitched blade turbines of $T/3$ and $T/2$ diameter, in vessels up to 1.83 m diameter. Three sparger designs were tested: a point sparger, a small ring sparger ($D_S = 0.54D$), and a large ring sparger ($D_S = 0.82D$). Refer also to Bujalski et al (1988) and Bujalski et al (1990). These workers concluded that the flow patterns observed with downward pumping pitched blade turbines can be unstable due to the counter current flow of gas and liquid in the impeller region. The largest instabilities were found to occur with small diameter impellers ($D < T/3$) of low blade number (i.e. 4) and a centrally mounted point sparger. For downward pumping impellers the best geometry studied, in terms of achieving complete gas dispersion at the lowest power draw with the lowest torque fluctuations, was a large diameter ($D = T/2$), six blade impeller with a large ring sparger ($D_S = 0.82D$) at a sparger clearance of $T/6$.

Figure 1.12, from Bujalski (1987), shows the flow patterns observed with downward pumping pitched blade turbines with a large ring sparger ($D_S = 0.82D$) positioned directly below the centre of the impeller. At low impeller speeds the gas bubbles rise straight through the impeller blades with little or no dispersion, figure 1.12(a). Gas flow dominates the hydrodynamics and only a weak liquid circulation is observed. At higher impeller speeds there is some dispersion of gas in the upper part of the vessel but large quantities of gas still rise rapidly up the shaft, figure 1.12(b). At higher impeller speeds large bubbles still rise up the shaft, though less frequently, and gas periodically surges down very close to the vessel base, figure 1.12(c). At higher speeds this periodicity disappears and gas is dispersed throughout the vessel, figure 1.12(d).

Chapman (1981) found that for small diameter impellers ($D = T/4$) over a narrow range of impeller speeds the flow pattern was unstable and oscillated, without external stimulus, between that shown in figure 1.12(c) and that shown in figure 1.12(d). With large impellers ($D = T/2$) no sudden transition in bulk flow pattern was observed, and the transition from figure 1.12(c) to figure 1.12(d) was gradual.

Chapman (1981) defined two impeller speeds:

N_c Minimum impeller speed that just overcomes the up flow of gas from the sparger and prevents direct gas flow into the impeller, i.e. the indirect / direct loading transition.

N_{CD} Minimum impeller speed at which gas is well dispersed and the flow pattern is stable.

Chapman (1981) and Nienow et al (1983) found that large diameter impellers ($D = T/2$) achieved complete gas dispersion at a lower impeller speed and power draw than a small diameter impeller ($D = T/4$), but flow pattern instabilities occurred over a wider range of impeller speeds, i.e. (N_{CD} - N_c) was larger. A 6 blade impeller was also found to

achieve complete gas dispersion at a lower impeller speed and power draw than a four blade impeller, and the range of unstable operating conditions was narrower. Thus large diameter impellers with six blades were recommended. Generally a downward pumping impeller with a large projected blade area will be less susceptible to a decrease in pumping capacity when gas cavities form on the blades, Bakker (1992), which explains why they are also less susceptible to direct gas loading.

Chapman (1981) developed a theoretical correlation for prediction of N_c, based on a momentum balance between the downward liquid flow from the impeller and the upward gas and entrained liquid flow from the sparger:

$$N_c = 11.7 \frac{Q_G^{0.5}}{D^{1.63}} \qquad \text{...Eqn (1.13)}$$

This correlation agreed well with Chapman's own experimental data.

Warmoeskerken et al (1984) developed an empirical relationship between N_c, gas flow rate and the blade angle to the horizontal (θ) (blade angles of 30, 45 and 60° were tested). For $D = 0.4T$ and $T = 0.44$ m:

$$N_c = 125 \frac{Q_G^{0.5}}{\sin \theta}$$

For these tests a ring sparger of diameter $0.43D$ was mounted at a clearance of $0.23D$ below the impeller. The effect of impeller diameter was not studied but the exponent on gas flow rate is the same as in Chapman's correlation, equation 1.13.

For a large diameter ($D = T/2$), six blade impeller with a large ring sparger ($D_S = 0.82D$) at a sparger clearance of $T/6$, Bujalski et al (1988) found that complete dispersion of gas was correlated, for vessels up to 1.83 m diameter, by:

$$Fl_{CD} = 0.08\, Fr^{0.75}$$

This can be rearranged to:

$$N_{CD} = 5.45 \frac{Q_G^{0.4}}{D^{1.5}} \qquad \text{...Eqn (1.14)}$$

Muskett (1987a) studied four blade, 45° pitch blade turbines with $D = T/2$, in vessels of 0.61 m and 2.73 m diameter. With a sparger diameter of $0.6D$ and a sparger clearance of $0.2D$. Muskett found that the transition from indirect to direct loading could be described by:

$$N_c = 8.8 \frac{Q_G^{0.53}}{D^{2.1}} \qquad \text{...Eqn (1.15)}$$

The exponents on Q_G and D, in equations 1.14 and 1.15 are again similar to those developed theoretically by Chapman et al, equation 1.13. However, each correlation is valid only for the specific geometry studied and range of variables tested.

Muskett (1987) showed that at large scale (for T = 2.73 m) downward pumping four blade 45° pitched blade turbines became directly loaded with gas at flow numbers of approximately 0.03. For most industrial applications the flow number would be in excess of this value and therefore the impeller would be directly loaded.

Power draw

Nienow et al (1983) and Warmoeskerken et al (1984) observed the gas cavities that form on the blades of downward pumping pitched blade turbines. The different cavity structures are shown in Figure 1.13. At low gas flow rates the trailing vortex from each blade becomes filled with small bubbles forming a vortex cavity. Increased gas flow results in the formation of a clinging cavity which is attached to the impeller blade. The formation of large cavities occurs simultaneously on all blades, Nienow et al (1983), resulting in the transition from indirect to direct gas loading, Warmoeskerken et al (1984), and a sharp drop in the power draw of the impeller. Comparing the gassed power data for downward pumping pitched blade turbines in figure 1.14, from Nienow et al (1983), it can be seen that the power falls much more sharply for a small diameter (D = T/3) impeller than it does for a large diameter impeller (D = T/2), and that for a given impeller diameter, fewer blades result in a sharper power fall.

Operation close to this steep fall in power can result in large torque fluctuations (±50% of the average value), Chapman (1981). The torque instabilities reported by Chapman (1981) were not detected by Warmoeskerken et al (1984), but Chapman did comment that large diameter six blade impellers are less susceptible to these fluctuations, (Warmoeskerken et al studied a six blade impeller with D = 0.4T).

After the steep fall in power, the gassed power slowly increases with increasing gas flow rate, see figure 1.14. This is caused by the increased liquid flow which is swept into the impeller region by the bubbles and which opposes the flow generated by the impeller, Warmoeskerken et al (1984). This generates a dynamic pressure against which the impeller is pumping, increasing the power consumption.

Incomplete gas dispersion and fluctuating power draw are both undesirable operating conditions. It is therefore important that downward pumping pitched blade turbines are operated at sufficiently high impeller speed to avoid the instabilities associated with the direct/indirect loading transition, Chapman (1981).

Prediction of gassed power draw

No correlations exist for predicting the gassed power draw of a downward pumping pitched blade turbine. Chapman (1981) recommended that $N > N_c$ to avoid the instabilities associated with the direct / indirect loading transition. Under these operating conditions the gassed power draw is similar to the ungassed power draw, see figure 1.14, i.e.:

$$P_g/P_u \approx 0.8 \text{ to } 1.0$$

1.2.1.3 Upward pumping pitched blade turbines

Flow patterns

The flow patterns produced by an upward pumping pitched blade turbine are shown in figure 1.15, from Bujalski (1987). At low impeller speeds, the gas bubbles pass straight between the impeller blades with little or no dispersion, figure 1.15(a). At higher speeds, the radial component of the impeller discharge carries gas bubbles to the vessel wall but the region below the impeller is virtually devoid of bubbles, figure 1.15(b). Higher speeds result in gas bubbles being swept into the region below the impeller (complete dispersion), figure 1.15(c). At even higher speeds, the bubble velocities in the recirculation loops increase, and the loops themselves oscillate vigorously up and down the lower regions of the vessel, figure 1.15(d). Thus upward pumping impellers disperse gas extremely well, achieving complete dispersion at very low speeds and powers without instabilities. As with downward pumping impellers, the flow pattern transitions were less pronounced with larger diameter impellers, i.e. $T/2$ compared to $T/3$, Chapman (1981).

Although upward pumping impellers are directly loaded with gas at all times, this does not lead to poor gas dispersion as is the case with downward pumping impellers. However, Bujalski (1987) found that sparger design does have a significant effect on gas dispersion with upward pumping impellers because the sparger design affects the exact position where the gas enters the impeller blades. Bujalski concluded that the best geometry, in terms of achieving complete gas dispersion at lowest power draw and minimising flow and torque instabilities, was the same as for downward pumping pitched blade turbines. That is, a large diameter ($D = T/2$) six blade impeller with a large ring sparger ($D_S = 0.82D$,) mounted $T/6$ below the impeller. For this geometry the minimum impeller gas flow number for complete gas dispersion was correlated by:

$$Fl_{CD} = 12\times10^{4}\, Fr^{5}\, T^{2.8} \qquad \text{...Eqn (1.16)}$$

i.e. $N_{CD} \propto Q_G^{0.1}$

Thus large increases in gas flow rate result in only a very small increase in the impeller

speed required to achieve complete dispersion. The independence of the mixing characteristics is attributable to the co-current flow of gas and liquid through the impeller, Chapman et al (1983). Nienow et al (1983) concluded that an upward pumping pitched blade turbine achieved complete gas dispersion at a lower power draw than a downward pumping pitched blade turbine, at all gas flow rates, or a Rushton turbine, but only at high gas flow rates.

For upward pumping pitched blade turbines, flooding is difficult to define. The rapid transition from indirect to direct loading, found with downward pumping impellers, is not observed and flow instabilities can have periods of minutes, Nienow et al (1985b).

Muskett (1987b), defined flooding for upward pumping pitched blade turbines as the condition where no bulk flow instabilities occurred, and showed that:

$$N_F \propto Q_G^{0.25}$$

Bujalski (1987) developed the following flooding correlation:

$$Fl_F = 6000\, Fr^{2.7}\, T^{1.55}$$

i.e. $N_F \propto Q_G^{0.16}$

and Machon et al (1992) found that:

$$N_F \propto Q_G^{0.20}$$

The exponents on Q_G are all similar, but the above correlations are strictly valid only for the specific geometries stated. However, in all of these studies the power input at flooding was always well below normal industrial operating limits. For example, Muskett (1987) found that, even at a very high gas flow rate of 2.8 vessel volumes per minute, the flooding conditions of the impeller corresponded to only 0.25 W/kg. Thus for the majority of industrial operations, upward pumping pitched blade turbines are unlikely to be flooded.

Power draw

Nienow et al (1983) concluded that the same cavity types are found on upward pumping pitched blade turbines as are found on downward pumping pitched blade turbines. However, upward pumping impellers do not undergo such dramatic changes in flow regime as downward pumping impellers. As a result, the gassed power consumption is relatively independent of gas flow rate, compared to a downward pumping pitched blade turbine or a Rushton turbine, see figure 1.14. As with downward pumping pitched blade turbines, small diameter impellers ($D = T/3$) give a sharper fall in power than large diameter impellers ($D = T/2$).

Despite the flow oscillations observed in figure 1.15(d), significant fluctuations in torque were not detected by Chapman (1981). Torque instabilities are small compared to downward pumping impellers and maximum torque instabilities, found with small diameter impellers ($D = T/3$), were only ±20% of the average value, Chapman (1981).

Prediction of gassed power draw

No correlations exist for predicting the gassed power draw of a upward pumping pitched blade turbine.

Bujalski (1987) found that P_g/P_u could fall as low as 0.5 for upward pumping pitched blade turbines at very high gas flow rates (3.5 vvm). However, under normal operating conditions ($N_F < N < 2xN_{CD}$), $P_g/P_u \approx 0.8$ to 0.9 for a six blade impeller, Bujalski et al (1990).

1.2.1.4 LE20 impellers

No literature information is available on the flow patterns or gassed power draw of the LE20 impeller. However, in many respects all downward pumping impellers exhibit similar hydrodynamic behaviour to downward pumping pitched blade turbines, Nienow (1987). As shown in figure 1.11, the flow produced by an LE20 impeller is similar to that produced by a pitched blade turbine.

Blade width and blade angle have an effect on P_g/P_u for downward pumping pitched blade turbines. As blade angle and width are reduced the indirect / direct loading transition occurs at lower gas flow rates and P_g/P_u falls off more sharply, Warmoeskerken et al (1984). For the impellers studied in this thesis, see chapter 2, the total projected area of the LE20 blades was similar to that of the pitched blade turbines. However, the LE20 had fewer blades and the blade angle to the horizontal was shallower.

1.2.2 Multiple impellers

This section reviews the literature on gas liquid flow patterns and power draw of multiple impeller combinations.

Several workers have studied combinations of impellers and simply commented on the quality of gas dispersion observed visually. This work is reviewed first, followed by separate reviews of more detailed studies with:

a) multiple Rushton turbines
and b) combination of mixed impeller designs

1.2.2.1 Comparison of impeller combinations

Kuboi and Nienow (1982) studied eight dual impeller combinations in a standard geometry vessel ($H = T$) of 0.45 m diameter:

1. 2 × RT
2. 2 × 4PBT (bottom pumping up + top pumping down)
3. 2 × 4PBT (bottom pumping down + top pumping up)
4. 2 × 4PBT (both pumping up)
5. 2 × 4PBT (both pumping down)
6. RT (bottom) + 4PBT (top, pumping up)
7. RT (bottom) + 4PBT (top, pumping down)
8. 4PBT (bottom, pumping down) + RT (top)

All impellers had a diameter of $T/3$, and the impeller separation was equal to D. The impeller combinations were compared on the basis of a visual assessment of the quality of gas dispersion. Combinations 3, 8 and especially 5 suffered from the flow instabilities encountered with all downward pumping impellers at impeller speeds just sufficient to overcome the upward movement of gas, see section 1.2.1.2. Upward pumping impellers do not suffer from this problem but their ability to disperse gas is somewhat restricted at low speeds and when placed in the upper position they were seen to gather in gas and discharge it immediately through the dispersion surface. Thus combination 3 gave poor gas dispersion at low speeds and combination 4, though very stable, was unable to produce more than a minimum of gas dispersion until very high speeds were reached. Combination 7 was quite good but it did show slight instabilities. Combination 1 produced the best gas dispersion, closely followed by combination 2. However, combination 2 produced complete dispersion of gas at a much lower power level than combination 1. Combination 6 was also recommended but found to produce unstable flow patterns. Figure 1.16 shows the flow patterns observed with the recommended impeller combinations (1, 2 and 6).

Machon et al (1985) studied combinations 1, 6 and 7, (using six blade PBTs) in a 0.29 m diameter vessel with $H = 2T$, $D = T/3$ and $S = 3D$. Based on visual observations of the quality of gas dispersion it was concluded that the dual disc turbine combination produced a good dispersion, as did the disc turbine below an upward pumping PBT. As Kuboi and Nienow found, the combination of a disc turbine below a downward pumping PBT was unsuitable for gas dispersion. This was due to the relatively narrow range of operating conditions over which a good dispersion was observed.

Chiampo & Conti (1992) studied the same impeller combinations as Machon et al (1985), (using mixed flow turbines (MFT), i.e. Rushton turbines with the blades at 45° to the disc, rather than pitched blade turbines). A 0.39 m diameter vessel was used with $H = 2T$, $D = T/3$ and $S = 3D$. It was concluded that the RT + 6MFT (pumping up) combination was better for gas dispersion than the dual Rushton turbine combination or the RT + 6MFT (pumping down) combination.

1.2.2.2 Multiple Rushton turbines

Multiple Rushton turbines represent a 'standard' multiple impeller combination for many researchers. It is also a combination which is commonly found in industry.

Ungassed flow patterns and power draw

Hudcova et al (1987) and Chiampo et al (1991) studied the effect of impeller separation on the ungassed flow patterns and power draw of identical dual Rushton turbines. Both sets of workers used fully baffled, flat bottomed vessels with impellers of $T/3$ diameter and an impeller clearance of $T/3$. Vessel diameters were 0.29 m, 0.56 m (both Hudcova) and 0.39 m (Chiampo). The impeller separation was varied from $0.2D$ to $4D$. The flow patterns are shown in figure 1.17, and the power draw is shown in figure 1.18, which includes data from several other workers who studied dual Rushton turbines of $T/3$ diameter.

At an impeller separation of $0.2D$ the two impellers were touching, as shown in figure 1.17. The flow pattern at this separation was the same as that found with a single impeller. Blade height has a significant effect on the power drawn by a Rushton turbine, Palmer (1987). The Rushton turbines used in these tests had a blade height of $0.2D$ so for two touching impellers the effective blade height was $0.4D$. An increase in blade height from $0.2D$ to $0.4D$ has been shown to increase the power draw of flat blade turbines by 140%, Bates et al (1963). However, as shown in figure 1.18, the measured power draw of the two touching Rushton turbines was only 20 to 30 % greater than for a single impeller. This is probably the result of reduced impeller pumping capacity when two horizontal discs are present, as is the case with two touching Rushton turbines, see figure 1.19. The zone between the horizontal discs will effectively act as a solid body, or very thick disc, restricting the amount of liquid pumped by the blades. Palmer (1987) showed that as disc thickness increases the power draw of a Rushton turbine falls.

The power drawn by the dual Rushton turbines increased rapidly up to an impeller separation of $0.6D$. Up to this separation the flow pattern remained the same as for a single impeller and the increased power draw was the result of the increase in effective blade height.

For the separation range $0.6D < S < 1.3D$ one circulation loop was observed for each impeller, with the discharge flow from the lower impeller leaving at 45° up from the horizontal and that from the upper impeller leaving at 45° down from the horizontal. The liquid between the impellers rotated as a solid body. Kuboi & Nienow (1985) also observed this flow pattern at an impeller separation equal to D, see figure 1.16 (combination 1 figure (b)). In this range of impeller separation there was only a modest increase in power draw because there was no significant change in the bulk flow pattern and increased separation only resulted in an increase in the amount of liquid in solid body rotation.

At impeller separations greater than $1.3D$ the zone between the impellers became turbulent and for separations greater than $1.6D$ the characteristic radial discharge and figure of eight flow pattern developed for each Rushton turbine, see figure 1.17, and the dual impellers achieved full power draw, i.e. $P_2 = 2 \times P_1$, (where P_2 is the total power draw of dual impellers, and P_1 is the power draw of a single impeller).

Cronin (1988) studied the effect of impeller separation on the power draw of dual Rushton turbines, of identical design, in a vessel of 0.72 m diameter. For $D = T/3$ full power draw was not achieved until the impeller separation reached $1.5D$, very similar to Hudcova and Chiampo's results above. However, for larger diameter impellers ($D = T/2$) maximum power draw was not achieved until a larger impeller separation of $2D$ was used. In similar tests Smith et al (1987), studying triple Rushton turbines in a vessel of 0.64 m diameter with $D = 0.4T$, found that full power draw was not achieved until an impeller separation of $1.75D$. Cronin plotted his data with that of Smith et al (1987), Hudcova et al (1987) and the one data point of Kuboi and Nienow (1982) showing that as impeller diameter increased, a larger impeller separation was required for full power draw to be achieved, see figure 1.20. Cronin concluded that large diameter impellers require more volume for the flow patterns to mature and therefore for full power draw to be achieved.

Gbewonyo et al (1988) studied dual Rushton turbines ($D = 0.38T$) in a 0.8 m diameter vessel, and found that full power was drawn at an impeller separation of $1.67D$. Impeller separation was not varied but this single data point also agrees with Cronin's conclusion above.

Bader (1987) studied combinations of up to 4 Rushton turbines, each with 8 blades, in a 0.60 m diameter vessel with $D = 0.40T$. Bader concluded that equally spaced turbines drew equal amounts of power. This was not quite true as Bader's data, figure 1.21, shows:

For a single impeller:	Po = 4.9
For 2 impellers:	Po = 8.9
For 3 impellers:	Po = 12.7
For 4 impellers:	Po = 16.5

The multiple impeller combinations drew 84 to 91% of the maximum potential power draw (based on multiples of the single impeller power number). This translates into P_2/P_1 values, for comparison with Cronin's results in figure 1.20, of 1.68 to 1.82. The power reduction measured by Bader at an impeller separation of D agrees well with the observations of Cronin, Smith and Hudcova.

Chiampo (1991) found that the impeller separation required to achieve full power draw was also a function of the impeller speed. As impeller speed was increased for dual Rushton turbines ($D = T/3$) the minimum impeller separation required for full power draw fell from $1.9D$ to $1.6D$. Chiampo's results suggest that although radial flow impellers produce more intense local recirculation loops at higher impeller speeds, the

interaction between the impellers is actually reduced.

Thus the impeller separation required to achieve full power draw is a function of impeller speed and diameter and potentially there could be a scale effect. For design purposes it would be safer to assume that full power draw will only be achieved at impeller separations greater than $2D$.

Roustan (1985), Magelli et al (1987), Abrardi et al (1988) and Nocentini et al (1988) did not study the effect of impeller separation on power draw but they all found that full power draw was achieved for multiple Rushton turbines with $S > 2D$. Thus for $S > 2D$, where the flow interactions between the impellers are minimised, the total ungassed power draw for a multiple Rushton turbine combination is simply the sum of the powers that the individual impellers would draw if mounted alone in a standard geometry vessel, i.e., from equation 1.4:

$$\text{Total power draw} = A\ \rho_L\ N^3\ (Po_1 D_1^5 + Po_2 D_2^5 \ldots + Po_n D_n^5)$$

...Eqn (1.17)

where $A = 1.0$

This equation only holds for impeller clearances (c_l) $\geq T/4$ for flat based vessels (optimum clearance recommended by Nienow et al (1977)) and $\geq T/3$ for standard dished based vessels, see figure 2.1. Cronin (1988) found that for smaller clearances the lower circulation loop of a Rushton turbine did not have enough room to fully form, resulting in reduced impeller pumping capacity and power draw.

Flooding of the lowest impeller

In vessels fitted with multiple disc turbines, of identical design, Kuboi and Nienow (1982), Roustan (1985), Smith et al (1987), Abrardi et al (1988) and Nocentini et al (1988a) observed that with the lowest impeller flooded the upper impellers could still maintain a good gas dispersion, as shown in figure 1.22. The small amount of gas dispersion produced by the lowest impeller, even when flooded, is enough to make the dispersion duty of the upper impellers much easier. Roustan (1985) and Smith et al (1987) found that, for a fixed impeller speed, the gas flow rate required to flood the upper impeller, in a dual identical turbine combination, was approximately twice that needed to flood the lowest impeller.

With the flow pattern shown in figure 1.22, visual observation of the dispersion surface (the only visual observation possible in most industrial vessels) would suggest an acceptable gas dispersion with a uniform distribution of gas across the whole cross sectional area of the surface. This is obviously not the case in the lower half of the vessel and shows that visual observation of the dispersion surface cannot always be used as a reliable indicator of agitator performance when multiple impellers are fitted to the

shaft.

The separation distance between impellers can significantly affect the flooding and complete dispersion conditions of the lowest impeller. Hudcova et al (1987) found that if the separation between identical Rushton turbines was large enough so that flow interactions between the impellers were minimised, i.e. $S > 2D$, the lowest impeller flooded at the same operating conditions as it did when mounted alone in a standard geometry vessel. Machon et al (1991) reached the same conclusion for an impeller separation of $3D$. Flooding of the lowest impeller could therefore be predicted from equation 1.1, for a standard Rushton turbine. For a smaller separation, i.e. $0.5 < S/D < 1.5$, the impeller flow patterns combined to produce upward flow through the lower disc turbine, refer to figure 1.17(b), and the lowest Rushton turbine flooded at lower gas flow rates.

Abrardi et al (1988) studied a 0.39 m diameter vessel fitted with dual Rushton turbines of identical design, with $H = 5T/3$, $D = T/3$ and $S = 2D$. The flooding and complete dispersion transitions for the lowest impeller were found to occur at different operating conditions to when it was mounted alone in the vessel with $H = T$. The presence of the upper impeller had a stabilising effect on the flooded condition, i.e. less gas could be dispersed for a given impeller speed. This is the same trend as observed by Hudcova et al (1987) but at a larger impeller separation. Abrardi et al observed that flooding and loading often coexist on the lowest impeller in a dual turbine system, making determination of the flooding loading transition uncertain. This was also observed by Machon et al (1991) for a single Rushton turbine, refer to section 1.2.1.1.

Gassed power draw

Hudcova et al (1987) studied single and dual Rushton turbines ($D = 0.33T$) in a vessel of 0.56 m diameter ($H = 1$ or $2T$). They found that the total gassed power draw of dual Rushton turbines varied significantly with impeller separation in the range $0.2D < S < 3D$. No clear trends were evident in Hudcova's data. Chiampo et al (1991) studied the effect of impeller separation on the gassed power draw of dual Rushton turbines, for conditions of complete gas dispersion only. Gassed power draw was found to increase with increasing impeller separation in a similar way to the ungassed power. Full gassed power draw was achieved at an impeller separation of $2D$. At lower impeller separations the presence of gas between the impellers prevented solid body rotation and as a result the power did not fall of as much as it did ungassed.

Roustan (1985), Abrardi et al (1988) and Warmoeskerken and Smith (1988) concluded that the lowest impeller in a combination of multiple, identical Rushton turbines had a similar gassed power to a single impeller mounted in a standard geometry vessel. However, this was only true for impeller separations greater than $1.5D$.

Numerous workers have observed that, even with impellers of identical design, the impellers in a multiple combination do not always all draw the same amount of power

when gassed, Hicks & Gates (1976), Nienow & Lilly (1979), Kuboi & Nienow (1982), Machon et al (1985c), Hudcova et al (1987), Bader (1987a), Magelli et al (1987), Abrardi et al (1988), Cronin (1988), Nocentini et al (1988a), Chiampo & Conti (1991), Lu and Yao (1991). All of these workers studied geometries in which the sparge gas was introduced below the lowest impeller, through a point or small ring sparger. As long as the lowest impeller is not flooded the sparge gas is dispersed as small bubbles throughout the cross section of the vessel. The upper impellers therefore operate in the dispersion already created by the lowest impeller and cavity development on the upper impellers is controlled by gas recirculation into the impeller blades, Smith et al (1987).

At high impeller speeds and gas recirculation rates the gas flow rate into the upper impellers will be the same as into the lowest impeller, so the gas cavities will be the same on all impellers. Warmoeskerken and Smith (1988) found that this occurred at conditions close to those predicted by equation 1.3. Thus for $N > N_R$ the upper impellers should draw the same power as the lowest impeller (assuming they are all of identical design), i.e.:

$$\left(\frac{P_g}{P_u}\right)_{multiple\ Rushtons} = \left(\frac{P_g}{P_u}\right)_{single\ Rushton}$$

However, this is unlikely to occur at large scale, Nienow (1987), and for most industrial vessels the impeller speed will be above that required to avoid flooding of the lowest impeller but below that required for high gas recirculation rates, i.e. $N_F < N < N_R$. Under these conditions the gas flow rate entering the upper impellers due to recirculation will only be a fraction of the sparger gas flow rate. The fraction of gas entering the upper impellers will depend on the exact geometry of the impellers and vessel and the operating conditions of impeller speed and gas flow rate. Various workers have estimated this fraction for their particular vessel geometries and test conditions:

Smith et al (1986):	40% for triple Rushton turbines with T = 0.64 m and $D = 0.4T$.
Hudcova et al (1987):	20% at low speed and 30% at higher speed for dual Rushton turbines with T = 0.56 m and $D = T/3$.
Lu and Yao (1991):	30 to 40% at low speed and 50% at higher speed for triple Rushton turbines with T = 0.64 m and $D = T/3$.

Based on these results it can be seen that 50 to 80% of the sparge gas bypasses the upper impellers completely. As a result the gas cavities found on the upper impellers will be smaller than those on the lowest impeller and the upper impellers will therefore draw more power than the lowest impeller, i.e.:

$$\left(\frac{P_g}{P_u}\right)_{multiple\ Rushtons} > \left(\frac{P_g}{P_u}\right)_{single\ Rushton}$$

Smith et al (1987) and Warmoeskerken and Smith (1988) studied a combination of three identical Rushton turbines (T = 0.64 m, $H = 3T$, $D = 0.4T$, $S = 2.5D$). A flexible vane sensor, positioned in the outlet stream of each impeller, was used to determine the gas cavity structure present on the blades of the impeller. It was found that, for a fixed impeller speed, 3-3 cavities developed on the upper impellers at higher sparger gas flow rates than they did on the lowest impeller. The 3-3 cavity transition, which occurred at the same conditions for the top and middle impellers, was correlated by:

$$Fl \times Fr = C \qquad \text{...Eqn (1.18)}$$

where C is a constant for a particular scale and geometry.

Warmoeskerken and Smith (1988) modified the cavity regime flow map, developed by Warmoeskerken and Smith (1985) for single Rushton turbines, so that it could be extended to multiple Rushton turbine combinations, see figure 1.23. The value of the constant C, in equation 1.18, can be determined from the intersection of the gross recirculation and 3-3 cavity development lines (equations 1.3 and 1.5).

Abrardi et al (1988 and 1990), Magelli et al (1987) and Nocentini et al (1988) found, for multiple small diameter (D = $T/3$ and $T/5$) Rushton turbines, that P_g/P_u was independent of impeller speed, for $N > N_F$, and only a function of gas flow rate. Roustan (1985) also found that, for a given gas flow rate and $N > N_F$, P_g/P_u was independent of impeller speed, but this was only true for the smaller impeller diameters studied, i.e. $D/T < 0.37$. Roustan concluded that larger diameter impellers produced more gas recirculation and power draw was therefore more sensitive to impeller speed (P_g/P_u fell with increasing impeller speed).

Nocentini et al (1988) also found that for a single impeller, Po_g only had a very slight dependence on impeller speed when gas was sparged uniformly across the cross section of the vessel base. In this arrangement the single impeller behaved in the same way as the upper impellers in a multiple turbine configuration, i.e. only small vortex clinging cavities were formed on the impeller blades. The same effect is observed when a large ring sparger is used with a single impeller, Nienow and Allsford (1985), Nienow et al (1986) and Nienow et al (1988).

1.2.2.3 Mixed impeller combinations

As stated earlier, multiple Rushton turbines represent the 'standard' multiple impeller combination for many researchers. However, there is a great deal of interest in studying combinations of axial flow impellers, mainly from the requirement of some processes to have good top to bottom mixing in tall vessels.

Ungassed power draw

Kuboi and Nienow (1982) measured the ungassed power draw of two mixed impeller combinations in a standard geometry vessel ($H = T$) of 0.45 m diameter:

1. 2 × 4PBT (bottom pumping up + top pumping down)
2. RT (bottom) + 4PBT (top, pumping up)

All impellers had diameters of $T/3$ and in all cases the impeller separation was equal to D. For combination 2, A (the constant in equation 1.17) was equal to 0.90. The power numbers of both impellers were found to be low compared to measurements in a standard geometry vessel. For the dual pitched blade turbine combination (combination 1), A was equal to 1.12. The power numbers of both impellers were higher, than when each was mounted alone in a standard geometry vessel, because when combined the impellers pumped against each other and the resistance to flow was increased.

Machon et al (1985) studied two mixed impeller combinations:

1. RT + 4PBT (pumping up)
2. RT + 4PBT (pumping down)

The impeller separation was $3D$ and in each case $A = 1.0$. Thus at large impeller separations equation 1.17 holds for combinations of different impeller designs.

Chiampo et al (1991) is the only worker who has studied a wide range of impeller separations for combinations of different impeller designs. Three mixed impeller combinations were tested in a flat bottomed vessel of 0.39 m diameter:

1. RT + 6MFT (pumping up)
2. RT + 6MFT (pumping down)
3. 6MFT (pumping up) + 6MFT (pumping down)

All impellers had diameters of $T/3$. The impeller clearance from the vessel base was also $T/3$. The impeller separation was varied from $0.2D$ to $4D$. For combination 1, full power draw was achieved at an impeller separation of $1.5D$ (similar to dual Rushton turbines of $T/3$ diameter, see section 1.2.2.2). For combination 2, full power draw was not achieved until a much larger impeller separation of $2.8D$ was used. For impeller separations less than $1.6D$ there was a large degree of flow interaction. For $1.6D < S < 2.8D$ there was a progressive disengagement of the flow patterns and it was not until $S > 2.8D$ that the flow patterns became completely independently. Combination 3 was found to give similar results to combination 2. As with dual Rushton turbines the minimum impeller separation required for full power draw was found to be sensitive to impeller speed for all combinations.

Flooding of the lowest impeller

Machon et al (1985) studied the effect of upper impeller design on the conditions at which the lowest impeller (always a Rushton turbine) flooded. However, flooding was determined from the minimum in the P_g/P_u versus Fl_G curve at constant gas flow rate, rather than visual observations. Kuboi and Nienow (1982) showed that this minimum in the power curve is actually associated with the onset of complete gas dispersion, NOT flooding. The mixed impeller combinations studied, by Machon et al, in a 0.29 m diameter vessel with $H = 2T$, were:

1. RT + 4PBT (pumping down)
2. RT + 4PBT (pumping up)

The diameter of all impellers was $T/3$ and the impeller separation was $3D$. For combination 1 the minimum in the P_g/P_u versus Fl curve at constant gas flow rate could not be determined. The results for combination 2 showed that there were significant differences in the complete dispersion conditions compared to a dual Rushton turbine combination, suggesting that even at the large separation studied there was significant interaction between the impellers. However, the author's admitted that considerable inaccuracies were involved in the estimation of the minimum in the power curves. Machon et al (1991b) studied the same impeller combinations in the same vessel and used a conductivity probe technique to determine the flooding / loading transition. They concluded that the flooding to loading transition for the lowest impeller (always the Rushton turbine) was unaffected by the design of the upper impeller at an impeller separation of $3D$.

As with multiple Rushton turbines, Machon et al (1991b) observed hysteresis around the flooding point of the lowest impeller for all combinations studied. Within the hysteresis limits the flow pattern was unstable with flooding, loading or a mixture of both flow regimes existing at the same time.

Gassed power draw

Kuboi and Nienow (1982) measured the power draw of each impeller in two mixed impeller combinations ($T = 0.45$ m, $H = T$, $D = T/3$, $S = D$):

1. $2 \times$ 4PBT (bottom pumping up + top pumping down)
2. RT (bottom) + 4PBT (top, pumping up)

As the recirculation loop formed for the downward pumping PBT in combination 1 the power fell very rapidly. For combination 2, changes in flow patterns resulted in small changes in the total power draw, but the power draw of the individual impellers was found to vary significantly, e.g. as the power of one impeller fell by 40% the power of the other impeller rose by 20%, so there were large local torque changes.

Abrardi et al (1990) measured the total gassed power draw of two mixed impeller combinations:

1. RT + 4PBT (down)
2. RT + 4PBT (up)

As found with multiple Rushton turbines, for $N > N_F$, Po_g was found to be independent of impeller speed for a given gas flow rate, and for each combination:

$$Po_g \propto Q_G^{0.33}$$

Chiampo et al (1991) studied the effect of impeller separation on the gassed power draw of two mixed impeller combinations:

1. RT + 6MFT (pumping up)
2. RT + 6MFT (pumping down)

Only conditions of complete gas dispersion were studied. Both combinations behaved in exactly the same way when gassed and full gassed power draw was achieved at an impeller separation of 2.5D for both combinations.

1.2.2.4 Prediction of gassed power draw

To account for the fact that upper impellers usually draw more power than the lowest impeller Hicks & Gates (1976) and Nienow & Lilly (1979) considered the lowest impeller as a single aerated impeller operating alone, and the upper impeller(s) as unaerated impeller(s) operating in a fluid of density equal to that of the gas-liquid mixture. Thus, for dual Rushton turbines, the following equation was developed:

$$\left(\frac{P_g}{P_u}\right)_{2\ impellers} = \frac{1}{2}\left(\left(\frac{P_g}{P_u}\right)_{1\ impeller} + (1 + \varepsilon_G)\right) \qquad \text{...Eqn (1.19)}$$

Kuboi and Nienow (1982) concluded that this equation gave a closer fit to dual Rushton turbine power measurements (T = 0.45 m, $H = T$, $D = T/3$, $S = D$) than the assumption that:

$$\left(\frac{P_g}{P_u}\right)_{2\ impellers} = \left(\frac{P_g}{P_u}\right)_{1\ impeller}$$

Kuboi and Nienow (1982) also compared equation 1.19 with power measurements from a combination of dual pitched blade turbines (lowest pumping up and upper pumping down). For $N_F < N < N_{CD}$ equation 1.19 predicted a constant value of P_g/P_u within 10% of that measured, but at high recirculation rates equation 1.19 predicted a rise in P_g/P_u while a fall was observed.

Hudcova et al (1987) showed that equation 1.19 worked well for dual Rushton turbines (T = 0.56 m, $H = 2T$, $D = T/3$, $S = 3D$) at low gas flow rates and was quite useful considering its simplicity. However, both Kuboi and Nienow, and Hudcova et al concluded that equation 1.19 is conceptually incorrect because it is known that the power draw of an aerated impeller is related to the gas cavity structure present on the blades, see section 1.2.1, and NOT to the apparent density of the gas liquid dispersion. In addition, Hudcova et al found that equation 1.19 overestimated the power draw of the upper impeller.

Machon et al (1985) measured the power draw of three impeller combinations in a 0.29 m diameter vessel ($H = 2T$, $D = T/3$, $S = 3D$):

1. 2 × RT
2. RT + 6PBT (pumping down)
3. RT + 6PBT (pumping up)

The empirical curve fit developed by Kurdna (1965) for single Rushton turbines, see section 1.2.1, was used to correlate the power data for each impeller combination. Machon concluded that the data from each dual impeller combination fitted Kurdna's correlation very well ($r > 0.978$ in all cases) with the following coefficients:

2 × RT	K=1.44	K'=0.066
RT + 6PBT (pumping down)	K=1.62	K'=0.055
RT + 6PBT (pumping up)	K=1.46	K'=0.042

Although, for a given impeller speed and gas flow rate, the absolute power draw of each combination was very different, Machon concluded that there was little difference in the P_g/P_u values of the different impeller combinations.

With dual Rushton turbines ($D = T/3$), Roustan (1985) found that data from two scales (T = 0.43 m and 0.78 m) produced the same curve when plotted as P_g/P_u versus $V_{sg}/(gT)^{0.5}$, see figure 1.24. This follows from Roustan's observation that P_g/P_u was independent of impeller speed and was only affected by gas flow rate. This conclusion only applied to impellers with $D < 0.37T$.

Bader (1986) studied 2, 3 and 4 Rushton turbines in a 100 gallon vessel (T = 0.60 m, $D = 0.4T$, $S = D$, H = 2, 3 and 4T respectively). For a given impeller speed and gas flow rate P_g/P_u did not change significantly as the number of impellers was increased. Bader used the following equation for estimating the power draw of the upper impellers:

$$P_g = P_u \left(\frac{1}{1 + \varepsilon_G} \right) \qquad \text{...Eqn (1.20)}$$

This is a density correction factor similar to that proposed by Hicks & Gates (1975) and Nienow and Lilly (1979), see equation 1.19. Bader found that this equation overestimated the actual power draw of the upper impellers (Hudcova et al (1987) made

the same comment about equation 1.19). Bader developed his own empirical curve fit for single Rushton turbine power data, taking into account the effects of impeller clearance from the vessel base, impeller submergence below the liquid surface, and surface aeration effects. This correlation was modified slightly for application to multiple impeller combinations, the basic assumption being that all impellers drew the same power, for a given impeller speed and gas flow rate, except for the top impeller which drew less power due to surface aeration effects.

Bader (1987a) compared experimental power measurements from a 1000 gallon vessel (T = 1.22 m, $D = 0.46T$, $S = D$) and a 30,000 gallon vessel (T = 3.63 m, $D = 0.34T$, $S = 1.5D$) with his own correlation (developed from measurements in a 100 gallon vessel), from Bader (1986). Both the 1000 and 30,000 gallon vessels were fitted with five Rushton turbines. The correlation predictions agreed well with the measurements from the 1000 gallon vessel, which was of a similar geometry to the 100 gallon vessel. For the 30,000 gallon vessel the correlation predictions were consistently low (this was attributed to different number of blades on each impeller and a smaller D/T ratio compared to the 100 gallon vessel). Bader concluded that his own correlation was not applicable to the 30,000 gallon vessel because of the significantly different geometry compared to the vessel from which his correlation was developed.

Bader (1987b) predicted the gassed power draw for a combination of four identical Rushton turbines, in a 150 m^3 vessel, using Calderbank's correlations for the lowest impeller, see section 1.2.1, Equation 1.20 was used for the upper impellers. Thus this approach was very similar to that proposed by Hicks and Gates (1976) and Nienow and Lilly (1979). The estimation of gas holdup at each impeller position included a correction factor for pressure differences in the vessel, i.e. due to gas expansion in this large scale reactor, the power draw of the impellers decreased from bottom to top. Bader concluded that this approach produced reasonable values of gassed power draw.

Nocentini et al (1988) measured the gassed power draw of a single Rushton turbine in a 0.23 m diameter vessel using two different sparger designs. A small ring sparger which introduced all of the sparge gas directly into the impeller region, and a spiral sparger which distributed gas uniformly across the vessel cross sectional area. The impeller was found to draw more power with the spiral sparger because less gas flowed into the impeller region and the size of the gas cavities was reduced (same effect as when a large ring sparger is used, Nienow and Allsford (1985), Nienow et al (1986) and Nienow et al (1988)). The power draw of multiple (2 and 4) Rushton turbines was then measured ($D = T/5$, $S = 5D$) in the same vessel, fitted with the small ring sparger. It was found that, for a given impeller speed and gas flow rate, P_g/P_u for the multiple Rushton turbine combinations could be estimated using:

$$\left(\frac{P_g}{P_u}\right)_{multiple\ impellers} = \frac{1}{n}\left(\frac{P_g}{P_u}\right)_{1,\ ring} + \frac{(n-1)}{n}\left(\frac{P_g}{P_u}\right)_{1,\ spiral}$$

where n = number of impellers

This approach illustrates the reason why the upper impellers draw more power than the lowest impeller, but for predictive purposes this equation cannot be used without experimental data with ring and spiral spargers.

Abrardi et al (1988) studied a 0.39 m diameter vessel fitted with dual Rushton turbines of identical design, with $H = 5T/3$, $D = T/3$ and $S = 2D$. Abrardi et al found that Calderbank's correlations for single Rushton turbines, see section 1.2.1, agreed with the experimental results from the dual Rushton turbine combination at low flow numbers only. At high flow numbers Calderbank's correlations underestimated P_g/P_u for the dual impellers. The use of equation 1.19 for the upper impellers again only agreed with Abrardi's measurements at low flow numbers. Abrardi concluded that both correlation methods are unsuitable for multiple impellers. Abrardi also concluded that the gassed power draw of multiple impellers is strongly influenced by the hydrodynamic regimes of the different impellers. Thus, it was concluded, generalised empirical correlation are of no use, a correlation is needed which is based on the different hydrodynamic regimes.

Seichter et al (1992) measured the gassed power draw of triple Rushton turbines at four scales: 0.15, 1.5, 15 and 150 m^3 ($H = 2.5T$, $D = 0.35$ to $0.43\ T$). The experimental data were compared with the correlations of Calderbank, Kurdna, and Michel and Miller, see section 1.2.1, and that of Roustan (1985). Michel and Miller's correlation was the only one which fitted the experimental data, which it did very well. Data for a range of large diameter ($D = 0.63T$) axial flow impeller combinations (exact details of impeller design were not given) incorporating five to seven impellers pumping up or down, were also found to fit this correlation with the same correlation exponents. As a result Seichter et al concluded that the effects on gassed power draw of the number, diameter, design and pumping direction of the impellers was negligible. However, Nienow (1977) pointed out that the Michel and Miller correlation is essentially a plot of N^3D^5 versus N^7D^{13}, which is capable of correlating anything.

1.3 GAS HOLDUP

The gas holdup in a reactor (ε_G) is defined as the volume of dispersed gas divided by the total volume of the dispersion, i.e.:

$$\varepsilon_G = V_G / (V_L + V_G) \qquad \text{...Eqn (1.21)}$$

where: V_G = Volume of gas in dispersion
V_L = Volume of liquid

Holdup is affected by:

- bubble generation at the impeller
- distribution and circulation of the bubbles
- growth and coalescence of the bubbles during circulation

The typical range of holdup observed in industrial vessels is 5 to 15%, Bader (1987a).

Holdup is an important parameter because, for a fixed volume reactor, the gas holdup determines the maximum liquid volume and therefore the maximum product formed. However, gas-liquid reactors are not designed to achieve a particular value of gas holdup, they are designed to achieve a particular mass transfer rate between the two phases and gas holdup is a consequence of that design.

Andrew (1982) concluded that holdup is proportional to mass transfer coefficient in low viscosity liquids over the range of power inputs encountered in industrial stirred tank fermenters. For rigid spheres of a given size:

$$a = \frac{6\varepsilon_G}{d_b}$$

(where the 6 comes from the volume of a sphere divided by its surface area). Andrew concluded that, for non coalescing low viscosity media at low gas holdup and 20°C:

$$\frac{k_L a}{\varepsilon_G} = 0.4\ s^{-1}$$

Thus although mass transfer is the desired process result, for comparative purposes, holdup is an adequate parameter. From the experimental stand point, holdup is much easier to measure than mass transfer rate and holdup is less sensitive to external parameters such as trace contamination.

1.3.1 Single impellers

The general form of the relationship between gas holdup and impeller speed, at constant gas flow rate, is shown in figure 1.25. This is a non linear relationship, with the points A to D corresponding to the different flow patterns of figure 1.1. The flow pattern development from figure 1.1(a) to figure 1.1(c) results in a steady increase in overall gas holdup. Further increases in impeller speed result in more gas recirculation into the impeller region, figure 1.1(d), which has a diminishing effect on the overall gas holdup.

Numerous researchers have measured gas holdup in standard geometry vessels fitted with a single impeller. Most research has been conducted at small scale and there is a large degree of uncertainty in literature holdup correlations, Davies (1986).

Two forms of correlation have been developed in the literature and these will be reviewed separately. Firstly, holdup can be correlated with independent system variables such as impeller speed, gas flow rate, D/T ratio, etc.. Secondly, holdup can be correlated with gassed power and superficial gas velocity.

Correlation of holdup with independent variables

For a given liquid, impeller type, scale and D/T ratio, holdup can be correlated by:

$$\varepsilon_G = \alpha\ (N)^{\beta}\ (Q_G)^{\gamma} \qquad \text{...Eqn (1.22)}$$

where:
N = impeller rotational speed
Q_G = Volumetric gas flow rate

from Muskett (1987b).

This equation is the dimensional form of dimensionless equations such as:

$$\varepsilon_G = \alpha'\ (Fl_G)^{\beta'}\ (Fr)^{\gamma'}\ (Re)^{\omega'}$$

where:
Fl_G = Gas flow number
Fr = Impeller froude number
Re = Impeller Reynolds number

Typical values of β and γ in equation 1.22 are:

$0.8 < \beta < 1.2$
$0.35 < \gamma < 0.6$

from Tatterson (1991).

Numerous correlations based on independent variables can be found in the literature, for

example refer to Van Dierendonck (1968), Hassan and Robinson (1977), Roustan (1978), Yung et al (1979) and Hughmark (1980). All of these correlations have been validated by experimental data but only from very small scale (T < 0.5 m). Mann (1983a) concluded that the correlation of Yung et al:

$$\varepsilon_G = 0.52\ Fl_G^{0.5}\ We^{0.65} \left(\frac{D}{T}\right)^{1.4}$$

had the most sound theoretical basis, presumably because it is the only one, of the above correlations, which contains the Weber number. Weber number relates inertial forces (which act to break up the gas bubble) to interfacial tension forces (which act to hold the gas bubble together) and is therefore related to average bubble size and hence overall gas holdup.

Warmoeskerken (1986) correlated holdup from geometrically similar vessels over a range of scales (T up to 1.2 m) using:

$$\varepsilon_G = 0.177\ (N)^{0.9}\ (Q_G)^{0.40}\ (D)^{0.10}$$

Muskett (1987) measured holdup in a 2.7 m diameter vessel and found that although some of the above literature correlations give similar predictions at small scale they all give very different predictions at large scale. The correlations of Hassan and Robinson, and Yung et al significantly overestimated Muskett's gas holdup data at the 2.7 m scale. As noted above, Yung et al used Weber number in their correlation, and Weber number increases with scale. Any correlation which includes Weber number will have strong scale effects which Muskett concluded are totally spurious. Warmoeskerken's correlation gave a closer fit to Muskett's large scale data, but still overestimated holdup at the 2.7m scale.

Warmoeskerken's correlation does not correlate data for different D/T ratios or different impeller designs. Muskett (1987b) concluded that further research is required to quantify the effects of geometry and scale on this type of correlation. This would involve systematic variation of all the correlation parameters over a wide range to obtain industrially useful correlations. Until this work is complete the more robust correlation method based on power input and gas superficial velocity was recommended.

Correlation of holdup with power draw and superficial gas velocity

The effects of impeller type, D/T ratio and scale, can be successfully correlated using:

$$\varepsilon_G = \alpha\ (\varepsilon_m)^{\beta}\ (V_{sg})^{\gamma} \qquad \text{...Eqn (1.23)}$$

where: ε_m = Impeller power draw per unit mass of liquid
V_{sg} = Superficial gas velocity

This equation is dimensional and has a poor theoretical basis, but it consistently produces high correlation coefficients and good data fits. The correlation is based on the principle of the average bubble size being related to the size of the smallest turbulent eddies which, as Kolmogoroff showed, is a function of the power input. Under turbulent conditions the forces that control bubble size can be identified as the inertial forces due to dynamic pressure fluctuations, and surface tension forces, Parthasarathy et al (1991). The inertial forces tend to deform the bubbles whereas the surface tension forces resist the deformation. Inertial forces increase with increasing power input and so bubble sizes are reduced.

In reality the turbulent energy dissipation rates vary significantly with position in a stirred vessel. Thus with freely coalescing media the local bubble size also varies with position in the vessel, as observed by Greaves and Barigou (1988). Bubble sizes will only approach a uniform size if bubble coalescence is heavily repressed. Under these conditions the minimum bubble size will be determined by the maximum local energy dissipation rate, which occurs at the impeller, and these small bubbles will not coalesce as they move away from the impeller into regions of lower energy dissipation.

In scale up, N/N_{CD} is approximately constant at constant ε_m and V_{sg}, Muskett (1987), which may indicate a fundamental mechanism behind the success of this correlation approach when scaling up. N_{CD} is the impeller speed required to achieve complete dispersion of gas, so N/N_{CD} is related to the degree of gas dispersion.

It is not standard industrial practice to scale up at constant V_{sg}, it is more common to use constant vessel volumes of gas per minute (VVM), on the basis of maintaining mean gas residence time and reaction stoichiometry constant. However, Warmoeskerken (1986), Muskett (1987) and Bujalski et al (1988) showed that the use of gas flow rate Q_G, or VVM gave a much poorer data fit than superficial gas velocity V_{sg} when used in equation 1.23.

The difficulties with using equation 1.23 for predicting gas holdup are that the impeller power draw must be predicted, and appropriate values of α, β and γ selected. As shown in section 1.2.1 prediction of gassed impeller power draw is not simple, and it is also a function of V_{sg}. There is also a significant degree of variation in the correlation exponents between different workers and different scales. Typical values of β and γ for equation 1.23 are:

$0.20 < \beta < 0.53$ (but usually $\beta = 0.3$)
$0.36 < \gamma < 0.75$

from Tatterson (1991).

The variation in these exponents is a result of different measuring techniques and correlation of data from different flow regimes.

Van't Riet (1975) found that data from a range of disc turbine designs fitted one correlation:

$$\varepsilon_G = 1.43\ (\varepsilon_m)^{0.33}\ (V_{sg})^{0.67} \qquad \text{...Eqn (1.24)}$$

Chapman et al (1983) found that holdup data from several totally different impeller designs (two sizes of disc turbine, a pitched blade turbine pumping up and a pitched blade turbine pumping down) correlated together using:

$$\varepsilon_G = 1.97\ (\varepsilon_m)^{0.31}\ (V_{sg})^{0.67} \qquad \text{...Eqn (1.25)}$$

Chapman's data fell within ±25% of this correlation showing that, for a given power draw and superficial gas velocity, there was little difference in holdup for the impeller designs studied.

Muskett (1987) did observe slight differences in the holdup measured for different impeller designs. At constant ε_m and low V_{sg} a downward pumping PBT gave higher holdup than an upward pumping PBT of the same dimensions. At high V_{sg} the reverse trend was observed. Muskett related these observations to the direct and indirect gas loading regimes observed with downward pumping impellers, see section 1.2.2. A Rushton turbine produced the same holdup as an upward pumping PBT at low V_{sg}, but at high V_{sg} the Rushton turbine produced higher holdup than the upward pumping PBT.

As gas bubbles rise through a tall vessel the hydrostatic pressure falls and the gas expands. Some authors, e.g. Hubbard (1987), argue that the isothermal expansion energy of the gas (ε_{gas}) should be added to the impeller power draw when correlating holdup, i.e.

$$\varepsilon_G = \alpha\ (\varepsilon_m + \varepsilon_{gas})^{\beta}\ (V_{sg})^{\gamma} \qquad \text{...Eqn (1.26)}$$

where:

$$\varepsilon_{gas} = \left(\frac{Q\ \rho_G}{V_L}\right)\left(\frac{R\ T_L}{M}\right)\ln\left(\frac{p_{sparger}}{p_{at\ liquid\ surface}}\right)$$

The argument used to support the inclusion of ε_{gas} is that when the impeller power is zero equation 1.23 predict zero gas holdup, however, there is some gas holdup in the vessel because the vessel acts as a bubble column. Equation 1.26 is an attempt to correct for this limiting case.

Davies (1986) claimed that the inclusion of the gas isothermal expansion energy improved the fit of his data. Muskett (1987b), on the other hand, found that the inclusion of ε_{gas} could not be justified on statistical grounds.

Influence of gas cavity regime

Warmoeskerken (1986) found that when vortex cavities are present on the blades of a Rushton turbine, flow is radial and small bubbles are produced by the rapid spinning action of the roll vortices. With large cavities, the fluid flow from a disc turbine is more tangential and larger gas bubbles break away from the cavities. Large cavities reduce the pumping capacity of the impeller and hence the degree of turbulence in the vessel. Gas holdup is determined by the relative effects of the bubble buoyancy forces and the fluid motion so it may be expected that separate correlations are required for each cavity regime.

Smith and Warmoeskerken (1985) obtained improved data fits when the holdup data, for a single Rushton turbine, was separated into the two main cavity regimes:

1. vortex/clinging cavities
2. 3-3 cavities

Refer to section 1.2.1.

The resulting correlations were:

Vortex/clinging regime:

$$\varepsilon_G = 0.62\ (N)^{1.6}\ (Q_G)^{0.45}$$

3-3 regime:

$$\varepsilon_G = 1.67\ (N)^{0.7}\ (Q_G)^{0.75}$$

Davies (1986) also obtained an improved data fit by separating his holdup data into the same two regimes. Davies correlated his data (including the isothermal expansion energy of the gas) as follows:

Vortex/clinging regime:

$$\varepsilon_G = 0.138\ (\varepsilon_m + \varepsilon_{gas})^{0.40}\ (\varepsilon_{gas})^{0.35}$$

3-3 regime:

$$\varepsilon_G = 0.229\ (\varepsilon_m + \varepsilon_{gas})^{0.20}\ (\varepsilon_{gas})^{0.49}$$

The above correlations show significant differences in holdup behaviour between the two cavity regimes. The dependency of holdup on impeller power/speed was greater in the

vortex/clinging regime, and the exponent on gas flow was lower in the vortex/clinging regime. Thus the gas flow rate becomes a significant factor in determining the dispersion hydrodynamics when the large cavity structure is present. Most of Muskett's (1987a) holdup data were in the 3-3 cavity regime, but he did conclude that the few data points that he had for the vortex/clinging regime were significantly lower than the predicted values from correlations based solely on the 3-3 regime.

Greaves & Barigou (1988) measured local bubble size distributions in a 1.0 m diameter vessel fitted with a single impeller. They concluded that at low gas flow rates bubble breakage is mainly responsible for determining bubble size in the impeller region but at high gas flow rates bubble coalescence becomes more important. Thus at low gas flow rates an increase in impeller speed has a significant effect on bubble sizes in the impeller region, but at high gas flow rates an increase in impeller speed has little effect on bubble sizes in the impeller region. These conclusions agree with the exponents on impeller speed reported above for the different cavity regimes. Vortex/clinging cavities occur at low gas flow rates and 3-3 cavities occur at high gas flow rates.

1.3.2 Multiple impellers

Roustan (1985) studied the effect of impeller speed on the evolution of gas holdup for a dual Rushton turbine combination, see figure 1.26. As the impeller speed was increased from zero the gas holdup increased slowly until the upper impeller became loaded with gas (N_{L2}). Holdup then increased rapidly until the bottom impeller became loaded with gas (N_{L1}). As impeller speed was increased above N_{L1} there was a linear increase in gas holdup. If Roustan had studied even higher impeller speeds the gas holdup would have started to level out due to the diminishing effect on gas holdup of increased gas recirculation, (the same effect as seen in standard geometry vessels).

Nocentini et al (1988) and Cronin (1988) also observed the holdup discontinuity at N_{LI}. Industrial vessels usually require high interfacial area for mass transfer and so should not be operating below N_{LI}.

Very few papers have been published on the measurement of gas holdup in multiple impeller systems. Most data refers to multiple disc turbine combinations and only one recent paper, Chiampo et al (1991), presents holdup data for mixed impeller combinations.

Correlation of data

Magelli et al (1987) measured gas holdup in a small non standard vessel (T = 23 cm, $H = 4T$) fitted with four Rushton turbines ($D = 0.4T$). It was found that, for a given power/unit mass and superficial gas velocity, the holdup values were the same as for a single impeller in a standard geometry vessel and could be correlated by equation 1.24 proposed for standard vessels by Van't Riet (1975):

$$\varepsilon_G = 1.43\ (\varepsilon_m)^{0.33}\ (V_{sg})^{0.67} \qquad \text{...Eqn (1.27)}$$

Cronin (1988) also concluded that Van't Riet's correlation adequately described holdup data measured for two dual disc turbine combinations ($D = T/3$ and $D = T/2$) in a 0.72 m diameter vessel.

Nocentini et al (1988) concluded that the holdup correlations proposed by Chapman (1983):

$$\varepsilon_G = 1.97\ (\varepsilon_m)^{0.31}\ (V_{sg})^{0.67}$$

and Hassan and Robinson (1977):

$$\varepsilon_G = 0.113\ (Q\ N^2\ /\ \sigma_{GL})^{0.57}$$

where: σ_{GL} = Gas liquid interfacial tension

which were both developed from single impeller data, adequately described their multiple impeller measurements. Other literature correlations for predicting gas holdup for single impeller configurations proved inadequate for interpreting Nocentini's tall vessel data.

Roustan (1985), studied two non standard vessels, both $H = 2T$, with $T = 0.43$ m and 0.78 m. Two or three Rushton turbines were mounted in these non standard vessels. Roustan found that the addition of a third turbine, to an existing dual turbine combination (while maintaining $H = 2T$, i.e. reducing the impeller spacing), increased the power draw but did not result in an increase in the gas holdup for a fixed impeller speed and gas flow rate. Roustan concluded that the gas holdup depends on the degree of turbulence but that it is above all related to the circulation pattern in the vessel. The addition of a third impeller increased the power dissipation but it would not have improved the liquid circulation, in fact it probably would have made liquid mixing worse due to increased compartmentalisation, see section 1.4.

Abrardi et al (1988), studied two vessels of $T = 0.39$ m, one with $H = T$ fitted with a single Rushton turbine, and the other with $H = 5T/3$ fitted with two Rushton turbines. For a given impeller speed and gas flow rate it was found that the gas holdup produced by a dual turbine system was greater than that produced by a single turbine, see figure 1.27. Abrardi et al concluded that when correlating holdup data with impeller speed and gas flow rate a factor is needed to account for the number of impellers, or better a separate contribution from the lowest impeller to that of the upper impellers. Abrardi et al also concluded that Roustan's data (1985), showed a further increase in holdup when changing from two to three impellers at constant impeller speed. This was not the conclusion drawn by Roustan himself who claimed that there was no difference between his dual and triple impeller combinations, see above. Roustan tabulated his holdup data and this has been plotted in figure 1.28, showing that Roustan's conclusion is the correct one.

When compared on the basis of power / unit mass and superficial gas velocity, Abrardi et al concluded that holdup was independent of the number of impellers used. Thus a single correlation was proposed covering both single and dual impeller systems:

$$\varepsilon_G = 0.21\ (\varepsilon_m\ (1 - \varepsilon_G))^{0.27}\ (V_{sg})^{0.65}$$

It is not known why Abrardi et al chose to correlate their holdup data with the inconvenient term $\varepsilon_m\ (1 - \varepsilon_G)$ rather than just ε_m. Unfortunately Abrardi et al did not tabulate their holdup data. To investigate the effect of the $(1-\varepsilon_G)$ term in the above correlation Roustan's data (1985) for non standard vessels ($H = 2T$ fitted with 2 and 3 Rushton turbines) was used. The resulting correlations were obtained:

$$\varepsilon_G = 0.48\ (\varepsilon_m)^{0.35}\ (V_{sg})^{0.76} \qquad \text{...Eqn (1.28)}$$

$$\varepsilon_G = 0.51\ (\varepsilon_m\ (1 - \varepsilon_G))^{0.35}\ (V_{sg})^{0.77} \qquad \text{...Eqn (1.29)}$$

The inclusion of $(1 - \varepsilon_G)$ on the right hand side of the correlation had negligible effect on the correlation exponents and produced a marginally worse data fit. Thus the only difference between the two correlating methods seems to be that equation 1.28 is easier to use for predicting holdup.

The exponents on ε_m and V_{sg} produced by correlating Roustan's data are very similar to the exponents reported by Magelli et al (1987), Cronin (1988) and Nocentini et al (1988). Considering the uncertainty surrounding holdup correlations in standard geometry vessels, there is a surprising degree of agreement between the holdup correlations reported for tall multiple Rushton turbine combinations.

Chiampo et al (1991) measured holdup for three different dual impeller combinations ($H = 2T$, $T = 0.39$ m, and $D = T/3$):

1. $2 \times$ RT
2. RT + 4MFT (top, pumping up)
3. RT + 4MFT (top, pumping down)

For all experiments the gas was completely dispersed. In spite of the different bulk flow patterns produced by the three impeller combinations it was found that for a given impeller speed and gas flow rate all impeller combinations produced the same gas holdup. As mentioned above, Roustan (1985) drew the same conclusion for dual and triple Rushton turbine combinations.

For a given impeller speed and gas flow rate the difference in gassed power draw between Chiampo's impeller combinations was never greater than 25%. For Roustan's impeller combinations the difference in power draw was never greater than 36%. Assuming that equation 1.27 can be applied to all of these impeller combinations (i.e. for a given gas flow rate $\varepsilon_G \propto \varepsilon_m^{0.33}$) the maximum difference in holdup measured with the different impeller combinations would be expected to be only 9.7%. This is within

the holdup measurement error bands of ±20%, Chapman (1983), so any difference would probably be lost in the experimental error.

Influence of gas cavity regime

With multiple Rushton turbines large cavities only form on the upper impellers at much higher sparger gas flow rates than those which lead to the formation of large cavities on the lowest impeller, see section 1.2.2.2. Thus there are three possible cavity regimes:

1. Vortex/clinging cavities on all impellers.
2. 3-3 cavities on the lowest impeller + vortex/clinging cavities on the upper impellers.
3. 3-3 cavities on all impellers.

This assumes that the cavity regime is the same on all upper impellers, which may not be true in very deep tanks where the gas expands significantly. As shown in section 1.3.1 gas cavity regimes have a significant effect on the correlation of holdup data for a single impeller. The effect of different cavity regimes on the correlation of holdup data for multiple impeller systems has not been investigated in the literature.

1.4 LIQUID MIXING

Good gas dispersion and high mass transfer rates are usually the main objective for the designer of a gas liquid agitator. However, liquid mixing can also play an important role in determining the product yield of many chemical reactions. Some processes require a well mixed liquid with no stagnant regions, and a uniform distribution of material, e.g. nutrients and dissolved oxygen in fermentation processes. Other processes require plug flow of liquid through the equipment, (with agitated vessels this condition can be approached by using a number of well mixed vessels in series, or using one tall vessel in which the liquid mixing is staged).

Many researchers have investigated the effects of impeller design, operating conditions and scale on liquid mixing times in standard geometry vessels without gas, refer to the recent review by Grenville (1992). Gas sparging is known to have a significant effect on impeller power draw, see section 1.1, but very few workers have investigated the effect of aeration on liquid mixing times.

1.4.1 Single impellers

Einsele and Finn (1980) found that, for a single Rushton turbine in standard geometry vessels up to 0.76 m in diameter, liquid mixing time increased with increasing gas flow rate at a given impeller speed. The decrease in impeller power draw, caused by aeration, did not fully account for the increased liquid mixing time and it was found that:

$$\frac{\theta_{with\ gas}}{\theta_{ungassed}} = 1 + fn(\varepsilon_G)$$

The effect of holdup on blend time was found to be the same regardless of whether the holdup material was gas or particles of the same average diameter. Therefore, it was concluded that the reduction in mixing efficiency was caused by suppression of turbulent eddies due to the presence of the holdup material.

Bryant and Sadeghzadeh (1979) used a neutrally buoyant radio transmitter to monitor circulation times in a 0.9 m diameter vessel fitted with a flat blade turbine (exact details of impeller not given). It was concluded that, for a given impeller speed, liquid circulation time increased linearly with gas flow rate. However, it was also concluded that gas flow rate had negligible effect on the terminal liquid mixing time. Using the same experimental technique Middleton (1979) measured circulation times in standard geometry vessels, of 0.18, 0.61 and 1.83 m diameter, fitted with a single Rushton turbine. At constant impeller speed increasing gas flow rate was found to increase the mean circulation time.

1.4.2 Multiple impellers

1.4.2.1 Liquid mixing times

Cooke et al (1988) measured aerated liquid mixing times in standard geometry vessels (T up to 1.8 m) and a tall vessel (H = 3T, T = 0.3 m) fitted with three impellers. For a given geometry it was found that:

$$\theta_{95\%} \propto \varepsilon_m^{-0.33}$$

Mixing times with triple Rushton turbines were significantly longer than mixing times measured with a single Rushton turbine in a standard geometry vessel. Triple axial flow impellers were found to mix the liquid in approximately half the time taken by the triple Rushton turbines. This illustrates how poor top to bottom mixing is with multiple Rushton turbines.

Cronin (1988) measured liquid mixing times with dual Rushton turbines (T = 0.72 m, H = 2T) using an iodine starch decolourisation method. As the impeller separation was reduced the ungassed liquid mixing time increased due to changing flow patterns and reduced power draw. When compared on the basis of power input per unit volume, liquid mixing times were independent of impeller separation.

For an impeller separation equal to the vessel diameter the shortest ungassed mixing times were obtained when tracer was added to the lower circulation loop of the upper Rushton turbine. Mixing times were 40% longer when tracer was added to the liquid surface. Intermediate mixing times were measured for all other tracer addition points. Ungassed, $N\theta_{95\%}$ was constant for a given geometry and tracer addition point.

For a single Rushton turbine at a given power per unit mass the liquid mixing time was approximately four times longer in a tall ($H = 2T$) vessel compared to a standard geometry ($H = T$) vessel. Single and dual Rushton turbines were then compared in a tall ($H = 2T$) vessel. On the basis of equal power input per unit volume the dual impellers produced slightly shorter mixing times than the single impeller. Thus it was concluded that for high aspect ratio vessels, i.e $H > T$, multiple impellers are required for adequate mixing.

Cronin found that aeration had a significant effect on liquid mixing time. In a dilute CMC solution (pseudoplastic model fluid) gassing reduced the liquid mixing time at low impeller speeds and increased the liquid mixing time at high impeller speeds. Thus for a given gas flow rate, Nθ was not constant. The gassed liquid mixing times were found to be longer than the ungassed mixing times for power inputs > 1 W/kg.

Mahmoudi and Yianneskis (1991) studied the effect of impeller separation and rotational speed on ungassed liquid mixing time for dual Rushton turbines ($T = 0.29$ m, $D = T/3$). At large impeller separations the flow from each turbine was horizontal. At small

impeller separations the flow from the two turbines were directed towards each other merging together halfway between the impellers. This flow pattern was observed by Kuboi and Nienow (1982) and Hudcova et al (1987), see figures 1.16 and 1.17(b). The variation in flow pattern was founds to affect the liquid mixing time with merging flow producing smaller mixing times. At intermediate separations the flow pattern was unstable changing from one to the other with time.

Abrardi et al (1990) measured ungassed and gassed liquid mixing times for three dual impeller combinations:

2 × RT
1 × RT + 1 × PBT (pumping up)
1 × RT + 1 × PBT (pumping down)

In all cases $N\theta$ was constant without gas showing that liquid exchange between the impeller regions was proportional to ND^3. The value of $N\theta$ was lower for the two RT + PBT combinations than with the dual RT combination. However $N\theta$ was always much higher than for a single impeller in a $H = T$ vessel, showing that the exchange between impellers was significantly lower than the circulation induced by each impeller.

For the dual Rushton turbine combination at high impeller speeds, the liquid mixing time increased with gas flow rate due to the reduction in impeller pumping capacity. With gas $N\theta$ was still roughly constant. For the dual Rushton turbine and RT + PBT (pumping down) combinations the gassed mixing times were similar to the ungassed mixing times for a given power input. In both cases:

$$\theta_{gassed} \propto \varepsilon_m^{-0.33}$$

The RT + PBT (pumping down) combination produced similar results to the 2RT combination when gassed. For the RT + PBT (pumping up) combination gassed mixing times were lower than ungassed mixing times except at very high impeller speeds. With the lowest impeller flooded the liquid mixing time was reduced due to improved axial mixing around the lowest impeller.

1.4.2.2 Structured liquid mixing models

Lelli et al (1972), Fajner (1982) and Nocentini (1988) measured the liquid phase residence time distribution in ungassed vessels fitted with four Rushton turbines (H = 4T, T = 0.08 to 0.23 m).

Fajner et al (1982) compared their experimental results with three ideal models for liquid mixing:

a) Cascade of well mixed cells with exchange flows (one cell per turbine)
b) One dimensional diffusion model

c) Perfect mixing

The local concentration was found to be constant across the plane of each impeller supporting the cascade model, but concentration gradually changed in the central core of the vessel between adjacent impellers, supporting the diffusion model. Thus neither model was found to correspond exactly to the true liquid mixing. It was concluded that both the cascade model and the diffusion model were satisfactory and that perfect mixing was not a good model for the liquid mixing.

In the cascade of well mixed cells model, liquid exchange flows occur across the horizontal section between two impellers where the adjoining circulation flows meet. The liquid exchange flow regulates the mixing rate and the flow patterns observed with multiple Rushton turbines indicate that the back flow cell model is adequate, Ando et al (1985).

Oosterhaus and Kossen (1983 and 1984) concluded that for vessels fitted with multiple impellers, even when the liquid phase mixing time is equal to or greater than the characteristic mass transfer time, the liquid phase cannot be assumed to be perfectly mixed. So for scale up, correlations developed in standard geometry vessels (in which the liquid has been assumed perfectly mixed) have to be replaced by a reactor model in which the bulk liquid mixing is taken into account. Jury and Schneider (1988) also concluded that to be able to model the mixing behaviour in a triple impeller stirred tank reactor a structured model which reflects the actual flow pattern is required.

Singh (1986) concluded that knowledge of mixing in multiple impeller reactors would be helpful in scale up, for estimating substrate distributions and for optimisation of impeller and vessel geometries. However, it was also concluded that mixing time is itself not sufficient to characterise mixing because it does not provide information on fluid segregation in the vessel.

Bader (1986) claimed that application of the cascade of cells model to multiple impeller agitated vessels has the advantage of considering the individual effect of each impeller rather than considering the whole vessel as a black box. The major weakness of the model is the limited information available for quantifying the parameters in the model. Reliable correlations for upper turbine gassed power, k_La as a function of agitation and aeration and exchange flows do not exist.

Manna et al (1991) concluded that mixing time is useful for comparing with transfer time or reacting time to estimate the controlling mechanism of the process. However, a quantitative definition of the mixing performance is only possible by defining a model which takes into account the internal hydrodynamics of the vessel. A cascade of well mixed cells model was recommended for multiple impellers. Using colour change experiments observed the main mixing boundaries for a dual Rushton turbine combination (T = 0.39 m, H = 0.65 m, D = T/3). As a result a three cell model was used with the cell boundaries located between the two impellers and at the centre line of the upper impeller, see figure 1.29.

Numerous versions of the cascade of well mixed cells model have been applied to multiple impeller geometries. Manfredini and Cavallera (1983) and Bader (1986 & 1987) modelled the liquid mixing in industrial size vessels (112 m^3 and 40 m^3 respectively), each fitted with four Rushton turbines, as four well mixed cells (one cell per impeller) connected by exchange flows, see figure 1.30. For a dual Rushton turbine geometry (V_L = 19 m^3) Oosterhaus and Kossen (1983) and Nishikawa et al modelled the liquid mixing as a series of well mixed agitator controlled zones and bubble controlled zones all connected by exchange flows. Jury and Schneider (1988) used a two cell exchange flow model for a single impeller and a six cell model for a triple impeller combination. Although the above workers assumed models which included exchange flows non of them actually attempted to measure the exchange flows.

Fajner et al (1982) estimated the exchange flows in their simple cascade model, for a multiple Rushton turbine combination, from residence time distribution experiments (assuming that all exchange flows were equal). For Reynolds numbers < 8000 the exchange flows were found to increase with impeller speed. For Re > 8000 the exchange flows were independent of impeller speed for a given geometry:

For six blade turbines: $$\frac{F}{N D^3} = 0.275$$

For four blade turbines: $$\frac{F}{N D^3} = 0.246$$

For four and six blade turbines under turbulent conditions good agreement was obtained with the relation defined by Miyauchi et al (1966):

$$\frac{F}{N D^3} \propto Po^{\frac{1}{3}}$$

Bader (1986b) measured residence time distributions for multiple Rushton turbines at three scales and modelled the liquid mixing using a cascade of well mixed cells (one cell per impeller). Bader assumed that all exchange flows in his model were equal and found that:

100 gallon vessel, 4×RT : $$\frac{F}{N D^3} = 0.34$$

1000 gallon vessel, 5×RT: $$\frac{F}{N D^3} = 0.14$$

30000 gallon vessel, 5×RT: $$\frac{F}{N D^3} = 0.40$$

All tests were conducted under gassed conditions with Q_G = 0.4 VVM. It was concluded that these results were similar to those of Fajner et al (1982).

Singh et al (1986) assumed a three cell mixing model for a triple Rushton turbine combination at four scales (0.1 to 40 m^3). The upper and lower exchange flows, which were assumed to be equal, were estimated from liquid mixing experiments conducted with fast response pH probes and pulse addition of tracer. It was concluded that:

$F = 0.5\ Q_I$ where Q_I is the impeller pumping capacity ($= N_Q\ N\ D^3$)

$If\ Q_G < Q_{G,F}$: $F_{gassed} \approx F_{ungassed}$

and $If\ Q_G > Q_{G,F}$: $F_{gassed} > F_{ungassed}$

Thus it was concluded that the point of departure of the exchange flows from the ungassed value, for a given impeller speed, can be used to determine the flooding point.

Kuboi and Nienow (1986) modelled the liquid phase mixing, for several dual impeller combinations, as a series of well mixed zones corresponding to the circulation loops observed in the vessel. A flow follower technique was presented for determination of liquid exchange flows between the circulation loops. Viscous newtonian and non Newtonian liquids were tested but the effects of aeration were not studied.

1.5 MASS TRANSFER

The main objective of contacting a gas with a liquid is usually to achieve mass transfer between the two phases. For most gas dispersion processes the liquid phase chemical or biochemical reaction would not proceed at the required rate if the transfer of one of the reactants from the gas phase to the liquid phase became limited. Mass transfer is therefore one of the most important aspects of equipment design.

For sparingly soluble gasses the mass transfer between gas and liquid is described by:

$$J = k_L a \, (C_{Li} - C_L) \qquad \text{...Eqn (1.30)}$$

where

J	=	mass transfer rate (kg/m3s)
k_L	=	liquid side mass transfer coefficient (m/s)
a	=	interfacial area per unit volume of liquid (m^2/m^3)
C_L	=	Concentration in the bulk liquid (kg/m^3)
C_{Li}	=	Concentration at the liquid interface (kg/m^3) (assumed to be in equilibrium with the bulk gas concentration, i.e. $C_{Li} = KC_G$)
C_G	=	Concentration in the bulk gas (kg/m^3)

Equation 1.30 is based on the assumption that $k_L << K\,k_G$, where k_G is the gas side mass transfer coefficient, so that the liquid side resistance to mass transfer limits the overall mass transfer rate. In practice it is important to check that this assumption holds for a particular process because it can affect the choice of equipment and the scale up method, Middleton (1985). All mass transfer studies in this thesis were concerned with the transfer of oxygen from air to water. Oxygen is sparingly soluble in water and so equation 1.30 does apply to this system.

1.5.1 single impellers

Many researchers have measured $k_L a$ values in standard geometry vessels. As with gas holdup the most successful correlations are of the form:

$$k_L a = \alpha \, (\varepsilon_m)^{\beta} \, (V_{sg})^{\gamma} \qquad \text{...Eqn(1.31)}$$

This correlation has been found effective even though much of the fundamental fluid mechanics information does not appear explicitly.

For the transfer of oxygen to water, Van't Riet (1979) reported the range of exponents in the literature as:

$$0.1 < \beta < 0.7$$
$$0.4 < \gamma < 1.0$$

Literature values of α, β and γ vary significantly from researcher to researcher because of the differences in system geometries, vessel scales, range of experimental variables tested, and experimental methods employed, Chandrasekharan and Calderbank (1981).

Van't Riet (1979) reviewed mass transfer results from many sources and concluded that for oxygen mass transfer from air to water:

$$k_L a \propto (\varepsilon_m)^{0.4} (V_{sg})^{0.5}$$

Muskett (1987) correlated data from a wide range of scales (T = 0.61 m to 2.67 m) and produced a very similar correlation:

$$k_L a \propto (\varepsilon_m)^{0.41} (V_{sg})^{0.49}$$

This correlation holds for all impeller designs studied, so long as the gas is effectively dispersed. However, this correlation only applies to oxygen transfer from air to clean water. Clean water is a freely coalescing medium. If bubble coalescence is suppressed, e.g. by the addition of salt to the liquid, the average bubble size will be reduced and a will increase significantly. The exponents β and γ in equation 1.31 also change with the bubble coalescence behaviour of the system, refer to Van't Riet (1979).

1.5.2 Multiple impellers

Ramanarayanan and Sharma (1982) measured a and $k_L a$ in a 0.2 m diameter vessel, using chemical methods. Up to three Rushton turbines were studied. a and $k_L a$ were found to be practically independent of superficial gas velocity and to vary linearly with impeller speed. a and $k_L a$ were not affected by the number of impellers for the geometry studied.

Nishikawa et al (1984) studied the effect of impeller separation on $k_L a$ for dual paddle and turbine impellers. $k_L a$ was found to increase with impeller separation in a similar manner to power draw, see section 1.2.2. $k_L a$ reached a maximum steady value for $S > 1.5D$. Machon et al (1988) also studied the effect of impeller separation on overall $k_L a$ values for dual Rushton turbines in a 0.29 m diameter vessel ($H = 2T$). For a given power input and superficial gas velocity, $k_L a$ was found to increase with impeller separation up to $S = 3T$.

Cronin (1988) measured overall mass transfer rates in a baker's yeast fermentation. For a given power input per unit mass and superficial gas velocity $k_L a$ with dual Rushton turbines in a tall vessel ($H = 2T$) was found to be greater than $k_L a$ for a single Rushton turbine in a standard ($H = T$) vessel.

Several researchers have claimed that retrofitting multiple Rushton turbines with axial flow impellers can improve the mass transfer rate for a given power input. Lally et al (1985) retrofitted the upper impellers in a multiple Rushton turbine combination with

axial flow hydrofoils (Lightnin A310s). It was concluded that the new combination derived all the benefits of gas dispersion from the remaining Rushton turbine, in the lowest impeller position, while using less power to provide the same mass transfer, liquid blending and heat transfer. Gbewonyo et al (1986) studied the effect of retrofitting dual Rushton turbines with dual axial flow impellers (Prochem Maxflos). The axial flow impellers were found to be 40% more energy efficient in terms of oxygen mass transfer than the dual Rushton turbines when tested in a viscous mycelial fermentation broth. The benefit observed with the axial flow impellers was attributed entirely to the improved bulk liquid mixing. In their paper Gbewonyo et al referred to two presentations from the Henniker mixing conference of 1985: Tyler et al reported improved k_La following the retrofit of triple Rushton turbines with triple axial flow impellers (Lightnin A315s), and Krone et al reported an improvement in k_La when using a combination of an axial flow hydrofoil (Lightnin A310) plus a Rushton turbine compared with dual Rushton turbines.

1.5.3 Gas phase mixing with multiple impellers

Abrardi et al (1988) conducted gas residence time measurements with a dual Rushton turbine combination in a 0.39 m diameter vessel ($H = 5T/3$). At low stirrer speeds the gas was found to flow as a plug through the vessel. At higher stirrer speeds the gas phase mixing was intermediate between plug flow and perfect mixing.

Nocentini et al (1988) studied the residence time distribution of the gas phase (following the pulse injection of a hydrocarbon) in a tall vessel ($H = 4T$, $T = 0.23$ m) fitted with four Rushton turbines. The gas phase mixing was found to be intermediate between plug flow and perfect mixing.

1.6 CONCLUSIONS

Single impellers

Gas dispersion with single standard geometry Rushton turbines has been extensively studied in the literature. Empirical correlations have been developed for predicting the main bulk flow pattern transitions, and the gas cavity regimes on the impeller blades. The effect of gas cavities on impeller power draw is qualitatively understood, however it is difficult to accurately relate cavity size and shape to impeller power draw, and designers still have to rely on empirical correlations. Many power correlations can be found in the literature, mostly based on small scale data. The most successful power correlations are those which consider the effects of different cavity regimes. Correlations from Smith (1989) are presented which, although still empirical in nature, do consider the effects of different cavity regimes and are based on a wide range of scales (vessel diameters up to 2.7 m).

Single pitched blade turbines have been studied by several workers, although not as extensively as the Rushton turbine. Empirical correlations exist for predicting the main flow pattern transitions but each correlation is geometry specific. Downward pumping impellers are inherently unstable due to the counter current flow of gas and liquid in the impeller region, and operation close to the direct / indirect loading regime can result in large torque and flow pattern instabilities. For most industrial applications downward pumping pitched blade turbines would be directly loaded with gas. LE20 impellers have not been studied previously but, in many respects, this impeller design should be similar to a downward pumping pitched blade turbine.

Upward pumping impellers are very stable and disperse gas very effectively with less torque and flow pattern instabilities than downward pumping impellers. For the majority of industrial applications, upward pumping pitched blade turbines are unlikely to be flooded.

For single impellers no generally applicable correlations exist for relating gas holdup or mass transfer rates to independent system parameters, such as impeller speed, D/T ratio, liquid physical properties, etc.. The most successful correlation method, for both parameters, is:

$$\varepsilon_G \text{ or } k_La = \alpha\,(\varepsilon_m)^{\beta}\,(V_{sg})^{\gamma}$$

The exponents in these correlations vary with the range of conditions tested, and a wide range of exponents have been reported in the literature. Generally, for air dispersion into water, ε_G and k_La have been found to be independent of impeller design for a given ε_m and V_{sg} (for non flooded impellers). Several workers have shown that correlation of holdup data is improved if the impeller cavity regimes are considered separately.

Few workers have studied the effect of aeration on liquid mixing. Limited results show

that liquid mixing times can increase or decrease with gas flow rate, depending on the impeller speed.

Multiple impellers

For multiple impellers the separation between impellers has a major effect on the hydrodynamics. Generally, for multiple Rushton turbines, at separation distances less than $2D$ the flows from each impeller can interact affecting power draw and the flow pattern transitions of the lowest impeller. For large impeller separations $S > 2D$ the lowest impeller behaves in the same way as it does when mounted alone in a standard geometry vessel, in terms of flow patterns and power draw. The effect of impeller separation is a function of impeller diameter, speed, design and probably scale. For a combination of axial flow impellers there is greater interaction between the impellers and the impeller separation may need to be as large as $3D$ to eliminate flow interactions.

For most industrial operating conditions, the upper impellers of a multiple impeller combination will only see a fraction of the sparger gas flow rate. The hydrodynamics and power draw of the upper impellers will therefore be significantly different to the lowest impeller. For predicting the gassed power draw of multiple impellers it is important to account for the cavity structure on each impeller. Currently, different cavity regimes can only be estimated for multiple Rushton turbines. Several workers have presented empirical correlations for the prediction of multiple impeller gassed power draw. However, none of these correlations takes account of the different cavity structures present on the impellers.

Based on visual observations of gas dispersion quality it can be concluded that the general trends observed with single impellers are directly applicable to multiple impellers. For example, downward pumping impellers can be subject to instabilities, while multiple Rushtons or combinations of Rushtons with upward pumping impellers are good for gas dispersion.

Several workers have measured the individual power draw of multiple Rushton turbines and compared these measurements to single impeller results. However, the same approach has not been taken for other impeller designs, such as pitched blade turbines.

Several workers have found that the correlation developed by Van't Riet (1975), for single impeller configurations, adequately describes holdup data from multiple Rushton turbine combinations. The effect of the different cavity regimes on gas holdup correlations has not been investigated for multiple impellers. Only one recent study has been published on holdup measurements with multiple impellers of mixed designs, and it was concluded that gas holdup was independent of impeller combination.

Aeration has a significant effect on liquid mixing times but the effect depends on the number and type of impellers used. Aeration can increase, decrease or have no effect on liquid mixing time.

In tall tanks, fitted with multiple Rushton turbines, the liquid phase is not well mixed. Mixing time is not sufficient to characterise liquid mixing in tall vessels because it gives no indication of fluid segregation. For scale up and prediction of reactant / product distributions in a reactor, a structured model of the liquid phase mixing is required which takes account of the actual two phase flow patterns. A structured model would also be of benefit in selection of optimum reactant addition points which have a large effect on the rate of mixing. A cascade of well mixed zones has been shown to be a good approximation to the liquid mixing in multiple impeller systems, as has the one dimensional diffusion model. The cascade model has the advantage of considering the individual effect of each impeller rather that considering the whole vessel as a black box. The major limitation of this modelling approach is the lack of data on upper impeller power draw, exchange flows between cells and k_La in the upper cells.

1.7 STRUCTURE OF THIS THESIS

This thesis is arranged in the following chapters:

1. Literature review (includes detailed review of gas dispersion with multiple impellers and a summary review of gas dispersion with single impellers).

2. Experimental facilities (describes facilities and experimental techniques).

3. Flow patterns and power draw (presents visual observations of two phase flow patterns and measurements of impeller power draw).

4. Gas holdup (presents measurements of overall gas holdup).

5. Liquid mixing (studies into effect of aeration on liquid mixing times, local mixing rates and liquid mixing models).

6. Mass transfer (incorporates liquid mixing models with measurements of dissolved oxygen transients to calculate local k_La).

7. Economic analysis (compares options for improving mass transfer rates in an existing reactor).

8. Conclusions and suggestions for future work.

CHAPTER 2

EXPERIMENTAL DETAILS

2.1 INTRODUCTION

This chapter describes the experimental facilities, instrumentation and techniques adopted in this thesis.

2.2 EXPERIMENTAL FACILITIES

2.2.1 Vessels

The standard vessel geometry is shown in figure 2.1. This vessel was used for studying the hydrodynamics of single impellers. This vessel had a dished bottom, with the radius of curvature equal to the vessel diameter. Four equally spaced baffles were fitted to the vessel extending from above the dispersion surface to the tan line. All baffles had a width of $T/12$ and a wall clearance of $T/60$, giving a total distance from the vessel wall to the outside baffle edge of $T/10$. The standard vessel was 0.61 m in diameter and manufactured from Perspex to allow visual observation of the flow patterns.

The tall vessel geometry is shown in Figure 2.2. This vessel geometry was exactly the same as the standard vessel except that the vessel height was three times the vessel diameter. Two geometrically identical tall vessels, of 0.61 m and 0.95 m diameter, were studied. The 0.61 m diameter vessel was manufactured from Perspex to allow visualisation of the flow patterns. The 0.95 m diameter vessel was manufactured from stainless steel, and supplied by APV Ltd. The baffles were not continuous, with a gap of $0.21T$ at half the vessel height.

The ungassed liquid depth was fixed at $2.4T$ giving a liquid volume of 420 litres in the 0.61 m diameter vessel, and 1570 litres in the 0.95 m diameter vessel. This liquid level was chosen to allow a maximum gas holdup of 20% at both scales.

2.2.2 Impellers

Three different impeller designs were used in this study:

1. Rushton turbine (RT)
2. 4 blade, 45° pitched blade turbine (PBT)
3. LE20 (a proprietary axial flow impeller, manufactured by APV Ltd)

The impellers are shown in figure 2.3 and the dimensions are given in tables 2.1 to 2.3. The Rushton turbines had a nominal diameter of $T/3$, while the PBT and LE20 impellers had nominal diameters of $T/2$. The LE20 impellers were sized to give the same

ungassed power draw as a Rushton turbine at a given impeller speed. The pitched blade turbines were not sized in this way and drew approximately twice the ungassed power of a Rushton turbine for a given impeller speed.

Four triple impeller combinations were studied in the 0.61 m diameter vessel:

1. 3 × RT (all of identical design)
2. 1 × RT (lowest position) + 2 × LE20s (both pumping down)
3. 1 × RT (lowest position) + 2 × PBTs (both pumping down)
4. 1 × RT (lowest position) + 2 × PBTs (both pumping up)

Only combinations 1 and 2 were studied in the 0.95 m diameter vessel.

The impeller positions in the tall vessel geometry are shown in Figure 2.2.

2.2.3 Spargers

The sparge ring was positioned centrally below the lowest impeller. The hole pitch circle diameter (pcd) was $0.84D_{RT}$ and the sparge holes faced upwards. The sparger holes were positioned $0.2D_{RT}$ below the lower edge of the impeller blades.

The dimensions of the sparge rings are given in Figure 2.4.

2.2.4 Test fluids

The only liquid used for this study was tap water. This is a liquid in which bubbles freely coalesce. The test vessels were maintained in a clean condition, and the test liquid was replaced at regular intervals to prevent the build up of contaminants which could inhibit the coalescence behaviour of the gas bubbles.

Two gases were used in this study: air, and oxygen free nitrogen. Air was supplied from an oil-free screw compressor. The nitrogen was stored as a liquid (storage facilities supplied by BOC Ltd) and vapourised, using atmospheric heat exchangers, as required. The flow rate of both gases was measured by rotameter.

All experiments were conducted at ambient pressure and temperature. The temperature of the liquid and the inlet gas (at the rotameter) were measured for all tests, using thermocouples.

All gas flow rates quoted in this thesis are correct at the sparger hydrostatic pressure.

2.3 INSTRUMENTATION AND EXPERIMENTAL TECHNIQUES

2.3.1 Flow patterns

The bulk flow patterns of the different multiple impeller combinations tested were observed visually. Visual observations were aided by the use of the iodine / thiosulphate, starch decolourisation method, refer to Cronin (1988) for details.

2.3.2 Impeller power draw

The power draw of the impellers was determined by simultaneously measuring the shaft rotational speed and the shaft torque. Power draw was then calculated from:

$$P = 2 \pi N \Lambda$$

Both vessels studied were fitted with a.c. motors. The shaft rotational speed was fixed using a variable frequency controller. This allowed the speed to be fixed anywhere in the following ranges:

0.61 m vessel:	0 to 350 rpm
0.95 m vessel:	0 to 420 rpm

To measure the shaft rotational speed a toothed wheel was fixed to the shaft. The rotating teeth interrupted a beam of light producing a binary output from a receiving photoelectric cell. Knowing the number of teeth on the wheel and the rate at which teeth passed the light detector the shaft rotational speed could be calculated and displayed on a digital readout. The accuracy of this method was $\pm$ 1 revolution / minute.

The torque drawn by the impellers was measured using semi-conductor strain gauges mounted directly on the shaft. Strain gauges were fitted to the shaft just above each impeller position. Thus three sets of strain gauges were fitted to the shafts in the tall vessels. The lowest gauge measured the torque on the bottom impeller, the middle gauge measured the total torque of the middle and bottom impellers, and the upper gauge measured the total torque of all three impellers. Thus by subtraction the torque drawn by each impeller could be calculated.

All three strain gauges were calibrated by applying known loads to a level arm attached to the shaft while the shaft was supported horizontally. The voltage output from each gauge was recorded as a function of the applied torque (always found to be a linear relationship). A least squares linear regression through this data produced the torque calibration factors. The calibrations were checked by conducting power measurements with a single impeller, of known power number, in the lowest impeller position.

Because the strain gauges were mounted between the impellers, they had to operate submerged in the test fluid. The gauges were therefore covered with waterproof material. The calibration routine was repeated at regular intervals to ensure that water was not penetrating the waterproofing material and affecting the strain gauge outputs.

The alignment of the strain gauges had to be checked to ensure that they were only measuring torsional forces and not bending forces. The alignment was checked by applying a bending load to the shaft and recording the gauge output voltages. In all cases the gauges showed a negligible response to the bending force indicating that the gauges were correctly aligned.

The agitator shafts in the tall vessels were fitted with bottom steady, anti friction bearings. The torque zero level was measured with the shaft rotating at a low speed (15 rpm) to eliminate the small shaft torque produced by the bottom bearing. This zero level was then subtracted from the torque measured with the shaft rotating at test speed.

For the 0.95 m diameter vessel, telemetry was used to transmit the strain gauge output signal from the shaft, to pick ups mounted on the vessel support framework. Figure 2.5 is a schematic of the torque instrumentation chain for this vessel. The voltage signal from the strain gauges was first amplified by an operational amplifier mounted on the shaft. The amplified voltage signal was then converted to a frequency modulated signal and transmitted as a radio wave. This radio wave was collected by aerials fixed to the vessel support framework. The frequency modulated signal was converted back to voltage modulation (by units manufactured by Astech Electronics Ltd) before being filtered and amplified and finally sampled by a PDP 11 laboratory computer. The PDP 11 was fitted with a 12 bit analogue to digital converter giving a resolution of 1 in 4096 over a range of ± 5 Volts. Six windows of 2048 data points were taken for each test condition with a sampling frequency of 100 Hz. Electrical noise was filtered out using a low pass filter set at 25 Hz. The accuracy of the torque measurement method was ± 3%, and allowing for errors in speed measurement, the power measurements were accurate to within ± 5%.

The 0.95 m diameter vessel was positioned outside of the main laboratory and no problems were encountered due to stray radio signals. However, the 0.61 m diameter vessel was positioned inside the main laboratory surrounded by other mixing vessels and potential sources of electrical interference. For this reason, this vessel was not fitted with telemetry equipment, it was fitted with slip rings to minimise electrical interference problems. The torque instrumentation chain for this vessel is shown schematically in figure 2.6.

Pitched blade turbines were studied pumping up and down. To achieve this the same impellers had to be rotated clockwise for upward pumping and anticlockwise for downward pumping. It was therefore necessary to determine the strain gauge calibrations in both directions of rotation. The calibration factors were checked by fitting a single Rushton turbine to the shaft and measuring its power number in both direction of rotation. For a range of impeller speeds, in the fully turbulent regime, the

average values were:

Clockwise:	Po = 4.78 (rsd = 0.5%)
Anticlockwise:	Po = 4.77 (rsd = 0.9%)

Thus the direction of shaft rotation had negligible effect on the power measurements.

2.3.3 Gas holdup

The methods available for measuring overall gas holdup in an agitated vessel were reviewed by Muskett (1987b). Muskett used an ultrasonic level detector to measure the difference in surface level between the ungassed state and the agitated, aerated state. This method, which was also used by Davies (1986) and Bujalski (1987), was adopted for this work.

The level change was measured using an ultrasonic level detector (Endress & Hauser Ltd., FMU2780 gauge with DU213 head). The level detector was positioned over the centre of a quadrant formed by two baffles, see figure 2.7. In accordance with the manufacturers instructions a vertical tube was fitted over the unit to reduce errors from stray ultrasonic signals reflected from the vessel internals.

The level detector had a voltage output range from 0 to 5 Volts. For calibration of the level detector the vessel was first filled with water to the ungassed operating depth, and the voltage output from the level detector was set to approximately 0.5 Volts. The vessel was then filled with water to the maximum expected dispersion level, and the voltage output from the level detector was set at approximately 4.5 Volts. The linearity of the level detector output was checked by reducing the liquid level, in stages, back to the ungassed operating depth, and plotting liquid depth against voltage output. In all cases the linearity of the detector output was excellent. The 0.61 m diameter vessel was made from perspex, and the 0.95 m diameter steel vessel was fitted with vertical sight glasses, so both vessels allowed accurate calibration of the level detector. Visual checks were regularly made of the gas dispersion level during the experiments, and excellent agreement was always obtained with the reading from the level detector.

Data acquisition was carried out using a PDP 11 laboratory computer fitted with a -5 to +5 Volt analogue to digital converter. The signal was filtered using a low pass filter set at 1.0 Hz to remove instrumentation noise. Data was collected at a sample frequency of 25 hz in four successive windows each lasting forty seconds. The measured holdup from each sample window was monitored to ensure no increasing or decreasing trends were present in the data, i.e. the dispersion had reached a steady state condition. The average level change over the four sample windows was then calculated.

2.3.4 Liquid mixing

Liquid mixing rates were measured by adding a pulse of electrolytic tracer (NaCl solution) to the liquid surface and recording the subsequent conductivity fluctuations using conductivity probes at different positions.

Khang and Levenspiel (1975) designed a conductivity probe for single phase liquid blending work, see figure 2.8. These probes were tested in gas liquid dispersions and found to be very sensitive to the presence of gas bubbles. All conductivity probes work by measuring the conductivity between two electrodes, and the response time of conductivity probes is generally in the order of a few milliseconds. Air has a much lower conductivity than salt solution so when a gas bubble passes between the probe electrodes the measured conductivity falls very rapidly. When the gas bubble leaves the conductivity measuring zone the conductivity signal returns rapidly to the correct value for the local salt concentration. Thus gas bubbles produce sharp downward spikes in the conductivity response curves, for example see figure 2.9(a). The problem with the Khang and Levenspiel probes was that one electrode consisted of a coiled wire, see figure 2.8, which tended to trap air bubbles. Probes supplied by EDT ltd, also shown in figure 2.8, were tested and found when carefully positioned, to be less susceptible to interference from gas bubbles than the Khang and Levenspiel probes. Figure 2.9 compares the conductivity responses of the EDT probe with that of a Khang and Levenspiel probe under identical conditions in a gas liquid dispersion (at a high gas flow rate). As gas holdup increased even the EDT probes became susceptible to interference from gas bubbles and under these conditions a course plastic mesh (mesh size approximately 2 mm $\times$ 2 mm) was wrapped around the probe tip, see figure 2.10. This mesh was found not to change the measured liquid mixing time but it did help to deflect some of the gas bubbles producing a cleaner conductivity signal. Even with the use of the mesh the EDT conductivity probes could not be used with gas holdup in excess of 10%.

The conductivity probes were energised by a conductivity meter manufactured by the instrumentation department of BHR Group Ltd. The output of the meter was a 0 to 200 mV analogue signal, directly proportional to the measured conductivity. The conductivity meter was designed to eliminate electrical interference between the probes. The conductivity instrumentation chain is shown in figure 2.11. The signal from the conductivity meter was amplified to $\pm$5 Volts, which was the input voltage range of the analogue to digital converter (ADC) used. Before passing to the ADC the signal was passed through anti-aliasing filters, the low pass cut off frequency of which depended on the sampling rate of the ADC. The computer collected 4096 data points for each experiment regardless of the sample time. The sample time was set so that it was three to four times the liquid mixing time. The conductivity transients were stored on the computer's hard disc for later analysis.

Clean tap water was used as the continuous phase of all experiments. In this liquid bubbles freely coalesce, i.e. every time two bubbles collide they coalesce to form one larger bubble. At high salt concentrations, bubble coalescence is suppressed by

electrostatic repulsion caused by ions collecting at the gas liquid interface. The degree of coalescence repression depends on the salt concentration and the valency of the salt ions. For sodium chloride (the tracer used in these mixing experiments) bubble coalescence is repressed above a concentration of 0.17 mol/l, refer to figure 2.12 from Oolman and Blanch (1985). A reduction in bubble coalescence would have a significant effect on mean bubbles size, gas holdup and potentially liquid mixing time. To avoid these hydrodynamic changes the vessel was drained and refilled with fresh water after a maximum of three mixing time experiments. Thus all experiments were conducted in a freely coalescing medium.

2.3.5 Mass transfer

The rate of transfer of oxygen from the gas to the liquid was measured using the dynamic gassing out technique. The impeller speed and air flow rate were set to the required values, and when the two phase flow patterns were fully established, the gas was changed from air to oxygen free nitrogen, at the same flow rate, to deoxygenate the liquid. When steady low values of dissolved oxygen level were recorded by all oxygen probes, (three probes were used in these experiments) the computer recording of the electrode output voltage was initiated. Ten to fifteen seconds later the gas was rapidly changed from nitrogen to air. The gas supply system was arranged so that this change could be completed as rapidly as possible. A manually operated three way valve was used to change between the nitrogen and air supplies. The gas supply system is shown in figure 2.13. The computer recording of the oxygen probe responses continued for five minutes allowing sufficient time for the system to reach equilibrium. Thus for each experiment, three dissolved oxygen transients were recorded.

The oxygen concentration in the liquid phase was measured using 'Electrosense' fast response oxygen probes, see figure 2.14. A thin membrane isolates the probe electrodes from the environment but allows oxygen and certain other gasses to enter. When a polarising voltage is applied across the sensor, oxygen which has passed through the membrane, reacts at the cathode causing a current to flow. The membrane passes oxygen at a rate proportional to the difference across it in partial pressure of oxygen. As the oxygen partial pressure varies both the oxygen diffusion through the membrane and the probe current change proportionately.

The probes had to be positioned in vigorously agitated regions to prevent gas bubbles clinging to the membrane and adversely affecting the probe readings.

The probes exhibited first order response characteristics with time constants from 0.5 to 1.5 seconds. Typically, oxygenation of the liquid was complete in 40 to 60 seconds and it was found, for all experiments, that the probe response time had negligible effect on the measured dissolved oxygen transients.

CHAPTER 3

FLOW PATTERNS AND POWER DRAW

3.1 INTRODUCTION

As shown in chapter 1, the power dissipated into a gas liquid dispersion directly influences liquid mixing, bubble sizes, gas holdup and the mass transfer rate. Thus the process requirements determine the minimum acceptable power input from the impellers. Most process designers will include a degree of over design to ensure that this minimum requirement is achieved. However, motor and compressor power costs represent the major running costs of a gas liquid reactor, and it is therefore important not to over design too much, or the process could become uneconomic.

The gassed power draw of an impeller is usually lower than its ungassed power draw. To avoid the requirement for very large motors, large scale reactors are often fitted with two speed motors: low speed for ungassed conditions, and high speed for gassed conditions, Hicks and Gates (1976). In these cases the gassed power draw and torque of the impellers determines the motor / gearbox selection and the shaft design. Thus it is also from mechanical design requirements that it is necessary to be able to predict accurately the gassed power draw of an agitator.

As shown in chapter 1, there are no reliable correlations available for predicting the power draw and torque of multiple impellers under gassed conditions. The only correlations presented in the literature are empirical curve fits which are geometry and scale specific.

In this chapter power measurements are presented, for a range of impeller speeds and gas flow rates, for single impellers mounted in standard geometry vessels, and combinations of those impellers in the tall vessel geometry. The power draw of each impeller in the multiple impeller combinations was measured separately using shaft mounted strain gauges, refer to chapter 2, allowing direct comparison with the single impeller measurements. The objective of this work was to identify relationships between the power draw of single impellers and multiple impeller combinations.

Four different triple impeller combinations were studied in the 0.61 m diameter tall vessel:

1. 3 × RT (all of identical design)
2. 1 × RT (lowest position) + 2 × LE20 (both pumping down)
3. 1 × RT (lowest position) + 2 × 4PBT impellers (both pumping down)
4. 1 × RT (lowest position) + 2 × 4PBT impellers (both pumping up)

The second objective of this work was the comparison of the power draw of these impeller combinations.

To help with the interpretation of the gassed power data, observations of the gas liquid flow patterns are also presented. Visual observations were not possible in the larger (T = 0.95m) stainless steel vessel, but power measurements were made with combinations 1 and 2.

One futher objective of this work was to determine the best method of predicting gassed power draw for multiple impeller combinations. A method of estimating the gassed power draw for multiple Rushton turbines is presented which takes account of the different hydrodynamic regimes on the lowest and upper impellers. The results of this estimation method are compared with the experimental measurements reported in this chapter, and with recent literature data from a larger, industrial scale (150 m^3) vessel.

3.2 RESULTS FROM THE 0.61 m DIAMETER VESSEL

Four triple impeller combinations were studied in this vessel:

1. 3 × RT (all of identical design)
2. 1 × RT (lowest position) + 2 × LE20 (both pumping down)
3. 1 × RT (lowest position) + 2 × 4PBT impellers (both pumping down)
4. 1 × RT (lowest position) + 2 × 4PBT impellers (both pumping up)

The diameter of the Rushton turbines was 0.315T. The diameter of all the LE20 and pitched blade turbine impellers was approximately 0.5T. Details of the vessel and impellers are given in chapter 2.

The same Rushton turbine was used as the lowest impeller in all four combinations, and the same pitched blade turbines were used in combinations 3 and 4. The only difference between combinations 3 and 4 was the direction of shaft rotation.

3.2.1 Ungassed power numbers

3.2.1.1 Single impellers

The ungassed power number of each impeller was measured in a standard geometry vessel of 0.61 m diameter, at a clearance of $T/3$ above the base, see figure 2.1. For all tests the impeller Reynolds number was greater than 10^4 (i.e. fully turbulent conditions), and the impeller speed was never high enough to draw gas down from the surface. In all cases, power number was found to be constant over the range of impeller speeds studied, see figure 3.1 which shows data for one impeller of each design. The average power number of each impeller is given in table 3.1.

Palmer (1987) conducted an extensive literature review of impeller power numbers, including the influence of impeller and blade geometries. Using Palmer's work, it was

possible to predict the ungassed power number of the Rushton and pitched blade turbines used in this thesis (LE20 impellers were not included in Palmer's review). Based on the impeller dimensions given in tables 2.1 and 2.2, the predicted ungassed power numbers were as follows:

Rushton turbine	:	4.71
PBT (pumping down):		1.33

The measured power numbers of the three Rushton turbines, see table 3.1, were all within 4% of the predicted value. The measured power numbers of the downward pumping pitched blade turbines, see table 3.1, were both within 3% of the predicted value. Slight differences in the measured power numbers of impellers, of the same design, were caused by minor geometrical differences such as sharpness of the blade edges.

The pitched blade turbines were found to have 4 to 6% higher power numbers when pumping up compared to the same impellers pumping down. This difference is close to the limits of experimental accuracy (±5%), as reported in section 2.3.2, so it is difficult to say, from the single impeller data alone, if there is a real effect of pumping direction on power number.

The measured power numbers of the LE20 impellers were within 3% of the manufacturers value of 0.35 (data from APV Ltd).

3.2.1.2 Multiple impellers

The ungassed power numbers for each impeller in the four combinations studied are given in table 3.2. The impeller separation for all combinations was 0.495 m, i.e. 2.6D for the Rushton turbines, and 1.6D for the larger LE20s and pitched blade turbines.

The power numbers of the Rushton and pitched blade impellers in the multiple impeller combinations were all within ±5% of their standard geometry values given in table 3.1. The power numbers of the LE20s, however, were 9% higher in the multiple impeller combination than when mounted alone in the standard geometry vessel.

For multiple impellers:

$$\text{Total power draw} = \rho_L N^3 \Sigma(Po\ D^5)$$

From table 3.2 the $\Sigma(Po\ D^5)$ for the triple Rushton turbine combination:

$$\Sigma(Po\ D^5)_C = (4.23 + 4.58 + 4.95) \times (0.191)^5 = 3.50\times10^{-3}$$

From table 3.1 the total of the individual Rushton turbine powers:

$$\Sigma(Po\ D^5)_I = (4.52 + 4.69 + 4.78) \times (0.191)^5 = 3.56\times10^{-3}$$

Thus $$\frac{\Sigma(PoD^5)_I}{\Sigma(PoD^5)_C} = 1.02$$

Similarly for the other impeller combinations:

Combination 2: $$\frac{\Sigma(PoD^5)_I}{\Sigma(PoD^5)_C} = 1.06$$

Combination 3: $$\frac{\Sigma(PoD^5)_I}{\Sigma(PoD^5)_C} = 0.99$$

Combination 4: $$\frac{\Sigma(PoD^5)_I}{\Sigma(PoD^5)_C} = 1.01$$

Except for combination 2, the total of the ungassed power draw of the triple impeller combinations was equal (±2%) to the sum of the individual impeller power draw from the standard geometry vessel.

3.2.2 Gas liquid flow patterns and power draw

The gassed power data are presented as plots of gassed power draw (P_g), or gassed to ungassed power ratio (P_g/P_u), versus gas flow number (Q_G/ND^3) at a range of constant impeller speeds. Thus the horizontal axis of all plots (gas flow number) is proportional to the gas flow rate. To simplify comparisons between single impellers and multiple impeller combinations containing impellers of different diameters, the gas flow number in all plots is based on the diameter of a Rushton turbine ($D = 0.315T$).

3.2.2.1 Single impellers

One impeller of each design was selected for visual observation of flow patterns and measurement of gassed power draw. These tests were conducted in a standard geometry vessel of 0.61 m diameter, see figure 2.1.

The flow patterns observed with a single Rushton turbine were the same as reported in chapter 1, refer to figure 1.1. The flow pattern transition from loading to flooding was determined by visual observation. For a fixed impeller speed this transition was defined as the gas flow rate at which the flow from the edges of the Rushton turbine blades changed from radial to vertical flow. The transition from flooding back to loading was also determined by visual observation, and the results are given in table 3.3. For a single Rushton turbine, the gas flow numbers at which the transition from loading to flooding was observed were 15% lower than those predicted from equation 1.1, from

Nienow (1977). This may be the result of a slightly smaller diameter of horizontal disc used on these impellers ($D_S = 0.68D$) compared with Nienow's impellers ($D_S = 0.75D$). The transition from flooding back to loading was found to occur at gas flow numbers 10 to 20% lower than the transition from loading to flooding.

Gassed power data, for a single Rushton turbine at three impeller speeds, are shown in figure 3.2(a). Gas flow rate had a significant effect on the power draw of this impeller with P_g/P_u falling as low as 0.43. Over the range of conditions studied, increased impeller speed resulted in only a slight reduction in power draw, due to increased gas recirculation. Data from Muskett (1987b), for a slightly larger Rushton turbine in the same scale of vessel, are included in figure 3.2(a) for comparison, and good agreement was obtained with the current data.

The flow patterns for single, downward pumping pitched blade turbines, and downward pumping LE20s, were similar to those reported in chapter 1, refer to figure 1.12.

Gassed power data for the downward pumping LE20 impeller are shown in figure 3.2(b). This impeller exhibited a sharp fall in power at very low gas flow numbers (corresponding to the indirect to direct loading transition, see section 1.2.1.2). In the direct loading regime large bubbles were observed rising from the impeller region and the power draw was independent of gas flow rate. The gassed power draw in the direct loading regime fell, as impeller speed was increased, due to increased gas recirculation.

Gassed power data for the downward pumping pitched blade turbine are shown in figure 3.2(c). Data from Muskett (1987b), for a four blade PBT, are included for comparison, and good agreement was obtained with the current data. At the highest gas flow rates studied the power draw of this impeller was still falling, i.e. it had not reached a steady value as observed with the LE20 impeller. This suggests that the transition from indirect to direct gas loading was not complete and that for all conditions studied this impeller was indirectly loaded with gas. Only at the lowest impeller speed and highest gas flow number were large bubbles observed rising from the impeller region, which are associated with the direct loading regime.

Gassed power data for the upward pumping pitched blade turbine are shown in figure 3.2(d). For a given impeller speed and gas flow rate the PBT drew more power pumping up than it did pumping down. This is the same trend observed by previous workers, see section 1.2.1.3.

The standard deviation of the torque signal was generally $\leq$10% of the mean value. The only exceptions to this occurred with the downward pumping pitched blade turbine, with the largest torque fluctuations (standard deviation of 22%) recorded at a low impeller speed and a gas flow number close to the direct / indirect loading transition. The largest torque fluctuations measured with the LE20 impeller had a standard deviation of 12%. In all cases, only high frequency torque fluctuations were observed. Large step changes in torque, as reported by Chapman (1981), were not observed under

any conditions with the impellers tested in this thesis.

3.2.2.2 Comparison of multiple impeller combinations

Figure 3.3 shows the effect of gas flow rate, for a range of fixed impeller speeds, on the total power draw of the four triple impeller combinations studied. The LE20 impellers were designed to draw the same ungassed power as the Rushton turbines, see chapter 2. Figures 3.2(a) and (b) show that, for a given impeller speed and gas flow rate, the single Rushton turbine and LE20 impellers behaved differently and drew different amounts of power. However, figure 3.3 shows that the 3RT and the RT+2×LE20 combinations actually had very similar gassed power draw over the whole range of impeller speeds and gas flow rates studied.

Ungassed, a single pitched blade turbine ($D \approx T/2$) drew approximately three times the power drawn by a single Rushton turbine ($D \approx T/3$), for a given impeller speed. At all speeds studied, both of the RT+2×PBT combinations drew approximately 2.4 times the ungassed power of the triple RT combination. When gassed, for all impeller speeds studied, both RT+2×PBT combinations maintained a higher power draw than the triple RT combination, with the upward pumping combination drawing more power than the downward pumping combination.

Figure 3.4 shows the effect of gas flow rate on the total P_g/P_u ratio for each impeller combination at a range of fixed impeller speeds. At low gas flow numbers there was little difference in the P_g/P_u ratios for the four impeller combinations studied. At high gas flow numbers the RT+2×PBT (pumping down) combination was most affected by gas, giving the lowest P_g/P_u values.

3.2.2.3 Triple Rushton turbines

The gas-liquid flow patterns observed with this impeller combination are shown in figure 3.5. At high impeller speeds and low gas flow rates, each Rushton turbine developed its own figure of eight flow pattern. With triple turbines, this resulted in a total of six distinct circulation loops in the vessel. As gas flow rate was increased, for a fixed impeller speed, the lowest Rushton turbine reached a point where it could no longer disperse gas below itself. At higher gas flow rates, the lowest Rushton turbine became flooded, and the flow around this impeller changed to one axial circulation loop. The middle and top Rushton turbines maintained their figure of eight flow patterns, giving a total of five distinct circulation zones in the vessel.

The measured power draw of each impeller in this impeller combination is shown in figure 3.6, for three constant impeller speeds and a range of gas flow rates. Figure 3.7 shows a flow map for this impeller combination, based on equations 1.1, 1.3 1.5 and 1.18, showing the experimental conditions at which power was measured.

At an impeller speed of 3.33 rps the middle and top turbines drew similar power, but significantly more power than the lowest turbine. These measurements support the prediction of the flow map, figure 3.7, that, for all gas flow rates tested at this impeller speed, large cavities were present on the lowest impeller and small cavities were present on the upper impellers.

As impeller speed was increased to 4.33 rps the P_g/P_u ratio of all impellers was slightly reduced due to increased gas recirculation. At this impeller speed the middle and top turbines again drew similar power and significantly more power than the lowest turbine. The flow map predicted large cavities on the lowest impeller and small cavities on the upper impellers except at the highest gas flow rate tested where 3-3 cavities were predicted for all three impellers. The flow map, however, makes no distinction between small 3-3 cavities and large 3-3 cavities.

As impeller speed was increased to 6.00 rps the P_g/P_u ratio of all impellers was again slightly reduced due to increased gas recirculation. The difference in power draw between the three impellers was less than found at lower impeller speeds. As impeller speed increases gas recirculation to the upper impellers also increases and at very high gas recirculation rates all impellers should draw the same power. The flow map shows that the power measurements at 6.00 rps were closer to the gross recirculation line than at lower speeds, and that none of the measurements were above this line. For gas flow numbers less than 0.10, the middle impeller drew more power than the top impeller. This can only be the result of greater gas recirculation into the top impeller compared to the middle impeller. It is unclear why this effect was observed only at this impeller speed but may be related to the baffle geometry (there was a gap in the baffles between the middle and top impellers, see chapter 2).

By comparing the power curves of the upper impellers with that of the lowest impeller, for a given P_g/P_u value, the fraction of gas recirculated into the upper impellers can be estimated, for example see figure 3.6(c). At a sparger gas flow number of 0.100 the effective gas flow number at the middle impeller was 0.036, thus 36% of the sparge gas was recirculated into the middle impeller under these conditions. At a sparger gas flow number of 0.056 the effective gas flow number at the top impeller was 0.036, thus 65% of the sparger gas flow rate was recirculated into the top impeller. Figures 3.6(a), (b) and (c) were analysed in this way, for a range of sparger gas flow rates, and the results are summarised in table 3.4. For a given gas flow rate, as impeller speed was increased the fraction of gas recirculated to the upper impellers increased. For a given impeller speed, as sparger gas flow rate was increased, a lower fraction of the sparger gas was recirculated to the upper impellers. At 3.33 and 4.33 rps, the gas flow rate into the top and middle impellers was similar, for a given impeller speed and gas flow rate, and varied from 28% to 54%. These values are similar to the values reported in the literature for multiple Rushton turbines of identical design, see section 1.2.2.2. At 6.00 rps, much more gas was recirculated into the top impeller compared to the middle impeller, as mentioned above.

Power measurements for a single disc turbine mounted in a standard geometry vessel are included in figures 3.6(a) and (b). For a given gas flow number, the lowest Rushton turbine drew up to 20% less power than it did when mounted alone in a standard geometry vessel.

Figures 3.6(a) and (b) also show the range of gas flow numbers over which the flooding / loading transition was observed for the lowest impeller in the triple turbine combination. The higher value of gas flow number corresponds to the transition from loading to flooding with increasing gas flow rate. The lower value of gas flow number corresponds to the transition from flooding back to loading with decreasing gas flow rate, refer to table 3.3. The flooding / loading region observed with the lowest Rushton turbine, mounted alone in a standard geometry vessel, is included for comparison. It can be seen that in the triple Rushton turbine combination flooding of the lowest impeller occurred at lower gas flow numbers than in the standard geometry vessel. At 6.00 rps, the lowest turbine was not flooded at the highest gas flow rate tested.

Table 3.3 also includes flooding loading observations at a reduced impeller spacing of 0.300 m. At this reduced impeller separation, the lowest Rushton turbine flooded at even lower gas flow numbers, for a given impeller speed.

3.2.2.4 1 Rushton turbine + 2 LE20 combination

The gas-liquid flow patterns observed with this impeller combination are shown in figure 3.8. At high impeller speeds and low gas flow rates, intense recirculation loops were formed below the blades of each LE20. This intense circulation loop was not observed with a single LE20 mounted in a standard geometry vessel because, at an impeller clearance of $T/3$, the circulation loop did not have room to form. In the tall vessel, the flow from the top LE20 did not combine with that of the middle LE20. Instead, a reverse circulation loop separated the impellers. The upper recirculation loop of the Rushton turbine did combine with the intense recirculation loop formed below the middle LE20. In total, four distinct circulation loops were observed. As gas flow rate was increased, for a fixed impeller speed, the Rushton turbine reached a point where it could no longer disperse gas below itself. However, the flow patterns above this impeller remained unchanged. At higher gas flow rates, the Rushton turbine became flooded, some gas rose directly into the middle LE20 and some gas was thrown out to the vessel wall by the pumping action of this impeller. The intense recirculation loops previously observed below the blades of each LE20 were no longer present. Only a small amount of gas seemed to be recirculated into the LE20s, and most of the gas rose very rapidly at the wall of the vessel. This rapid rise was occasionally disrupted by the formation of a small circulation loop between the LE20s.

Gassed power data for this impeller combination are shown in figure 3.9. At all impeller speeds studied, the lowest impeller (a Rushton turbine) drew slightly less power (up to 20% less) than it did when mounted alone in a standard geometry vessel.

Figures 3.9(a) and (b) also show the range of gas flow numbers over which the flooding / loading transition was observed for the Rushton turbine. It can be seen that the presence of the LE20 impellers in the tall tank reduced the gas flow numbers at which the Rushton turbine flooded and reloaded compared with a single Rushton turbine in a standard geometry vessel. Table 3.3 also includes flooding observations for this impeller combination at a reduced impeller separation of 0.300 m. When impeller separation was reduced, the lowest Rushton turbine flooded at higher gas flow numbers, for a given impeller speed.

When a Rushton turbine floods, the power draw of the impeller rises slightly, see section 1.2.1.1. This was observed at 4.33 rps but not at 3.33 rps (refer to figure 3.9(a) and (b)). However, visual observations confirmed that at 3.33 rps, the Rushton turbine was flooded above a gas flow number of 0.058. At the same time that the Rushton turbine flooded, the power of the top LE20 increased slightly and the power draw of the middle LE20 fell (this is clearly illustrated in figure 3.9(b) but can also be seen in figure 3.9(a)). As described above, when the Rushton turbine changed from the loaded to the flooded condition, some gas flowed directly into the middle LE20 and recirculation into the top LE20 was reduced. Thus the power measurements support the flow patterns described in figure 3.8.

At low impeller speeds, the top and middle LE20s drew different amounts of power for a given impeller speed and gas flow number. However, as impeller speed was increased this difference disappeared and, at 5.00 and 6.00 rps, both LE20s drew exactly the same power at a given gas flow rate.

The power draw of the LE20s in the tall vessel are compared with the power draw of a single LE20, mounted in a standard geometry vessel, in figure 3.10. At 3.33 rps, the middle LE20 drew similar power to the single impeller, but the top LE20 drew significantly more power with P_g/P_u exceeding 1.0 at very low gas flow numbers. This phenomenon was not observed with the single LE20 in a standard geometry vessel, but it has been observed with similar impeller designs (e.g. marine propellers) in standard geometry vessels at very low gas flow rates, Chapman et al (1983). This was attributed to the presence of just a few gas bubbles close to the surface of the impeller blades, causing detachment of the boundary layer flow from the blade surface and resulting in increased drag.

At 4.33 and 5.00 rps, the power curves of the middle and top LE20s developed the characteristic shape observed in the standard geometry vessel, i.e. high P_g/P_u at low gas flow numbers followed by a sharp fall in power corresponding to the transition from indirect to direct loading. The rapid fall in power occurred at higher sparger gas flow rates in the tall vessel than found in the standard geometry tank. This suggests that, as with multiple Rushton turbines, only a fraction of the sparge gas was recirculated into the LE20s in the tall vessel. From figure 3.10(c) it can be estimated that approximately 40% of the sparge gas was recirculated into the upper impellers before the indirect to direct loading transition occurred. Following the rapid fall in power, P_g/P_u for the

LE20s in the tall vessel levelled out at lower values than observed in the standard geometry vessel, suggesting that under these conditions gas recirculation was greater in the tall vessel. As discussed above, intense recirculation loops were observed below the LE20 impellers in the tall vessel which were not observed in a standard geometry vessel. The power data suggests that although gas was recirculating in these loops it did not actually enter the impeller blades until the transition from indirect to direct loading occurred.

3.2.2.5 Rushton turbine + 2 PBT (pumping down) combination

The gas-liquid flow patterns observed with this impeller combination are shown in figure 3.11. At high impeller speeds and low gas flow rates, intense recirculation loops were formed at the edges of the pitched blade turbine blades. Large reverse flow loops developed between all impellers and none of the impeller flow patterns combined. A total of six distinct circulation loops were observed in the vessel. As gas flow rate was increased, for a fixed impeller speed, the lowest Rushton turbine reached a point where it could no longer disperse gas below itself. However, the flow patterns above the Rushton turbine remained unchanged. At higher gas flow rates, the Rushton turbine became flooded. Gas rose straight up from the flooded Rushton turbine and was then thrown out to the vessel wall by the intense circulation loop produced by the middle PBT. A large axial circulation loop was formed around the Rushton turbine by the gas flow, with significant amounts of gas being carried downwards at the vessel wall as far as the Rushton turbine.

Gassed power data for this impeller combination are shown in figure 3.12. At 3.33 rps, the Rushton turbine drew the same gassed power as it did when mounted alone in a standard geometry vessel. However, at higher impeller speeds (4.33 and 5.00 rps) this impeller drew slightly less power (up to 20% less) in the tall tank.

At all speeds studied, the pitched blade turbines in the middle and top positions drew the same power as they did when mounted alone in the standard vessel, see figure 3.13. This suggests that all of the sparge gas was recirculated into the PBT blades by the intense recirculation loops shown in figure 3.11, and that under all conditions, the downward pumping PBTs were indirectly loaded, as they were in the standard geometry vessel, (i.e. gas entered the impeller blades from above rather than from below).

3.2.2.6 Rushton turbine + 2 PBT (pumping up) combination

The gas-liquid flow patterns observed with this impeller combination are shown in figure 3.14. At high impeller speeds and low gas flow rates, intense recirculation loops were formed at the edges of the pitched blade turbine blades, in exactly the same way as observed with the downward pumping PBTs, except for the opposite direction of circulation. A large reverse flow loop developed between the PBTs, but one did not form between the middle PBT and the Rushton turbine. A total of six distinct

circulation loops were observed. As gas flow rate was increased, for a fixed impeller speed, the lowest Rushton turbine reached a point where it could no longer disperse gas below itself. However, the flow patterns above the Rushton turbine remained unchanged. At higher gas flow rates, the Rushton turbine became flooded. Even with the Rushton turbine flooded, its upper circulation loop remained in place and gas was pushed out to the vessel wall to be incorporated into the intense recirculation loop around the middle PBT. Some gas was also carried down the centre of the vessel towards the Rushton turbine. At very high gas flow rates, the buoyancy of the gas would probably cause it to rise directly into the middle PBT, but such high gas flow rates were not studied.

Gassed power data for this impeller combination are shown in figure 3.15. The Rushton turbine drew slightly less power in this combination than it did when mounted alone in a standard vessel. At low speeds (3.33 and 4.33 rps), there was a slight difference between the power draw of the middle and top pitched blade turbines. In both cases, the top PBT drew more power than the middle PBT. In both cases the top PBT behaved in the same way as a single upward pumping PBT mounted in a standard vessel, see figure 3.16. At higher impeller speeds, the middle and top PBTs drew the same power as a single PBT in a standard vessel.

3.3 RESULTS FROM THE 0.95 m DIAMETER VESSEL

Two triple impeller combinations were studied in this vessel:

1. 3 Rushton turbines
2. 1 Rushton turbine (lowest position) + 2 LE20 impellers (both pumping down)

The vessel and impellers were geometrically identical to those tested at the smaller scale, refer to chapter 2. The 0.95 m diameter vessel was manufactured from stainless steel and although it was fitted with sight glasses, visual observation of the bulk flow patterns was not possible.

3.3.1 Ungassed power numbers

3.3.1.1 Single impellers

For the Rushton turbine geometry used in this vessel, see table 2.1, Palmer (1987) predicted an ungassed power number of 5.05.

The manufacturer's value of ungassed power number for the LE20 impellers at this scale was 0.35.

3.3.1.2 Multiple impellers

The ungassed power numbers of each impeller, in both impeller combinations are given in table 3.5. For both impeller combinations the power number of the lowest Rushton turbine was slightly higher (up to 6.7% higher) than its standard geometry value. The power numbers of both upper Rushton turbines in combination 1 were both lower than their standard geometry value, but by less than 5%. As observed in the 0.61 m diameter vessel, the power numbers of both LE20 impellers, in combination 2, were significantly higher (up to 20% higher in this vessel) than their standard geometry value.

Using the power numbers given in table 3.5 and section 3.3.1.1:

For combination 1: $$\frac{\Sigma(PoD^5)_I}{\Sigma(PoD^5)_C} = 0.99$$

For combination 2: $$\frac{\Sigma(PoD^5)_I}{\Sigma(PoD^5)_C} = 1.15$$

As found in the 0.61 m vessel, for the triple Rushton turbine combination, the total of the ungassed power measured in the tall tank, was equal to the sum of the individual impeller power from the standard geometry vessel. Again, this was not true for the RT+2×LE20 combination due to the higher power draw of the LE20 impellers in the tall vessel, compared to the standard vessel.

3.3.2 Gassed power draw

3.3.2.1 Triple Rushton turbines

Figure 3.17 shows the flow map for the power measurements in this vessel. The gassed power data are shown in figure 3.18. At the lowest impeller speed studied, 3.33 rps, the upper turbines drew more power than the lowest turbine. This agrees with the flow map which, for the lowest gas flow number studied, predicted smaller cavities on the upper impellers than on the lowest impeller. As impeller speed was increased, this difference between the power draw of the three impellers disappeared. As the flow map shows, most of the data above 3.33 rps lie in the region in which 3-3 cavities exist on all impellers. At the highest impeller speeds studied, the data are very close to the recirculation line, equation 1.3, which agrees with the observation that under these conditions all three impellers drew the same power.

Data for 7.00 rps is omitted from figure 3.18 because it is very similar to the power data of 6.33 rps.

3.3.2.2 Rushton turbine + 2 LE20 combination

The gassed power curves for this impeller combination are shown in figure 3.19.

The flatness of the LE20 power data indicates that, for the range of conditions studied in this vessel, the rapid fall in power observed with the LE20 impellers had already occurred, i.e. the LE20 impeller were directly loaded with gas.

As found in the 0.61 m diameter vessel, for a given impeller speed and gas flow rate, the total P_g/P_u values for this impeller combination were very similar to those of the triple Rushton turbine combination, see figure 3.20.

3.4 EFFECT OF SCALE

The effect of scale on the power data of the triple Rushton turbine combination is shown in Figure 3.21. Data are compared at constant Froude number and also at constant ungassed power draw. At constant Froude and gas flow number, the P_g/P_u ratios of each Rushton turbine are very similar at both scales. This is to be expected because Froude and gas flow numbers determine the gas cavity structure on the impeller blades. Scale up at constant ungassed power draw results in a lower Froude number at larger scale. As figure 3.21(b) shows, at constant ungassed power draw there is little difference between the gassed power data from both scales. This is because the two scales are not sufficiently different to result in a significant change in Froude number.

Figure 3.22 shows similar scale comparisons for the RT+2×LE20 combination. As with the triple Rushton turbine combination scale up at constant Froude and gas flow numbers results in the same P_g/P_u ratios for each impeller. No data are available for comparison of scale at constant ungassed power draw.

3.5 DISCUSSION OF RESULTS

3.5.1 Ungassed flow patterns and power draw

At an impeller separation of $0.8T$ in the tall vessel, the ungassed power numbers of the Rushton turbines ($D = 0.315T$) and the pitched blade turbines ($D = 0.5T$) were the same as measured in, or predicted for, the standard geometry vessels. The flow patterns observed around the blades of these impellers were very similar in both vessel geometries and there was no significant interaction between the impellers in the tall vessel. This was not true for the LE20 impellers ($D = 0.5T$), and significant differences in ungassed power number and flow patterns were observed between the standard and tall vessel geometries. At both scales, the LE20 impellers were found to have higher ungassed power numbers in the tall vessel compared to those measured in the standard

vessel geometry. In a standard geometry vessel, the flow patterns observed with a single LE20 impeller were similar to those observed with a single pitched blade turbine. That is, fluid flowed downward and out from the centre of the impeller, around the tips of the impeller blades and re-entered the impeller from above, see figure 1.12(d). With the LE20s in the tall vessel, this flow was also observed but an additional intense circulation loop was observed below the impeller blades, as shown in figure 3.8. This intense circulation loop did not have room to form in the standard geometry vessel because of the proximity of the vessel base. The LE20 power number was 9% higher in the 0.61 m diameter vessel and up to 20% higher in the 0.95 m diameter vessel showing that there is a significant scale effect.

In both the standard geometry and tall vessels, the pitched blade turbines had slightly higher ungassed power numbers when pumping up compared to when pumping down. This difference is at the limits of experimental accuracy but there does seem to be a systematic effect of pumping direction on power number. Muskett (1987b) observed the opposite trend, i.e. higher power number pumping down, with a six blade pitched blade turbine in a standard geometry vessel and explained this as a result of the downward pumping impeller experiencing higher resistance to flow because it had to pump against the vessel base. In the multiple impeller geometries studied in this thesis, the impellers were far from the vessel base and yet the same effect of pumping direction was observed in both the standard geometry and tall geometry vessels. Bujalski (1987) measured power numbers for upward and downward pumping six blade pitched blade turbines in standard geometry vessels of 0.29 to 1.83 m diameter and found that in some cases power number was higher when pumping up and in some cases power number was lower when pumping up, but there were no trends in his data. The maximum difference in power number was 6%, and for $D \leq T/2$, Bujalski concluded that power number was independent of pumping direction. In conclusion there seems to be a slight effect of pumping direction on power number, which is geometry specific, but from a design point of view is negligible.

3.5.2 Gassed flow patterns and power draw

For single impellers in the standard geometry vessel, the transition from indirect to direct loading occurred at lower gas flow numbers for the LE20 compared to the downward pumping pitched blade turbine. The pitched blade turbine had a similar total projected blade area (37% of the projected swept area) to the LE20 impeller (36% of the projected swept area). However, the LE20 only had three blades, compared with the four of the pitched blade turbine, and the blade angle (to the horizontal) of the LE20 was smaller, see tables 2.2 and 2.3. In addition, the ungassed power number of the PBT was 1.34 compared with 0.34 for the LE20, so for a given impeller speed the power draw of the pitched blade turbine was approximately four times that of the LE20. All of these factors helped the pitched blade turbine to avoid direct gas loading at higher gas flow numbers than the LE20.

Generally, in all the multiple impeller combinations studied, the lowest impeller (always a Rushton turbine) drew slightly less (maximum of 20% less) gassed power compared to a single Rushton turbine mounted alone in a standard geometry vessel.

Even with a large impeller separation of 0.8*T* the lowest impeller, in both the 3×RT and RT+2×LE20 combinations, flooded at lower gas flow numbers than when mounted alone in a standard geometry vessel. Previous workers have also reported this effect for multiple Rushton turbines but only at smaller impeller separation distances than tested here, Hudcova (1987) and Abrardi (1988), refer to section 1.2.2.2. At a reduced impeller separation of 0.49*T*, the gas flow number at which the lowest impeller flooded was again reduced for the 3×RT combination but it was increased for the RT+2×LE20 combination. Using a small impeller separation for multiple Rushton turbines results in flow interactions which produce up flow through the lowest impeller, refer to figures 1.16 and 1.17(b), (this flow pattern was observed in this work at an impeller separation of 0.49*T*). Thus the lowest impeller floods at lower gas flow rates. With the RT+2×LE20 combination at a small impeller separation, the down force from the middle LE20 on the lowest Rushton turbine was increased, stabilising the loading regime. The stabilising effect of the LE20 allowed the Rushton turbine to disperse more gas than it did when mounted alone in a standard geometry vessel.

With the RT+2LE20 combination, the rapid fall in power observed in the standard geometry vessel, associated with the transition from indirect to direct gas loading, was also observed in the tall vessel. Thus in the tall vessel, where the lowest impeller distributes the gas across the vessel cross section, the upper impellers can still become effectively directly loaded with gas. For all experiments in the 0.95 m diameter vesel the power data indicates that the LE20 impellers were directly loaded with gas.

For both RT+2×PBT combinations, the PBT impellers drew the same gassed power as they did in the standard geometry vessel. This was because, in both cases, the PBT impellers drew a lot of power and totally domimated the hydrodynamics in both vessels, producing intense localised recirculation loops.

Scale up at constant Froude and gas flow numbers produced the same gas cavity structures at both scales and therefore the P_g/P_u ratios are the same at both scales. For both Rushton turbines and LE20s gas cavities are determined by *Fr* and *Fl*. In scale up, power / unit mass would generally be maintained constant, so *Fr* would fall as scale increased, reducing gas recirculation to the upper impellers and resulting in higher P_g/P_u ratios.

3.6 PREDICTION OF GASSED POWER DRAW FOR MULTIPLE RUSHTON TURBINES

As section 1.2.1.1 showed, empirical correlations exist for predicting the gassed power draw of a single Rushton turbine. To extend the use of these correlations to multiple impellers the fraction of sparge gas which enters the upper impellers must be estimated. The power draw of the upper impellers can then be estimated based on this fraction of the sparger gas flow rate.

The flow maps shown in figures 3.8 and 3.16 can be used to estimate the fraction of sparger gas entering the upper impellers. For a given Froude number, equation 1.5 gives the gas flow number at which 3-3 cavities develop on the lowest impeller, and equation 1.18 gives the gas flow number at which 3-3 cavities develop on the upper impellers. The ratio of these two gas flow numbers gives an estimate of the percentage of gas entering the upper impellers. Thus, at low Froude numbers, this percentage is small and as Froude number increases it reaches 100% at the intersection of equations 1.5 and 1.3. This is a simplistic way of estimating the gas flow into the upper impellers because the gas recirculation rate into the upper impellers is also a function of the gas flow number. The percentage of gas flowing into the upper impellers tends to be higher at low gas flow numbers than it is at high gas flow numbers, Nienow et al (1979).

Table 3.6 shows a summary of the results of this analysis for both the 0.61 m and the 0.95 m vessels. The percentages given in table 3.6 for the 0.61 m vessel are similar to those given in table 3.4 which were estimated from the gassed power curves, see section 3.2.2.3. Using Smith's correlations, see section 1.2.1.1, and the percentage of gas flowing into the upper impellers, from table 3.6, the gassed power draw of each impeller was predicted, (this includes the effect of gas expansion as the gas rises through the vessel, assuming the gas to be ideal). The predictions are compared with the experimental power measurements in figure 3.23.

For the 0.61 m vessel the predictions are very good at 3.33 and 4.33 rps but not so good at 6.00 rps, with the predictions tending to be low. For the 0.95 m diameter vessel the predictions are good at 3.33 and 4.33 rps but again tend to under predict the true power draw at 6.33 rps. In terms of Froude number the power predictions are good for $Fr < 0.6$, but under predict power for $Fr > 0.7$.

Seichter (1992) compared gassed power measurements from as range of vessel scales up to 150 m^3 with various literature correlations, see section 1.2.2.2. The above approach for predicting gassed power draw was adopted for the vessel geometry described in Seichter's work. Seichter's vessel was 10 m deep so gas expansion has a significant effect on the estimated gas flow rate into each impeller region.

From equation 1.5 the gas flow number at which 3-3 cavities formed on the lowest impeller was:

$Fl_{3\text{-}3,L} = 0.0392$

From equation 1.18 the 3-3 cavity transition on the upper impellers occurred at:

$$Fl_{3\text{-}3,U} \times Fr = 0.0267 \qquad \text{...Eqn(3.1)}$$

Seichter's 150 m^3 vessel had a fixed impeller speed of 1 rps, and the impeller diameter was 1.46 m. Thus Fr = 0.149.

From equation 3.1: $Fl_{3\text{-}3,U} = 0.179$

All the Rushton turbines were of identical design, so the 3-3 cavity transition must occur at the same local gas flow rate for a given impeller speed. $Fl_{3\text{-}3,L}$ and $Fl_{3\text{-}3,U}$ are both based on the sparger gas flow rate. Thus the fraction of sparger gas entering the upper impellers is given by the ratio:

$$\frac{Fl_{3\text{-}3,L}}{Fl_{3\text{-}3,U}} = \frac{0.0392}{0.179} = 0.22$$

It was assumed that, as gas flowed up the vessel it expanded ideally, but only 22% of the corrected gas flow rate entered the upper impeller regions. The predictions of Smith's correlations are shown in figure 3.23(g). The top impeller draws less power than the middle impeller because of the gas expansion effect. The total P_g/P_u values predicted by this method are compared with Seichter's measured values showing good agreement. Again the predictions underestimate at low gas flow numbers and overestimate at high gas flow numbers, due to the influence of gas flow number on gas recirculation rates. The predictions using this method are closer to Seichter's measurements than any of the literature curve fits tested in Seichter's paper.

The advantage of this prediction method is that it takes account of the different cavity regimes found on the blades of the different impellers. The main limitations of this approach are that it is only as good as the empirical correlation for single Rushton turbines, and it does not account for the effect of gas flow number on recirculation into upper impellers.

3.7 CONCLUSIONS

Ungassed

1. The measured power number of the LE20 impeller, in a standard geometry vessel, was within 3% of the manufacturers value.

2. The measured power numbers of the Rushton turbine and pitched blade turbines, in a standard geometry vessel, were within 4% of those predicted by Palmer (1987).

3. The power numbers of the pitched blade turbines were up to 6% higher when pumping upward than they were when pumping downward. This effect of pumping direction on power number was observed in both a standard geometry vessel and a tall vessel showing that proximity to the vessel base was not an influencing factor (for $c_l > T/3$). In terms of design this is only considered to be a minor effect.

4. At an impeller separation of $0.8T$ in the tall vessel the power numbers of the Rushton turbines and pitched blade turbines were the same as measured in the standard geometry vessel. The flow patterns observed with both types of impeller were very similar in both vessel geometries and there was no significant flow interaction in the multiple impeller geometries.

5. The Power number of the LE20 was 9 to 20% higher in the tall vessel than in a standard geometry vessel. This is believed to be the result of the different flow patterns observed in the two vessel geometries. In the tall vessel an intense circulation loop was observed below the blades of the LE20 which did not form in the standard geometry vessel, due to the proximity of the vessel base.

Gassed

1. For a given impeller speed the LE20 impellers became directly loaded with gas at lower gas flow numbers than the downward pumping pitched blade turbines.

2. In all impeller combinations studied, the lowest impeller (always a Rushton turbine) generally drew slightly less gassed power (maximum of 20% less) compared to a single Rushton turbine mounted alone in a standard geometry vessel.

3. With multiple Rushton turbines at an impeller separation of $2.6D$ the flooding transition of the lowest impeller occurred at lower gas flow numbers than found with a single impeller mounted in a standard geometry vessel. For a smaller impeller separation of $1.6D$ the flooding transition was found to occur at even lower gas flow numbers. This was caused by flow interactions producing up flow through the lower impeller.

4. With the RT+2×LE20 combination at an impeller separation of 0.8T the flooding transition of the lowest impeller occurred at lower gas flow numbers than found with a single Rushton turbine mounted in a standard geometry vessel. For a smaller impeller separation of 0.49T the flooding transition was found to occur at higher gas flow numbers due to the stabilising effect of the down force from the middle LE20 impeller.

5. For all impeller combinations studied in the tall vessel, the flow patterns were compartmentalised. One top to bottom circulation loops was never observed.

6. For the triple Rushton turbine combination the upper impellers drew more power than the lowest impeller at low impeller speeds, because only a fraction of the sparger gas was recirculated into the upper impellers.

7. In the upper impeller positions, in the tall vessel geometry, the downward pumping LE20 impellers exhibited the sharp fall in power draw, associated with the indirect to direct gas loading transition, even though they were not directly sparged with gas.

8. For all test conditions studied in the 0.95 m diameter tall vessel, the LE20 impellers were directly loaded with gas.

9. For the RT+2×PBT combinations (PBTs pumping up or down) the pitched blade turbines drew the same gassed power as they did when mounted alone in a standard geometry vessel.

10. Although the total absolute gassed power draw of the impeller combinations studied were very different, the P_g/P_u ratios were similar for a given impeller speed and gas flow rate.

11. On scale up from the 0.61 m diameter vessel to the 0.95 m diameter vessel, the gassed power curves for a given impeller combination (3×RT and RT+2×LE20 combinations only) were very similar at constant Froude and gas flow numbers.

12. The cavity regime flow map developed by Smith et al (1987) was found to be useful in qualitatively describing the gassed power data from the triple Rushton turbine combination.

13. A method is presented for estimating the fraction of gas entering the upper impellers of a multiple Rushton turbine combination which makes use of the flow map approach developed by previous workers. This was combined with empirical correlations, for predicting the gassed power draw of a single Rushton turbine, to predict the gassed power draw of multiple Rushton turbines. This approach was found to work quite successfully at Froude numbers < 0.6. However, at $Fr > 0.7$ the method under predicted the power.

CHAPTER 4

GAS HOLDUP

4.1 INTRODUCTION

As discussed in chapter 1, it is important to be able to predict gas holdup in a gas liquid reactor because it determines the maximum liquid volume, in a fixed volume reactor, and therefore product yield. Overall gas holdup is also a relatively easy to measure parameter which, for the air water system at least, is approximately related to the interfacial area available for mass transfer. In standard geometry systems gas holdup has been shown to be related to power input and gas superficial velocity, and virtually independent of impeller design (assuming the gas is well dispersed).

This chapter presents gas holdup measurements for four triple impeller combinations at two scales. The aim of these experiments was to find holdup relationships between single and multiple impeller geometries, and to see if there are any significant differences in gas holdup between the multiple impeller combinations studied.

The gas holdup was measured using an ultrasonic level detector, refer to chapter 2.

4.2 RESULTS FROM THE 0.61m DIAMETER VESSEL

Four triple impeller combinations were studied in this vessel:

1. 3 Rushton turbines
2. 1 Rushton turbine + 2 LE20s (both pumping downwards)
3. 1 Rushton turbine + 2 PBTs (both pumping downwards)
4. 1 Rushton turbine + 2 PBTs (both pumping upwards)

Combinations 1 and 2 were designed to draw the same ungassed power for a given impeller speed. Combinations 3 and 4 were not designed in this way and, for a given impeller speed, drew significantly more power than combinations 1 and 2, see chapter 3.

The holdup measured with these four impeller combinations, at a range of impeller speeds and gas flow rates, are given in tables 4.1 to 4.4. The holdup data from each impeller combination were correlated using:

$$\varepsilon_G = \alpha\ (N)^{\beta}\ (Q_G)^{\gamma} \qquad \text{...Eqn(4.1)}$$

and $\varepsilon_G = \alpha\ (\varepsilon_m)^{\beta}\ (V_{sg})^{\gamma}$ ...Eqn(4.2)

The results are shown in tables 4.5 and 4.6. There was no significant difference between the two correlating methods in terms of the quality of fit of the data, when applied to a given impeller combination.

An F test showed that there was no significant difference between the 3RT and RT+2×LE20 correlations. This was true for a given impeller speed and gas flow rate, or a given power input and superficial gas velocity. F tests also showed that the RT+2×PBT (pumping up) and the RT+2×PBT (pumping down) correlations were each significantly different to the correlations for the other three impeller combinations.

The data from all four impeller combinations were combined and correlated, using equations 4.1 and 4.2. The results are given in tables 4.5 and 4.6. The data fit to these combined correlations was worse than for any of the individual data sets. F tests showed that the combined impeller speed / gas flow rate correlation was significantly different to both RT+2×PBT correlations. The combined power / superficial gas velocity correlation was significantly different to the RT+2×LE20 and the RT+2×PBT (pumping up) correlations.

In figure 4.1 the holdup data from all four impeller combinations are plotted against the 3RT correlation based on impeller speed and gas flow rate. This figure shows that at low gas holdup (below approximately 8%), for a given impeller speed and gas flow rate, both of the RT+2×PBT combinations produced significantly more holdup than the 3RT and RT+2×LE20 combinations. It was shown in Chapter 4 that, for a given impeller speed and gas flow rate, both of the RT+2×PBT combinations drew significantly more power than the 3RT and RT+2×LE20 combinations. At high gas holdup (above 8%) all four impeller combinations produced similar gas holdup for a given impeller speed and gas flow rate.

When compared at the same gassed power input and superficial gas velocity, see figure 4.2, all four impeller combinations produced similar gas holdup (below 8% holdup). At high holdup (above 8%) the holdup values for all four impeller combinations fall below the 3RT correlating line. As shown in chapter 1, gas holdup does tend to level out at high power inputs and gas velocities. At the highest gas holdups measured (13 to 15%) all four impeller combinations produced similar holdup but the power draw of the 1RT+2×PBT (pumping up) combination was 150% greater than the power draw of the 3RT combination.

The holdup data from the 3RT combination were recorrelated, including the isothermal expansion energy of the gas with the impeller power draw in equation 4.2, see table 4.15. The data fit to this correlation was slightly worse than for the correlation based solely on the impeller power draw, table 4.6. The inclusion of

gas expansion energy in the correlation increased the exponent on power input, from 0.31 to 0.34, and decreased the exponent on superficial gas velocity, from 0.75 to 0.71. An F test showed that the inclusion of gas expansion energy did produce a statistically different correlation.

Figure 3.9 shows the flow map for the 3RT combination at this scale, refer to chapter 3, section 3.2.2.3. Using this flow map, the holdup data for this impeller combination were separated into the three main cavity regimes:

a) Vortex / clinging cavities on all three disc turbines
b) 3-3 cavities on the lowest disc turbine and Vortex / clinging cavities on the upper disc turbines
c) 3-3 cavities on all three disc turbines

The data from each cavity regime were correlated using equations 4.1 and 4.2. The results are shown in tables 4.7 and 4.8. The quality of the data fit (judged from the standard error) was improved by separating the data into the cavity regimes. F-tests showed that the correlations for the different cavity regimes were statistically different to each other. Thus there is a significant difference in holdup behaviour between the different cavity regimes, as reported for single impeller geometries, refer to chapter 1, section 1.3.1. The exponent on impeller speed or power input, in cavity regime c, was approximately half of its value in cavity regimes a and b. This is the same trend as reported for single impeller geometries in chapter 1. The exponent on gas flow rate decreased slightly as the cavity regime changed from a through b to c. This is the opposite trend to that observed in single impeller geometries, see chapter 1.

4.3 RESULTS FROM THE 0.95m DIAMETER VESSEL

Two impeller combinations were studied in this vessel:

1. 3 Rushton turbines
2. 1 Rushton turbine + 2 LE20s (both pumping downwards)

The holdup data for each impeller combination are given in tables 4.9 and 4.10. The data for each impeller combination correlated well using equations 4.1 and 4.2, see tables 4.11 and 4.12. F-tests showed that the correlations for each impeller combination were statistically different (true for both correlation methods). The holdup data for both impeller combinations are compared with the 3RT correlations in figures 4.3 and 4.4.

In the 0.61m diameter vessel, combinations 1 and 2 were found to be very similar for the holdup range 1 to 15%. Figures 4.3 and 4.4 show that, for the same holdup range in the 0.95m diameter vessel, the two impeller combinations produced similar holdup. However, there is a systematic difference between the

two impeller combinations at holdup greater than 12%, where the 3RT combination maintained a higher holdup than the RT+2×LE20 combination. This was true for a given impeller speed and gas flow rate, and was slightly more pronounced at a given power input and superficial gas velocity.

The data from both impeller combinations were combined and correlated using equations 4.1 and 4.2. For each correlation method the combined correlation had a worse data fit than the correlations based on the individual data sets, refer to tables 4.11 and 4.12. The combined data correlations were both found to be statistically different to the RT+2×LE20 correlations.

The holdup data from the 3RT combination was recorrelated including the isothermal expansion energy of the gas with the impeller power draw in equation 4.2, see table 4.15. As found with the data from the 0.61 m diameter vessel, the inclusion of the gas expansion energy produced a statistically different correlation. Again the data fit to this correlation was slightly worse than for the correlation based solely on the impeller power draw, refer to table 4.12. The inclusion of gas expansion energy in the correlation increased the exponent on power input, from 0.18 to 0.22, and decreased the exponent on superficial gas velocity, from 0.57 to 0.54.

Figure 3.17 shows the flow map for the 3RT combination at this scale. The majority of the holdup data was in cavity regime 'c' (3-3 cavities on all three Rushton turbines) with only two data in cavity regime 'b' (3-3 cavities on the lowest disc turbine and Vortex / clinging cavities on the upper Rushton turbines) and one data in cavity regime 'a' (Vortex / clinging cavities on all three Rushton turbines). Thus there is insufficient data at this scale to produce correlations for all of the different cavity regimes. The correlations based on the data from cavity regime 'c' are given in tables 4.13 and 4.14 and are virtually identical to the overall correlation.

4.4 SCALE UP

Two impeller combinations were studied in both the 0.61m and 0.95m diameter vessels:

1. 3 Rushton turbines
2. 1 Rushton turbine + 2 LE20s (both pumping downwards)

For a given impeller combination, the hold up correlations (based on equations 4.1 and 4.2) from the 0.95 diameter vessel were statistically different to the correlations for the 0.61m diameter vessel. All the correlation exponents were lower at the larger scale.

The data from both scales, for a given impeller combination, were combined and

correlated using equations 4.1, 4.2 and:

$$\varepsilon_G = \alpha\ (N)^{\beta}\ (Q)^{\gamma}\ (T)^{\varpi} \qquad \text{...Eqn(4.3)}$$

Refer to tables 4.16, 4.17 and 4.18. For equations 4.1 and 4.2 the standard error increased, compared to the correlations for a given scale. F tests showed that there was little difference between the three correlation methods, and in all cases the data was within ±20% of the correlation. The scale up correlations, based on power and superficial gas velocity, are shown in figures 4.5 and 4.6.

The 3RT data from both scales was separated into the two main cavity regimes and correlated together. The results are given in tables 4.16 to 4.18. F tests showed that the quality of data fit was significantly improved when the cavity regimes were considered separately.

4.5 COMPARISON OF STANDARD AND TALL VESSEL GEOMETRIES

The gas holdup data from all four impeller combinations tested, and both scales, were correlated with data from single, standard geometry Rushton turbine mounted in standard geometry vessels of diameter 0.61 m and 2.67 m. The resulting correlation was:

$$\varepsilon_G = 1.79\ (\varepsilon_m)^{0.34}\ (V_{sg})^{0.72}$$

See figure 4.7. The only data point which falls significantly outside ±20% of this correlation is for the RT+2×PBT (pumping up) combination at high gas flow rates.

This correlation is very similar to those developed, for single impeller geometries, by Van't Riet (1975) and Chapman (1981), refer to chapter 1, section 1.3.2.

4.6 DISCUSSION

Figure 4.8, from Bakker (1992), shows the distribution of energy dissipation rates in stirred vessels fitted with single Rushton and pitched blade turbines. For both impeller designs, energy dissipation rates are high in the impeller discharge region, but much lower in the bulk of the liquid. For a freely coalescing system, the bubble size distribution would therefore vary widely, with small bubbles close to the impeller and larger bubbles in the bulk of the liquid. The literature on standard geometry vessels showed that although there are difference in local bubble size distributions, in terms of overall gas holdup there is little difference between impellers for a given power input and superficial gas velocity.

The results presented in this chapter show that slight differences in overall gas holdup were observed for different combinations of triple impellers. Different impeller cavity regimes were also found to have a statistically significant effect on overall gas holdup, for the triple Rushton turbine combination. However, all of these effects were minor, and holdup data from all four triple impeller combinations correlated well (±20%) with holdup data from single impeller configurations using

$$\epsilon_G = 1.79\ (\epsilon_m)^{0.34}\ (V_{sg})^{0.72}$$

For the data fitted to this correlation, the maximum liquid depth tested was 2.7 m. Thus the gas would have expanded by approximately 10% between the sparger and the dispersion surface. For very deep tanks, gas expansion could double the local value of V_{sg} between the bottom and top of the vessel, making the selection of an appropriate value of V_{sg} difficult.

The above correlation only applies to the range of experimental conditions tested. At the highest power inputs and superficial gas velocities studied, the gas holdup tended to level out, refer to figure 4.7. Thus this holdup correlation would over predict holdup at power inputs and superficial gas velocities greater than those tested in this thesis. This could be a problem on scale up because, assuming that gas flow rate is scaled with liquid volume, the superficial gas velocity would increase with scale potentially taking it outside the range of application of this correlation.

Warmoeskerken (1975) and Chapman (1981) measured holdup up to 9% in standard geometry vessels. Roustan (1985), Magelli (1987), Nocentini (1988) and Abrardi et al (1988) also only measured gas holdup up to 9% for multiple Rushton turbines. Chiampo (1991) did not observe a difference in holdup for dual combinations of RT and PBT impellers, but again the highest gas holdup measured was only 8%.

In this work, holdup was measured up to 20%. Below 8 to 12%, depending on scale, little difference was found between the different impeller combinations tested, which agrees with the conclusions of the above workers. However, at higher gas holdup there were systematic differences between the impeller combinations, (although still within ±20% of the overall correlation), for a given power input and gas flow rate.

In the 0.95 m diameter vessel the RT+2×LE20 combination produced lower holdup than the 3RT combination, for holdup > 12%. This is probably related to the fact that, for all tests in this vessel, the LE20 impellers were directly loaded with gas, see chapter 3. When directly loaded, in the standard geometry vessel, large gas cavities were observed on the LE20 blades which occasionally broke away to produce large gas bubbles with short residence times.

In the 0.61 m diameter vessel, gas holdups up to only 13% could be achieved. At the highest level of holdup measured, the RT+2×PBT (upward pumping) combination had to dissipate 150% more power, compared to the 3RT combination, to achieve this holdup. Kuboi and Nienow (1982) noted that when upward pumping pitched blade turbines are used as upper impellers they can, under some conditions, gather in gas bubbles and discharge them directly to the dispersion surface, refer to chapter 1, section 1.2.2.1. The gas holdup data for the RT+2×PBT (pumping up) combination could be indicating the same effect as observed by Kuboi and Nienow. However, this is based on one data point and further work needs to be done at high gas holdups (>13%) to confirm the data trends.

4.7 CONCLUSIONS

1. For each impeller combination studied, holdup data were correlated equally well using:

$$\epsilon_G = \alpha\ (N)^{\beta}\ (Q_{\underline{G}})^{\gamma} \qquad \text{...Eqn(4.1)}$$

or $$\epsilon_G = \alpha\ (\epsilon_m)^{\beta}\ (V_{\underline{sg}})^{\gamma} \qquad \text{...Eqn(4.2)}$$

These correlations only apply to the range of conditions tested. Gas holdup does not keep increasing with increasing power input and gas flow rate, and tends to level out at high holdups.

2. The holdup correlations for the different impeller combinations were statistically different.

3. The holdup correlations for the 3RT combination were improved by correlating the data from the different cavity regimes separately. The correlations from the different cavity regimes were also statistically different to each other. The exponent on $\epsilon_{\underline{m}}$ in the large cavity regime was approximately half its value in the small cavity regime.

4. As vessel scale increased, from 0.61 m to 0.95 m diameter, the exponents on power input and superficial gas velocity both decreased for a given impeller geometry.

5. For a given impeller combination the data from two scales correlated well using equations 4.1, 4.2 or:

$$\epsilon_G = \alpha\ (N)^{\beta}\ (Q)^{\gamma}\ (T)^{\omega} \qquad \text{...Eqn(4.3)}$$

All three correlation methods produced similar data fits.

6. At low gas holdup, less than 8% in the 0.61 m vessel, and less than 12% in the 0.95 m vessel, all impeller combinations studied produced the same gas holdup for a given power input and superficial gas velocity.

7. At high gas holdups, greater than 8% in the 0.61 m vessel, and greater than 12% in the 0.95 m vessel, slight differences were observed between the impeller combinations:

   - in the 0.61 m vessel the RT+2×LE20 combination produced lower holdup than the 3RT combination.
   - in the 0.95 m vessel the RT+2×PBT (pumping up) combination had to disperse 150% more power than the 3RT combination to achieve a gas holdup of 13%.

8. Despite conclusions 2, 3, 4 and 7, gas hold up data from a range of vessel geometries ($H = T$ & $H = 2.4T$), scales (T = 0.61 m, 0.95 m & 2.73 m) and impeller configurations (1RT, 3RT, RT+2×LE20 & RT+2×PBT) correlated well together (±20%) using:

$$\varepsilon_G = 1.79(\varepsilon_m)^{0.34}(v_{sg})^{0.72}$$

   This correlation is very similar to those of Van't Riet (1975) and Chapman (1981) which were developed for air dispersion into water using single impellers.

   Thus to a first approximation gas holdup is independent of vessel geometry and impeller configuration for a given ϵ_m and V_{sg} below flooding.

9. The inclusion of gas isothermal expansion energy, in equation 4.1, did produce statistically different holdup correlations but with a slightly worse data fit. The inclusion of gas expansion energy reduced the exponent on power and increased the exponent on gas velocity.

CHAPTER 5

LIQUID MIXING

5.1 INTRODUCTION

Liquid mixing can directly influence the yield and / or selectivity of a chemical reaction. In addition, many fermentation processes require a uniform environment with minimal nutrient and dissolved oxygen concentration gradients. Thus one objective of this chapter is to investigate the effects of operating parameters, including impeller combination, impeller speed and gas flow rate, on liquid blend times.

A series of experiments were conducted in the 0.95 m diameter vessel to investigate the effects of operating conditions on the mass transfer rate from gas to liquid. Two impeller combinations were studied:

1. 3×RT
2. RT+2×LE20

These experiments, described in chapter 6, involved the measurement of dissolved oxygen transients at three locations in the vessel. The shape of each dissolved oxygen transient was determined by the local oxygen mass transfer rate from the gas to the liquid, and by the rate at which dissolved oxygen was transfered to and from other parts of the vessel. For vessels in which the liquid cannot be assumed to be perfectly mixed, accurate determination of local mass transfer rates, from the experimental dissolved oxygen transients, requires a reactor model which includes a structured model for the liquid phase mixing. For multiple Rushton turbines several workers have shown that a model consisting of a cascade of perfectly mixed cells (one cell per turbine) connected by liquid exchange flows is a good approximation to the liquid mixing. Thus a three cell cascade model was assumed for both impeller combinations in the 0.95 m diameter vessel. The second objective of the liquid mixing studies presented in this chapter was to define all parameters within the assumed liquid mixing model.

Further liquid mixing experiments are also presented in this chapter which investigate in detail, the validity of the three cell cascade model for both impeller combinations.

5.2 LIQUID MIXING IN THE 0.95 m DIAMETER VESSEL

5.2.1 Assumed liquid mixing model

In the 0.95 m diameter vessel, three conductivity probes were used to investigate the effects of operating parameters on liquid mixing. The probe positions are shown in figure 5.1. These probe positions were the same as the dissolved oxygen probe positions

used for the mass transfer experiments, refer to chapter 6. The liquid phase mixing was assumed to consist of three perfectly mixed cells connected by exchange flows, see figure 5.2. The boundaries between the cells were assumed to be located mid way between the impellers.

200 ml of tracer (saturated sodium chloride solution) were added to the dispersion surface using a solenoid operated valve. The tracer addition point is shown in figure 5.1. Examples of the three conductivity transients obtained following addition of tracer to the liquid surface, are shown in figures 5.3 and 5.4. The conductivity responses were normalised from 0 (conductivity at start of test) to 1.0 (conductivity of homogeneous liquid at end of test).

The ungassed cell volumes, for the assumed liquid mixing model, were as follows:

$V_T = 0.595\ m^3$

$V_M = 0.546\ m^3$

$V_B = 0.447\ m^3$

When gassed the liquid was displaced upward, reducing the liquid volume in the lower cells but increasing the liquid volume in the top cell (the cell boundaries were assumed to be in the same positions, except for the dispersion surface). With the gas completely dispersed, i.e. $N > N_{CD}$ (N_{CD} estimated from equation 1.2), the gas was assumed to be uniformly distributed throughout the vessel. For $N < N_{CD}$ the liquid volume of each cell was estimated assuming no gas dispersion below the lowest impeller, but uniform gas holdup above this impeller.

The exchange flows in the assumed liquid mixing model were calculated from the following equations (refer to appendix 1):

$$F_t = \frac{(V_m + V_b)}{area\ 1} \qquad \text{...Eqn (A1.33)}$$

and

$$F_b = \frac{V_b}{area\ 2} \qquad \text{...Eqn (A1.34)}$$

Where areas 1 and 2 are the areas between the response curves, see figure 5.5. If the area between the response curves is small, i.e. the probes produce similar response curves, the liquid mixing between the cells must be good, and the exchange flow will be large. If the area between the response curves is large the mixing between the cells must be poor, and the exchange flows will be small.

From Appendix 1 the calculation of exchange flows followed these three steps:

i) Calculation of area under each response curve, from tracer injection to equilibrium, using Simpson's rule.

ii) Calculation of area between adjacent response curves by subtraction.

iii) Calculation of exchange flows from equations A 1.33 and A 1.34.

Exchange flows were determined for the same experimental conditions at which the dissolved oxygen transients were measured. Thus the assumed liquid mixing model and the measured exchange flows provide the full description of the liquid phase mixing required for accurate determination of local mass transfer coefficients, see chapter 6.

The rest of this chapter will present the effects of operating parameters on exchange flows and liquid mixing times in the 0.95 m diameter vessel. Further work will also be presented, which was conducted at smaller scale, to investigate the validity of the assumed liquid mixing model for both impeller combinations.

5.2.2 Exchange flows

5.2.2.1 Ungassed

The exchange flows, for each impeller combination, are shown in Tables 5.1 and 5.2. The values reported are the average of six experiments, and the values in brackets are the relative standard deviation about the mean value.

The ungassed exchange flows for each impeller combination were correlated as:

$$F = a\,(N)\,b \qquad \text{...Eqn (5.1)}$$

The results are given in Table 5.3.

Each correlation was compared, using the F test, with:

$$F = a\,(N)L0 \qquad \text{...Eqn (5.2)}$$

For the 1RT+2xLE20 combination there was no difference between the two correlations at the 95% significance level. For the bottom exchange flow of the 3RT combination the same was true. There was, however, a significant difference for the top exchange flow of the 3RT combination (however, this difference was only caused by one high data point at an impeller speed of 2 rps).

The exchange flows for each combination were also correlated using:

$$F = a\,(z\,m)b \qquad \text{...Eqn (5.3)}$$

The results are shown in Table 5.4 and Figure 5.6.

Each correlation was compared, using the F test, with:

$$F = a\ (\ \varepsilon_m\ )^{0.33} \qquad \text{...Eqn (5.4)}$$

In all cases there was no difference, at the 95% significance level, between equations 5.3 and 5.4.

From table 5.4 it can be seen that, for a given power per unit mass, the RT+2×LE20 combination produced exchange flows 100 to 150% larger than the 3×RT combination.

Singh et al (1988) calculated exchange flows for a 3×RT combination in a tall vessel. They related their exchange flow values to the impeller pumping capacities and found that:

F_t (assumed to be equal to F_b) = 0.50 Q_I

Where Q_I = impeller pumping capacity = $N_Q\ N\ D^3$

For the 3×RT combination studied in this thesis:

$$F_t = 0.36\ N\ D^3$$

and $F_b = 0.38\ N\ D^3$

For a six blade Rushton turbine N_Q = 0.75, Revill (1982).

$\therefore$ $F_t = 0.48\ Q_{I,\,RT}$

and $F_b = 0.51\ Q_{I,\,RT}$

Very similar to the results of Singh et al (1988).

For the 1RT+2×LE20 combination:

$$F_t = 0.15\ N\ D^3$$

and $F_b = 0.20\ N\ D^3$

For an LE20 impeller N_Q = 0.60 (manufacturers data)

$\therefore$ $F_t = 0.25\ Q_{I,\,LE20}$

and $F_b = 0.33\ Q_{I,\,LE20}$

Although the LE20's produced higher absolute values of exchange flow compared with the Rushton turbines, the exchange flows for the RT+2×LE20 combination were a lower fraction of the LE20's pumping capacity.

5.2.2.2 3×RT combination with gas

Figure 5.7 shows the effect of aeration on the exchange flows, for the 3×RT combination at a range of impeller speeds. In all cases, for a given impeller speed the liquid exchange flows were reduced by aeration. With aeration the top exchange flow was reduced by 14 to 24%, and the bottom exchange flow by 22 to 41%. The top exchange flow increased significantly when the lowest impeller became flooded. With the lowest impeller flooded the lower exchange flow would be expected to increase, not the upper exchange flow, because flooding improves axial mixing around the lowest impeller.

Considering the liquid mixing model shown in figure 5.2 it is unlikely that the power draw of the top impeller would influence the lower exchange flow. Similarly it is unlikely that the power draw of the lowest impeller would influence the upper exchange flow. Thus the exchange flows were plotted against the local power input, where:

$$\text{Local power input for top exchange flow} = \frac{P_t+P_m}{V_t+V_m}$$

$$\text{and local power input for bottom exchange flow} = \frac{P_m+P_b}{V_m+V_b}$$

Where:
V_t = volume of top cell in liquid mixing model
V_m = volume of middle cell in liquid mixing model
V_b = volume of bottom cell in liquid mixing model
P_t = power input of top impeller
P_m = power input of middle impeller
P_b = power input of bottom impeller

Ungassed, the local power draw in the lower part of the vessel was approximately 20% greater than the local power draw in the upper part of the vessel. When gassed, the local power draw in the lower part of the vessel was still slightly greater than in the upper part of the vessel.

The exchange flows for this impeller combination are compared with local power input in Figure 5.8. This figure shows that the top exchange flow was constant for a given power input, regardless of the gas flowrate. The only exception to this occurred when the lowest impeller was flooded and F_t was found to be larger than under non flooded gassed conditions. For the lower exchange flow, the gassed data lie on the same line as the ungassed data, except for one low data point. Both flooded data points also lie on the same line as the ungassed and gassed, non flooded data.

5.2.2.3 1RT+2×LE20 combination with gas

Figure 5.9 shows the effect of aeration on the exchange flows for the RT+2×LE20 combination. The top exchange flow was reduced by 26 to 51%. The bottom exchange flow was reduced by 43 to 78%.

The exchange flows are plotted versus local power in Figure 5.10. As found with the 3RT combination, the top exchange flow was constant for a given power input regardless of the gas flowrate. However, this was not true for the bottom exchange flow where, for a given power input, the aerated exchange flows were lower than the unaerated exchange flows. In addition the difference between the ungassed and gassed lower exchange flows increased as the power input decreased.

5.2.2.4 Comparison of impeller combinations with gas

Figure 5.11 shows all the aerated exchange flow data, for both impeller combinations (flooding data omitted). For a given power input the RT+2×LE20 combination produced a higher exchange flow in the upper part of the vessel compared to the 3×RT combination. In the lower part of the vessel the 3×RT combination achieved a similar exchange flow to the RT+2×LE20 combination at low power input, but at higher power the RT+2×LE20 combination produced higher exchange flows.

5.3 EXPERIMENTS TO DETERMINE VALIDITY OF THREE CELL LIQUID MIXING MODEL

These experiments were conducted in a Perspex, 0.61 m diameter vessel. Six conductivity probes were positioned in the vessel, as shown in figure 5.12. 60 ml of tracer (saturated sodium chloride solution) were added to the dispersion surface using a solenoid operated valve. The tracer addition point is shown in figure 5.12.

Examples of the conductivity transients obtained following addition of tracer to the liquid surface are shown in figures 5.13 and 5.14. All conductivity responses were normalised from 0 (conductivity at start of test) to 1.0 (conductivity of homogeneous liquid at end of test). For a perfectly mixed liquid phase the responses of all six probes would be identical. For the triple Rushton turbine combination with and without gas, see figure 5.13, the shape of the response curves from the top of the vessel were very different to those from the bottom of the vessel, showing that the liquid was far from perfectly mixed.

The use of six conductivity probes allowed the assumption of a six cell cascade model for the liquid phase mixing, as shown in figure 5.15. Comparing this model with the experimental response curves of figure 5.13(a) it can be seen that the probes in cells 1 and 2 produced very similar responses, indicating that the mixing between these two cells was good. It can also be seen that the probes in cells 2 and 3 produced very

different responses, indicating that the liquid mixing between these two cells was poor. Thus visual assessment of the response curves shown in figure 5.13(a) indicates that there was good mixing between cells 1 and 2, cells 3 and 4, and cell 5 and 6, and that there was poor mixing between cells 2 and 3, and cells 4 and 5. Thus just by looking at the raw conductivity response curves it can be concluded that, for triple Rushton turbines without aeration, the liquid mixing can be approximated by a three cell model, as shown in figure 5.2. When gassed, see figure 5.13(b), the triple Rushton turbine combination produced fairly similar response curves to the ungassed responses shown in figure 5.13(a), except that there is slightly more difference between responses 3 and 4.

For the RT+2×LE20 combination ungassed, see figure 5.14(a), all probe responses reached equlibrium very quickly showing that the liquid was relatively well mixed. When gassed, however, see figure 5.14(b), it took longer for the probes to reach equilibrium and there was greater difference in the shapes of the response curves.

The exchange flows in the six cell liquid mixing model can be quantified by measuring the areas between adjacent response curves. The mathematics of this analysis are given in appendix 1. From appendix 1 the exchange flows were calculated from the following equations:

$$F_1 = \frac{(4 \times V_M + V_B)}{Area\ 1} \qquad \text{...Eqn (A1.32)}$$

$$F_2 = \frac{(3 \times V_M + V_B)}{Area\ 2} \qquad \text{...Eqn (A1.31)}$$

$$F_3 = \frac{(2 \times V_M + V_B)}{Area\ 3} \qquad \text{...Eqn (A1.30)}$$

$$F_4 = \frac{(V_M + V_B)}{Area\ 4} \qquad \text{...Eqn (A1.29)}$$

$$F_5 = \frac{V_B}{Area\ 5} \qquad \text{...Eqn (A1.28)}$$

where :

V_T = volume of liquid in top cell of model (cell 1)
V_M = volume of liquid in each middle cell (cells 2 to 4)
V_B = volume of liquid in bottom cell of model (cell 6)
Area 1 = area between conductivity response curves 1 and 2
Area 2 = area between conductivity response curves 2 and 3
Area 3 = area between conductivity response curves 3 and 4
Area 4 = area between conductivity response curves 4 and 5
Area 5 = area between conductivity response curves 5 and 6

In this analysis the liquid volumes V_T, V_M and V_B include the effect of gas displacement of liquid from the lower cells into the top cell, see Appendix 1.

From Appendix 1 the calculation of exchange flows followed these three steps:

i) Calculation of area under each response curve, from tracer injection to equilibrium, using Simpson's rule.

ii) Calculation of area between adjacent response curves by subtraction.

iii) Calculation of exchange flows from equations A1.28 to A1.32.

5.3.1 Effect of tracer addition point

The effect of tracer addition point was investigated, for the 3×RT combination, using the thiosulphate / iodide starch decolourisation method, refer to Cronin (1988). Overall mixing times were estimated visually as the time from sulphite addition to the time when the last colour disappeared. Three addition points were studied, refer to figure 5.15:

1. Liquid surface (cell 1 of liquid mixing model)
2. Below the middle impeller (cell 4 of model)
2. Outflow from the middle impeller (boundary between cells 3 and 4 of model)

The results for two impeller speeds, ungassed, are given in table 5.5. For each impeller speed the longest mixing time was recorded for surface addition, and the shortest mixing time was recorded for addition to the outfow from the middle impeller. At the lowest impeller speed studied there was a factor of four between the longest and shortest mixing times.

If the six cell model, shown in figure 5.15, is a good representation of the liquid mixing the calculated exchange flows should be independent of the tracer addition point. Using the conductivity method, identical experimental conditions were repeated for two tracer addition points:

a) Addition to the liquid surface (i.e. cell 1 of the model)
b) Addition just below the middle impeller (i.e. cell 4 of the model)

The mathematical relationships between the exchange flows and the areas between the conductivity response curves are different for the different tracer addition points, refer to Appendix 1.

The results of these experiments are shown in table 5.6. As found with the decolourisation method, the overall liquid mixing time was much shorter when the tracer

was added below the middle impeller, compared to surface addition. Although the overall mixing times were different for the two tracer addition points the exchange flows were very similar, illustrating the robustness of the 6 cell model for this impeller combination.

As shown in figures 5.13 and 5.14, when six probes are used in this small scale vessel the areas between the conductivity response curves can be very small, making accurate measurement of these areas difficult, particularly when signal noise caused by gas bubbles is present, refer to chapter 2. The purpose of these experiments was to locate the main boundaries to liquid mixing so that an appropriate liquid model could be defined. Thus the six cell exchange flows reported in this chapter are presented as qualitative rather than quantitative values.

The six cell exchange flows measured for the two impeller combinations over a range of impeller speeds and gas flow rates are given in tables 5.7 and 5.8. For the triple Rushton turbine combination at an impeller speed of 3.33 rps and no gas, the conductivity responses show that the main boundaries to mixing were located between the impellers, i.e. F_2 and F_4, refer to figure 5.13(a). The calculated values of exchange flow for these boundaries were 14 and 10 l/s respectively, from table 5.7. The conductivity responses also indicate that for these conditions F_1, F_3 and F_5 were higher, again refer to figure 5.13(a). Table 5.7 gives these exchange flows as 28, 35 and 32 l/s respectively. It should be noted that figures 5.13 and 5.14 are examples of individual experiments, and that the exchange flows given in tables 5.7 and 5.8 are the average values from six experiments. Based on this type of comparison with other experimental conditions, exchange flows $\leq$ 25 l/s have been chosen as a general indicator of the significant boundaries to mixing. These boundaries are indicated by the symbol B in tables 5.7 and 5.8. In addition, for exchange flows > 60 l/s the two cells can be assumed to be very well mixed together. Thus in tables 5.7 and 5.8 exchange flows > 60 l/s are represented by ∞.

5.3.2 Exchange flows (3×RT combination)

The six cell exchange flows measured for the triple Rushton turbine combination over a range of impeller speeds and gas flow rates are given in table 5.7.

Ungassed, the main mixing boundaries were generally located at F_1, F_2 and F_4. Thus the liquid mixing ungassed can be approximated by a four cell model.

When gassed the main mixing boundaries were always located at exchange flows F_2, F_3 and F_4 (except under flooded conditions when F_1 was very low). The main boundaries to mixing are compared with the flow patterns in figure 5.16. Thus when gassed, below flooding a four cell model, as shown in figure 5.17, should adequately describe the liquid mixing for this impeller combination.

5.3.3 Exchange flows (RT+2×LE20 combination)

The six cell exchange flows measured for the RT+2×LE20 combination are given in table 5.8. The top exchange flow F_1 is missing from this table due to a problem with the conductivity probe in cell 1, which was only discovered following completion of the test programme. However, good axial mixing was observed around the top impeller of this combination, see chapter 3, indicating that F_1 should be high for all conditions.

Ungassed, all the exchange flows were very high (compared to the values reported for the 3×RT combination) showing that the liquid was well mixed with no major boundaries to mixing.

When gassed significant boundaries to mixing developed at F_2, F_3 and F_4 although not always all at the same time. F_3 appears to be the strongest boundary to mixing when these impellers are gassed. Poor axial mixing in the middle of the vessel is explained by the reduced axial pumping capacity of the LE20 impellers when gassed, and the circulation loops described in chapter 3, and shown again in figure 5.16. F_5 remained high for all conditions as, it is assumed did F_1. Thus as with the triple Rushton turbine combination the four cell mixing model shown in figure 5.17 should be adequate for describing the liquid phase mixing for this impeller combination under gassed conditions.

5.3.4 Choice of liquid mixing model

The liquid mixing model shown in figure 5.17 seems to be simplest, realistic model which is applicable to both impeller combinations under gassed conditions. For ungassed conditions, a five cell model would be required because F_1 was low for the 3RT combination.

For the mass transfer experiments, which were conducted in the 0.95 m diameter vessel prior to these liquid mixing experiments, one of the dissolved oxygen probes was positioned at the same liquid depth as the middle impeller. Thus when considering the liquid mixing model shown in figure 5.17, one dissolved oxygen probe was positioned at the boundary between the two middle cells. Thus the dissolved oxygen level measured by this probe has to be considered as an average of the dissolved oxygen levels in the central two cells of the four cell liquid mixing model. This effectively forces the assumption of the three cell liquid mixing model shown in figure 5.2.

5.4 LIQUID MIXING TIMES

Liquid mixing times were calculated at both scales, from the same conductivity responses used to determine exchange flows. Mixing times were measured from the time that the tracer injection valve was opened.

The time varying concentration in the vessel at any point can be regarded as being represented by a steady concentration, equal to the mean concentration in the vessel, and a time varying component:

$$C(t) = C_m + C'(t)$$

where:

$C(t)$	=	local concentration at time t
C_m	=	mean concentration in the vessel
$C'(t)$	=	local fluctuating component of concentration at time t

The root mean square (RMS) concentration fluctuation over a time t^* is given by

$$\sigma_c^2 = \frac{1}{t^*}\int_0^{t^*}(C(t) - C_m)^2 dt)^{\frac{1}{2}}$$

$$= \frac{1}{t^*}\int_0^{t^*}(C'(t))^2 dt)^{\frac{1}{2}}$$

This approach is commonly used for dealing with problems involving turbulent fluctuating quantities, and the RMS is generally used to characterise the fluctuating quantity. The situation in a mixing vessel is complicated since the concentration fluctuations are transient. Not only C, but σ_c^2 is a function of t^*, the time over which integration takes place. This problem can be overcome by calculating σ_c^2 for small sections along the conductivity time history during its entire length, Ruszkowski (1985). The conductivity across each probe was measured 4096 times during each experiment and σ_c^2 was calculated over a short section of the trace, i.e. 32 data points as recommended by Ruszkowski (1985). This section was then moved forward by 4 points to carry out the next calculation. Thus a series of estimates of the root mean square concentration fluctuation were obtained:

$$\sigma_c^2(i) = \frac{1}{32}\sum_{4i}^{4i+31}(C_j - C(\infty))^2 \qquad i = 0, 1, ...1016$$

where:

$\sigma_c(i)$	=	the i^{th} estimate of the root mean square concentration fluctuation
C_j	=	concentration of the j^{th} data point
$C(\infty)$	=	concentration in liquid when mixing is complete

from Grenville (1991).

Only the overall liquid mixing times are reported in this work. For this calculation the data from all three probes were converted into a root mean square concentration:

$$C_{j,RMS} = \left(\frac{1}{3}(C_{j,1}^2 + C_{j,2}^2 + C_{j,3}^2)\right)^{\frac{1}{2}}$$

where $C_{j,1}$ is the concentration of the j^{th} data point measured at probe 1, etc.

Thus $C_{j,RMS}$ is substituted into the above equation to calculate $\sigma_{c,RMS}^2(i)$.

The performance of different impeller types in blending operations is usually assessed by measuring the time taken to reach a pre-specified degree of homogeneity. For this purpose a mixing index, M, is defined:

$$M = \frac{(\Delta c - \sqrt{\sigma_{c,\,RMS}^2})}{\Delta c}$$

where: $\Delta C = C(\infty) - C(0)$

$C(0)$ = initial concentration before tracer addition

M expresses the reduction in the root mean square concentration fluctuation as a fraction of the total change in concentration due to the injection of tracer. When M = 1.0 the tracer concentration is homogeneous at the scale of measurement (0.5 cm^3 for the EDT probes used in these tests).

The mixing time, θ, was defined as the time taken to reach a specified value of M. For blending of liquids in agitated vessels a value of 0.95 is usually selected, Grenville (1991), i.e. the blending process is 95% complete. However, in these gas liquid studies it was often difficult to define the 95% mixing time due to the noise in the conductivity data produced by the presence of the gas bubbles. Thus for this work a value of 0.80 was selected for M. $\theta_{80\%}$ is therefore the time at which the liquid blending process was 80% complete.

Each experiment was repeated six times and the mixing times reported in this chapter are the average values of those six tests. The relative standard deviation given with each mixing time was calculated using:

$$RSD = \frac{\sigma_\theta}{\bar{\theta}} \times 100\ \%$$

Mixing times for different degrees of homogeneity can be calculated from $\theta_{80\%}$ using:

$$\frac{\theta_{n\%}}{\theta_{80\%}} = \frac{\ln\left(1.0 - \frac{n}{100}\right)}{\ln(1.0 - 0.80)}$$

Thus 95% mixing times are 86% longer than the 80% mixing times given in this chapter.

In the 0.61 m diameter vessel, six conductivity probes were used. For the mixing time analysis probes 1, 3 and 6 were selected for determination of the mixing time.

Mixing times are included in tables 5.1. 5.2, 5.6, 5.7 and 5.8.

5.4.1 Ungassed liquid mixing times

Ungassed liquid mixing times, for both impeller combinations in the 0.95 m diameter vessel, are plotted against power input in figure 5.18(a). Only the average liquid mixing times for each impeller speed are shown in this figure.

For the triple Rushton turbine combination:

$\theta_{80\%} = 28.1\ \varepsilon_m^{-0.27}$ ($R^2 = 0.847$ for 26 data points)

and for the RT+2×LE20 combination:

$\theta_{80\%} = 15.4\ \varepsilon_m^{-0.25}$ ($R^2 = 0.884$ for 31 data points)

At this scale, for a given power input per unit mass, the RT+2×LE20 combination mixed the liquid in approximately 55% of the time taken by the triple Rushton turbine combination.

The same data were correlated with impeller speed:

For the triple Rushton turbine combination:

$\theta_{80\%} = 79.8\ N^{-0.82}$ ($R^2 = 0.847$ for 26 data points)

and for the RT+2×LE20 combination:

$\theta_{80\%} = 44.7\ N^{-0.85}$ ($R^2 = 0.890$ for 31 data points)

Using the F-test (at the 95% significance level) the triple Rushton turbine correlation was found not to be statistically different to:

$\theta_{80\%} = a\ N^{-1.00}$ ...Eqn (5.5)

i.e. $N\theta_{80\%}$ was constant.

For the RT+2×LE20 combination the best fit correlation was statistically different to equation 5.5. Thus $N\theta_{80}$ was not constant.

Ungassed liquid mixing times, for both impeller combinations in the 0.61 m diameter vessel, are plotted against power input in figure 5.18(b).

For each impeller combination the mixing times were correlated against power per unit mass:

For the triple Rushton turbine combination:

$\theta_{80\%} = 24.8\ \varepsilon_m^{-0.27}$ ($R^2 = 0.896$ for 18 data points)

and for the RT+2×LE20 combination:

$\theta_{80\%} = 9.6\ \varepsilon_m^{-0.25}$ ($R^2 = 0.884$ for 23 data points)

Thus for a given power input per unit mass, at this scale, the RT+2×LE20 combination mixed the liquid in approximately 40% of the time taken by the 3RT combination.

The same data were also correlated with impeller speed:

For the 3RT combination:

$\theta_{80\%} = 71.4\ N^{-0.81}$ ($R^2 = 0.898$ for 18 data points)

and for the RT+2×LE20 combination:

$\theta_{80\%} = 31.6\ N^{-0.74}$ ($R^2 = 0.867$ for 23 data points)

Using the F-test (at the 95% significance level) both correlations were found not to be statistically different to equation 5.5. Thus for both impeller combinations at this scale $N\theta_{80\%}$ can be considered constant.

5.4.2 Effect of aeration on liquid mixing times

Figure 5.19 shows the effect of gas flow rate on power draw and liquid mixing for the triple Rushton turbine combination at a range of impeller speeds in the 0.95 m diameter vessel. As discussed in chapter 3, aeration reduced the power draw of the impellers. At each impeller speed, liquid mixing time increased as gas flow rate was increased. The only exceptions to this occurred at 3.33 rps when the lowest impeller was flooded. Under these conditions the liquid mixing time was much shorter than the non flooded and ungassed tests for that impeller speed. It is interesting to note that flooding is bad from a gas dispersion viewpoint, but appears to be good in terms of liquid mixing.

Figure 5.20 shows the effect of gas flow rate on the power draw and liquid mixing time for the RT+2×LE20 combination at a range of impeller speeds in the 0.95 m diameter vessel. For each impeller speed, aeration reduced the power draw of the impellers and increasing the liquid mixing time. Unlike the triple Rushton turbine combination, flooding of the lowest impeller had no significant effect on the liquid mixing time compared to non flooded conditions at the same impeller speed.

Figure 5.21 shows the liquid mixing times, for each impeller combination, plotted against power per unit mass. The line shown on each diagram is the best fit line

through the ungassed data points. For the triple Rushton turbine combination the gassed liquid mixing times lie on the same line as the ungassed data. Thus for a given power input, liquid mixing time was independent of impeller speed and gas flow rate, and as power per unit mass was increased liquid mixing time was reduced. The flooded data points lie well below the ungassed and gassed data points of the same power input, showing that flooding of the lowest impeller improved the liquid mixing per unit power. For the RT+2×LE20 combination the gassed liquid mixing times lie above the ungassed data, showing that liquid mixing time for this impeller combination was not solely a function of power input. The one flooded data point lies close to the aerated data points of the same power input showing that, compared to non flooded conditions at the same gassed power draw, flooding of the lowest impeller had no significant effect on liquid mixing for this impeller combination.

Figure 5.22 shows a comparison of the liquid mixing times for the two impeller combinations in the 0.95 m diameter vessel. At low power inputs (< 1 W/kg) the RT+2×LE20 combination produced similar mixing times, when gassed, to the 3×RT combination. At higher power inputs (> 1 W/kg) the RT+2×LE20 combination produced 20% shorter mixing times, when gassed, than the ungassed 3×RT combination.

Figure 5.23 shows the liquid mixing times, for each impeller combination, in the 0.61 m diameter vessel plotted against power per unit mass. The line shown on each diagram is again the best fit line through the ungassed data points. For each impeller combination the trends in the data are exactly the same as observed in the 0.95 m diameter vessel, refer to figure 5.21.

5.4.3 Effect of scale on liquid mixing times

The mixing times for the triple Rushton turbine combination at both scales are compared in figure 5.24. The flooded data are not included in this comparison. For a given power per unit mass the mixing times in the 0.95 m diameter vessel were approximately 12% larger than the mixing times in the 0.61 m diameter vessel. The ungassed and gassed data from both scales were correlated together well using:

$$\theta_{80\%} = 28.5\ \varepsilon_m^{-0.30}\ T^{0.25}$$

see table 5.9 and figure 5.25.

The mixing times for the RT+2×LE20 combination at both scales are compared in figure 5.26. For a given power per unit mass the ungassed liquid mixing times from the 0.95 m vessel were approximately 63% larger than the ungassed mixing times from the 0.61 m diameter vessel. On the same basis the gassed mixing times were approximately 40% larger in the 0.95 m diameter vessel than in the 0.61 m diameter vessel. Because there was a significant difference between the ungassed and gassed mixing times for this impeller combination the two data sets were correlated separately across the two scales.

For the ungassed data:

$$\theta_{80\%} = 16.5\ \varepsilon_m^{-0.26}\ T^{1.10}$$

see table 5.9 and figure 5.27(a)

and for the gassed data (excluding the flooded data):

$$\theta_{80\%} = 25.2\ \varepsilon_m^{-0.34}\ T^{0.77}$$

see table 5.9 and figure 5.27(b)

5.5 DISCUSSION

5.5.1 Effect of tracer addition point

For dual Rushton turbines Cronin (1988) found that liquid mixing times with addition of tracer to the liquid surface were 40% longer than mixing times with tracer addition to the lower circulation loop of the upper turbine. In section 5.3.1 it was shown that for triple Rushton turbines, surface tracer addition produced liquid mixing times up to 300% longer than tracer addition to the outlet flow from the middle turbine. In both cases surface addition produced longer mixing times because the tracer had to mix across more mixing boundaries. The more boundaries there are to axial mixing the longer it will take to blend the tracer. This has important implications for processes that require short liquid mixing times, or uniform concentrations throughout the liquid phase. The optimum number and position of addition points will depend on exactly how many boundaries there are to axial mixing and their locations. This will be very geometry specific and influenced by factors such as the number of impellers, design of impellers, distance between impellers, impeller speed and gas flow rate.

5.5.2 Choice of liquid mixing model

For the triple Rushton turbine combination with gas the main boundaries to axial mixing were located between adjacent impellers and at the centre line of the middle impeller. No significant boundary to mixing was measured at the centre line of the bottom impeller under any conditions. This may be associated with the proximity of the vessel base preventing symetrical flow above and below this impeller. A significant boundary to mixing was found at the centre line of the top impeller, but only for ungassed conditions. Thus mixing boundaries can form at the centre line of Rushton turbines but this seems to be very sensitive to the system geometry. This can have important implications for selection of chemical addition point(s) because, as discussed above in section 5.5.1, the liquid mixing time is very sensitive to the number of mixing boundaries that the tracer has to cross. Manna et al (1991) studied dual Rushton

turbines and also observed a significant mixing boundary at the centre line of only one of the impellers (this was the upper impeller of the two, again suggesting that the proximity of the vessel base prevents a mixing boundary forming at the lowest impeller).

In terms of modelling the liquid mixing for the triple Rushton turbine combination, under gassed but non flooded conditions, a four cell model (shown in figure 5.7) should be adequate because it includes the three main mixing boundaries found in the vessel. For ungassed conditions the top cell of this model would need to be considered as two separate cells to account for the low value of $F_{\underline{1}}$.

For the RT+2×LE20 combination there were no significant mixing boundaries when ungassed and the liquid was relatively well mixed. With gas, however, significant mixing boundaries developed between adjacent impellers and at the centre line of the middle impeller. Formation of mixing boundaries in these areas can be associated with the liquid flow patterns (there are several recirculation loops in this part of the vessel which from visual observation did not seem to combine into one top to bottom mixing pattern) and the loss of axial pumping capacity of the LE20 impellers when gassed. Thus when gassed, the same four cell mixing model as described above for the triple Rushton turbine combination, seems to be a good approximation to the liquid mixing for this impeller combination.

Due to the positioning of the dissolved oxygen probes during the mass transfer experiments, refer to section 5.2.1, the four cell model described above had to be simplified to a three cell model, as shown in figure 5.2. Thus the significant mixing boundary found at the centre line of the middle impeller, for both impeller combinations, was ignored for the analysis of the mass transfer data, see chapter 6.

5.5.3 Liquid mixing without aeration (T = 0.95 m)

At a given power input per unit mass the RT+2×LE20 combination produced exchange flows approximately double (and liquid mixing times approximately half) those produced by the 3×RT combination. Due to the radial flow produced by the Rushton turbines the triple turbine combination produced the compartmentalised flow pattern described in chapter 3. The flow produced by the LE20 impellers was not vertical but was approximately 45° to the horizontal. Thus as reported in chapter 3 the RT+2×LE20 combination did not produce one large top to bottom circulation loop, see figure 5.16. However, compared to the triple Rushton turbine combination there was less compartmentalisation of the flow pattern and as a result the top to bottom mixing was more rapid. The exchange flow and mixing time measurements showed that although one large top to bottom recirculation loop was not formed by the RT+2×LE20 combination, the liquid was effectively well mixed due to good exchange between the observed recirculation loops.

For the triple Rushton turbine combination the upper and lower exchange flows were very similar for a given impeller speed. As shown in figure 5.16 the flow patterns

between the top and middle impellers were very similar to the flow patterns between the middle and bottom impellers, which explains the similarity in the exchange flows. For the RT+2×LE20 combination, at a given impeller speed, the lower exchange flow was generally larger than the upper exchange flow. Again visual observations of the flow patterns suggested that the flow of the middle LE20 combined well with the flow from the Rushton turbine, but that the flow between the top LE20 and the middle LE20 did not combine as well, due to the formation of a reverse flow loop between the impellers, see figure 5.16.

With the two triple impeller combinations studied in the 0.95 m diameter vessel the ungassed exchange flows were directly proportional to impeller speed and as a result the ungassed liquid mixing times were indirectly proportional to impeller speed. This is the same conclusion drawn for single impellers in standard geometry vessels, under fully turbulent conditions, Grenville (1992).

For both impeller combinations ungassed:

$$F \propto N D^3$$

The results from this thesis, for the multiple Rushton turbine combination, agree well with the assumption of Singh et al (1988) that:

$$F = 0.5\ Q_l$$

The results for the RT+2×LE20 combination show that:

$$F = 0.25 \text{ to } 0.33\ Q_l$$

Thus a lower fraction of the LE20 pumping capacity is converted into useful axial flow. Most of the LE20 flow seems to have gone into the intense recirculation loops wich were observed below each LE20, see figure 5.16.

5.5.4 Liquid mixing with aeration (T = 0.95 m)

For both impeller combinations studied, aeration reduced the power draw of the impellers and increased the liquid mixing time. For both impeller combinations aeration resulted in a greater reduction in the lower exchange flow than in the upper exchange flow. This was related to the greater reduction in power draw to the lower half of the vessel caused by aeration.

Singh et al. (1986), and Nocentini et al. (1983) found for triple Rushton turbine combinations, at a given impeller speed, that there was no significant difference between the aerated and unaerated exchange flows below flooding. The data reported in this thesis differs from these workers because it shows that the reduction in power caused by the formation of gas cavities on the impellers did result in lower exchange flows and

longer mixing times.

For a given power input the exchange flows and liquid mixing time measured with the triple Rushton turbine combination were independent of gas flow rate below flooding. Aeration reduces the pumping capacity of these radial flow impellers but below flooding the bulk flow pattern remained the same, i.e. each impeller pumped radially and a circulation loop formed above and below each impeller. The results presented in this chapter show that the rate of mixing across the boundaries between the circulation loops was solely a function of the turbulence in the liquid phase. With the lowest impeller flooded, mixing times measured with the triple Rushton turbine combination were significantly reduced because the axial flow around the flooded impeller broke up the compartmental flow pattern in the lower part of the vessel, refer to figure 3.5. Singh et al (1988) also observed this effect. Although the liquid mixing was improved with the lowest impeller flooded it should be noted that the gas dispersion in the lower part of the vessel was significantly worse.

When the lowest impeller of the 3RT combination flooded, the upper not the lower exchange flow increased (assuming the three cell model). This indicates that the three cell model is not a good model under flooded conditions. The fact that in reality the probe positioned at the same depth as the middle impeller was measuring conductivity at the boundary between two cells, may be the reason for the confused result. The six cell model showed an increase in the exchange flows in the lower half of the vessel, when conditions changed from non flooded to flooded, indicating that the use of six probes gives a more realistic picture of what is happening in the vessel.

When gassed the pumping capacity of the LE20 impellers is also reduced by the formation of gas cavities on the impeller blades. However, because the LE20 impellers are axial pumping the reduction in pumping capacity has a direct affect on the axial mixing in the vessel. In addition, as the axial flow from the LE20 impellers is reduced it becomes less likely that the flow patterns between impellers will combine. The exchange flow data showed that ungassed the liquid was well mixed with this impeller combination, but that with gas significant boundaries to mixing were formed around the middle impeller. Thus the liquid mixing times with gas were significantly greater than without gas.

With gas, at low power inputs (< 1 W/kg), the 3×RT and RT+2×LE20 combinations produced similar liquid mixing times. As power input was increased the aerated RT+2×LE20 combination produced shorter mixing times than the ungassed 3RT combination. For the LE20 impellers higher power input would go directly into producing axial flow and therefore better top to bottom mixing. For the multiple Rushton turbines higher power mainly produces more radial flow rather than axial flow. At higher power inputs than tested in this thesis it is therefore expected that the liquid mixing performance of the LE20 combination would improve more rapidly than that of the multiple Rushton turbine combination.

5.5.5 Effect of scale

Only a very narrow range of vessel scale was studied (0.61 m and 0.95 m diameter) so the conclusions drawn in this thesis need to be verified by test work at a third scale (preferably larger).

The correlations given in section 5.4.3 show that for a given power input per unit mass the liquid mixing times increased more with scale for the RT+2LE20 combination than with the triple Rushton turbine combination.

For the 3×RT combination: $\theta_{80\%} \propto T^{0.25}$

For the RT+2×LE20 combination: $\theta_{80\%} \propto T^{0.77 \text{ to } 1.00}$

For standard geometry vessels fitted with a single impeller:

$$\theta_{80\%} \propto T^{0.67}$$

from Grenville (1992).

The different scale up relationships may be related to slight differences in bulk flow patterns as scale changes. What ever the reason, these results have significant implications for scale up of processes that require good bulk mixing at large scale.

5.6 CONCLUSIONS

5.6.1 Effect of tracer addition point

1. For the triple Rushton turbine combination, at a given impeller speed and gas flow rate, addition of tracer to the liquid surface resulted in liquid mixing times 300% longer than when tracer was added to the outlet flow from the middle impeller.

2. As the number of impellers is increased it becomes increasingly important to avoid surface addition of material if that material needs to be mixed rapidly throughout the vessel. (This only applies if the flow patterns are compartmentalised, e.g. multiple radial flow impellers or any impellers that are spaced widely apart).

5.6.2 Choice of liquid mixing model

1. The cascade of six well mixed cells model is robust for the triple Rushton turbine combination, i.e. the calculated exchange flows are independent of tracer addition point.

2. For the two triple impeller geometries studied, the liquid mixing with aeration can be characterised by a four cell cascade model with the main mixing boundaries positioned half way between adjacent impellers and at the centre line of the middle impeller.

3. For interpretation of the dissolved oxygen transients a simplified three cell model had to be used in this work due to the positioning of the dissolved oxygen probes in the initial mass transfer work. This model ignores the presence of a significant mixing boundary at the centreline of the middle impeller, (true for both impeller combinations tested).

5.6.3 Liquid mixing times without aeration

1. At a given scale, the RT+2×LE20 combination mixed the liquid in 40 to 55% of the time taken by the triple Rushton turbine combination. This was a direct result of the compartmentalised flow patterns produced by the Radial flow turbines which impeded top to bottom mixing.

2. For each impeller combination at both scales:

$$\theta_{80\%} \propto N^{\approx -0.8}$$

and $$\theta_{80\%} \propto \varepsilon_m^{\approx -0.26}$$

However, in most cases the data were not statistically different to:

$$\theta_{80\%} \propto N^{-1.0}$$

or $$\theta_{80\%} \propto \varepsilon_m^{\approx -0.33}$$

5.6.4 Liquid mixing times with aeration

1. For the triple Rushton turbine combination, aeration reduced the power draw of the impellers and increased the mixing time of the liquid. For a given power per unit mass the liquid mixing time was independent of impeller speed and gas flow rate, as long as the lowest impeller was not flooded.

2. For the RT+2LE20 combination, aeration reduced the power draw of the impellers and increased the mixing time of the liquid. For a given power per unit mass the gassed liquid mixing times were 50 to 90% longer than the ungassed mixing times.

3. The triple Rushton turbine combination produced shorter liquid mixing times when the lowest Rushton turbine was flooded, due to break up of the compartmental flow pattern in the lower part of the vessel.

4. For the RT+2LE20 combination, flooding of the Rushton turbine had no significant effect on liquid mixing time compared to aerated, non flooded conditions at a similar power draw.

5. At low power inputs, the 3×RT and RT+2×LE20 combinations produced similar aerated liquid mixing times. At higher power inputs the RT+2×LE20 combination produced shorter aerated liquid mixing times than the ungassed 3RT combination.

6. For a given power per unit mass, liquid mixing time increased with scale for a given impeller combination. Scale had a much greater effect on the mixing times measured with the RT+2×LE20 combination than with the 3×RT combination.

5.6.5 Ungassed exchange flows (three cell model, T = 0.95 m)

1. For the triple Rushton turbine combination $F_t \approx F_b$. This agrees with the visual observations reported in chapter 3, i.e. the flow patterns observed between the top and middle impellers were similar to those between the middle and bottom impellers.

2. Generally for the RT+2×LE20 combination $F_b > F_t$. This again agrees with the visual observations from chapter 3 which indicated that the flow from the middle impeller combined with that of the bottom impeller, but that the flow of the top and middle impellers did not combine.

3. At a given scale and power input, the exchange flows for the RT+2×LE20 combination were greater than with the 3×RT combination (100% greater in the top half of the vessel and 150% higher in the lower half of the vessel). This agrees with the trends observed with liquid mixing times, i.e. for a given power input mixing time was shorter for the RT+2×LE20 combination.

4. Although the LE20s produced higher absolute values of exchange flow compared with the disc turbines, the LE20 exchange flows were a lower fraction of the impeller pumping capacity.

For the 3RT combination:

$$F_t = 0.48\ Q_{I\ DT}$$

$$F_b = 0.51\ Q_{I\ DT}$$

For the 1RT+2LE20 combination:

$$F_t = 0.25\ Q_{I\ LE20}$$

$$F_b = 0.33\ Q_{I\ LE20}$$

5. Generally for both impeller combinations:

$$F_t \text{ and } F_b \propto N^{1.00}$$

and $$F \propto \varepsilon_m^{0.33}$$

which agrees with the conclusions for liquid mixing time.

5.6.6 Exchange flows with aeration (three cell model, T = 0.95 m)

1. For both impeller combinations at a given impeller speed the exchange flows with aeration were lower than the exchange flows without aeration. Aeration had a greater effect on the axial flow impellers:

   For the 3RT combination:

   F_t reduced by 14 to 24%
   F_b reduced by 22 to 41%

   For the 1RT+2LE20 combination:

   F_t reduced by 26 to 51%
   F_b reduced by 43 to 78%

   For both impeller combinations the reduction in exchange flows was greater in the lower half of the vessel, as a result of the greater power loss due to aeration in this section of the vessel.

2. For the 3×RT combination both exchange flows were constant for a given power input, and independent of impeller speed and gas flow rate. This agrees with the trend observed with liquid mixing time.

3. For the RT+2×E20 combination the top exchange flow was constant for a given power input, independent of impeller speed and gas flowrate. However, this was not true for the lower exchange flow which, for a given power input, was lower with aeration than without aeration. This again agrees with the trend observed for liquid mixing time but shows that the liquid mixing was reduced mainly in the lower half of the vessel.

4. For the 3RT combination, at a gas flowrate above the flooding point of the bottom impeller there was an increase in one of the exchange flows. This was caused by a breakdown of the compartmental flow patterns produced by the 3RT combination. This effect was not seen with the 1RT+2LE20 combination.

5. When the lowest impeller, in the 3RT combination, flooded the upper not the lower exchange flow increased. This may indicate that the three cell model is not a good model under these conditions.

5.6.7 Comparison of impeller combinations (with aeration)

1. In the top half of the vessel the RT+2×LE20 combination produced a higher exchange flow than the 3RT combination at a given power input.

2. In the bottom half of the vessel the two impeller combinations produced similar exchange flows at low power inputs. At higher power inputs the 1RT+2LE20 combination produced a higher exchange flow than the 3RT combination.

CHAPTER 6

MASS TRANSFER

6.1 INTRODUCTION

This chapter presents the results of the mass transfer experiments conducted with two impeller combinations in the 0.95 m diameter vessel:

1. 3×RT
2. RT+2×LE20

Dissolved oxygen transients, following a step change from nitrogen to air sparging, were measured at three locations in the vessel, see figure 6.1. The experimental procedure is described in chapter 2.

The aim of this work was to determine local mass transfer coefficients for each impeller region of the impeller combinations tested, and to compare the impeller combinations in terms of these local mass transfer coefficients.

6.2 LIQUID AND GAS PHASE MIXING MODELS

Accurate interpretation of the three dissolved oxygen transients requires realistic models for both the liquid and gas phase mixing.

6.2.1 Gas phase mixing model

As discussed in section 1.5.3, previous workers have shown that in tall vessels fitted with multiple impellers, the gas phase mixing is close to plug flow at low impeller speeds, but as the impeller speed is increased the degree of back mixing increases. Even at high power inputs the gas phase does not become perfectly mixed and there is always a significant time lag in the system. As discussed in section 1.2, the degree of gas recirculation in an agitated vessel, and therefore the degree of gas back mixing, is very difficult to quantify. For this analysis it will be assumed that the gas is in plug flow.

Following the step change from nitrogen to air sparging, oxygen transfers from the gas to the liquid reducing the oxygen concentration of the gas. In addition the gas bubbles expand as they rise through the vessel due to the reduction in hydrostatic pressure. This gas expansion increases the interfacial area available for mass transfer but decreases the concentration of oxygen in the gas phase. Muskett (1987b) concluded that, for standard geometry vessels ($H = T$), depth effects must be included in any rigorous model of the gas phase. For the tall vessels studied in this thesis, the influence of depth effects will be even greater than in standard geometry vessels.

Muskett (1987b) gave a set of equations describing a system with the gas in plug flow which included the effects of depth on gas density and bubble volume:

$$\frac{\delta(Q_G C_G)}{\delta x} = -A(1 - \varepsilon_G)\, k_L a\, (KC_G - C_L) + A\, \varepsilon_G \frac{\delta C_G}{\delta t} \qquad \text{...Eqn (6.1)}$$

where:

Q_G = Gas volumetric flow rate
C_G = Concentration of oxygen in the gas
A = Vessel cross sectional area
ε_G = Gas holdup
k_La = Mass transfer coefficient
K = Equilibrium constant (= C_G / C_{Li})
C_L = Concentration of oxygen in the liquid
t = time

$$\frac{\delta(\rho_G Q_G)}{\delta x} = -A(1 - \varepsilon_G)\, k_La\, (KC_G - C_L) \qquad \text{...Eqn (6.2)}$$

where: ρ_G = Gas density

$$\frac{\delta C_L}{\delta t} = \frac{k_La}{H} \int_0^H (KC_G - C_L)\, dx \qquad \text{...Eqn (6.3)}$$

where: H = Liquid depth

$$\rho_G = \frac{P_0 + \rho_L\, g\, (H - x)}{R\, T} \qquad \text{...Eqn (6.4)}$$

where:

ρ_L = Liquid density
R = Gas constant
T = Temperature

Muskett (1987b) converted these partial differential equations into ordinary differential equations by considering the gas phase as ten consecutive well mixed elements. Thus a total of 11 simultaneous differential equations were used (10 for the gas phase and 1 for the liquid) to describe mass transfer in a standard geometry vessel in which the liquid phase was assumed to be perfectly mixed. Equations 6.1 to 6.4 were thus rewritten as follows:

$$\frac{\delta C_G}{\delta x} = \frac{(C_{Gn} - C_{Gn-1})}{\Delta x} \qquad \text{...Eqn (6.5)}$$

$$\frac{\delta Q_G}{\delta x} = \frac{(Q_{Gn} - Q_{Gn-1})}{\Delta x} \qquad \text{...Eqn (6.6)}$$

For the lowest element, i.e. n = 1:

$$\frac{d(C_{Gn})}{dt} = Q_{Gn}\, \frac{(C_{Gn} - C_{Gi})}{\Delta x} + C_{Gn}\, \frac{(Q_{Gn} - Q_{Gi})}{\Delta x} - A\, (1 - \varepsilon_G)\, k_La\, (KC_{Gn} - C_L) \qquad \text{...Eqn (6.7)}$$

where the subscript i denotes inlet gas conditions.

For the n^{th} element, where $n > 1$:

$$\frac{d(C_{Gn})}{dt} = Q_{Gn}\frac{(C_{Gn} - C_{Gn-1})}{\Delta x} + C_{Gn}\frac{(Q_{Gn} - Q_{Gn-1})}{\Delta x} - A\,(1 - \varepsilon_G)\,k_La\,(KC_{Gn} - C_L) \qquad \text{...Eqn (6.8)}$$

The overall mass balance is:

$$Q_{Gn} = \frac{-R\,T\,k_La\,A\,(1 - \varepsilon_G)\,(KC_{Gn} - C_L)\,\Delta x + Q_{Gn-1}\,(P_0 + \rho_L\,g\,(H - x))}{P_0 + \rho_L\,g\,(H - x) - \rho_L\,g\,\Delta x} \qquad \text{...Eqn (6.9)}$$

Finally, the expression for the liquid phase concentration in each well mixed cell (with 10 elements for the gas phase in each cell) is:

$$\frac{dC_L}{dt} = \frac{k_La}{L}\sum_{n=0}^{n=10}(KC_{Gn} - C_L)\,\Delta x \qquad \text{...Eqn(6.10)}$$

6.2.1 liquid mixing model

For the tall vessels studied in this thesis the liquid was modelled as three perfectly mixed cells. The gas phase was considered as 10 consecutive elements for each cell of the liquid mixing model (giving a total of 30 elements for the whole vessel). The gas phase was thus modelled as plug flow with no back mixing. The effect of the liquid exchange flows on the dissolved oxygen concentration in each cell of the liquid mixing model was included in the model by considering dissolved oxygen mass balances for each cell:

$$\frac{dC_{LB}}{dt} = \frac{F_B}{V_{LB}}(C_{LM} - C_{LB}) \qquad \text{...Eqn(6.11)}$$

$$\frac{dC_{LM}}{dt} = \frac{F_T}{V_{LM}}(C_{LT} - C_{LM}) + \frac{F_B}{V_{LM}}(C_{LB} - C_{LM}) \qquad \text{...Eqn(6.12)}$$

$$\frac{dC_{LT}}{dt} = \frac{F_T}{V_{LT}}(C_{LM} - C_{LT}) \qquad \text{...Eqn(6.13)}$$

Where: C_{LT} = Dissolved oxygen level in top cell

C_{LM} = Dissolved oxygen level in middle cell
C_{LB} = Dissolved oxygen level in bottom cell
F_t = Upper exchange flow
F_b = Lower exchange flow
V_{LT} = Liquid volume in top cell
V_{LM} = Liquid volume in middle cell
V_{LB} = Liquid volume in bottom cell

6.3 ANALYSIS OF DISSOLVED OXYGEN TRANSIENTS

The parameters entered into the model were:

- Liquid temperature measured during mass transfer experiment (°C)
- Liquid volume of each cell in liquid mixing model (m^3)
- Gas flow rate at sparger pressure and temperature (m^3/s)
- Gas holdup
- Dissolved oxygen probe response times (s)
- Upper and lower exchange flows (from tables 5.7, 5.8 or estimated from figures 5.8 or 5.10).

The analysis programme then read the three dissolved oxygen transients, which had been stored on the computer's hard disc, and normalised them from 0 (zero dissolved oxygen level) to 1.0 (equilibrium dissolved oxygen level).

The three response curves were deconvoluted, to take account of the response lag of the dissolved oxygen probes, using:

$$C_{L\ Actual} = \tau_L \frac{dC_{L\ Measured}}{dt} + C_{L\ Measured}$$

where: τ_L = first order response time of dissolved oxygen probe

Refer to Chapman et al (1977). In all cases this deconvolution had negligible effect because of the very short response times of the probes, see chapter 2, section 2.3.5.

A first guess for the k_La value in each cell (k_La_1) was calculated by assuming the simple model of no depletion in the gas phase and no exchange flows between the cells, see Appendix 4. A second estimate for the k_La in each cell (k_La_2) was calculated by assuming the simple plug flow model for the gas phase, again refer to Appendix 4. A third value of k_La in each cell was calculated from:

$$k_La_3 = k_La_1 + (k_La_2 - k_La_1)$$

For each of the three initial guesses for k_La in the bottom cell, equations 6.5 to 6.13 were solved using a fourth order Runge Kutta numerical technique (time step of 0.08 s) to produce three calculated liquid phase transients for this cell. A sum of errors squared was calculated between each of the calculated transients and the measured transient. The analysis program then optimised the value of k_La to achieve the minimum sum of errors squared between the calculated and measured responses. The optimised value of k_La for the bottom cell was then fixed for the rest of the analysis. The k_La in the bottom cell was optimised first because the k_La in the bottom cell

determines the oxygen concentration of the gas entering the middle cell.

The analysis then moved on to the middle and finally the top cell, where the same procedure was followed to optimise k_La. Thus the analysis always achieved the best possible fit to the experimental response curves, within the constraints of the gas and liquid phase mixing models.

Temperature has a significant effect on the value of k_La. During the mass transfer experiments the liquid temperature varied from 12 to 20 °C. Thus for comparative purposes, all k_La values reported in tables 6.1 and 6.2 were corrected to 20 °C using:

$$k_La_{(20°C)} = \frac{k_La_{(T_L)}}{[1 + 0.02665\ (T_L - 20)]}$$

from Smith, Van't Riet, Middleton (1977)

6.4 RESULTS

6.4.1 Simple model

The k_La values, assuming the simple model shown in figure 6.2, are given in tables 6.1 and 6.2. The impeller combinations are compared on the basis of these k_La values in figure 6.3. The 3RT data from each cell were correlated using:

$$k_La = \alpha\ (\varepsilon_m)^{\beta}\ (V_{sg})^{\gamma}$$

The correlations given in figure 6.3 are based only on the data from the 3RT combination.

In the bottom cell the exponent on ε_m is 0.31 and the exponent on V_{sg} is 0.81, both very similar to the exponents on the gas holdup correlations reported in chapter 4. Figure 6.3 shows that in the bottom cell, the impellers produced the same k_La for a given power and gas velocity. This is to be expected as a Rushton turbine was used in this cell for both impeller combinations.

In the middle cell the correlation of the Rushton turbine data produced exponents of 0.17 on ε_m and 0.62 on V_{sg}. For k_La values < 0.08 the LE20 impeller produced similar k_La to the Rushton turbine. However, for k_La > 0.08 the LE20 produced k_La values which were generally lower than the Rushton turbine.

In the top cell the correlation of the Rushton turbine data produced exponents of 0.13 on ε_m and 0.49 on V_{sg}. There is a lot of scatter in the LE20 k_La values with half of the data on the Rushton turbine correlating line and half the data below it.

6.4.2 Exchange flow model

This model, which includes the liquid exchange flows between the well mixed cells, is shown in figure 6.4.

The effect of introducing liquid exchange flows is shown in figure 6.5. During the dynamic mass transfer experiments, at any given time between the initial and final equilibrium conditions, the oxygen concentration in the bottom cell was higher than the oxygen concentration in the middle cell. Similarly the oxygen concentration in the middle cell was higher than the oxygen concentration in the top cell. Thus for the top cell, the introduction of a liquid exchange flow results in a net gain of oxygen. Therefore as the liquid exchange flow is increased, the k_La required to achieve a given dissolved oxygen transient, as measured in the top cell, decreases. For the bottom cell the introduction of a liquid exchange flow results in a net loss of oxygen. Thus as the liquid exchange flow is increased, the k_La required to achieve a given dissolved oxygen transient, as measured in the bottom cell, increases.

An example of the sensitivity of the calculated k_La values, to the liquid exchange flows (assumed to be equal at the top and bottom of the vessel for this sensitivity analysis), are shown in figure 6.6. As discussed above, the top cell k_La decreases and the bottom cell k_La increases with increasing exchange flow. For a given set of experimental response curves, the middle cell k_La can increase or decrease depending on the relative dissolved oxygen concentrations in the three cells. Figure 6.6 shows that it is important to accurately define the liquid exchange flows if the correct k_La are to be determined, and an accurate comparison of the two impeller combinations made.

The k_La values assuming the exchange flow model (exchange flows from chapter 5), are given in tables 6.1 and 6.2. As discussed in chapter 5, exchange flows could not be measured for gas holdup greater than 10%, so for these conditions the exchange flows were estimated, for a given power input, from figures 5.8 and 5.10.

Figure 6.7 shows the resulting k_La values, from this model, for the bottom cell only. The k_La values at high power and gas velocity are in excess of 0.2 s^{-1}. These k_La values are extremely high for oxygen transfer from air to water in an agitated vessel which are typically 0.07 s^{-1} ($\pm$0.05). The most likely cause of these high k_La values is that the exchange flows in the lower part of the vessel are being overestimated. This indicates that figure 5.8 cannot be used to estimate exchange flows at high gas holdup, and that high gas holdup does reduce exchange flows for a given power input, (exchange flows were not measured at high gas holdup due to the excessive noise on the conductivity response curves, refer to chapter 5).

The k_La values greater than 0.2 s^{-1} were removed from the following comparisons, as were the associated k_La values from the middle and top cells, (any error in the bottom cell k_La would introduce errors into the upper cells due to errors in gas depletion).

The impeller combinations are compared on the basis of the exchange flow model k_La values in figure 6.8. The 3RT data from each cell were correlated using:

$$k_La = \alpha\ (\varepsilon_m)^{\beta}\ (V_{sg})^{\gamma}$$

The correlations given in figure 6.8 are based only on the data from the 3RT combination.

In the bottom cell, the exponent on ε_m is 0.52 and the exponent on V_{sg} is 0.92, both higher than the simple model k_La. Generally, the bottom cell impellers produced the same k_La for a given power and gas velocity, as was found with the simple model. Three of the RT+2×LE20 data points are much higher than the correlation, which would

not be expected, and again may suggest overestimation of the exchange flows for these conditions.

In the middle cell the correlation of the Rushton turbine data produced exponents of 0.07 on ε_m and 0.53 on V_{sg}. The scatter in the data is much greater than found with the simple model, and the data from both impeller combinations are equally scattered about the correlation.

In the top cell the correlation of the Rushton turbine data produced exponents of 0.04 on ε_m and 0.58 on V_{sg}. In this cell, there is not too much scatter in the Rushton turbine data but there is a lot of scatter in the LE20 data. The introduction of exchange flows into the model significantly reduced some of the LE20 k_La values relative to the Rushton turbine k_La values. However, some of the LE20 k_La values have not been reduced, and remain of a similar order to the Rushton turbine data.

6.5 DISCUSSION

The power results, presented in chapter 3, indicated that the LE20 impellers were directly loaded with gas for the whole range of experiments conducted in the 0.95 m diameter vessel. When a single LE20 impeller, mounted in a standard geometry vessel, was directly loaded large gas bubbles were observed breaking away from the impeller region and rising rapidly to the liquid surface. The holdup results, presented in chapter 4, showed that at high gas holdup the RT+2×LE20 combination produced slightly less gas holdup than the 3RT combination, at a given power input and superficial gas velocity. It would therefore be expected, from the power and holdup results, that at high superficial gas velocities, the interfacial area produced by the RT+2×LE20 combination would be lower than that produced by the 3RT combination.

The simple mass transfer model (which ignored liquid mixing between cells) indicates that, in the upper impeller positions, the LE20 impellers produced the same k_La values as the Rushton turbines at low superficial gas velocities. At high superficial gas velocities the LE20 impeller in the middle cell produced lower k_La than the equivalent Rushton turbine. These results agree with the expected trends above. In the top cell there was too much scatter in the LE20 data to draw any definite conclusions.

It was shown that liquid exchange flows have a significant effect on the calculated k_La values in each cell. The aim of measuring three cell exchange flows and incorporating them into the mass transfer analysis, was to remove the effects of liquid mixing from the simple model k_La values, hopefully reducing the scatter in the LE20 data particularly in the top cell, and clarify the comparison of the impeller combinations in terms of local k_La. The results of the exchange flow model analysis show that this approach did not work, and it is believed that this is a result of inaccuracies in the assumed liquid mixing model.

It was shown, in chapter 1, that the exchange flow model has been used by several previous workers to model multiple Rushton turbine combinations (with one well mixed cell per impeller). The six cell liquid mixing work, reported in chapter 5, showed that the three cell exchange flow model was only realistic for the triple Rushton turbine combination at low impeller speeds and ungassed. At high impeller speeds or any gas sparged conditions this model does not apply to this impeller combination due to the formation of significant mixing boundaries at the plane of some of the Rushton turbines

(the top RT when ungassed, and the middle RT when gassed). The same effect was recently observed by Manna et al (1991).

Liquid mixing with multiple impellers is very geometry specific. This work and that of Manna et al (1991) show that significant mixing boundaries do not form at the plane of Rushton turbines positioned close to the vessel base. This is presumably the effect of the turbine discharge flow being slightly deflected by the non symmetric flow pattern around this impeller. Mixing boundaries can form in the upper Rushton turbine positions but the strength of these boundaries seems to be a function of the operating conditions, i.e. impeller speed and gas flow rate. For the RT+2×LE20 combination significant mixing boundaries were measured at the plane of the middle LE20 and mid way between the impellers. These boundaries were associated with the local flow loops observed in these regions. The two RT+2×PBT combinations were also shown to produce strongly compartmentalised flow patterns but it is difficult, just from visual observations, to judge where the main boundaries to liquid mixing are located, and therefore to decide what is the most appropriate model for the liquid mixing.

Of the workers who have previously attempted to measure liquid exchange flows, most only used one probe (to measure outlet residence time distributions) and only one worker used two probes to define liquid exchange flows for a triple Rushton turbine combination. This thesis shows that liquid mixing models for multiple impeller combinations can only be assessed accurately from liquid mixing experiments in which multiple probes are used, (preferably one probe positioned in each of the observed flow compartments).

6.6 CONCLUSIONS

1. Analysis of the dissolved oxygen transients using a simple liquid mixing model (three well mixed cells with no exchange flows) indicate that when LE20 impellers are used as upper impellers, they produce slightly lower k_La values, at high superficial gas velocities, than Rushton turbines in the same positions.

2. The inclusion of liquid exchange flows in the mass transfer model increased the scatter in the calculated k_La values, indicating that the assumed liquid mixing model was incorrect.

3. The determination of local k_La was limited by the ability to accurately define a liquid mixing model and the ability to measure the liquid exchange flows within that model (particularly difficult at gas holdups greater than 10%).

4. Definition of an accurate liquid mixing model, for multiple impeller systems, requires experiments with multiple liquid mixing probes, (one probe per flow loop / compartment).

5. In chapter 5 it was concluded that, for the 3RT combination, liquid exchange flows were constant for a given power input, and independent of impeller speed and gas flow rate. Analysis of the mass transfer data indicates that at high gas holdup (> 12%) this conclusion does not hold, and that liquid exchange flows are reduced for a given power input.

CHAPTER 7

ECONOMIC ANALYSIS

7.1 INTRODUCTION

This chapter will consider the economics of the options available for improving mass transfer in an agitated gas liquid reactor. It will be assumed that the mass transfer rate must be increased by 10% and the aim of this chapter is to define the most cost effective method of achieving this.

It is assumed that mass transfer from gas to liquid is the rate limiting step of the process and that any increase in mass transfer rate will result in a corresponding increase in product yield with no loss of product quality. Increased mass transfer may result in increased heat generation by the process which may require additional heat transfer equipment. In addition increased product yield could require significant modifications to the down stream processes, e.g. separators, filters and dryers. Increased production may also reduce the market price of the product. All of these costs need to be considered and compared with the benefits of increased product yield before the decision is made to increase the mass transfer rate. It is assumed in this analysis that once the decision to increase mass transfer rate has been made then additional heat transfer and down stream processing equipment will have to be purchased, and that the cost will be the same regardless of which option is chosen to actually achieve the increased mass transfer rate.

7.2 OPTIONS AVAILABLE FOR IMPROVING MASS TRANSFER

Mass transfer rate = $k_L a \, \Delta C$

Thus the mass transfer rate can be increased by increasing $k_L a$ (the mass transfer coefficient) and / or ΔC (the concentration driving force between the two phases).

Van't Riet (1979) reviewed mass transfer results from many sources and concluded that for oxygen transfer from air to water in agitated vessels:

$$k_L a \propto (\varepsilon_m)^{0.4} (V_{sg})^{0.5} \qquad \text{...Eqn (7.1)}$$

Muskett (1987) found very similar exponents for agitated vessels up to 2.67 m in diameter.

Thus $k_L a$ can be increased by increasing the power input to the dispersion or by increasing the gas flow rate (taking care not to flood the impeller). Assuming that the process will not allow a reduction in the oxygen level in the liquid phase, ΔC can only be increased by increasing the oxygen concentration in the gas phase. This can be achieved by increasing the pressure in the vessel or by addition of pure oxygen.

Thus the four options which will be considered for improving mass transfer rates are:

1. Increase the power input to the dispersion
2. Increase the gas flow rate

3. Increase the pressure in the process vessel
4. Enrich the gas

7.3 ECONOMIC BACKGROUND

The costs involved in any process change (equipment or operational) can be divided into capital costs and additional running costs. Capital costs are the costs incurred during the installation of additional process equipment and / or changes to operating procedures, and include all associated modifications required for complete process operation. The total capital cost consists of direct and indirect costs. Direct costs include: purchase of land, support steelwork, process equipment, pipe work and instrumentation and lost production during the retrofit (down time). Indirect costs include: planning time, administration, procurement, supervision, construction / installation expenses. New equipment or operating procedures can incur additional running costs due to increased labour, power consumption, or maintenance requirements. If a more energy efficient device is installed the additional running costs could be negative reflecting the reduced electricity consumption.

For situations where existing facilities are present and the choice is to replace / modify or stick with the existing equipment, net present worth and discounted cash flow methods give the soundest results for maximising the overall future worth of a concern, Peters and Timmerhaus (1991). Thus the net present value method will be used to compare the options given in section 7.2. The net present value of a project is initial capital cost plus the amount of money which must be invested at the start of the project to be able to pay the annual running costs in future years. For this method a project life has to be specified as well as the interest rate, which is assumed to be constant over the project life.

For this analysis the project life will be assumed to be 10 years and the interest rate will be assumed to be 10%. The sensitivity of these parameters will be discussed in section 7.6.

Assuming simple interest compounding:

$$R = I_0 (1 + i)^n$$

where:
I_0 = initial investment
R = amount available after n interest periods
i = interest rate

Thus the present value of a future investment is given by:

$$I_0 = \frac{R}{(1 + i)^n}$$

Relating this equation to the annual running costs of an agitator:

R = annual running cost
i = annual interest rate
I_0 = amount of money which would have to be invested now to realise R after n years

Summing the discounted running costs over the life time of the equipment gives an

e pression or t e net present v lue of the total future annua nni g costs

(

where pro ect life (e s)

Thus:

The total net present v ue of a project is the sum of he net present value of the capi l costs, , (represented as a one of pa ment at the st of th roject) and the net present value of the nnin costs, i.e.:

hus in comp ng the process o tions desc bed n section . the actors that need to be considered e the xed capital re uired to achieve the retro t and the a dit onal annual nning costs ese costs wi be estimated in secti n 7. .

7.4 TS SS I T T FIT O T O

ll pr ess options will involve additional capital and operating sts which are process d site speci c Thus numerous simplifying assumptions have had to be made to generalise the economic comp s n of the four options considered.

7.4 cre se the po er i p t to the di pe si

rom e uation 7.

h s to c ie a 10% increase in the gasse po er aw of the impel ers per nit mass of li uid must be increased by %.

or impure asses such as a' an increase in due to an increased power per unit mass would result in more gas depletion, thus reducing *C* and the mass ansfer rate. For this anal sis it will be assumed that gas depletion is negligible and that ncreased deple on, due to the increased power aw, has a negligible effect on *C*. or air wate dispersion gas holdup increases with power input in he sa e way as hus a increase in power input will increase gas hold p by appro imatel %. ost indust 'al vessels will already be op rating at maximum capacity so an inc ease in gas holdup coul only be accommodat d b educing the li uid volume in the vessel and therefore reducing the product ield. The effect of this on the process economics will depend on the reduction in li uid volume, the concen ation of product in the li uid and the sales p 'ce of the prod ct. hus for s mplicity it is assumed that the vessel can accommodate

in ath d n h e reduced.

h a se duadce goenucir c c uee u gtehl cecos n

For a given process:

$$Power \propto \frac{P_g}{P_u} Po\ N^3\ D^5$$

In some cases it would be possible to increase the gassed power draw of the agitator without increasing the ungassed power draw or torque. For example, if the agitator is fitted with a Rushton turbine, a centrally mounted point sparger and a single speed motor, the point sparger could be changed for a large ring sparger, Nienow and Allsford (1985), or the flat blades of the Rushton turbine could be changed for concave blades, Warmeoskerken and Smith (1989). These options if available have the advantage of not requiring any motor or gearbox modifications. However, this is unlikely to be the case for large scale production facilities which are usually fitted with two speed motors, (low speed for ungassed conditions and high speed for gassed conditions) so that the motor is fully utilised under gassed conditions. Thus in most cases a 27% increase in power could only be satisfied by fitting a larger motor to the agitator, modifying the gearbox, and perhaps modifying the impellers.

The simplest retrofit option, and the one involving the lowest capital cost, would be to keep the existing impellers and increase the impeller rotational speed. In this case:

$$\text{Power} \propto N^3$$

and $$\text{Torque} \propto N^2$$

Thus a 27% increase in power would require an 8.3% increase in impeller speed and this would result in a 17% increase in torque. For this analysis it is assumed that the existing shaft design can safely cope with the increased torque demand and that the new impeller speed is well below the shaft critical speed. It will also be assumed that the agitator speed can be increased by simply changing the gear ratios in the existing gearbox, and that the existing motor and gearbox mountings can safely handle the increased mechanical loads. Finally it will be assumed that the retrofit can be completed during a scheduled shut down period so that the costs involved with lost production can be eliminated (costs that will be very process specific).

Modification of the impellers would involve much higher capital costs. However, it is difficult to generalise these costs because they are sensitive to material of construction and the exact design of impellers used, e.g. in-house or proprietary design.

The worst case scenario, in terms of capital cost, would be if the existing gearbox and shaft cannot safely handle the increased torque. In this case the motor, gearbox, shaft and probably the impellers would have to be replaced, massively increasing the cost of the retrofit. Grenville (1992) showed that the capital cost of a complete agitator (assuming stainless steel wetted parts) can be estimated from:

$$C_C = 488\ \Lambda^{0.484} \qquad \text{...Eqn (7.2)}$$

Where: Λ = Shaft torque

This analysis will consider two cases for achieving a 27% increase in impeller power draw:

a) Operation of existing agitator at higher impeller speed requiring a larger

motor and modification of the existing gearbox.

b) Complete replacement of the agitator.

Muskett (1987) gave the relative costs for the main items of an agitator showing that the largest costs are associated with the gearbox and mechanical seal. The motor typically only represents 5% of the total cost of an agitator. From equation 7.2 it will be assumed that the capital costs associated with scenario 'a' can be estimated from:

$$C_C = 0.10 \times 488\ \Lambda^{0.484}$$

The factor of 0.10 accounts for the motor cost and the additional costs of installation and gearbox modifications.

The main additional operating cost of increasing the agitator power draw is the cost of electricity (principal cost of operating an agitator, Meyer and Kime, (1976)). The additional power draw of the impellers is 27% greater than the current power draw, i.e:

$$P_A = 1.27\ E_M\ P$$

where:
P_A = Additional power draw of impellers (kW)
E_M = Motor efficiency
P = Current power draw of motor

The motor efficiency takes into account of energy losses in the gearbox and bearings and will be assumed to be 90%, i.e. $E_M = 0.9$.

The annual cost of this extra power draw can be estimated from:

$$C_{pow} = P_A\ t_{op}\ C_{elec} \qquad \text{...Eqn (7.3)}$$

t_{op} = Production hours per year (hr)
C_{elec} = Cost of electricity (£/kW hr)

t_{op} will be assumed as 8000 hours / year and the cost of electricity will be assumed to be 0.0717 £/kW hr, Eastern Electricity plc (1992).

7.4.2 Increase the gas flow rate

From equation 7.1:

$$k_La \propto (V_{sg})^{0.5}$$

Thus to achieve a 10% increase in k_La, V_{sg} (the superficial gas velocity) must be increased by 21%. The maximum superficial gas velocity is limited by the flooding point of the impeller.

As assumed in section 7.4.1 the gas depletion is assumed to be negligible so the effect of increasing V_{sg} on the concentration driving force is also assumed to be negligible. Gas holdup increases with V_{sg} in the same way as k_La. Therefore a 21% increase in V_{sg} will result in a 10% increase in gas holdup. As discussed in section 7.4.1 it is assumed

for this analysis that the vessel can accommodate a 10% increase in gas holdup and that the liquid volume does not have to be reduced. It will also be assumed that the existing agitator is operating under conditions where the impeller power draw is insensitive to the gas flow rate. Thus the increased gas flow rate does not reduce the power input to the dispersion.

It will be assumed that there is sufficient capacity in the existing gas compressor to supply the required increase in gas flow rate and that the required increase in gas flow will not flood the impeller. Thus there are no capital costs associated with this option.

The costs involved in increasing the gas flow rate are assumed to equal the cost of the extra electrical energy consumed by the compressor. Compressor efficiencies are usually expressed as isentropic efficiencies, i.e. on the basis of an adiabatic reversible process. Isothermal efficiencies are sometimes quoted and design calculations are simplified when isothermal efficiencies are used. In either case the efficiency is defined as the ratio of the power required for the ideal process to the power actually consumed. For reciprocating compressors isothermal efficiencies are about 50 to 70%, Peters and Timmerhaus (1991).

Expressions for the theoretical power requirements of gas compressors can be obtained from the basic equations of thermodynamics. For an ideal gas undergoing an isothermal compression (PV = constant) the theoretical power requirement for any number of stages can be expressed as follows:

$$Power = P_1 \, Q_G \, ln(P_2/P_1)$$

where: P_1 = Inlet pressure (Pa)
P_2 = Discharge pressure (Pa)
Q_G = Volumetric flow rate of gas at inlet conditions (m^3/s)

It is assumed that the discharge pressure is dominated by the static head of liquid in the process vessel, i.e. pressure losses in the gas supply pipework are negligible.

The power consumed by the compressor is calculated from:

$$Power = E_C \, P_1 \, Q_G \, ln(P_2/P_1) \qquad \text{...Equation 7.4}$$

where: E_C = Isothermal efficiency of the compressor (assumed to equal 0.6)

The additional power draw of the compressor is calculated from:

$$Power = E_C \, P_1 \, \Delta Q_G \, ln(P_2/P_1)$$

where: ΔQ_G = Increase in gas flow rate (m^3/s)

The annual cost of this increased power draw is estimated from equation 7.3.

7.4.3 Increase the pressure in the process vessel

Takahashi et al (1986) showed that for a given volumetric gas flow rate at the sparger, pressure has no effect on the power draw or bubble sizes produced by a Rushton turbine.

Assuming that as soon as oxygen is transferred from the gas to the liquid it is utilised in some chemical reaction so that the concentration of oxygen in the liquid phase is very low, then ΔC can be increased by 10% if the concentration in the gas phase is increased by 10%.

For an ideal gas $P_1V_1 = P_2V_2$ (assuming isothermal compression)

Thus for a given mass of oxygen, M_{O2}, the concentration is increased by 10% when:

$$\frac{M_{O_2}}{V_1} \; 1.10 = \frac{M_{O_2}}{V_2}$$

so $$\frac{V_1}{V_2} = 1.10$$

i.e $$\frac{P_2}{P_1} = 1.10$$

It will be assumed that the existing gas compressor can supply gas at the higher pressure with no reduction in the gas flow rate. Thus assuming that the existing vessel is safely rated to handle the increased pressure then there are no capital costs associated with this option.

The only cost involved is the additional electricity consumed by the compressor, which can be calculated from equations 7.4 and 7.3.

7.4.4 Use enriched gas

When using pure oxygen for process enhencement a number of safety issues should be addressed, usually in conjunction with a knowledgeable authority. The prime concerns are the compatibility of materials that wil be in contact with increased oxygen concentrations, for example in the air main supplying the fermenter, and the interfacing of the pure oxygen addition with the process operation.

Air contains 21% oxygen by volume. Enriched air containing up to 25% by volume of oxygen may be substantially handled the same as air. Above 25% by volume of oxygen a detailed safety study should be considered, and above 30% by volume of oxygen the materials in contact must be compatible with pure oxygen use.

Before oxygen enrichment:

$$\text{Oxygen flow rate} = 0.21 \times Q_{AIR}$$

As assumed in section 7.2, ΔC can be increased by 10% if the oxygen concentration in the gas is increased by 10%. Assuming that the air flow into the vessel ($Q_{G,AIR}$) is maintained at 1.0 VVM, i.e:

$$Q_{G,AIR} = V_L$$

For a 10% increase in the oxygen concentration of the inlet gas:

$$\frac{(Q_{G,\,OXYGEN} + 0.21\ Q_{G,\,AIR})}{Q_{G,\,TOTAL}} = 1.10 \quad 0.21$$

where $Q_{G,\,TOTAL} = Q_{G,\,AIR} + Q_{G,\,OXYGEN}$

Thus $Q_{G,\,OXYGEN} = 0.0273\ V_L$ ...Eqn (7.5)

The enriched gas inlet concentration will therefore be 23.1% so it can be handled as normal air so long as safety interlocks prevent safety excursions above 25%.

Because of the quantities required the oxygen is stored as a liquid to minimise storage space requirements. BOC Ltd install the storage vessel, the vapouriser, pressure gauges, safety devices and control equipmant ready to connect to the vessel supply line. Capital costs for the gas user include a concrete plinth for the storage vessel and the pipe work from the storage facility to the vessel.

BOC Ltd were asked to supply installation costs for three of the vessels given in table 7.1:

Pilot scale: £ 6000

Small scale: £ 10,000

Large scale: £ 20,000

BOC Ltd were also asked to supply running costs for three of the vessel scales given in table 7.1 (assuming Q_G = 1 vvm, and vessel back pressure = 1 bar):

Pilot scale: £ 4,500 to 5000 / year

Small scale: £ 20,000 to 22,000 / year

Large scale: £ 250,000 to 275,000 / year

These costs include a regular service and emergency maintenance as well as the cost of the liquid oxygen (oxygen demand varies with air flow, from equation 7.5).

7.5 RESULTS

In this analysis it is assumed that the correlations in section 7.4 apply for the range of gas flow rates, back pressures and power inputs covered in this section. As the basis for comparison it is assumed that the project life is 10 years and that the interest rate is constant at 10%.

Figure 7.1 shows the effect of scale on the total net present costs associated with the five process options for improving mass transfer. For this comparison initial operating conditions of Q_G = 1 vvm, ε_m = 2 W/kg, and a back pressure = 1 bar were assumed. At all scales the lowest costs are associated with option 4, increase back pressure. The

highest running costs are associated with option 5, inlet gas enrichment. Gas enrichment is actually much more expensive than option 2, which involves complete replacement of the agitator, including motor, gearbox, shaft and impellers, to achieve a higher impeller power draw.

Figures 2 to 5 show a comparison of the process options for the large scale vessel (T = 3.8 m) at a range of gas flow rates, vessel back pressures and power inputs.

Figure 2 compares the process options for a range of power inputs (0.5 to 5 W/kg) at a low gas flow rate (1 vvm) and a low back pressure (1 bar). Options 3 and 4 are independent of impeller power draw because they are only a function of compressor power draw and back pressure. For power inputs > 2 W/kg the conclusions are the same as for figure 1. At lower power levels the cost involved in increasing power by 27% (options 1 and 2) decrease and become comparable to option 4 (increasing back pressure) at 0.5 to 1 W/kg.

Figure 3 is the same as figure 2 except that the back pressure has been increased to 5 bar, (the gas flow rate remains at 1 vvm). For a vessel operating at higher pressure the costs associated with option 3 (increasing the gas flow rate) are significantly increased but the costs associated with options 1, 2 and 4 remain unchanged. Thus at a gas flow rate of 1 vvm the cheapest option for improving k_La is to increase the back pressure, regardless of the existing vessel pressure and the impeller power draw (above 0.5 to 1 W/kg).

Figure 4 is the same as figure 2 except that the gas flow rate has been increased to 5 vvm, (the back pressure remains at 1 bar). Compared with figure 2 the costs of options 3 and 4 have increased significantly but the costs of options 1 and 2 remain unchanged. Keeping the gas flow rate at 5 vvm and increasing the back pressure to 5 bar, figure 5, all costs remain the same except those for option 3 which increase further. Thus at high gas flow rates options 1 and 2 (increasing power draw) have the lowest costs except for high power inputs (> 4 W/kg) where increasing back pressure becomes the cheapest option.

Figures 6 to 9 are the same as figures 2 to 5 except that they apply to the pilot scale vessel (T = 0.61 m). Generally the conclusions are the same as the large scale vessel. There is, however, a greater difference between options 1 and 2 so the costs associated with increasing the power draw of the impellers is more sensitive to the capital costs of the retrofit.

The sensitivity of this economic comparison to project life and interest rate are shown in figures 7.10 and 7.11. For very short project lives (less than 6 months) running costs are minimised and the total cost of the various options is dominated by the capital costs. Thus the costs associated with option 2 (complete agitator retrofit) are an order of magnitude higher than those for option 1 (motor retrofit), and the costs associated with option 3 (increased gas flow rate) and option 4 (increase back pressure) are an order of magnitude lower than option 1. For very short project lives it is also cheaper to enrich the inlet gas with oxygen (option 5) than it is to completely retrofit the agitator (option 2).

For project lives greater than 1 year, the comparison of costs is dominated by the running costs. For options 1, 2, 3 and 4 the running costs consist entirely of electrical power costs. For option 5 the running costs are dominated by the cost of liquid oxygen.

For projects lasting more than one year, the comparison of costs is independent of the project life. Option 4 (increasing back pressure) is always the cheapest option, and option 5 (enriching the inlet gas) is always the most expensive option.

The effect of interest rates is similar for all options, see figure 7.11. This comparison is based on a project life of 10 years so the total costs are dominated by the running costs. The total net present value decreases with interest rate because at higher interest rates less money has to be invested now to realise a specified sum at some future date.

7.6 DISCUSSION

One major assumption in this analysis is that the oxygen demand of the process is constant during the whole batch time. Under these conditions oxygen enrichment of the inlet gas is the most expensive option for improving mass transfer rate, due to the relatively high running costs. For many processes, for example fermentations, the oxygen demand changes significantly with time. In these cases oxygen enrichment may be the easiest method of achieving high mass transfer rates during these periods of peak demand. The main advantage of oxygen enrichment is flexibility, i.e. easy on / off control.

One other factor which has been ignored from this analysis, because of the process specific nature of the costs involved, is the effect of the process change on the gas holdup in the vessel. Gas holdup will not affected by oxygen enrichment so the liquid volume would not have to be reduced, as it probably would be with increased power draw or increased gas flow rate. Higher levels of oxygen enrichment will allow a reduction in gas holdup (although this will reduce k_La) and an increase in the liquid volume resulting in more product per batch. However, as mentioned in section 7.4.4, the safe operation of the process may require significant plant modifications if high levels of air enrichment are to be considered.

Throughout this analysis the gas has been assumed to be ideal. As a result a 10% increase in pressure produces a 10% increase in gas concentration. This assumption may be acceptable at low pressures but will not be realistic at very high pressures due to the non ideal behaviour of the gas. For this reason this analysis is limited to pressure less than 5 bar.

k_La is very system specific and the exponents on ε_m and V_{sg} vary with coalescence behaviour and liquid rheology. Generally as liquid viscosity increases the exponent on ε_m increases and the exponent on V_{sg} decreases. Thus for viscous liquids options 1 and 2 will become relatively cheaper and option 3 will become relatively more expensive. Options 4 and 5 will be independent of liquid rheology. Thus for typical fermenter operating conditions ($\varepsilon_m \approx 2$ W/kg and $Q_G \approx 1$ vvm, Bader (1987)) increasing the vessel back pressure is the cheapest option for improving mass transfer rates. This agrees with the conclusion of Bader (1987) who noted that pressure increase is common practice for dissolved oxygen control in fermenters. Bader also concluded that oxygen enrichment has a high potential for control of dissolved oxygen levels if low cost oxygen is available.

7.7 CONCLUSIONS

1. For a gas flow rate of 1 vvm, increasing back pressure offers the cheapest option for improving mass transfer rates in an existing gas liquid reactor. This is true regardless of the initial operating pressure.

2. For a high gas flow rate of 5 vvm, the costs associated with increasing the back pressure are higher than those associated with increasing the power input from the impellers. At large scale increasing the power input is the cheapest option, even if this requires a complete agitator retrofit. At small scale increasing power input is the cheapest option but only if the capital costs of the retrofit can be minimised.

3. Oxygen enrichment of the inlet gas, assuming enrichment during the whole process cycle and not just at peak periods, is the most expensive option for improving mass transfer rates. This is because whilst capital costs are relatively low, the running costs are relatively high. For projects of short duration (one or two months) oxygen enrichment would have comparable or even lower total costs than the other options considered.

CHAPTER 8

OVERALL CONCLUSIONS AND SUGGESTIONS FOR FUTURE WORK

8.1 INTRODUCTION

In this research work, air dispersion into water was studied in tall vessels fitted with four different multiple impeller combinations:

1. 3×RT
2. RT+2×LE20 (pumping down)
3. RT+2×PBT (pumping down)
4. RT+2×PBT (pumping up)

One objective of this work was to improve understanding of how impellers behave in the lower and upper positions of multiple impeller combinations, and to determine if any literature correlations for single impellers could be applied to multiple impeller combinations. The purpose of retrofitting multiple Rushton turbines with axial flow impellers is to improve liquid mixing and / or mass transfer rates. Additional objectives of thesis were therefore to investigate the effects of impeller design and operating conditions on these important design parameters.

8.2 CONCLUSIONS

For design of gas liquid reactors it is important to know the maximum gas flow rate that can be dispersed before flooding. The work presented in this thesis showed that the design of the upper impellers had a significant effect on the flooding behaviour of the lowest impeller (always a Rushton turbine). At a large impeller separation of $0.8T$ the lowest impeller flooded at lower gas flow rates than when mounted alone in a standard geometry vessel (true when upper impellers were Rushton turbines or LE20s). At a lower impeller separation of $0.5T$, the use of Rushton turbines in the upper positions further reduced the flooding gas flow rate of the lowest turbine. However, at the same impeller separation of $0.5T$, the use of LE20 impellers in the upper positions significantly increased the flooding gas flow rate of the lowest turbine. It was the down flow produced by the LE20 that stabilised the loading regime for the lowest turbine. Thus at low impeller separations (approximately $< 0.5T$) the selection of upper impeller design can significantly affect the maximum gas flow rate that can be dispersed by the lowest impeller. This work suggests that downward pumping impellers are the best choice for the upper positions if flooding of the lower impeller must be avoided.

Previous workers have concluded that the use of downward pumping impellers above a Rushton turbine can result in large flow and torque instabilities. It was also observed in this work that, when downward pumping impellers are used in the upper impeller positions, they can become effectively directly loaded with gas, as they do when sparged in standard geometry vessels. For downward pumping impellers of low blade number and low blade angle, this can lead to rapid changes in power draw and the instabilities referred to above. Thus impellers of large projected blade area and large blade angle, e.g. four or preferably six blade 45° pitched blade turbines, are recommended for the upper impeller positions.

At an impeller separation of 0.8*T*, the ungassed power numbers of the Rushton and pitched blade turbines tested were the same in the tall vessel geometry as they were in the standard vessel. This was not true for the LE20 impellers because these impellers produced significantly different local flow patterns in the tall vessel, compared to the standard vessel, and as a result drew more power.

For an impeller separation of 0.8*T*, the lowest impeller in all combinations tested, (always a Rushton turbine) drew slightly less gassed power than it did when mounted alone in a standard geometry vessel. This difference is not considered to be very significant from a design point of view. The large diameter pitched blade turbines studied drew the same gassed power in the tall vessel as they did in the standard geometry vessel. This was because these impellers had large diameters and high power draw and therefore the local hydrodynamics were dominated by gas recirculation. The Rushton turbine and LE20 impellers drew different gassed power when positioned in the upper positions of the tall vessel, compared to when they were positioned alone in a standard geometry vessel. These impellers imparted much less power into the dispersion and therefore the gas recirculation rates into these impellers were lower. Although the power draw of the impeller combinations tested was very different, the total P_g/P_u ratios were similar for a given impeller speed and gas flow rate.

A method was presented for estimating the fraction of gas entering the upper impellers for multiple Rushton turbines, based on the flow maps developed by previous workers. This was combined with an empirical correlation for prediction of gassed power of a single Rushton turbine, to predict the gassed power draw of multiple Rushton turbines. The power predictions were found to work well for $Fr < 0.6$, but for $Fr > 0.7$ the predictions under estimated the measured power draw.

The holdup data correlated equally well with power input and superficial gas velocity, or impeller speed and gas flow rate. The correlations were found to be statistically different for each impeller combination studied. The different cavity regimes found on the blades of multiple Rushton turbines were also found to have a significant effect on the correlation of gas holdup data. For a given power input and superficial gas velocity slight differences were observed between the impeller combinations studied, but only at high gas holdup (> 12%). However, all of these effects were minor and all of the tall vessel data could be correlated well (±20%) with single Rushton turbine data from standard geometry vessels of 0.61 and 2.67 m diameter using:

$$\varepsilon_G = 1.79\ (\varepsilon_m)^{0.34}\ (V_{sg})^{0.72}$$

Thus, for the range of conditions studied, overall gas holdup was independent of vessel geometry and impeller combination.

Tracer addition point had a large effect on the measured liquid mixing time. For the triple Rushton turbine combination tested in this thesis surface addition of tracer resulted in a liquid mixing time 300% longer than when tracer was added to the outlet from the middle impeller. To optimise the position of reactant feed streams the designer needs to know where the main boundaries to axial mixing are located. This thesis shows that, for all impeller combinations tested, the flow patterns were compartmentalised, i.e. a single top to bottom circulation loop was not observed for any test conditions. Strong mixing boundaries were found at the plane of Rushton turbines, and between axial flow impellers. The position of axial mixing boundaries is sensitive to impeller design, impeller separation, impeller speed and gas flow rate.

For ungassed conditions, at a given scale, the RT+2×LE20 combination mixed the liquid in 40 to 55% of the time taken by the 3RT combination. Although flow patterns with RT+2×LE20 combination were compartmentalised by local flow loops, they were not as compartmentalised as the 3RT combination. In all cases $N\theta$ was approximately constant for a given impeller geometry under fully turbulent conditions.

Aeration had a significant effect on liquid mixing for both the 3RT and RT+2×LE20 combinations. Aeration reduced the power draw of all impellers and increased the liquid mixing time. For multiple Rushton turbines the liquid mixing was constant for a given power input, up to gas holdup of 10%, regardless of the gas flow rate. Analysis of the mass transfer data suggested that this was not true at higher holdup and that under these conditions the liquid mixing time increased for a given power input. With the lowest impeller flooded the liquid mixing time was reduced due to break up of the compartmentalised flow pattern. Thus, for this impeller combination, flooding was good for liquid mixing but obviously bad for gas dispersion.

For the RT+2×LE20 combination, aeration had a greater effect than observed with the 3RT combination. For a given power input the liquid mixing time was larger with gas than without gas. Flooding of the lowest impeller had negligible effect on liquid mixing because the vessel contents were not as compartmentalised as with the 3RT combination. Liquid mixing time with the RT+2×LE20 combination was strongly affected by aeration because the gas cavities which formed on the blades of the LE20 impellers directly reduced axial liquid pumping. Thus when gassed, this impeller combination produced the same liquid mixing time as the 3RT combination at a given power input. The aim of retrofitting two of the Rushton turbines with LE20s was to improve liquid mixing, but the results in this thesis show that very little benefit was actually achieved. At higher power inputs the gassed liquid mixing times with the RT+2×LE20 combination appeared to be decreasing at a faster rate than those of the 3RT combination, suggesting that the RT+2×LE20 combination would give shorter liquid mixing times at higher power inputs.

Liquid mixing with multiple impellers is very geometry specific. This work showed that significant mixing boundaries do not form at the plane of Rushton turbines positioned close to the vessel base. This is presumably the effect of the turbine discharge flow being slightly deflected by the non symmetric flow pattern around this impeller. However, mixing boundaries can form in the upper Rushton turbine positions, and the strength of these boundaries seems to be a function of the operating conditions. For the RT+2×LE20 combination, significant mixing boundaries were measured at the plane of the middle LE20 and mid way between the impellers. These boundaries were associated with the local flow loops observed in these regions. The two RT+2×PBT combinations were also shown to produce strongly compartmentalised flow patterns but only visual observations were made of these impeller combinations and it was difficult to judge where the main boundaries to liquid mixing were located. This could only be assessed from liquid mixing experiments in which probes are positioned in each of the observed flow compartments.

Several previous workers have used exchange flow models to describe liquid phase mixing with multiple Rushton turbine combinations (with one well mixed cell per impeller). Of the workers who actually attempted to measure the liquid exchange flows in their models, most only used one probe, (to measure outlet residence time distributions) and only one worker used two probes to define liquid exchange flows for a triple Rushton turbine combination. In this thesis liquid mixing experiments were

conducted with six probes, one positioned in each flow loop. The results showed that the three cell exchange flow model was only realistic for the triple Rushton turbine combination at low impeller speeds when ungassed. At high impeller speeds, or any gas sparged conditions, this model did not apply to this impeller combination, due to the formation of significant mixing boundaries at the plane of some of the Rushton turbines (the top RT when ungassed, and the middle RT when gassed).

The effect of scale on liquid mixing times was very different for the two impeller combinations tested, though it is accepted that a narrow range of scales was tested and that further tests at a larger scale are needed to check the trends observed in this work.

Analysis of the mass transfer data, assuming a simple liquid mixing model (which ignored liquid mixing between cells) indicated that, in the middle impeller position, the LE20 impeller produced the same k_La values as the Rushton turbine at low superficial gas velocities. At high superficial gas velocities the LE20 impeller produced lower k_La than the Rushton turbine. These results agree with the expected trends from the power and holdup data. In the top cell there was too much scatter in the LE20 data to draw any definite conclusions. The assumption of a three cell exchange flow model, as the basis for the calculation of local k_La values, increased the scatter in the k_La data, again indicating that the assumed liquid mixing model was incorrect.

The ability to accurately determine local k_La in this work was limited by the ability to define an appropriate mixing model for the liquid phase, and the ability to accurately determine liquid exchange flows within that model. For multiple impeller systems, a realistic liquid mixing model can only be determined by the use of multiple probes, one for each liquid recirculation loop.

8.2 SUGGESTIONS FOR FUTURE WORK

The gas flow rate at which the lowest impeller floods defines the operating limit for the reactor. If selection and positioning of the upper impellers can increase the maximum gas flow rate then this can have direct benefits for the process. Thus it would be useful to study in detail the effects of impeller separation and upper impeller design on flooding of the lowest impeller.

The pitched blade turbines used in this study produced strongly compartmentalised flow patterns. In terms of liquid mixing time, when gassed, there was little difference between multiple Rushton turbines and LE20 impellers. It would be interesting to measure liquid mixing times with multiple pitched blade turbines, over a wide range of operating conditions, to see if they offer any advantages over multiple Rushtons. The degree of compartmentalisation in tall vessels is very geometry specific, and there are many parameters that could be studied, e.g. impeller design, diameter and separation. The aim of this work would be to define the optimum agitator design for good liquid mixing in gassed processes. The effect of tracer addition point on liquid mixing time would also be very geometry specific but important for optimisation of reactant addition points.

The use of conductivity probes to determine local exchange flows was limited to gas holdups less than 10%, due to interference of the gas bubbles on the conductivity response curves. The k_La analysis suggested that some of the liquid mixing conclusions based on gas holdups less than 10% do not hold for gas holdups greater than 10%. To

investigate this further would require refinement of the experimental technique presented in this thesis. One option would be the use of fast response pH probes which should be less susceptible to interference from gas bubbles than conductivity probes.

Tall vessels are often used for gas dispersion into viscous liquids. It would be useful to study the effects of liquid rheology on liquid exchange flows and local mass transfer rates. In viscous liquids the dynamic response mass transfer method used in this work cannot be used. A steady state mass transfer method must be used, and Appendix 5 details one such method. Several problems were initially encountered with the method described in appendix 5, but these problems were solved and the method is now being used successfully at BHR Group Ltd for mass transfer studies in standard geometry vessels.

REFERENCES

Abrardi, V.
Rovero, G.
Sicardi, S.
Baldi, G.
Conti, R.
"Sparged vessels agitated by multiple turbines", Proc. of 6th Euro. Conf. on Mixing, Pavia, Italy, (1988), BHRA, Fluid Eng., Cranfield, U.K., pp. 329-336.

Abrardi, V.
Rovero, G.
Baldi, G.
Sicardi, S.
Conti, R.
"Hydrodynamics of a gas liquid reactor stirred with a multi impeller system", Trans. IChemE, Vol. 68, Part A, (November 1990), pp. 516-522.

Ando, K.
Fukuda, T.
Endoh, K.
"Encyclopedia of Fluid Mechanics", Volume 2, Chapter 28, p. 783, Edited by Cheremisinoff, N.P., Gulf Publishing Co., (1985).

Andrew, S.P.S.
"Gas-liquid mass transfer in microbiological reactors", Trans. IChemE., Vol. 60, No. 1, pp. 3-13, (1982).

Bader, F.G.
"Mass transfer in a multi turbine fermenter. 1. Gassed and ungassed power inputs", Proc. of Int. Conf. on Bioreactor Fluid Dynamics, Cambridge, U.K., (1986), BHRA, Cranfield, U.K., paper 20, pp. 269-280.

Bader, F.G.
"Modelling mass transfer and agitator performance in multi turbine fermenters", Biotech. & Bioeng., Vol. 30, pp. 37-51, (1987a).

Bader, F.G.
"Improvements in multi-turbine mass transfer models", Biotechnology Processes, (Edited by Ho, C.S. & Oldshue, J.Y.), AIChE, pp. 96-106, (1987b).

Bajpai, R.
Sohn, P.U.
"Staged models for mixing in stirred bioreactors", Biotechnology Processes (Edited by Ho, C.S. & Oldshue, J.Y.), AIChE, pp. 13-21, (1987).

Bakker, A.
"Hydrodynamics of stirred gas-liquid dispersions", PhD Thesis, Delft University of Technology, (1992).

Balmer, G.J.
Moore, I.P.T.
Nienow A.W.
"Aerated and unaerated power and mass transfer characteristics of Prochem agitators", Biotechnology Processes, Edited by Ho, C.S. and Oldshue, J.Y., AIChE, (1987), pp.116-127.

Bates, R.L.
Fondy, P.L.
Corpstein, R.R.
"An examination of some geometric parameters of impeller power", I&EC Process Design and Development, Vol. 2, No. 4, (1963), pp. 310-314.

Bruijn, W.
Van't Riet, K.
Smith, J.M.
"Power consumption with aerated Rushton turbines", Trans. I.ChemE., Vol. 52, (1974) pp. 88-104.

Bryant, J.
Sadeghzadeh, S.
"Circulation rates in stirred and aerated tanks", Proc. of 3rd Euro. conf. on mixing, York, U.K., (1979), BHRA, Paper F3, pp. 325-336.

Bujalski, W.
"Three phase mixing: Studies of geometry, viscosity and scale", PhD Thesis, University of Birmingham, (1987).

Bujalski, W.
Konno, M.
Nienow, A.W.
"Scale up of 45° pitch blade agitators for gas dispersion and solid suspension", Proc. 6th Eur. Conf. on mixing, Pavia, Italy, BHRA Fluid Eng., Cranfield, England, (1988), pp. 389-398.

Bujalski, W.
Nienow, A.W.
Huoxing, L.
"The use of upward pumping 45° pitched blade turbine impellers in three phase reactors", Chem. Eng. Sci., Vol. 45, No. 2, (1990), pp. 415-421.

Calderbank, P.H.
"Physical rate processes in industrial fermentation. Part 1: The interfacial area in gas-liquid contacting with mechanical agitation", Trans. Inst. Chem. Eng., Vol. 36, (1958), pp. 443-463.

Chandrasekharan, K.
Calderbank, P.H.
"Further observations on the scale up of aerated mixing vessels", Chem. Eng. Sci., Vol. 36, (1981), pp. 819-823.

Chapman, C.M.
"Studies of gas liquid particle mixing in stirred vessels", PhD Thesis, University College London, (1981).

Chapman, C.M.
Gibilaro, L.G.
Nienow, A.W.
"A dynamic response technique for the estimation of gas liquid mass transfer coefficients in a stirred vessel", Chem. Eng. Sci., Vol. 37, No. 6, (1982), pp. 891-896.

Chapman, C.M.
Nienow, A.W.
Middleton, J.C.
"Surface aeration in a small, agitated and sparged vessel", Biotechnol. and Bioeng., Vol. 22, (1980), pp. 981-993.

Chapman, C.M.
Nienow, A.W.
Cooke, M.
Middleton, J.C.
"Particle-gas-liquid mixing in stirred vessels, Part 2: Gas liquid mixing", Chem. Eng. Res. Des., Vol. 61, (1983a), pp. 82-94.

Chapman, C.M. Nienow, A.W. Cooke, M. Middleton, J.C. "Particle-gas-liquid mixing in stirred vessels, Part 3: Three phase mixing", Chem. Eng. Res. Des., Vol. 61, (1983b), pp. 167-181.

Chapman, C.M. Nienow, A.W. Cooke, M. Middleton, J.C. "Particle-gas-liquid mixing in stirred vessels, Part 4: Mass transfer and final conclusions", Chem. Eng. Res. Des., Vol. 61, (1983c), pp. 182-185.

Chiampo, F. Guglielmetti, R. Manna, L. Conti, R. "Gas liquid mixing in a multiple impeller stirred vessel", Proc. of 7th Euro. Conf. on Mixing, Brugge, Belgium, (1991), pp. 333-342.

Chiampo, F. Conti, R. "Complete dispersion of gas in stirred vessels with double impellers", Proc. of Conf. on Recent Progress in Process Engineering: Industrial Agitation, Vol. 6, No. 19, Toulouse, France, (1992).

Cooke, M. Dawson, M.K. Nienow, A.W. Moody, G. Whitton, M.J. "Mass transfer in aerated agitated vessels: Assessment of the NEL / Hickman steady state method", Proc. of 7th Euro. Conf. on Mixing, Brugge, Belgium, (1991), pp. 409-418.

Cooke, M. Middleton, J.C. Bush, J.R. "Mixing and mass transfer in filamentous fermentations", Proc. of 2nd Conf., Cambridge, U.K., (1988), BHRA The Fluid Engineering Centre, Cranfield, U.K., Paper B1, pp.37-64.

Cronin, D.G. "The design of a pilot scale protofermenter and its application to mixing power consumption, heat transfer and mass transfer studies", PhD Thesis, University of Birmingham, (1988).

Davies, S.N. "The evaluation of gas liquid mass transfer coefficients in gas sparged agitated vessels", PhD Thesis, University College London, (1986).

Dickey, D.S. "Turbine agitated gas dispersion: Power, flooding and holdup", Proc. VI IFS, London, Canada, (1980), pp. 483-488.

Einsele, A. "Scaling up of bioreactors, theory and reality", Abstracts of the 5th int. fermentation symposium, Berlin, (1976), Session 4 : Mass and energy transfer and scale up, p.69.

Einsele, A. Finn, R.K. "Influence of gas flow rates and gas holdup on blending efficiency in stirred tanks", Ind. Eng. Chem. Process Des. Dev., Vol. 19, (1980), pp.600-603.

Fajner, D.
Magelli, F.
Pasquali, G.
"Modelling of non-standard mixers stirred with multiple impellers", Chem. Eng. Commun., Vol. 17, (1982), pp. 285-295.

Frijlink, J.J.
Kolijn, M.
Smith, J.M.
"Suspension of solids with aerated pitched blade turbines", Fluid Mixing II, IChemE Symposium Series No. 89, (1984), pp. 49-58.

Gbewonyo, K.
DiMasi, D.
Buckland, B.C.
"The use of hydrofoil impellers to improve oxygen transfer efficiency in viscous mycelial fermentations", Proc. of Int. Conf. on Bioreactor Fluid Dynamics, Cambridge, England, (1986), BHRA, Cranfield, U.K. Paper 21, pp. 281-299

Greaves, M.
Barigou, M.
"The internal structure of gas-liquid dispersions in a stirred reactor", Proc. of 6th Euro. Conf. on Mixing, Pavia, Italy, (1988), BHRA, Cranfield, U.K., pp. 313-320.

Greaves, M.
Kobbacy, K.A.
"Measurement of bubble size distribution in turbulent gas-liquid dispersions", Chem. Eng. Res. Des., Vol. 62, (1984), pp. 3-12.

Grenville, R.K.
"Blending of viscous Newtonian and pseudo-plastic fluids", PhD Thesis, Cranfield Institute of Technology, (1992).

Hassan, I.T.
Robinson, C.W.
"Stirred tank mechanical power requirement and gas holdup in aerated aqueous phases", AIChE J., Vol. 23, No. 1, (1977), pp. 48-56.

Hicks, R.W
Gates, L.E.
"How to select turbine agitators for dispersing gas into liquids", Chem. Eng., (July 19th 1976), pp. 141-148.

Hubbard, D.W.
Harris, L.R.
Wierenga, M.K.
"Scale up for polysaccharide fermentations", AIChE Annual meeting (1987), New York, paper 175b.

Hubbard, D.W.
"Scale up strategies for bioreactors", Biotechnology Processes (Edited by Ho, C.S. & Oldshue, J.Y.), AIChE, pp. 168-184, (1987).

Hudcova, V.
Nienow, A.W.
Machon, V.
"Gas liquid dispersion with dual Rushton turbine impellers", CHISA Conf., Prague, Czechoslovakia, (1987), paper E 6.3.

Hughmark, G.A.
"Power requirements and interfacial area in gas liquid turbine agitated systems", Ind. Eng. Chem. Process Des. Dev., Vol. 19, (1980), pp.638-641.

Jury, W.
Schneider, G.
Moser, A.
"Modelling approach to industrial bioreactors", Proc. of 6th Euro. Conf. on Mixing, Pavia, Italy, (1988), BHRA, Cranfield, U.K., pp. 451-456.

Khang, S.J.
Fitzgerald, T.J.
"A new probe and circuit for measuring electrolyte conductivity", Ind. Eng. Chem. Fundam., Vol. 14, pp. 208-213, (1975)

Kuboi, R.
Nienow, A.W.
"The power drawn by dual impeller systems under gassed and ungassed conditions", Proc. of 4th Euro. Conf. on Mixing, Noordwijkerhout, The Netherlands, (1982), BHRA, Cranfield, U.K., paper G2, PP. 247-260.

Kudrna, V.
"Power input of a rotational stirrer in aerated liquids", PhD Thesis, Prague Institute of Chemical Technology, (1965).

Lelli, U.
Magelli, F.
Sama, C.
"Backmixing in multistage mixer columns", Chem. Eng. Sci., Vol. 27, (1972), pp.1109-1117.

Linek, V.
Benes, P.
Sinkule, J.
"The hollow blade agitator for mass transfer in gas liquid bioreactors", Trans. IChemE, Vol. 69, Part C, September (1991).

Lopes De Figuerdo, M.M.
Calderbank, P.H.
"The scale up of agitated mixing vessels for specified oxygen dissolution rates", Chem. Eng. Sci., Vol. 34, (1978), pp. 1333-1338

Lu, W.M.
Yao, C.L.
"Gas dispersion in a multi stage impeller stirred tank", Proc. of 7th Euro. Conf. on Mixing, Brugge, Belgium, (1991), pp.351-358.

Machon, V.
Fort, I.
Antosova, E.
et al.
"Gas flooding of an inclined blade impeller", Proc. of Conf. on Recent Progress in Process Engineering: Industrial Agitation, Toulouse, France, (1991a), pp. 636-645.

Machon, V.
Hudcova, V.
Vlcek, J.
Lepsova, P.
"The flooding loading transition in multi impeller aerated stirred vessels", Proc. of 7th Euro. Conf. on Mixing, Brugge, Belgium, (1991b), pp.343-350.

Machon, V.
McFarlane, C.M.
Nienow, A.W.
"Power input and gas holdup in gas liquid dispersions agitated by axial flow impellers", Proc. of 7th Euro. Conf. on Mixing, Brugge, Belgium, (1991c), pp. 243-249.

Machon, V.
Vlcek, J.
Hudcova, V.
"Multi-impeller gas liquid contactors", Proc. of 6th Euro. Conf. on Mixing, Pavia, Italy, (1988), BHRA, Cranfield, U.K., pp. 351-360.

Machon, V.
Vlcek, J.
Skrivanek, J.
"Dual impeller systems for aeration of liquids: An experimental study", Proc. of 5th Euro. Conf. on Mixing, Wurzburg, Germany, (1985), BHRA, Cranfield, U.K., paper 16, pp. 155-169.

Magelli, F.
Nocentini, M.
Fajner, D.
Pasquali, G.
"Fluid dynamic behaviour of multiple impeller systems", Paper presented at the Engineering Foundation Conference Mixing XI, New England College, New Hampshire, USA, (1987).

Mahmoudi, S.M.
Yianneskis, M.
"The variation of flow pattern and mixing time with impeller spacing in stirred vessels with two Rushton impellers", Proc. of 7th Euro. Conf. on Mixing, Brugge, Belgium, (1991), pp. 17-24.

Manfredini,R.
Cavallera, V.
Marini, L.
Donati, G.
"Mixing and oxygen transfer in conventional stirred fermenters", Biotech. and Bioeng., Vol. 25, (1983), pp. 3115-3131.

Mann, R.
"Gas liquid mixing in stirred vessels", IChemE Symposium Series No. 94, (1983a), IChemE., Rugby, U.K., pp.335-351.

Mann, R.
"Gas-liquid contacting in mixing vessels", IChemE Industrial Fellowship Report, (1983b), IChemE., Rugby, U.K..

Manna, L.
Chiampo, F.
Rovero, G.
Sicardi, S.
"Mixing time in vessels stirred by multiple impellers", Proc. of 7th Euro. Conf. on Mixing, Brugge, Belgium, (1991), pp. 111-120.

Mehta, V.D
Sharma, M.M.
"Mass transfer in mechanically agitated gas liquid contactors", Chem. Eng. Sci., Vol. 26, (1971), pp. 461-479.

Michel, B.J.
Miller, S.A.
"Power requirements of gas-liquid agitated systems", AIChE J., Vol. 8, No. 2, (1962), pp. 262-266.

Middleton, J.C.
"Measurement of circulation within large mixing vessels", Proc. of 3rd Euro. conf. on mixing, York, U.K., (1979), BHRA, Paper A2, pp. 15-36.

Middleton ,J.C.
"Gas dispersion and mixing", Chapter 17 in "Mixing in the process industries", Edited by Harnby, N., Edwards, M.F., and Nienow, A.W., (1985), Butterworths.

Miller, D.N.
"Scale up of agitated vessels for gas liquid mass transfer", AIChE Journal, Vol. 20, No. 3, (1974), pp. 445-453.

Miyauchi, T.
Mitsutake, H.
Harase, I.
"Longitudinal dispersion in rotating impeller types of contactors", AIChE J., Vol. 12, (1966), p.508.

Muskett, M.J.
"The measurement of shaft power and bending levels for a series of impeller types and vessel internals in a 0.61 m diameter tank", FMP report 007, BHR Group, Cranfield, U.K., (1985).

Muskett, M.J.
"Experimental work in a tall mixing vessel equipped with three Rushton turbines", FMP interim report 1003, BHR Group, Cranfield, U.K., (1986a).

Muskett, M.J.
"Further power and hold-up measurements for gas liquid dispersions", FMP interim report 1009, BHR Group, Cranfield, U.K., (1986b).

Muskett, M.J.
"Gas liquid research review", FMP 030, BHR Group, Cranfield, U.K., (1987a).

Muskett, M.J.
"Gas liquid dispersion in stirred tanks: Scale up and agitator comparison", PhD Thesis, Cranfield Institute of Technology, (1987b).

Nienow, A.W.
Allsford, K.V.
"Effect of sparger type on gas dispersion by Rushton turbines", IChemE Symposium Series No. 94, (1985a), IChemE., Rugby, U.K., pp.31-34.

Nienow, A.W.
Chapman, C.M.
Middleton, J.C.
"Gas recirculation rate through impeller cavities and surface aeration in sparged agitated vessels", Chem. Eng. J., Vol. 17, (1979a), pp. 111-118.

Nienow, A.W.
Haozhung, W.
Huoxing, L.
Allsford, K.V.
"The advantage of using large ring spargers with standard Rushton turbines in gassed reactors", Proceedings of World Congress III of Chemical Engineering, Tokyo, Japan, Society of Chemical Engineering Japan, Vol. III, (1986), pp.354-357.

Nienow, A.W.
Huoxing, L.
Haozhung, W.
et al.
"The use of large ring spargers to improve the performance of fermenters agitated by single and multiple standard Rushton turbines", Proc. of the 2nd Int. Conf. on Bioreactors, Cambridge, (1988), BHRA Fluid Eng., Cranfield, England, Paper D2, pp. 159-177.

Nienow, A.W.
Konno, M.
Bujalski, W.
"Studies on three-phase mixing: A review and recent results", Proc. of 5th Euro. Conf. on Mixing, Wurzburg, Germany, (1985b), BHRA, Cranfield, U.K., paper 2, p. 1.

Nienow, A.W.
Kuboi, R.
Chapman, C.M.
Allsford, K.
"The dispersion of gases into liquids by mixed flow agitators", Proc. of Int. Conf. on Physical Modelling of Multi-Phase Flow, Coventry, England, Paper K1, BHRA Fluid Eng., Cranfield, England, (1983).

Nienow, A.W.
Lilly, M.D.
"The power drawn by multiple impellers in sparged, agitated vessels", Biotech. and Bioeng., Vol. 21, (1979b), pp. 2341-2345.

Nienow, A.W.
Wisdom, D.J.
Middleton, J.C.
"The effect of scale and geometry on flooding, recirculation and power in gassed stirred vessels", Proc. 2nd Eur. Conf. on mixing, Cambridge, Paper F1, BHRA Fluid Eng., Cranfield, England, (1977).

Nienow, A.W.
Warmoeskerken, M.
Smith, J.M.
Konno, M.
"On the flooding / loading transition and the complete dispersal condition in aerated vessels agitated by a Rushton turbine", Fifth European conference on mixing, Wurzburg, Germany, Paper 15, (1985c).

Nienow, A.W.
"Gas dispersion performance in fermenter operation : A critical review", Annual AIChE meeting (1987), paper 174a.

Nienow, A.W.
"Gas dispersion performance in fermenter operation", Chem. Eng. Progress, (February 1990), pp. 61-71.

Nishikawa, M.
Nishioka, S.
Kayama, T.
"Gas absorption in an aerated mixing vessel with multistage impellers", Journal of Chem. Eng. Japan, Vol. 17, No. 5, (1984), pp. 541-543.

Nocentini, M.
Magelli, F.
Pasquali, G.
Fajner, D.
"A fluid dynamic study of a gas liquid, non standard vessel stirred by multiple impellers", Chem. Eng. J., Vol. 37, (1988a), pp. 53-59.

Nocentini, M.
Magelli, F.
Pasquali, G.
"On the modelling of the gas behaviour of gas-liquid vessels stirred with multiple impellers", Proc. of 6th Euro. Conf. on Mixing, Pavia, Italy, (1988b), BHRA, Cranfield, U.K., pp.337-344.

Oldshue, J.Y.
Post, A.
Weetman, R.J.
Coyle, C.K.
"Comparison of mass transfer characteristics of radial and axial flow impellers", Proc. of 6th Euro. conf. on mixing, Pavia, Italy, (1988), BHRA, Cranfield, U.K., pp. 345-350.

Oosterhuis, N.M.
Kossen, N.W.
"Oxygen transfer in a production scale bioreactor", Chem. Eng. Res. Des., Vol. 61, (1983), pp. 308-312.

Oosterhuis, N.M.
Kossen, N.W.
"Dissolved oxygen concentration profiles in a production scale bioreactor", Biotech. and Bioeng., Vol. 26, (1984), pp. 546-550.

Palmer, M.H.
"Design guide for impeller power numbers", FMP 028, April (1987).

Palmer, M.H.
"Shaft design guide", FMP 033, September (1988).

Parthasarathy, R.
Jameson, G.J.
Ahmed, N.
"Bubble break up in stirred vessels - Predicting the sauter mean diameter" Trans. IChemE., Vol. 69, Part A, July (1991).

Ramanarayanan, K.A.
Sharma, M.M.
"Mass transfer characteristics of multiple impeller agitated gas liquid contactors", Ind. Eng. Chem. Process Des. Dev., Vol. 21, (1982), pp. 353-355.

Ritchi, J.
"POWER-TK version 1.0 user manual release 1.0", FMP 044, September 1990.

Roustan, M.
Charles, J.M.
Martinet, J.P.
"Methode de determination du coefficient de transfert de matiere gas liquide en regime transitoire", Int. Symp on Mixing, Mons, Belgium, (1978), paper C1-1.

Roustan, M.
"Power consumed by Rushton turbines in non standard vessels under gassed conditions", Proc. 5th Eur. Conf. on Mixing, Wurzburg, (1985), BHRA, Cranfield, U.K., paper 14, pp. 127-261.

Ruszkowski, S.R.
"The FMP method for measuring mixing times", FMP008, BHR Group, Cranfield, U.K., (1985).

Seichter, P.
Mazoch, J.
Slama, V.
"Scale up of power input in gas-liquid systems with multiple stirrers", Proc. of Conf. on Recent Progress in Process Engineering: Industrial Agitation, Vol. 6, No. 19, Toulouse, France, (1992).

Singh, V.
Hensler, W.
Fuchs, R.
"On-line determination of mixing parameters in fermenters using pH transients", Proc. of Int. Conf. on Bioreactor Fluid Dynamics, Cambridge, U.K., (1986), BHRA, Cranfield, U.K., paper 18, p. 231-256.

Smith, J.M.
Private communication (1989).

Smith, J.M
Van't Riet, K.
Middleton, J.C.
"Scale up of agitated gas liquid reactors for mass transfer", Proc. of 2nd Euro. conf. on mixing, Cambridge, U.K., (1977), BHRA, Cranfield, U.K., Paper F4.

Smith, J.M.
Warmoeskerken, M.
"The dispersion of gases in liquids with turbines", Proc. of 5th Euro. conf. on mixing, Wurzburg, Germany, (1985), BHRA, Cranfield, U.K., Paper 13.

Smith, J.M.
Warmoeskerken, M.
Zeef, E.
"Flow conditions in vessels dispersing gases in liquids with multiple impellers", Biotechnology Processes (Edited by Ho, C.S. & Oldshue, J.Y.), AIChE, pp. 107-115, (1987).

Sridar, T.
Potter, O.E.
"Gas holdup and bubble diameters in pressurised gas-liquid stirred vessels", Ind. Eng. Chem. Fundam., Vol. 19, (1980), pp. 21-26.

Tatterson, G.B.
"Fluid mixing and gas dispersion in agitated tanks", McGraw-Hill, (1991).

Van't Riet, K.
"Turbine agitator hydrodynamics and dispersion performance", PhD Thesis, University of Delft, (1975).

Warmoeskerken, M.M.
Smith, J.M.
"Description of the power curves of turbine stirred gas liquid dispersions", Proc. 4th Eur. Conf. on Mixing, Noordwijkerhout, The Netherlands, (1982), BHRA, Cranfield, U.K., paper G1, pp. 237-246.

Warmoeskerken, M.M.
Speur, J.
Smith, J.M.
"Gas liquid dispersion with pitched blade turbines", Chem. Eng. Commun., Vol. 25, (1984), pp.11-29.

Warmoeskerken, M.M.
"Gas liquid dispersing characteristics of turbine agitators", Phd Thesis, University of Delft, (1986).

Warmoeskerken, M.M.
Smith, J.M.
"Impeller loading in multi turbine vessels", Proc. of Second Int. Conf. on Bioreactor Fluid Dynamics, Cambridge, U.K., (1988), BHRA, Cranfield, U.K., paper D3, pp. 179-197.

Whitton, M.J.
"Power and mass transfer studies in a tall vessel equipped with three impellers", Proc. of 2nd Bioreactor Conf., Cambridge, U.K., (1988a), BHRA, Cranfield, U.K., paper D1, p. 135-158.

Whitton, M.J.
"Measurement of mass transfer coefficients for gas liquid mixing tests in the 0.61m and 2.67m tanks", FMP interim report 1017, BHR Group Ltd, Cranfield, U.K., (1987).

Whitton, M.J.
"Mass transfer, power and hold-up measurements in a tall mixing vessel", FMP interim report 1022, BHR Group Ltd, Cranfield, U.K., (1988b).

Whitton, M.J. "Influence of liquid viscosity and sparge ring geometry on the power drawn by a Rushton turbine", FMP interim report 1037, BHR Group Ltd, Cranfield, U.K., (1988c).

Whitton, M.J. "Liquid mixing times with multiple impellers and the effect of aeration", FMP interim report 1044, BHR Group Ltd, Cranfield, U.K., (1990a).

Whitton, M.J. "Compartmentalisation in tall tank fermenters: Exchange flows between compartments and the effects of aeration in a 0.95m tank", FMP interim report 1054, BHR Group Ltd, Cranfield, U.K., (1990b).

Whitton, M.J. "Power and gas holdup in tall vessels fitted with multiple impellers: Measurements at 0.61 m scale and comparison with 0.95 m scale", FMP interim report 1055, BHR Group Ltd, Cranfield, U.K., (1991a).

Whitton, M.J. "Mass transfer in aerated agitated vessels: Assessment of the NEL / Hickman steady state method", FMP report 047, BHR Group Ltd, Cranfield, U.K., (1991b).

Yung, C.N.
Wong, C.W.
Chang, C.L. "Gas holdup and aerated power consumption in mechanically stirred tanks", Can. J. Chem. Eng., Vol. 57, No.6, (1979), pp. 672-676.

APPENDIX 1: CALCULATION OF EXCHANGE FLOWS

A1.1 INTRODUCTION

This appendix presents the mathematical analysis of the conductivity response data to produce exchange flows for the multiple cell liquid mixing models described in chapter 5. The detailed mathematics are presented for the six cell mixing model. Exactly the same approach was applied to the less complex three cell model but the detailed mathematics are not presented for the sake of brevity.

The liquid phase mixing model for the 0.61 m diameter vessel is shown in Figure A1.1. The model consists of six perfectly mixed cells connected by the liquid exchange flows F_1 to F_5. The cell boundaries were assumed to be at the centre line of each impeller and half way between the impellers. Due to the position of the impellers and the shape of the vessel base the volume of each cell was not the same. The ungassed cell volumes were:

Top cell ($V_1 = V_T$):	0.0853 m^3
Middle cells (V_2 to $V_5 = V_M$):	0.0721 m^3
Bottom cell ($V_6 = V_B$):	0.0462 m^3

With aeration, liquid was displaced by the gas but the position of the cell boundaries was assumed to remain unchanged, (except for the dispersion surface which increases with holdup). Thus as gas holdup increased, the liquid volume in the lower cells V_2 to V_6 decreased, and the liquid volume in the top cell V_1 increased.

For cells 2 to 5 the gas holdup was assumed to be uniform, i.e. under gassed conditions:

$$V_2 = V_3 = V_4 = V_5 = V_M = 0.0721 \times (1 - \varepsilon_G)$$

The gas holdup below the bottom impeller, i.e. cell 6, depended on the degree of gas recirculation below the lowest impeller. The minimum impeller speed at which gas was completely dispersed below the lowest impeller (N_{CD}) was assumed to be defined by:

$$N_{CD}^2 = 5\ Q\ (\ g\ T\ )^{0.5}\ /\ D^4 \qquad \text{from equation 1.2}$$

For $N > N_{CD}$, (i.e. gas was dispersed below the lowest impeller):

$$V_B = 0.0462 \times (1 - \varepsilon_G)$$

For $N < N_{CD}$, (i.e. gas was not dispersed below the lowest impeller):

$$V_B = 0.0462$$

The liquid volume in the top cell was equal to its ungassed volume plus the liquid volume displaced from the lower cells. Thus for $N < N_{CD}$:

$$V_T = 0.0853 + 4 \times (0.0721 \times \varepsilon_G)$$

and for $N > N_{CD}$:

$$V_T = 0.0853 + 4 \times (0.0721 \times \varepsilon_G) + (0.0462 \times \varepsilon_G)$$

For the few experiments conducted with the lowest impeller flooded it was assumed that there was no gas dispersion below the lowest impeller but that gas holdup was uniform above this impeller.

Although the liquid volume in each cell varied with experimental conditions the liquid in each cell was always assumed to be perfectly mixed. The maximum gas holdup during the liquid mixing tests was 10%.

A1.2 CALCULATION OF EXCHANGE FLOWS FOR SURFACE ADDITION OF TRACER

Six conductivity probes were used in the 0.61 m diameter vessel, one in each cell, allowing the separate determination of all five exchange flows. Pulse addition of tracer was made to the liquid surface, i.e. cell 1.

The determination of the exchange flows begins by writing a mass balance for the tracer in each well mixed cell, refer to figure A1.1:

Cell 1:

$$V_T \frac{dC_1}{dt} = F_1 C_2 - F_1 C_1 + q \qquad \text{...Eqn (A1.1)}$$

Cell 2:

$$V_M \frac{dC_2}{dt} = F_1 C_1 + F_2 C_3 - F_1 C_2 - F_2 C_2 \qquad \text{...Eqn (A1.2)}$$

Cell 3:

$$V_M \frac{dC_3}{dt} = F_2 C_2 + F_3 C_4 - F_2 C_3 - F_3 C_3 \qquad \text{...Eqn (A1.3)}$$

Cell 4:

$$V_M \frac{dC_4}{dt} = F_3 C_3 + F_4 C_5 - F_3 C_4 - F_4 C_4 \qquad \text{...Eqn (A1.4)}$$

Cell 5:

$$V_M \frac{dC_5}{dt} = F_4 C_4 + F_5 C_6 - F_4 C_5 - F_5 C_5 \qquad \text{...Eqn (A1.5)}$$

Cell 6:

$$V_B \frac{dC_6}{dt} = F_5 C_5 - F_5 C_6 \qquad \text{...Eqn (A1.6)}$$

The tracer is assumed to be added as a perfect pulse. Therefore the total amount of tracer added:

$$\int_0^\infty q(t)dt = V_{TOTAL} C_\infty \int_0^\infty \delta(t)dt$$

where $\delta(t)$ is the Dirac delta function such that

$$\int_0^\infty \delta(t)dt = 1$$

If the final concentration C_∞ is normalised to 1:

$$\int_0^\infty q(t)dt = V_{TOTAL} \int_0^\infty \delta(t)dt$$

or

$$q(t) = V_{TOTAL}\,\delta(t)$$

where:

$$V_{TOTAL} = (4V_M + V_T + V_B)$$

Substituting for q in Eqn A1.1:

$$V_T\frac{dC_1}{dt}=F_1C_2-F_1C_1+V_{TOTAL}\delta(t) \qquad \text{...Eqn (A1.7)}$$

Taking the Laplace transforms of equations A1.7 and A1.2 to A1.6:

$$F_1\bar{C}_2-(F_1+sV_T)\bar{C}_1=-V_{TOTAL} \qquad \text{...Eqn (A1.8)}$$

$$F_1\bar{C}_1+F_2\bar{C}_3-(F_1+F_2+sV_M)\bar{C}_2=0 \qquad \text{...Eqn (A1.9)}$$

$$F_2\bar{C}_2+F_3\bar{C}_4-(F_2+F_3+sV_M)\bar{C}_3=0 \qquad \text{...Eqn (A1.10)}$$

$$F_3\bar{C}_3+F_4\bar{C}_5-(F_3+F_4+sV_M)\bar{C}_4=0 \qquad \text{...Eqn (A1.11)}$$

$$F_4\bar{C}_4+F_5\bar{C}_6-(F_4+F_5+sV_M)\bar{C}_5=0 \qquad \text{...Eqn (A1.12)}$$

$$F_5\bar{C}_5-(F_5+sV_B)\bar{C}_6=0 \qquad \text{...Eqn (A1.13)}$$

Equations A1.8 to A1.13 can be simplified by introducing the following notation:

$$\bar{F}_{mn}=F_m+F_n+sV \qquad \text{...Eqn (A1.14)}$$

with

$$\bar{F}_{01}=F_1+sV_T \quad ; \quad F_0=0$$

and

$$\bar{F}_{56}=F_5+sV_B \quad ; \quad F_6=0$$

Equations A1.8 to A1.13 can thus be written:

$$-\bar{F}_{01}\bar{C}_1+F_1\bar{C}_2=-V_{TOTAL} \quad \text{...Eqn (A1.15)}$$

$$F_1\bar{C}_1-\bar{F}_{12}\bar{C}_2+F_2\bar{C}_3=0 \quad \text{...Eqn (A1.16)}$$

$$F_2\bar{C}_2-\bar{F}_{23}\bar{C}_3+F_3\bar{C}_4=0 \quad \text{...Eqn (A1.17)}$$

$$F_3\bar{C}_3-\bar{F}_{34}\bar{C}_4+F_4\bar{C}_5=0 \quad \text{...Eqn (A1.18)}$$

$$F_4\bar{C}_4-\bar{F}_{45}\bar{C}_5+F_5\bar{C}_6=0 \quad \text{...Eqn (A1.19)}$$

$$F_5\bar{C}_5-F_5\bar{C}_6=0 \quad \text{...Eqn (A1.20)}$$

These equations are now solved using standard Gaussian elimination, Bajpai et al (1980). This procedure is detailed in Appendix 2.

From Appendix 2:

$$\bar{C}_1=\frac{V_{TOTAL}}{\bar{F}_{01}}+\frac{F_1}{\bar{F}_{01}}\bar{C}_2 \quad \text{...Eqn (A2.1)}$$

$$\bar{C}_2=\frac{-V_{TOTAL}F_1}{\bar{F}_{01}K_1}-\frac{F_2}{K_1}\bar{C}_3 \quad \text{...Eqn (A2.2)}$$

$$\bar{C}_3=\frac{-V_{TOTAL}F_1F_2}{\bar{F}_{01}K_1K_2}+\frac{F_3}{K_2}\bar{C}_4 \quad \text{...Eqn (A2.3)}$$

$$\bar{C}_4=\frac{V_{TOTAL}F_1F_2F_3}{\bar{F}_{01}K_1K_2K_3}-\frac{F_5}{K_3}\bar{C}_5 \quad \text{...Eqn (A2.4)}$$

$$\bar{C}_5=\frac{V_{TOTAL}F_1F_2F_3F_4}{\bar{F}_{01}K_1K_2K_3K_4}+\frac{F_5}{K_4}\bar{C}_6 \quad \text{...Eqn (A2.5)}$$

$$\bar{C}_6=\frac{-V_{TOTAL}F_1F_2F_3F_4F_5}{\bar{F}_{01}K_1K_2K_3K_4K_5} \quad \text{...Eqn (A2.6)}$$

(K_1 to K_5 are defined in Appendix 2)

From Laplace transform theory:

$$\int_0^\infty C_n(t)dt - \int_0^\infty C_{(n+1)}(t)dt = \lim_{s \to 0}(\bar{C}_n - \bar{C}_{(n+1)}) \qquad \text{...Eqn (A1.21)}$$

= area between concentration response curves for probes n and n+1.

The solution to equations A2.1 to A2.6 is therefore evaluated in the $s \rightarrow 0$ limit.

$\bar{C}_6$ can be estimated from binomial expansion of the terms $\bar{F}_{01}, K_1, K_2, K_3, K_4$ and K_5 up to the terms containing s, i.e. all terms with s to the power 2 and above are neglected.

From equation A1.14:

$$\bar{F}_{01}^{-1} = (F_1 + sV_T)^{-1}$$

$$= \frac{1}{F_1}\left(1 - \frac{sV_T}{F_1}\right) + 0(s^2) \qquad \text{...Eqn (A1.22)}$$

From Appendix 2:

$$K_1^{-1} = \left(\frac{F_1^2}{\bar{F}_{01}} - \bar{F}_{12}\right)^{-1}$$

$$= \left(\frac{F_1^2}{F_1}\left(1 - s\frac{V_T}{F_1}\right) - F_1 - F_2 - sV_M\right)^{-1}$$

$$= \frac{-1}{F_2}\left(1 + \frac{s(V_M + V_T)}{F_2}\right)^{-1}$$

Binomial expansion gives:

$$K_1^{-1} = \frac{-1}{F_2}\left(1 - \frac{s(V_M + V_T)}{F_2}\right) + 0(s^2) \qquad \text{...Eqn (A1.23)}$$

From Appendix 2:

$$K_2^{-1}=(\frac{F_2^2}{K_1}+\bar{F}_{23})^{-1}=(F_3+s(2V_M+V_T))^{-1}$$

Binomial expansion gives:

$$K_2^{-1}=\frac{1}{F_3}(1-\frac{s(2V_M+V_T)}{F_3}) \qquad \text{...Eqn (A1.24)}$$

K_3^{-1} and K_4^{-1} are expanded in the same way, giving:

$$K_3^{-1}=\frac{-1}{F_4}(1-\frac{s(3V_M+V_T)}{F_4}) \qquad \text{...Eqn (A1.25)}$$

and

$$K_4^{-1}=\frac{1}{F_5}(1-\frac{s(4V_M+V_T)}{F_5}) \qquad \text{...Eqn (A1.26)}$$

Finally:

$$\begin{aligned} K_5^{-1}&=(\frac{F_5^2}{K_4}-\bar{F}_{56})^{-1} \\ &=(F_5(1-\frac{s(4V_M+V_T)}{F_5})-F_5-sV_B)^{-1} \\ &=\frac{-1}{s(4V_M+V_T+V_B)} \\ &=\frac{-1}{sV_{TOTAL}} \qquad \text{...Eqn (A1.27)} \end{aligned}$$

Substituting equations A1.22 to A1.27 into equation A2.6:

$$\bar{C}_6=V_{TOTAL}\frac{1}{s(4V_M+V_T+V_B)}(1-\frac{sV_T}{F_1})(1-\frac{s(V_M+V_T)}{F_2})(1-\frac{s(2V_M+V_T)}{F_3})(1-\frac{s(3V_M+V_T)}{F_4})(1-\frac{s(4V_M+V_T)}{F_5})$$

$$=[\frac{1}{s}-\sum_{n=0}^{n=4}\frac{(V_T+nV_M)}{F_{n+1}}]+0(s^2) \qquad \text{as } s \rightarrow 0$$

From Appendix 2:

$$-K_4\bar{C}_5+F_5\bar{C}_6=\frac{-V_{TOTAL}F_1F_2F_3F_4}{\bar{F}_{01}K_1K_2K_3K_4}$$

Rearranging:

$$\bar{C}_5=\frac{V_{TOTAL}F_1F_2F_3F_4}{\bar{F}_{01}K_1K_2K_3K_4}+\frac{F_5}{K_4}\bar{C}_6$$

Expanding to s^n, where $n < 2$:

$$\bar{C}_5=\frac{V_{TOTAL}}{F_5}[1-s\sum_{n=0}^{n=4}\frac{(V_T+nV_M)}{F_{n+1}}]+(1-\frac{s(4V_M+V_T)}{F_5})\bar{C}_6$$

$$=\frac{V_{TOTAL}}{F_5}+\bar{C}_6-\frac{s(4V_M+V_T)}{F_5}[\frac{1}{s}-\sum_{n=0}^{n=4}\frac{(V_T+nV)}{F_{n+1}}]$$

$$=\frac{V_{TOTAL}}{F_5}+\bar{C}_6-\frac{(4V_M+V_T)}{F_5}$$

Therefore,

$$(\bar{C}_5-\bar{C}_6)=\frac{V_B}{F_5} \qquad \text{...Eqn (A1.28)}$$

Thus, from equation A1.21, the difference in area below the conductivity response curves of probes 5 and 6:

$$=\frac{V_B}{F_5}$$

If the area between the conductivity response curves = 0, the liquid mixing between two cells is perfect, i.e. $F = \infty$. At the other extreme if there is no mixing between adjacent cells, $F = 0$ because the area between the response curves will be infinite. The relationship between F and the area between response curves is shown in figure A1.2.

The above derivation illustrates that only terms of the order $1/s$ contribute from $\bar{C}_6$ x sV since terms of the order 1 and above vanish in the limit.

This means that if $\bar{C}_5$ (or $\bar{C}_4$ etc) is used in the later stages only 1/s terms should be kept.

i.e. $\bar{C}_5$ (or $\bar{C}_4$ etc) = 1/s

From Appendix 2:

$$K_3\bar{C}_4+F_4\bar{C}_5=\frac{V_{TOTAL}F_1F_2F_3}{\bar{F}_{01}K_1K_2}$$

or

$$\bar{C}_4=-\frac{F_4}{K_3}\bar{C}_5+\frac{V_{TOTAL}F_1F_2F_3}{\bar{F}_{01}K_1K_2K_3}$$

$$=(1-\frac{s(3V_M+V_T)}{F_4})\bar{C}_5+\frac{V_{TOTAL}}{F_4}+0(s)$$

$$=\bar{C}_5-\frac{(3V_M+V_T)}{F_4}+\frac{(4V_M+V_T+V_B)}{F_4}$$

Thus:

$$(\bar{C}_4-\bar{C}_5)=\frac{(V_M+V_B)}{F_4} \qquad \text{...Eqn (A1.29)}$$

Thus, the difference in area below the conductivity response curves of probes 4 and 5:

$$=\frac{V_M+V_B}{F_4}$$

The same procedure can be applied to determine the relation ships between the conductivity response curves and the exchange flows F_3, F_2 and F_1. The results are:

$$(\bar{C}_3-\bar{C}_4)=\frac{(2V_M+V_B)}{F_3} \qquad \text{...Eqn (A1.30)}$$

$$(\bar{C}_2-\bar{C}_3)=\frac{(3V_M+V_B)}{F_2} \qquad \text{...Eqn (A1.31)}$$

$$(\bar{C}_1-\bar{C}_2)=\frac{(4V_M+V_B)}{F_1} \qquad \text{...Eqn (A1.32)}$$

Equations A1.22 to A1.26 only apply for tracer addition to cell 1, i.e. the liquid surface. If tracer is added to other cells in the vessel the relationships between exchange flows and conductivity response curves change.

For a three cell model there are only three cell concentrations (C_1, C_2, and C_3) and two exchange flows (F_t and F_b), see figure 5.14. For this model:

$$(\bar{C}_1-\bar{C}_2)=\frac{(V_M+V_B)}{F_t} \qquad \text{...Eqn (A1.33)}$$

and $$(\bar{C}_1-\bar{C}_2)=\frac{V_B}{F_b} \qquad \text{...Eqn (A1.34)}$$

A1.3 CALCULATION OF EXCHANGE FLOWS FOR SUB SURFACE TRACER ADDITION

Some conductivity response experiments were carried out with tracer addition to cell 4. In this case, equations A1.1 to A1.6 can be used to describe the tracer concentration in each cell with the following modifications:

Equation A1.1 becomes:

$$V_T\frac{dC_1}{dt}=F_1C_2-F_1C_1 \qquad \text{...Eqn (A1.35)}$$

Equation A1.4 becomes:

$$V_M\frac{dC_4}{dt}=F_3C_3+F_4C_5-F_3C_4-F_4C_4+q \qquad \text{...Eqn (A1.36)}$$

Solving these equations, in the limit $s \rightarrow 0$, yields the following:

$$(\bar{C}_1-\bar{C}_2)=\frac{-V_T}{F_1} \qquad \text{...Eqn (A1.37)}$$

$$(\bar{C}_2-\bar{C}_3)=\frac{-(V_M+V_T)}{F_2} \qquad \text{...Eqn (A1.38)}$$

$$(\bar{C}_3-\bar{C}_4)=\frac{-(2V_M+V_T)}{F_3} \qquad \text{...Eqn (A1.39)}$$

$$(\bar{C}_4-\bar{C}_5)=\frac{(V_M+V_B)}{F_4} \qquad \text{...Eqn (A1.40)}$$

$$(\bar{C}_5-\bar{C}_6)=\frac{V_B}{F_5} \qquad \text{...Eqn (A1.41)}$$

The terms for F_1, F_2 and F_3 are negative because when tracer is added to cell 4, probe 4 responds first followed by probes 3, 2 and then 1. Thus the area under curve 4 is larger than that under curve 3, which is larger than that under curve 2, etc..

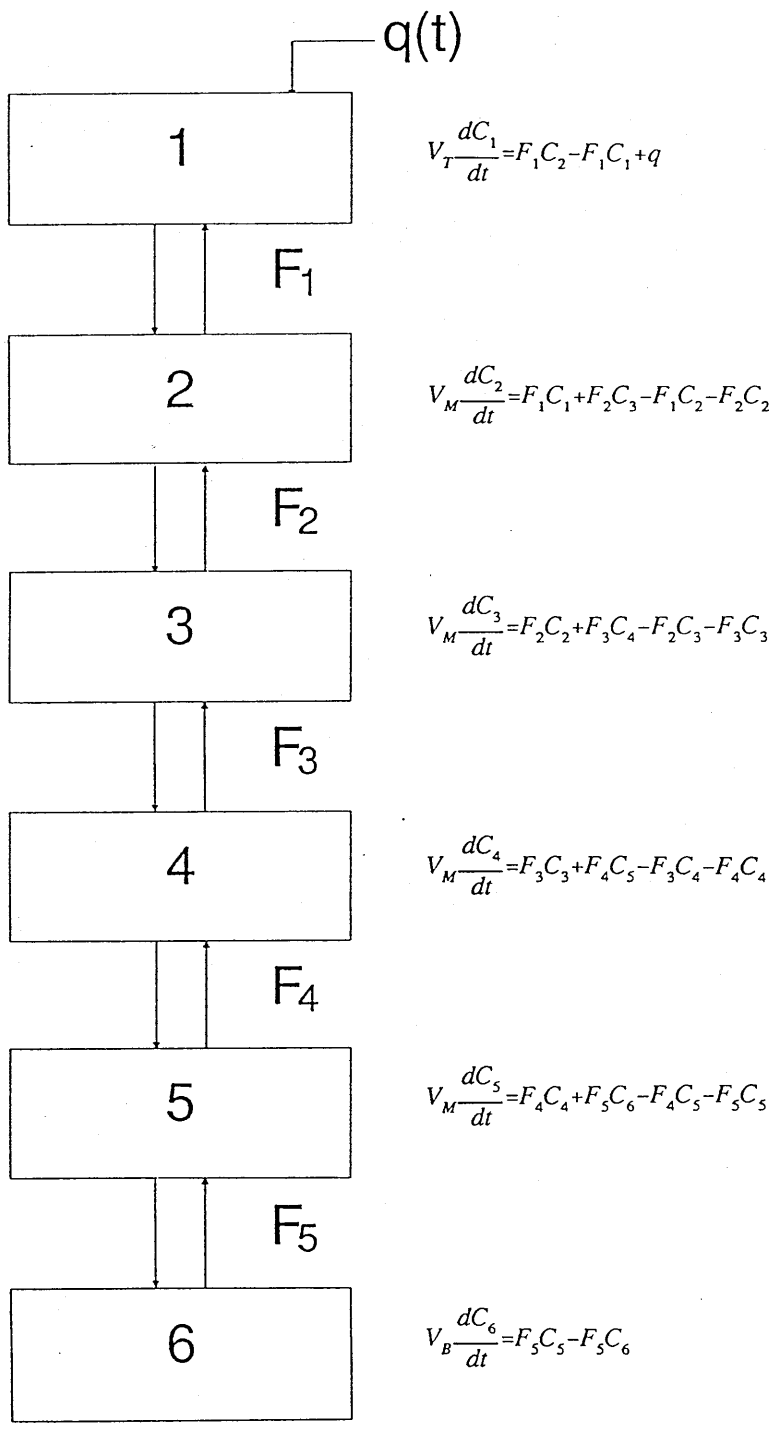
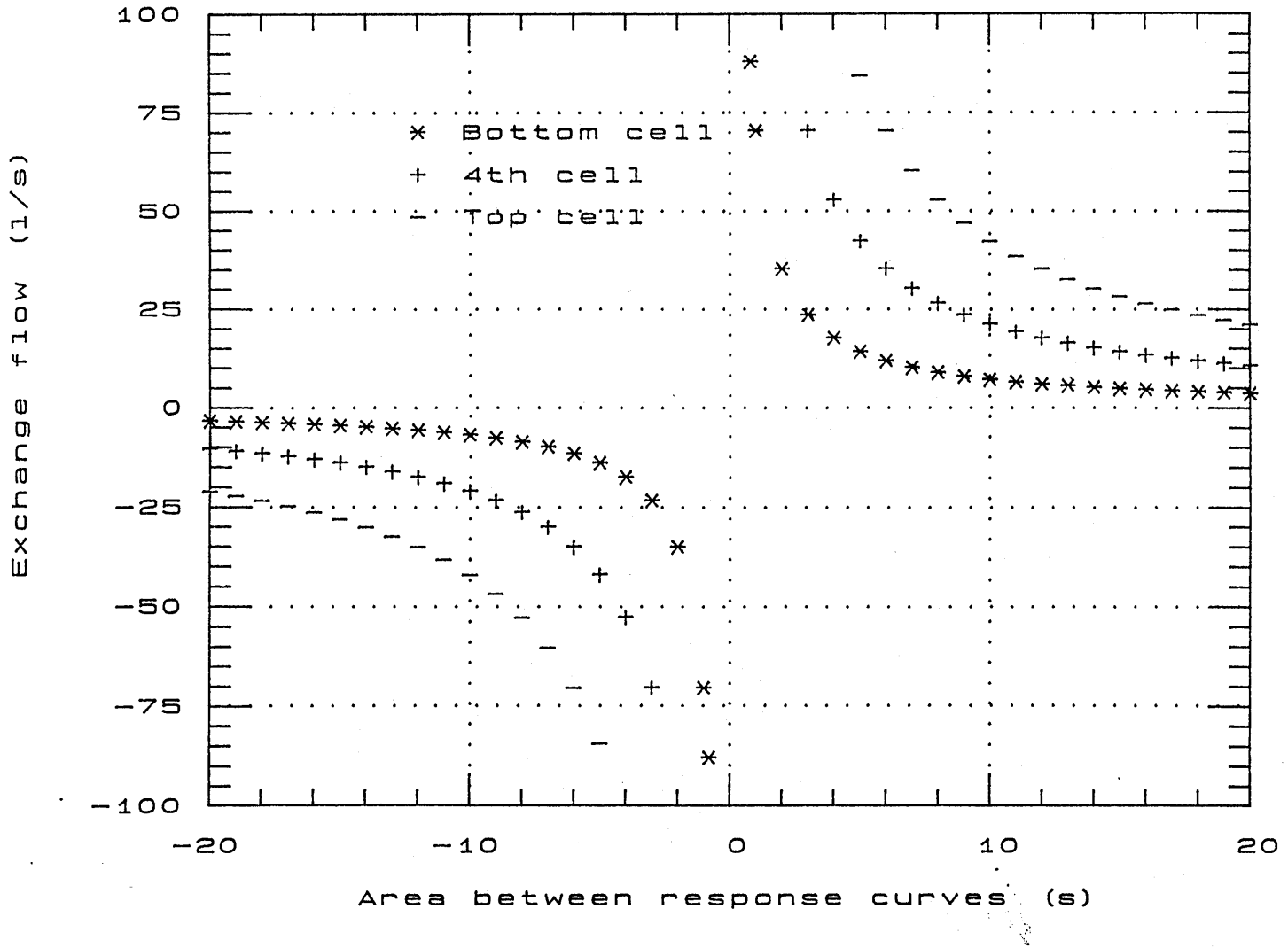


Figure A1.1: Tracer mass balances for six cell liquid mixing model.

Figure A1.2: Relationship between exchange flow values and area between conductivity response curves.



APPENDIX 2: SOLUTION OF DIFFERENTIAL EQUATIONS A1.15 TO A1.20 USING GAUSSIAN ELIMINATION.

Equations A1.15 to A1.20 can be represented as the following matrix:

	$\bar{C}_1$	$\bar{C}_2$	$\bar{C}_3$	$\bar{C}_4$	$\bar{C}_5$	$\bar{C}_6$	
(1)	$-\bar{F}_{01}$	F_1	0	0	0	0	$-V_{TOTAL}$
(2)	F_1	$-\bar{F}_{12}$	F_2	0	0	0	0
(3)	0	F_2	$-\bar{F}_{23}$	F_3	0	0	0
(4)	0	0	F_3	$-\bar{F}_{34}$	F_4	0	0
(5)	0	0	0	F_4	$-\bar{F}_{45}$	F_5	0
(6)	0	0	0	0	F_5	$-\bar{F}_{56}$	0

STEP 1: Eliminate C_1 from row 2 ($\frac{F_1}{\bar{F}_{01}}$ x (1) + (2)):

	$\bar{C}_1$	$\bar{C}_2$	$\bar{C}_3$	$\bar{C}_4$	$\bar{C}_5$	$\bar{C}_6$	
(1)	$-\bar{F}_{01}$	F_1	0	0	0	0	$-V_{TOTAL}$
(2)	0	$\frac{F_1^2}{\bar{F}_{01}}-\bar{F}_{12}$	F_2	0	0	0	$\frac{-V_{TOTAL}F_1}{\bar{F}_{01}}$
(3)	0	F_2	$-\bar{F}_{23}$	F_3	0	0	0
(4)	0	0	F_3	$-\bar{F}_{34}$	F_4	0	0
(5)	0	0	0	F_4	$-\bar{F}_{45}$	F_5	0
(6)	0	0	0	0	F_5	$-\bar{F}_{56}$	0

STEP 2: Eliminate C_2 from row 3 ($-\frac{F_2}{K_1}$ x (2) + (3)) where $K_1=\frac{F_1^2}{\bar{F}_{01}}-\bar{F}_{12}$

	$\bar{C}_1$	$\bar{C}_2$	$\bar{C}_3$	$\bar{C}_4$	$\bar{C}_5$	$\bar{C}_6$	
(1)	$-\bar{F}_{01}$	F_1	0	0	0	0	$-V_{TOTAL}$
(2)	0	K_1	F_2	0	0	0	$\frac{-V_{TOTAL}F_1}{\bar{F}_{01}}$
(3)	0	0	$-\frac{F_2^2}{K_1}-\bar{F}_{23}$	F_3	0	0	$\frac{V_{TOTAL}F_1F_2}{\bar{F}_{01}K_1}$
(4)	0	0	F_3	$-\bar{F}_{34}$	F_4	0	0
(5)	0	0	0	F_4	$-\bar{F}_{45}$	F_5	0
(6)	0	0	0	0	F_5	$-\bar{F}_{56}$	0

STEP 3: Eliminate C_3 from row 4 ($\frac{F_3}{K_2}$ x (3) + (4)) where $K_2=\frac{F_2^{\,2}}{K_1}+\bar{F}_{23}$

	$\bar{C}_1$	$\bar{C}_2$	$\bar{C}_3$	$\bar{C}_4$	$\bar{C}_5$	$\bar{C}_6$	
(1)	$-\bar{F}_{01}$	F_1	0	0	0	0	$-V_{TOTAL}$
(2)	0	K_1	F_2	0	0	0	$\frac{-V_{TOTAL}F_1}{\bar{F}_{01}}$
(3)	0	0	$-K_2$	F_3	0	0	$\frac{V_{TOTAL}F_1F_2}{\bar{F}_{01}K_1}$
(4)	0	0	0	$\frac{F_3^{\,2}}{K_2}-\bar{F}_{34}$	F_4	0	$\frac{V_{TOTAL}F_1F_2F_3}{\bar{F}_{01}K_1K_2}$
(5)	0	0	0	F_4	$-\bar{F}_{45}$	F_5	0
(6)	0	0	0	0	F_5	$-\bar{F}_{56}$	0

STEP 4: Eliminate C_4 from row 5 ($-\frac{F_4}{K_3}$ x (4) + (5)) where $K_3=\frac{F_3^2}{K_2}-\bar{F}_{34}$

	$\bar{C}_1$	$\bar{C}_2$	$\bar{C}_3$	$\bar{C}_4$	$\bar{C}_5$	$\bar{C}_6$	
(1)	$-\bar{F}_{01}$	F_1	0	0	0	0	$-V_{TOTAL}$
(2)	0	K_1	F_2	0	0	0	$\frac{-V_{TOTAL}F_1}{\bar{F}_{01}}$
(3)	0	0	$-K_2$	F_3	0	0	$\frac{V_{TOTAL}F_1F_2}{\bar{F}_{01}K_1}$
(4)	0	0	0	K_3	F_4	0	$\frac{V_{TOTAL}F_1F_2F_3}{\bar{F}_{01}K_1K_2}$
(5)	0	0	0	0	$-\frac{F_4^2}{K_3}-\bar{F}_{45}$	F_5	$\frac{V_{TOTAL}F_1F_2F_3F_4}{\bar{F}_{01}K_1K_2K_3}$
(6)	0	0	0	0	F_5	$-\bar{F}_{56}$	0

STEP 5: Eliminate C_5 from row 6 ($\frac{F_5}{K_4}$ x (5) + (6)) where $K_4=\frac{F_4^2}{K_3}-\bar{F}_{45}$

	$\bar{C}_1$	$\bar{C}_2$	$\bar{C}_3$	$\bar{C}_4$	$\bar{C}_5$	$\bar{C}_6$	
(1)	$-\bar{F}_{01}$	F_1	0	0	0	0	$-V_{TOTAL}$
(2)	0	K_1	F_2	0	0	0	$\frac{-V_{TOTAL}F_1}{\bar{F}_{01}}$
(3)	0	0	$-K_2$	F_3	0	0	$\frac{V_{TOTAL}F_1F_2}{\bar{F}_{01}K_1}$
(4)	0	0	0	K_3	F_4	0	$\frac{V_{TOTAL}F_1F_2F_3}{\bar{F}_{01}K_1K_2}$
(5)	0	0	0	0	$-K_4$	F_5	$\frac{-V_{TOTAL}F_1F_2F_3F_4}{\bar{F}_{01}K_1K_2K_3}$
(6)	0	0	0	0	0	$\frac{F_5^2}{K_4}-\bar{F}_{56}$	$\frac{-V_{TOTAL}F_1F_2F_3F_4F_5}{\bar{F}_{01}K_1K_2K_3K_4}$

SUMMARY OF RESULTS

$$\bar{C}_1 = \frac{V_{TOTAL}}{\bar{F}_{01}} + \frac{F_1}{\bar{F}_{01}}\bar{C}_2 \qquad \text{...Eqn (A2.1)}$$

$$\bar{C}_2 = \frac{-V_{TOTAL}F_1}{\bar{F}_{01}K_1} - \frac{F_2}{K_1}\bar{C}_3 \qquad \text{...Eqn (A2.2)}$$

$$\bar{C}_3 = \frac{-V_{TOTAL}F_1F_2}{\bar{F}_{01}K_1K_2} + \frac{F_3}{K_2}\bar{C}_4 \qquad \text{...Eqn (A2.3)}$$

$$\bar{C}_4 = \frac{V_{TOTAL}F_1F_2F_3}{\bar{F}_{01}K_1K_2K_3} - \frac{F_5}{K_3}\bar{C}_5 \qquad \text{...Eqn (A2.4)}$$

$$\bar{C}_5 = \frac{V_{TOTAL}F_1F_2F_3F_4}{\bar{F}_{01}K_1K_2K_3K_4} + \frac{F_5}{K_4}\bar{C}_6 \qquad \text{...Eqn (A2.5)}$$

$$\bar{C}_6 = \frac{-V_{TOTAL}F_1F_2F_3F_4F_5}{\bar{F}_{01}K_1K_2K_3K_4K_5} \qquad \text{...Eqn (A2.6)}$$

where:

$$K_1 = \frac{F_1^{\,2}}{\bar{F}_{01}} - \bar{F}_{12}$$

$$K_2 = \frac{F_2^{\,2}}{K_1} + \bar{F}_{23}$$

$$K_3 = \frac{F_3^{\,2}}{K_2} - \bar{F}_{34}$$

$$K_4 = \frac{F_4^{\,2}}{K_3} - \bar{F}_{45}$$

$$K_5 = \frac{F_5^{\,2}}{K_4} - \bar{F}_{56}$$

APPENDIX 3: TK SOLVER MODEL EQUATIONS FOR ECONOMIC ANALYSIS

VARIABLE SHEET

St	Input	Name	Output	Unit	Comment
					Cost-Benefit Analysis Calculation tk-Solver Program Version 1.1 20/08/92
	.61	T		m	Vessel Diameter
		H	1.17	m	Ungassed liquid depth
		VL	.329		Vessel Volume
	3.33	N		rps	Impeller speed
	500000	BPRESS		Pa	Back pressure
	10	IR		%	Nominal Interest Rate
	10	LIFE		Years	Operating Life
		DISFAC	6.145	-	Discount Factor
	.0717	CELEC		£/kWhr	Cost per Unit of Power
	8000	HRSPYR		Hours	Hours per Year Operation
L	.165	POWI		kW	Power draw
		XPOWI	.05	kW	Extra power draw
		XPOWIC	28	£	Extra annual Power Cost
		CAPM	145	£	Captial cost of motor retrofit
		CAPA	1450	£	Capital cost of agitator retrofit
		DPOWIC	174	£	Discounted Running Cost
L		TOTCOS1	319	£	Total NPV of motor retrofit
L		TOTCOS2	1625	£	Total NPV of agitator retrofit
L		COSVOL1	971	£/m^3	NPV cost / vol. for option 1
L		COSVOL2	4938	£/m^3	NPV cost / vol. for option 2
		XQ	.006	m^3/s	Extra gas flow rate
		P1	612814	Pa	Compressor outlet pressure
		XPOWC	1.75	kW	Extra compressor power
		XPOWCC	1004	£	Extra compressor costs
		DPOWCC	6168	£	Discounted extra running costs
L		TOTCOS3	6168	£	Total net present value of option 2
L		COSVOL3	18746	£/m^3	NPV cost / vol. for option 3
		POW1	8.33	kW	Existing compressor power draw
		P2	674096	Pa	New compressor output pressure
		POW2	8.77	kW	New compressor power draw
		XPOWP	.441	kW	Extra power draw of compressor
		XPOWCP	253	£	Extra compressor power costs
		DPOWCP	1555	£	Discounted extra running costs
L		TOTCOS4	1555	£	Net present value of option 4
L		COSVOL4	4727	£/m^3	NPV cost / vol. for option 4
	6000	CAPO2		£	Capital costs of oxygen supply
	4500	RUNC		£	Running costs for oxygen supply
L		TOTCOS5	33651	£	Net present value of option 5
L		COSVOL5	102272	£/m^3	NPV cost / vol. for option 5

RULE SHEET

S Rule

```
"Geometric relationships

H=1.92*T
VL=0.165*((T/0.61)^3)+((H-T)*3.142*(T^2)/4)

"Existing operating conditions

C POWI=2000*VL
Q=5*VL/60
VSG=Q/((T^2)*3.142/4)

"Discount factor

I=IR/100
DISFAC=((1+I)^LIFE-1)/(I*(1+I)^LIFE)

"increased power draw

TORQ=(POWI+XPOWI)/(2*3.142*(1.08*N))
CAPM=0.1*488*TORQ^0.484
CAPA=488*TORQ^0.484
XPOWI=0.27*(1/0.9)*POWI
XPOWIC=(XPOWI/1000)*HRSPYR*CELEC
DPOWIC=XPOWIC*DISFAC
TOTCOS1=CAPM+DPOWIC
TOTCOS2=CAPA+DPOWIC
COSVOL1=TOTCOS1/VL
COSVOL2=TOTCOS2/VL

"increased gas flow rate

XQ=0.21*Q
P1=(BPRESS+101325)+9.81*1000*H
XPOWC=(1/0.6)*XQ*101325*LN(P1/101325)
XPOWCC=(XPOWC/1000)*HRSPYR*CELEC
DPOWCC=XPOWCC*DISFAC
TOTCOS3=DPOWCC
COSVOL3=TOTCOS3/VL

"increase operating pressure

POW1=(1/0.6)*Q*101325*LN(P1/101325)
P2=1.1*P1
POW2=(1/0.6)*Q*101325*LN(P2/101325)
XPOWP=POW2-POW1
XPOWCP=(XPOWP/1000)*HRSPYR*CELEC
DPOWCP=XPOWCP*DISFAC
TOTCOS4=DPOWCP
COSVOL4=TOTCOS4/VL

"enrich inlet gas

DRUNC=RUNC*DISFAC
TOTCOS5=CAPO2+DRUNC
COSVOL5=TOTCOS5/VL
```

APPENDIX 4: SIMPLE MODELS FOR k_La ESTIMATION.

A4.1 No depletion model for gas phase mixing

This model assumes that the gas concentration throughout the vessel is equal to the inlet concentration at the sparger.

$$\frac{dC_L}{dt} = k_La\ (KC_G - C_L) \qquad \text{...Eqn (A4.1)}$$

For no depletion of the gas phase:

$$KC_{G\ (t>0)} = KC_{G\ (t=\infty)} = C_{L\ (t=\infty)}$$

Normalising equation A4.1 by dividing by $C_{L\ (t=\infty)}$:

$$\frac{dC_L^*}{dt} = k_La\ (1 - C_L^*)$$

Integrating:

$$-\ ln\ (1 - C_L^*) = k_La\ t$$

Thus a plot of $-\ ln\ (1 - C_L^*)$ versus t will give a straight line of gradient k_La.

Each measured dissolved oxygen response was fitted to this straight line approximation (for C_L^* values ranging from 0.1 to 0.9) using least squares regression. The gradient of this line is the no depletion k_La.

A4.2 Simple plug flow model for gas phase mixing

This simple model assumes that the gas phase concentration is not time dependent, i.e.:

$$\frac{dC_G}{dt} = 0$$

A mass balance over the whole vessel gives:

$$\Delta\ C = \frac{1}{\beta H}\ (KC_G - C_L)\ (1 - e^{-\beta H}) \qquad \text{...Eqn(A4.2)}$$

where: $$\beta H = \frac{K\ H\ (1 - \varepsilon_G)\ k_La}{V_{sg}}$$

$$\frac{dC_L}{dt} = k_L a \, \Delta \, C$$

Substituting from equation A4.2, then normalising and integrating:

$$- \ln (1 - C_L^*) = \frac{k_L a \, (1 - e^{-\beta H}) \, t}{\beta H}$$

Thus a semi log plot of $- ln (1 - C_L^*)$ versus t, will be a straight line of gradient m.

where: $$m = \frac{k_L a \, (1 - e^{-\beta H})}{\beta H}$$

Thus:

$$k_L a = \frac{V_{sg}}{K \, H \, (1 - \varepsilon_G)} \ln \left(1 - \frac{m \, K \, H \, (1 - \varepsilon_G)}{V_{sg}} \right)^{-1}$$

APPENDIX 5: MASS TRANSFER METHOD FOR VISCOUS LIQUIDS

Poster presented at the 7th European conference on mixing, Brugge, Belgium, September 1991.

MASS TRANSFER IN AERATED AGITATED VESSELS : ASSESSMENT OF THE NEL/HICKMAN STEADY STATE METHOD

Cooke, M	ICI Chemicals and Polymers Ltd, U.K.
Dawson, M.K.	The University of Birmingham, U.K.
Moody, G.	National Engineering Laboratory Executive Agency, U.K.
Nienow, A.W.	The University of Birmingham, U.K.
Whitton, M.J.	British Hydromechanics Research Group Ltd, U.K.

1. INTRODUCTION

Many industrial chemical and biochemical processes are limited by the rate at which oxygen can transfer from a gas phase to a liquid phase. The optimisation of gas liquid mass transfer rates in stirred tank reactors, which are commonly used for these processes, is therefore of great interest to industry. The hydrodynamics of this type of process are very complicated and the majority of development work to date has been based on empirical research. A number of experimental methods for investigating these systems have been developed but each method has its limitations.

The majority of published data is confined to the air-water system. Industrial fluids, however, are usually more viscous than water and quite often of non-Newtonian rheology. There is therefore a need for researchers to extend their work into more industrially relevant fluids. One of the stumbling blocks to achieving this is that the experimental methods developed for measuring oxygen transfer rates in the air-water system cannot easily be applied to rheologically-complex systems.

Hickman (1,2) published a novel experimental technique for measuring oxygen transfer rates in gas-liquid dispersions. This technique is potentially simple, low cost and applicable to rheologically-complex fluids.

However, following the instructions given in (2) researchers from Birmingham University, British Hydromechanics Research Group and ICI, have experienced a number of difficulties with the experimental method.

The aims of this paper are to describe the problems encountered with this method, provide solutions to these problems, and clarify the optimum conditions for achieving accurate oxygen transfer measurements.

2. MASS TRANSFER MEASUREMENT

The equation describing oxygen transfer between a gas and a liquid is:

Mass transfer rate = $k_L a\ (\ H_e c_G - c_L\ )$

The parameters of interest are k_L, the liquid film transfer coefficient, and a, the interfacial area per unit volume of liquid. However, it is very difficult to separate a from k_L so usually the combined parameter $k_L a$ is measured.

Experimental methods for measuring $k_L a$ can be divided into transient and steady state methods.

2.1 Transient methods

One example of a transient method is the dynamic gassing out technique which consists of sparging the vessel with pure nitrogen until all oxygen has been stripped from the liquid.

The sparge gas is then rapidly changed from nitrogen to air. By recording the oxygen concentration of the liquid with time, k_La can be calculated (3). However, this calculation requires an assumption about the degree of gas phase mixing, which can lead to large errors (4). However, this error can be reduced (4,5) if the off gas concentration is also recorded (two-probe technique).

2.2 Steady state methods

In this case the concentration of oxygen in each phase is constant with time, as oxygen transfers between the two phases. To achieve this steady state, oxygen must be continuously generated in one phase and continuously removed, at the same rate, from the other phase.

Two examples of steady state techniques are the sulphite method (6), and the yeast culture method (7). In both cases the chemicals used, and/or produced during the experiments, can alter the bubble size distribution and mass transfer characteristics of the system under study. Additional problems include the difficulty of determining the reaction order with the sulphite method (11), and the poor reproducibility of yeast fermentations (7).

3. NEL/HICKMAN TECHNIQUE (1,2)

3.1 Description

Hydrogen peroxide (BDH Ltd, GPR, 30% wt./vol.) is continuously added to the liquid phase where it is broken down by the enzyme Catalase (BDH Ltd or Sigma Chemicals Ltd, bovine liver extract, $2x10^5$ enzyme units (EU) /ml).

$$2H_2O_2 \rightarrow 2H_2O + O_2$$

$$r = k\,[H_2O_2]^A\,[cat]^B$$

This reaction rate is first order with respect to hydrogen peroxide (i.e. A=1) and independent of catalase concentration over a wide range (i.e. B=0).

Thus oxygen is continuously produced in the liquid phase. This oxygen is then stripped from the liquid by a continuous flow of air through the vessel. Initially hydrogen peroxide and oxygen accumulate in the liquid phase until a steady state is reached where the reaction rate is balanced by the peroxide addition rate and the rate of oxygen production is equal to the rate of oxygen transfer from the liquid phase to the gas phase.

i.e. $r = Q / V_L$

and $r/2 = OTR = k_La\,\Delta c$

The oxygen concentration driving force is estimated from the liquid dissolved oxygen level and an assumed gas phase mixing model.

For the calculation of k_La the only parameters required are

- Concentration and feed rate of hydrogen peroxide
- Dissolved oxygen concentration at steady state
- Gas flow rate and pressure
- Liquid volume
- Temperature
- Henry's law constant

Hickman (2) claimed that the k_La values obtained from this method were independent of peroxide feed rate and catalase concentration over a wide range of test conditions.

3.2 Experimental equipment and test fluids

Figure 1 shows a typical experimental set up. The range of scales studied was 5l to 5000l.

The authors have used the NEL/Hickman method in the following liquids:

- Deionised water
- 0.1M KCl, or NaCl, solution
- 25 ppm Poly Propylene Glycol solution
- Sodium Carboxy Methyl Cellulose solutions
- Celbi Eucalypt paper fibre suspensions

Two or more dissolved oxygen probes (Electrosense or Schott Gerat (model CG867) polarographic probes) were zeroed and spanned in the agitated, aerated vessel.

A metering pump was used to give an accurate and steady flow of peroxide into the vessel. The peroxide was discharged beneath the liquid surface into a well mixed region.

A suitable amount of catalase enzyme was added to the liquid, see Section 5.1.1. Peroxide was metered into the vessel at a fixed rate until a dissolved oxygen steady state was achieved. The experiment could then be repeated over a range of conditions.

The dissolved oxygen level at steady state (controlled by the peroxide feed rate) was always in the range 130% to 300% of the saturated dissolved oxygen level (8).

The production of water and/or the presence of hydrogen peroxide can affect the rheology of some model fluids. Regular rheological tests are therefore recommended.

The oxygen concentration of the exit gas may also be measured, this gives a check on the oxygen balance of the system.

4. PROBLEMS ENCOUNTERED

4.1 Catalase activity

There has to be a minimum concentration of active catalase in the vessel for the assumption of first order reaction rate, with respect to hydrogen peroxide, to hold. If there is insufficient active catalase either a pseudo steady state will be achieved or no steady state will be achieved at all. A pseudo steady state is a steady dissolved oxygen level which is lower than that which would be obtained in the presence of sufficient catalyst. This leads to an over estimation of k_La.

This problem can manifest itself either through insufficient initial active catalase or through loss of catalase activity with time.

Catalase activity loss can be caused by the following:

Temperature
pH
ionic strength
fluid dynamics
Substrate inhibition

Within the temperature range studied, 10 to 25°C, no significant effect on catalase activity was found.

Departure from neutral pH will result in increased activity loss.

In 0.1M NaCl and KCl solutions a significant loss of activity was observed, compared to deionised water. In 0.1M K_2SO_4 solution, total activity loss occurred immediately.

We have no real evidence to suggest that fluid dynamics affect catalase activity.

High standing concentrations of peroxide have been shown to accelerate catalase activity loss.

In addition, catalase active life has been found to vary significantly with composition of the test medium.

4.2 Probe membrane effects

4.2.1 Mechanical integrity

The mechanical integrity of the dissolved oxygen probes is an essential prerequisite for accurate measurements. We have found that damaged/old membranes or a poor membrane seal to the probe will lead to errors. Where peroxide can contaminate the probe electrolyte, the probe response is found to drift steadily upwards even in the absence of catalase.

This problem will result in a high dissolved oxygen reading, leading to an underestimation of k_La.

4.2.2 Catalase attachment to probe surfaces

The following beaker tests were conducted with the dissolved oxygen probes:

TEST	ACTION	PROBE RESPONSE
1.	a) Expose to peroxide	No change
2.	a) Expose to catalase b) Wash with water c) Expose to peroxide	No change Probe reading increased

Test 1 shows that the probe membrane is not permeable to peroxide.

In test 2, the probe reading increased on exposure to peroxide because of the action of catalase. This catalase became attached to the probe during step 2(a) and was not removed by the water wash. The catalase, which also deposits on the vessel internals, can be deactivated using a 0.1M H_2SO_4 wash, after which the probes no longer respond to peroxide.

As above this problem can lead to the under estimation of k_La.

4.2.3 Position and orientation

As in all k_La measurement techniques, incorrect dissolved oxygen readings can result from poorly positioned probes. This can be caused by either local depletion of oxygen (polarographic probes consume oxygen) due to poor local mixing when compared with the bulk mixing, or air bubbles attaching to the probe membrane. The former gives low dissolved oxygen readings, i.e. over estimated k_La, the latter gives high dissolved oxygen readings, i.e. under estimated k_La. A suitable probe position is in the impeller discharge stream as shown in Fig.1.

5. SOLUTIONS TO TECHNICAL PROBLEMS

5.1 Catalase activity

5.1.1 Estimation of required initial catalase concentration

The minimum catalase concentration required for the break down of peroxide can be calculated as follows:

The first stage is to estimate the maximum k_La likely under the range of experimental conditions.

The maximum oxygen transfer rate is then calculated from:

$$OTR_{MAX} = k_La_{MAX} (c_L - H_ec_G)$$

At the maximum k_La, the peroxide induced equilibrium must be at least 130% of the air equilibrium, Section 3.2.

i.e. $c_L = 1.3 * c_{L\,(\text{AT AIR EQUILIBRIUM})}$

$c_{L\,(\text{AT AIR EQUILIBRIUM})}$ is easily measured.

H_e is estimated using literature data for the air- water system.

c_G is estimated from an ideal gas phase mixing model. The simplest assumption is the no depletion/enrichment model.

i.e. $c_G = c_{G\,(\text{AIR INLET})}$

The required peroxide feed rate is then calculated:

$Q_{MAX} = OTR_{MAX} * 2V_L$

The concentration of catalase required to break down a peroxide feed rate of Q_{MAX} in one minute can be calculated using the following information:

Catalase activity = $2x10^5$ EU/ml, and 1 EU decomposes 1 µml H_2O_2 /min, (9).

In practice, the authors have found that to achieve a steady state in a reasonable time and to avoid high standing concentrations of peroxide, the actual catalase concentration needs to be at least fifteen times this calculated value. Since the initial catalase concentration required is proportional to k_La, fig. 2, it is obviously very system dependent.

At high catalase concentrations (high k_La), surface effects due to catalase deposition are exacerbated. The coalescence behaviour of the system may also be affected.

5.1.2 Activity loss

Activity loss is minimised by avoiding large standing concentrations of peroxide in the liquid. This is achieved by running experiments at a high catalase concentration and the minimum allowable peroxide feed rate.

The standing peroxide concentration can be checked by adding a small quantity of catalase to the liquid during an experiment. The dissolved oxygen level will rapidly increase and then it should return to the original steady state level. If the resulting peak is very large, it shows that the standing concentration of peroxide is too high. If this occurs, more catalase should be added to the system. High concentrations of peroxide can be avoided by making periodic small additions of catalase to balance the activity loss.

In extreme cases of activity loss, k_La will be over-estimated, see Section 4.1. To avoid this situation, it is useful to measure the off gas oxygen concentration as this allows a check on the mass balance of the system. Any disagreement between the mass balance calculations and the oxygen concentration measurements indicates a problem.

A set of base line experimental conditions should be chosen and repeated at regular intervals to check the reproducibility of the results.

5.2 Probe care and checks

5.2.1 Mechanical integrity

The probes can be checked before use by starting the peroxide feed to the agitated, aerated vessel before adding any catalase (N.B. if the vessel has recently contained catalase, all traces of this must be deactivated with a 0.1M H_2SO_4 wash) . A significant increase in the probe dissolved oxygen reading indicates that peroxide is contaminating the probe's electrolyte. The probe must be completely stripped down and reassembled with a new membrane.

Improved reproducibility has been obtained, with the Electrosense probes, by using heavy duty (25 μm) polypropylene membranes (supplied by Uniprobe Ltd) rather than thin (10 μm) PTFE membranes. The heavy duty membranes also reduce the probe's consumption of oxygen helping to avoid the problems described in Section 4.2.3.

6. EXPERIMENTAL RESULTS

Experimental data for a Rushton turbine in a range of test liquids are given in figures 3 to 6.

In deionised water, fig. 3, and KCl solution, fig. 4, the steady state method gave good agreement with the transient two probe method. This indicates that the chemicals used in the NEL/Hickman method do not significantly affect the k_La of the test medium.

In PPG solution, fig. 5, and CMC solution, fig. 6, the steady state method gave k_La values significantly higher than the transient method. This was the result of the large hold up of tiny bubbles in these liquids.

The transient method described cannot be applied to systems which contain a large hold up of tiny bubbles (i.e. < 1mm in diameter) which have a long residence time compared with their equilibrium time. These bubbles act as an additional oxygen sink which slows down the transient response of the liquid phase, (10). Therefore, the transient method will always underestimate k_La.

A steady state method avoids the problem caused by the tiny bubble hold up because there are no transients to inhibit. Thus the steady state technique gives a better estimate of the system k_La.

7. CONCLUSIONS

1. The NEL/Hickman steady state method is relatively simple, effective and gives reproducible results if the correct procedures are followed.

2. For the measurement of oxygen mass transfer rates from air in systems containing very small bubbles a steady state experimental method is essential because the two-probe transient method will under estimate k_La.

3. The mechanical integrity and positioning of dissolved oxygen electrodes is vital to the successful implementation of the NEL/Hickman technique.

4. The concentration of <u>active</u> catalase in the system must be maintained at a level of at least fifteen times the stoichiometric requirement.

5. The technique has been successfully used to measure k_La values up to 0.5 s^{-1}. The high catalase concentrations required for these measurements increase the level of catalase deposition on vessel and probe surfaces.

8. ACKNOWLEDGEMENTS

Support from the following is gratefully acknowledged: NEL for work at the University of Birmingham (including M.K. Dawson) and members of the FMP consortium for work at BHR Group Ltd.

9. NOMENCLATURE

a	Specific interfacial area	m^2/m^3
c_G	Gas phase oxygen concentration	$kmol/m^3$
c_L	Liquid phase oxygen concentration	$kmol/m^3$
H_e	Henry's law constant	-

k	Reaction rate constant	$kmol/m^3s$
k_L	Liquid film transfer coefficient	m/s
OTR	Oxygen transfer rate	kmol/s
P_t	Impeller power input	kW/m^3
r	Reaction rate	$kmol/m^3s$
Q	Peroxide feed rate	kmol/s
V_L	Liquid volume	m^3
Δc	Concentration driving force	$kmol/m^3$
Vs	Superficial gas velocity	m/s
[cat]	Catalase concentration	$kmol/m^3$
$[H_2O_2]$	Peroxide concentration	$kmol/m^3$

10. REFERENCES

1. Hickman, A.D., Bioreactor Design Club Report, F TP/D/06, NEL, Scotland, (1987).
2. Hickman, A.D., Proc. 6th Euro. conf. mixing, Pavia, Italy, (1988), BHR Group, Cranfield, 369.
3. Dang, N.D.P., Karrer, D.A., Dunn, I.J., Biotech. & Bioeng., 19, (1977), 853.
4. Chapman, C.M., Gibilaro, L.G., Nienow, A.W., Chem. Eng. Sci., 37, (1982), 891.
5. Cooke, M., Proc. Particle Processing in Liquid Suspension, UCL, (1989), 125.
6. Midoux, N., Charpentier, J.C., Proc. 3rd Euro. conf. mixing, York, England, (1979), BHR Group, Cranfield, Paper F4.
7. Hickman, A.D., Nienow, A.W., Int. conf. on bioreactor fluid dynamics, Cambridge, England, (1986), BHR Group, Cranfield, Paper 22.
8. Dawson, M.K., Bioreactor Design Club Report, NEL, Scotland, (1990).
9. BDH Ltd, chemical supply data.
10. Heijnen, J.J., Van't Riet, K., Wolthuis, A.J., Biotech. & Bioeng., 22, (1980), 1945.
11. Thibault, J., Leduy, A., Davies, A., Can. J. Chem. Eng., 68, (1990), 324.

Figure 1: Experimental set up

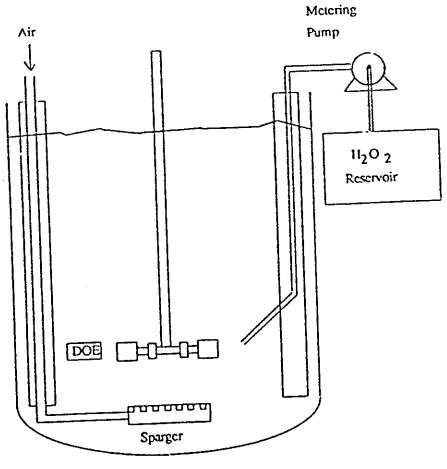


Figure 2: Minimum recommended catalase concentration

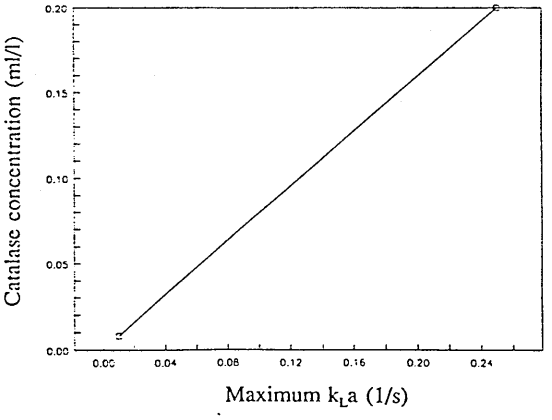


Figure 3

Air–Water Mass Transfer in a 0.3m Diameter Tank

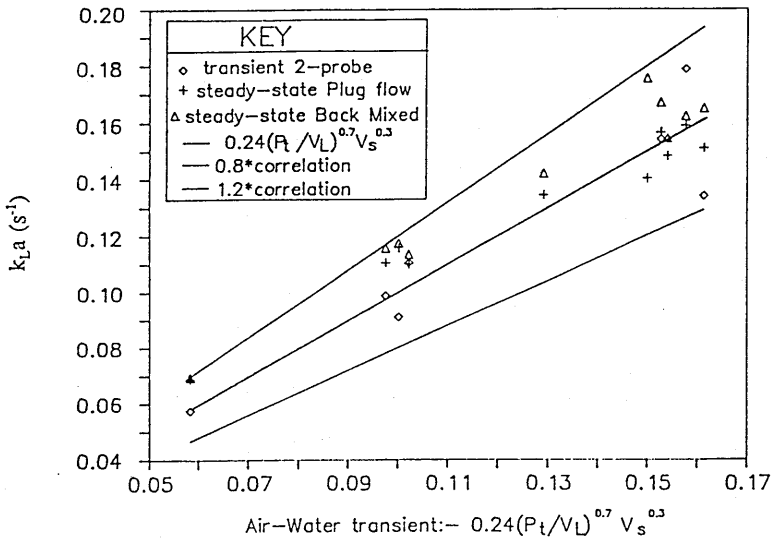


Figure 4

Air–0.1M KCl Mass Transfer in a 0.3m Diameter Tank

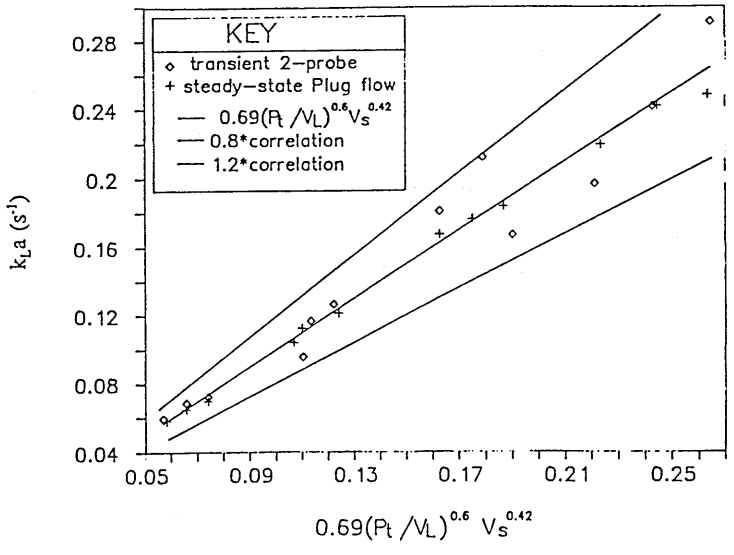


Figure 5

Air–25ppm PPG Mass Transfer in a 0.286m Diameter Tank

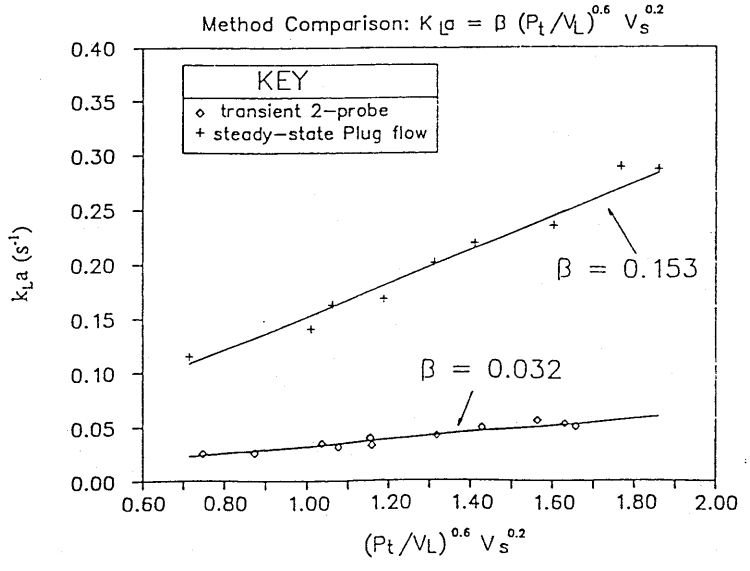
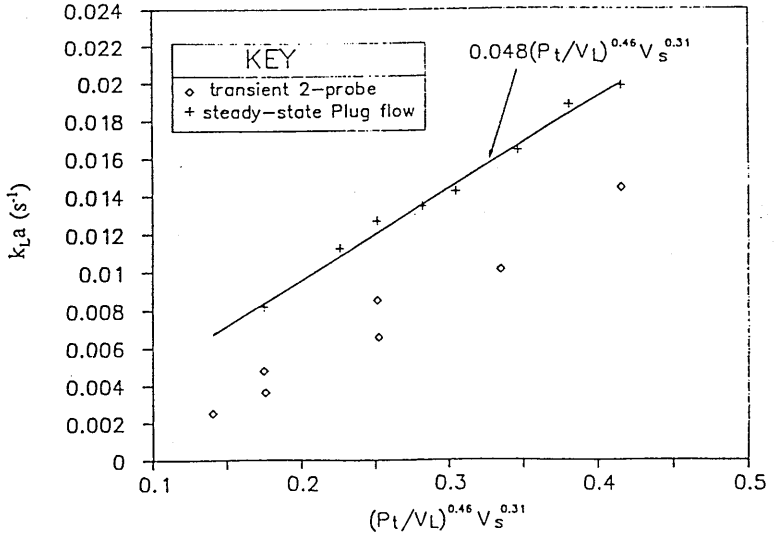


Figure 6

Air–0.4%CMC Mass Transfer in a 0.3M Diameter Tank



ERRATA

1.
Page 1, AUTHORS, Line 3, Reads : Moody, G.....
Should Read : Moody, G.W...

2.
Page 7, References, Column 1, Line 16, Reads : Report, FOTP/D/06, NEL, Scotland,
Should read : Report, FDTP/D/06, NEL, Scotland.

3.
Page 7, Nomenclature, Line 4, Reads : OTR Oxygen transfer rate kmol/s.
Should Read : OTR Oxygen transfer rate $kmol/m^3s$.

4.
Page 7, References, Column 2, Line 7, Reads :Liquid Suspension, UCL, (1989), 125.
Should Read : Liquid Suspension, University College London, (1989), 125.

5.
Page 6, Nomenclature, Insert between C and He: eu Enzyme Units.

6.
Page 5, Column 1, Line 17, Reads : decomposes 1µml H_2O_2/min, (9).
Should Read : decomposes $1x10^{-3}$ ml H_2O_2/min, (9).

REFEREES' COMMENTS AND QUESTIONS ANSWERED

Question 1

There is a conceptual problem regarding the way to account for the degree of gas phase mixing. This is correctly recalled as a potential source of large errors (Section 2.1), whilst perfect mixing is explicitly assumed throughout the paper. A comment on this seems to be in order, especially because the agreement of these results with those obtained with the two probe technique is fairly good (figs 3 & 4). In addition, the legend "steady-state plug flow" appears in figures 3 to 6 : this inconsistency should be properly amended or explained. Finally, the assumption of the no depletion/enrichment model is mentioned in Section 5.1.1 : it would be wise to mention whether this assumption is made just for the sake of initial catalase concentration estimation (which is acceptable) or in the whole paper (which could be questionable, unless properly explained).

Answer 1

Perfect mixing of the gas phase is not explicitly assumed throughout the paper.

Page 2, Column 2, Para.3 : O_2 conc. driving force is estimated from the liquid dO_2 level and an assumed gas phase mixing model.

The assumed model may either be 'plug-flow' or 'fully back mixed' depending upon system.

In practice the authors have found only small difference in resultant k_La values when either model is applied in water, C.M.C., etc.

Note fig 3 shows results with both plug-flow and back mixed models compared with 2-probe data. Both model data falls within ± 20% bands shown.

The assumption of no depletion/enrichment mentioned in Section 5.1.1 is made for the sake of initial [cat] estimation only.

Exit gas analysis data confirms enrichment values calculated using fully backed-mixed model in water.

O_2 Driving forces for Catalase technique are ≥ driving force for dynamic technique with either model.

Question 2

The definition of mass transfer rate at p.1 should actually be in terms of the overall coefficient, K_La. Since oxygen is sparingly soluble, then $K_L \approx k_L$. For clarity this should be stated explicitly.

Answer 2

Mass transfer rate $= k_La\ (Ci-C_L)$ (1)

$= k_Ga\ (Pc-Pi)$ (2)

Where $Pi = He.C_i$

Combining (1) and (2)

Mass transfer rate =

$$a\ (Pc/He-C_L).\ \left[\frac{1}{k_L} + \frac{1}{He.kc}\right]^{-1}$$

As $k_G > k_L$

Therefore $\frac{1}{k_L} >> \frac{1}{He.kc}$

Mass transfer rate $= k_La\ (C^*-CL)$

Where
$C^* = Pc/He$

$Ci = O_2$ conc. at interface $[mol.m^3]$

C_L = Liquid phase O_2 conc. $[mol.m^3]$

a = interfacial area $[m^2]$

P_c = Partial pressure O_2 in gas phase $[Nm^{-2}]$

P_i = " " " at interface $[Nm^{-2}]$

k_L = Liq. phase m.t. coeff. $[ms^{-1}]$

k_G = Gas phase m.t. coeff. $[ms^{-1}]$

Question 3

Section 3.2. The range of scales is given as 5l to 50001 : the form '5 to 5000 litre' is typographically clearer. More important, only two vessel sizes (0.3 and 0.286m diameter) are reported in the figures.

Answer 3

The range 5l to 50001 refers to those vessels in which the technique has been used.

The vessels of 0.3m and 0.286m diameter are those in which comparisons between NEL/Hickman and 2-probe have been conducted.

Question 4

Section 3.2. Apparently, experiments with K_2SO_4 solutions were also performed - in addition to KCl and NaCl.

Answer 4

The list of liquids Page 3, Col.1, Para.2 refers to those fluids in which the technique has been successfully applied.

In 0.1M K_2SO_4 activity loss occurred immediately and therefore the technique could not be applied.

Question 5

To get a correct measurement of dissolved oxygen concentration, wouldn't be better to use an auxiliary disk rotating in a parallel direction to the probe membrane.

Answer 5

Auxiliary Disc
Page 4, Col.2, 4.2.3 Probe position and orientation:
'A suitable probe position is in the impeller discharge stream as shown in Fig.1'.

An auxiliary disc will not do any good in the impeller discharge stream.

Problems with auxiliary disc., see:
König, B., Lipper, J. and Schügerl, K. Germ.Chem.Eng. 2, (1979), 371-377.

Can cause additional gas dispersion and changes local hydrodynamics giving too high k_La values.

Question 6

Section 5.1.1., you say that He is estimated using literature data for the air-water system. Don't you take the composition of water solution into account?

Answer 6

He estimation :
Literature data has been used corrected for temperature and salt concentration of the solution. As with other workers He water has also been used for C.M.C. solutions.

Question 7

It would be interesting to know the (apparent) viscosity of PPG and CCM solutions as well as the fluid dynamic regime under which the experiments were performed.

Answer 7

See M. Cooke

Question 8

Though the correlation of the results is clearly out of the scope of this paper, a few words about the agreement/disagreement of the results (figs 3 & 4) with published data could be interesting (e.g.: LINEK et al, Chem.Eng.J, vol 34, pp. 11-34, 1987).

Answer 8

Good agreement with stated reference for water

Ref $k_La = 4.95\times10^{-3}(P/V)^{0.593}\ Vs^{0.4}$

M K Dawson,
1:1/2:1 $k_La = 6.3\times10^{-3}\ (P/V)^{0.6}\ Vs^{0.43}$

Question 9

Section , paragraph 3 : don't you think that the chemical used in the NEL/Hickman method have an effect on gas bubble diameter?

Answer 9

Negligible
a) no increase in hold-up
b) Effect of non-coalescence e.g. k_La with salts shows typical enhancement with NEL/Hickman method which would not be the case if coalescence was significantly reduced by the catalase.

TABLE 2.1: Average dimensions of disc turbines, see figure 2.3

	T = 0.61 m	T = 0.95 m
Impeller diameter (D)	0.191 (0.31T)	0.297 (0.31T)
Blade Width (W)	0.039 (0.20D)	0.059 (0.20D)
Blade Length (L)	0.048 (0.25D)	0.074 (0.25D)
Disc diameter (D_d)	0.130 (0.68D)	0.203 (0.68D)
Blade / disc thickness (t)	0.005 (0.03D)	0.006 (0.02D)

TABLE 2.2: Average dimensions of pitched blade turbines, see figure 2.3

	T = 0.61 m
Swept diameter (D)	0.304 m (0.50T)
Blade Width (W)	0.070 m (0.23D)
Blade Length (L)	0.123 m (0.41D)
Blade thickness (t)	0.003 m (0.01D)
Blade angle (α)	45°

TABLE 2.3: Average dimensions of LE20 impellers, see figure 2.3

	T = 0.61 m	T = 0.95 m
Swept diameter (D)	0.313 m (0.51T)	0.505 m (0.53T)
Blade width at hub (W_1)	0.082 m (0.26D)	0.130 m (0.26D)
Blade width at tip (W_2)	0.070 m (0.22D)	0.110 m (0.22D)
Blade angle at hub (α_1)	30°	30°
Blade angle at tip (α_2)	25°	25°

TABLE 3.1: Individual impeller ungassed power numbers in standard geometry vessel, T = 0.61 m.

IMPELLER	DIAMETER mm	POWER NUMBER
RT (Top)	191 (0.31T)	4.52
RT (Middle)	190 (0.31T)	4.69
RT (Bottom)	191 (0.31T)	4.78
PBT (Top)	302 (0.49T)	1.43 (pumping up) 1.37 (pumping down)
PBT (Middle)	307 (0.50T)	1.42 (pumping up) 1.34 (pumping down)
LE20 (Top)	312 (0.51T)	0.35 (pumping down)
LE20 (Middle)	313 (0.51T)	0.34 (pumping down)

Maximum relative standard deviation was 1.4%

TABLE 3.2: Ungassed power numbers for triple impeller combinations (T = 0.61 m)

	3RT	1RT+2LE20 (Pumping down)	1RT+2PBT (Pumping down)	1RT+2PBT (pumping up)
TOP	4.23 (2.6)	0.38 (0.7)	1.35 (0.9)	1.45 (1.4)
MIDDLE	4.58 (1.7)	0.37 (4.2)	1.32 (0.5)	1.35 (2.5)
BOTTOM	4.95 (1.2)	4.83 (1.3)	4.77 (3.2)	5.00 (0.1)

Value in brackets = relative standard deviation (%)

TABLE 3.3: **Loading to flooding transition for a single Rushton turbine and the lowest Rushton turbine in the tall vessel**

N	RT*	RT	3×RT *S=2.6D*	3×RT *S=1.6D*	RT+2×LE20 *S=2.6D*	RT+2×LE20 *S=1.6D*
3.33	0.111	0.095 (0.075)	0.085 (0.063)	0.043 (0.032)	0.059 (0.057)	0.115 (0.089)
4.33	0.188	0.158 (0.139)	0.139 (0.108)	0.073 (0.035)	0.142 (0.117)	0.210 (-)

( ) : Transition from flooding back to loading
* : Prediction of equation 1.1

TABLE 3.4: **Fraction of sparge gas recirculated into upper impellers, estimated from power data, (triple Rushton turbine combination, (T = 0.61 m)**

N (rps)	Q_G (m^3/s)	Top (%)	Middle (%)
3.33	5.1×10^{-4}	28	33
4.33	5.1×10^{-4}	54	54
4.33	7.2×10^{-4}	44	39
4.33	8.8×10^{-4}	41	31
4.33	1.0×10^{-3}	41	29
6.00	9.6×10^{-4}	100	49
6.00	1.3×10^{-3}	84	40
6.00	1.6×10^{-3}	66	38

TABLE 3.5: **Ungassed power numbers for triple impeller combinations (T = 0.95 m)**

	3RT	**1RT+2LE20 (Pumping down)**
TOP	4.88	0.41
MIDDLE	4.84	0.42
BOTTOM	5.35	5.39

TABLE 3.6: Fraction of sparge gas recirculated into upper impellers, estimated from flow maps, (triple Rushton turbine combination, (T = 0.61 m)

T	N	Fr	$Fl_{3\text{-}3,L}$	$Fl_{3\text{-}3,U}$	Percentage
0.61	3.33	0.216	0.037	0.173	21%
	4.33	0.365	0.037	0.102	37%
	6.00	0.701	0.037	0.053	70%
0.95	3.33	0.336	0.039	0.117	33%
	4.33	0.568	0.039	0.069	57%
	5.33	0.860	0.039	0.046	86%
	6.33	1.213	0.039	0.033	120%*
	7.00	1.483	0.039	0.027	148%*

* : Assumed = 100%

TABLE 4.1: Holdup data for 3RT combination (T=0.61 m)

N (rps)	Q_G (m^3/s)	ε_m (W/kg)	ε_G (-)
3.33	0	0.322	0
3.33	6.67e-4	0.272	0.0139
3.33	9.67e-4	0.256	0.0191
3.33	1.23e-3	0.262	0.0233
3.33	1.53e-3	0.249	0.0285
3.33	1.83e-3	0.233	0.0286
3.33	2.13e-3	0.232	0.0319
4.33	0	0.726	0
4.33	9.67e-4	0.585	0.0234
4.33	1.53e-3	0.530	0.0344
4.33	2.13e-3	0.492	0.0440
4.33	2.77e-3	0.460	0.0542
4.33	3.40e-3	0.416	0.0595
4.33	3.73e-3	0.375	0.0670
5.00	0	1.092	0
5.00	9.67e-4	0.911	0.0294
5.00	2.13e-3	0.732	0.0506
5.00	3.40e-3	0.625	0.0714
5.00	5.50e-3	0.519	0.0905
6.00	0	1.901	0
6.00	9.67e-4	1.462	0.0330
6.00	2.13e-3	1.165	0.0544
6.00	3.40e-3	1.053	0.0724
6.00	5.50e-3	0.880	0.1002
6.00	1.02e-2	0.669	0.1373

TABLE 4.2: Holdup data for RT+2×LE20 combination (T=0.61 m)

N (rps)	Q_G (m^3/s)	ε_m (W/kg)	ε_G (-)
3.33	0	0.327	0
3.33	6.67e-4	0.297	0.0145
3.33	9.67e-4	0.275	0.0214
3.33	1.23e-3	0.256	0.0268
3.33	1.53e-3	0.254	0.0306
3.33	1.83e-3	0.246	0.0325
3.33	2.13e-3	0.219	0.0359
4.33	0	0.708	0
4.33	9.67e-4	0.641	0.0266
4.33	1.53e-3	0.518	0.0390
4.33	2.13e-3	0.420	0.0473
4.33	2.77e-3	0.374	0.0569
4.33	3.40e-3	0.375	0.0655
4.33	3.73e-3	0.383	0.0690
5.00	0	1.040	0
5.00	9.67e-4	0.934	0.0309
5.00	2.13e-3	0.572	0.0493
5.00	3.40e-3	0.516	0.0650
5.00	5.50e-3	0.487	0.0869
6.00	0	1.797	0
6.00	9.67e-4	1.468	0.0354
6.00	2.13e-3	0.969	0.0540
6.00	3.40e-3	0.877	0.0724
6.00	5.50e-3	0.793	0.0983
6.00	1.02e-2	0.770	0.1325

TABLE 4.3: Holdup data for RT+2×PBT combination (pumping down) (T=0.61 m)

N (rps)	Q_G (m^3/s)	ε_m (W/kg)	ε_G (-)
3.33	0	0.738	0
3.33	6.67e-4	0.660	0.0205
3.33	9.67e-4	0.608	0.0271
3.33	1.23e-3	0.565	0.0324
3.33	1.53e-3	0.521	0.0358
3.33	1.83e-3	0.431	0.0386
3.33	2.13e-3	0.395	0.0417
4.33	0	1.622	0
4.33	9.67e-4	1.354	0.0382
4.33	1.53e-3	1.007	0.0487
4.33	2.13e-3	0.811	0.0558
4.33	2.77e-3	0.746	0.0638
4.33	3.40e-3	0.680	0.0707
5.00	0	2.497	0
5.00	2.13e-3	1.259	0.0553
5.00	3.40e-3	1.006	0.0725
5.00	5.50e-3	0.925	0.0946
6.00	0	4.316	0
6.00	3.40e-3	1.740	0.0816
6.00	5.50e-3	1.511	0.1119
6.00	1.07e-2	1.330	0.1506

TABLE 4.4: Holdup data for RT+2×PBT combination (pumping up)
(T=0.61 m)

N (rps)	Q_G (m^3/s)	ε_m (W/kg)	ε_G (-)
3.33	0	0.802	0
3.33	6.67e-4	0.748	0.0234
3.33	9.67e-4	0.709	0.0324
3.33	1.23e-3	0.653	0.0351
3.33	1.53e-3	0.611	0.0389
3.33	1.83e-3	0.594	0.0423
3.33	2.13e-3	0.541	0.0457
4.33	0	1.705	0
4.33	9.67e-4	1.487	0.0401
4.33	1.53e-3	1.235	0.0519
4.33	2.13e-3	1.031	0.0611
4.33	2.77e-3	0.915	0.0691
4.33	3.40e-3	0.894	0.0704
4.33	3.73e-3	0.868	0.0726
5.00	0	2.625	0
5.00	2.13e-3	1.535	0.0624
5.00	3.40e-3	1.304	0.0763
5.00	5.50e-3	1.219	0.0891
6.00	0	4.536	0.
6.00	1.07e-2	1.774	0.1316

TABLE 4.5: Hold-up correlations for different impeller combinations in the 0.61 m diameter vessel

$$\varepsilon_G = \alpha\ (N)^{\beta}\ (Q_G)^{\gamma}$$

	α	β	γ	R^2	F ratio	Standard Error	Number of data points
3RT	0.72	0.86	0.67	0.987	734	0.068	21
1RT+2×LE20 (pumping down)	0.76	0.71	0.63	0.981	517	0.075	21
1RT+2×PBT (pumping down)	0.37	0.82	0.51	0.985	529	0.064	17
1RT+2×PBT (pumping up)	0.24	0.81	0.43	0.974	287	0.070	16
Combined data from all four impeller combinations	0.80	0.62	0.61	0.925	458	0.145	75

TABLE 4.6: Hold-up correlations for different impeller combinations in the 0.61 m diameter vessel

$$\varepsilon_G = \alpha\ (\varepsilon_m)^{\beta}\ (v_{sg})^{\gamma}$$

	α	β	γ	R^2	F ratio	Standard Error	Number of data points
3RT	2.18	0.31	0.75	0.990	956	0.060	21
1RT+2×LE20 (pumping down)	1.85	0.26	0.72	0.979	467	0.079	21
1RT+2×PBT (pumping up)	0.72	0.28	0.53	0.968	224	0.079	16
1RT+2×PBT (pumping down)	1.22	0.28	0.63	0.984	485	0.067	17
All 4 combinations combined	1.44	0.28	0.67	0.969	1163	0.093	75

TABLE 4.7: Effect of cavity regimes on 3RT holdup correlations (T = 0.61 m).

$$\varepsilon_G = \alpha\ (N)^{\beta}\ (Q_G)^{\gamma}$$

	α	β	γ	R^2	F ratio	Standard Error	Number of data points
Flow regime 'a'	0.96	1.04	0.75	0.974	56	0.062	4
Flow regime 'b'	0.48	1.07	0.64	0.968	91	0.048	7
Flow regime 'c'	0.91	0.49	0.60	0.988	359	0.035	10
All 3RT data	0.72	0.86	0.67	0.987	734	0.068	21

Flow regime 'a' = Vortex / clinging cavities on all three impellers.
Flow regime 'b' = 3-3 cavities on bottom impeller + vortex / clinging cavities on upper impellers.
Flow regime 'c' = 3-3 cavities on all three impellers.

TABLE 4.8: Effect of cavity regimes on 3RT holdup correlations (T = 0.61 m).

$$\varepsilon_G = \alpha\ (\varepsilon_m)^{\beta}\ (V_{sg})^{\gamma}$$

	α	β	γ	R^2	F ratio	Standard Error	Number of data points
Flow regime 'a'	1.68	0.37	0.71	0.983	86	0.051	4
Flow regime 'b'	1.73	0.37	0.70	0.971	102	0.046	7
Flow regime 'c'	1.41	0.18	0.66	0.987	343	0.036	10
All 3RT data	2.18	0.31	0.75	0.990	956	0.060	21

Flow regime 'a' = Vortex / clinging cavities on all three impellers.
Flow regime 'b' = 3-3 cavities on bottom impeller + vortex / clinging cavities on upper impellers.
Flow regime 'c' = 3-3 cavities on all three impellers.

TABLE 4.9: Holdup data for 3RT combination (T=0.95 m)

N (rps)	Q_G (m^3/s)	ε_m (W/kg)	ε_G (-)
3.33	0	0.823	0
3.33	0.66e-2	0.521	0.0654
3.33	1.32e-2	0.382	0.0971
3.33	1.83e-3	0.361	0.1064 (F)
3.33	2.17e-3	0.366	0.1148 (F)
4.33	0	1.809	0
4.33	0.66e-2	1.039	0.0758
4.33	1.32e-2	0.856	0.1190
4.33	1.83e-2	0.711	0.1409
4.33	2.69e-2	0.639	0.1610
4.33	3.20e-2	0.640	0.1565
5.33	0	3.373	0
5.33	0.66e-2	1.888	0.0858
5.33	1.32e-2	1.593	0.1295
5.33	1.83e-2	1.387	0.1535
5.33	2.17e-2	1.192	0.1748
5.33	2.69e-2	1.090	0.1840
5.33	3.20e-2	1.050	0.1899
6.33	0	5.651	0
6.33	0.66e-2	3.145	0.0955
6.33	1.32e-2	2.454	0.1381
6.33	1.83e-2	2.288	0.1611
6.33	2.17e-2	1.954	0.1836
6.33	2.69e-2	1.891	0.1938
6.33	3.20e-2	1.732	0.2010
7.00	0	7.642	0
7.00	0.66e-2	4.305	0.1015
7.00	1.32e-2	3.274	0.1440
7.00	1.83e-2	2.929	0.1653
7.00	2.17e-2	2.693	0.1869
7.00	2.69e-2	2.544	0.1966

TABLE 4.10: Holdup data for RT+2×LE20 combination (T=0.95 m)

N (rps)	Q_G (m^3/s)	ε_m (W/kg)	ε_G (-)
3.33	0	0.935	0
3.33	0.66e-2	0.513	0.0658
3.33	1.32e-2	0.490	0.0886
3.33	1.83e-3	0.469	0.0999
4.33	0	2.056	0
4.33	0.66e-2	1.082	0.0754
4.33	1.32e-2	0.954	0.1124
4.33	1.83e-2	0.929	0.1289
4.33	2.17e-2	0.902	0.1334
4.33	2.69e-2	0.903	0.1391
4.33	3.20e-2	0.902	0.1476
4.83	0	2.853	0
4.83	0.66e-2	1.442	0.0802
4.83	1.32e-2	1.278	0.1193
4.83	1.83e-2	1.012	0.1377
4.83	2.17e-2	1.180	0.1516
4.83	2.69e-2	1.168	0.1572
4.83	3.20e-2	1.168	0.1605
5.33	0	3.834	0
5.33	0.66e-2	1.970	0.0851
5.33	1.32e-2	1.772	0.1249
5.33	1.83e-2	1.750	0.1443
5.33	2.17e-2	1.657	0.1582
5.33	2.69e-2	1.579	0.1668
5.33	3.20e-2	1.491	0.1784

TABLE 4.11: Hold-up correlations for different impeller combinations in the 0.95 m diameter vessel

$$\varepsilon_G = \alpha\ (N)^{\beta}\ (Q_G)^{\gamma}$$

	α	β	γ	R^2	F ratio	Standard Error	Number of data points
3RT	0.45	0.53	0.50	0.979	540	0.047	24
1RT+2×LE20	0.27	0.68	0.45	0.980	461	0.042	20
Combined data from both impeller combinations	0.34	0.61	0.48	0.973	770	0.052	44

TABLE 4.12: Hold-up correlations for different impeller combinations in the 0.95 m diameter vessel

$$\varepsilon_G = \alpha\ (\varepsilon_m)^{\beta}\ (v_{sg})^{\gamma}$$

	α	β	γ	R^2	F ratio	Standard Error	Number of data points
3RT	1.12	0.18	0.57	0.977	489	0.049	24
1RT+2×LE20	0.73	0.24	0.48	0.976	352	0.047	20
Combined data from both impeller combinations	0.93	0.21	0.53	0.950	408	0.070	44

TABLE 4.13: Effect of cavity regimes on 3RT holdup correlations (T = 0.95 m).

$$\varepsilon_G = \alpha\ (N)^{\beta}\ (Q_G)^{\gamma}$$

	α	β	γ	R^2	F ratio	Standard Error	Number of data points
Flow regime 'c'	0.44	0.50	0.48	0.965	278	0.047	21
All 3RT data	0.45	0.53	0.50	0.979	540	0.047	24

TABLE 4.14: Effect of cavity regimes on 3RT holdup correlations (T = 0.95 m).

$$\varepsilon_G = \alpha\ (\varepsilon_m)^{\beta}\ (V_{sg})^{\gamma}$$

	α	β	γ	R^2	F ratio	Standard Error	Number of data points
Flow regime 'c'	1.02	0.17	0.54	0.962	256	0.049	21
All 3RT data	1.12	0.18	0.57	0.977	489	0.049	24

Flow regime 'c' = 3-3 cavities on all three impellers.

TABLE 4.15: Correlation of holdup data including gas expansion energy.

$$\varepsilon_G = \alpha\ (\varepsilon_m + \varepsilon_{gas})^{\beta}\ (v_{sg})^{\gamma}$$

	α	β	γ	R^2	F ratio	Standard Error	Number of data points
3RT (T = 0.61 m)	1.69	0.34	0.71	0.988	812	0.065	21
3RT (T = 0.95 m)	0.93	0.22	0.54	0.971	389	0.055	24

TABLE 4.16: Scale up correlations for the 3RT and 1RT+2×LE20 combinations (T = 0.61 m and 0.95 m)

$$\varepsilon_G = \alpha\ (N)^{\beta}\ (Q_G)^{\gamma}$$

	α	β	γ	R^2	F ratio	Standard Error	Number of data points
3RT (all data)	0.39	0.72	0.54	0.981	1106	0.105	45
1RT+2×LE20	0.26	0.84	0.49	0.981	1024	0.092	41
3RT Cavity regime 'b'	0.38	0.96	0.59	0.985	262	0.056	9
3RT Cavity regime 'c'	0.41	0.50	0.46	0.983	860	0.058	31

Cavity regime 'b' = 3-3 cavities on the lowest disc turbine and Vortex / clinging cavities on the upper disc turbines
Cavity regime 'c' = 3-3 cavities on all three disc turbines

TABLE 4.17: Scale up correlations for the 3RT and 1RT+2×LE20 combinations (T = 0.61 m and 0.95 m)

$$\varepsilon_G = \alpha\ (N)^{\beta}\ (Q)^{\gamma}\ (T)^{\omega}$$

	α	β	γ	ω	R^2	F ratio	Standard Error	Number of data points
3RT (all data)	0.51	0.70	0.61	-0.44	0.985	955	0.092	45
1RT+2×LE20	0.37	0.76	0.55	-0.38	0.984	843	0.083	41
3RT Cavity regime 'b'	0.57	0.92	0.67	-0.28	0.985	175	0.056	9
3RT Cavity regime 'c'	0.50	0.51	0.52	-0.28	0.988	789	0.049	31

Cavity regime 'b' = 3-3 cavities on the lowest disc turbine and Vortex / clinging cavities on the upper disc turbines
Cavity regime 'c' = 3-3 cavities on all three disc turbines

TABLE 4.18: Scale up correlations for the 3RT and 1RT+2×LE20 combinations (T = 0.61 m and 0.95 m)

$$\varepsilon_G = \alpha\ (\varepsilon_m)^{\beta}\ (v_{sg})^{\gamma}$$

	α	β	γ	R^2	F ratio	Standard Error	Number of data points
3RT (all data)	1.87	0.28	0.72	0.984	1384	0.094	45
1RT+2×LE20	1.29	0.27	0.64	0.979	910	0.098	41
3RT Cavity regime 'b'	3.17	0.41	0.80	0.974	150	0.074	9
3RT Cavity regime 'c'	1.46	0.24	0.66	0.971	496	0.076	31

Cavity regime 'b' = 3-3 cavities on the lowest disc turbine and Vortex / clinging cavities on the upper disc turbines
Cavity regime 'c' = 3-3 cavities on all three disc turbines

Table 5.1: Liquid mixing data, 3RT combination, T = 0.95 m.

(Liquid mixing model shown in figure 5.2)

N (rps)	Q (m^3/s)	Power (W/kg)	Holdup	θ_{80} (s)	Exchange flows ($m^3/s \times 10^3$) F_T	F_B
2.0	0	0.18	0	46.9 (3%)	21.1 (20%)	18.8 (30%)
3.33	0	0.83	0	29.1 (12%)	31.3 (7%)	34.3 (8%)
3.33	0.0066	0.52	0.065	32.7 (6%)	26.4 (12%)	25.4 (16%)
3.33	0.0183 (F)	0.36	0.106	21.9 (10%)	26.8 (17%)	21.8 (8%)
3.33	0.0269 (F)	0.37	0.115	20.8 (10%)	36.7 (16%)	20.9 (12%)
4.33	0	1.81	0	23.5 (6%)	40.2 (7%)	44.2 (8%)
4.33	0.0066	1.04	0.076	29.8 (10%)	34.7 (8%)	26.2 (6%)

Table 5.1 (continued)

N (rps)	Q (m^3/s)	Power (W/kg)	Holdup	θ_{80} (s)	Exchange flows ($m^3/s \times 10^3$) F_T	F_B
4.33	0.0183	0.71	0.141	29.9 (11%)	32.4 (10%)	34.3 (13%)
4.33	0.0269	0.64	0.161	33.9 (12%)	30.6 (6%)	33.1 (21%)
4.83	0	-	0	19.8 (10%)	43.4 (6%)	-
4.83	0.0269	-	0.171[E]	23.9 (11%)	36.0 (7%)	25.4 (9%)
5.33	0	3.38	0	21.1 (13%)	45.3 (10%)	51.9 (6%)

E : Estimated from holdup correlation.

Table 5.2: Liquid mixing data, RT+2×LE20 combination, T = 0.95 m.

(Liquid mixing model shown in figure 5.2)

N (rps)	Q (m^3/s)	Power (W/kg)	Holdup	θ_{80} (s)	Exchange flows ($m^3/s \times 10^3$) F_T	F_B
1.0	0	0.02	0	42.6 (8%)	19.9 (0%)	23.9 (15%)
2.0	0	0.13	0	25.1 (6%)	32.6 (20%)	54.0 (17%)
3.33	0	0.94	0	17.0 (5%)	77.4 (20%)	94.5 (18%)
3.33	0.0066	0.51	0.066	31.3 (11%)	43.7 (15%)	30.5 (8%)
3.33	0.0183 (F)	0.47	0.105^E	34.4 (13%)	40.2 (16%)	20.6 (16%)
3.33	0.0269 (F)	-	0.122^E	32.4 (4%)	38.3 (9%)	22.5 (12%)
4.33	0	2.06	0	13.5 (23%)	81.5 (12%)	81.0 (17%)

Table 5.2 (continued)

N (rps)	Q (m^3/s)	Power (W/kg)	Holdup	θ_{80} (s)	Exchange flows ($m^3/s \times 10^3$) F_T	F_B
4.33	0.0066	1.08	0.075	22.6 (7%)	54.6 (13%)	-
4.33	0.0183	0.93	0.129	24.7 (22%)	60.1 (32%)	36.9 (25%)
4.33	0.0269	0.90	0.139	28.8 (5%)	47.0 (9%)	47.3 (24%)
4.83	0	2.85	0	11.0 (15%)	99.5 (8%)	140.0 (18%)
4.83	0.0066	1.44	0.080	22.0 (7%)	67.2 (10%)	65.8 (16%)
4.83	0.0183	1.01	0.134	23.3 (7%)	50.0 (17%)	57.2 (13%)
4.83	0.0269	1.17	0.157	20.5 (22%)	51.6 (22%)	52.3 (21%)

E : Estimated from holdup correlation.

Table 5.3 : Unaerated exchange flows correlated versus impeller speed

$$F = a\,(N)^b$$

	a	b	Correlation coefficient (r^2)	F ratio	95% confidence limits on b	Number of data points
F_t						
3RT	0.012	0.80	0.908	103	± 0.160	24
1RT+2LE20	0.019	1.05	0.947	254	± 0.134	31
F_b						
3RT	0.009	1.05	0.935	132	± 0.184	21
1RT+2LE20	0.025	1.00	0.850	62	± 0.225	26

Table 5.4: Unaerated exchange flows correlated versus power input

$$F = a\,(\,\varepsilon_m\,)^b$$

	a	b	Correlation coefficient (r^2)	F ratio	95% confidence limits on b	Number of data points
F_t						
3RT	0.033	0.27	0.908	103	± 0.054	24
1RT+2LE20	0.069	0.32	0.957	314	± 0.037	31
F_b						
3RT	0.035	0.35	0.935	132	± 0.062	21
1RT+2LE20	0.088	0.30	0.847	61	± 0.069	26

Table 5.5: Effect of tracer addition point on ungassed liquid mixing time. (T = 0.61 m, 3RT combination)

N (rps)	Tracer addition point (Refer to figure 5.15)	θ (s)
2.67	Liquid surface (cell 1)	77
2.67	Below middle impeller (cell 4)	53
2.67	Outflow from middle impeller (boundary of cells 3 and 4)	20
4.33	Liquid surface (cell 1)	43
4.33	Below middle impeller (cell 4)	19
4.33	Outflow from middle impeller (boundary of cells 3 and 4)	16

Table 5.6: Effect of tracer addition point on liquid mixing time and exchange flows. (T = 0.61 m, 3DT combination)

(Liquid mixing model shown in figure 5.15)

N (rps)	Q (m^3/s)	Tracer addition point (Refer to figure 5.15)	θ (s)	Exchange flows ($m^3/s \times 10^3$) F_1	F_2	F_3	F_4	F_5
3.33	0	Liquid surface (cell 1)	30.1 (8%)	20 (8%)	14 (14%)	35 (17%)	10 (0%)	32 (8%)
3.33	0	Below middle impeller (cell 4)	12.9 (10 %)	28 (43%)	9 (59%)	41 (9%)	8 (43%)	38 (15%)

Table 5.7: Liquid mixing data, 3RT combination, T = 0.61 m.

(Liquid mixing model shown in figure 5.15)

N (rps)	Q (m^3/s)	Power (W/kg)	Holdup	θ_{80} (s)	Exchange flows ($m^3/s \times 10^3$)				
					F_1	F_2	F_3	F_4	F_5
3.33	0	0.352	0	30.1 (8%)	28^B (8%)	14^B (14%)	35 (17%)	10^B (0%)	32 (8%)
3.33	1.67E-3	0.271	0.032	40.8 (6%)	∞	11^B (14%)	19^B (12%)	11^B (4%)	59 (10%)
3.33	5.00E-3 (F)	0.198	0.060	27.5 (13%)	12^B (27%)	19^B (26%)	25^B (27%)	24^B (22%)	59 (20%)
4.33	0	0.761	0	27.7 (4%)	18^B (24%)	15^B (10%)	55 (24%)	15^B (8%)	∞
4.33	3.33E-3	0.483	0.064	32.9 (5%)	31 (23%)	18^B (14%)	20^B (21%)	16^B (19%)	∞
4.33	6.67E-3	0.370	0.094	33.1 (2%)	26 (26%)	15^B (24%)	24^B (52%)	21^B (26%)	45 (23%)
5.33	0	1.397	0	22.1 (5%)	-	20^B (24%)	41 (16%)	19^B (4%)	∞

Table 5.7 (continued)

N (rps)	Q (m^3/s)	Power (W/kg)	Holdup	θ_{80} (s)	Exchange flows ($m^3/s \times 10^3$) F_1	F_2	F_3	F_4	F_5
5.33	1.67E-3	0.982	0.048	30.0 (6%)	34 (15%)	12^B (5%)	31 (20%)	16^B (12%)	∞
5.33	5.00E-3	0.715	0.099	25.1 (10%)	-	30 (35%)	23^B (27%)	15^B (13%)	∞ (26%)

(F): Lowest impeller flooded
B : Major boundary to mixing, see section 5.3

Table 5.8: Liquid mixing data, 1RT+2×LE20 combination, T = 0.61 m.

(Liquid mixing model shown in figure 5.15)

N (rps)	Q (m^3/s)	Power (W/kg)	Holdup	θ (s)	Exchange flows ($m^3/s \times 10^3$) F_1	F_2	F_3	F_4	F_5
3.33	0	0.330	0	13.0 (18%)	-	49 (17%)	38 (27%)	45 (10%)	∞
3.33	1.67E-3	0.260	0.032	24.9 (7%)	-	24[B] (3%)	15[B] (15%)	43 (1%)	∞
3.33	5.00E-3 (F)	0.230	0.068	24.1 (10%)	-	29 (20%)	21[B] (26%)	22[B] (24%)	∞
4.33	0	0.710	0	9.7 (7%)	-	∞	∞	54 (11%)	∞
4.33	3.33E-3	0.370	0.057	26.9 (5%)	-	42 (25%)	18[B] (9%)	21[B] (7%)	49 (17%)
5.33	0	1.270	0	9.4 (23%)	-	59 (22%)	∞	∞	∞

(F): Lowest impeller flooded
B : Major boundary to mixing, see section 5.3

Table 5.9 : Effect of scale on liquid mixing times

$$\theta_{80\%} = a\,(\,\varepsilon_m\,)^b\,(\,T\,)^c$$

	a	b	c	R^2	F ratio	Confidence limits on b (95%)	Confidence limit on c (95%)	Number of data points
3RT (all data)	28.5	-0.30	0.25	0.952	139	± 0.04	± 0.15	15
1RT+2LE20 (ungassed)	16.5	-0.26	1.10	0.983	461	± 0.04	± 0.30	8
1RT+2LE20 (gassed)	25.2	-0.34	0.77	0.467	36.7	± 0.29	± 0.87	9

Table 6.1: Mass transfer coefficients for the 3RT combination

Position	V_{sg} *(m/s)*	ε_m *(W/kg)*	k_La *(simple model)*	k_La *(exchange model)*
top		0.79	0.0683	0.0518
middle		1.23	0.0587	0.0729
bottom	0.0093	1.16	0.0525	0.0543
top		2.27	0.0694	0.0457
middle		3.52	0.0580	0.0559
bottom	0.0093	4.03	0.0629	0.0953
top		3.06	0.0737	0.0499
middle		4.75	0.0595	0.0554
bottom	0.0093	5.68	0.0610	0.0985
top		0.33	0.0780	0.0780
middle		0.37	0.0541	0.0722
bottom	0.0186	0.48	0.0520	0.0364 (F)
top		0.69	0.0840	0.0682
middle		0.96	0.0746	0.0869
bottom	0.0186	1.69	0.0705	0.0746
top		1.19	0.0994	0.0789
middle		1.86	0.0870	0.1043
bottom	0.0186	1.94	0.0743	0.0814
top		1.75	0.0968	0.0746
middle		2.82	0.0856	0.0931
bottom	0.0186	3.21	0.0906	0.1210

Table 6.1 (continued)

top		2.28	0.1021	0.0768
middle		3.73	0.0893	0.0947
bottom	0.0186	4.43	0.0976	0.1352
top		0.50	0.0989	0.0905
middle		0.84	0.0789	0.0715
bottom	0.0258	0.92	0.0962	0.1194
top		1.02	0.1054	0.0841
middle		1.54	0.0998	0.1027
bottom	0.0258	1.84	0.1238	0.1658
top		1.59	0.1042	0.0762
middle		2.73	0.1058	0.0905
bottom	0.0258	3.13	0.1370	0.2216
top		1.97	0.0970	0.0661
middle		3.35	0.1153	0.1035
bottom	0.0258	4.18	0.1423	0.2381
top		0.50	0.1133	0.1005
middle		0.78	0.0914	0.0985
bottom	0.0306	0.86	0.1253	0.1363
top		0.28	0.0835	0.0814
middle		0.41	0.0966	0.1235
bottom	0.0306	0.44	0.0688	0.0513 **(F)**
top		1.24	0.1152	0.0934
middle		2.17	0.1029	0.0572
bottom	0.0306	3.06	0.1759	0.2916

Table 6.1 (continued)

top		1.64	0.1306	0.1009
middle		3.13	0.1247	0.0797
bottom	0.0306	4.20	0.2092	0.3611
top		0.43	0.1173	0.1072
middle		0.72	0.1072	0.1196
bottom	0.0379	0.92	0.1226	0.1272
top		0.43	0.1051	0.0979
middle		0.72	0.0934	0.0941
bottom	0.0379	0.92	0.1074	0.1123
top		0.73	0.1182	0.1009
middle		1.25	0.1204	0.1270
bottom	0.0379	1.59	0.1340	0.1695
top		1.19	0.1199	0.1070
middle		2.19	0.1067	0.1201
bottom	0.0379	2.92	0.1220	0.1328
top		1.64	0.1136	0.0891
middle		2.74	0.1307	0.1206
bottom	0.0379	4.10	0.1705	0.2594
top		0.73	0.1252	0.1074
middle		1.20	0.1552	0.1572
bottom	0.0451	1.49	0.1489	0.1953
top		1.05	0.1391	0.1163
middle		2.00	0.1512	0.1295
bottom	0.0451	3.16	0.2114	0.3290

Table 6.2: Mass transfer coefficients for the RT+2×LE20 combination

Position	V_{sg} *(m/s)*	ε_m *(W/kg)*	k_La *(simple model)*	k_La *(exchange model)*
top		0.46	0.0477	0.0209
middle		0.58	0.0369	0.0511
bottom	0.0093	0.49	0.0391	0.0447
top		0.94	0.0562	0.0242
middle		1.16	0.0510	0.0519
bottom	0.0093	1.17	0.0636	0.1114
top		1.08	0.0570	0.0212
middle		1.32	0.0514	0.0621
bottom	0.0093	1.13	0.0558	0.1070
top		0.45	0.0594	0.1031
middle		0.55	0.0586	0.1173
bottom	0.0183	0.46	0.0403	0.0231 **(F)**
top		1.06	0.1117	0.0885
middle		1.47	0.0725	0.0637
bottom	0.0186	1.37	0.0915	0.1579
top		0.44	0.0871	0.0817
middle		0.55	0.0621	0.0817
bottom	0.0258	0.47	0.0650	0.0601 **(F)**
top		0.80	0.0750	0.0494
middle		1.10	0.0663	0.0877
bottom	0.0258	0.92	0.0830	0.1005

Table 6.2 (continued)

top		0.84	0.0690	0.0443
middle		1.20	0.0779	0.0871
bottom	0.0258	1.06	0.0948	0.1388
top		0.76	0.1181	0.1059
middle		1.09	0.0640	0.0745
bottom	0.0306	0.90	0.0900	0.1174
top		0.98	0.0843	0.0459
middle		1.43	0.0947	0.1439
bottom	0.0306	1.21	0.1114	0.1361
top		0.79	0.0984	0.0803
middle		1.05	0.0900	0.1413
bottom	0.0379	0.89	0.0986	0.0939
top		0.75	0.1113	0.0993
middle		1.08	0.0814	0.0897
bottom	0.0451	0.93	0.1352	0.1578
top		0.74	0.1276	0.1097
middle		1.10	0.1135	0.1319
bottom	0.0451	0.94	0.1182	0.1388

Table 7.1: Vessel scales considered for economic analysis

Scale	Pilot	Small	Medium	Large*
Vessel diameter (m)	0.61	1.6	3.0	3.8
Liquid depth (m)	1.15	3.1	5.8	7.3
Liquid volume (m^3)	0.30	6.0	39	80
Impeller speed (rpm)	200+	105+	70+	60

*: Large scale vessel dimensions and impeller speed taken from Manfredini and Cavallera (1983).

+: Impeller speed scaled down from large scale vessel assuming equal power per unit volume.

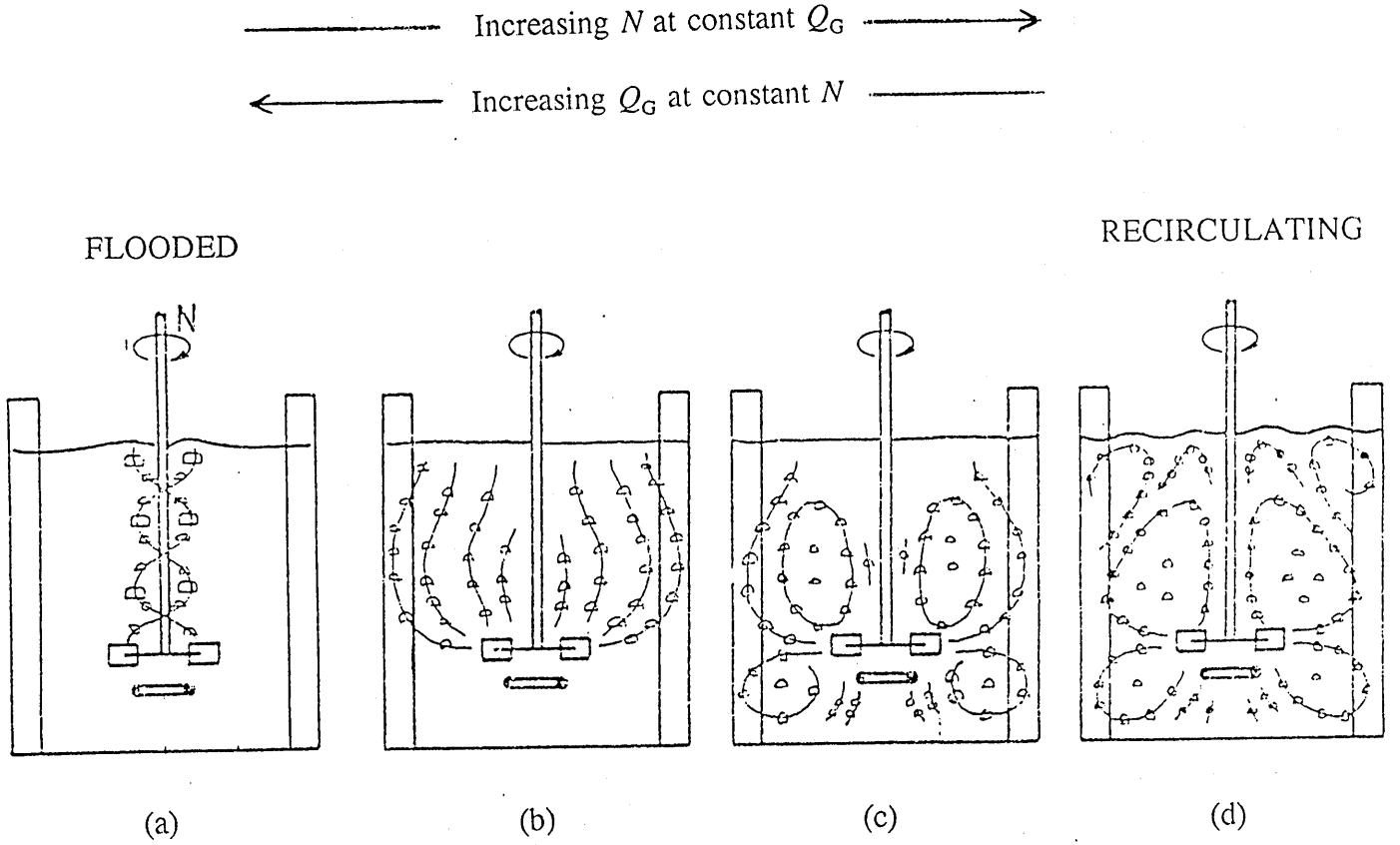


Figure 1.1: Gas liquid flow patterns for a single Rushton turbine, Nienow et al (1977).

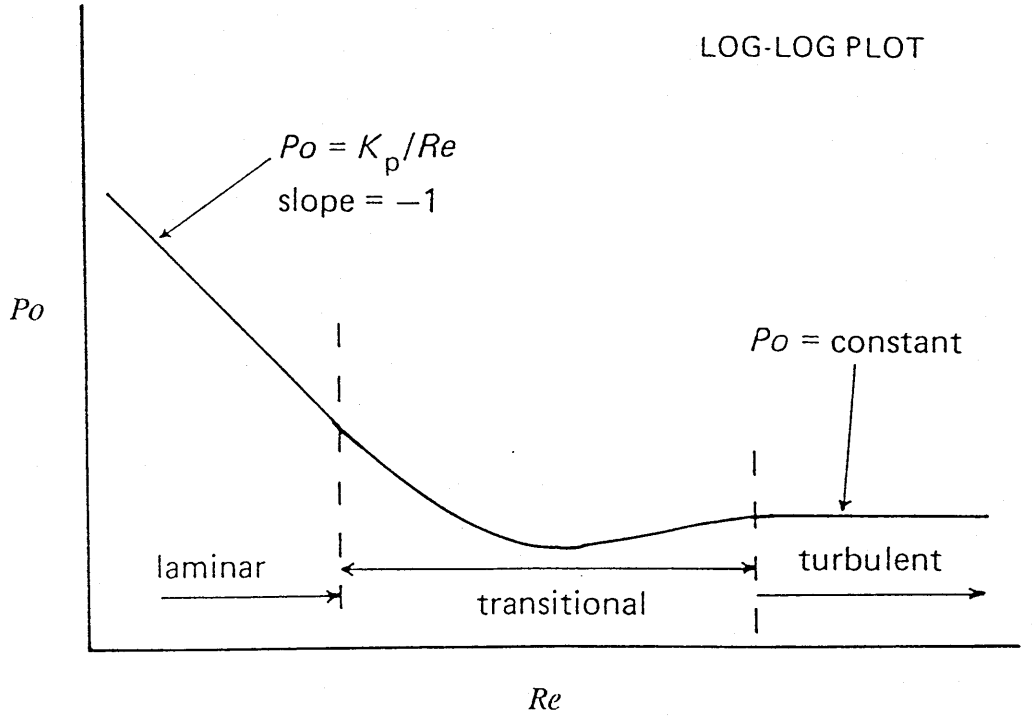
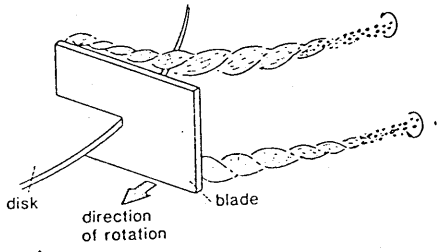
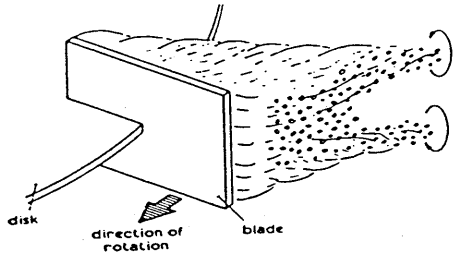


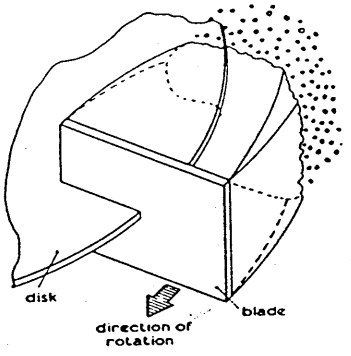
Figure 1.2: Effect of Reynolds number on Rushton turbine ungassed power number



(a): Vortex cavity

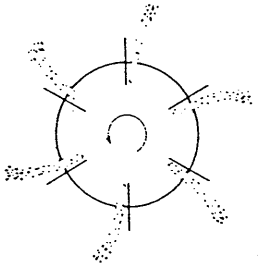


(b): Clinging cavity

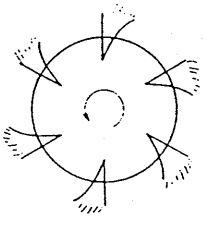


(c): Large cavity

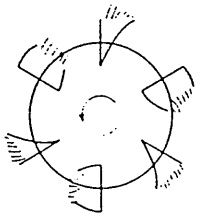
Figure 1.3: Gas cavities observed on the blades of a Rushton turbine, Van't Riet (1975).



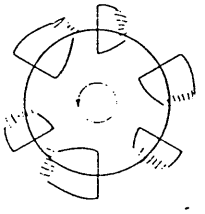
6 vortex cavities



6 clinging cavities



3 clinging and
3 large cavities



6 large cavities of
two different sizes

Figure 1.4: Gas cavity regimes for a six blade Rushton turbine, Warmoeskerken (1986).

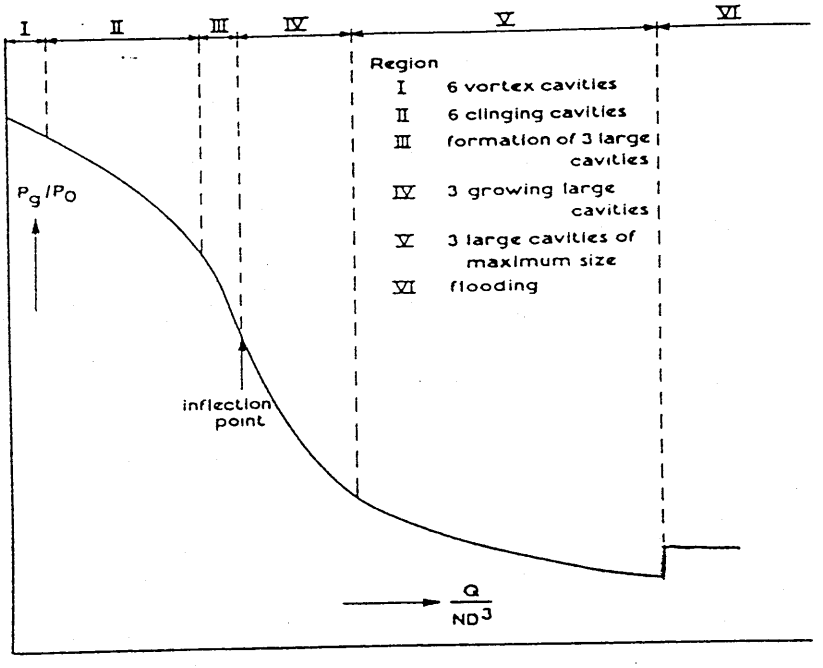


Figure 1.5: Relation between impeller cavity structure and power consumption, Warmoeskerken and Smith (1982).

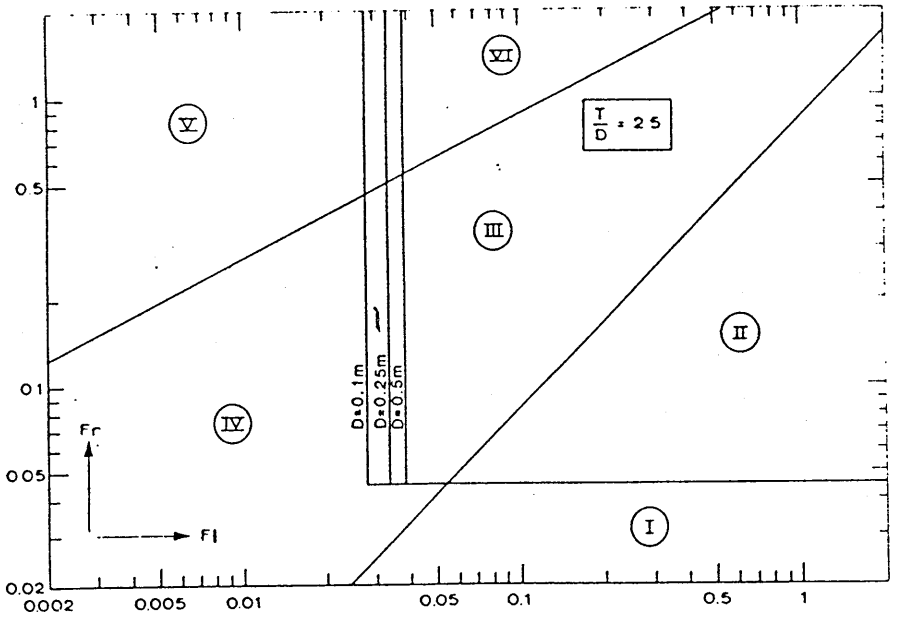


Figure 1.6: Flow map for a standard Rushton turbine in a standard geometry vessel, Smith and Warmoeskerken (1985).

Regimes: I Agitated bubble column
II Flooded
III 3-3 large cavities
IV 3-3 with recirculation
V Vortex cavities with recirculation
VI Vortex cavities without recirculation.

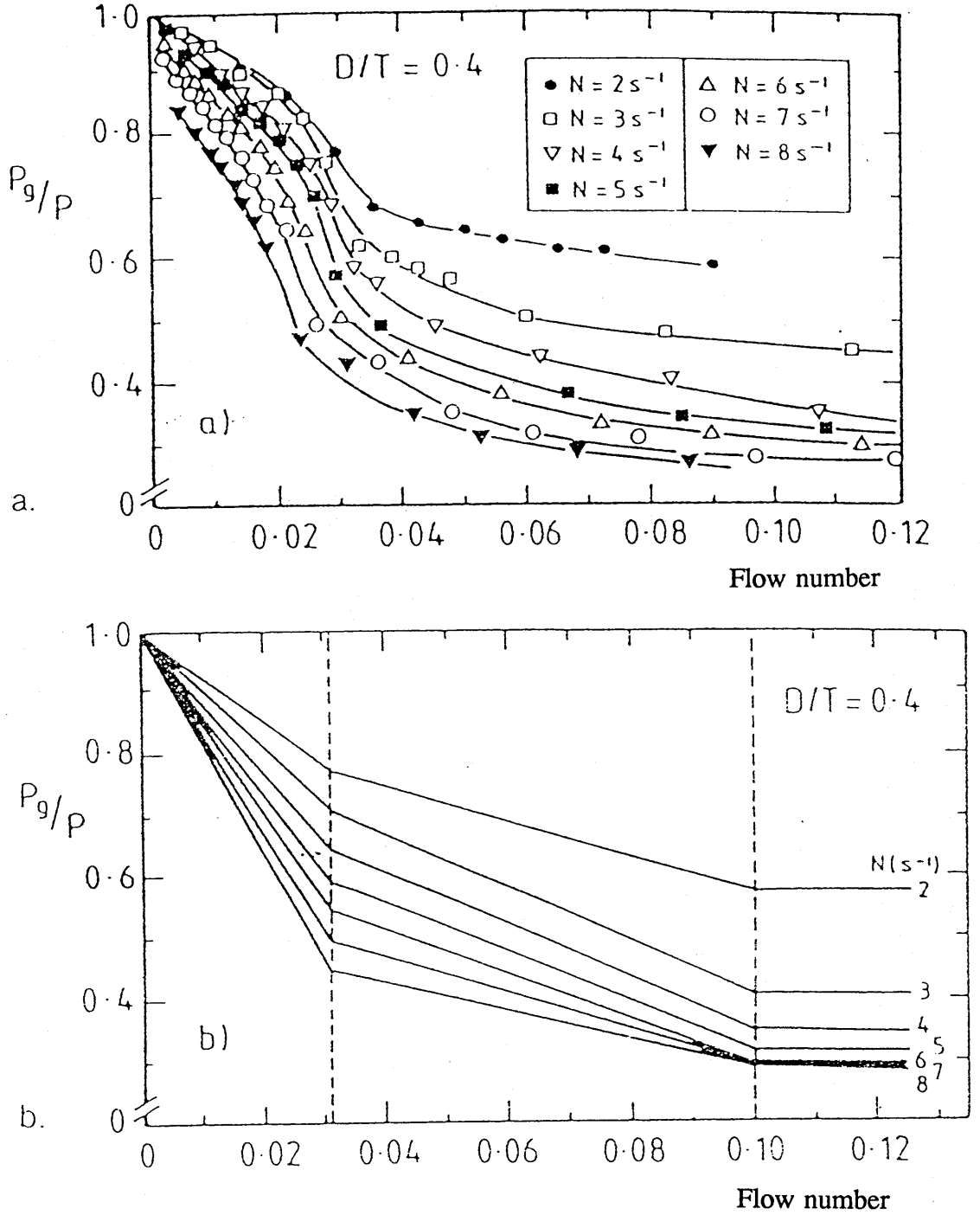
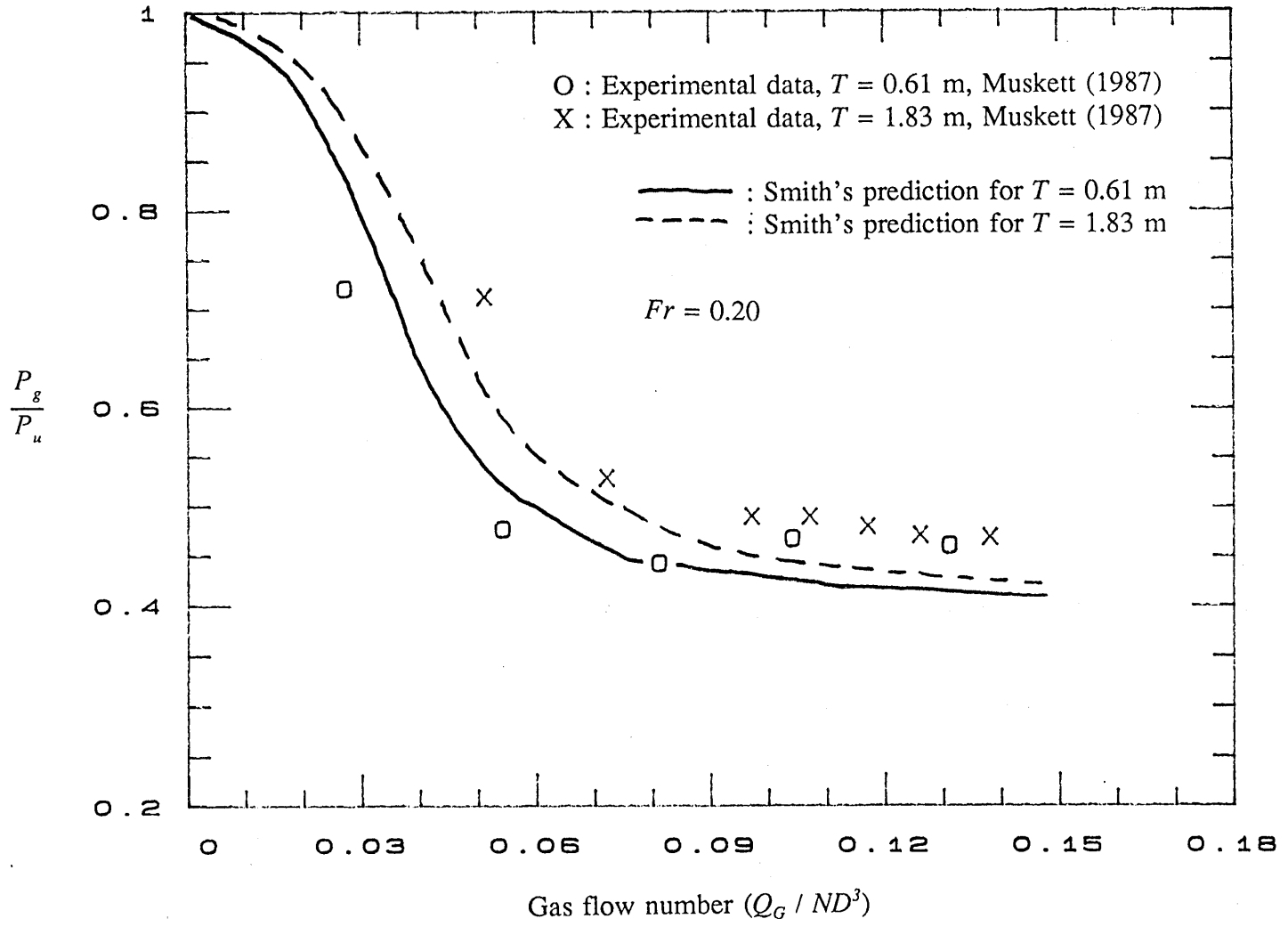


Figure 1.7: Measured gassed power curves for a standard Rushton turbine (T = 0.44 m) and comparison with the straight line approximations of Warmoeskerken (1986).

Figure 1.8: Effect of gas flow rate on the power draw of a Rushton turbine: Comparison of Smith's power predictions with experimental data.



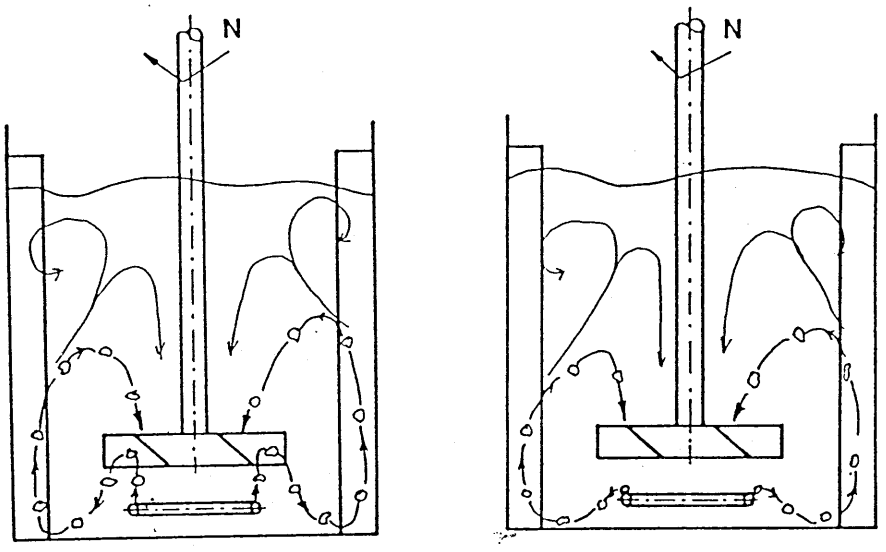


Figure 1.9: Gas loading regimes for a downward pumping impeller, Bujalski (1987).

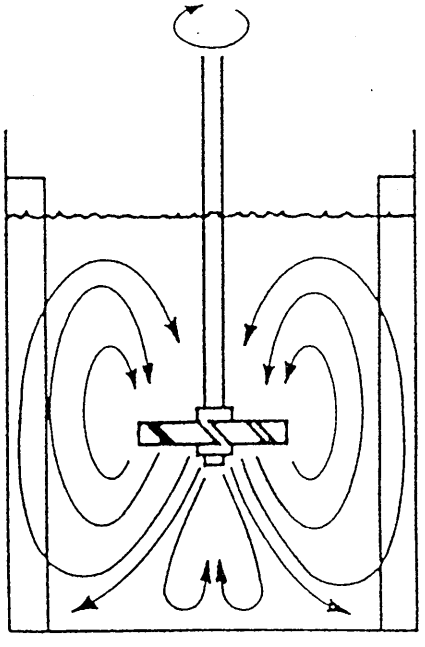
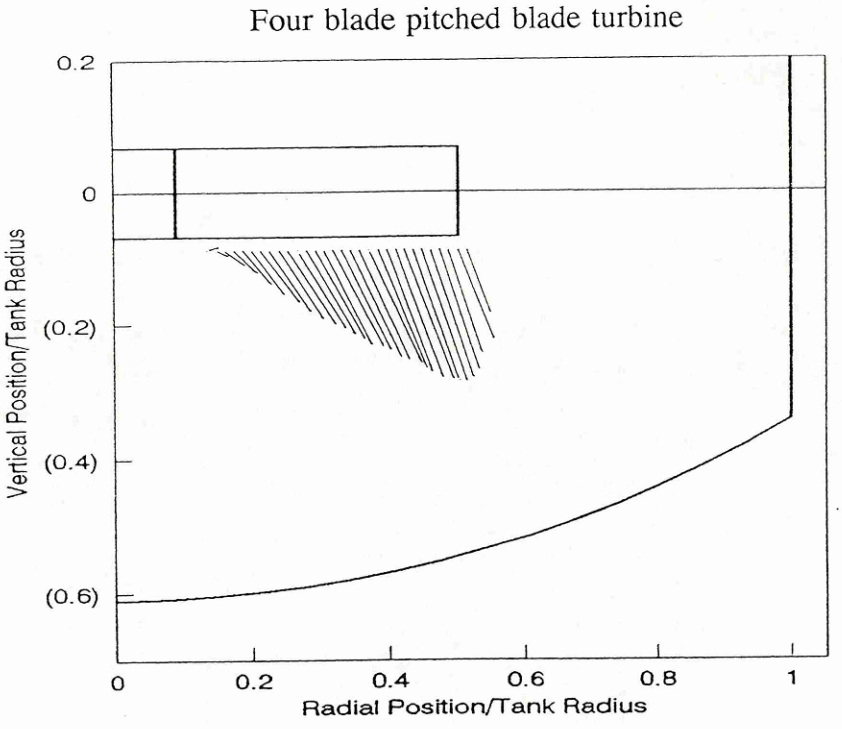


Figure 1.10: Region of upflow observed below a downward pumping impeller, Warmoeskerken et al (1984).



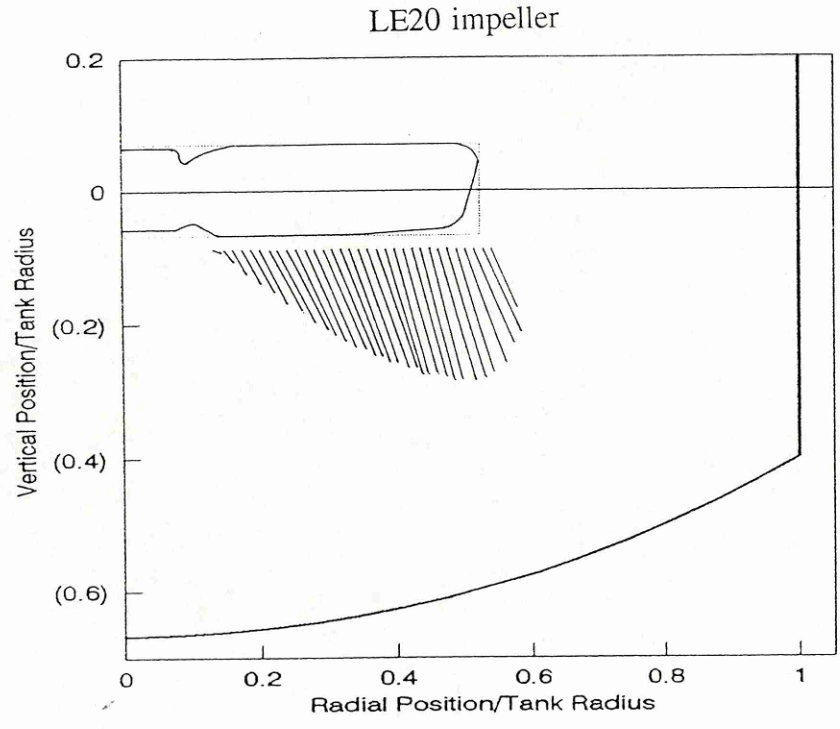


Figure 1.11: Ungassed flow profiles measured by laser doppler anemometry, Musgrove (1991).

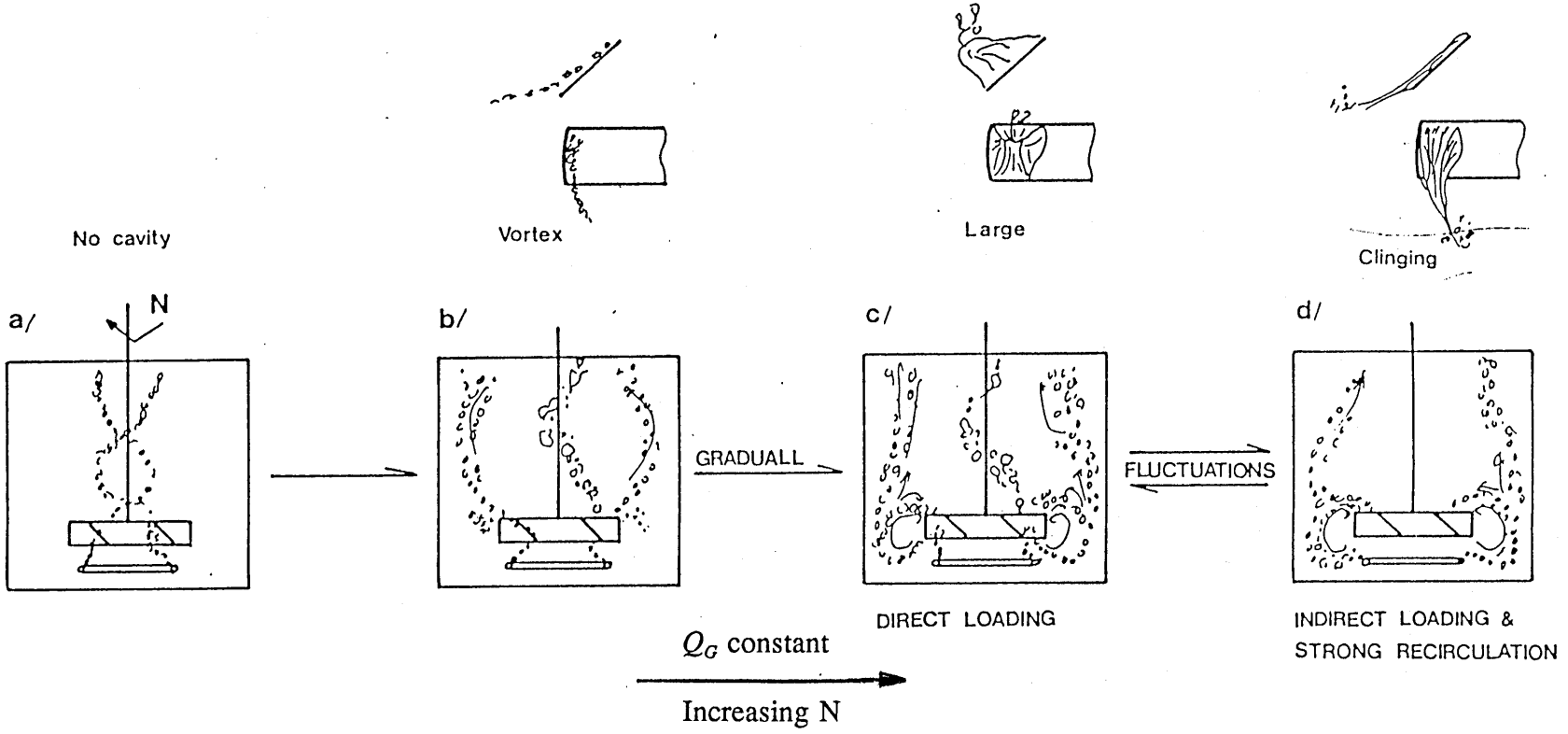


Figure 1.12: Change of flow pattern and gas cavity structure for a downward pumping pitched blade turbine, $D = T/2$, with a large ring sparger, Bujalski (1987).

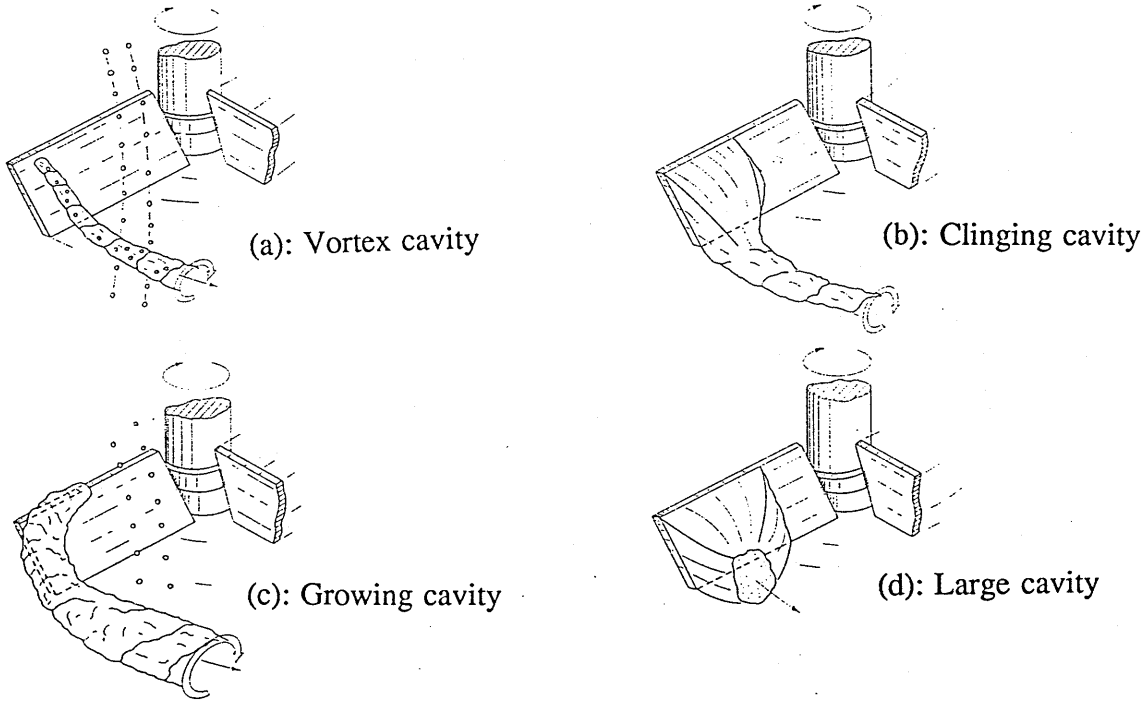


Figure 1.13: Gas cavity structures observed on the blades of downward pumping pitched blade turbines, Warmoeskerken et al (1984).

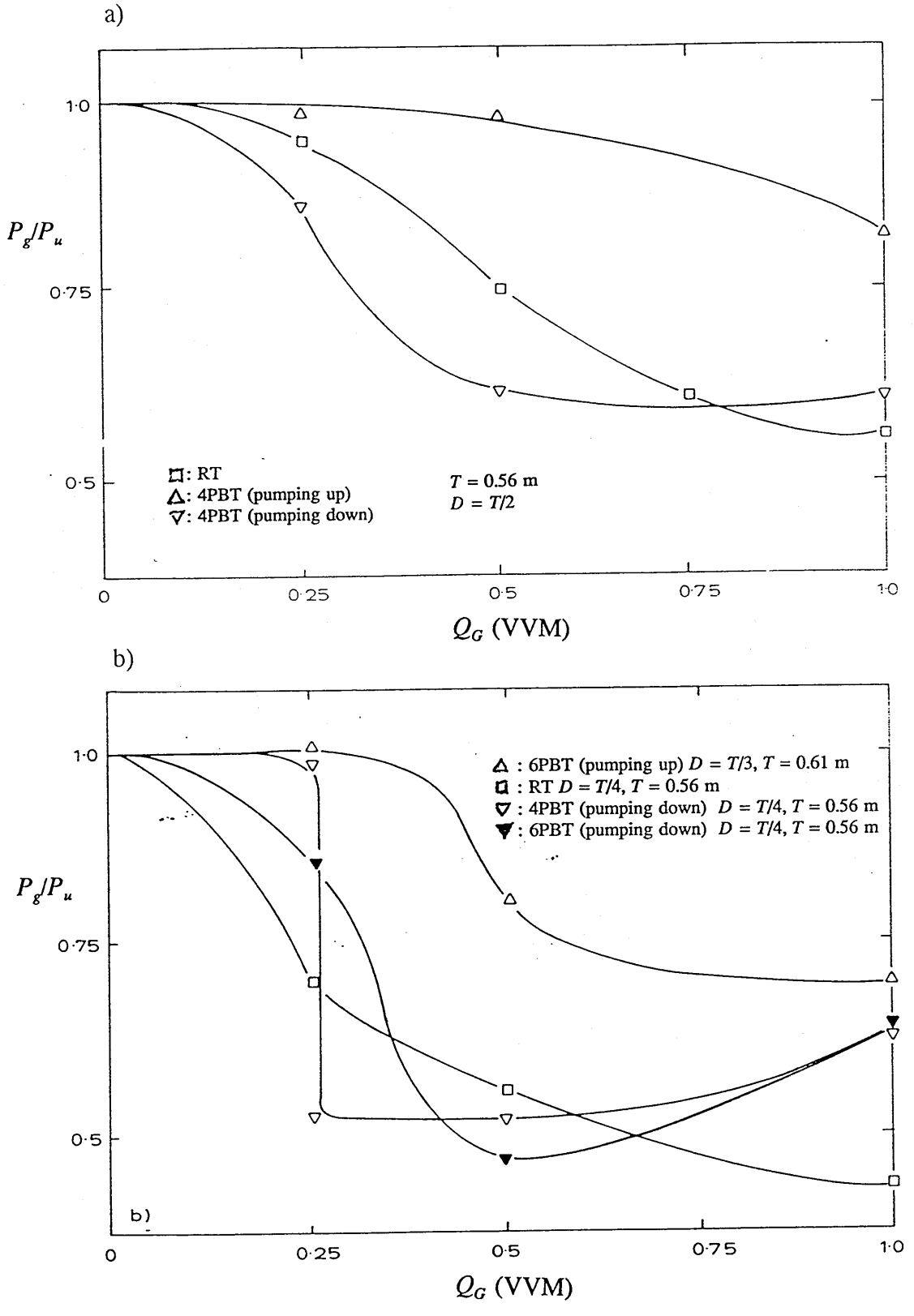
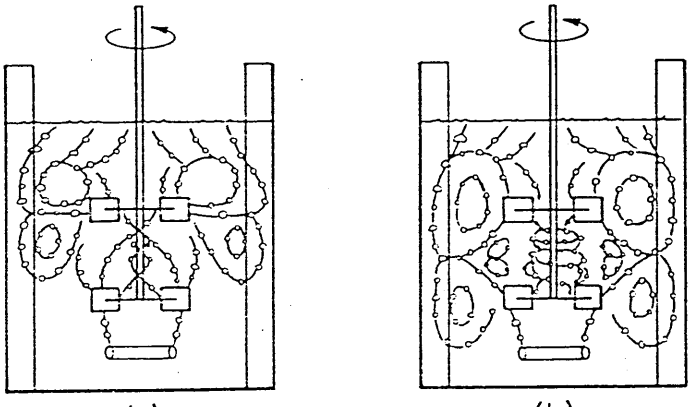


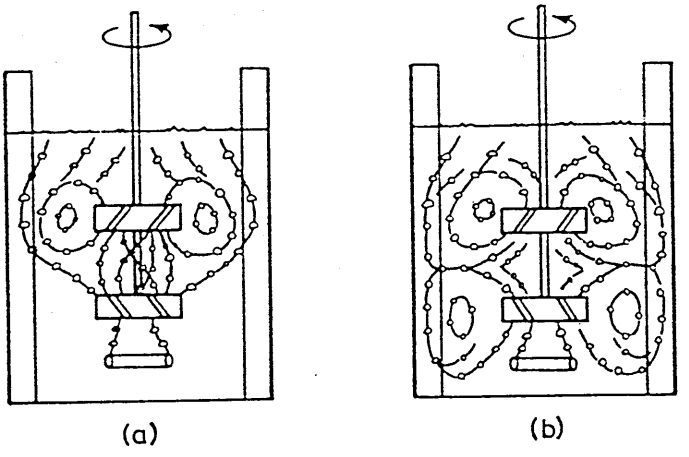
Figure 1.14: Decrease in P_g/P_u with increasing aeration rate, at constant impeller speed, for different impeller designs, Nienow et al (1983).

pumping pitched blade turbine, D - 7/2, with a large ring sparger, Bujalski (1987).

Combination 1: 2 × RT



Combination 2: 4PBT (bottom, pumping up) + 4PBT (top, pumping down)



Combination 6: RT + PBT (top, pumping up)

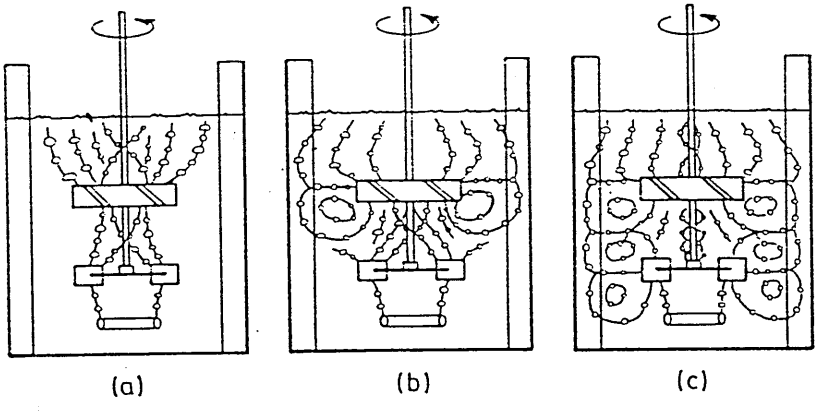


Figure 1.16: Gas liquid flow patterns observed with different dual impeller combinations, Kuboi and Nienow (1982).

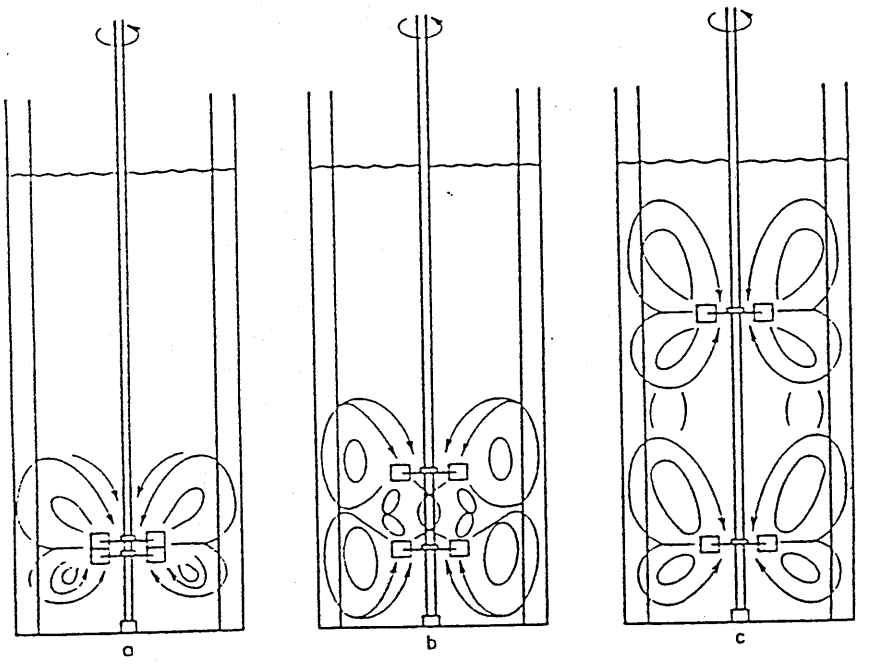
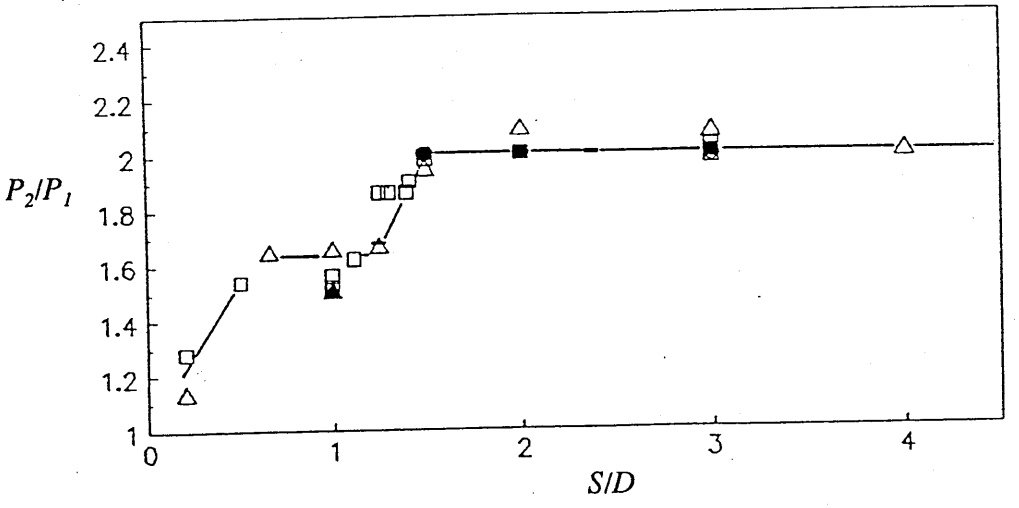
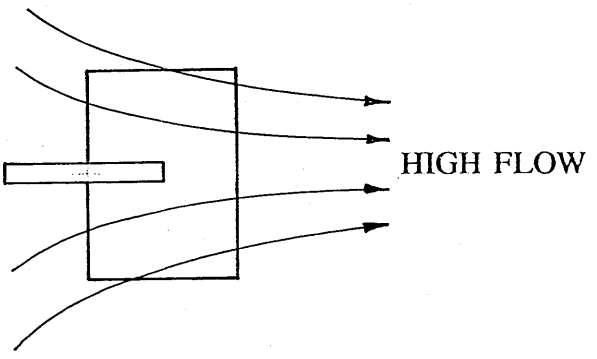


Figure 1.17: Ungassed flow patterns observed with dual Rushton turbines as a function of impeller spacing, Hudcova et al (1987).

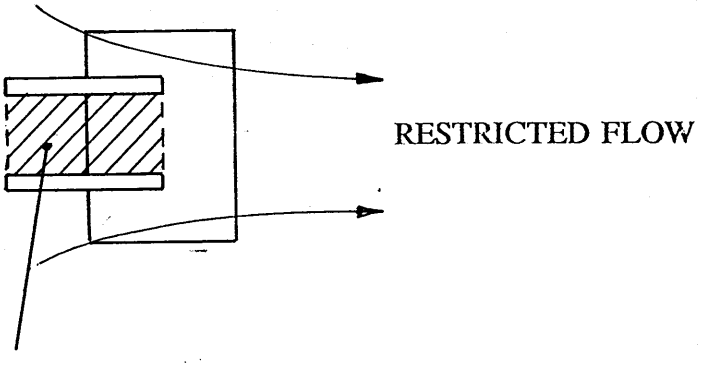


△ : Chiampo et al (1991)
□ : Hudcova et al (1987)
○ : Machon et al (1985)
▲ : Kuboi and Nienow (1982)
● : Abrardi et al (1988)
■ : Roustan (1985)

Figure 1.18: Effect of impeller separation on the ungassed power draw of dual Rushton turbines, Chiampo et al (1991).



a) Single Rushton turbine, W = 0.4D



b) Two touching Rushton turbines, each with W = 0.2D

Figure 1.19: Flow produced by two touching Rushton turbines and comparison with a single Rushton turbine of the same total blade width.

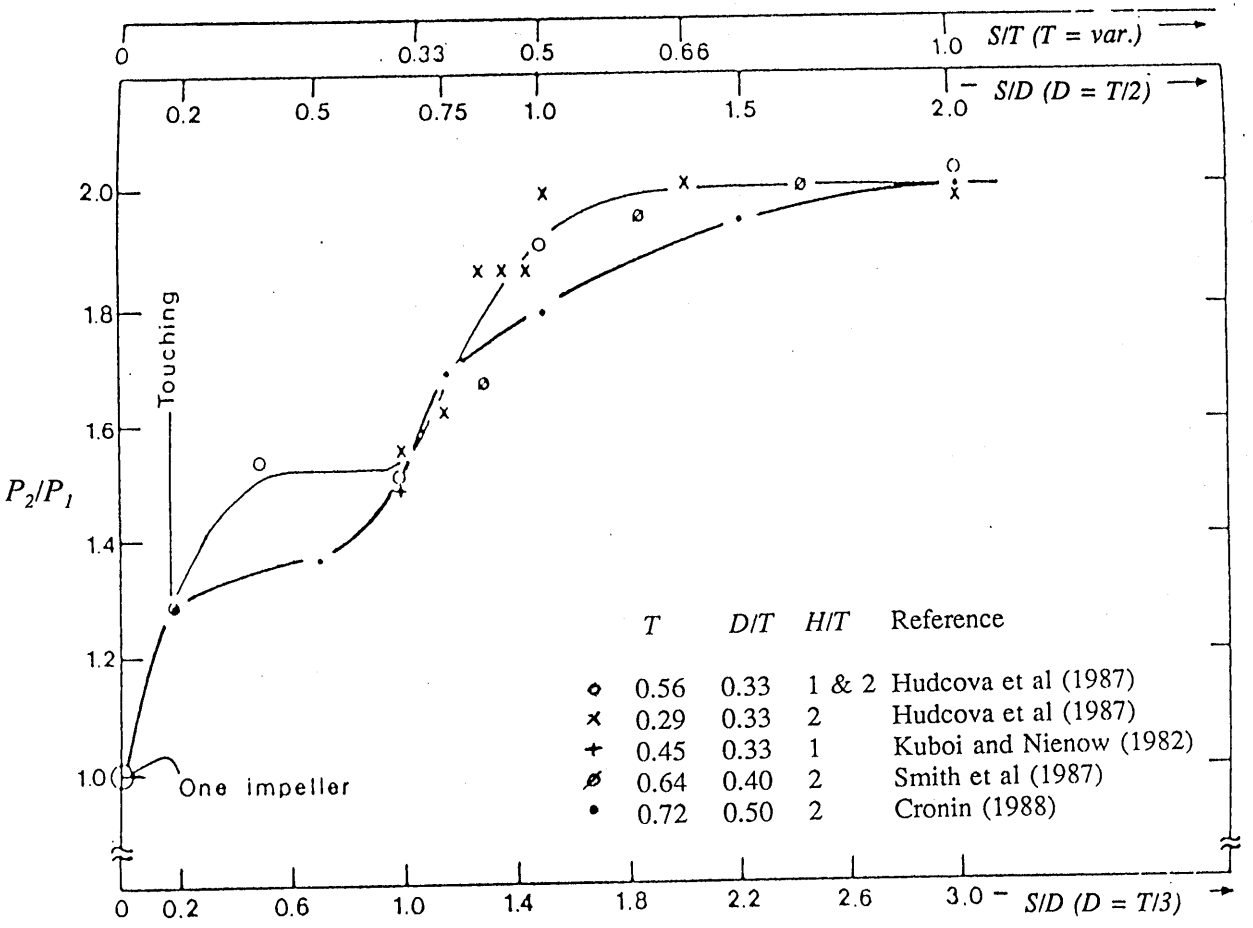


Figure 1.20: Effect of impeller separation on the ungassed power draw of dual Rushton turbines, Cronin (1988).

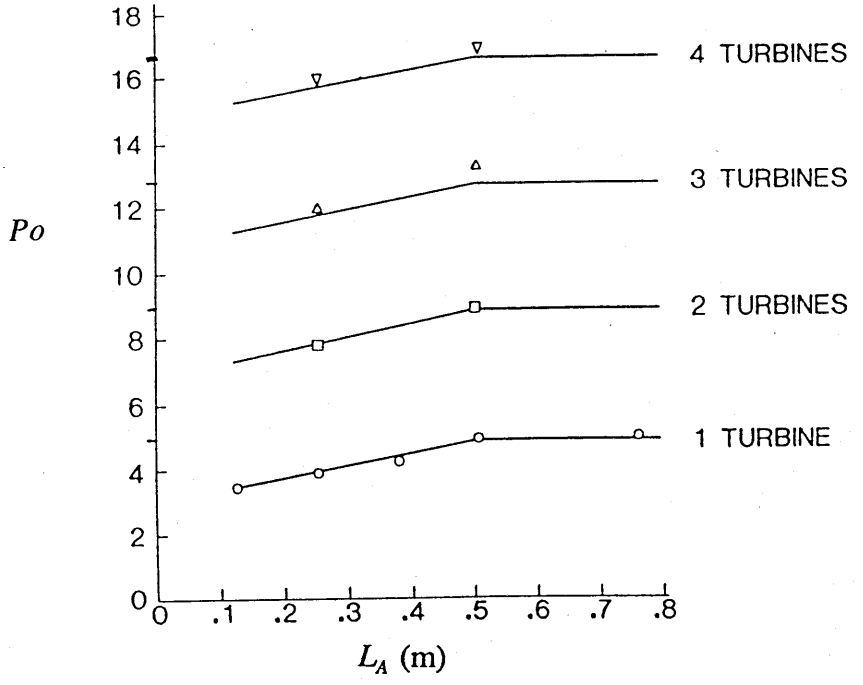


Figure 1.21: Ungassed power number as a function of liquid level above the top turbine for various numbers of turbines, Bader (1987).

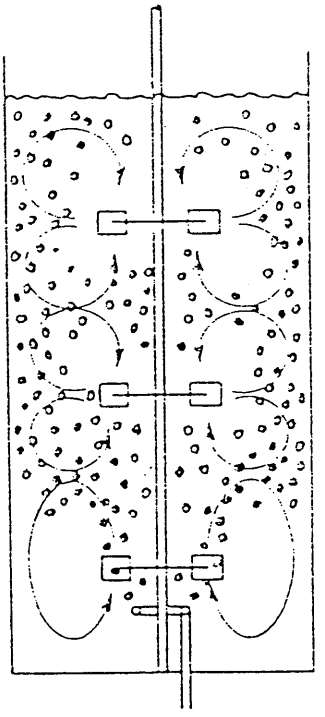


Figure 1.22: Gas liquid flow pattern for triple Rushton turbines, with the lowest impeller flooded, Smith et al (1987).

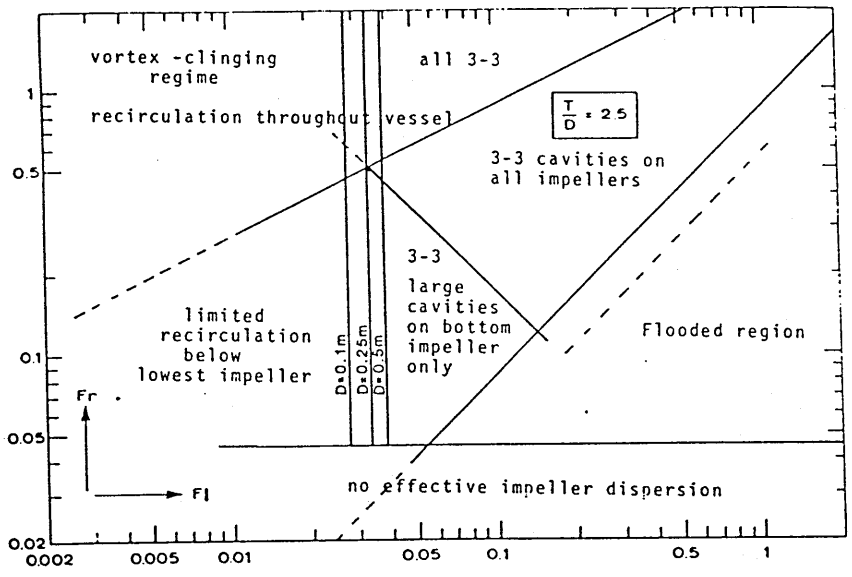


Figure 1.23: Generalised flow map for triple Rushton turbines, Smith et al (1987).

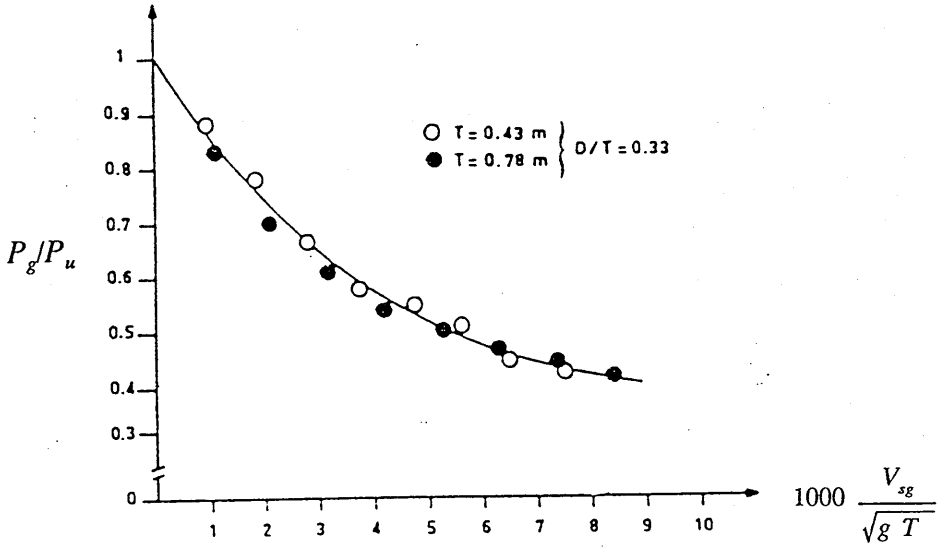


Figure 1.24: Plot of P_g/P_u versus $V_{sg}/\sqrt{gT}$ for dual Rushton turbines ($D = T/3$) at two scales (T = 0.43 and 0.78 m), Roustan (1985).

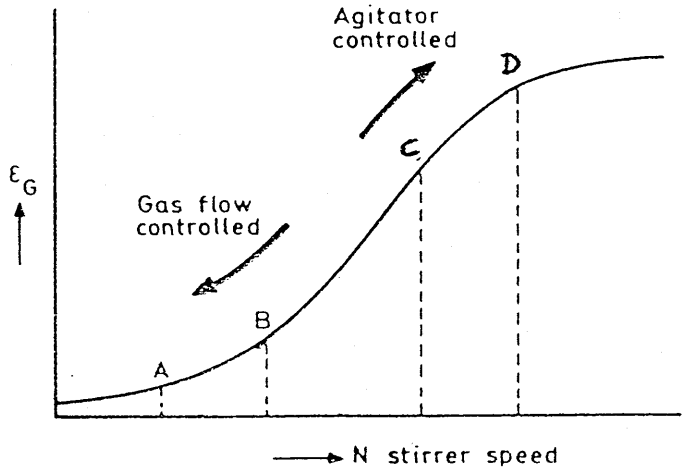


Figure 1.25: Evolution of gas holdup with increasing impeller speed at constant gas flow rate. Single Rushton turbine, $H = T$, Mann (1983).

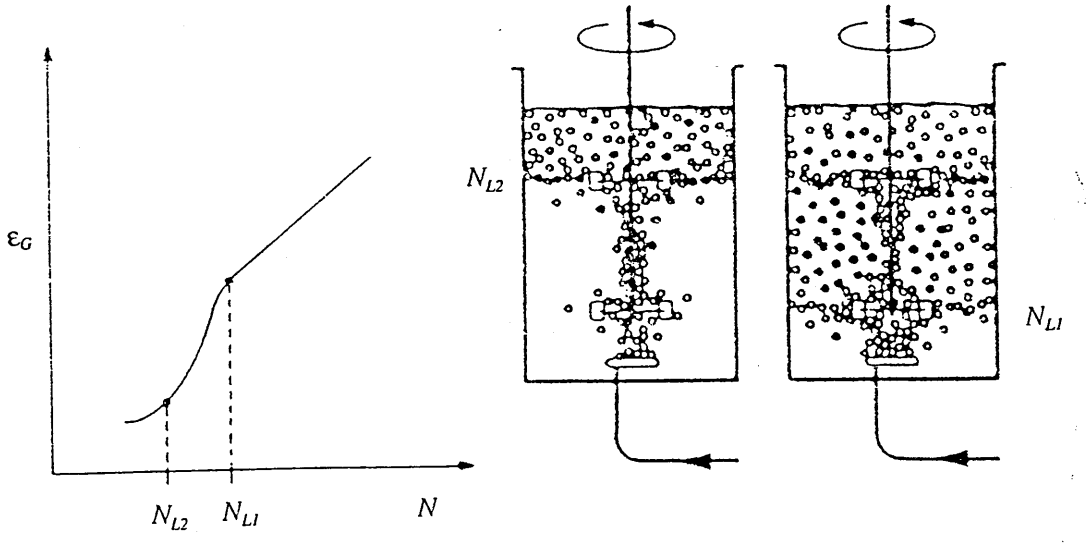


Figure 1.26: Evolution of gas holdup with multiple Rushton turbines, Roustan (1985).

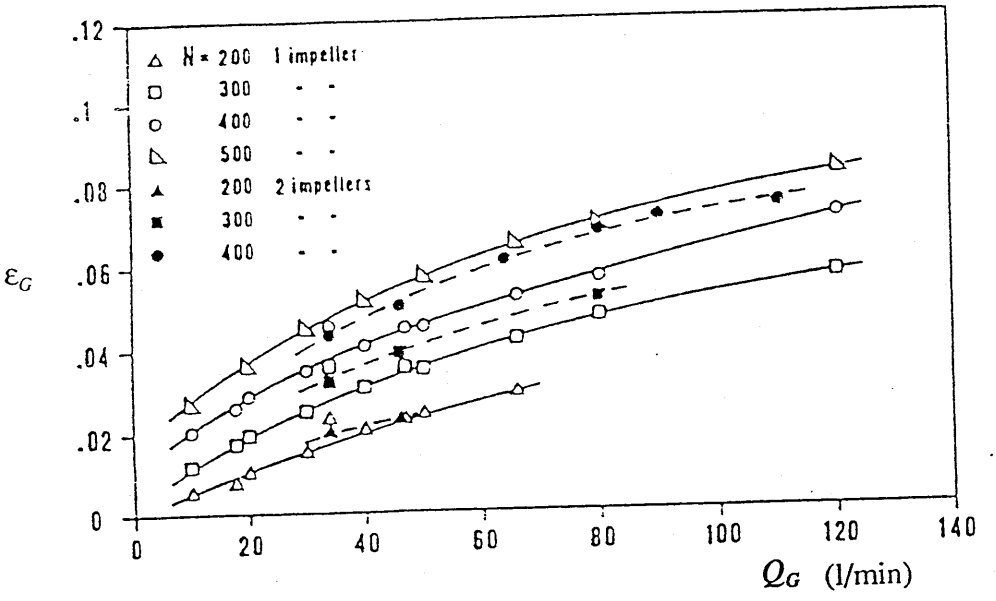


Figure 1.27: Comparison of gas holdup for a single Rushton turbine and dual Rushton turbines (constant impeller speed and gas flow rate), Abrardi et al (1988).

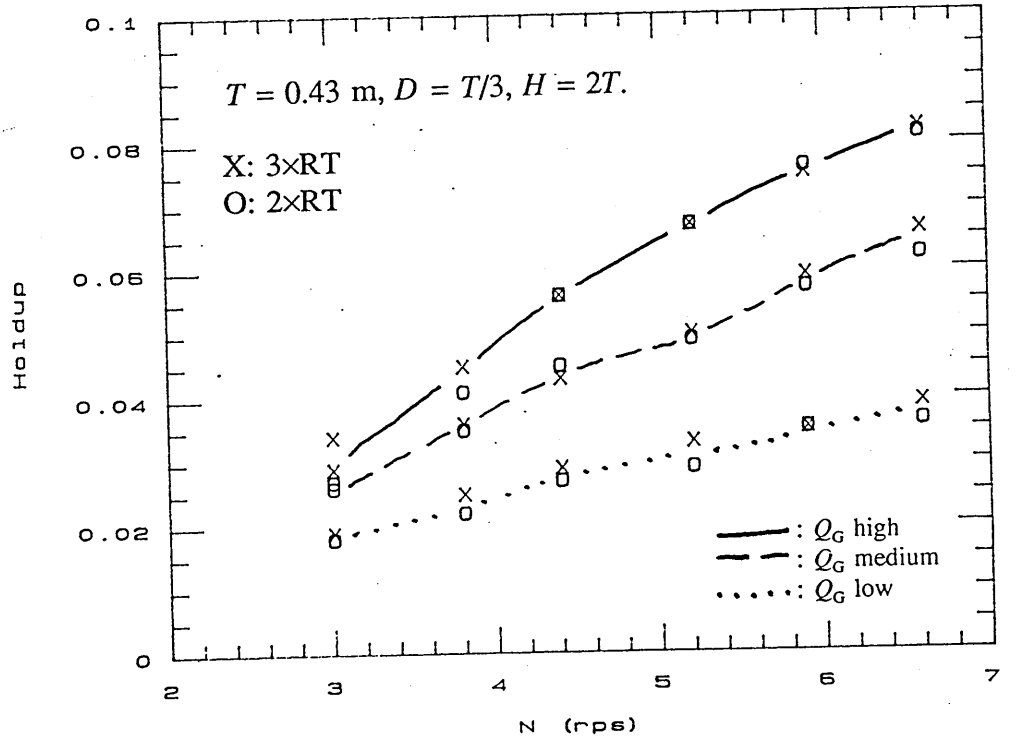


Figure 1.28: Comparison of dual and triple Rushton turbines, Roustan (1985).

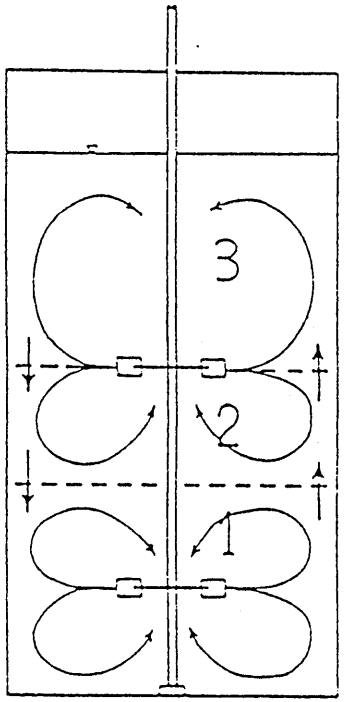


Figure 1.29: Three cell model used to describe liquid mixing for dual Rushton turbines, Manna et al (1991).

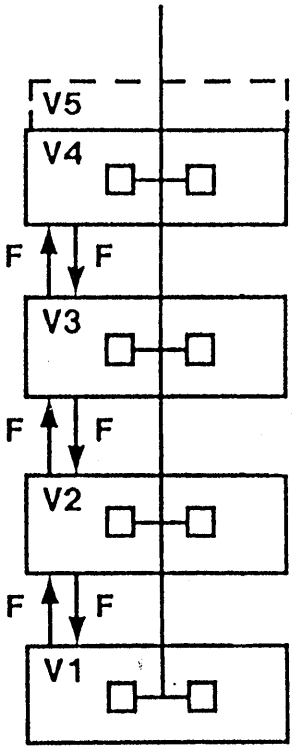


Figure 1.30: Four cell model used to describe liquid mixing for a combination of four Rushton turbines, Bader (1987).

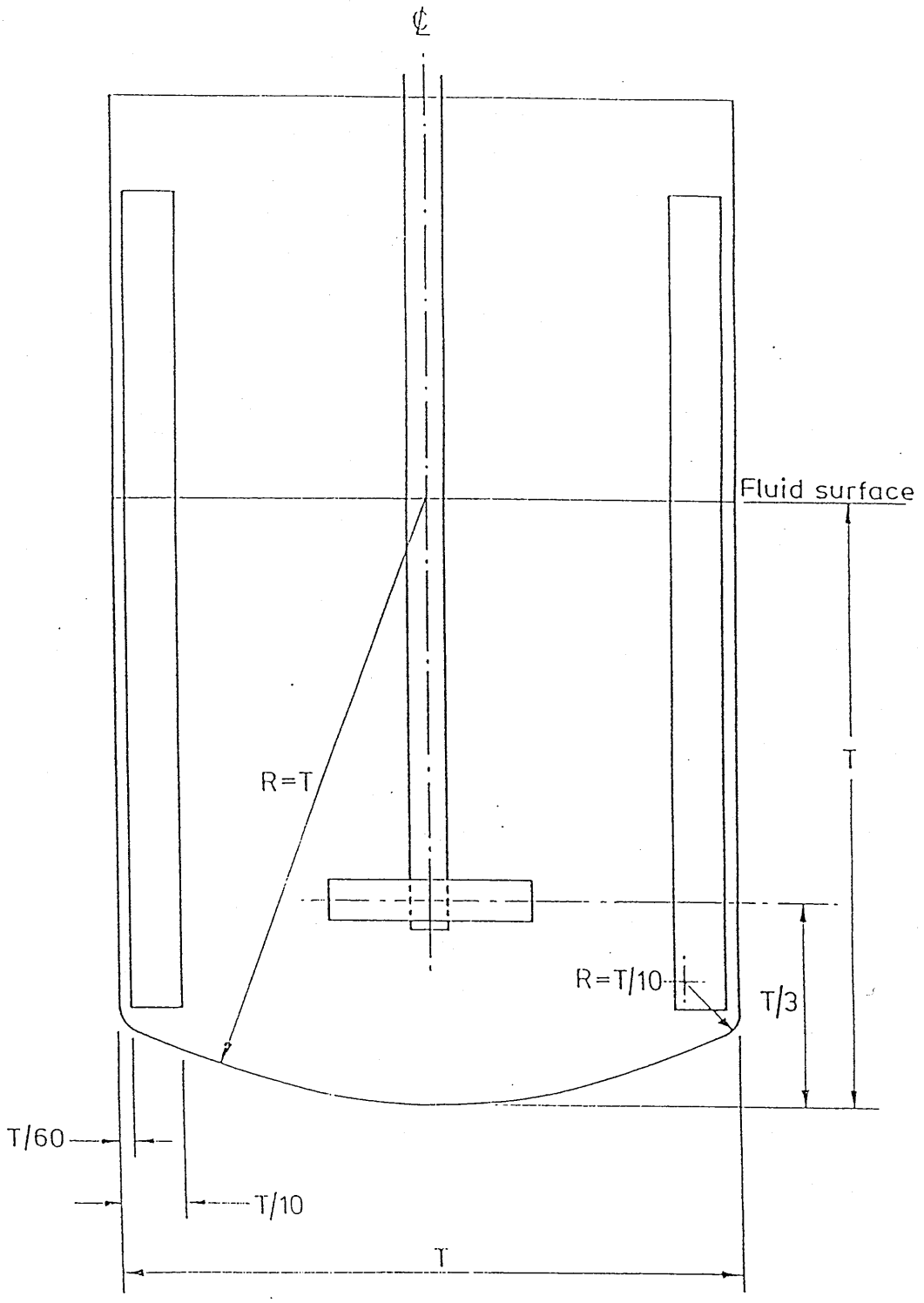


Figure 2.1: Standard geometry vessel, fitted with a single impeller

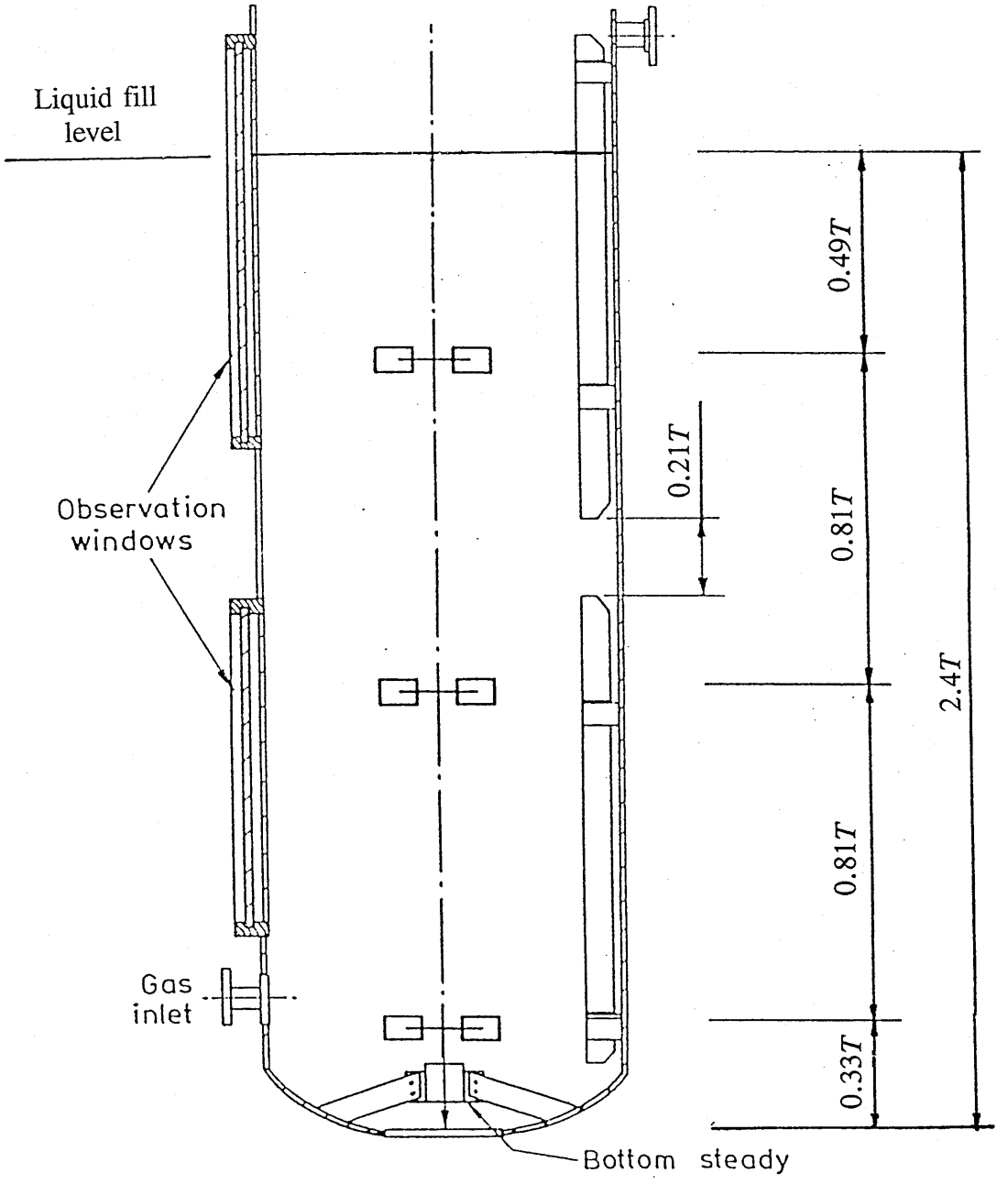
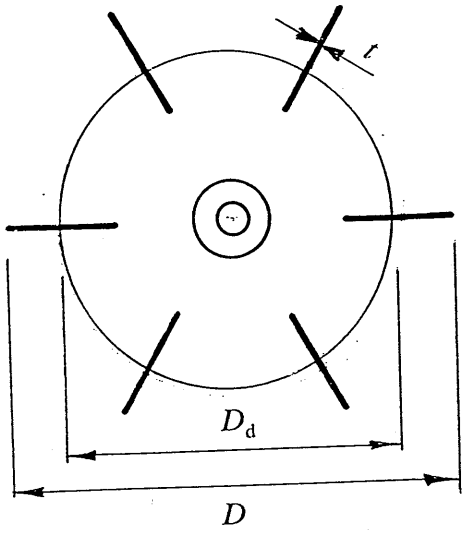


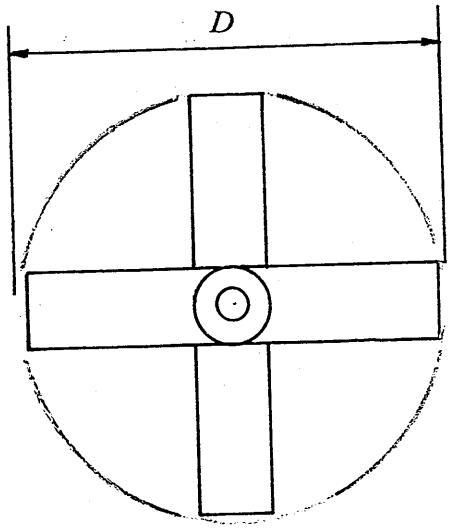
Figure 2.2: Tall vessel geometry, fitted with three impellers



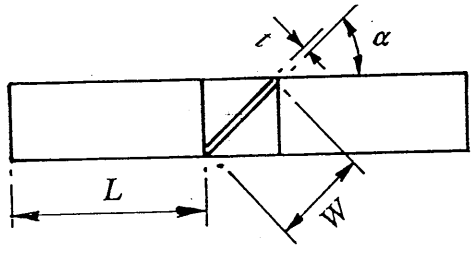
Rushton turbine

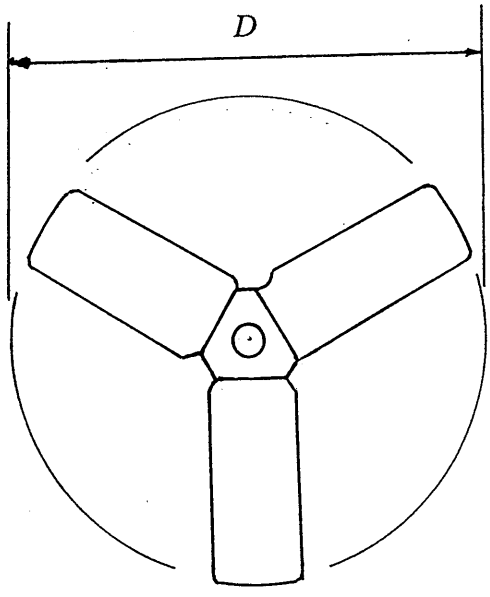
Standard dimensions:

$W = D/5,\ L = D/4,\ D_d = 0.75D$



Pitched blade turbine





LE20

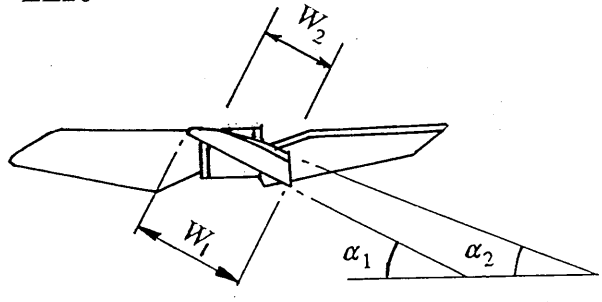
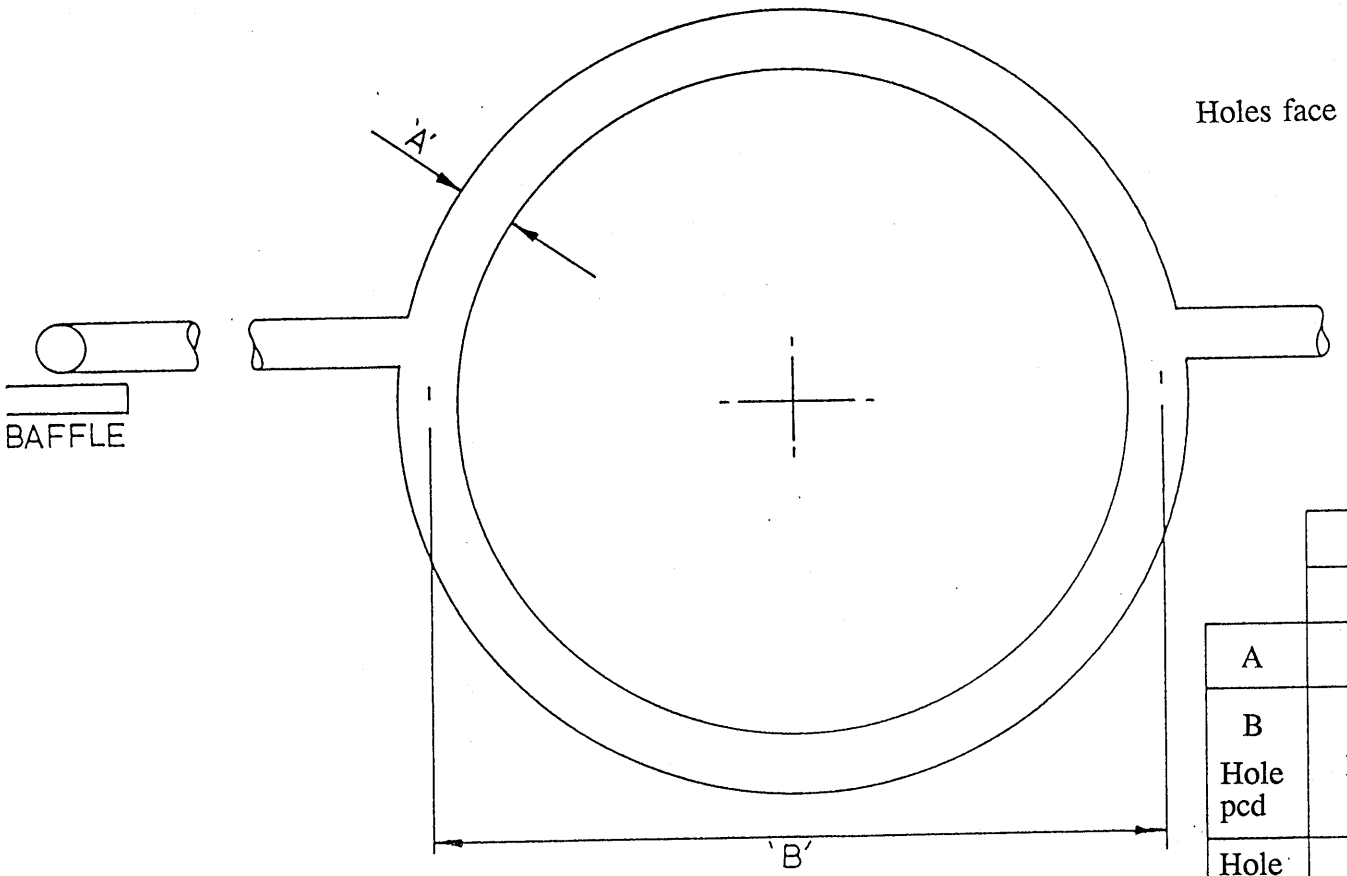


Figure 2.3: Impeller designs tested



	Vessel diameter	
	0.61 m	0.95 m
A	16 mm	50 mm
B Hole pcd	162 mm	250 mm
Hole dia.	2 mm	4 mm
No. of holes	30	50

Figure 2.4: Sparger geometry

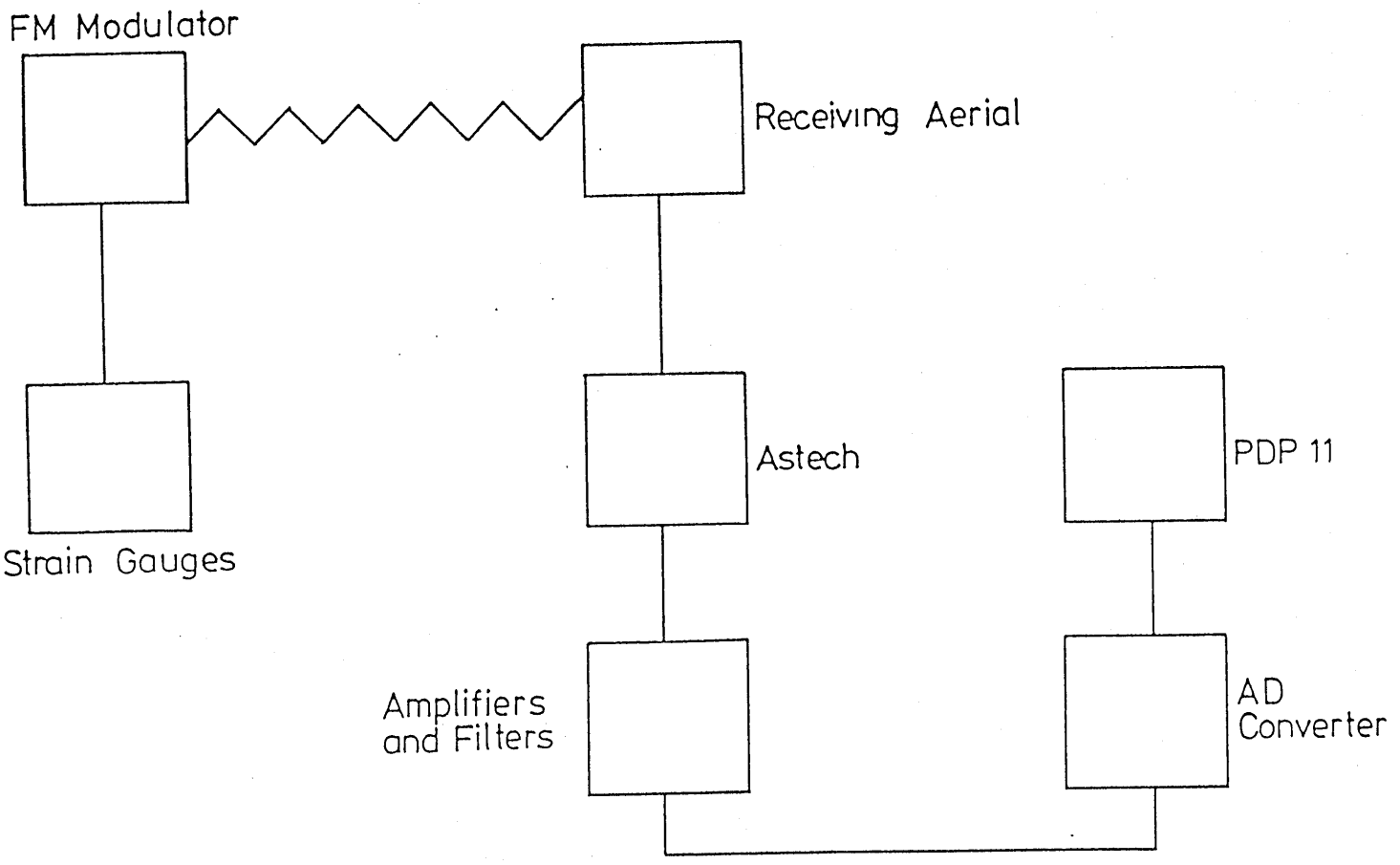


Figure 2.5: Instrumentation chain for strain gauge telemetry system

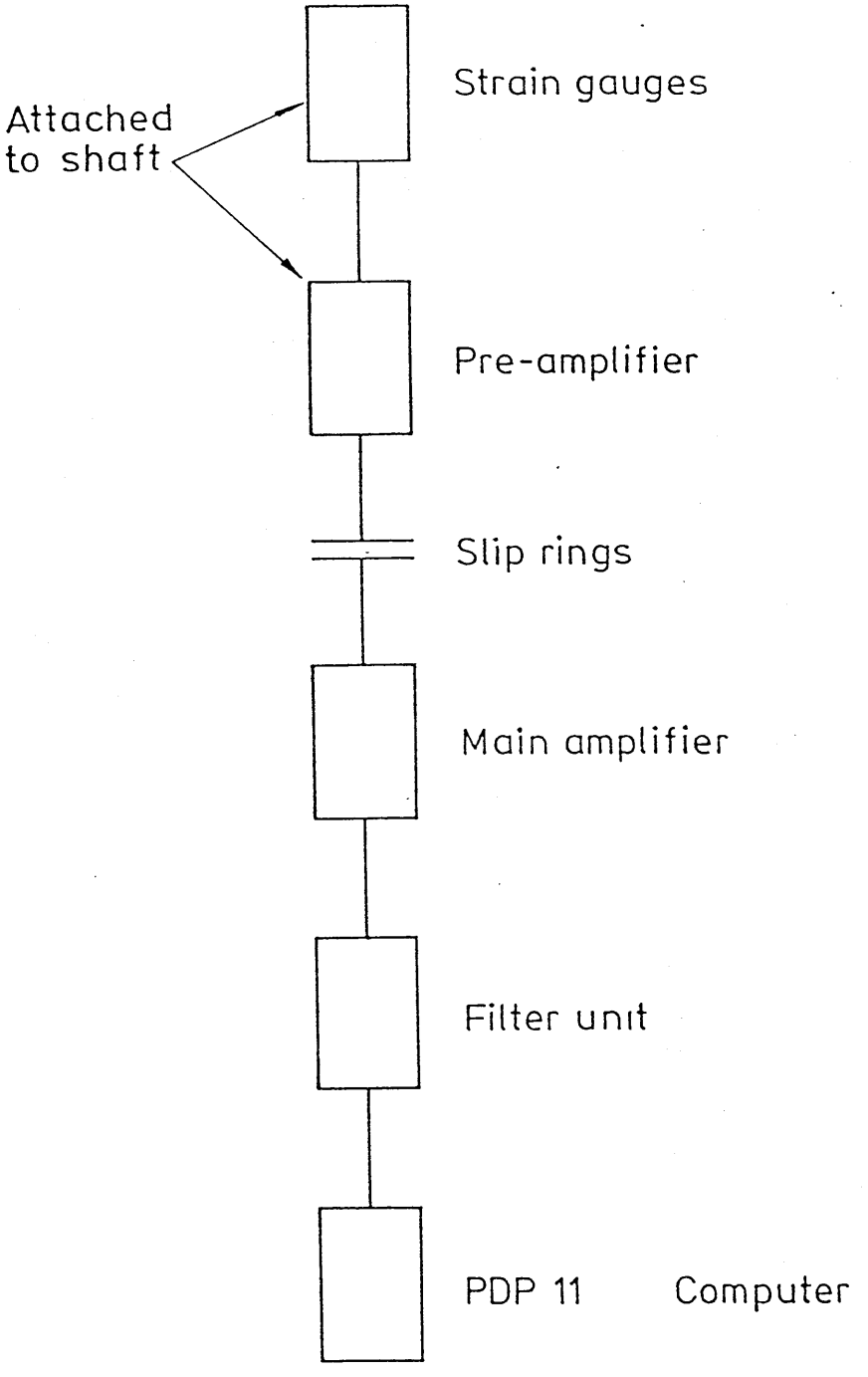


Figure 2.6: Instrumentation chain for strain gauge slip ring system

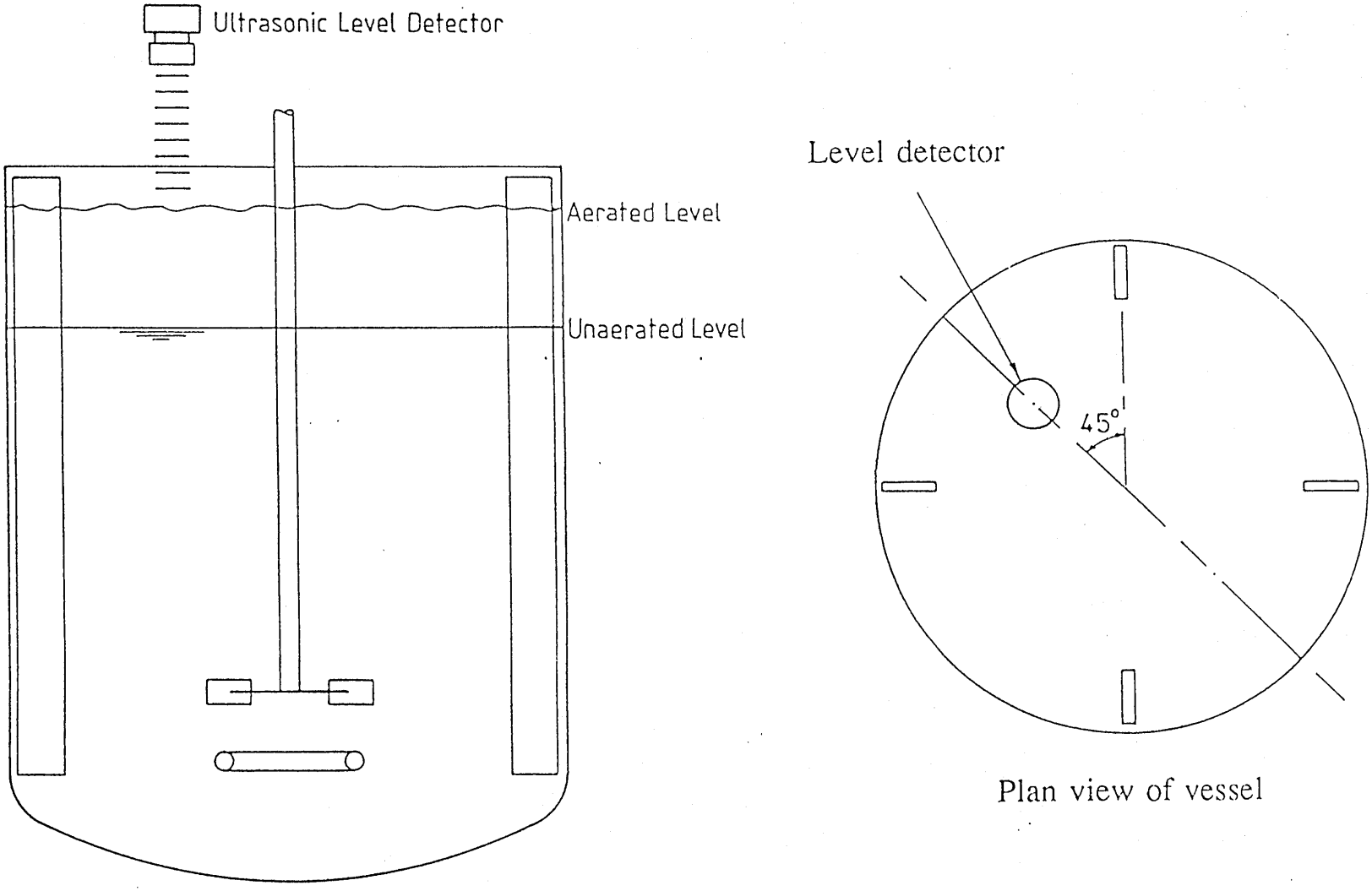


Figure 2.7: Position of ultrasonic level detector

Figure 2.8: Conductivity probe designs tested

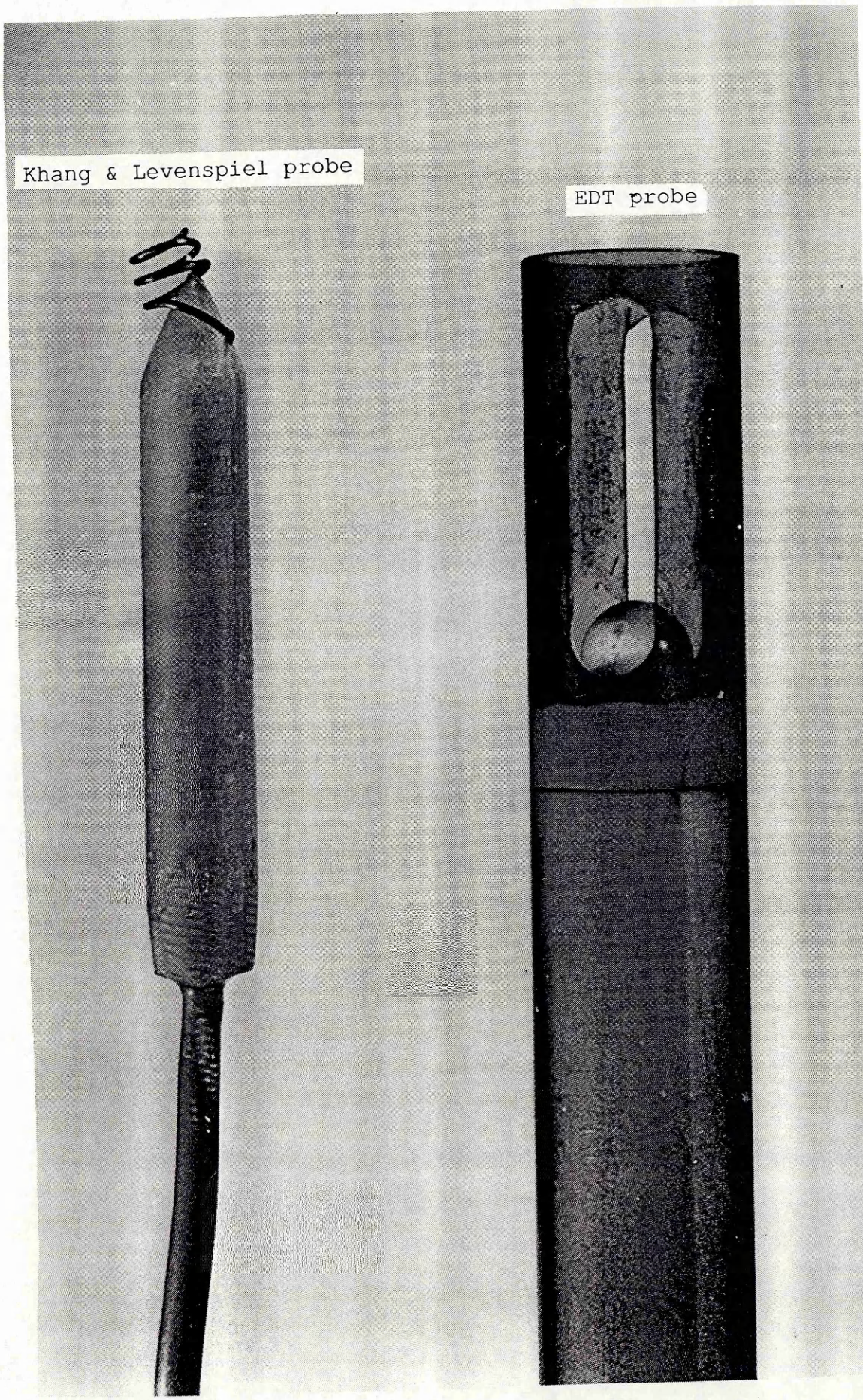
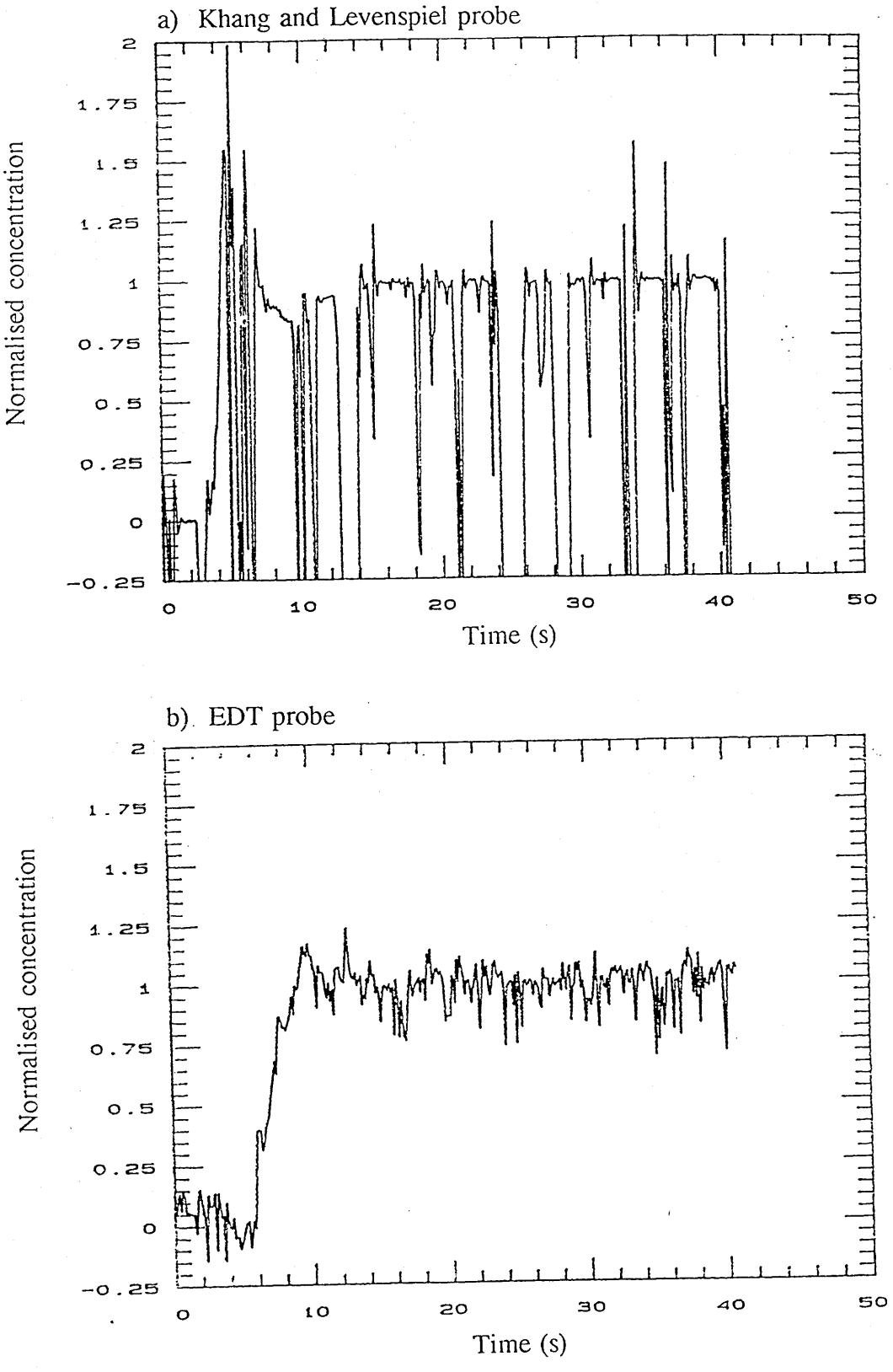


Figure 2.9: Comparison of conductivity probe responses in a gas liquid dispersion. Standard geometry vessel, probes in identical positions, Q_G = 1 vvm.



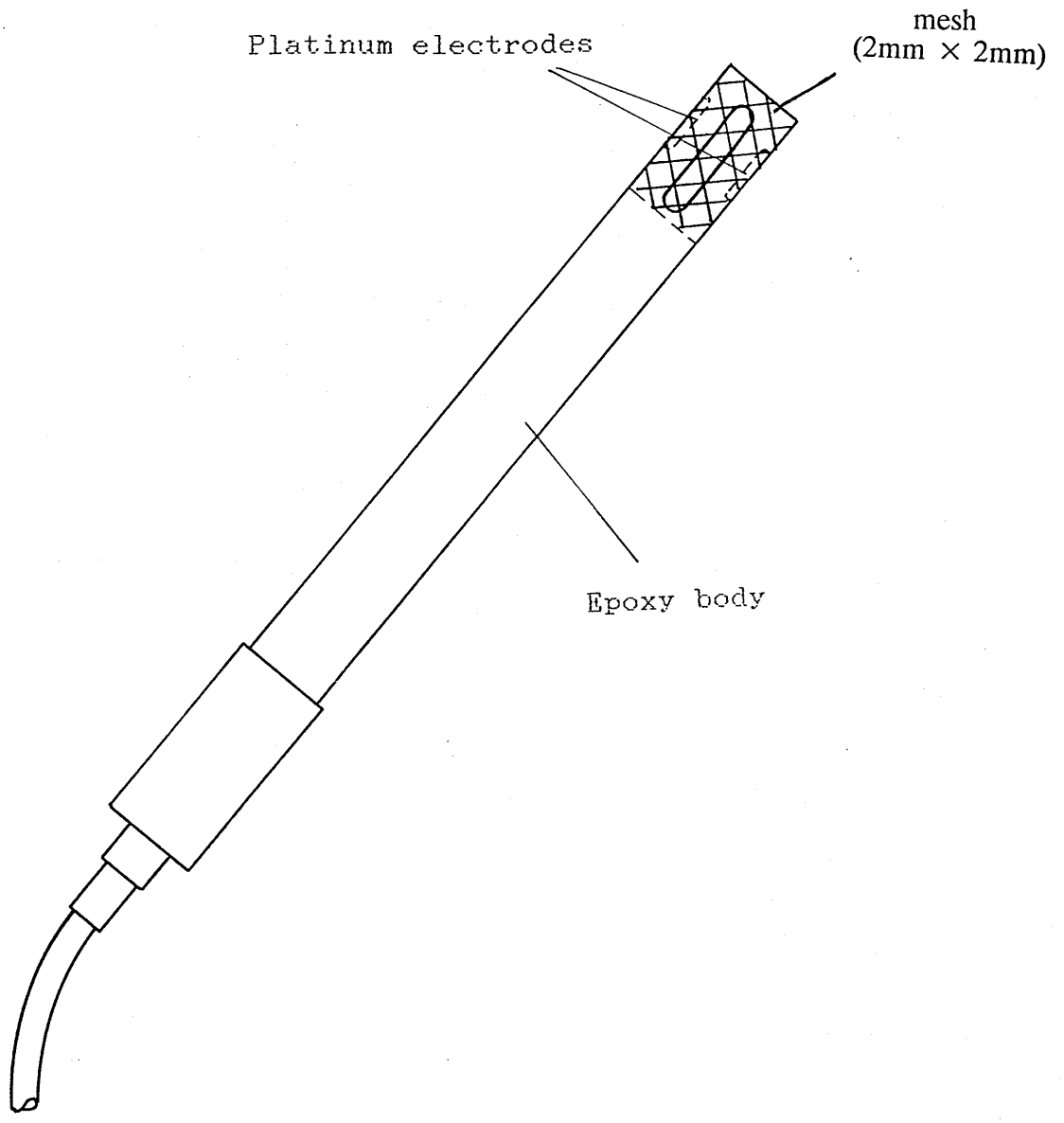


Figure 2.10: Schematic of EDT conductivity probe with mesh.

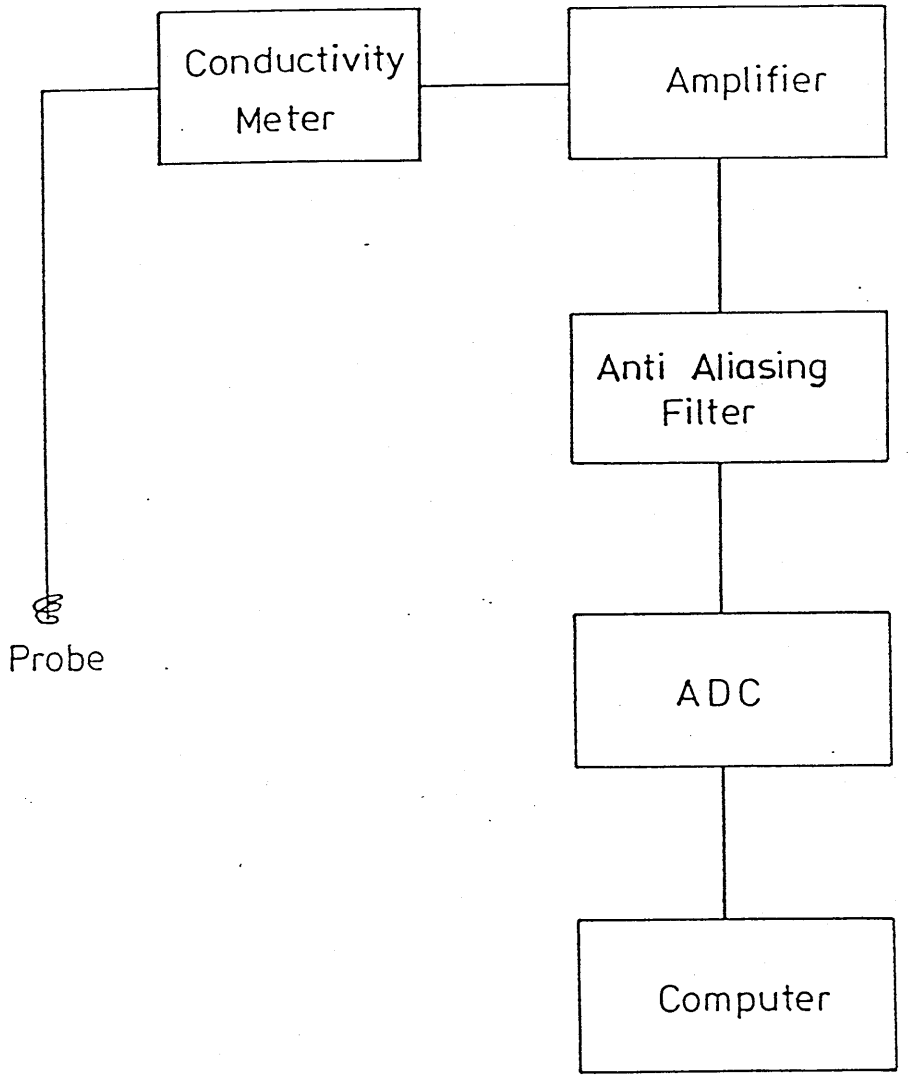
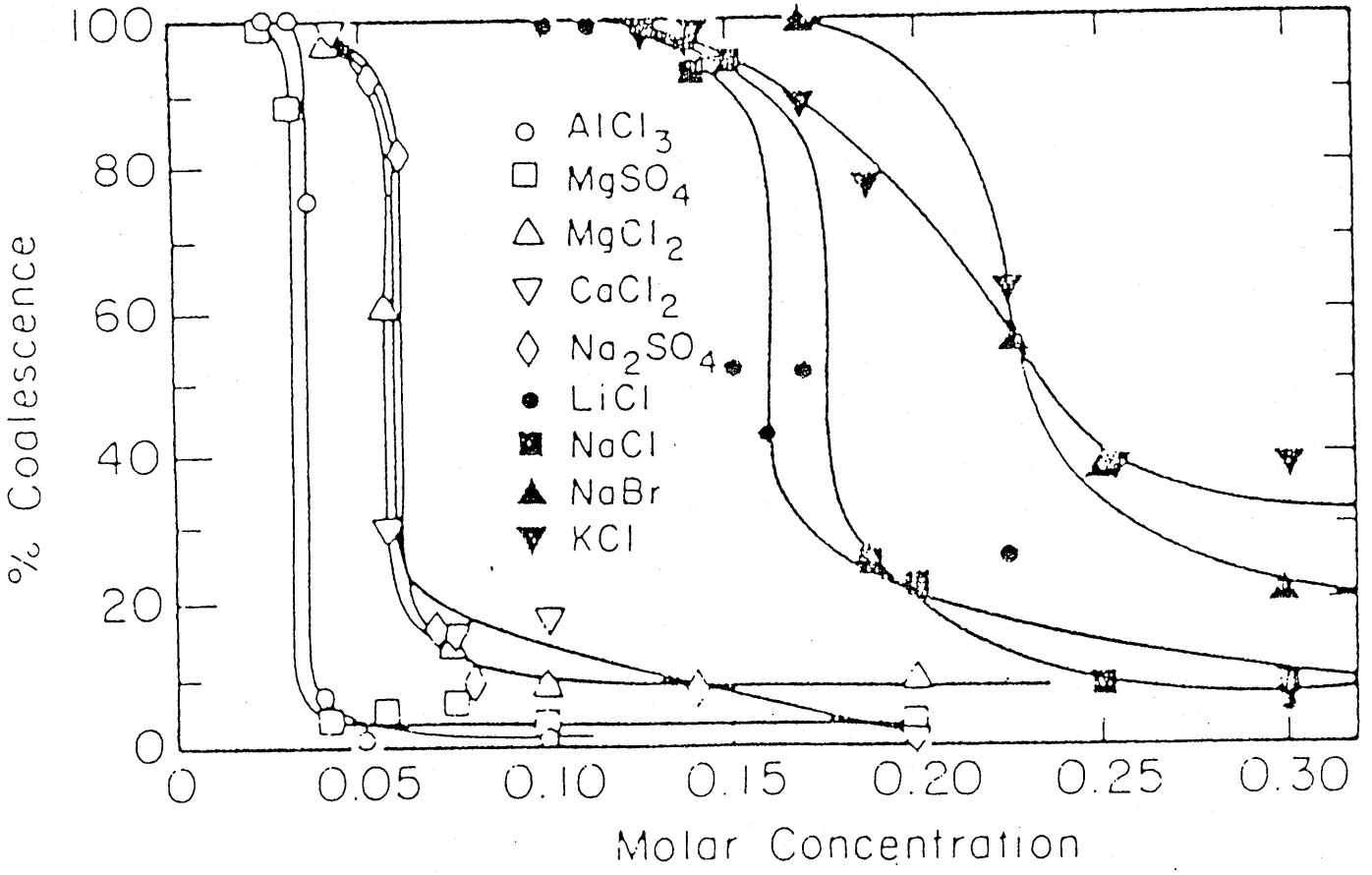


Figure 2.11: Instrumentation chain for conductivity measurement, Ruszkowski (1985).

Figure 2.12: Effect of salt concentration on coalescence behaviour of gas bubbles, Oolman and Blanch (1985).



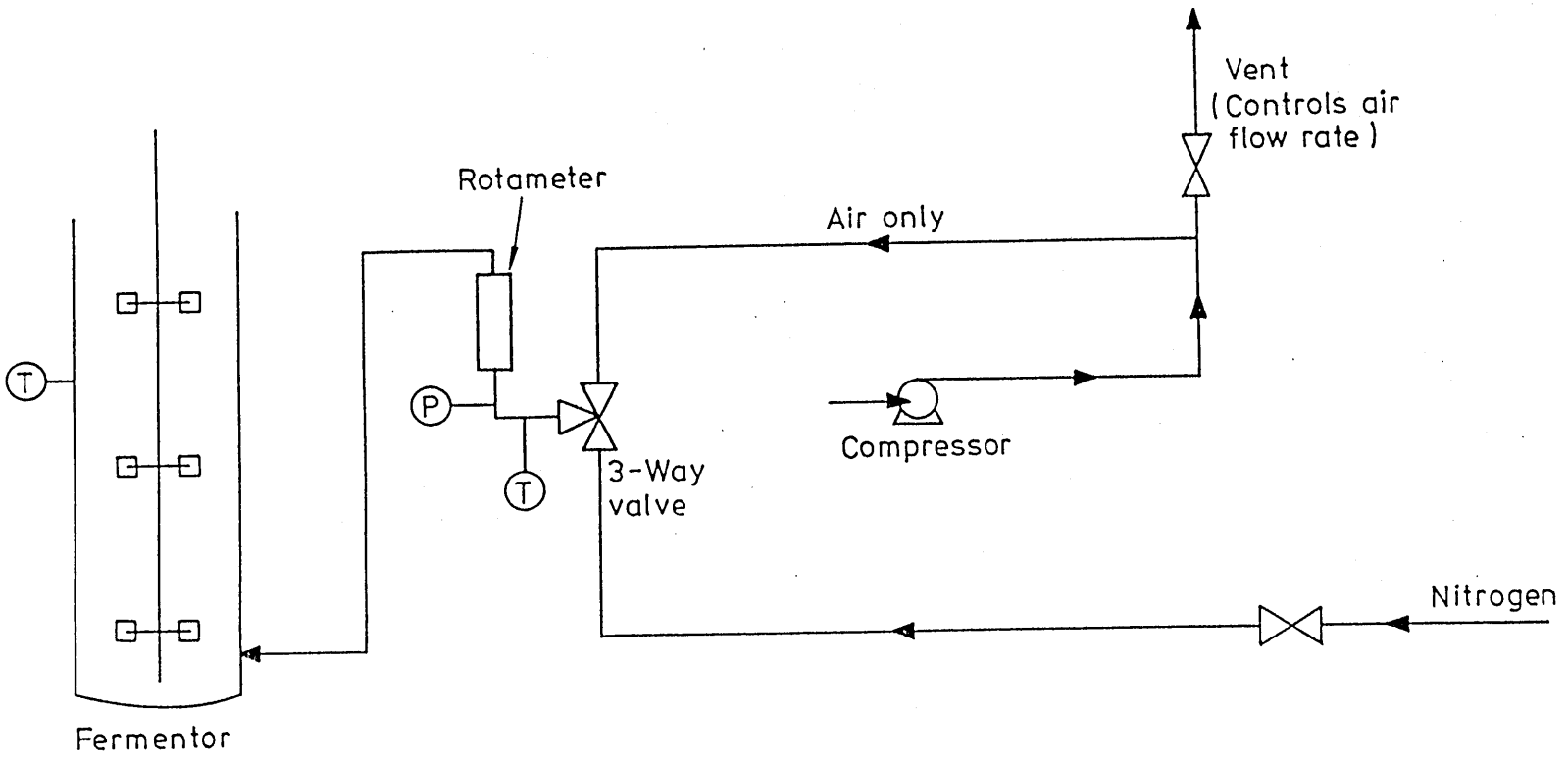


Figure 2.13: Gas supply system for dynamic mass transfer experiments.

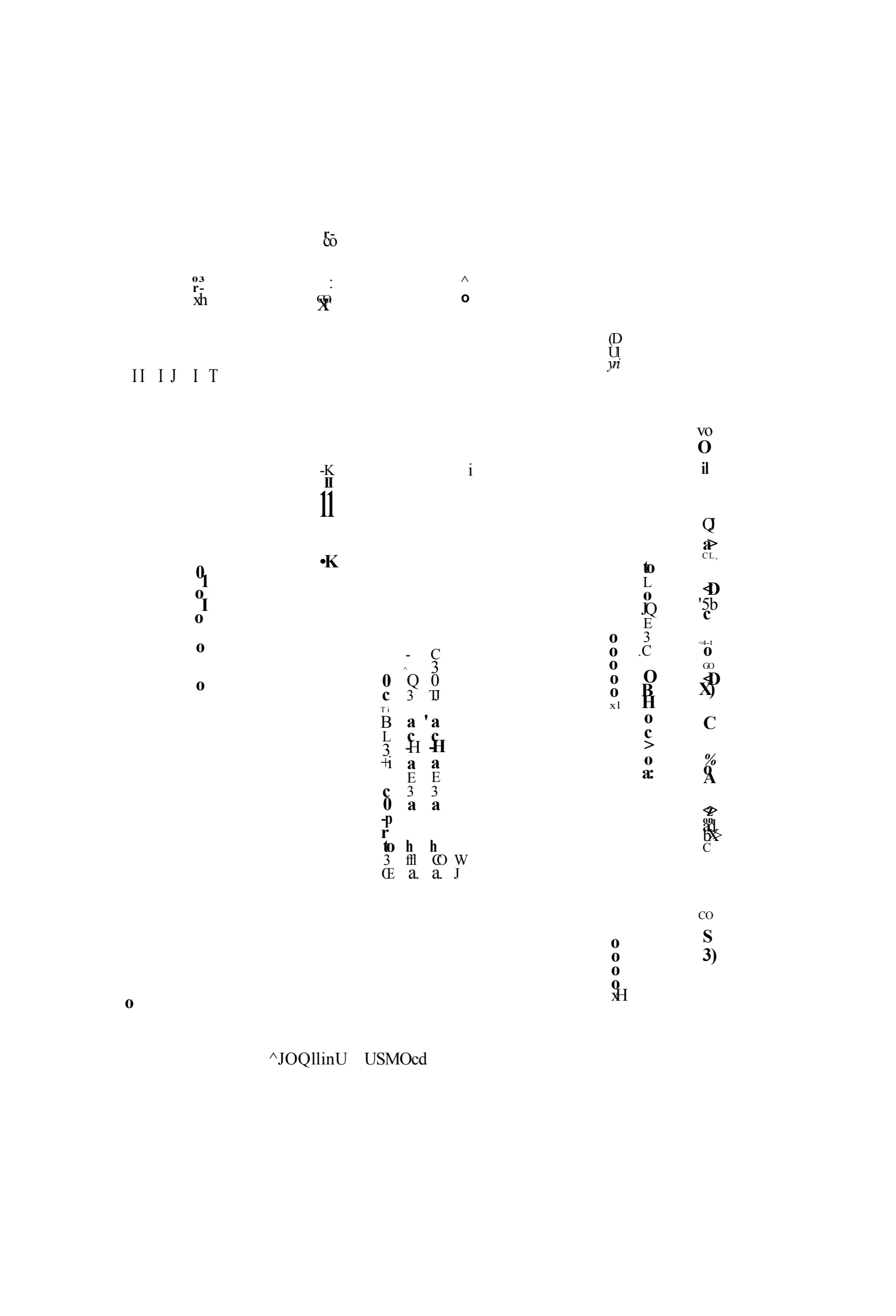
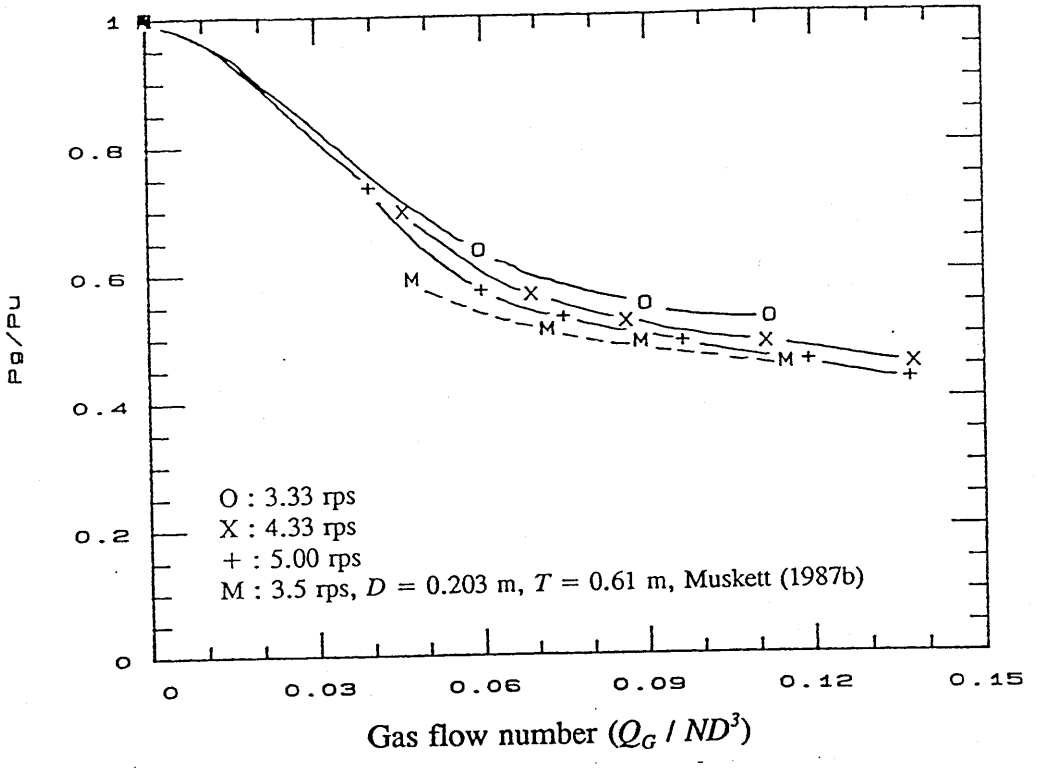


Figure 3.2: Gassed power draw of single impellers (T = 0.61 m).

a) Rushton turbine



b) LE20

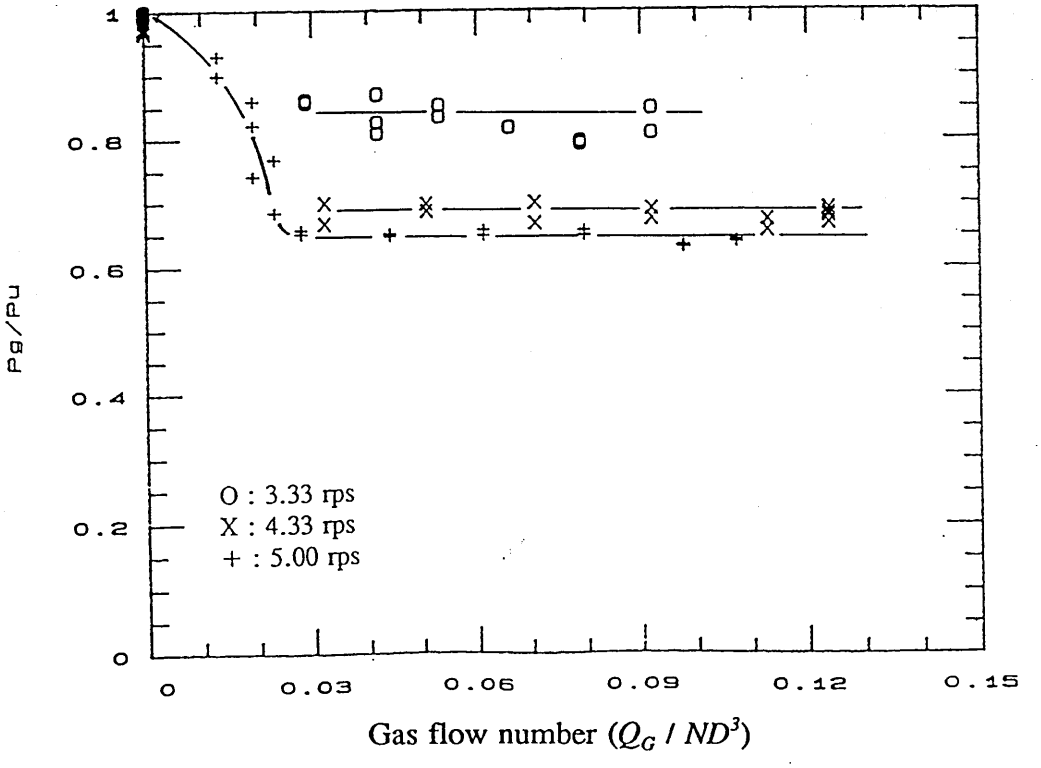
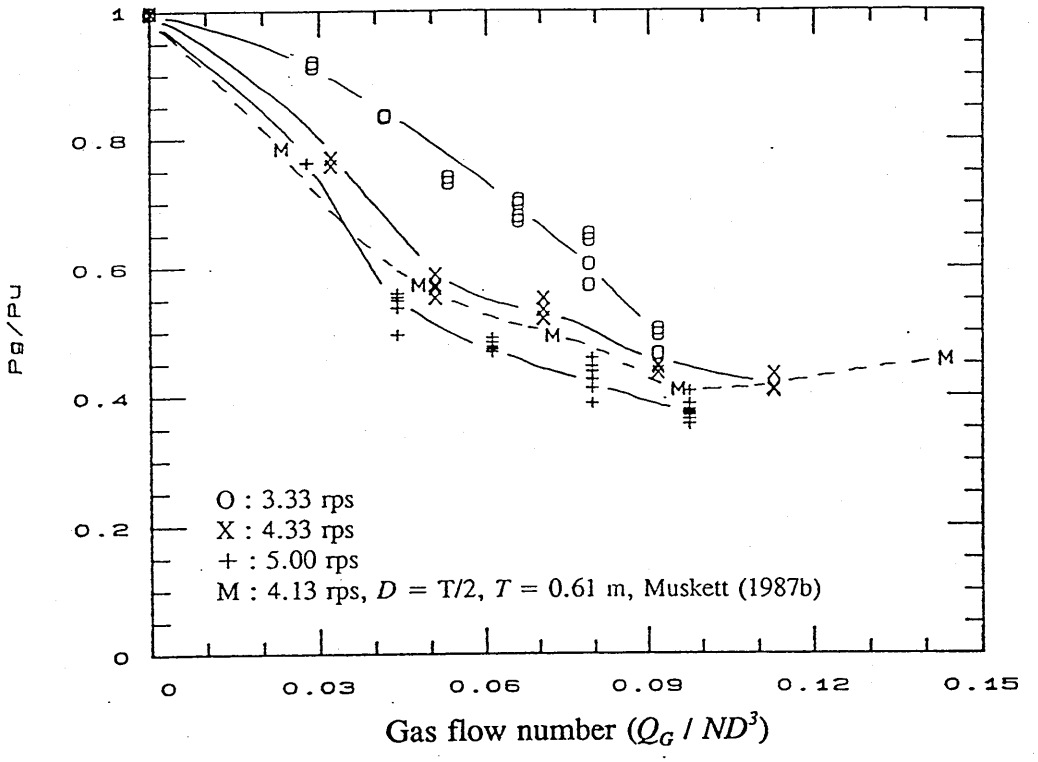


Figure 3.2: Gassed power draw of single impellers (T = 0.61 m).

c) PBT (pumping down)



d) PBT (pumping up)

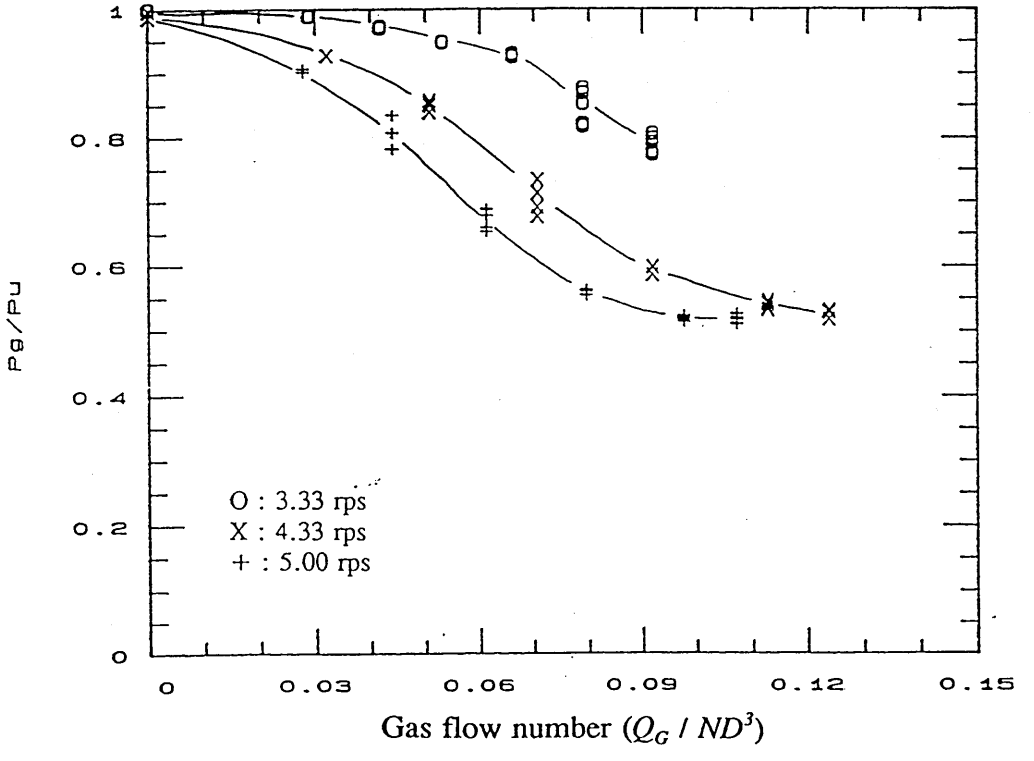
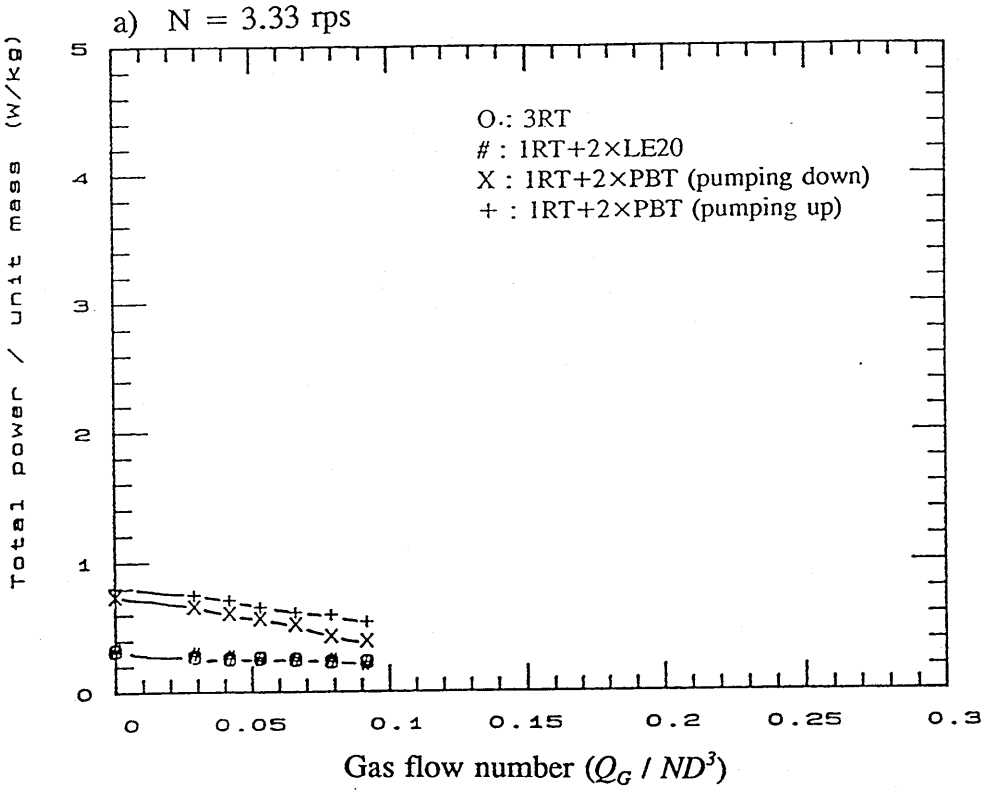


Figure 3.3: Comparison of total gassed power draw of multiple impeller combinations (T = 0.61 m).



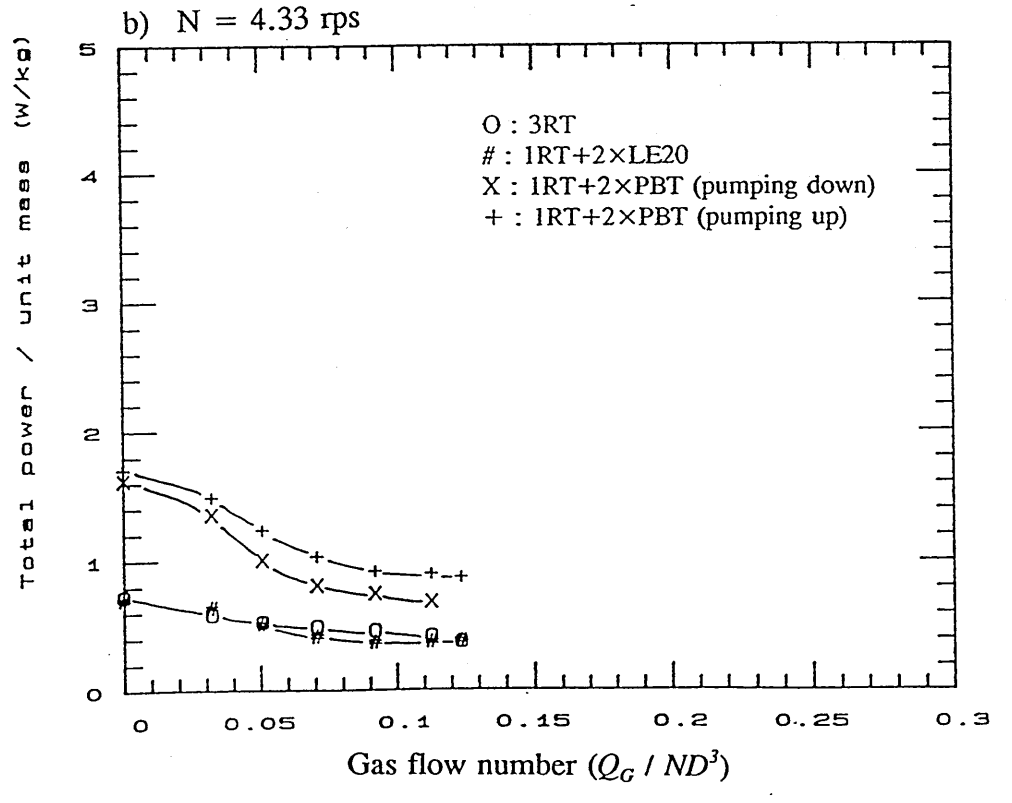
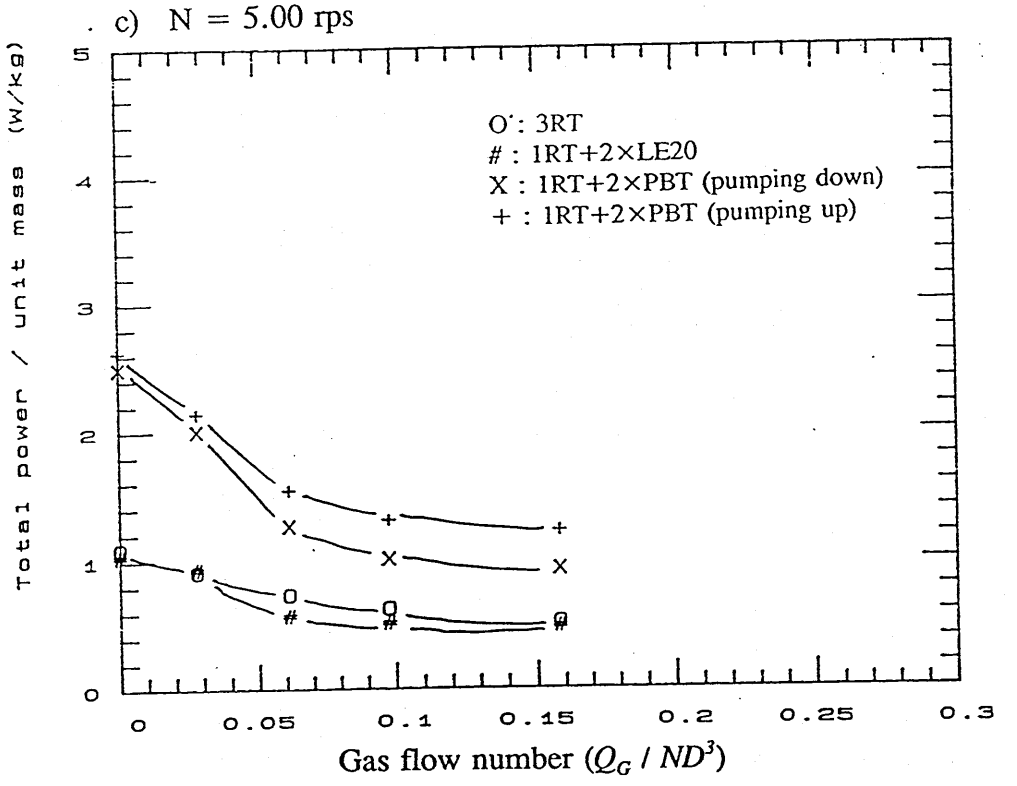


Figure 3.3: Comparison of total gassed power draw of multiple impeller combinations (T = 0.61 m).



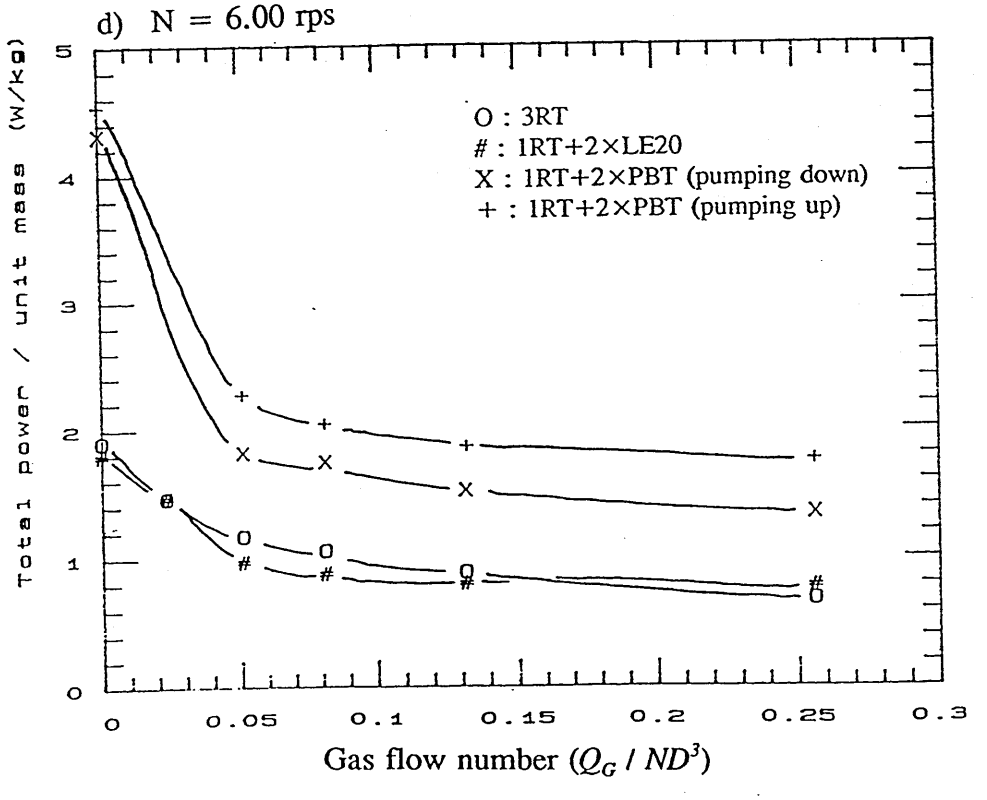
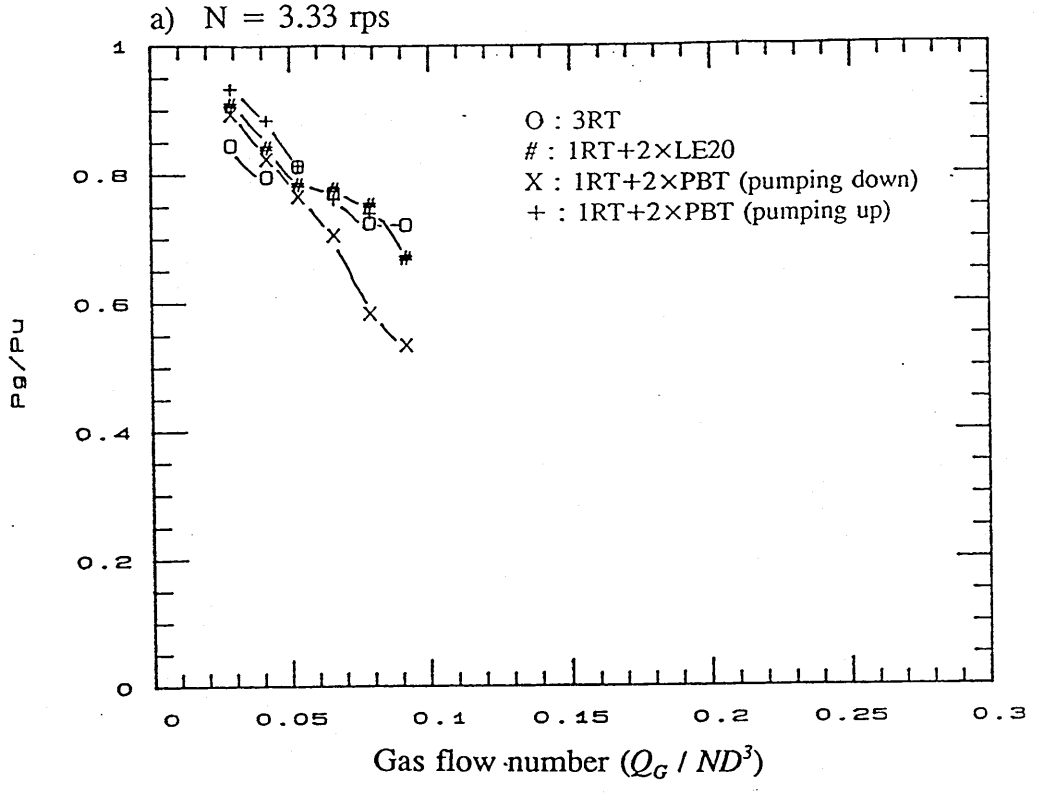


Figure 3.4: Comparison of total P_g/P_u ratio for multiple impeller combinations (T = 0.61 m).



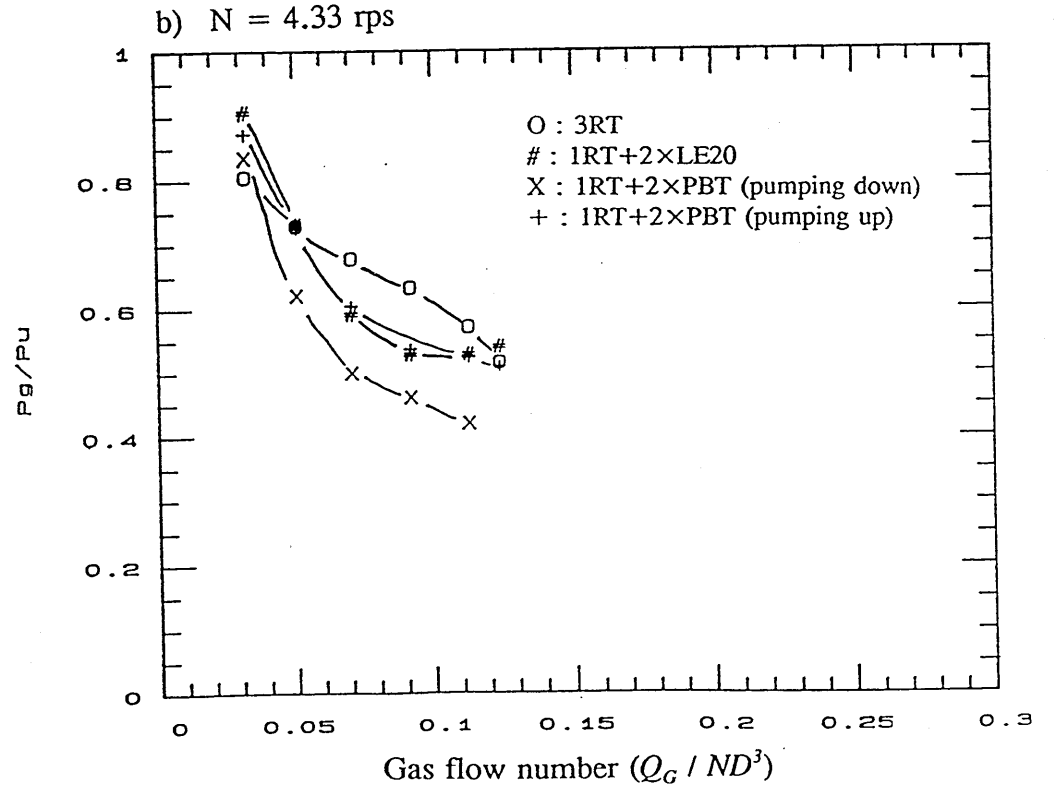
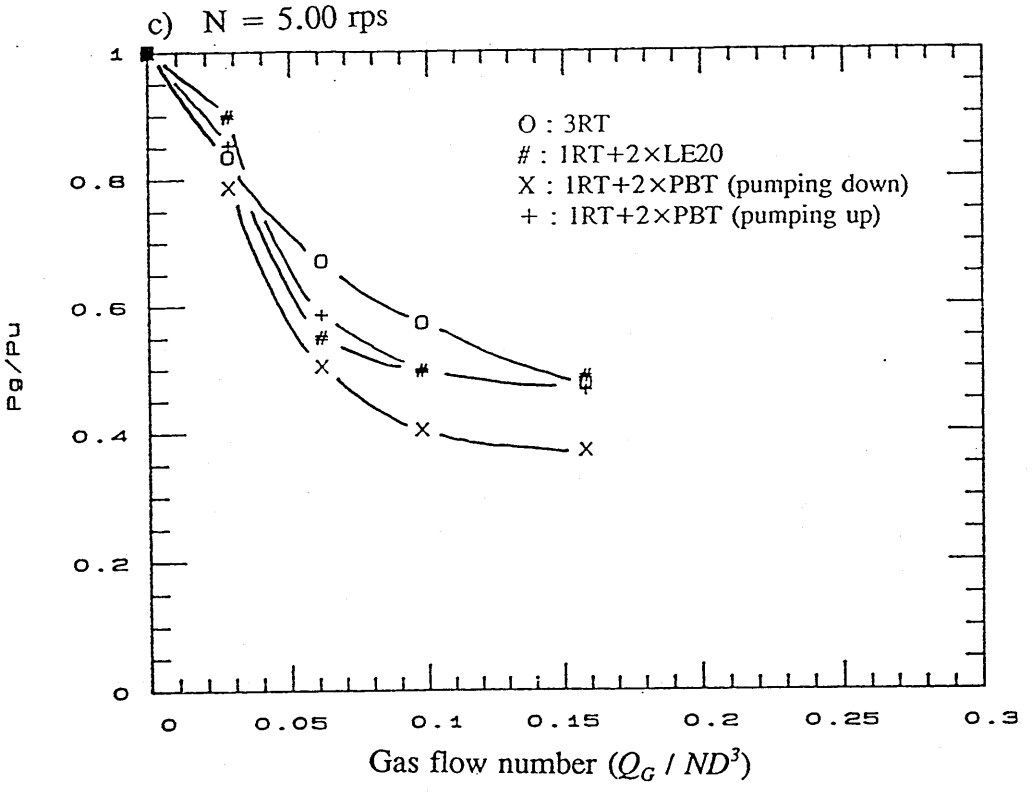


Figure 3.4: Comparison of total P_g/P_u ratio for multiple impeller combinations (T = 0.61 m).



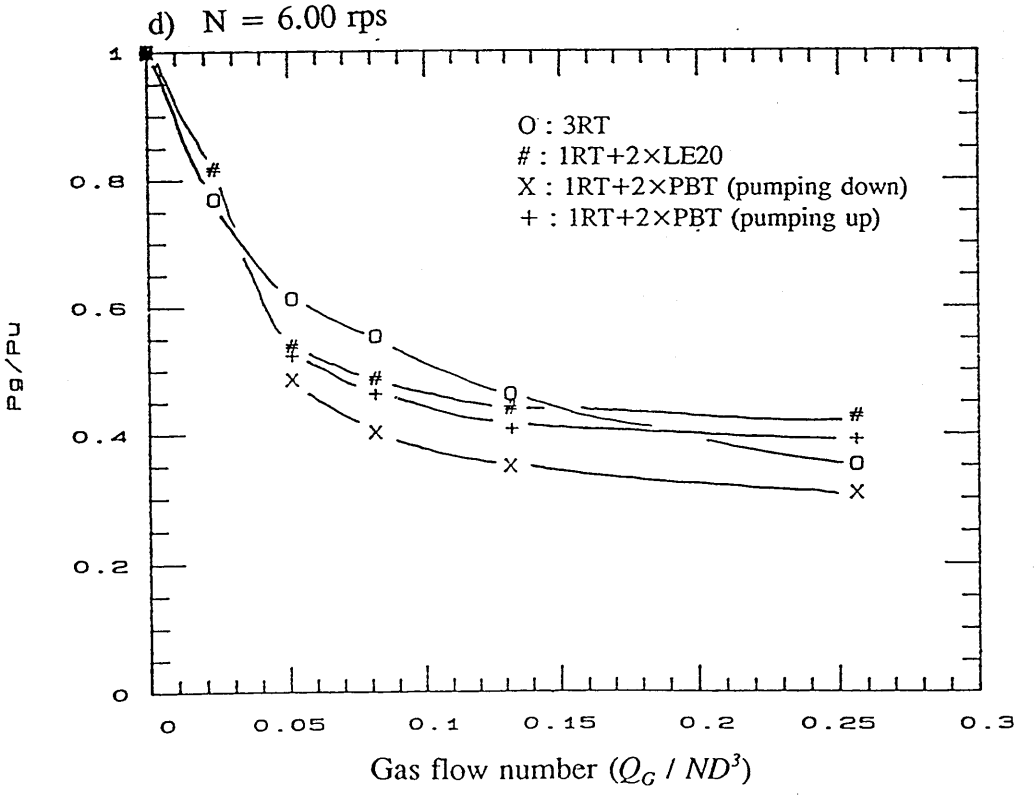


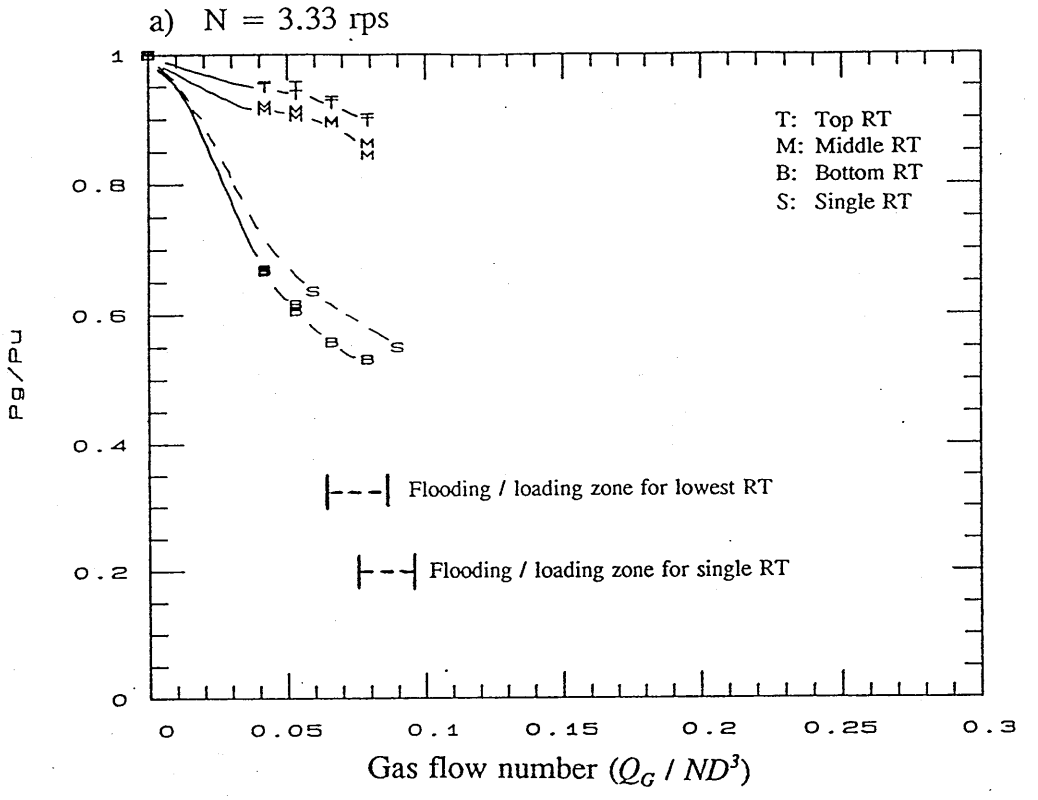
Figure 3.5: Gas liquid flow patterns observed with triple Rushton turbines (T - 0.61 m, s = 0.495 m)

6 circulation loops.
pas completely dispersed.

circulation loops.
N0 pas recirculated
below lowest impeller.

Lowest impeller fltxxled.
circulation loops.

Figure 3.6: Gassed power draw of triple Rushton turbine combination (T = 0.61 m).



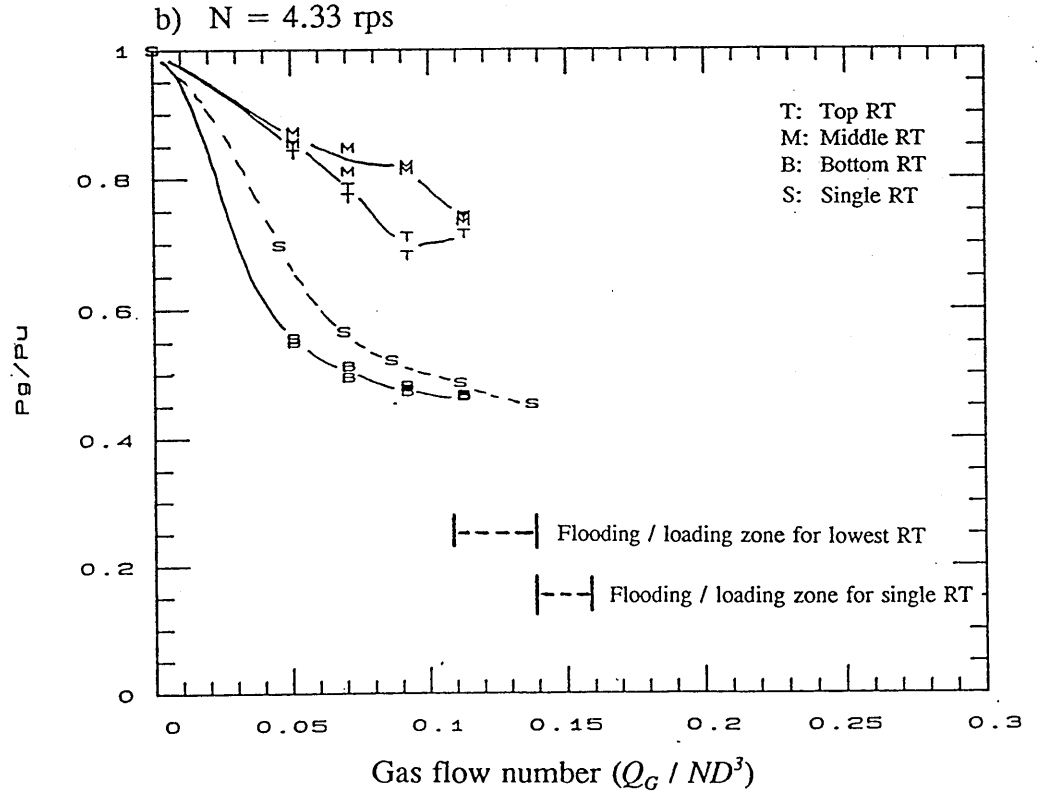


Figure 3.6: Gassed power draw of triple Rushton turbine combination (T = 0.61 m).

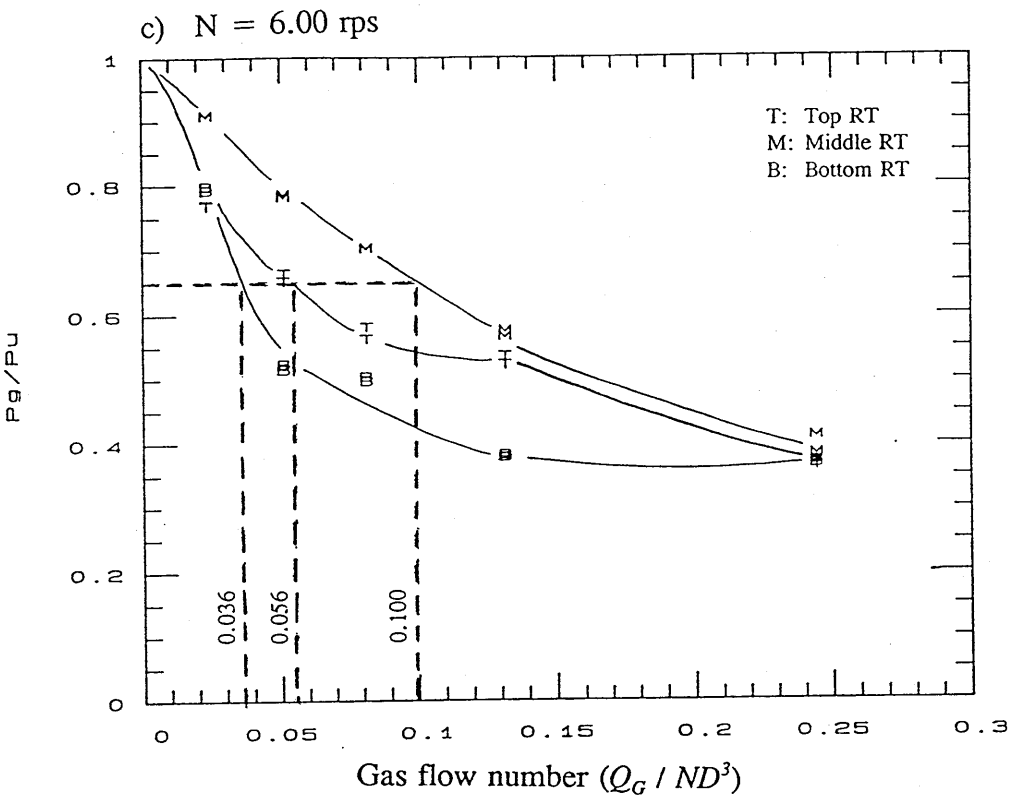


Figure 3.7: Flow map for triple Rushton turbines (T = 0.61 m).

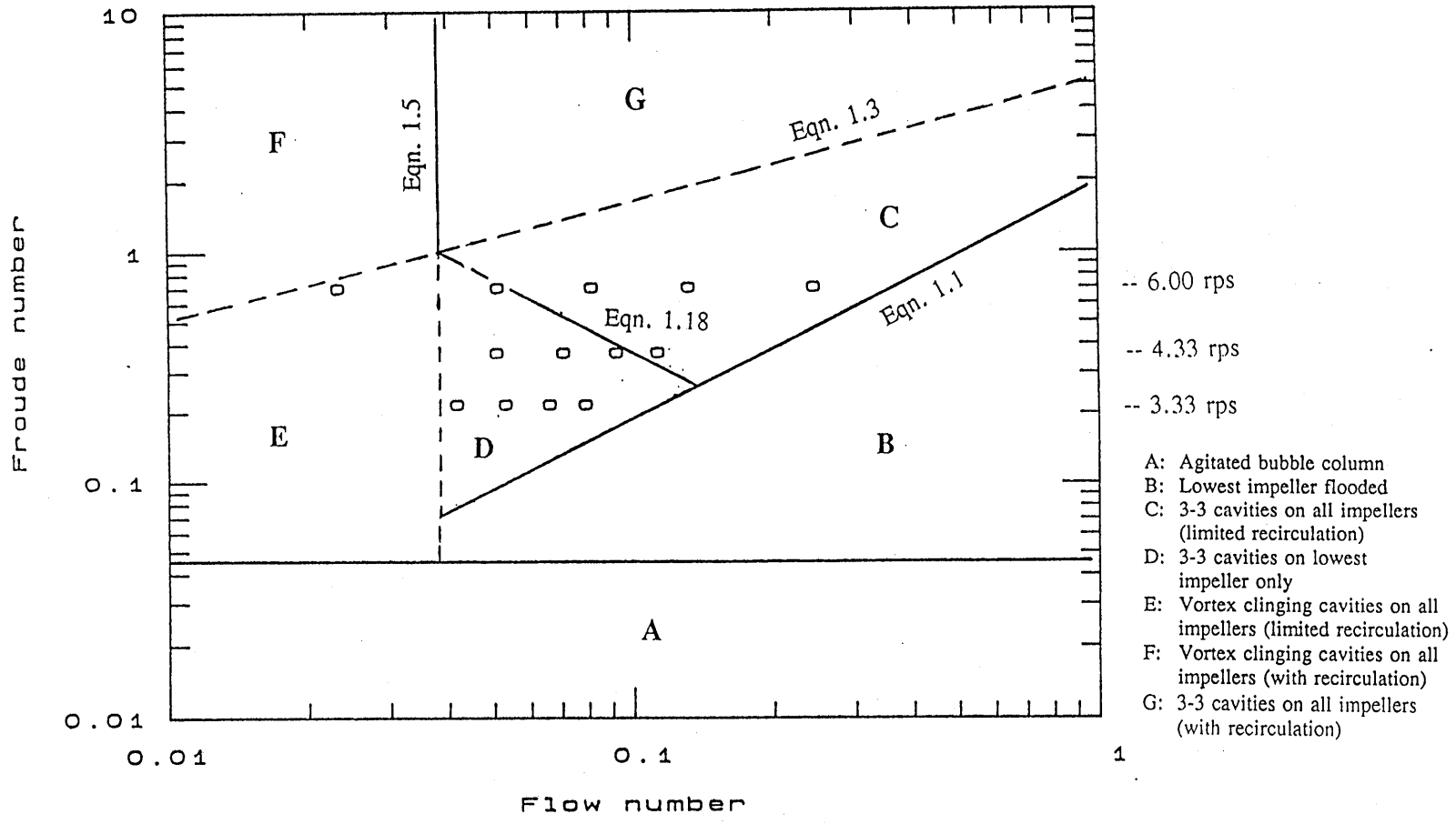


Figure 3.8: Gas liquid flow patterns observed with the 1RT+2×LE20 combination (T = 0.61 m, S = 0.495 m).

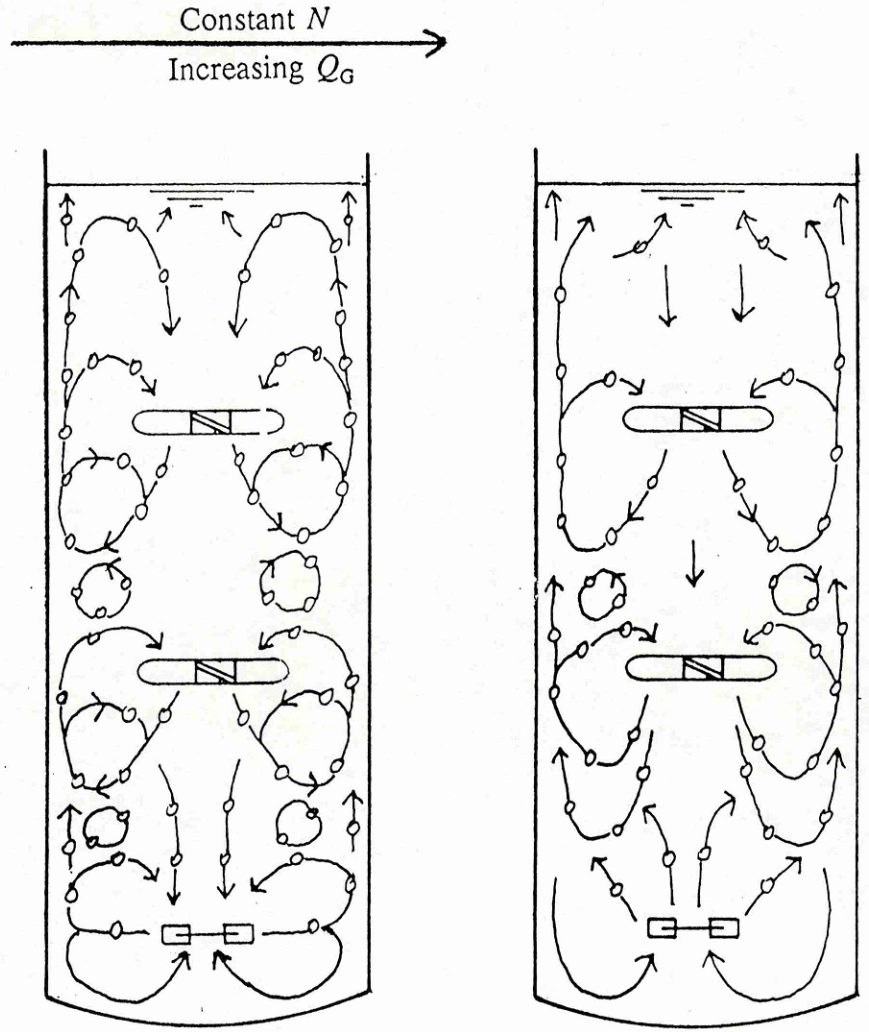
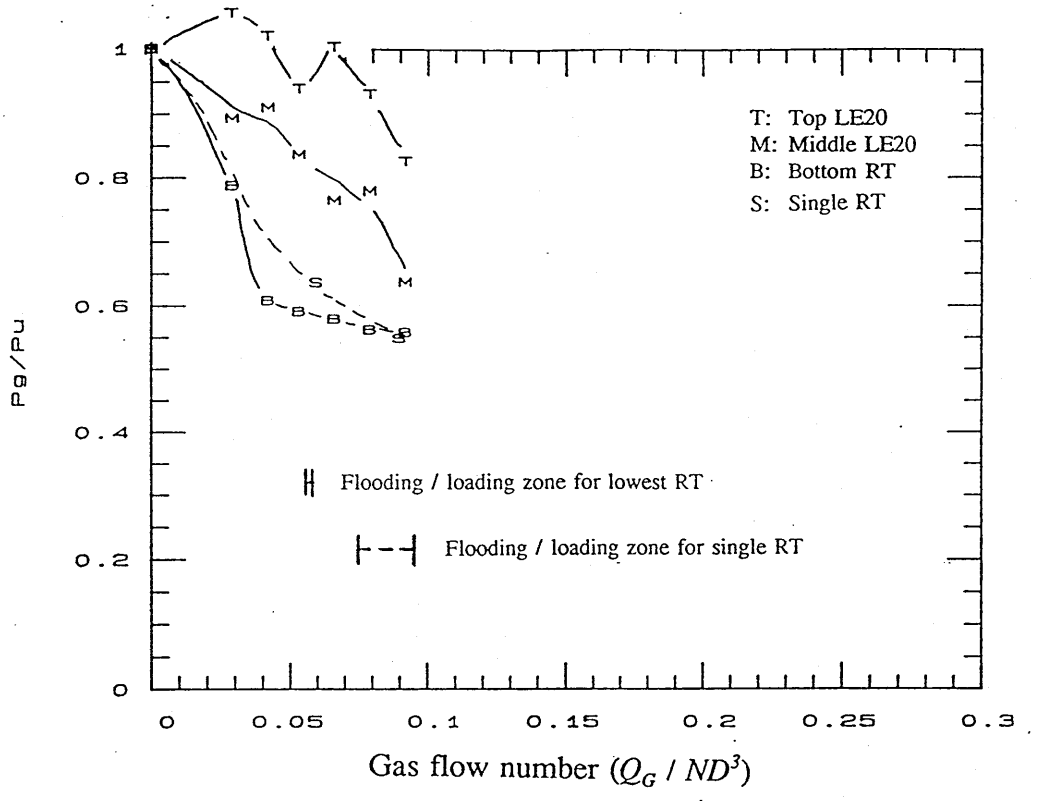


Figure 3.9: Gassed power draw of the 1RT+2×LE20 combination.

a) N = 3.33 rps



b) N = 4.33 rps

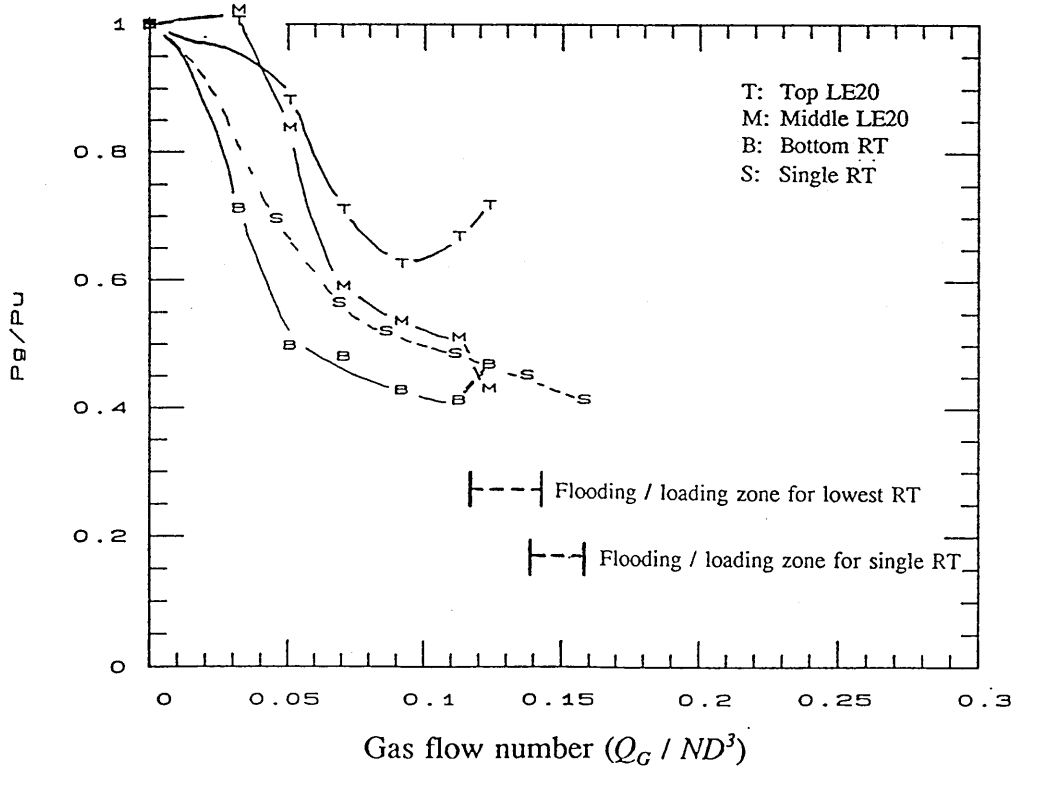
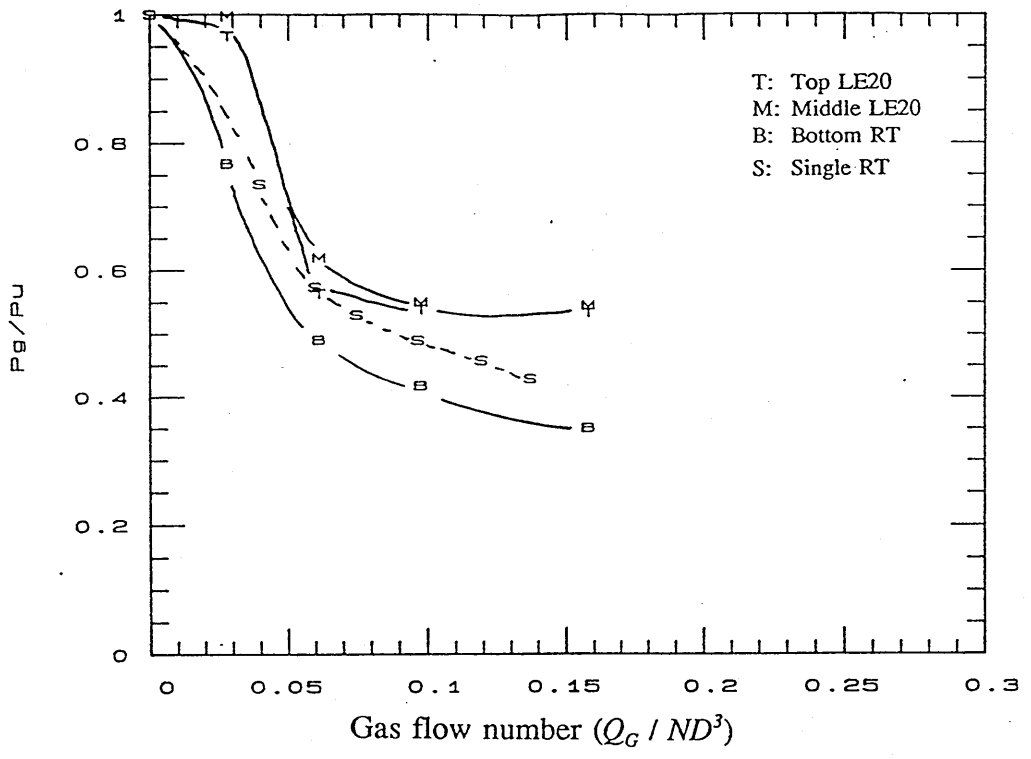


Figure 3.9: Gassed power draw of the 1RT+2×LE20 combination.

c) N = 5.00 rps



d) N = 6.00 rps

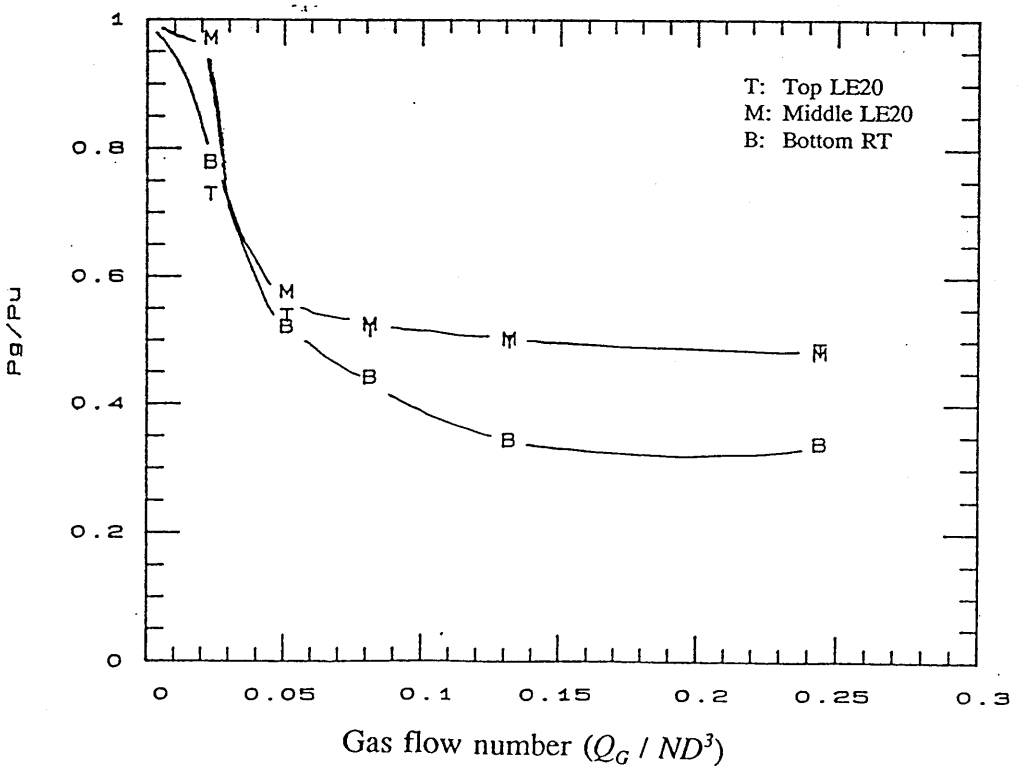
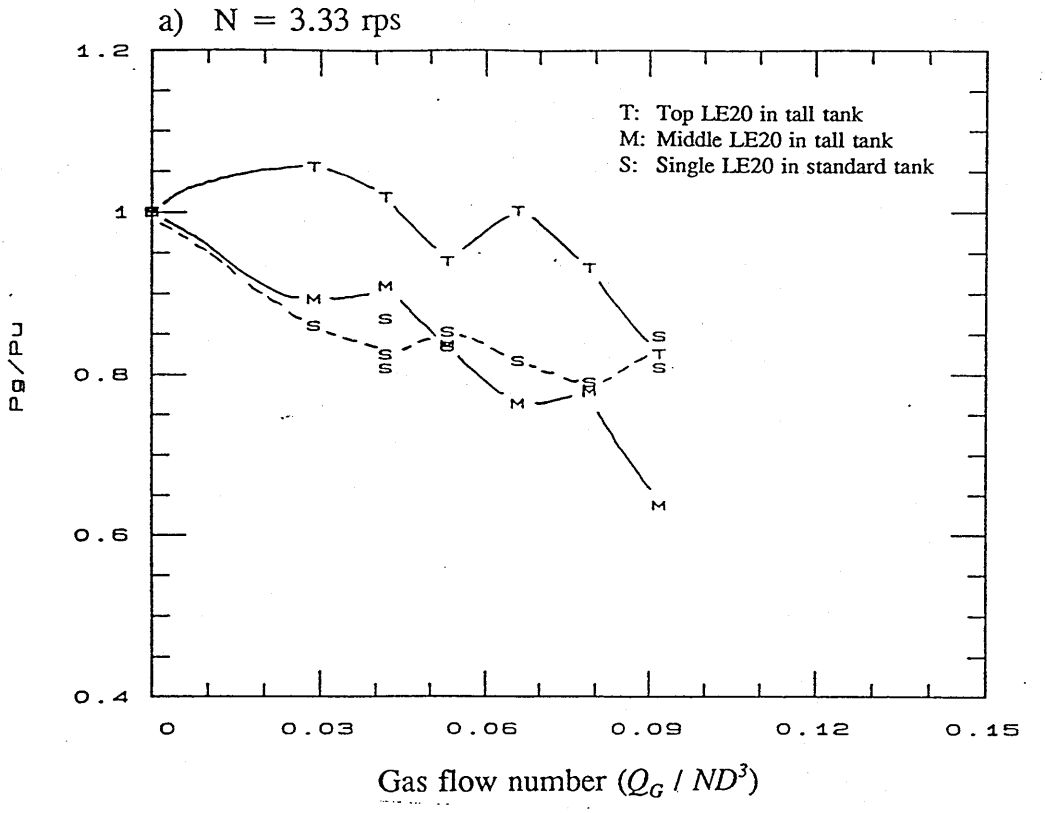


Figure 3.10: Comparison of gassed power draw for LE20 impellers in the tall tank and a standard tank.



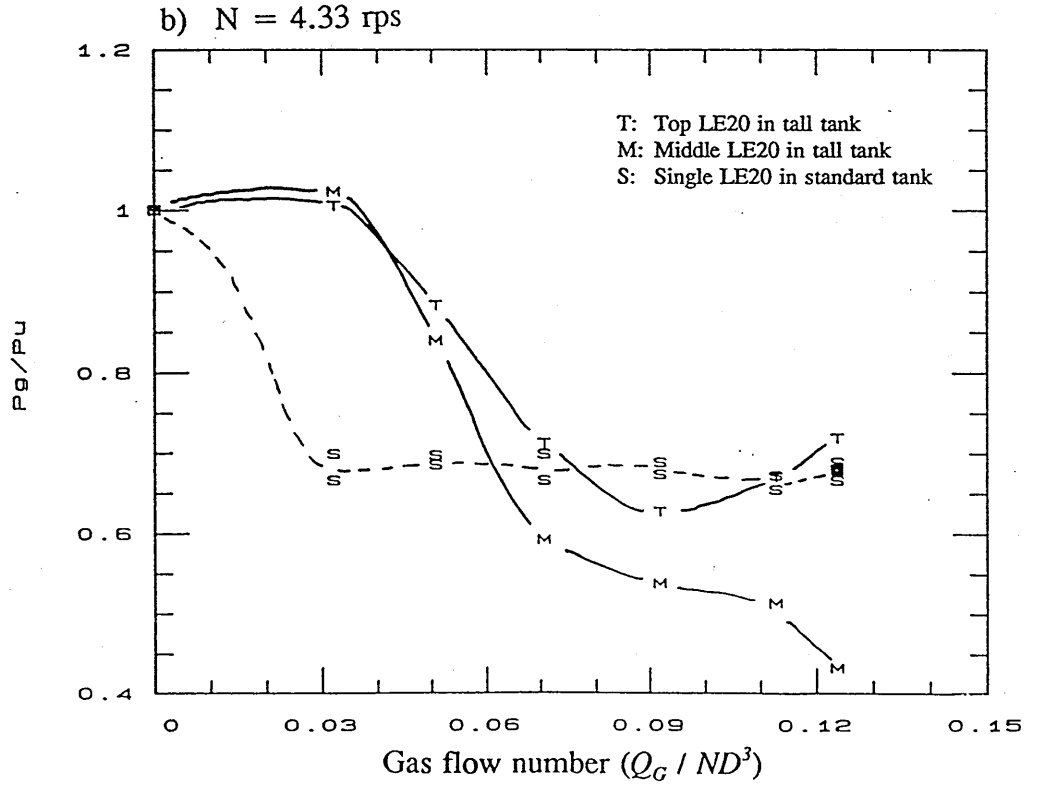


Figure 3.10: Comparison of gassed power draw for LE20 impellers in the tall tank and a standard tank.

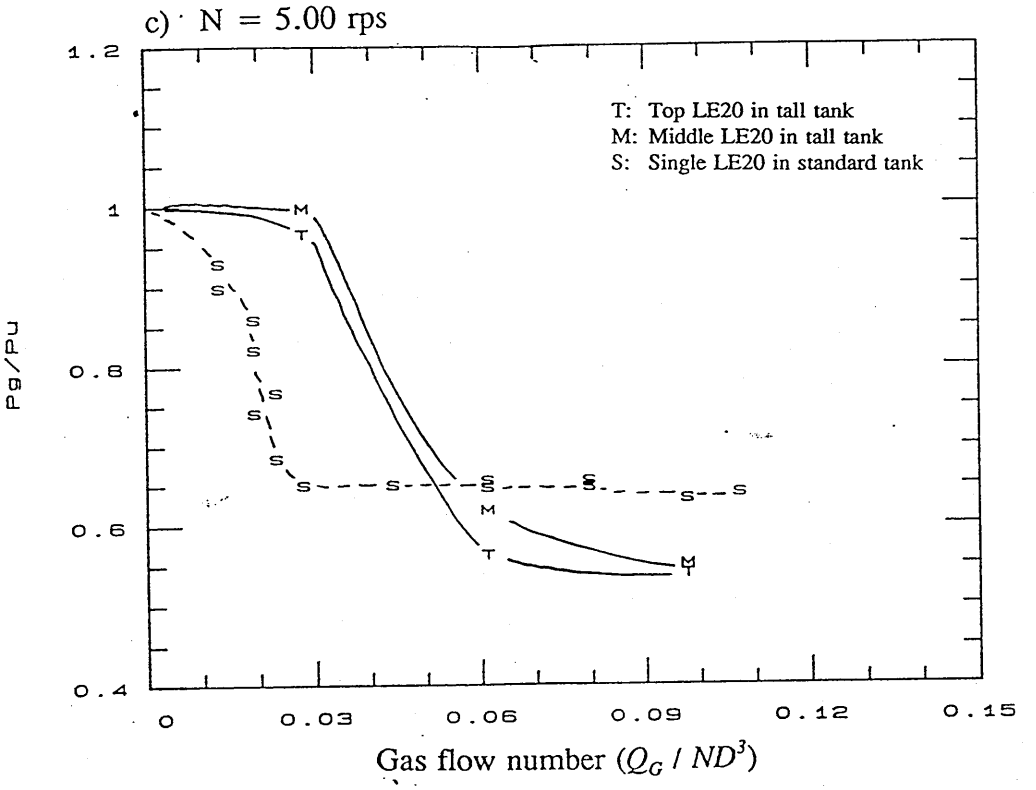


Figure 3.11: Gas liquid flow patterns observed with the 1RT+2×PBT (pumping down) combination (T = 0.61 m, S = 0.495 m).

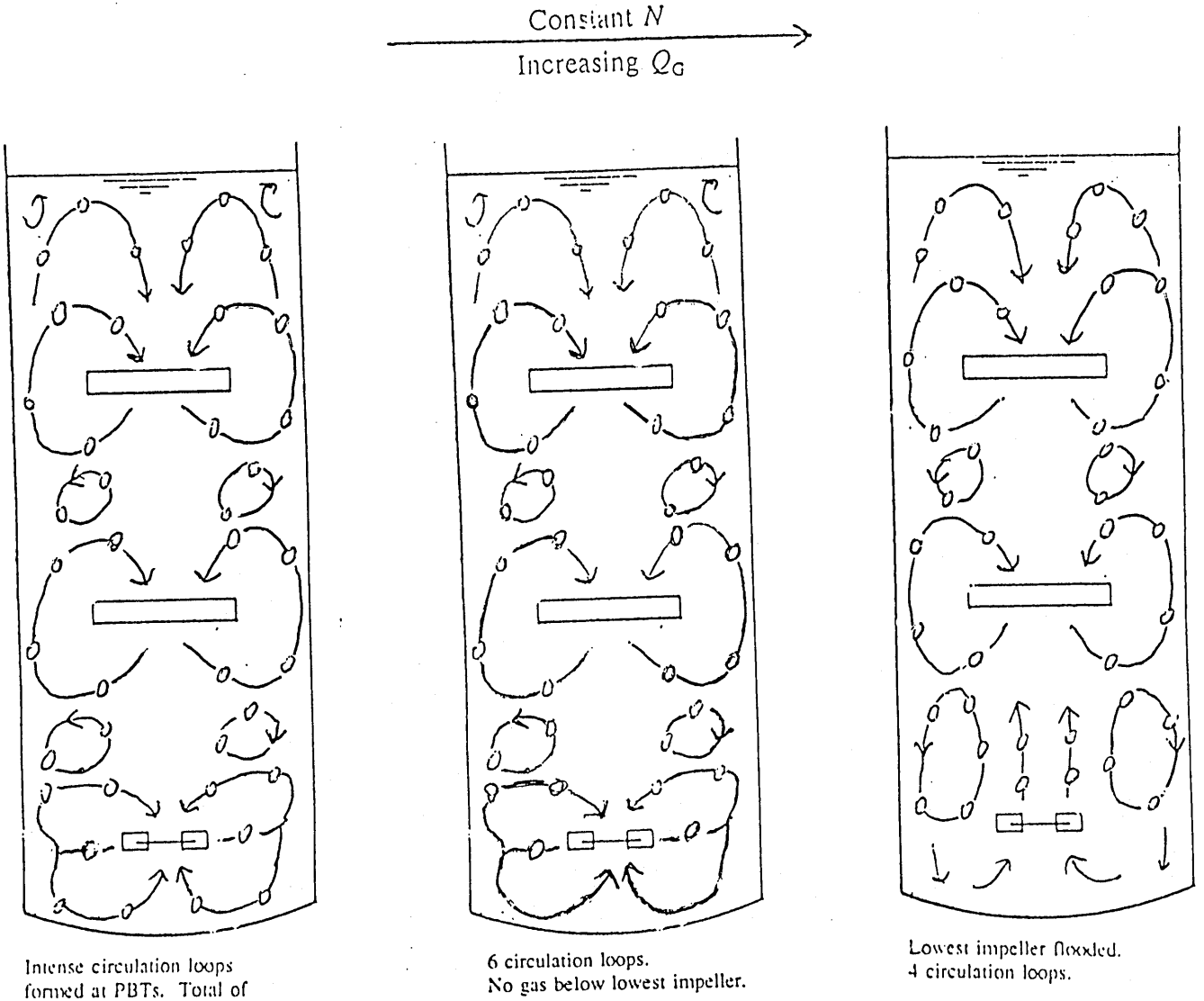
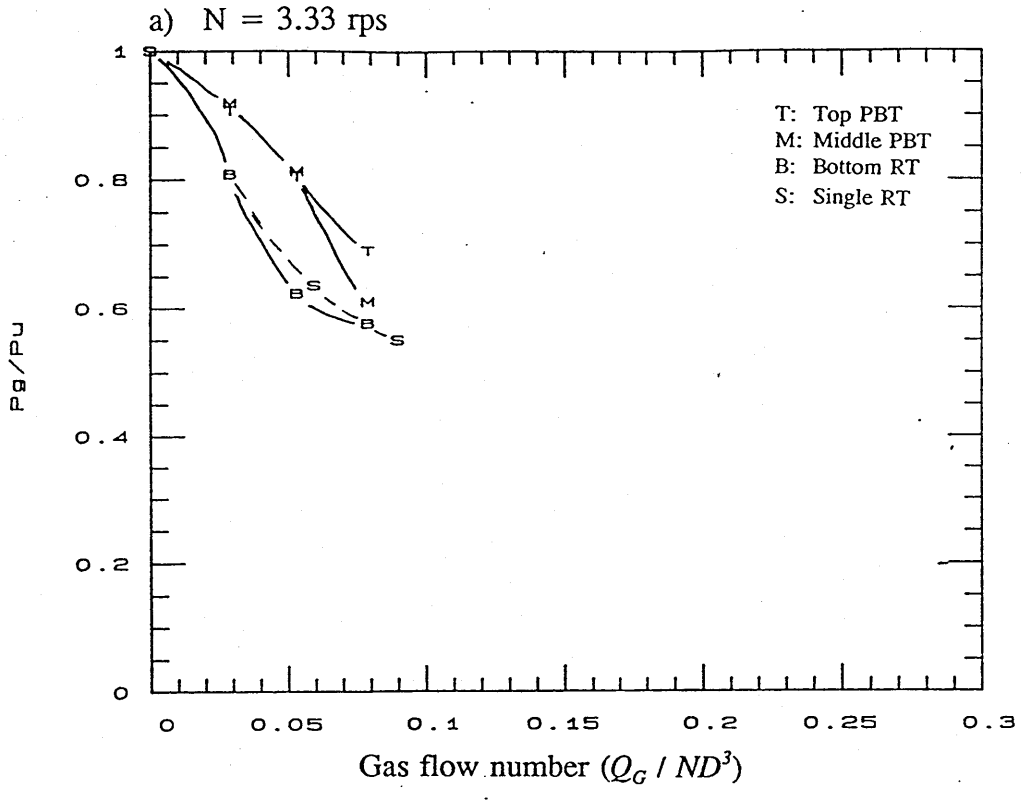


Figure 3.12: Gas liquid power draw of the 1RT+2×PBT combination (T = 0.61 m, S = 0.495 m).



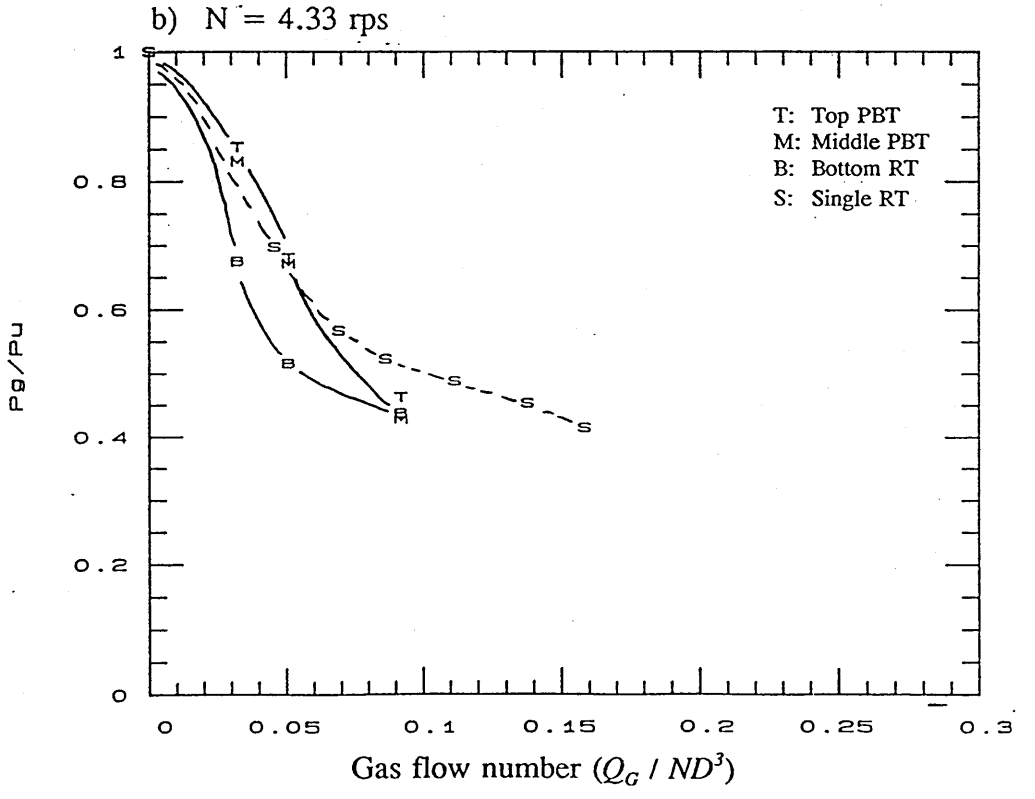
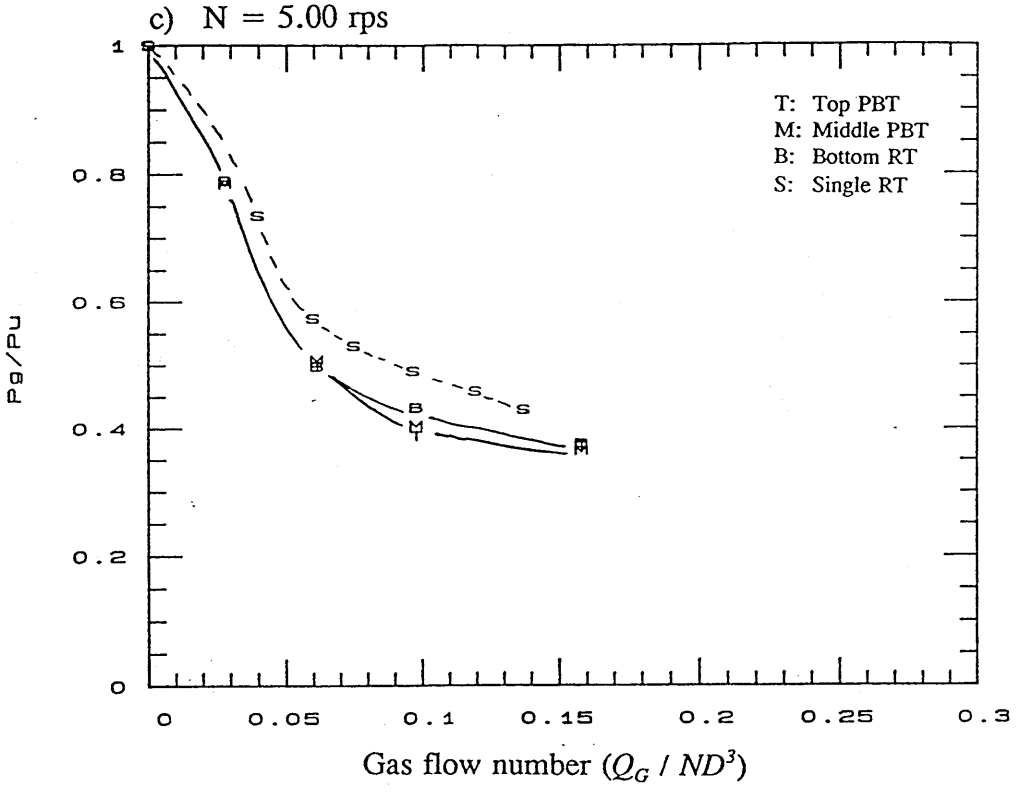


Figure 3.12: Gas liquid power draw of the 1RT+2×PBT combination (T = 0.61 m, S = 0.495 m).



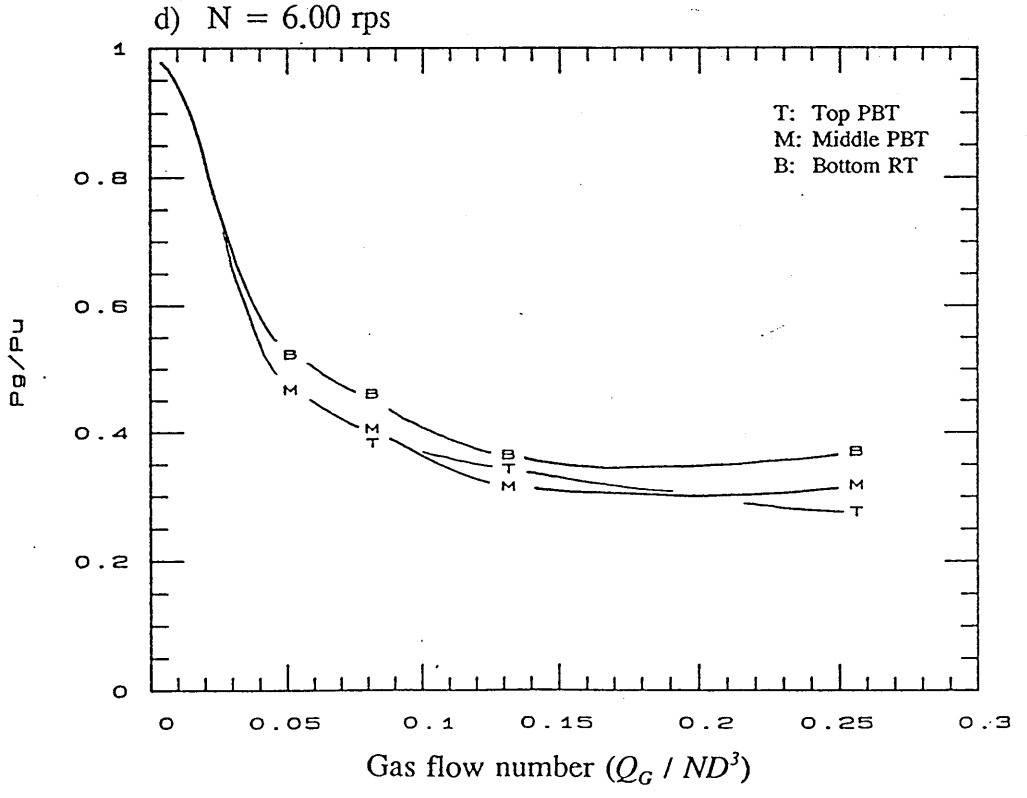
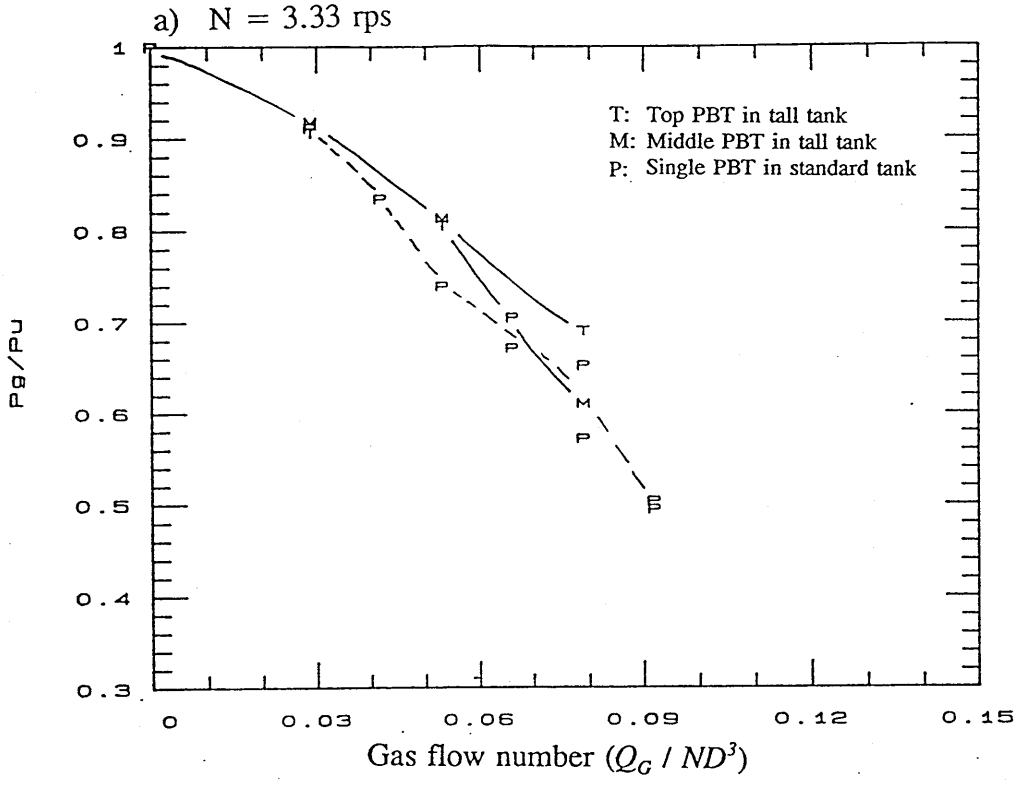


Figure 3.13: Comparison of gassed power draw for downward pumping PBT impellers in the tall tank and a standard tank.



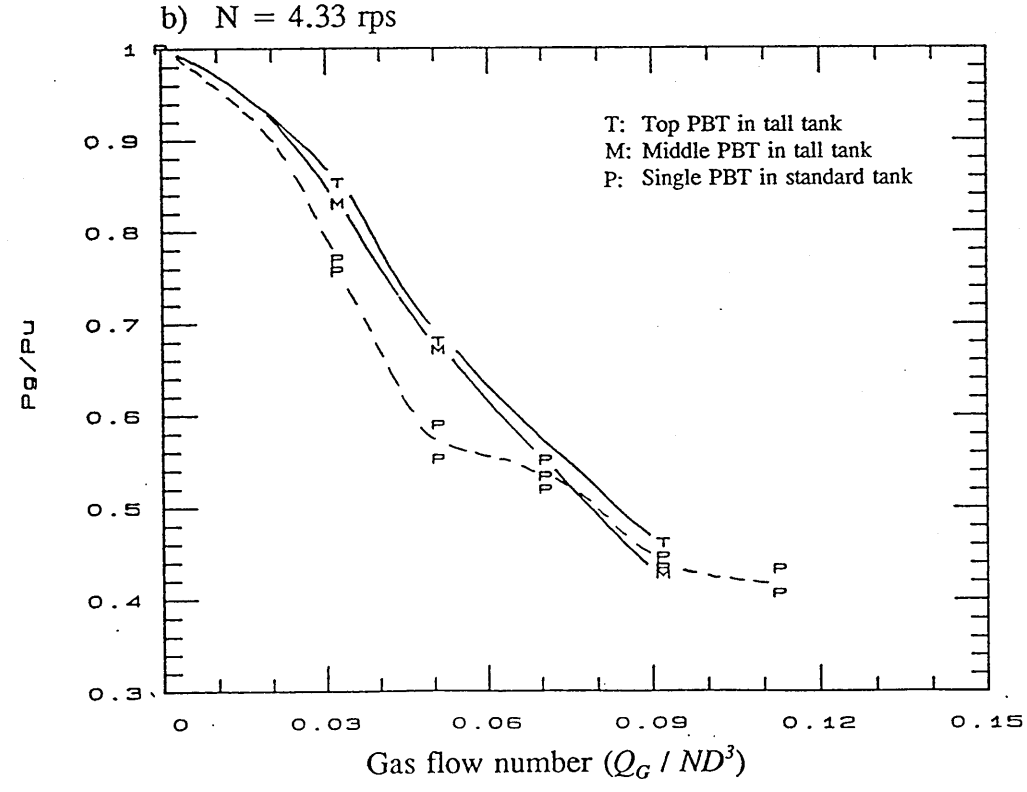


Figure 3.13: Comparison of gassed power draw for downward pumping PBT impellers in the tall tank and a standard tank.

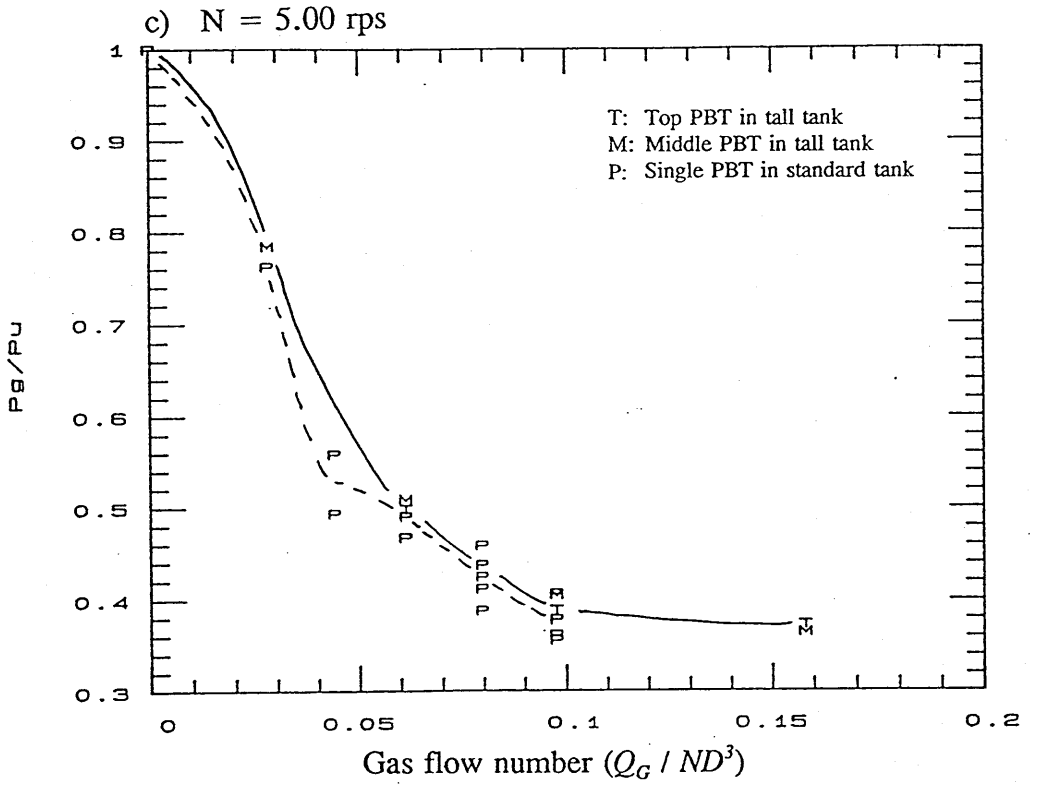


Figure 3.14: Gas liquid flow patterns observed with the 1RT+2×PBT (pumping up) combination (T = 0.61 m, S = 0.495 m).

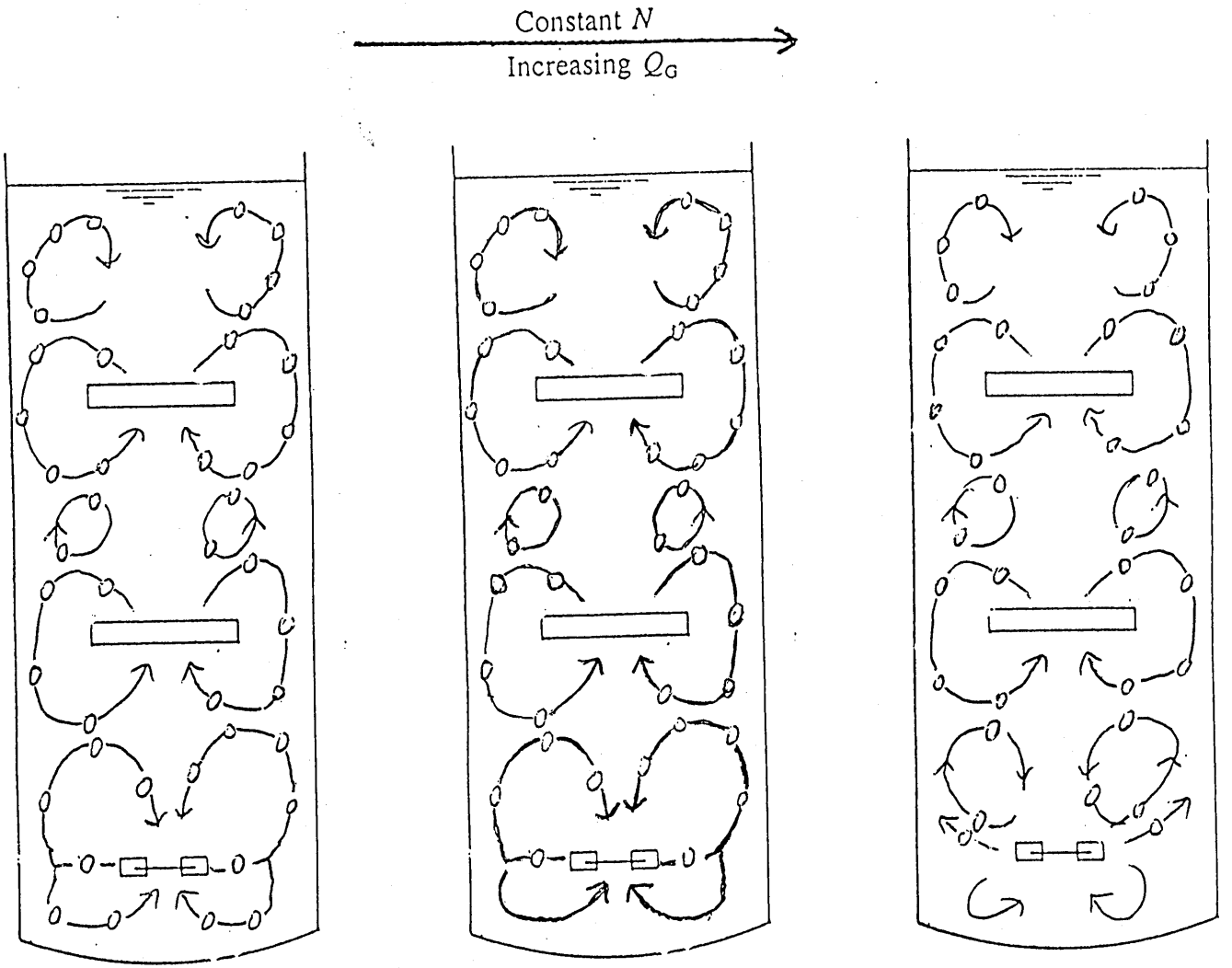
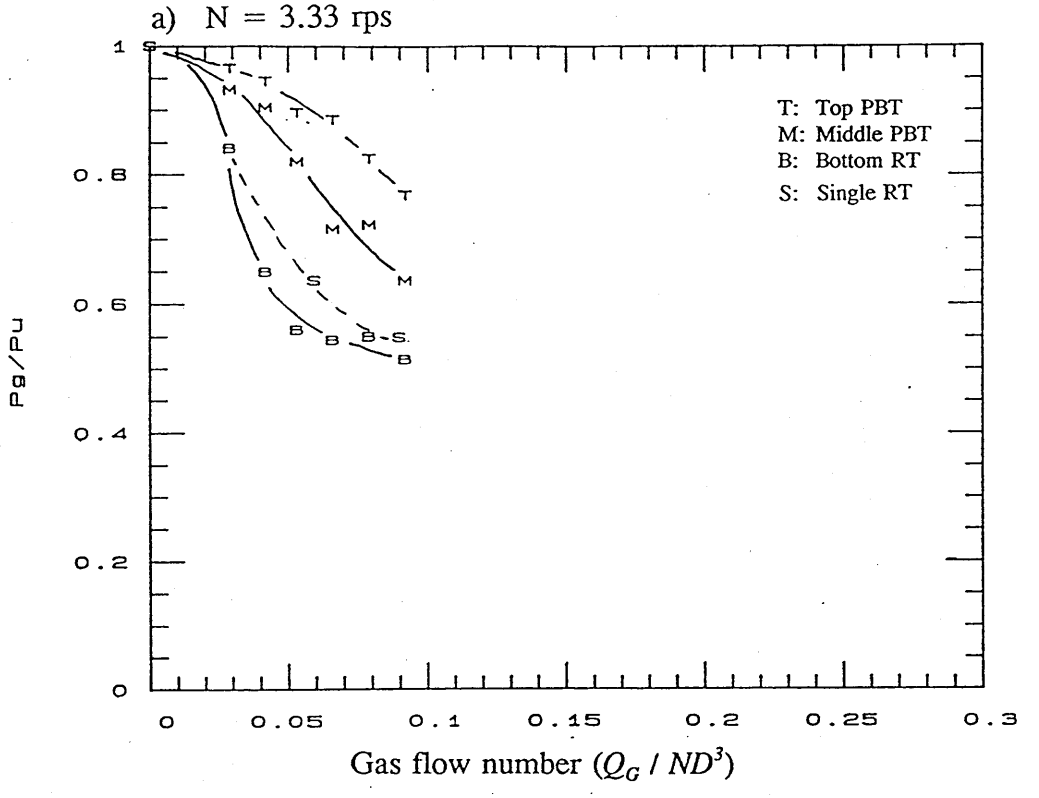


Figure 3.15: Gas liquid power draw of the 1RT+2×PBT (pumping up) combination (T = 0.61 m, S = 0.495 m).



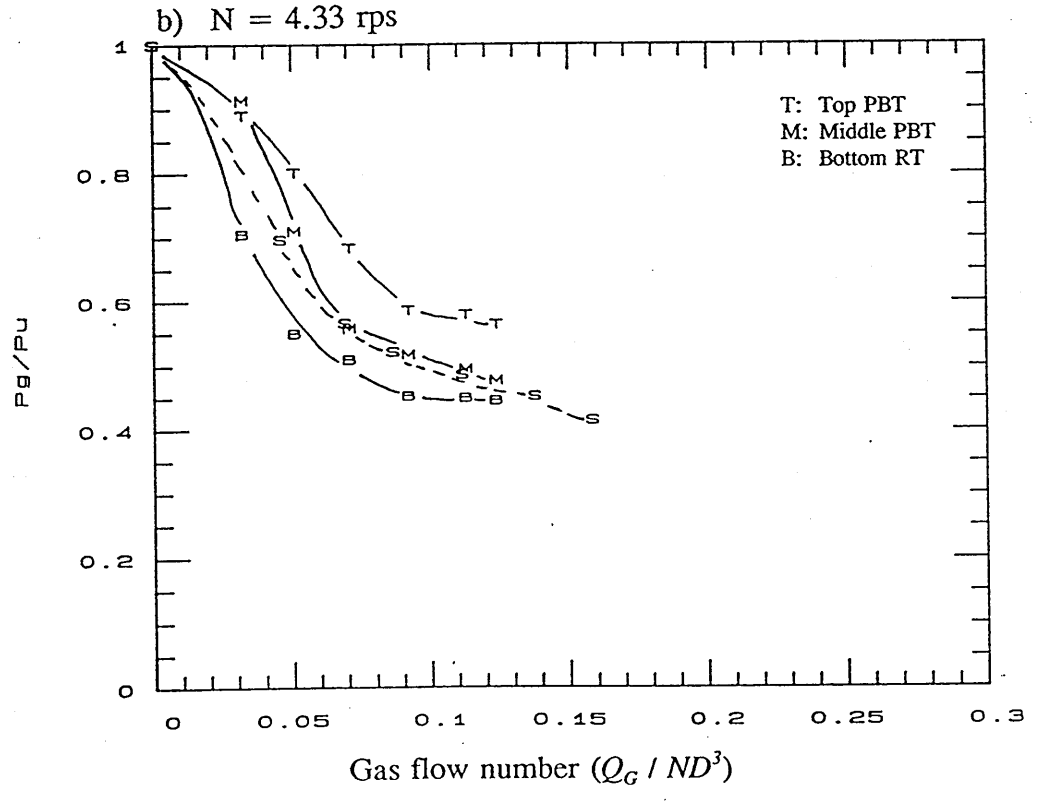
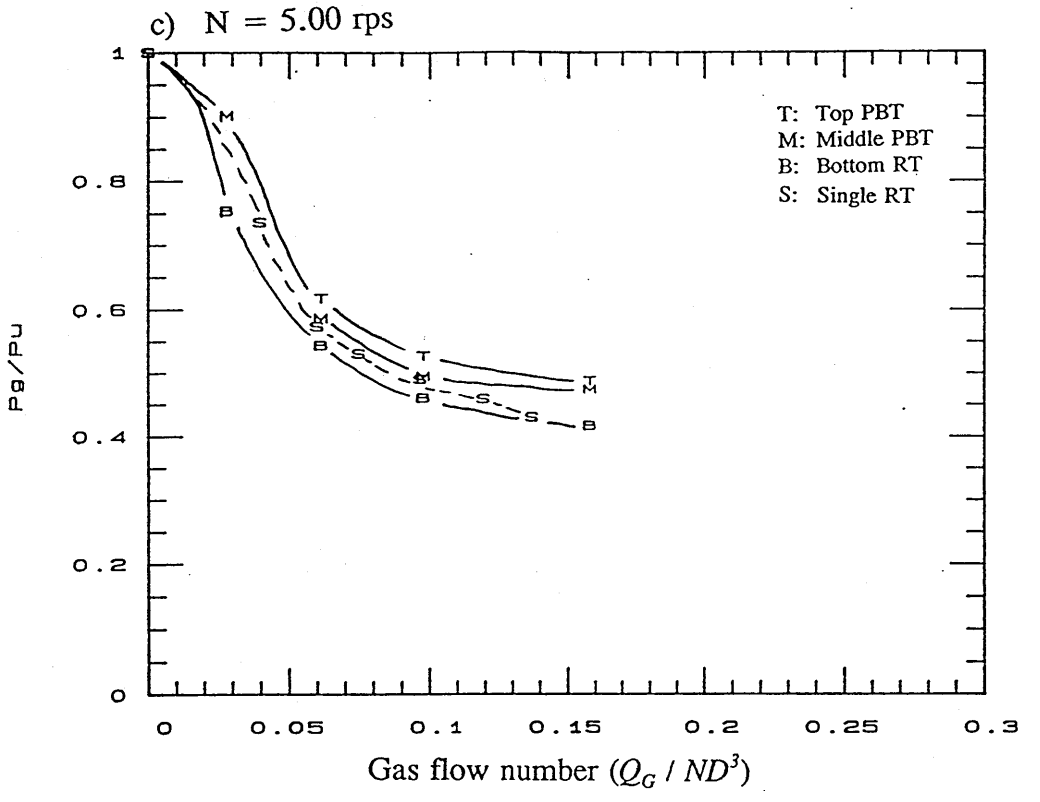


Figure 3.15: Gas liquid power draw of the 1RT+2×PBT (pumping up) combination (T = 0.61 m, S = 0.495 m).



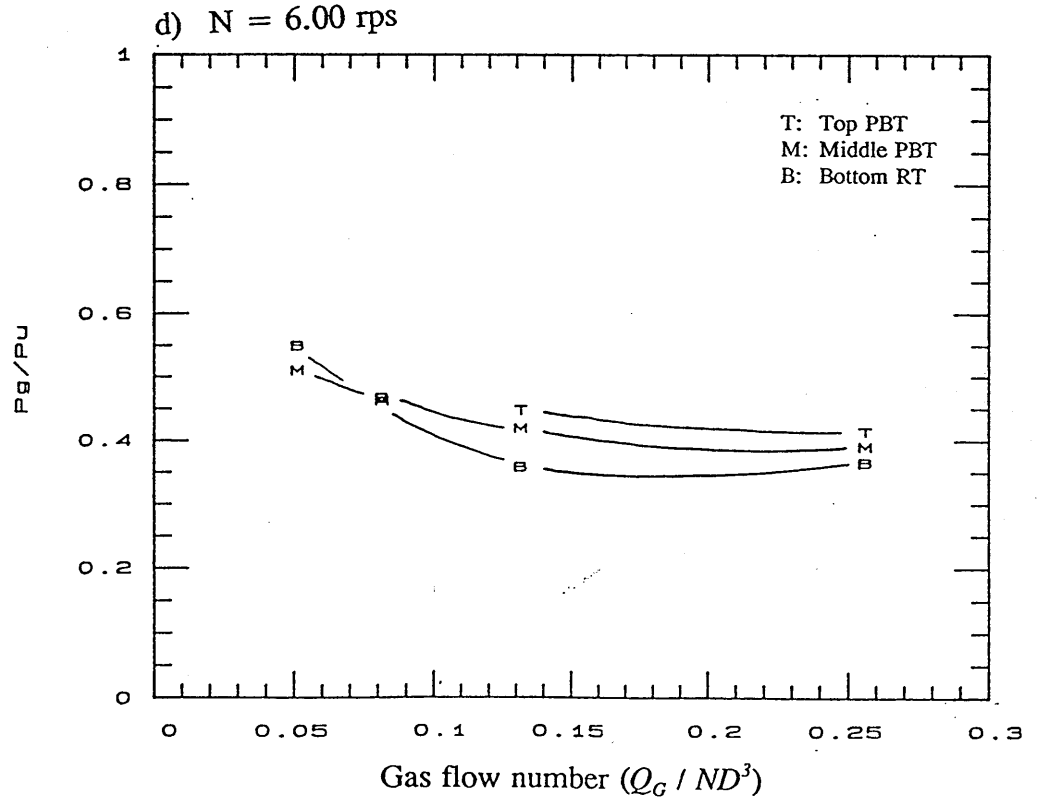
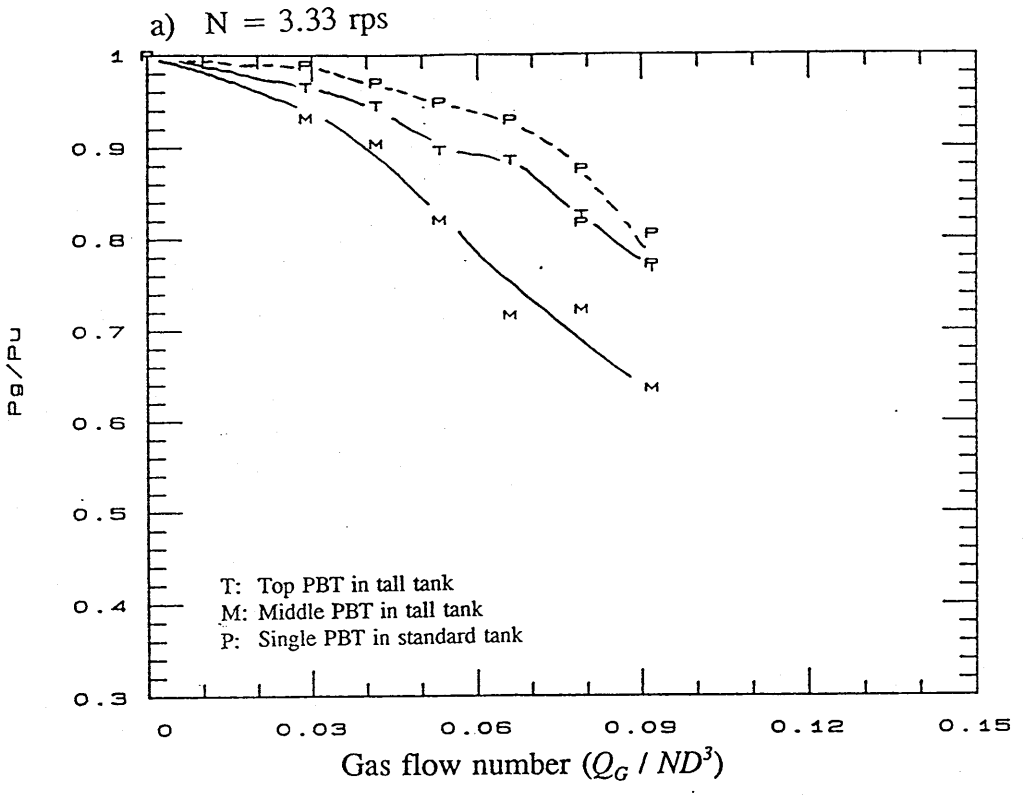


Figure 3.16: Comparison of gassed power draw for upward pumping PBT impellers in the tall tank and a standard tank.



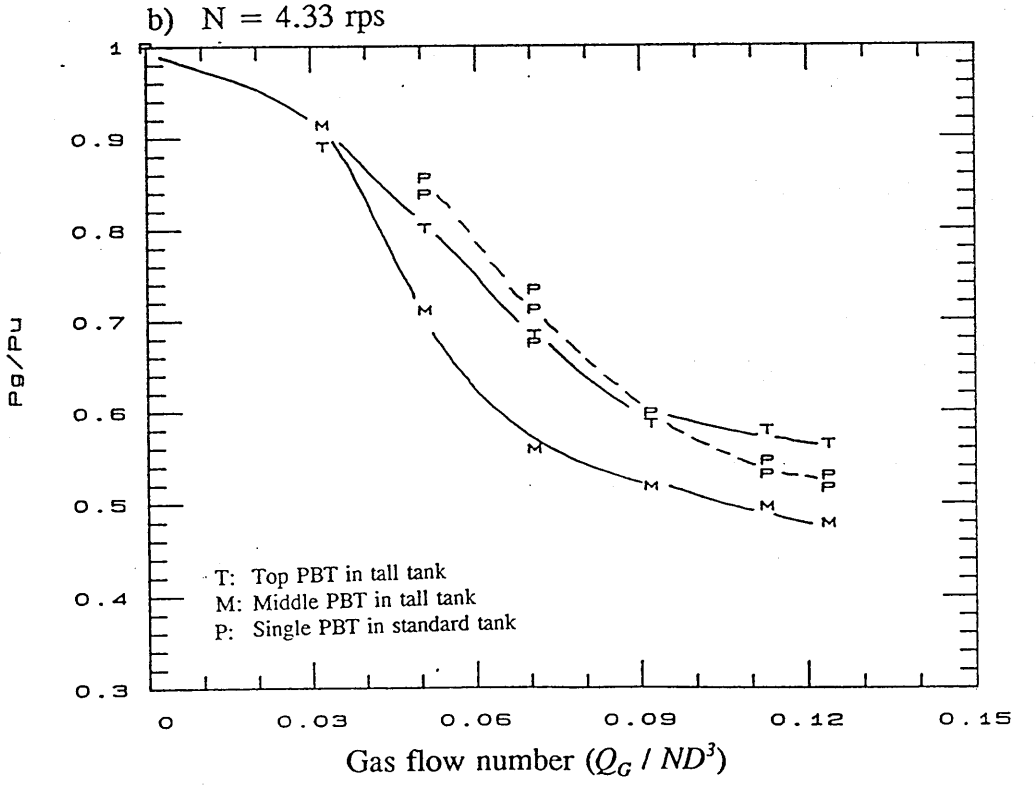


Figure 3.16: Comparison of gassed power draw for upward pumping PBT impellers in the tall tank and a standard tank.

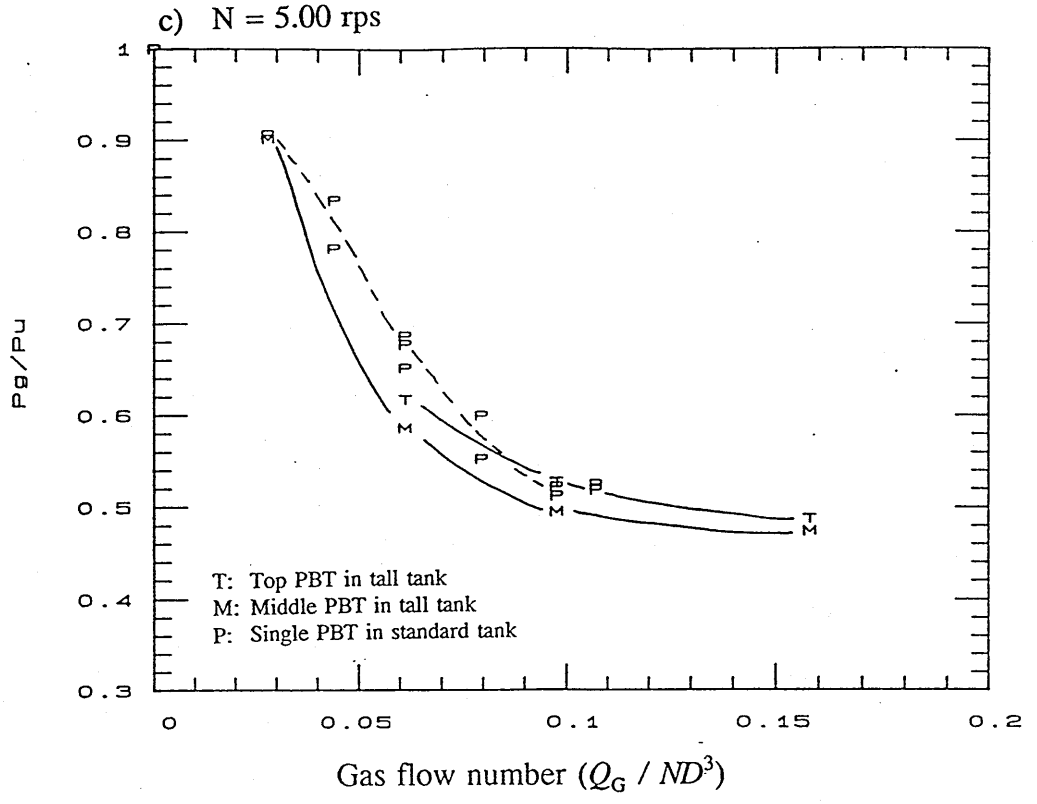


Figure 3.17: Flow map for triple Rushton turbines (T = 0.95 m).

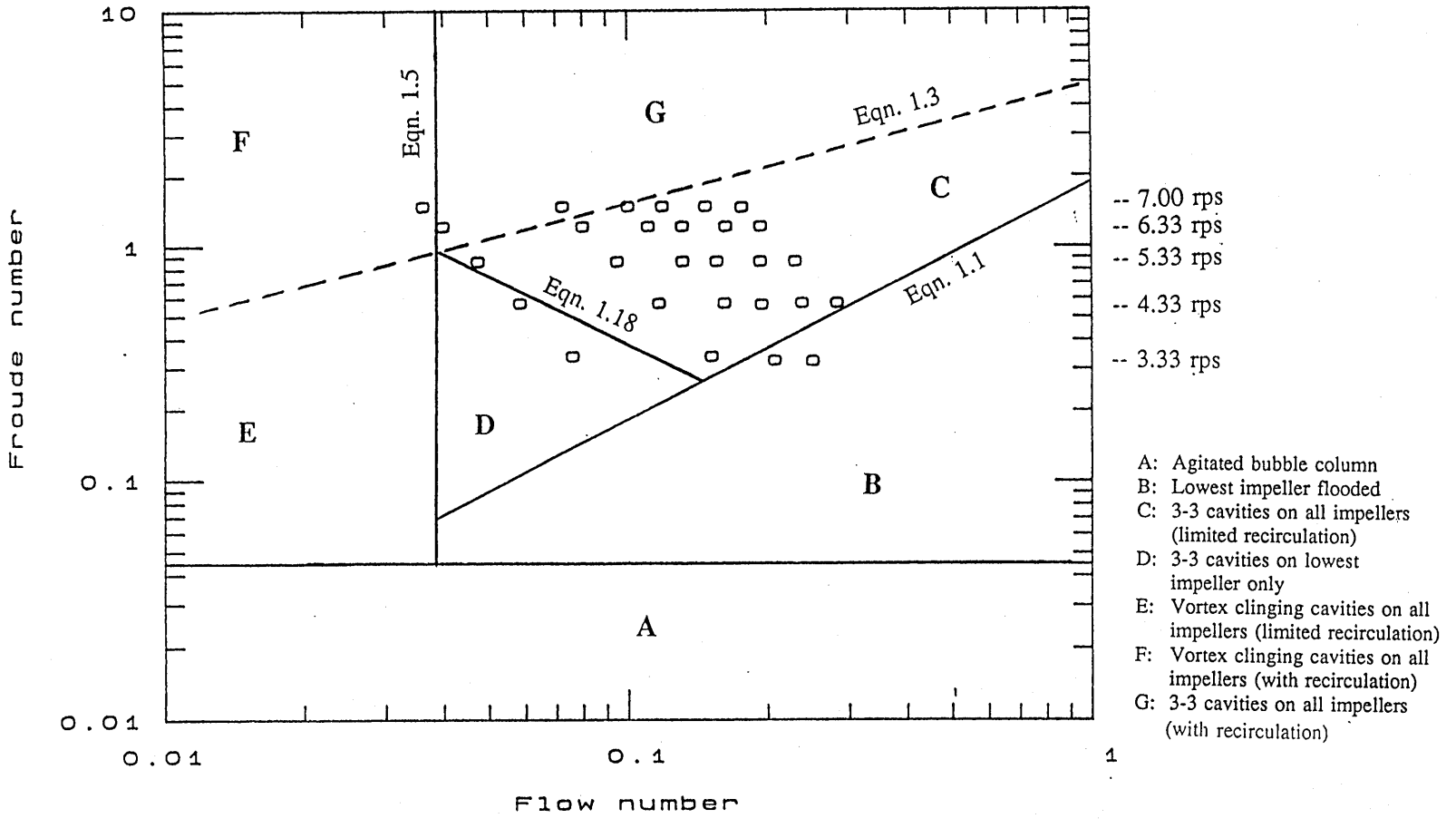
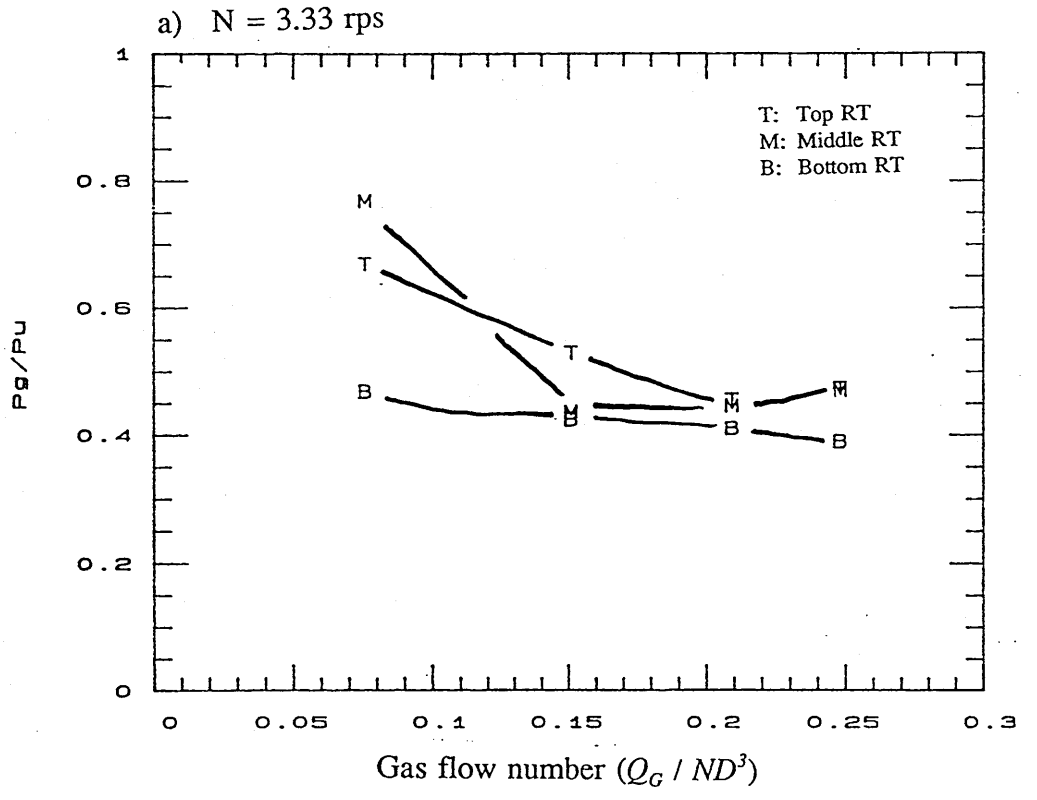


Figure 3.18: Gassed power draw of triple Rushton turbine combination (T = 0.95 m).



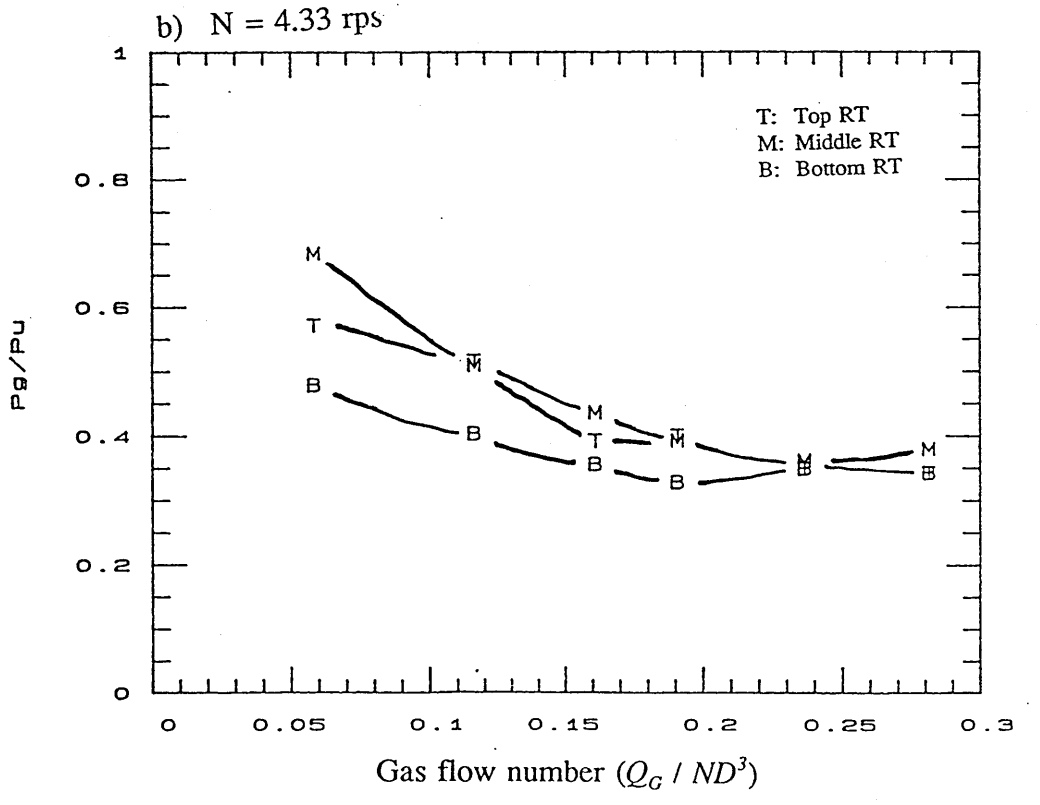
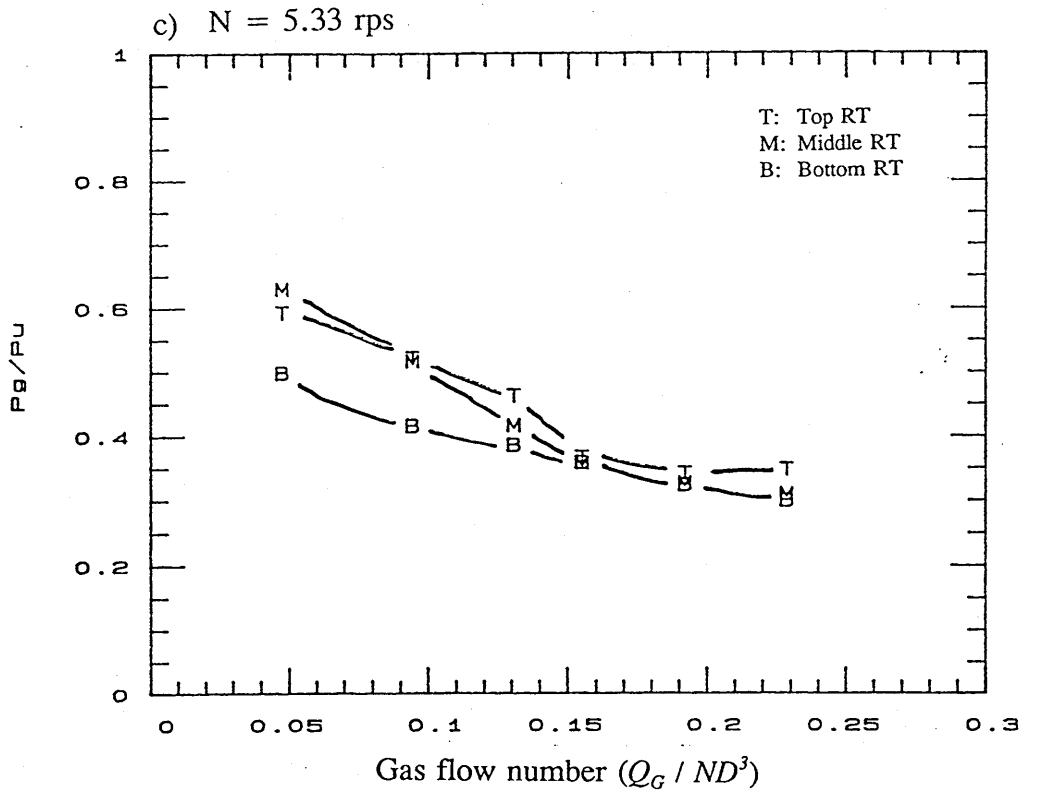


Figure 3.18: Gassed power draw of triple Rushton turbine combination (T = 0.95 m).



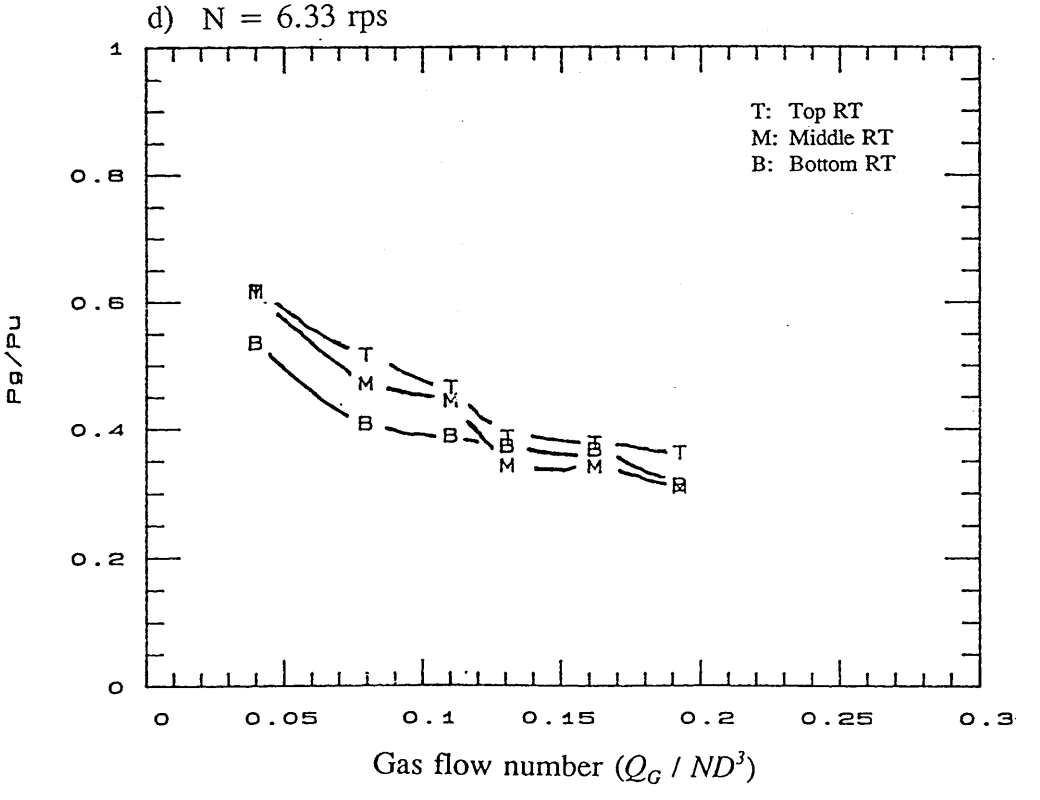
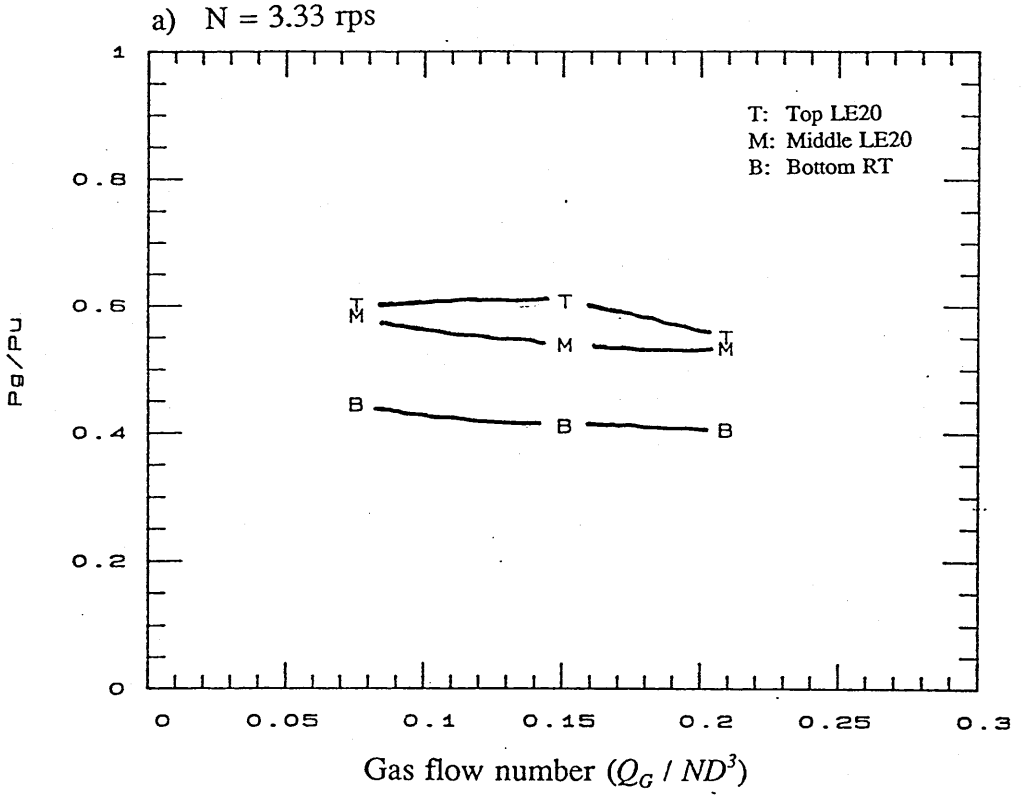


Figure 3.19: Gassed power draw of the 1RT+2×LE20 combination (T = 0.95 m).



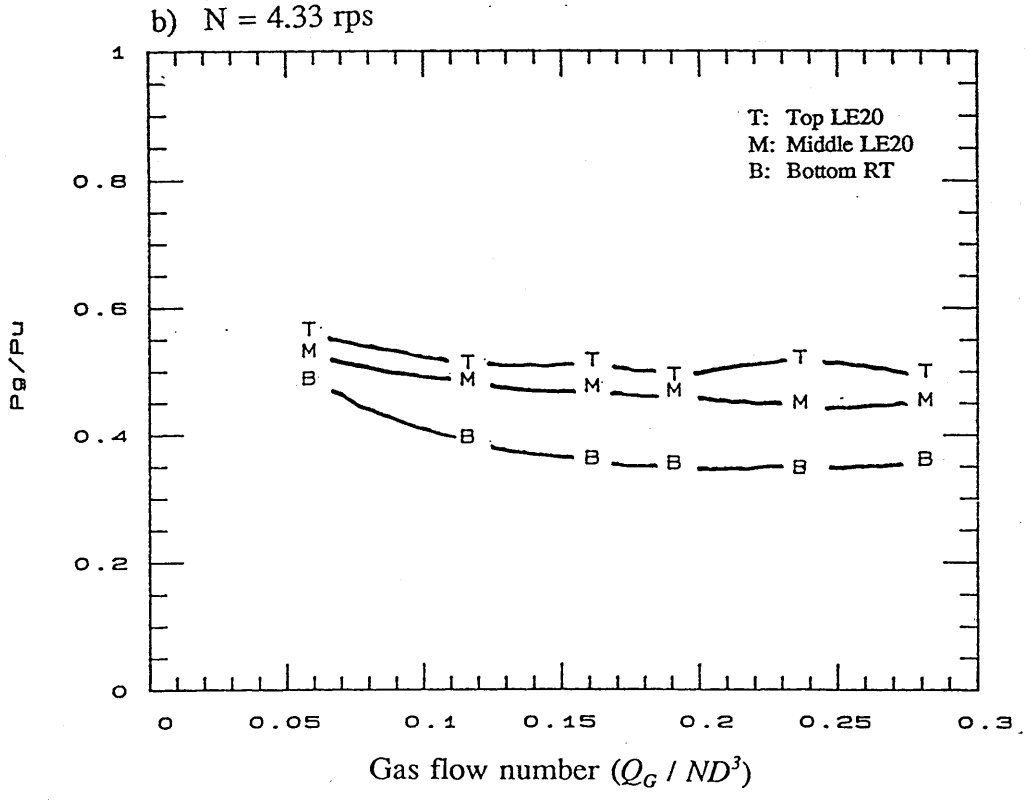


Figure 3.19: Gassed power draw of the 1RT+2×LE20 combination (T = 0.95 m).

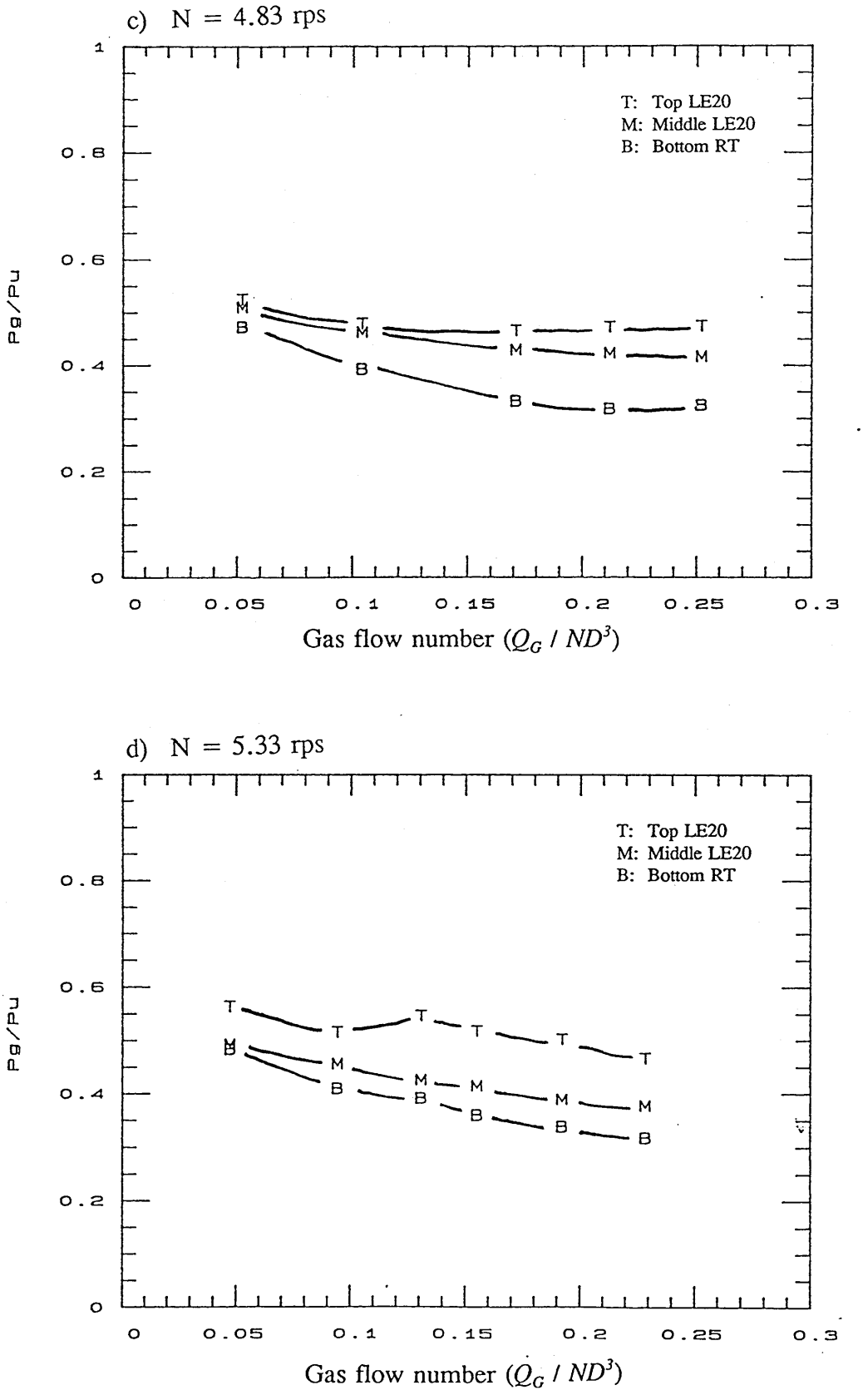
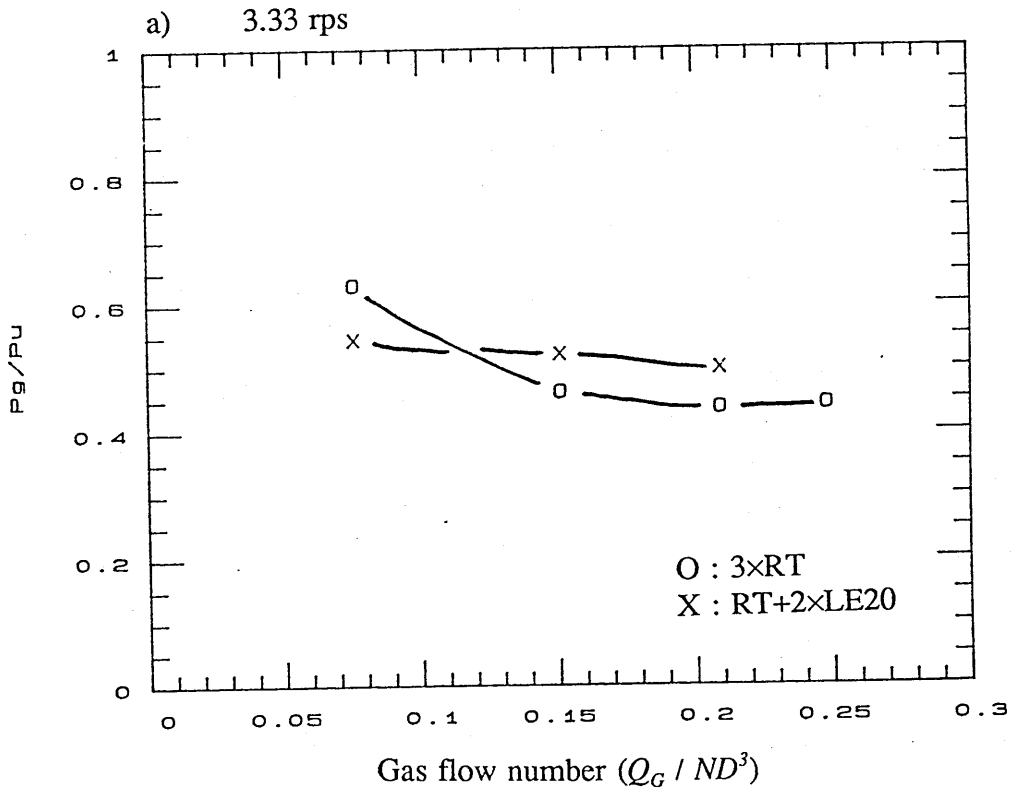


Figure 3.20: Total gassed power draw: Comparison of impeller combinations at given impeller speed T = 0.95 m



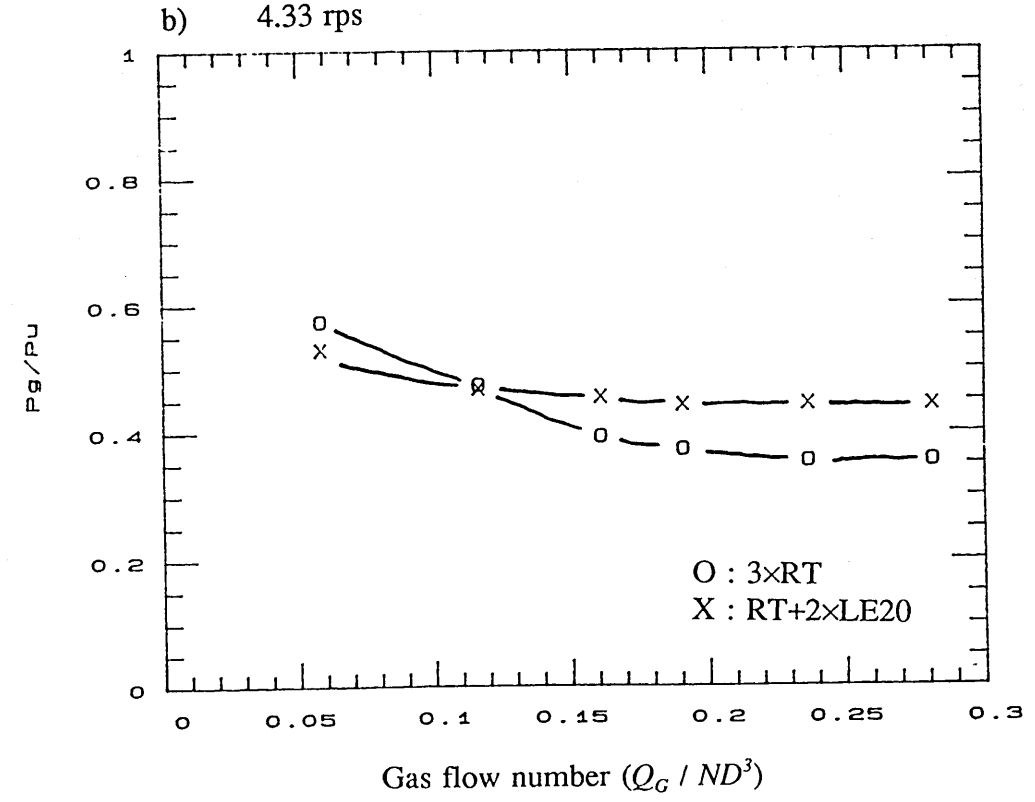


Figure 3.20: Total gassed power draw: Comparison of impeller combinations at given impeller speed T = 0.95 m

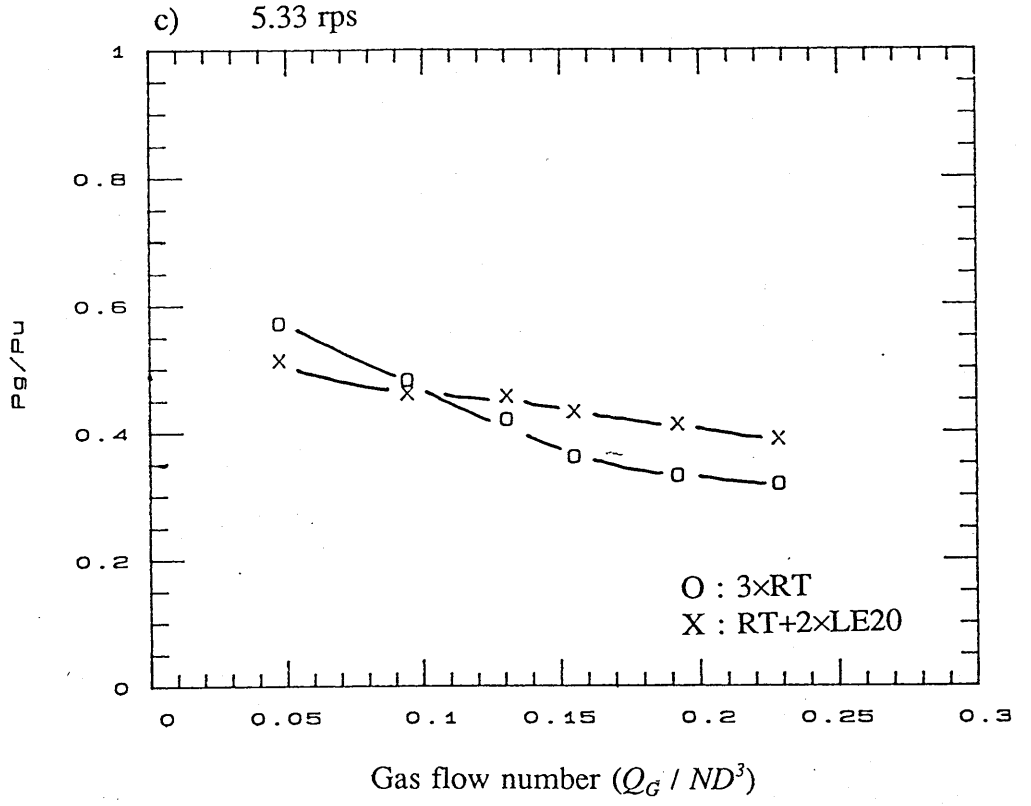
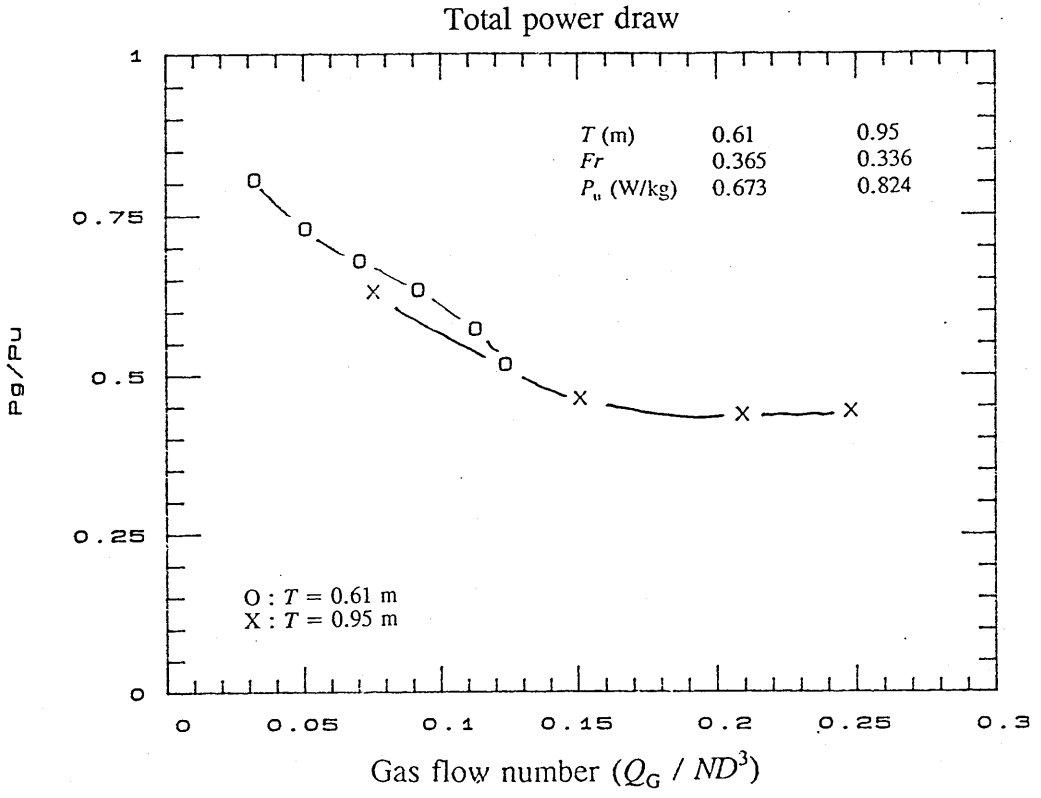


Figure 3.21: Comparison of power draw at different scales (3RT combination).

a) Constant Froude number



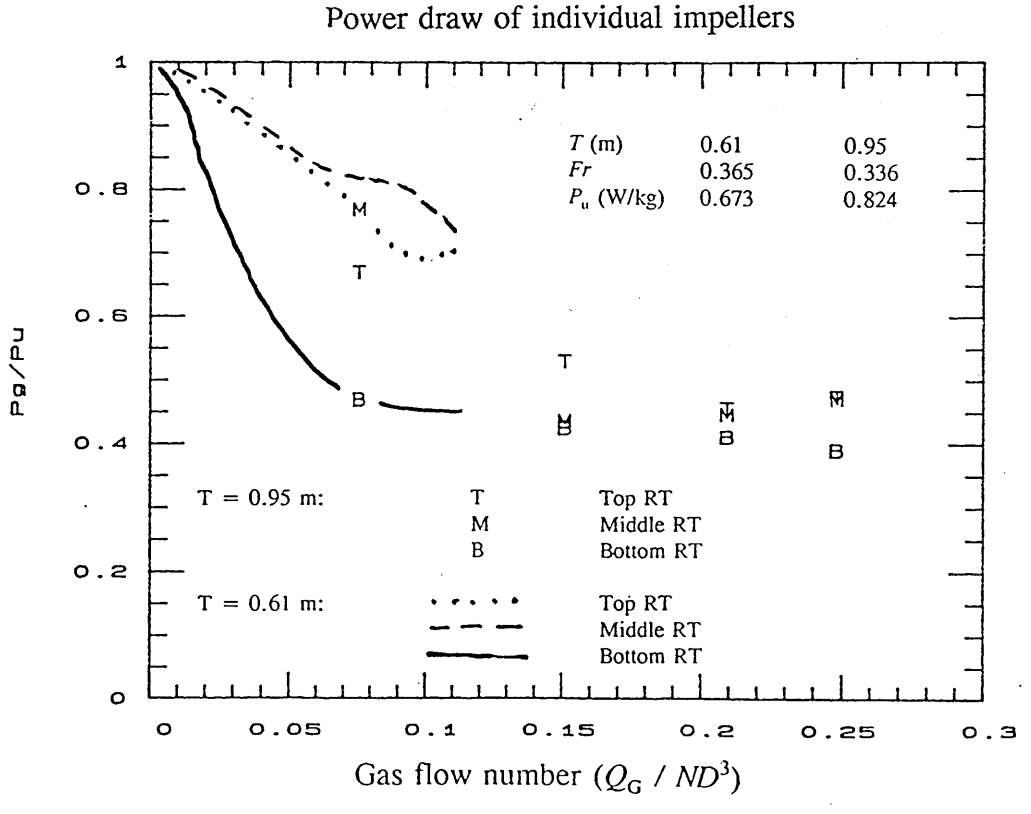
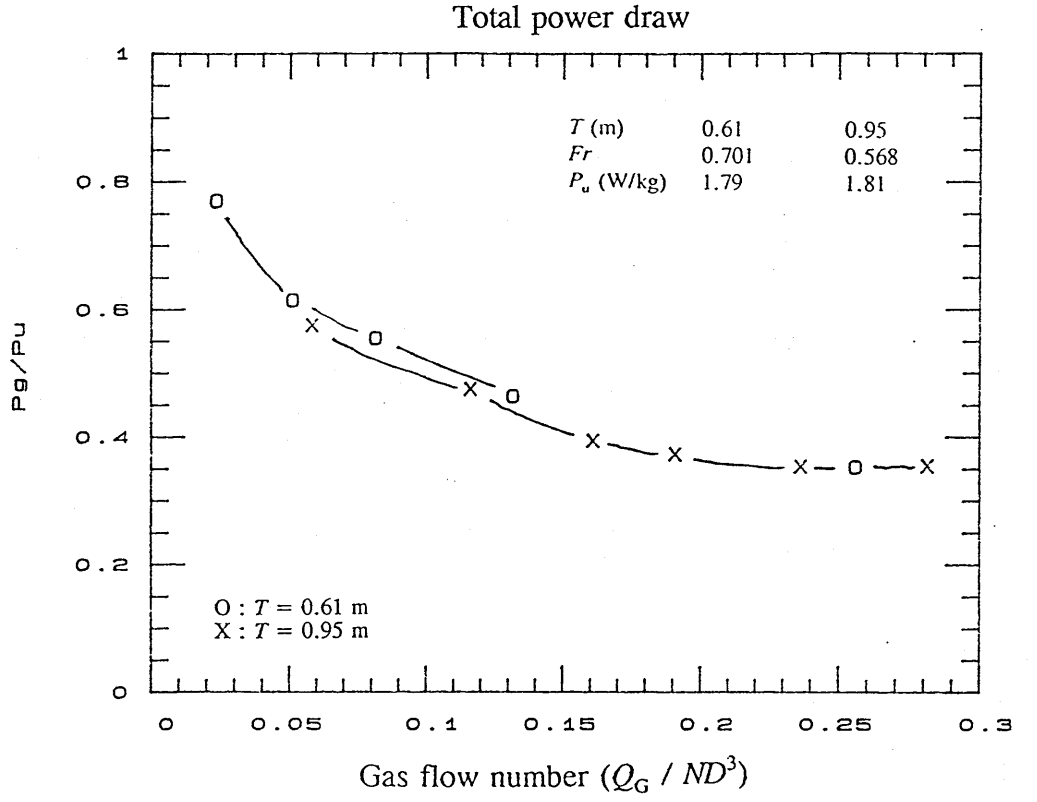


Figure 3.21: Comparison of power draw at different scales (3RT combination).

b) Constant ungassed power draw



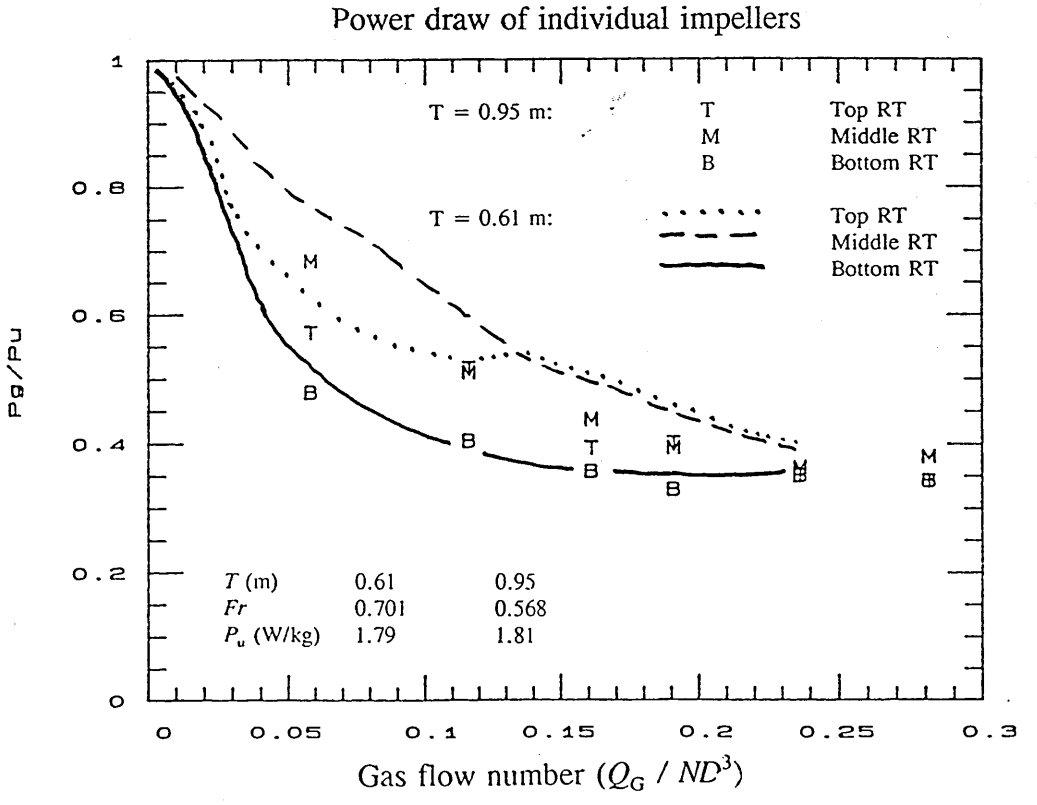
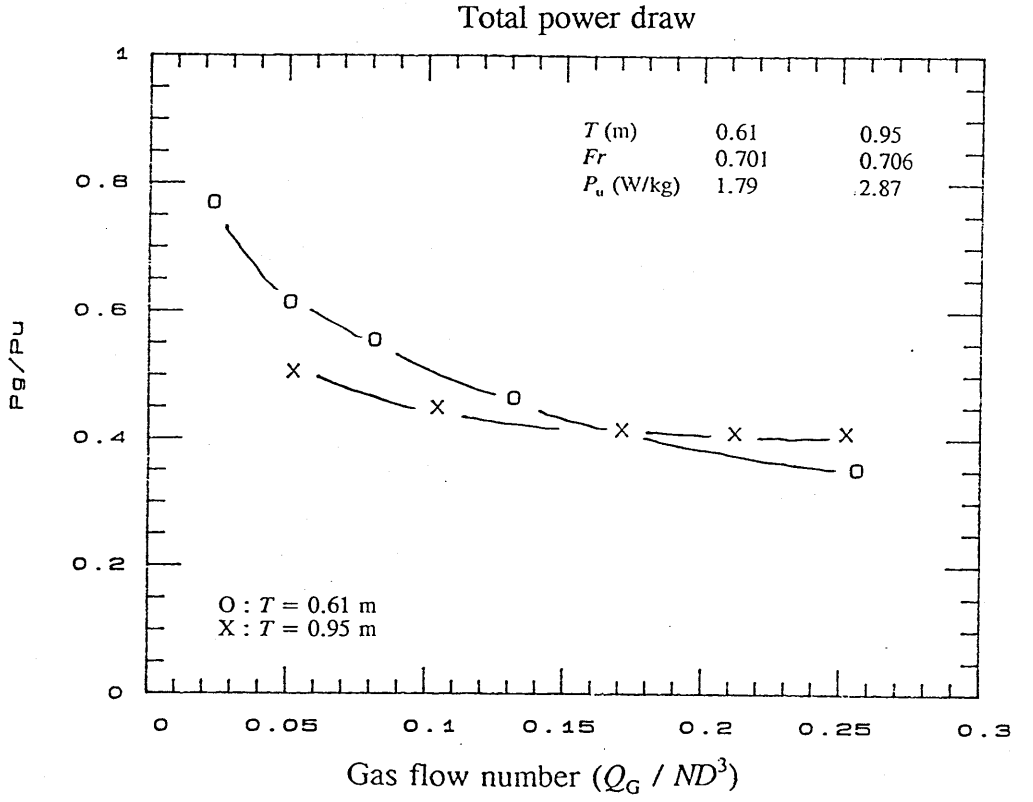


Figure 3.22: Comparison of power draw at different scales (1RT+2LE20 combination).

a) Constant Froude number



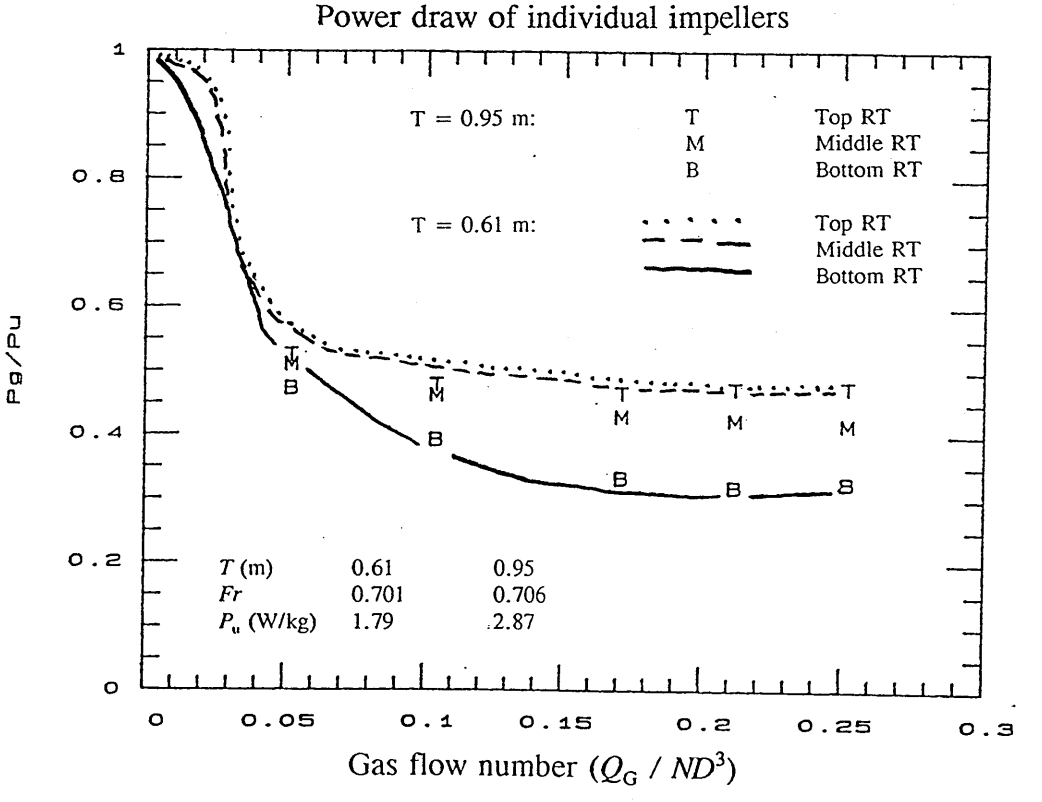
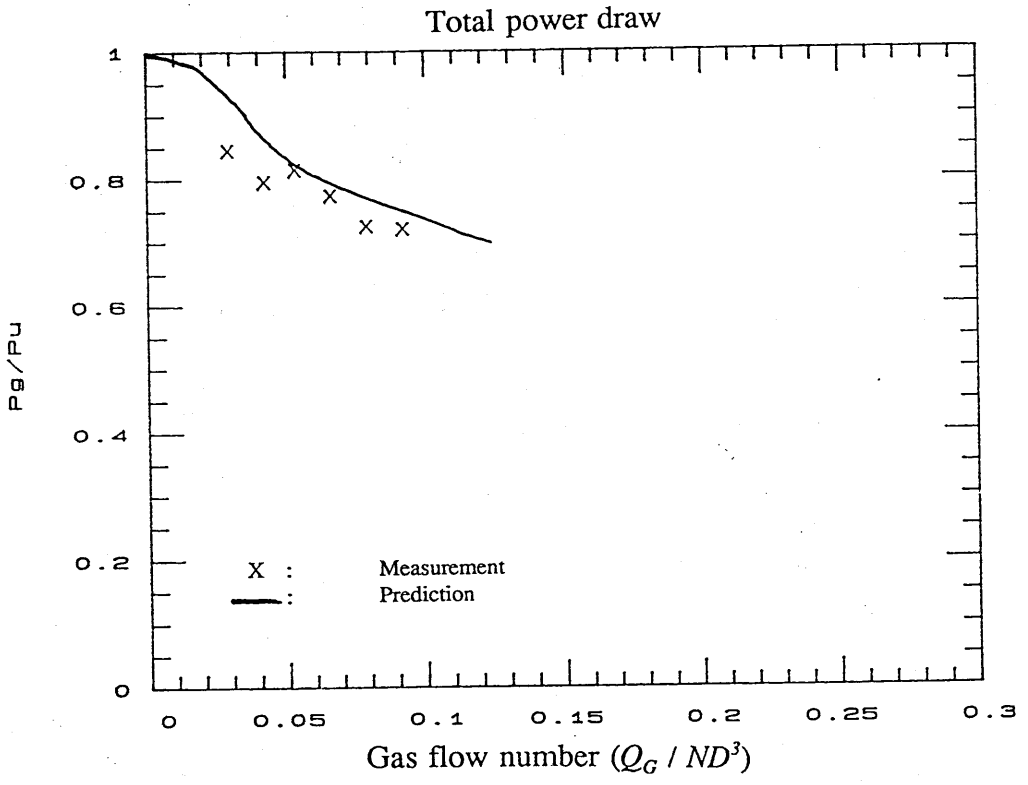


Figure 3.23: Prediction of gassed power draw for triple Rushton turbines.

a) T = 0.61 m, N = 3.33 rps



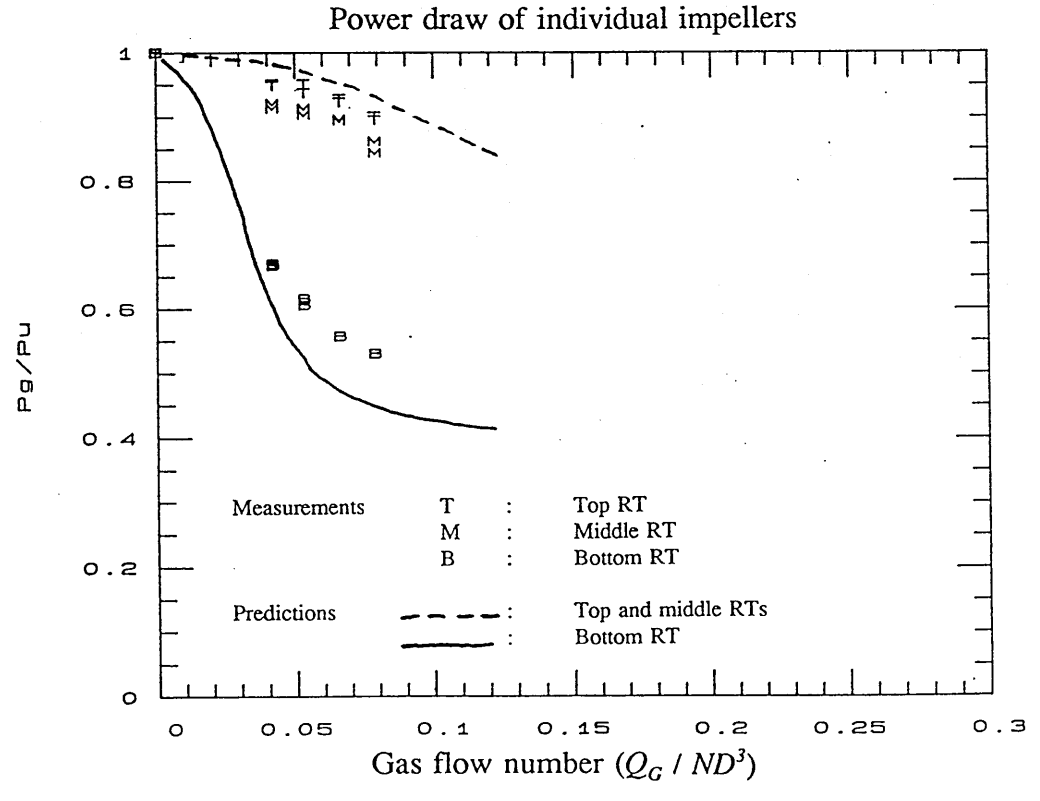
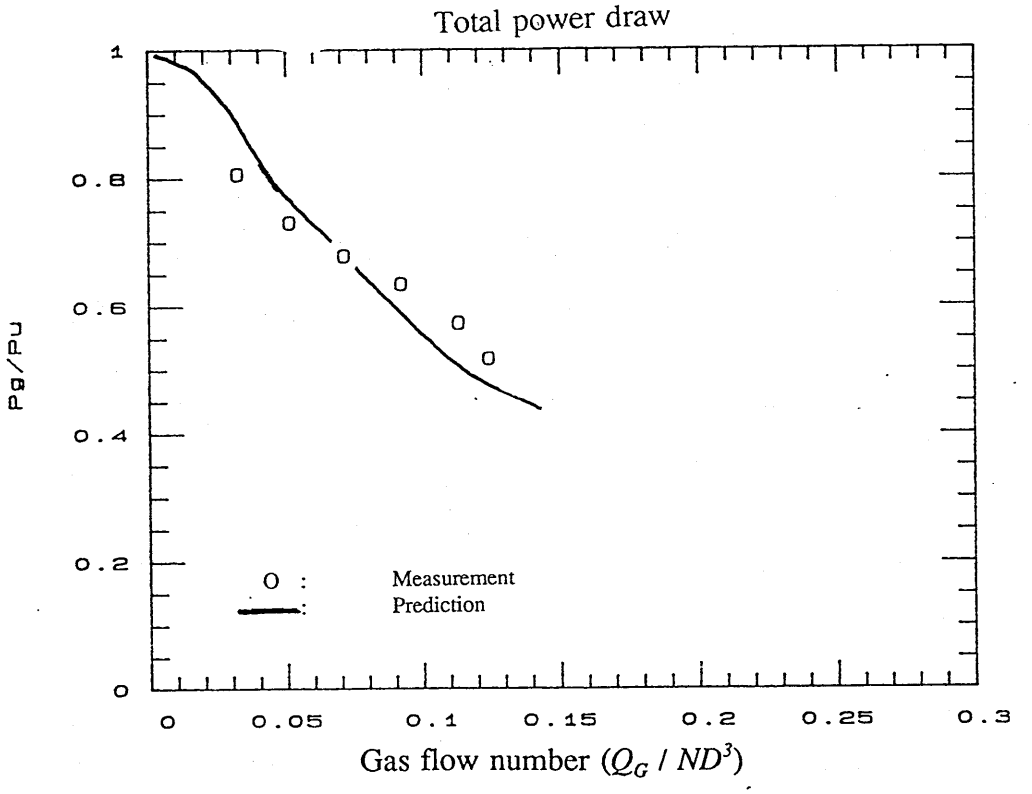


Figure 3.23: Prediction of gassed power draw for triple Rushton turbines.

b) T = 0.61 m, N = 4.33 rps



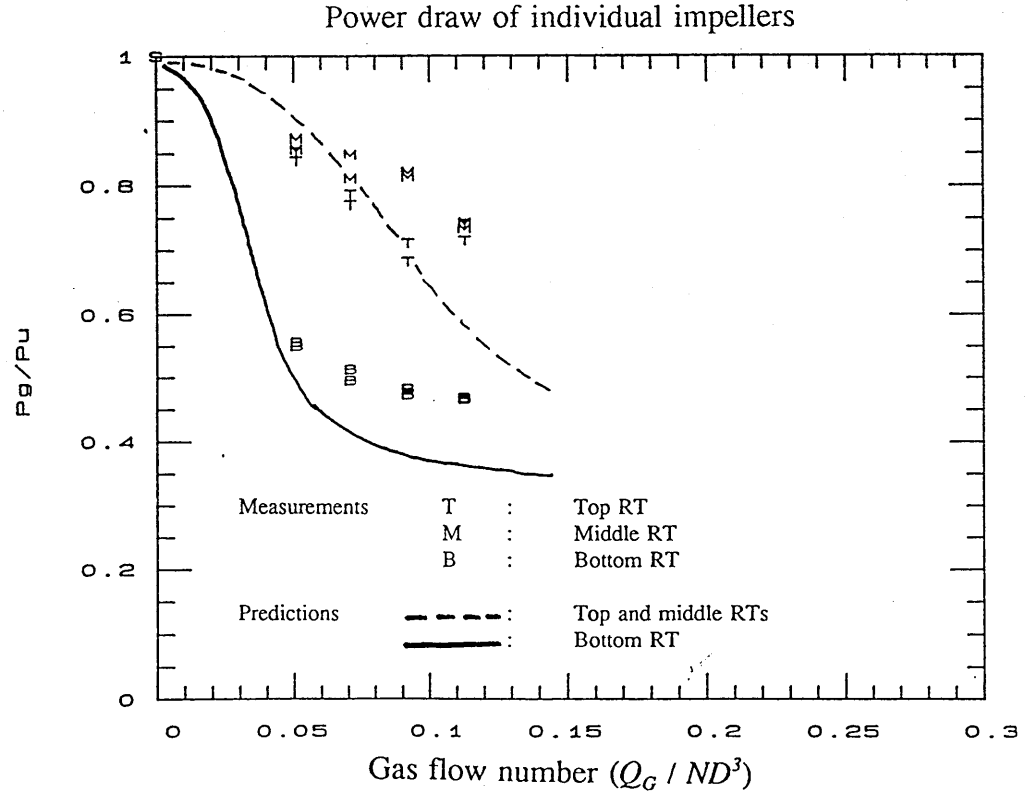
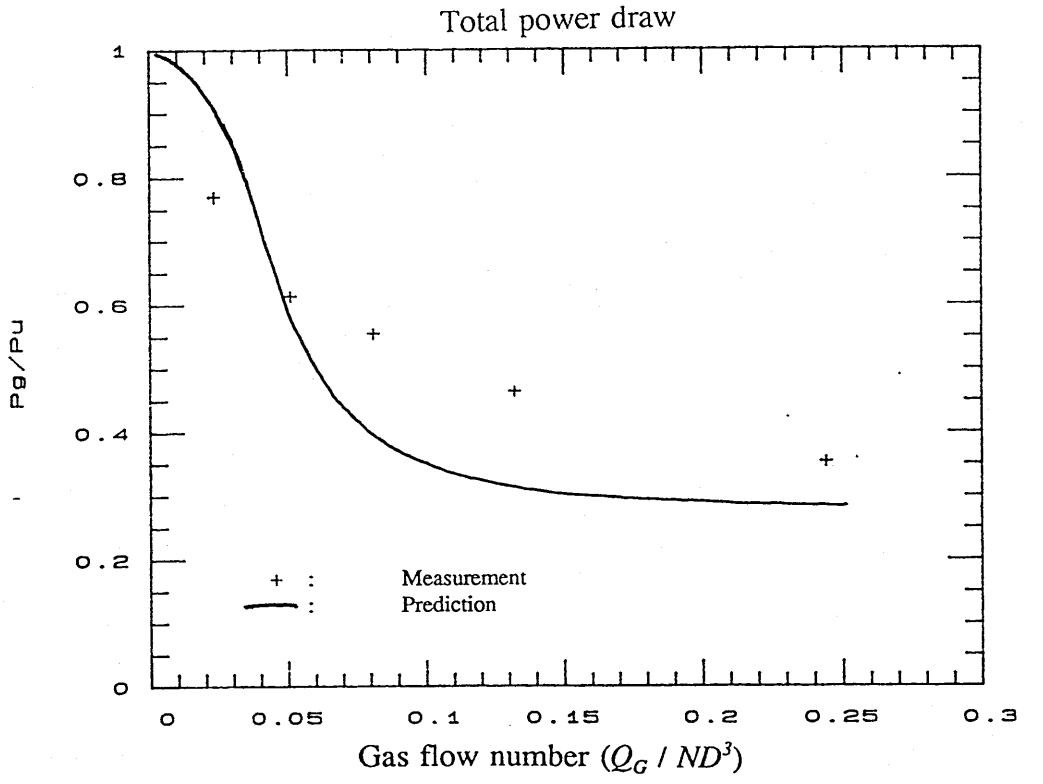


Figure 3.23: Prediction of gassed power draw for triple Rushton turbines.

c) T = 0.61 m, N = 6.00 rps



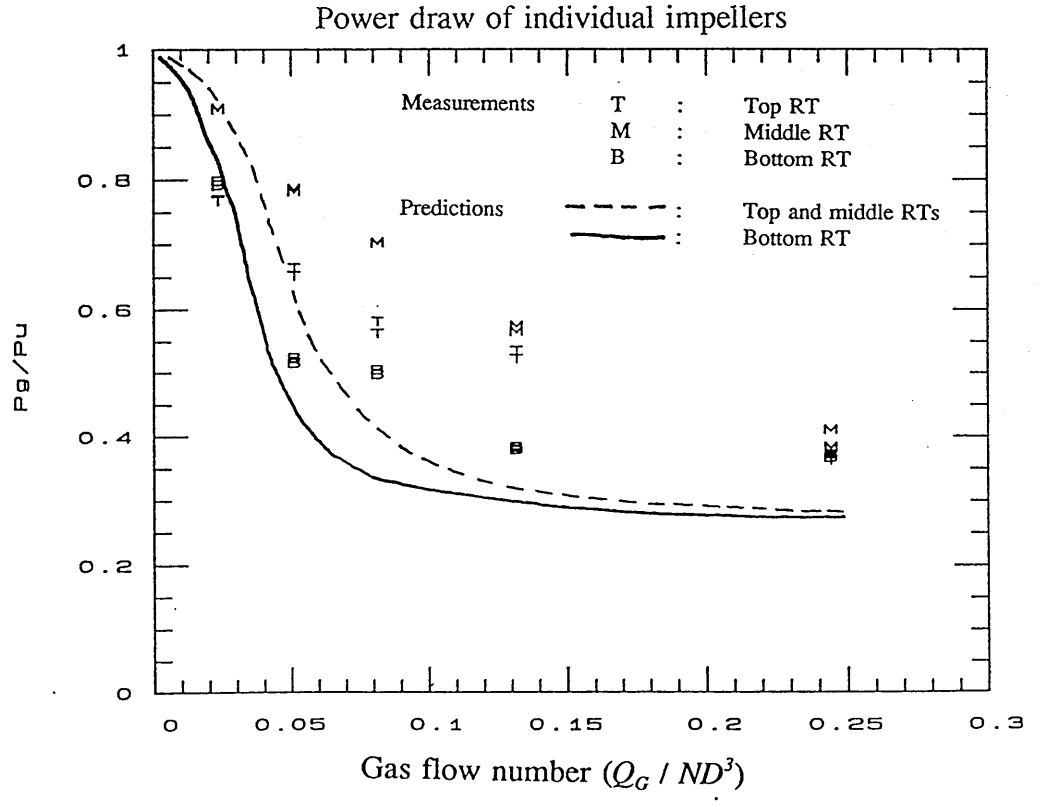
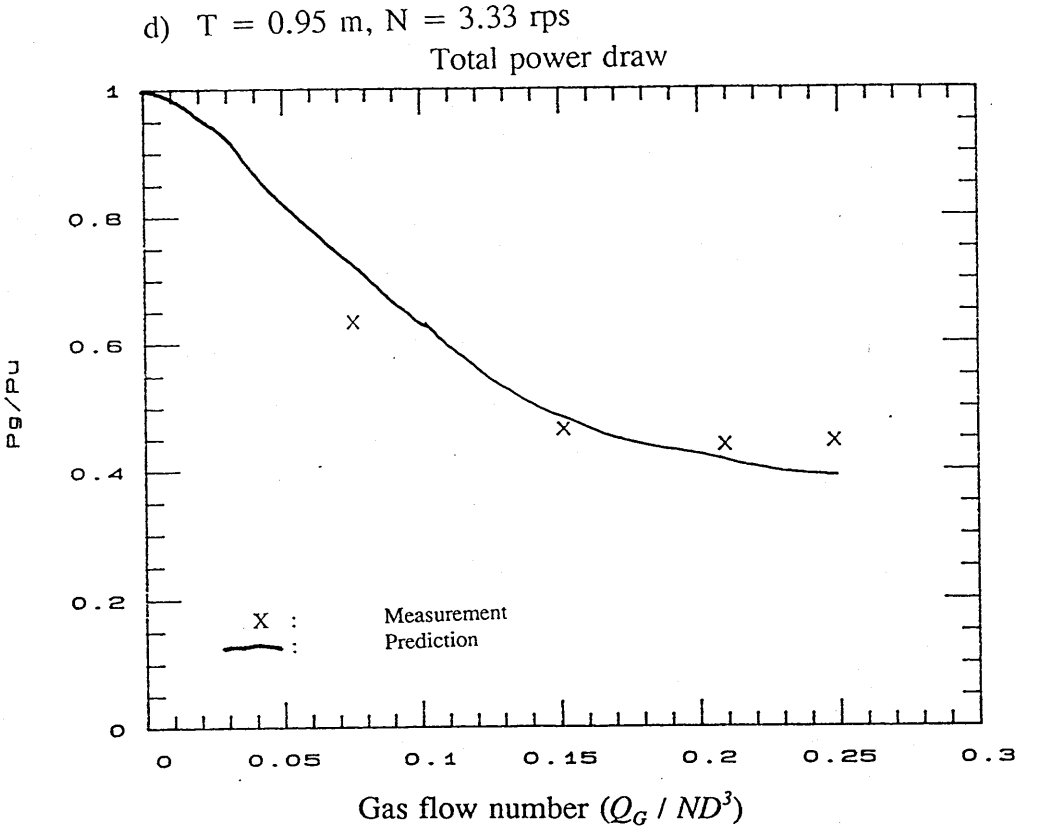


Figure 3.23: Prediction of gassed power draw for triple Rushton turbines.



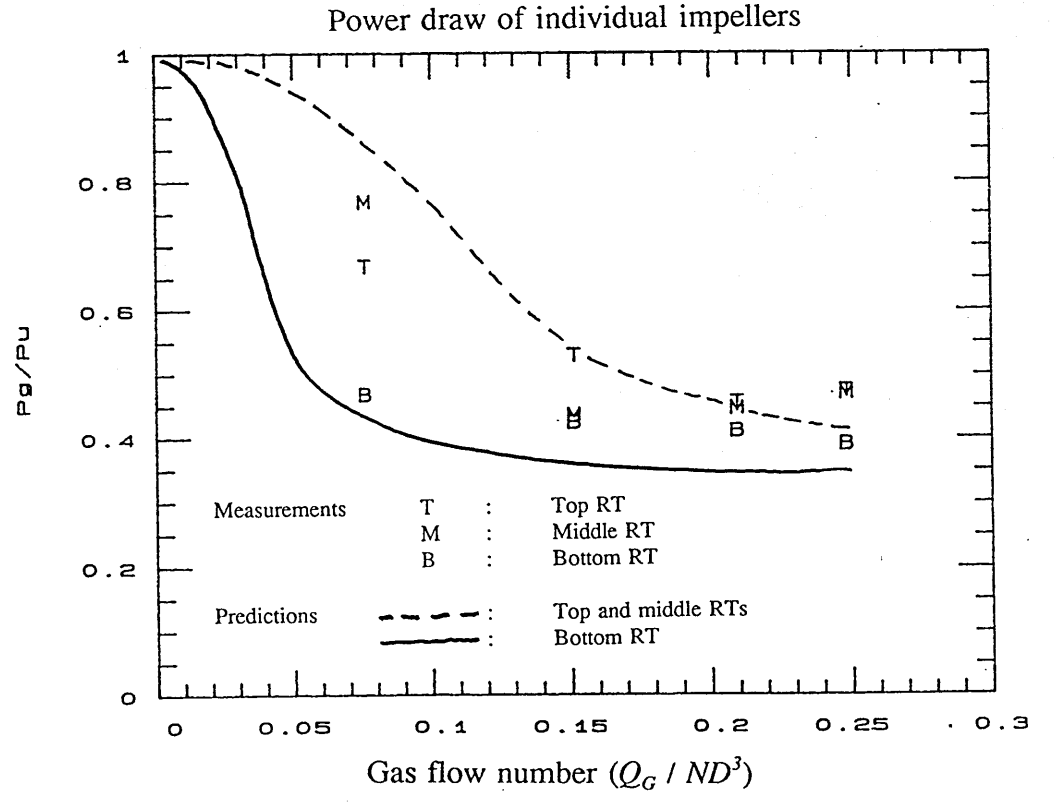
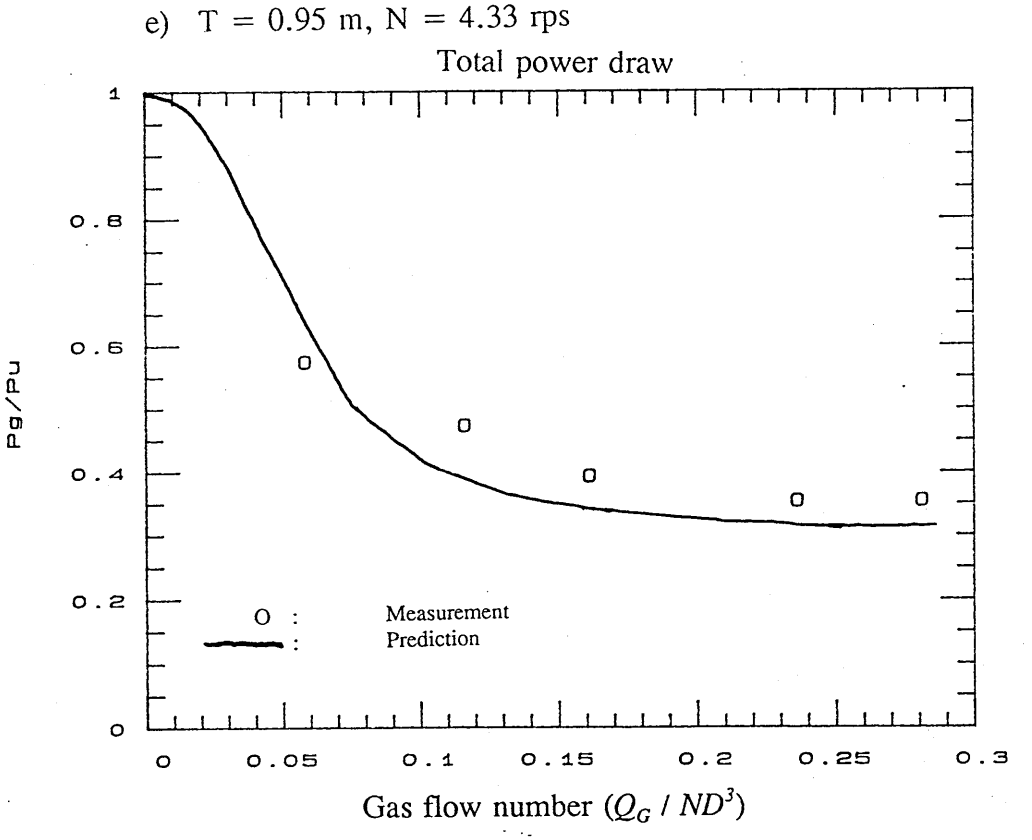


Figure 3.23: Prediction of gassed power draw for triple Rushton turbines.



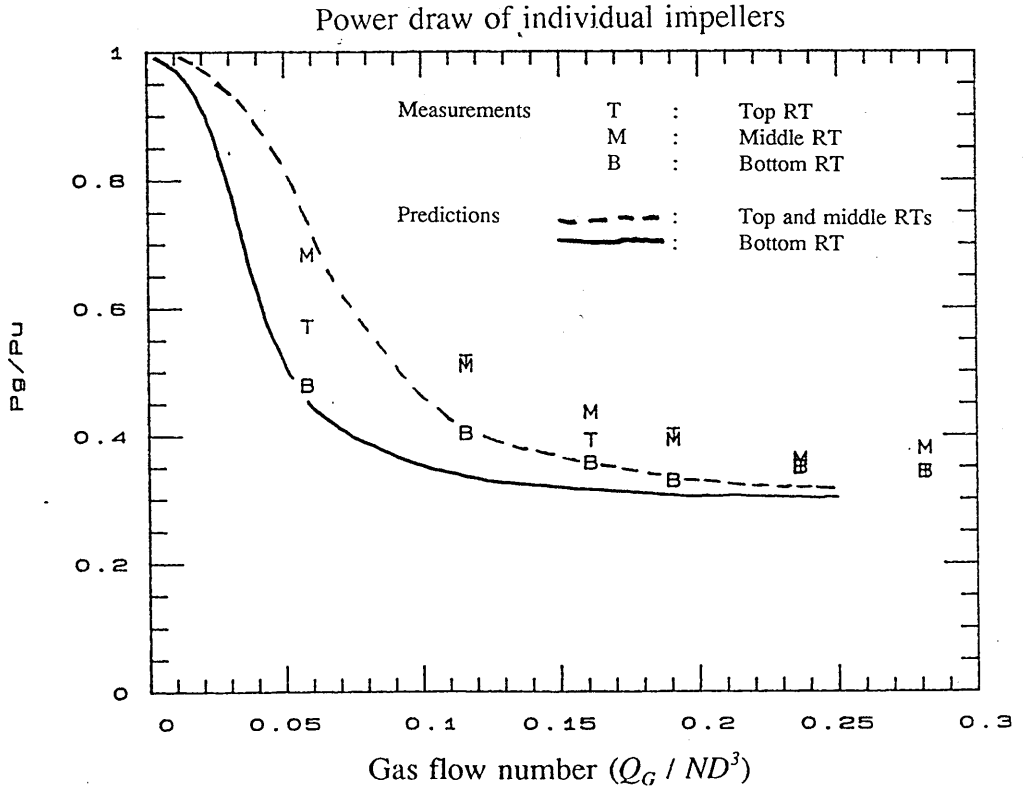


Figure 3.23: Prediction of gassed power draw for triple Rushton turbines.

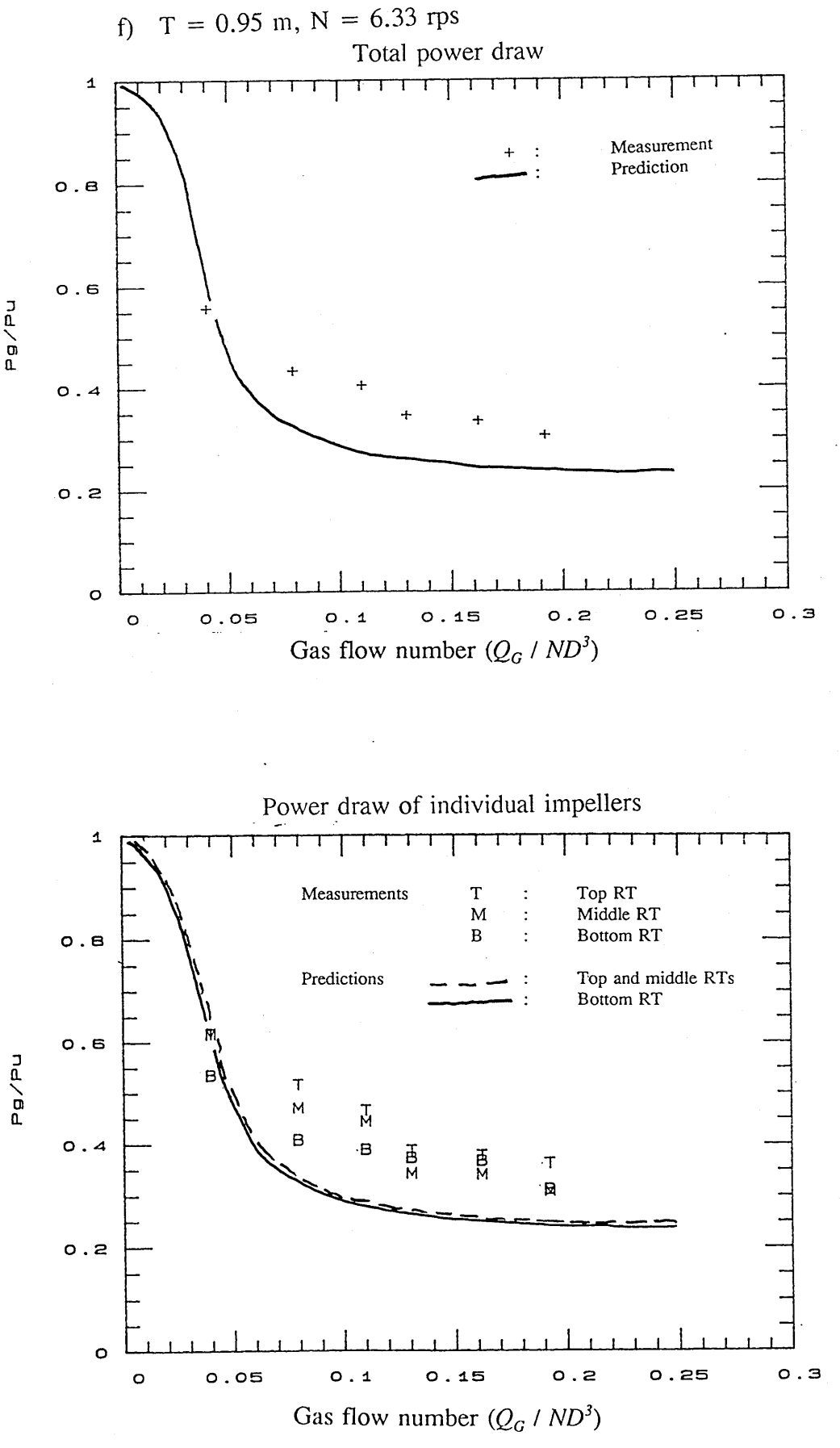
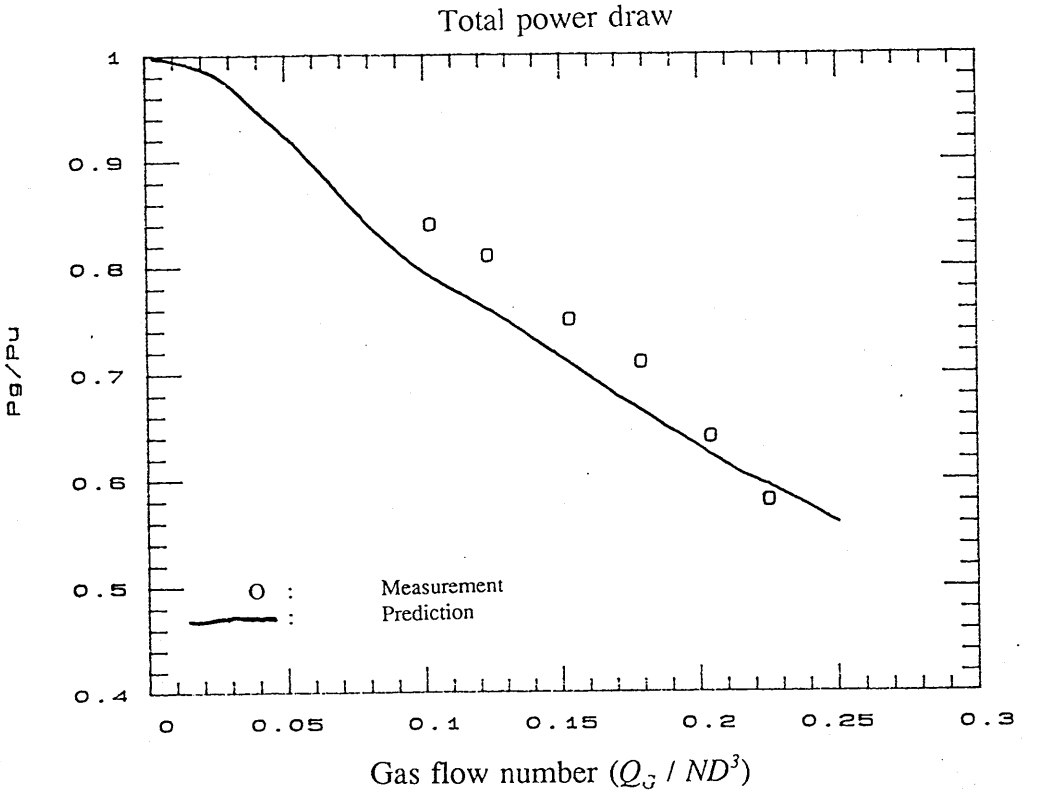


Figure 3.23: Prediction of gassed power draw for triple Rushton turbines.

g) Data from Seichter et al (1992), T = 4.00 m, N = 1.00 rps



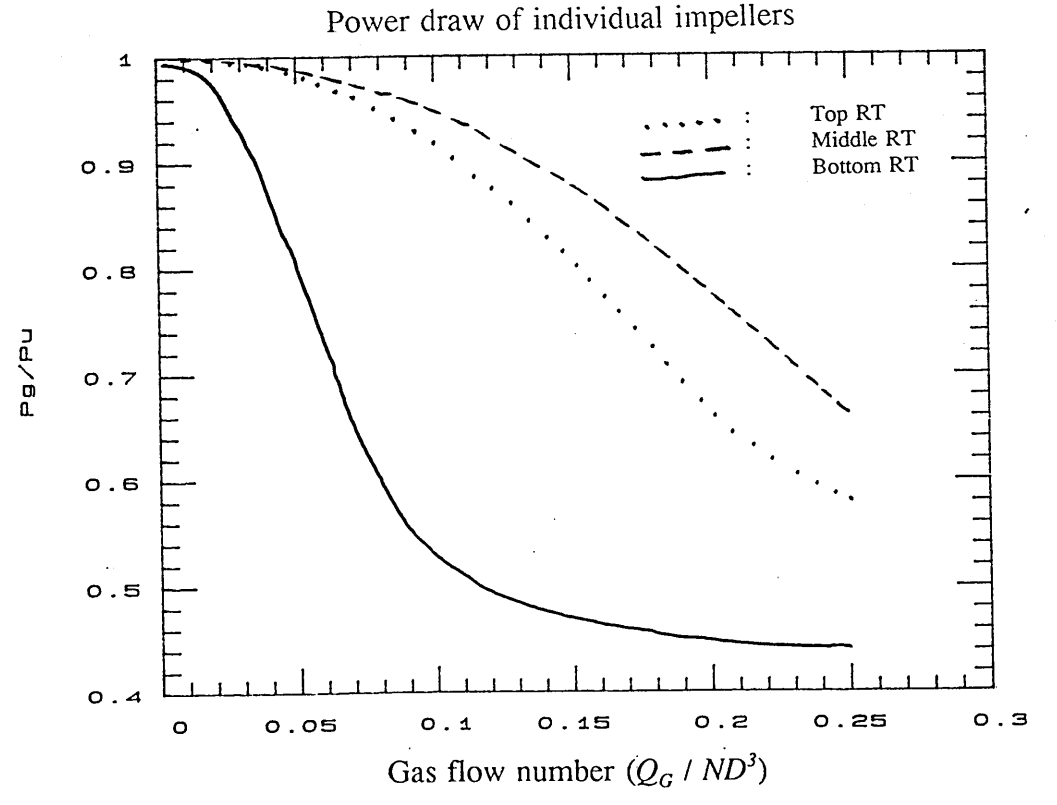


Figure 4.1: Comparison of impeller combinations at constant speed and gas flow rate (T = 0.61 m)

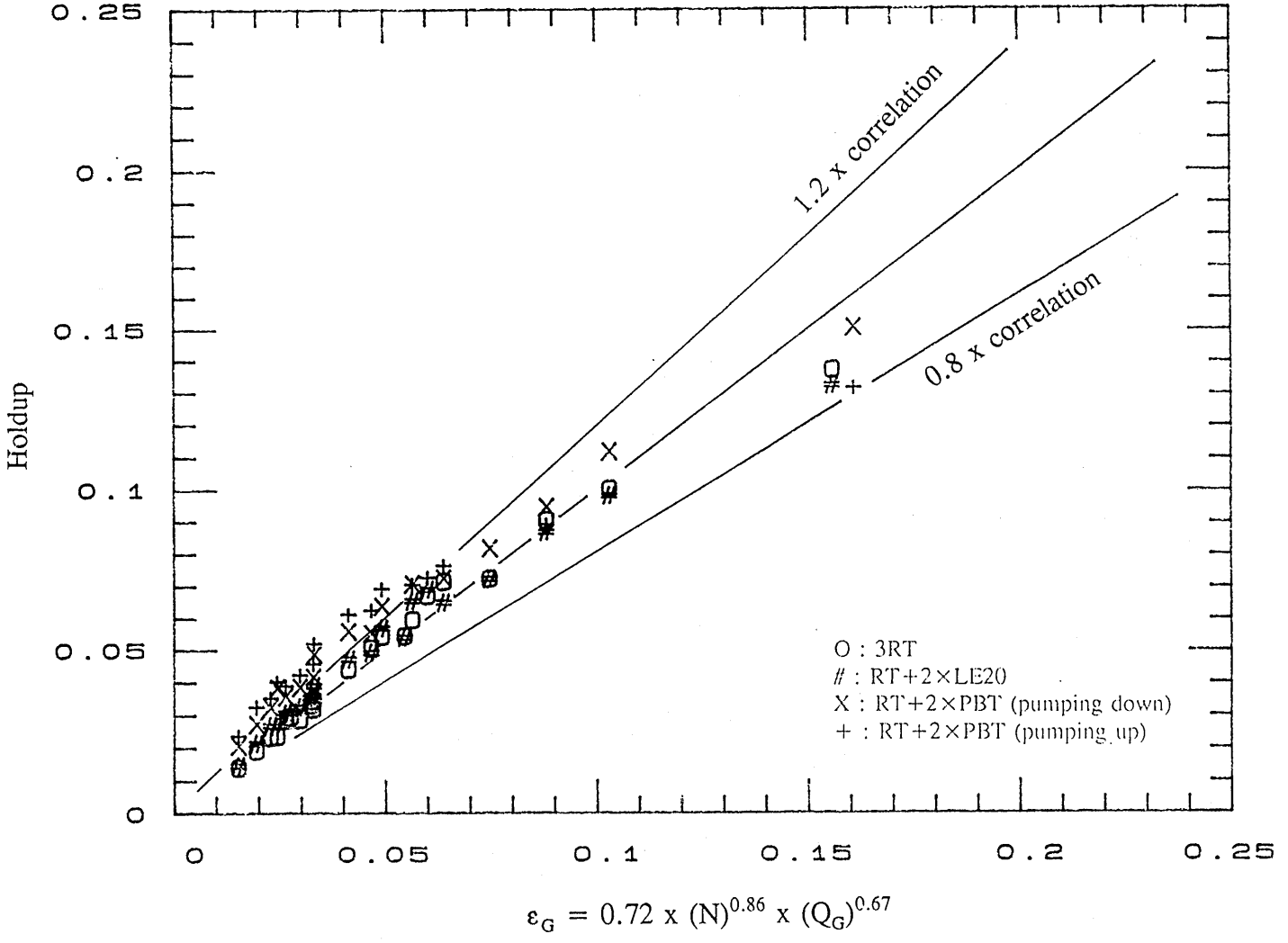
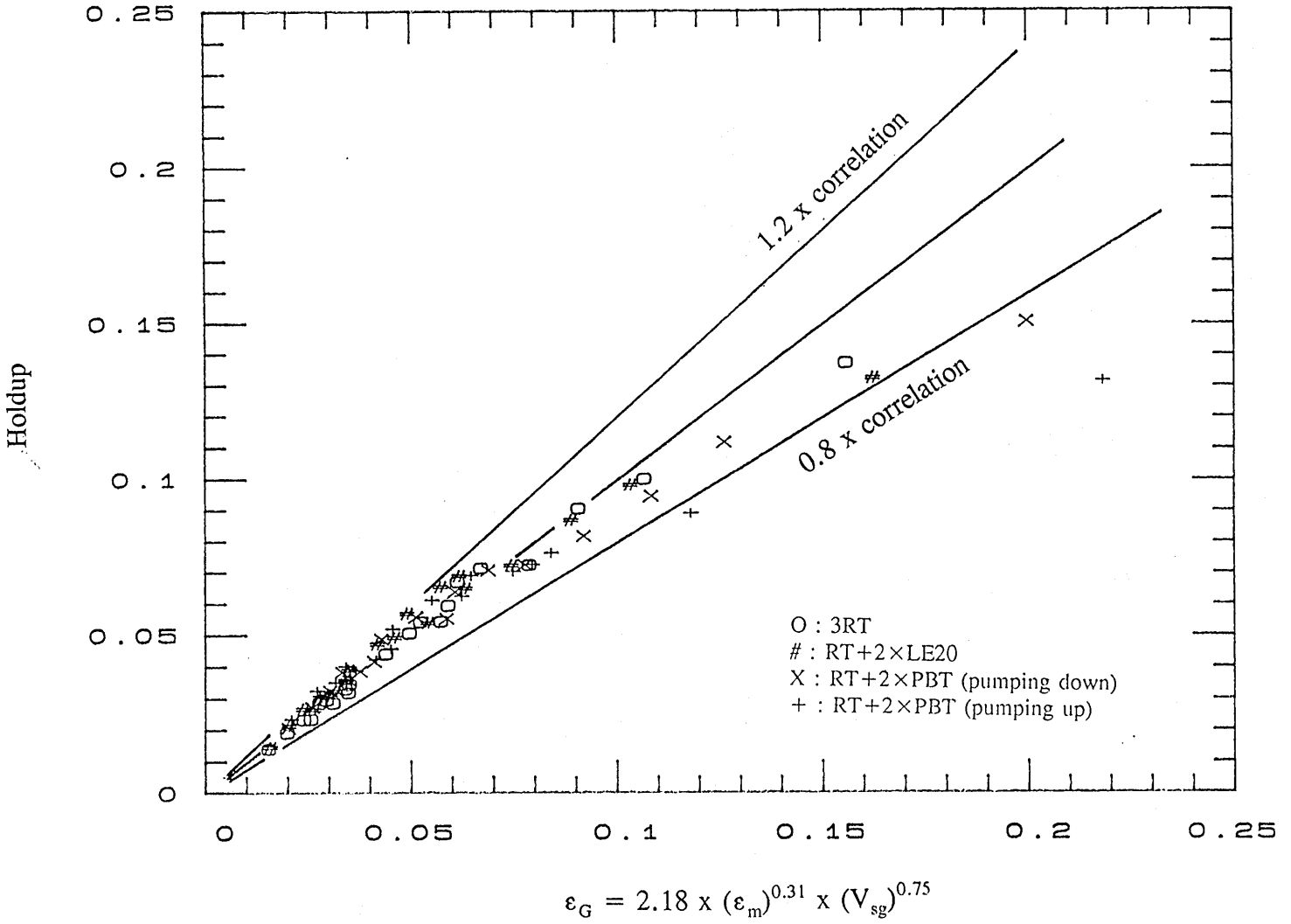


Figure 4.2: Comparison of impeller combinations at constant power and gas velocity (T = 0.61 m)



$$\varepsilon_G = 2.18 \times (\varepsilon_m)^{0.31} \times (V_{sg})^{0.75}$$

Figure 4.3: Comparison of impeller combinations at constant speed and gas flow rate (T = 0.95 m)

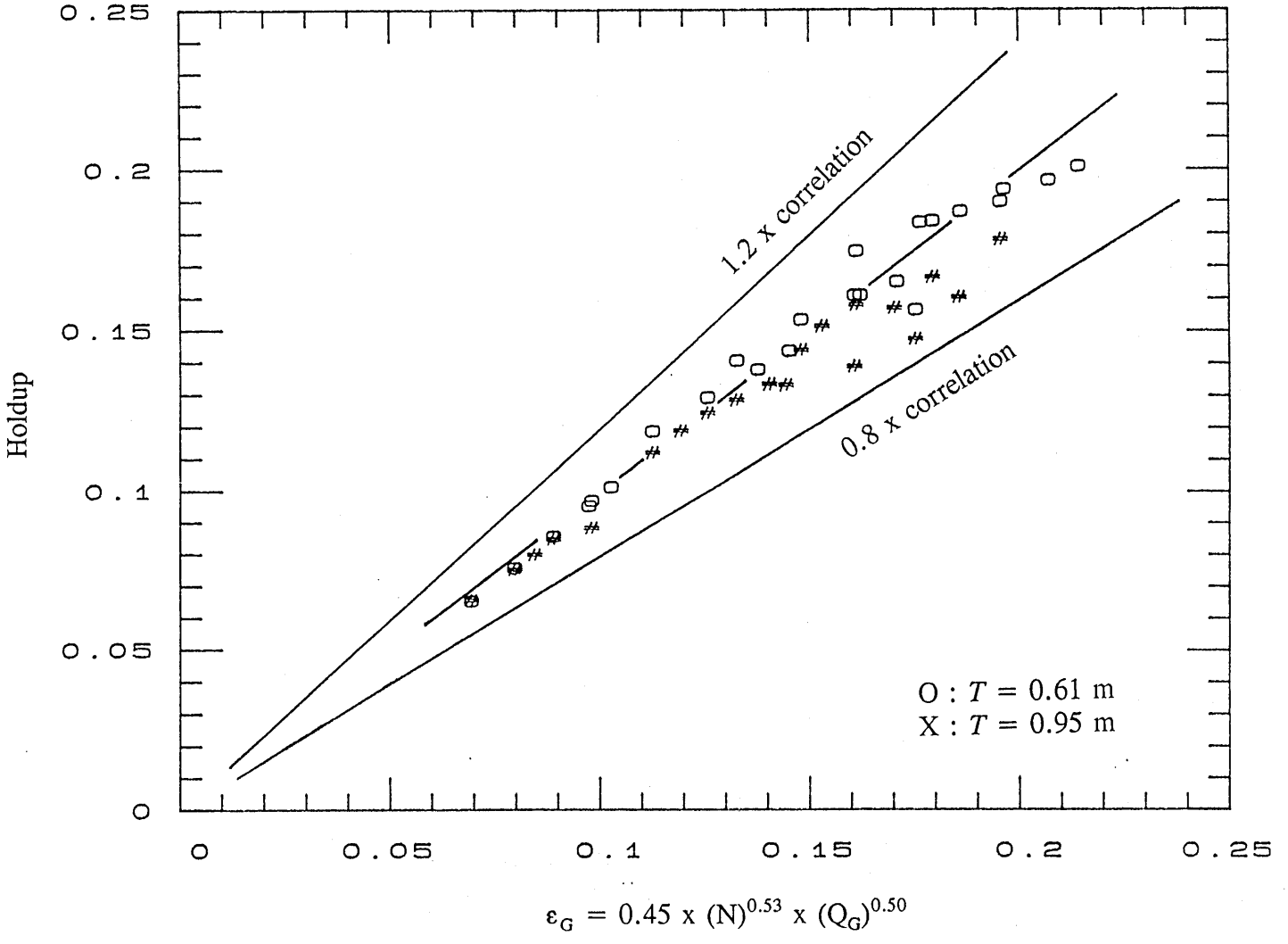
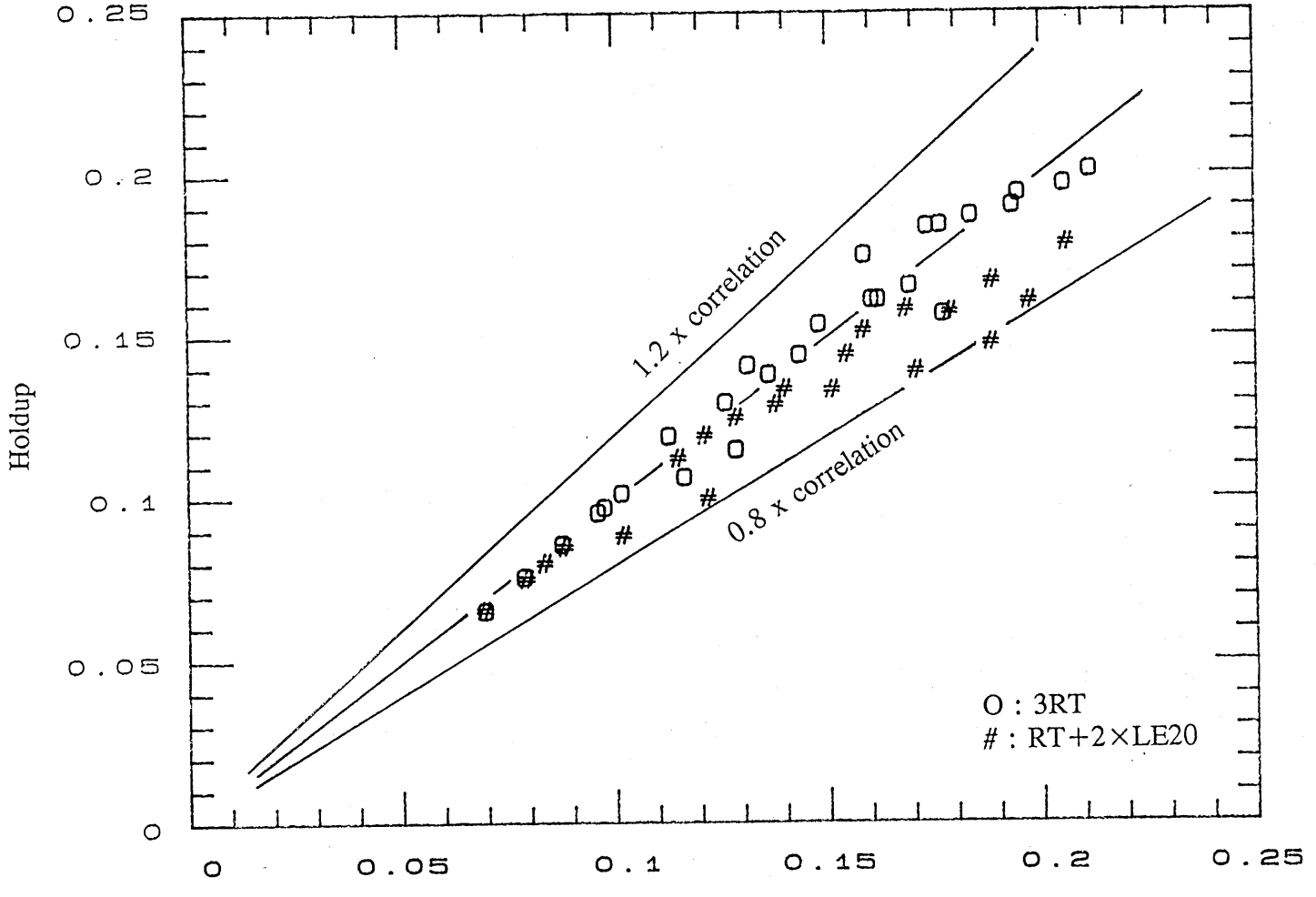
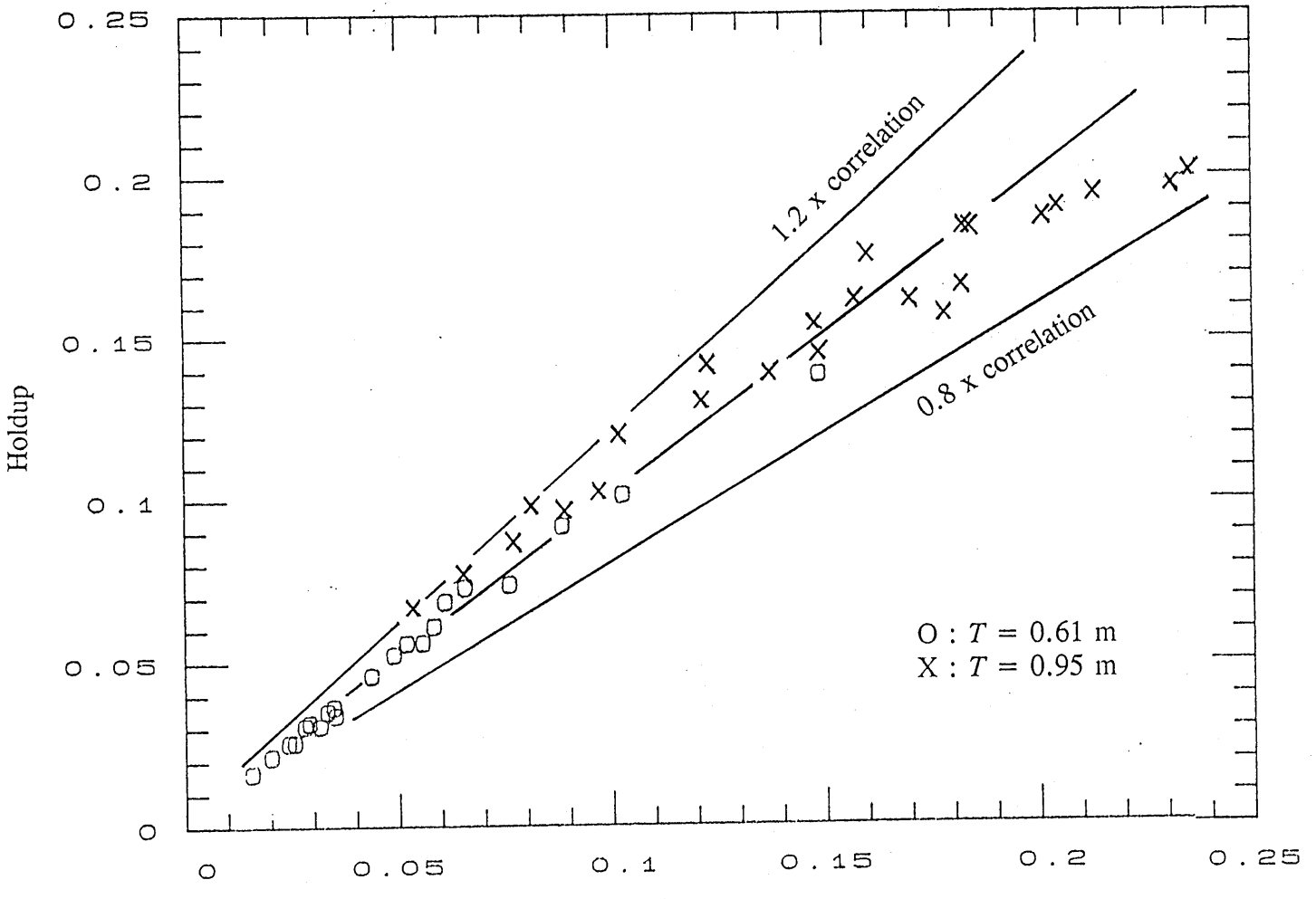


Figure 4.4: Comparison of impeller combinations at constant power and gas velocity (T = 0.95 m)



$$\varepsilon_G = 1.12 \times (\varepsilon_m)^{0.18} \times (V_{sg})^{0.57}$$

Figure 4.5: Scale up of 3RT combination



$$\varepsilon_G = 1.87 \times (\varepsilon_m)^{0.28} \times (V_{sg})^{0.72}$$

Figure 4.6: Scale up of RT+2×LE20 combination

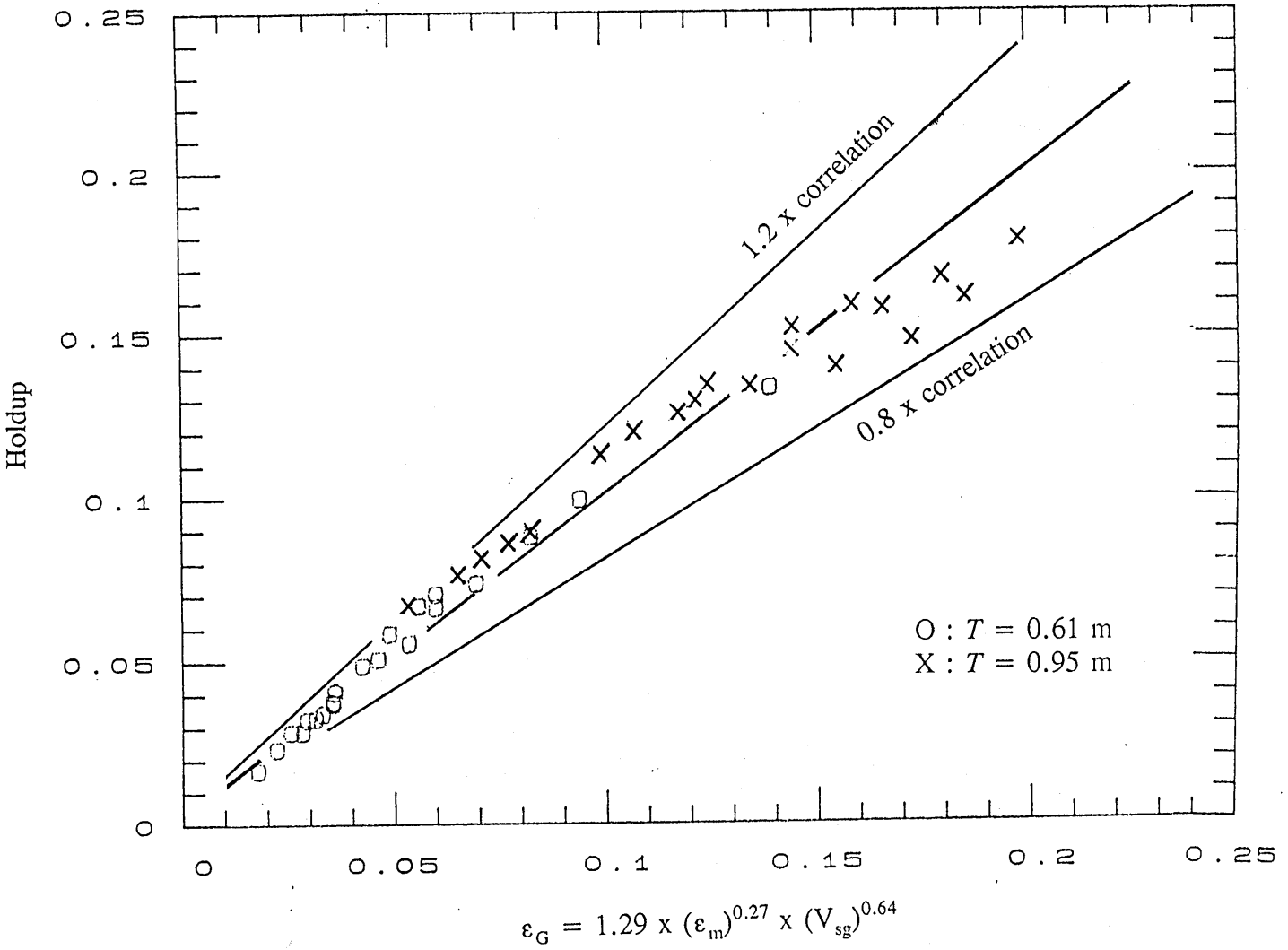
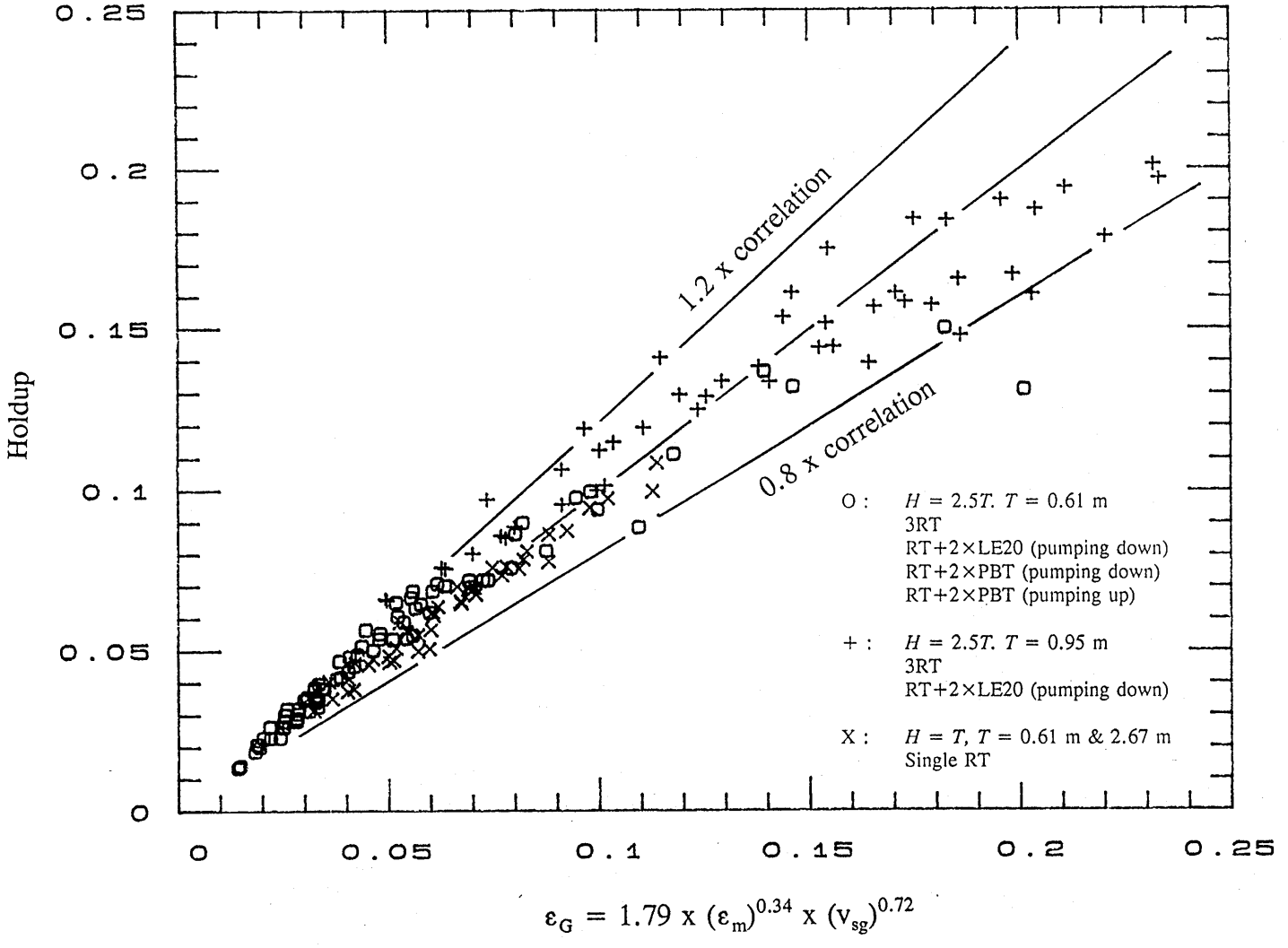
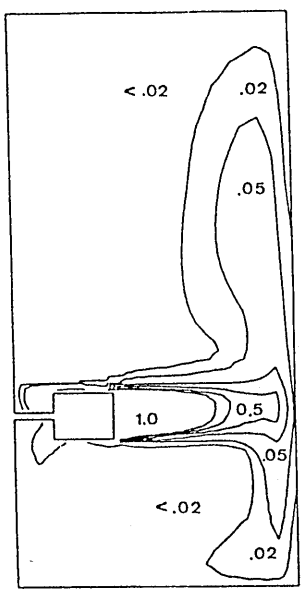


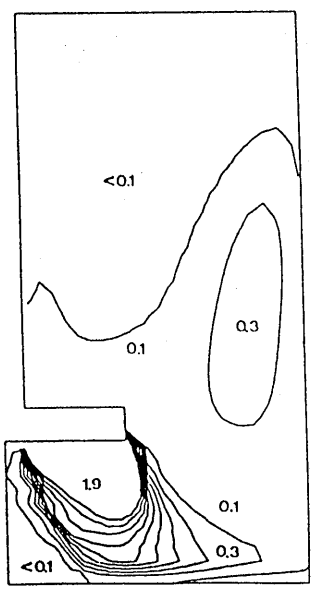
Figure 4.7: Holdup correlation for tall and standard geometry vessels



Rushton turbine



Pitched blade turbine
(pumping down)



Values in figures are of ε (W/kg)

Figure 4.8: Local energy dissipation rates for two impeller designs, at the same average power per unit mass, Bakker (1992).

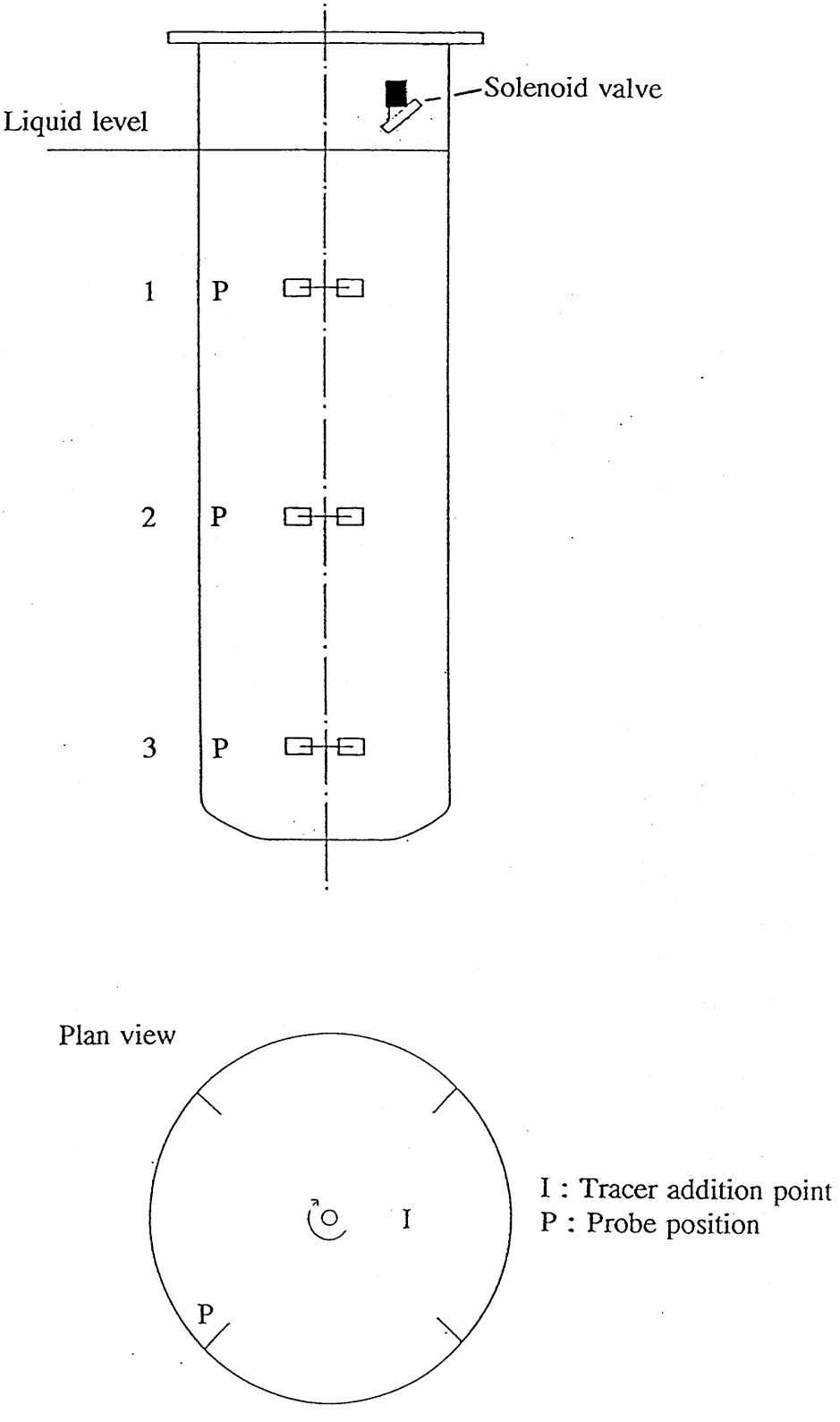


Figure 5.1: Tracer injection and conductivity probe positions (T = 0.95 m).

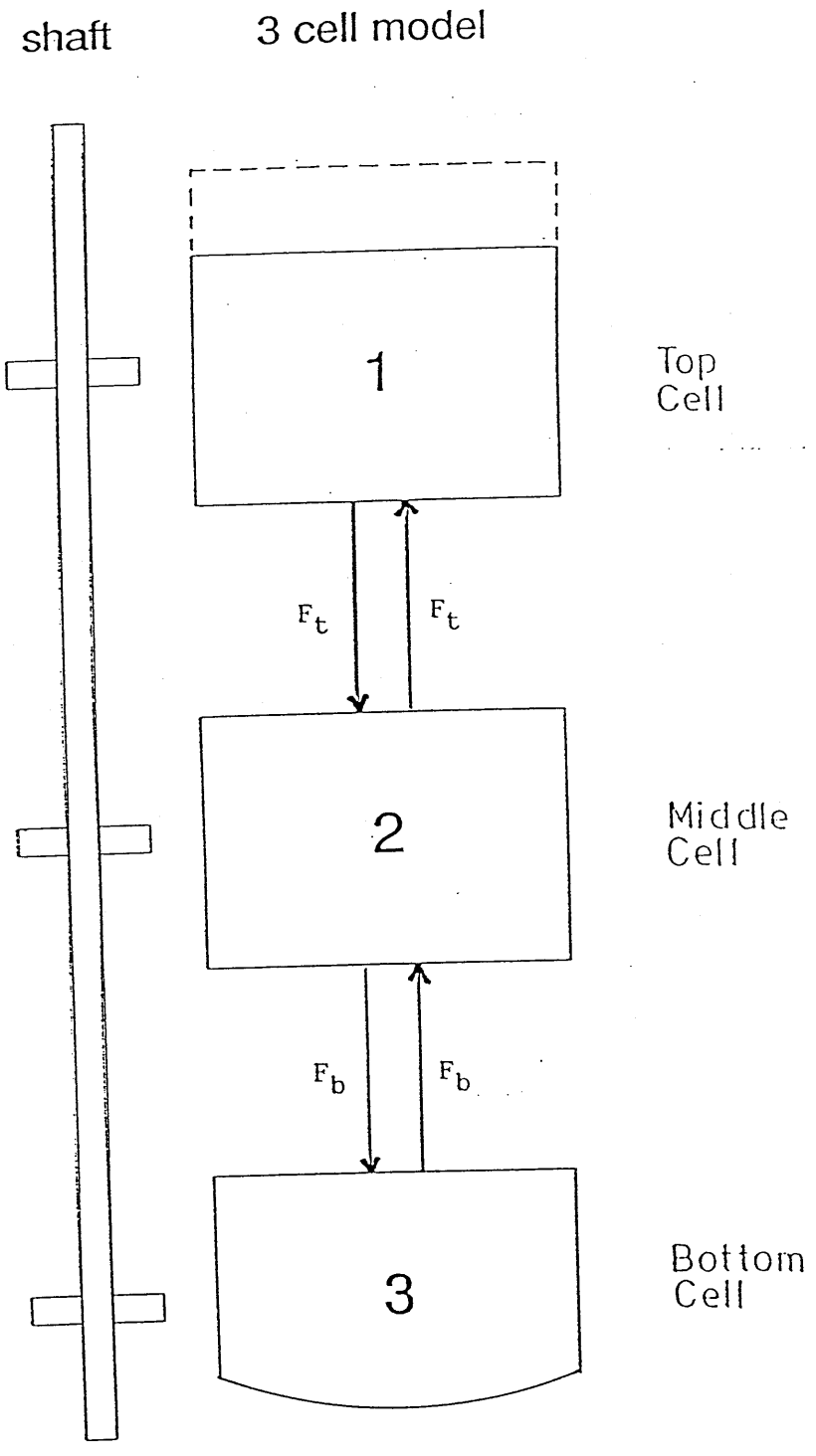
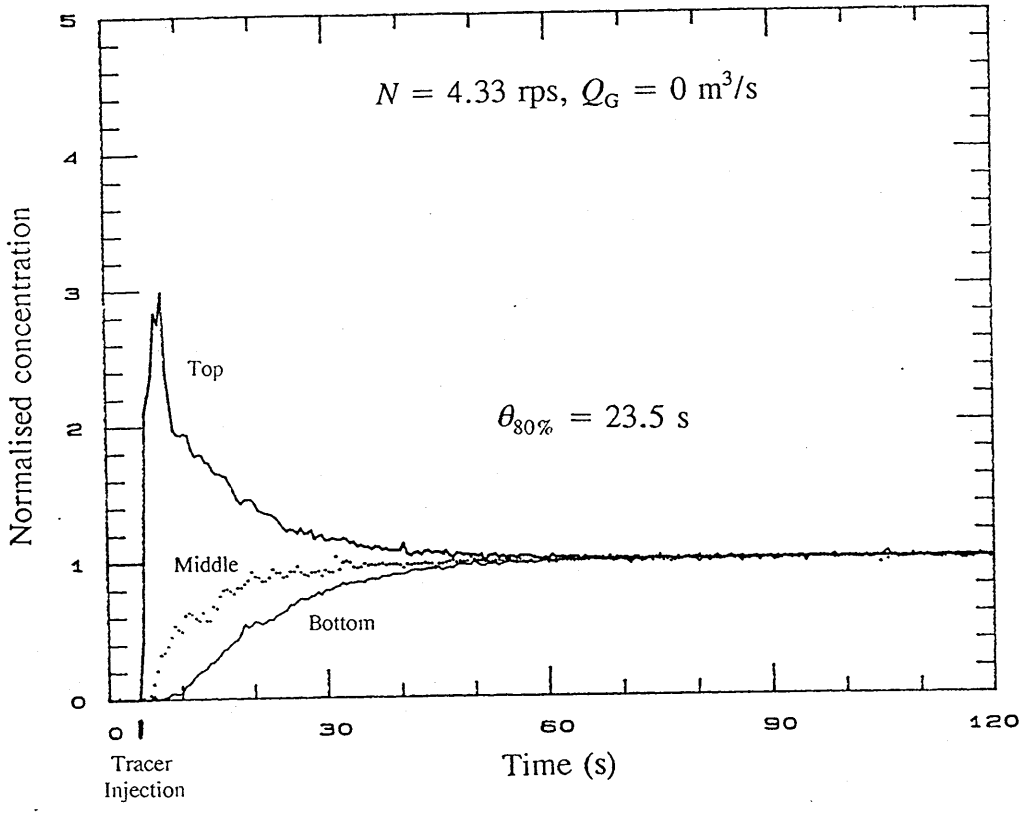


Figure 5.2: Three cell model for liquid phase mixing (three perfectly mixed cell connected by exchange flows).

Figure 5.3: Example of conductivity responses from tall vessel (triple Rushton turbine combination, T = 0.95 m)



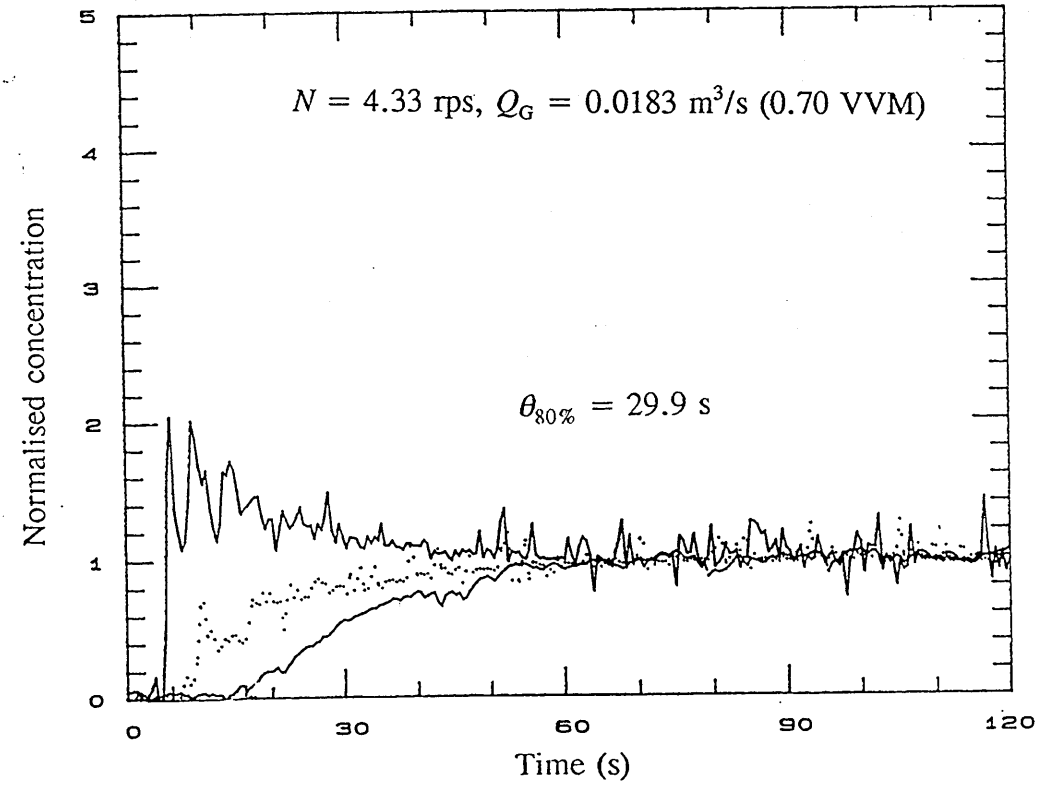
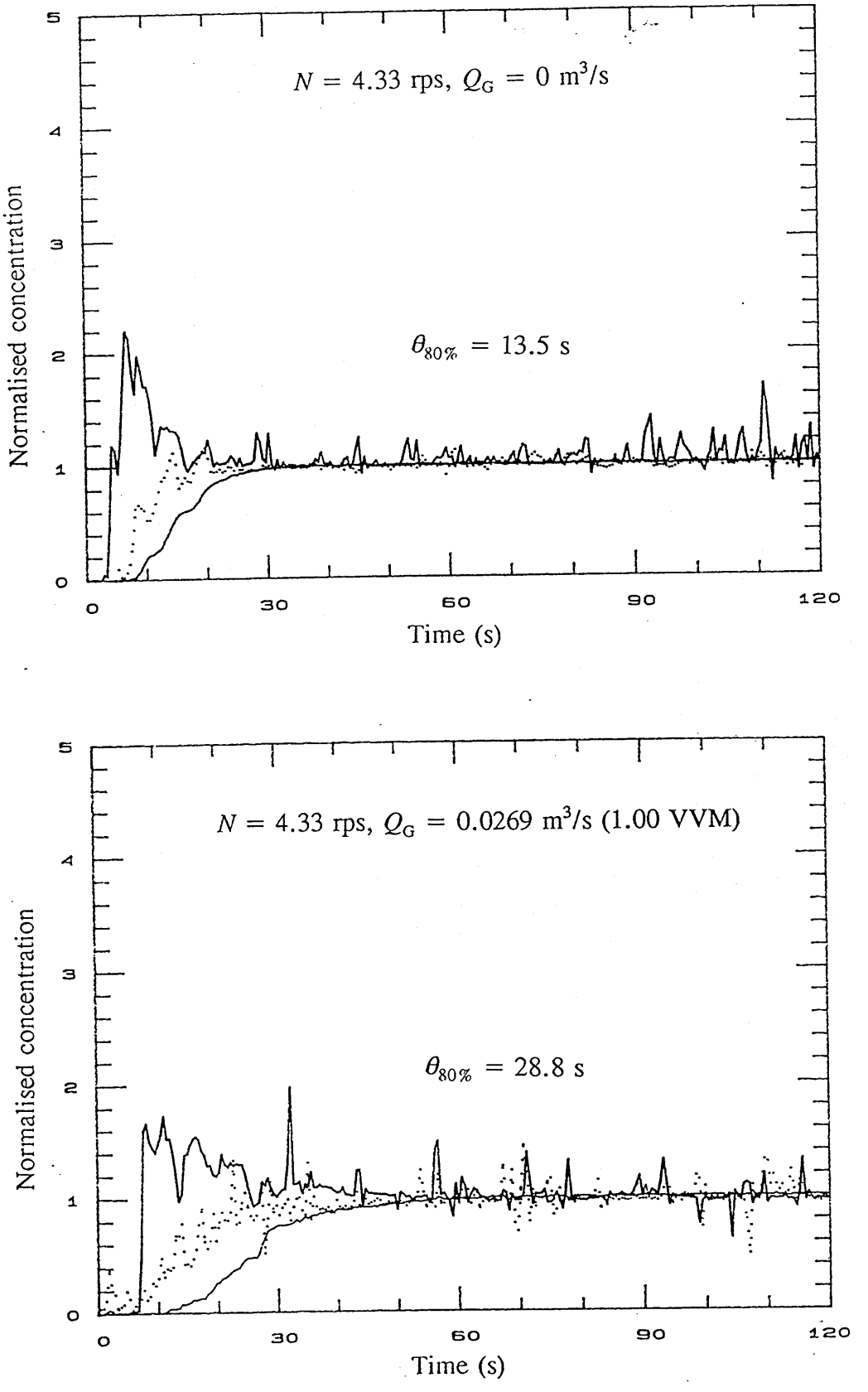


Figure 5.4: Example of conductivity responses from tall vessel (RT+2×LE20 combination, T = 0.95 m)



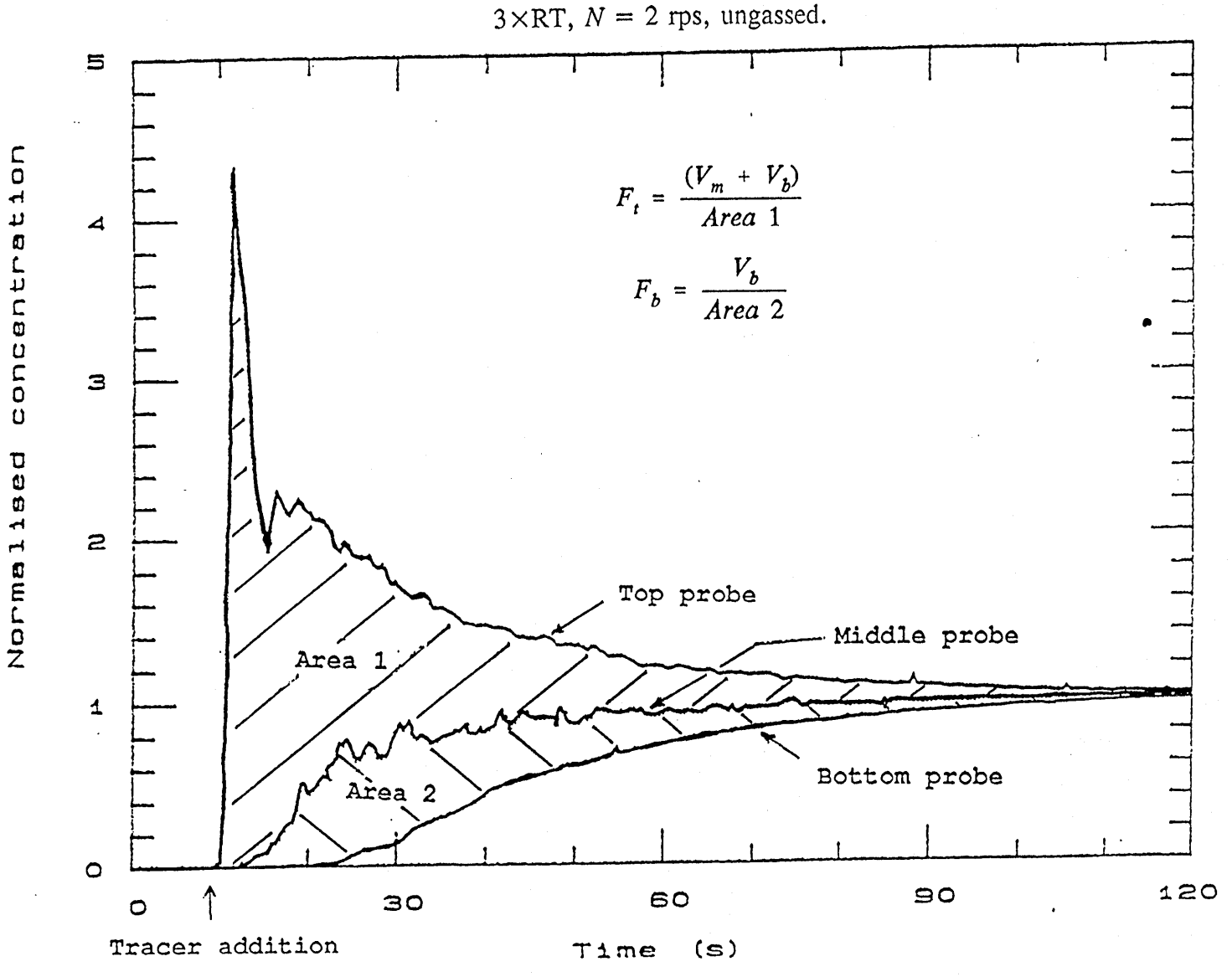
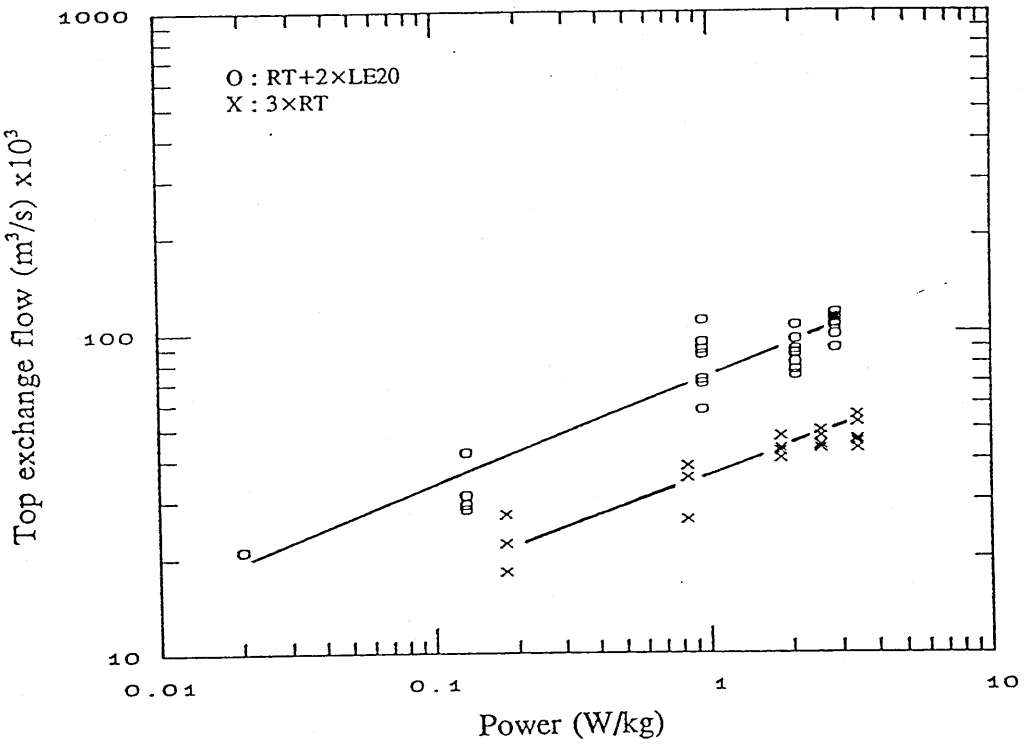


Figure 5.5: Example of how exchange flows F_t and F_b are determined from conductivity response curves.

Figure 5.6: Ungassed exchange flows versus power input.



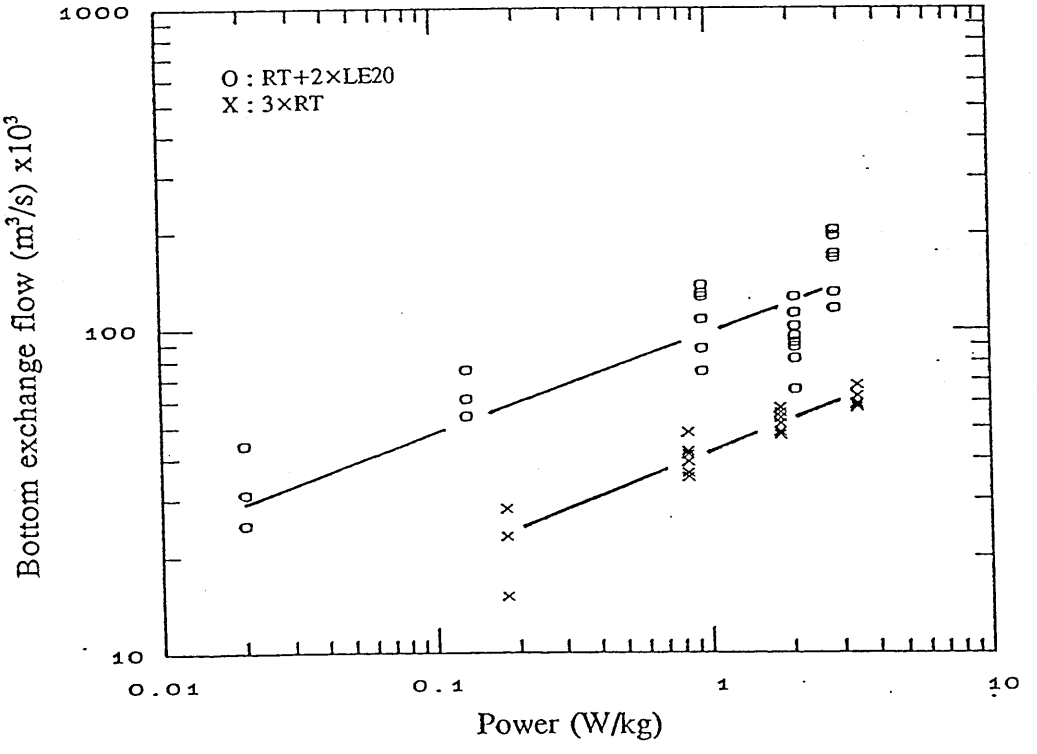
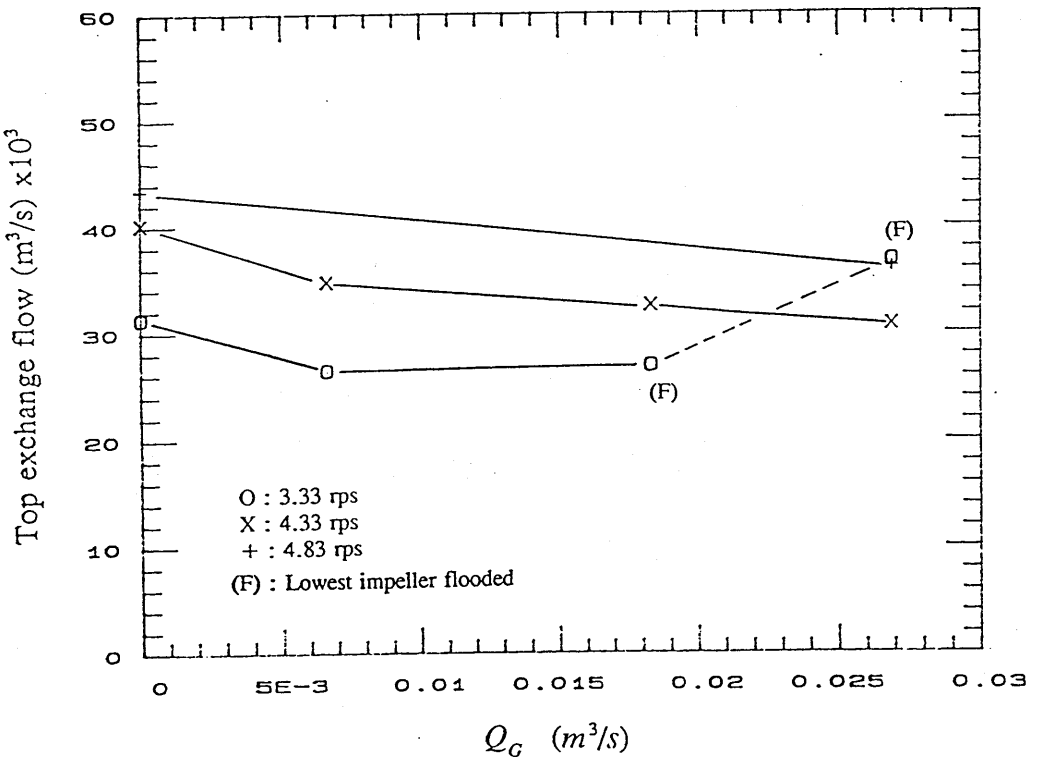


Figure 5.7: Effect of gas flow rate on exchange flows for the triple Rushton turbine combination (T = 0.95 m).



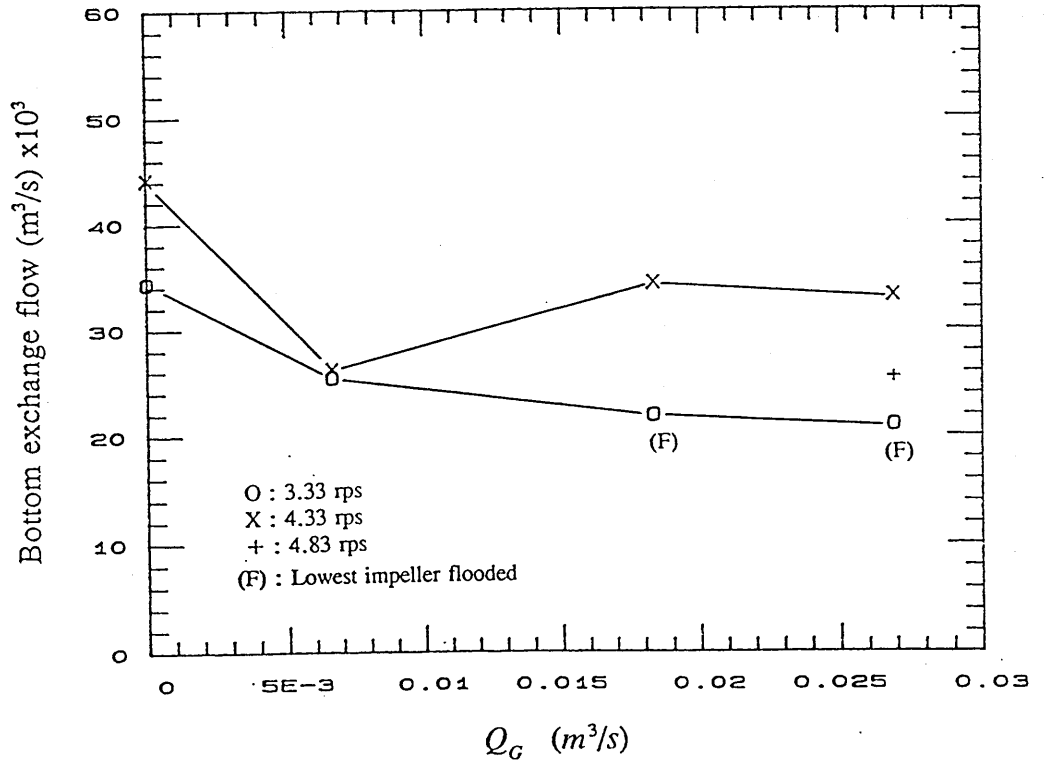
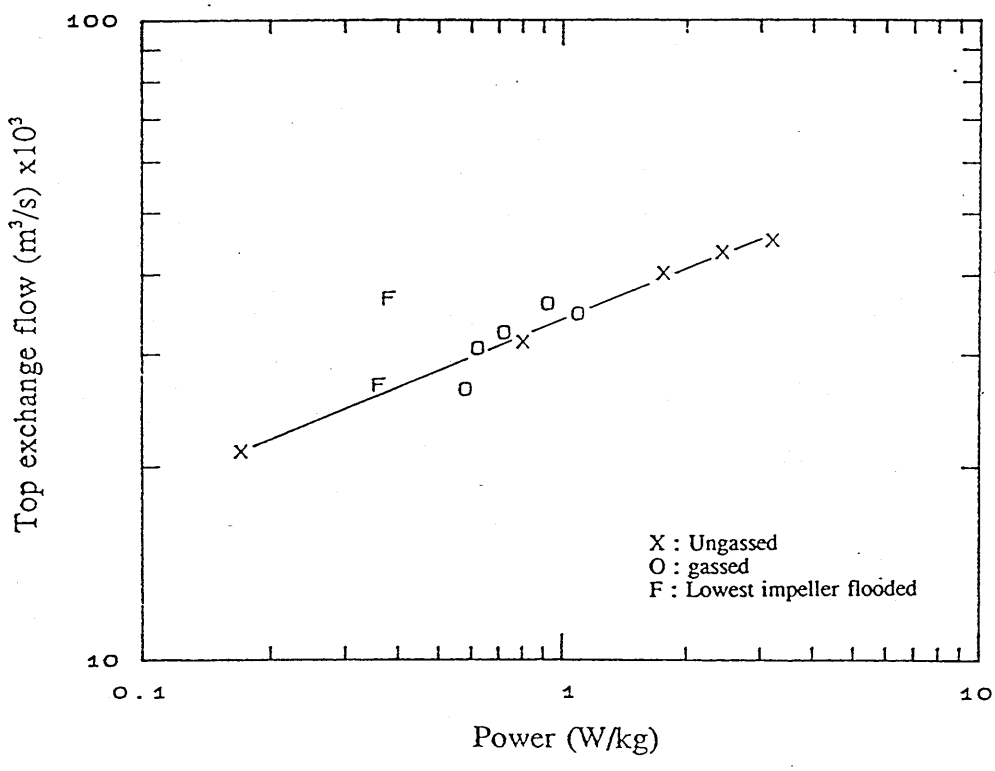


Figure 5.8: Effect of power input on exchange flows for the triple Rushton turbine combination (T = 0.95 m).



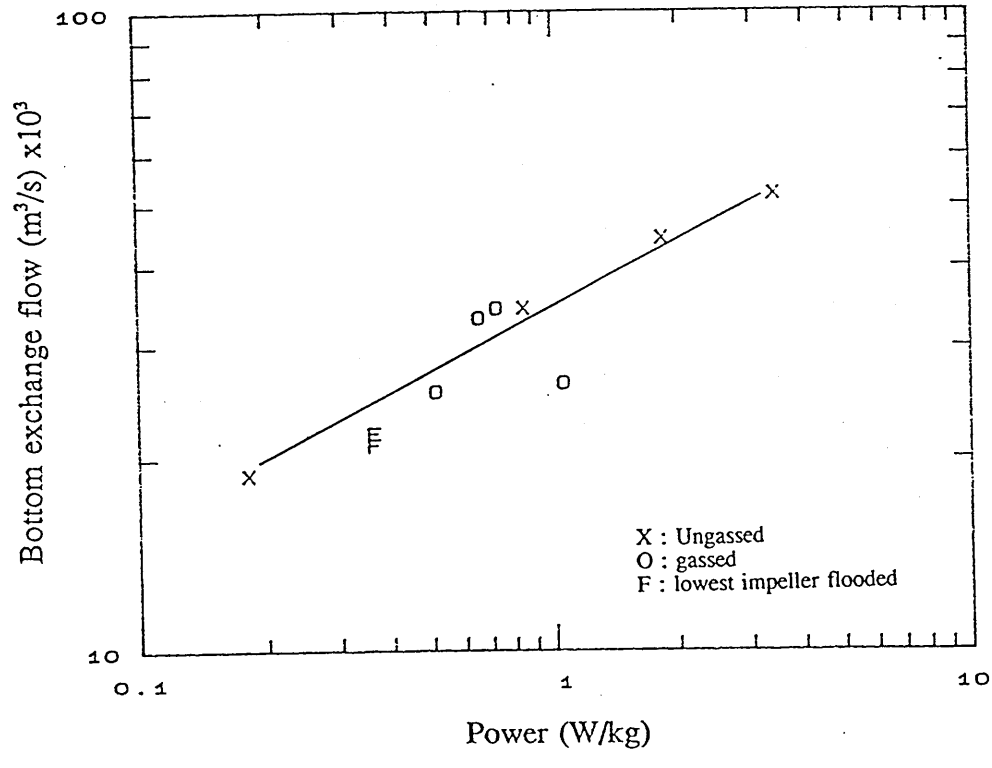
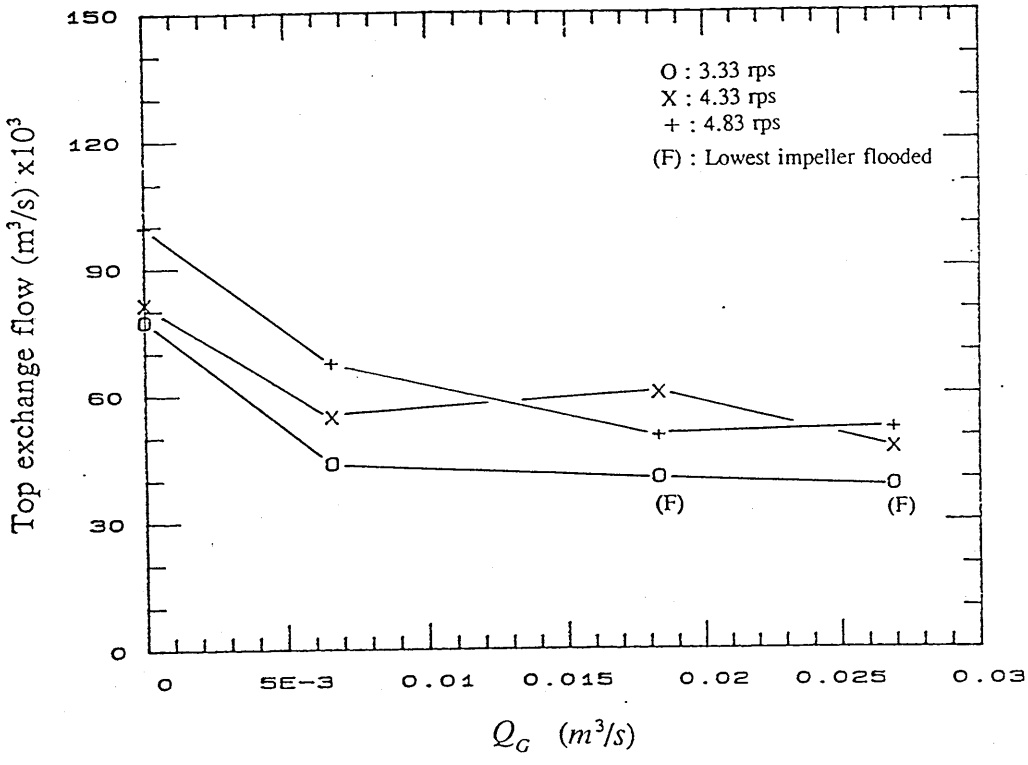


Figure 5.9: Effect of gas flow rate on exchange flows for the RT+2×LE20 combination (T = 0.95 m).



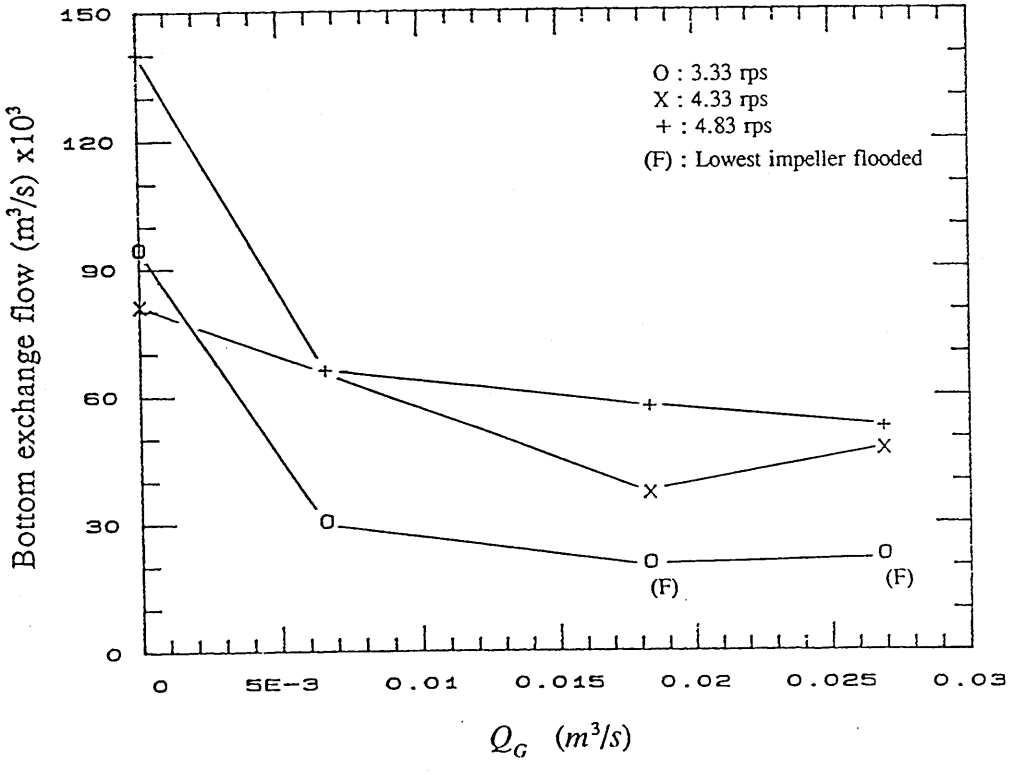
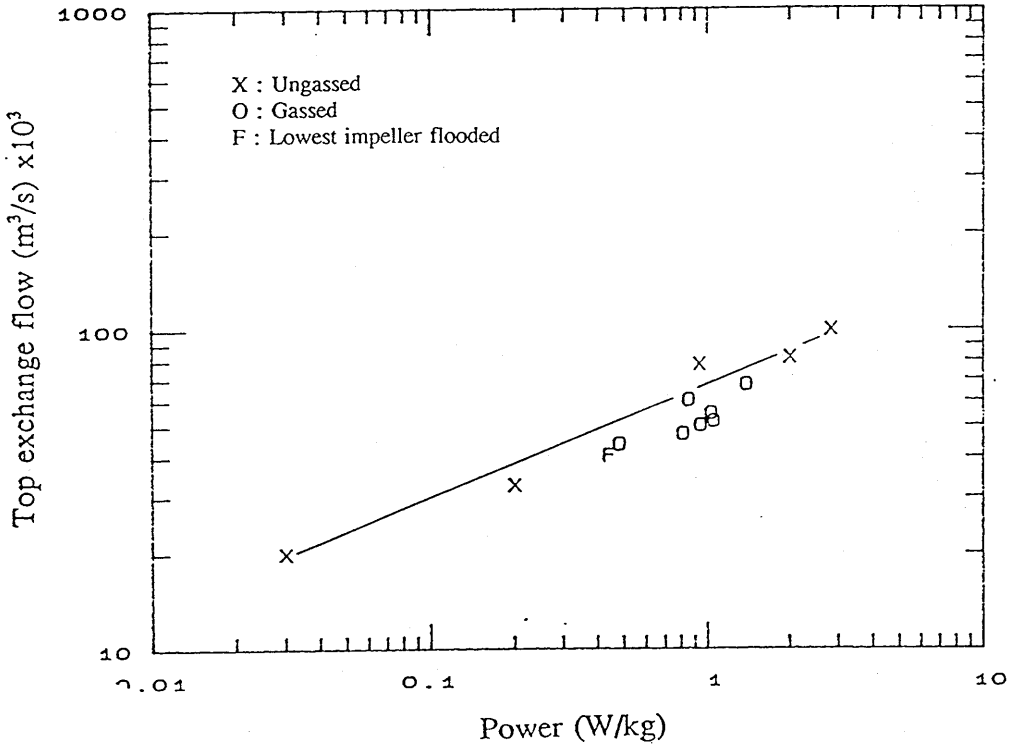


Figure 5.10: Effect of power input on exchange flows for the RT+2×LE20 combination (T = 0.95 m).



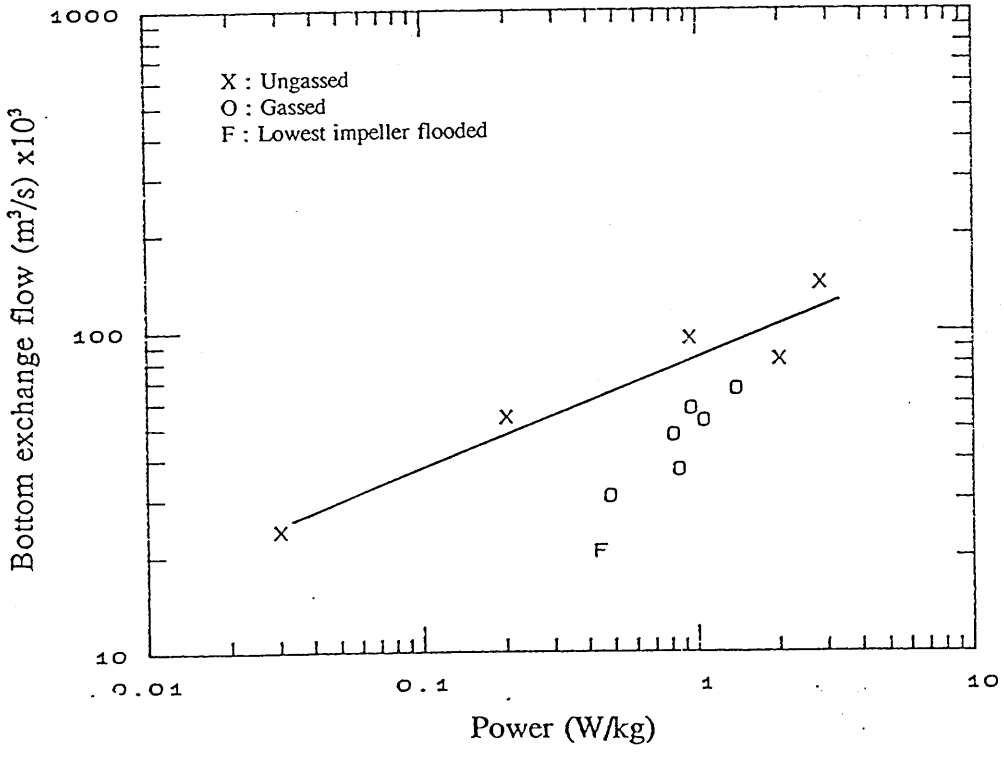
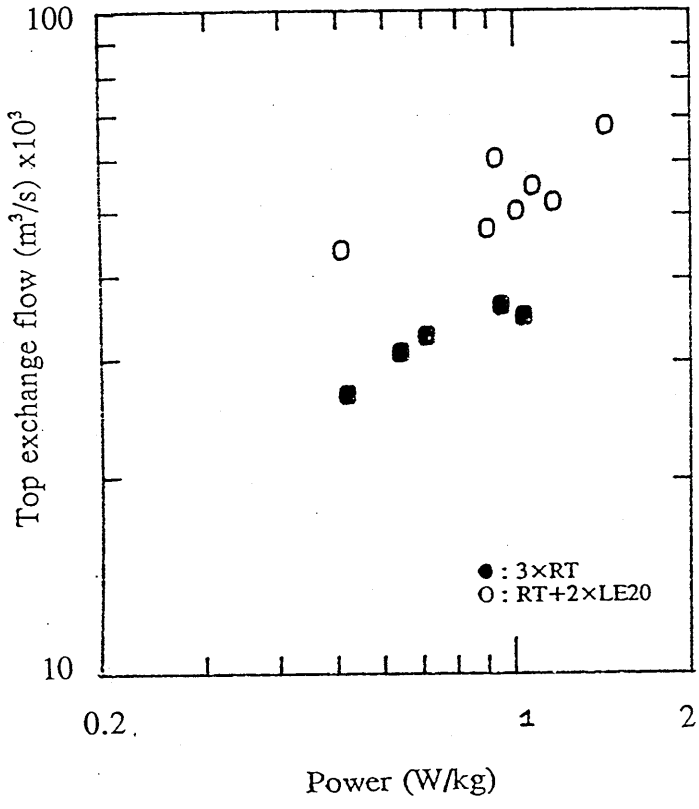
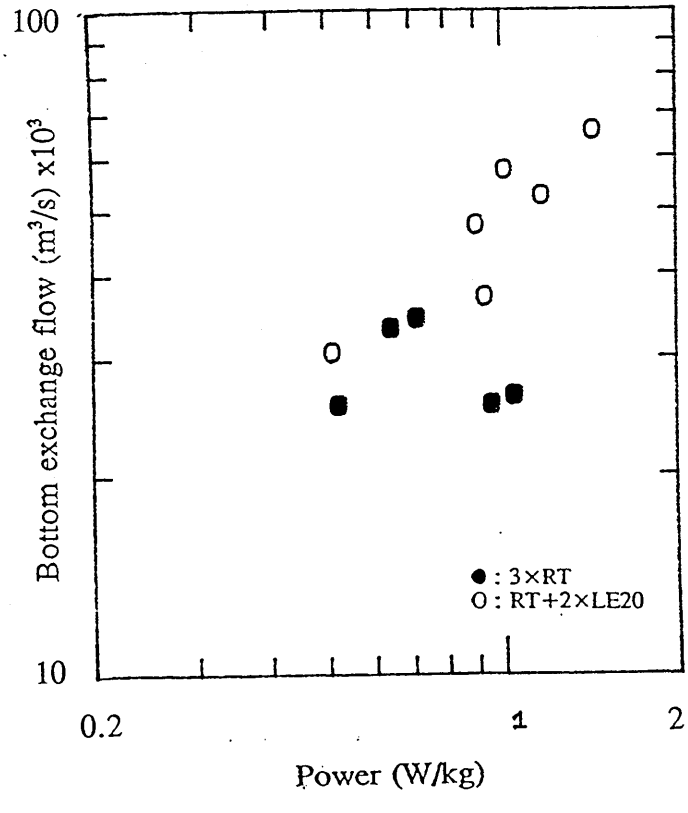


Figure 5.11: Comparison of liquid exchange flows when gassed ($T = 0.95$ m)





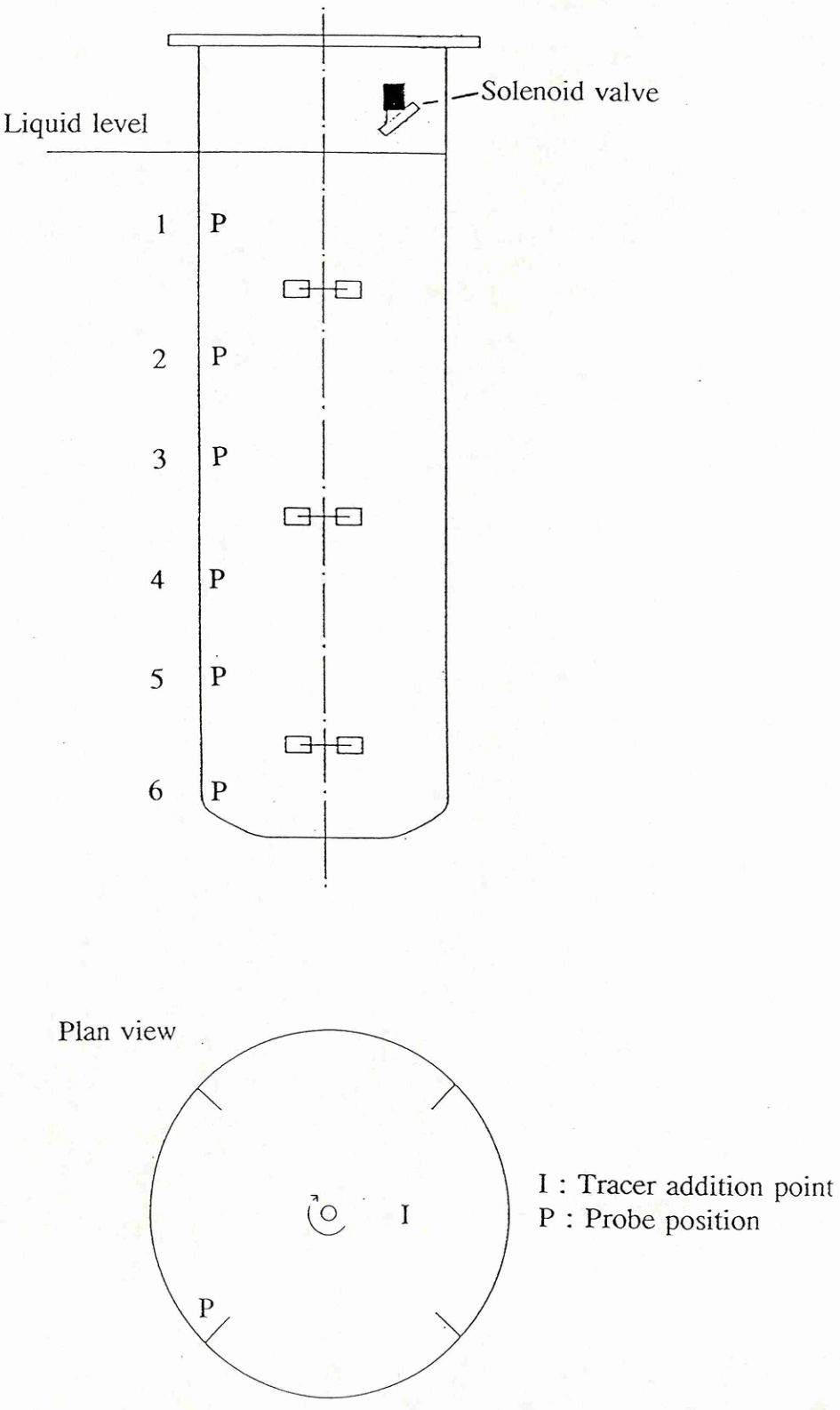


Figure 5.12: Tracer injection and conductivity probe positions ($T = 0.61$ m).

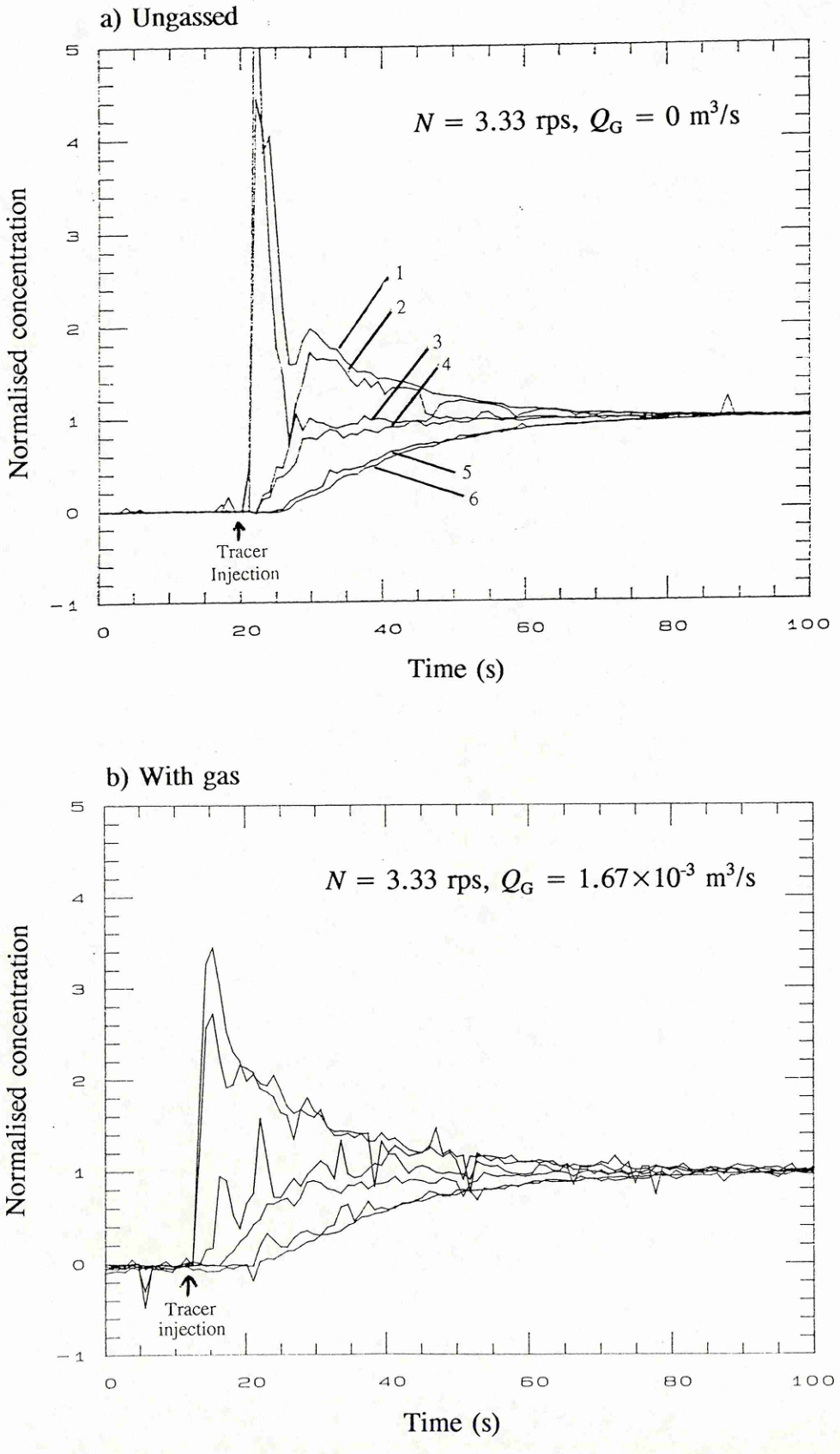
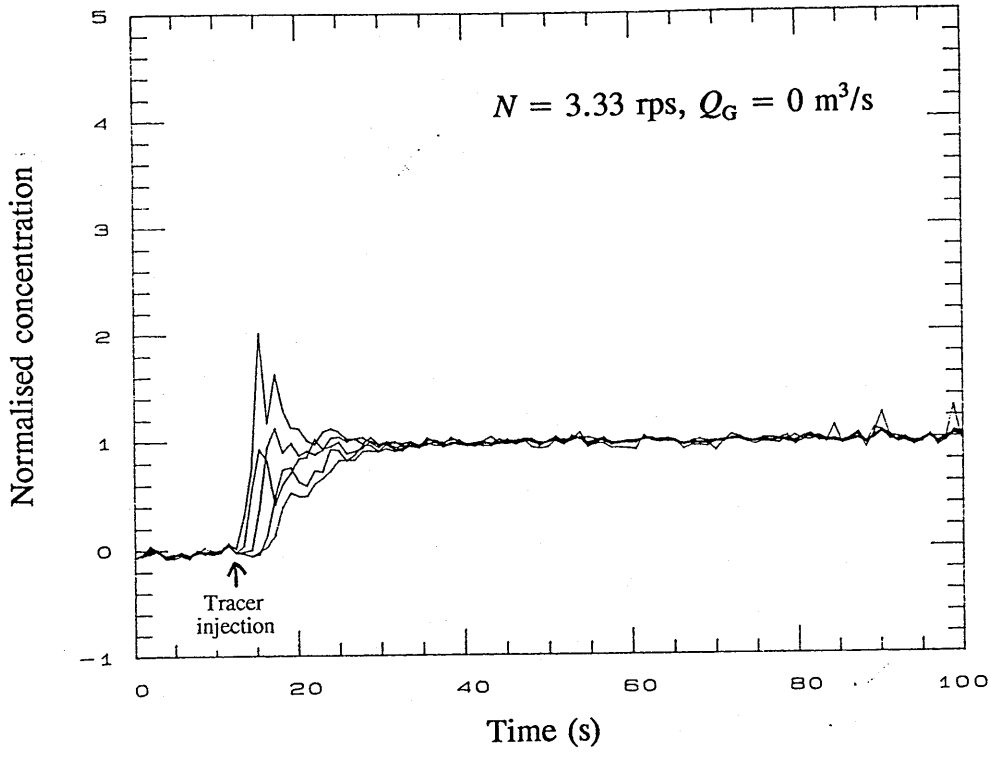


Figure 5.13: Example of conductivity responses from tall vessel (triple Rushton turbine combination, T = 0.61 m)



b) With gas

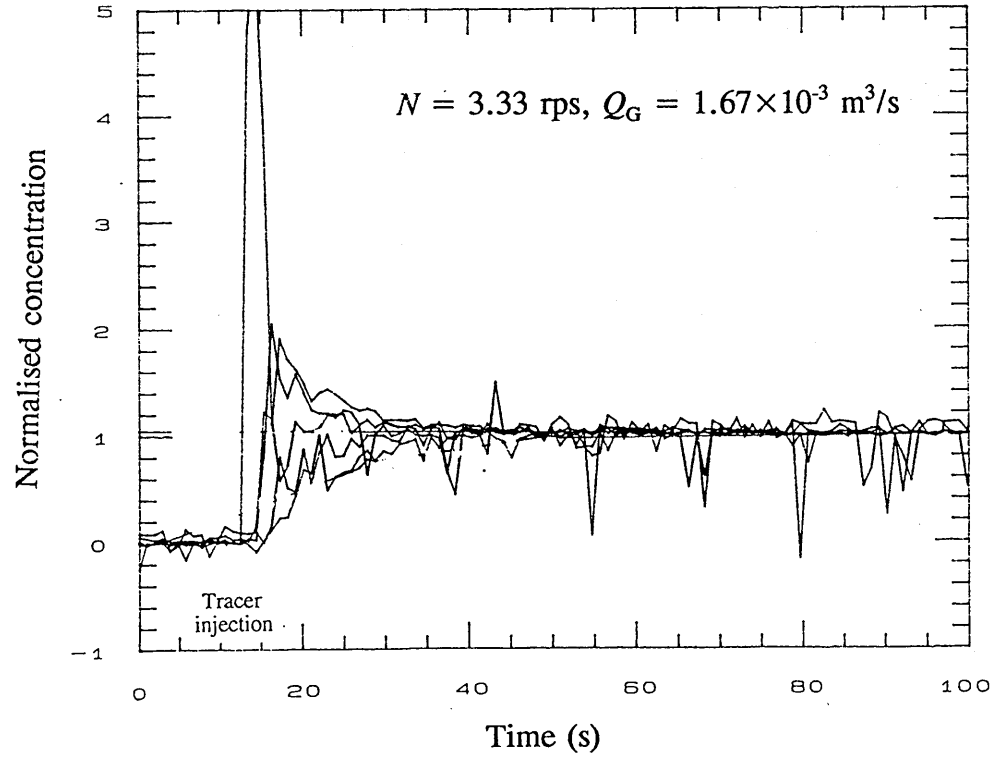


Figure 5.14: Example of conductivity responses from tall vessel (RT+2×LE20 combination, T = 0.61 m)

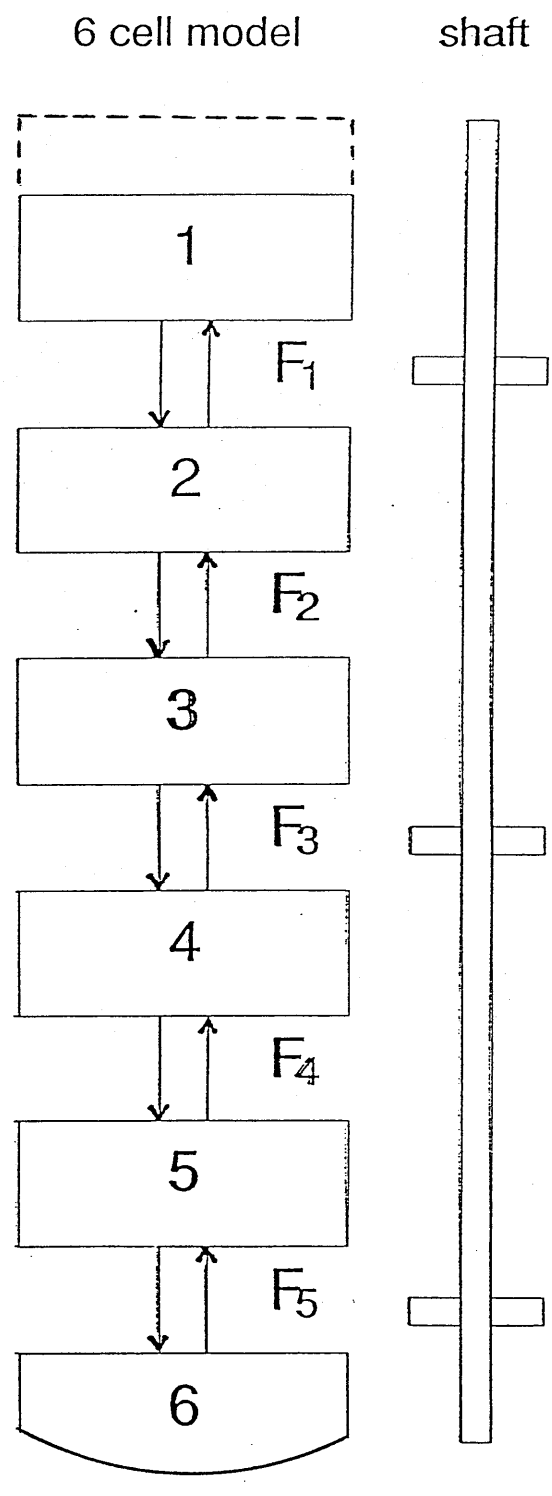


Figure 5.15: Six cell model for liquid phase mixing (six perfectly mixed cells connected by exchange flows).

3×RT combination

RT+2×LE20 combination

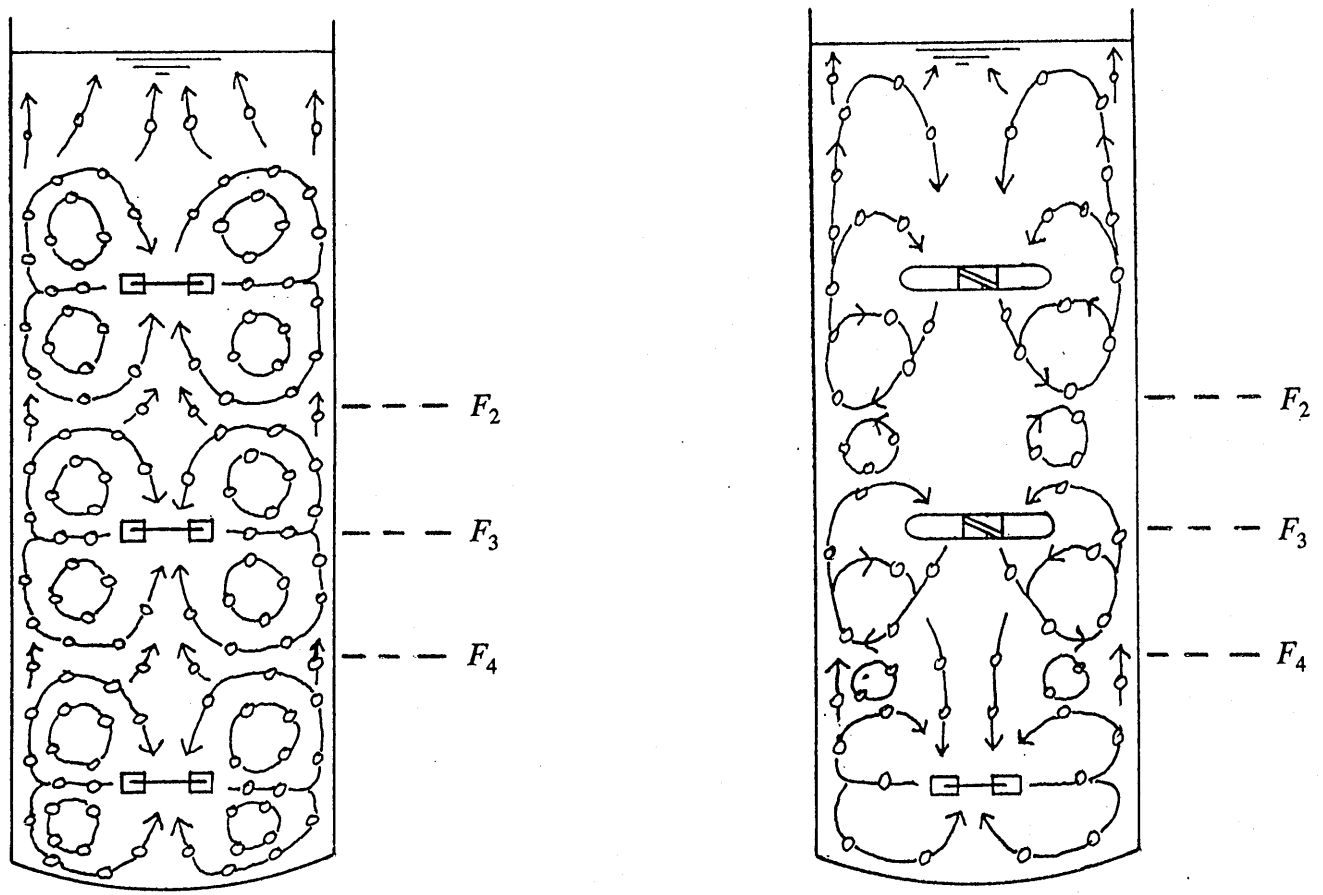


Figure 5.16: Flow patterns observations and main axial mixing boundaries.

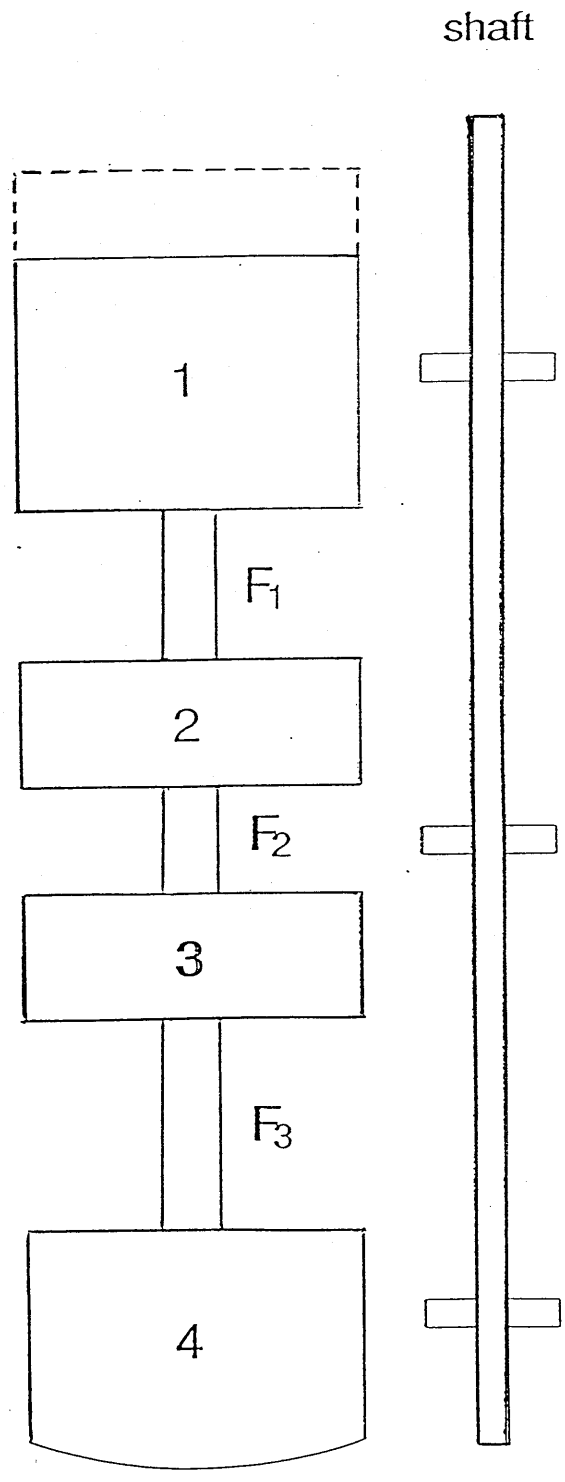
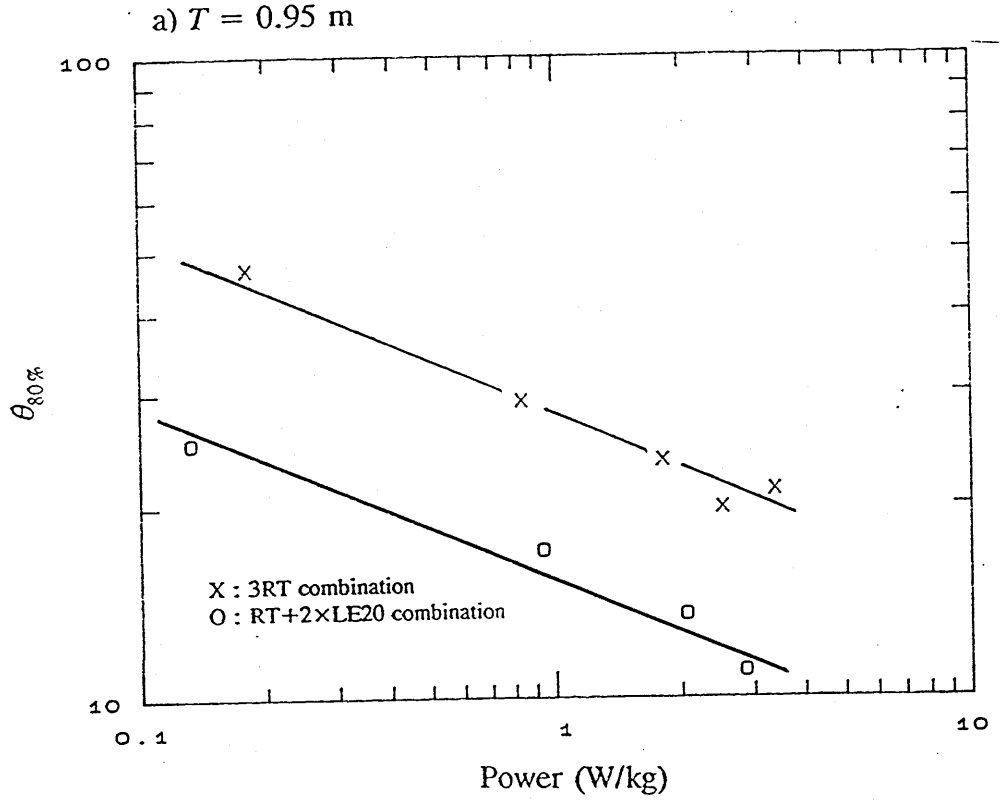


Figure 5.17: Four cell model for liquid phase mixing (four perfectly mixed cells connected by exchange flows).

Figure 5.18: Effect of power input on liquid mixing time.



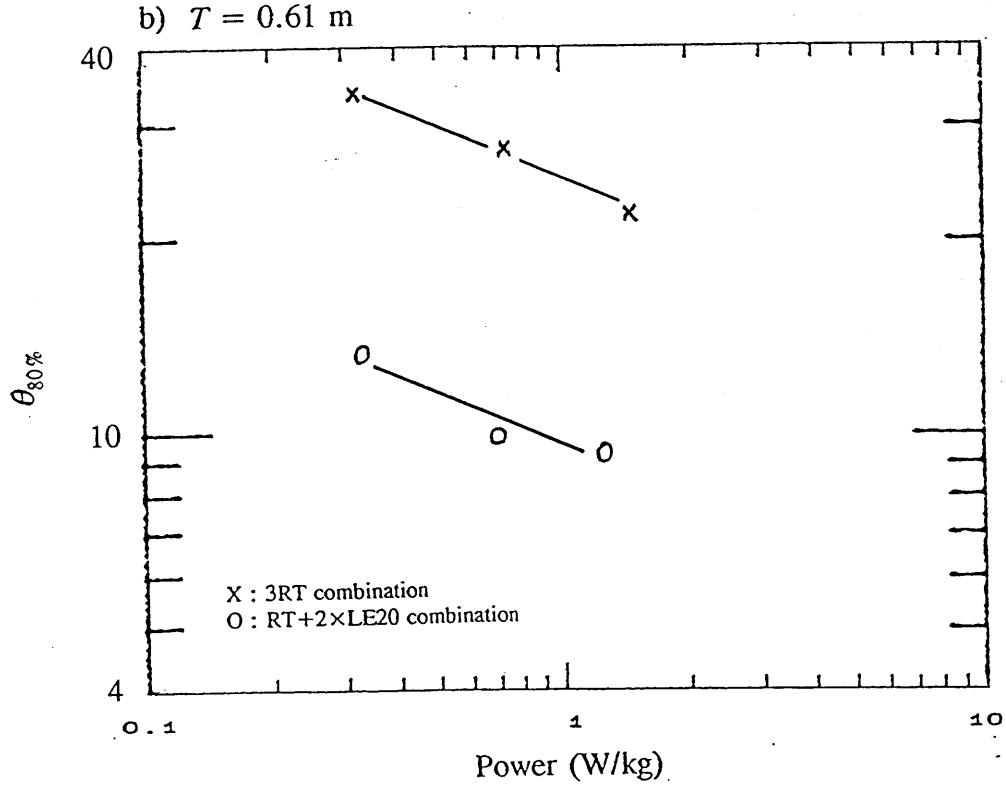
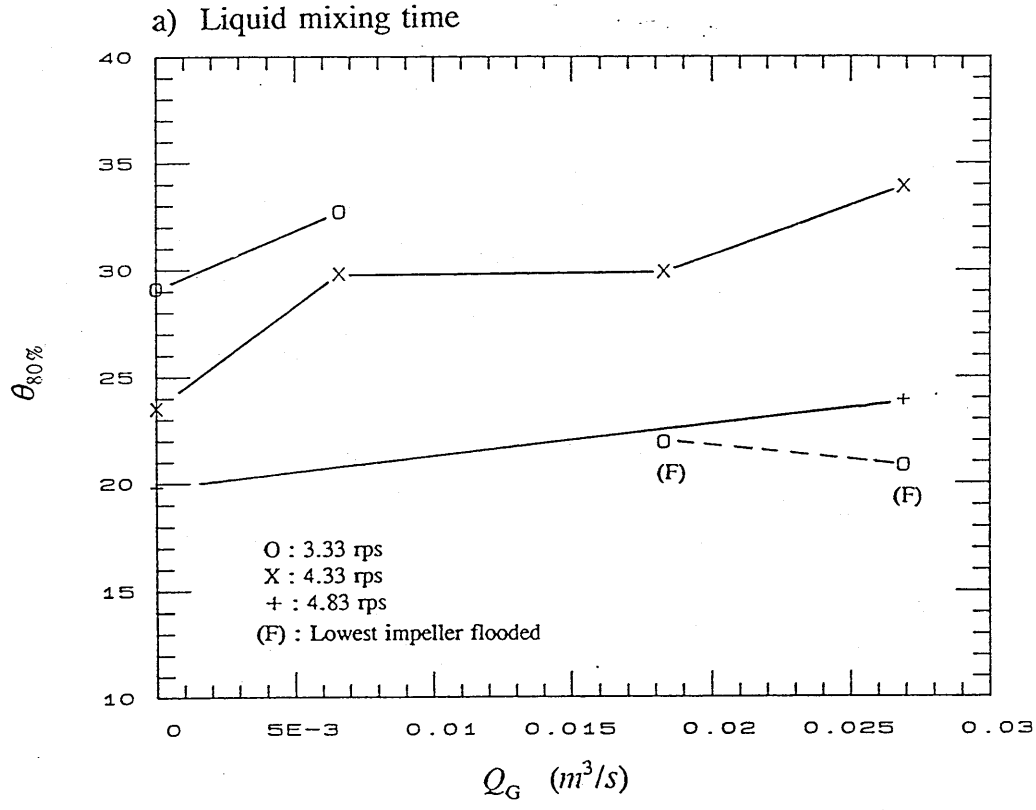


Figure 5.19: Effect of gas flow rate on triple Rushton turbine combination (T = 0.95 m).



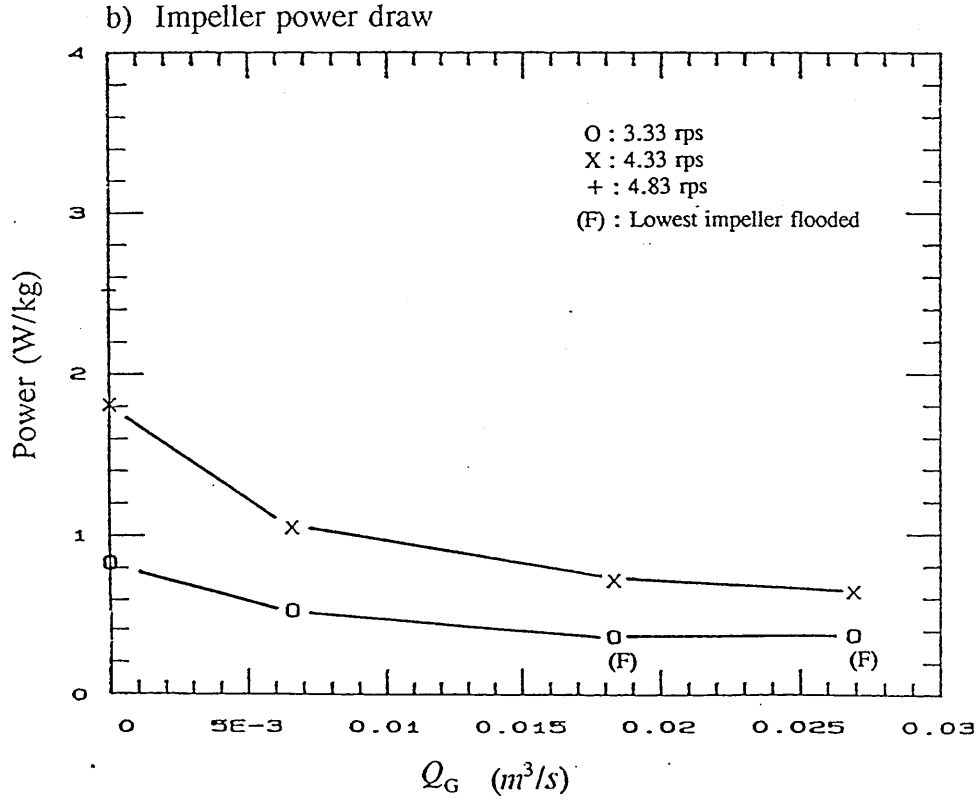


Figure 5.20: Effect of gas flow rate on the RT+2×LE20 combination. (T = 0.95 m).

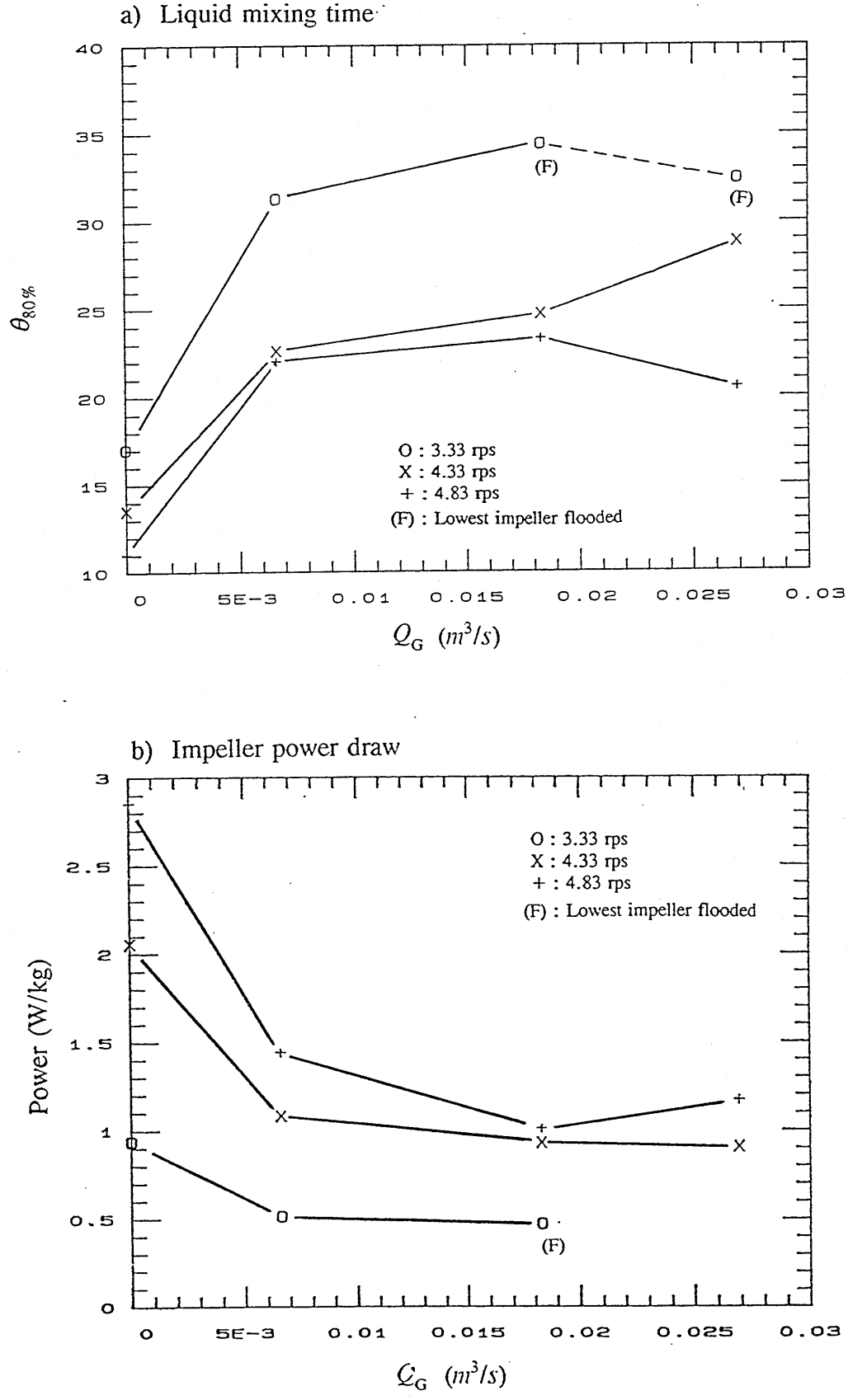
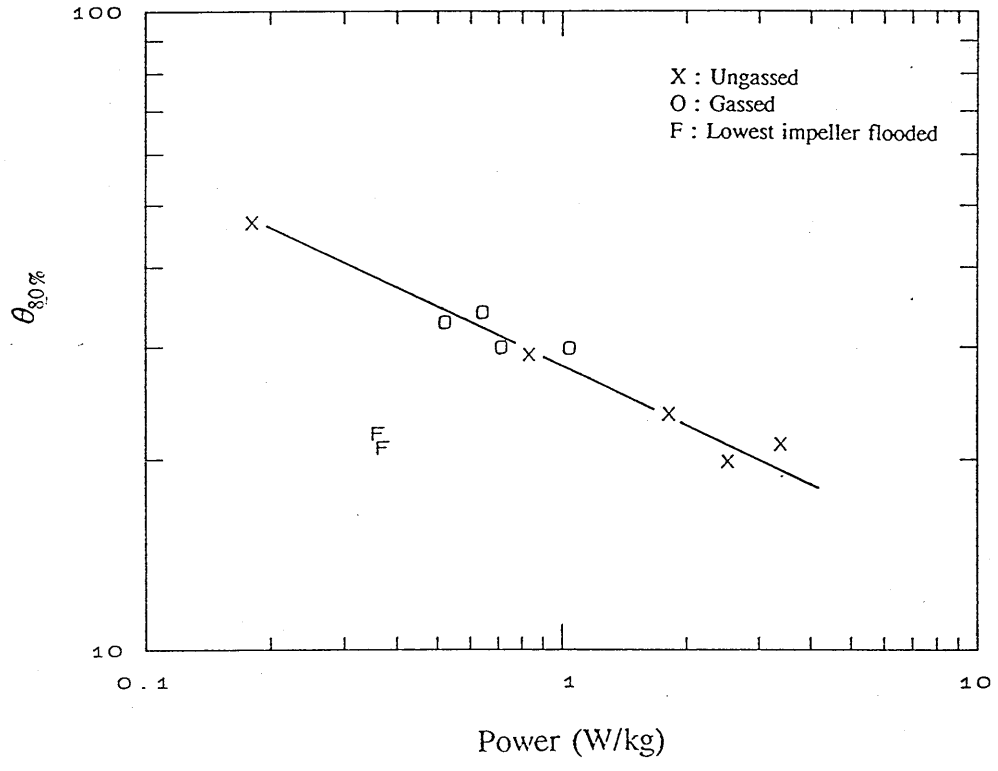


Figure 5.21: Effect of aeration and power draw on liquid mixing time (T = 0.95 m).

a) 3RT combination



b) RT+2×LE20 combination

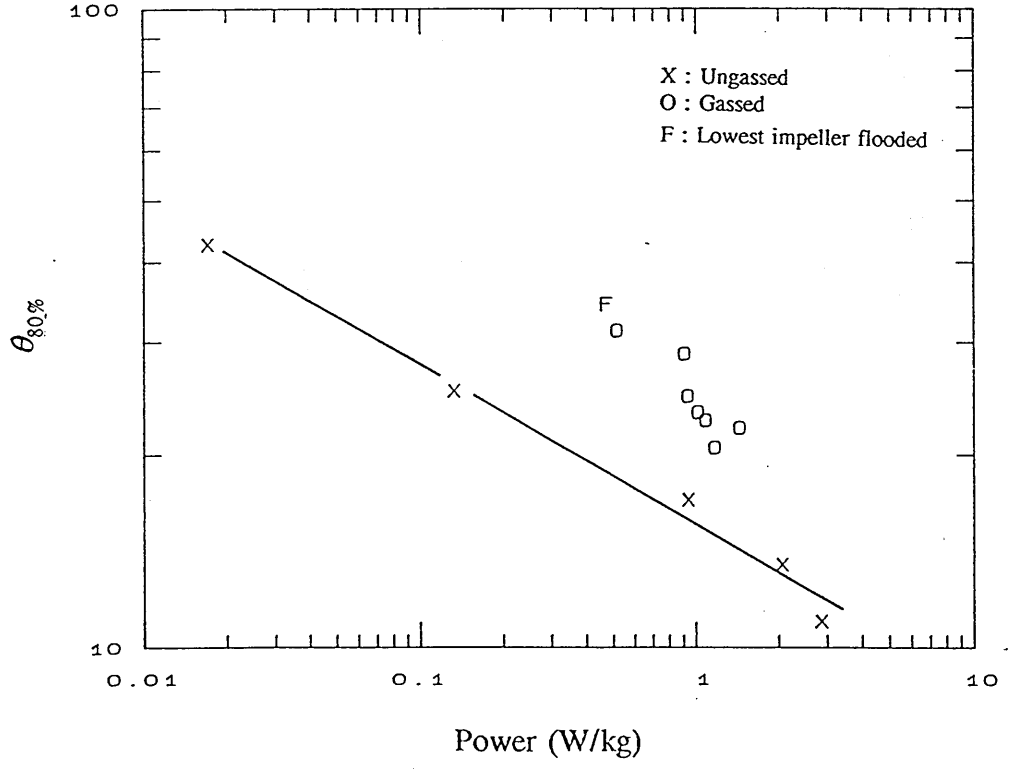


Figure 5.22: Comparison of impeller combinations (T = 0.95 m)

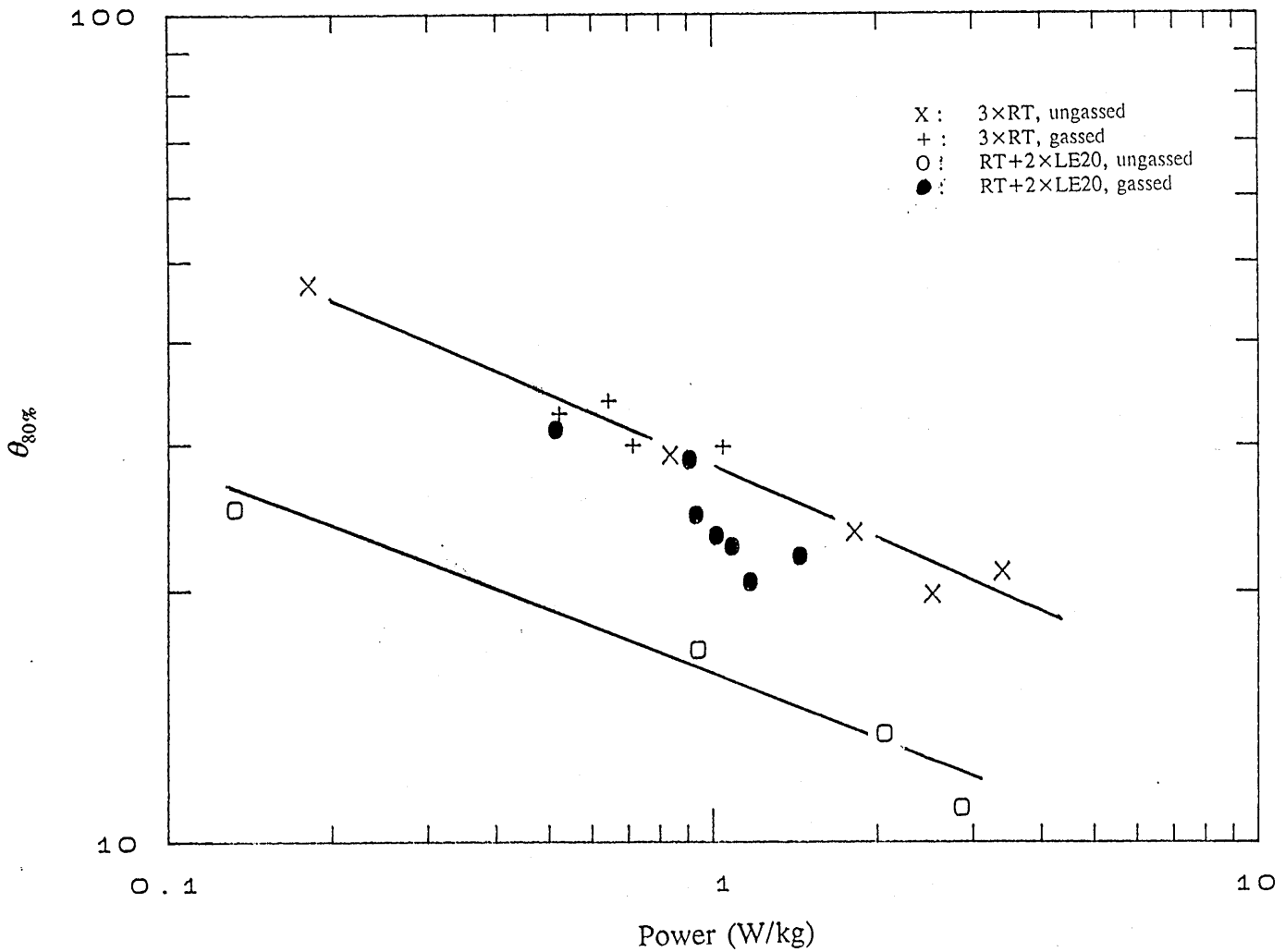
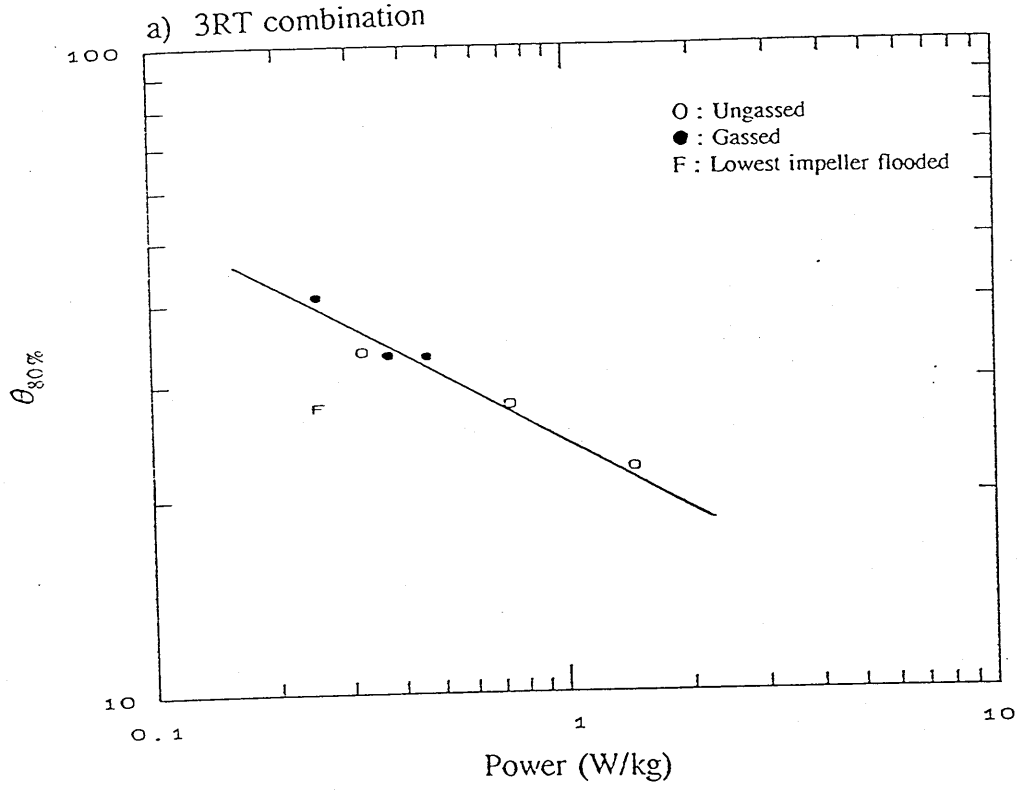


Figure 5.23: Effect of aeration and power draw on liquid mixing time (T = 0.61 m).



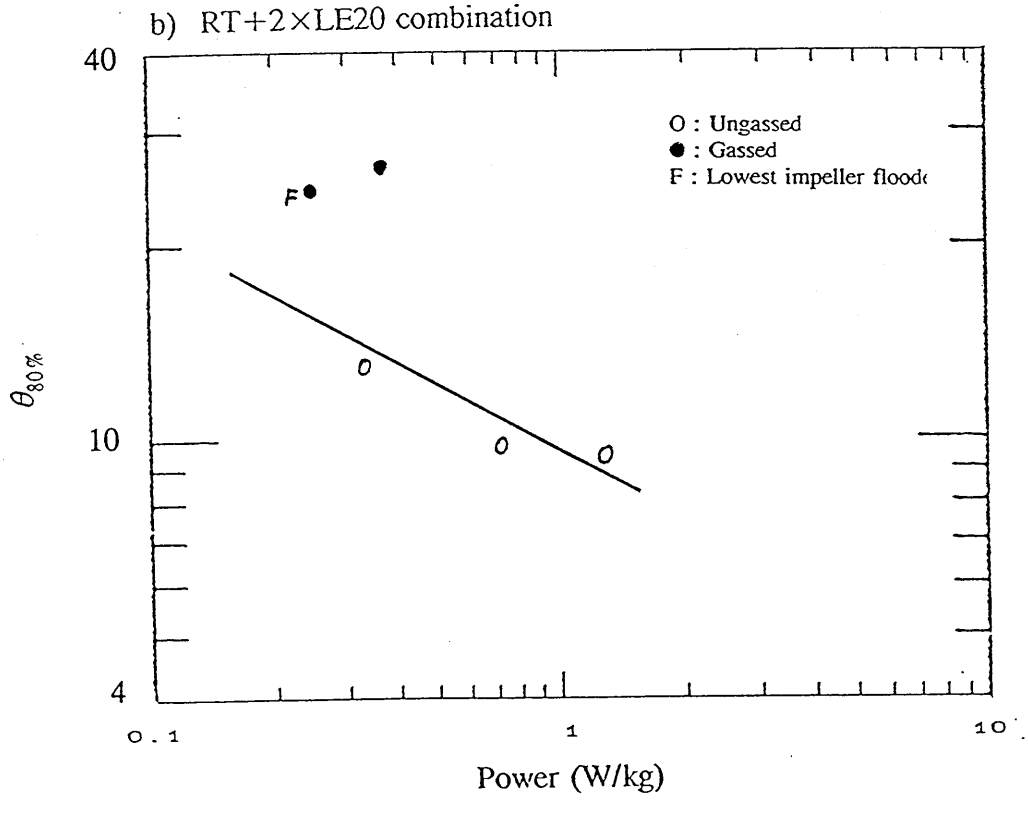


Figure 5.24: Effect of scale on liquid mixing time (3RT combination).

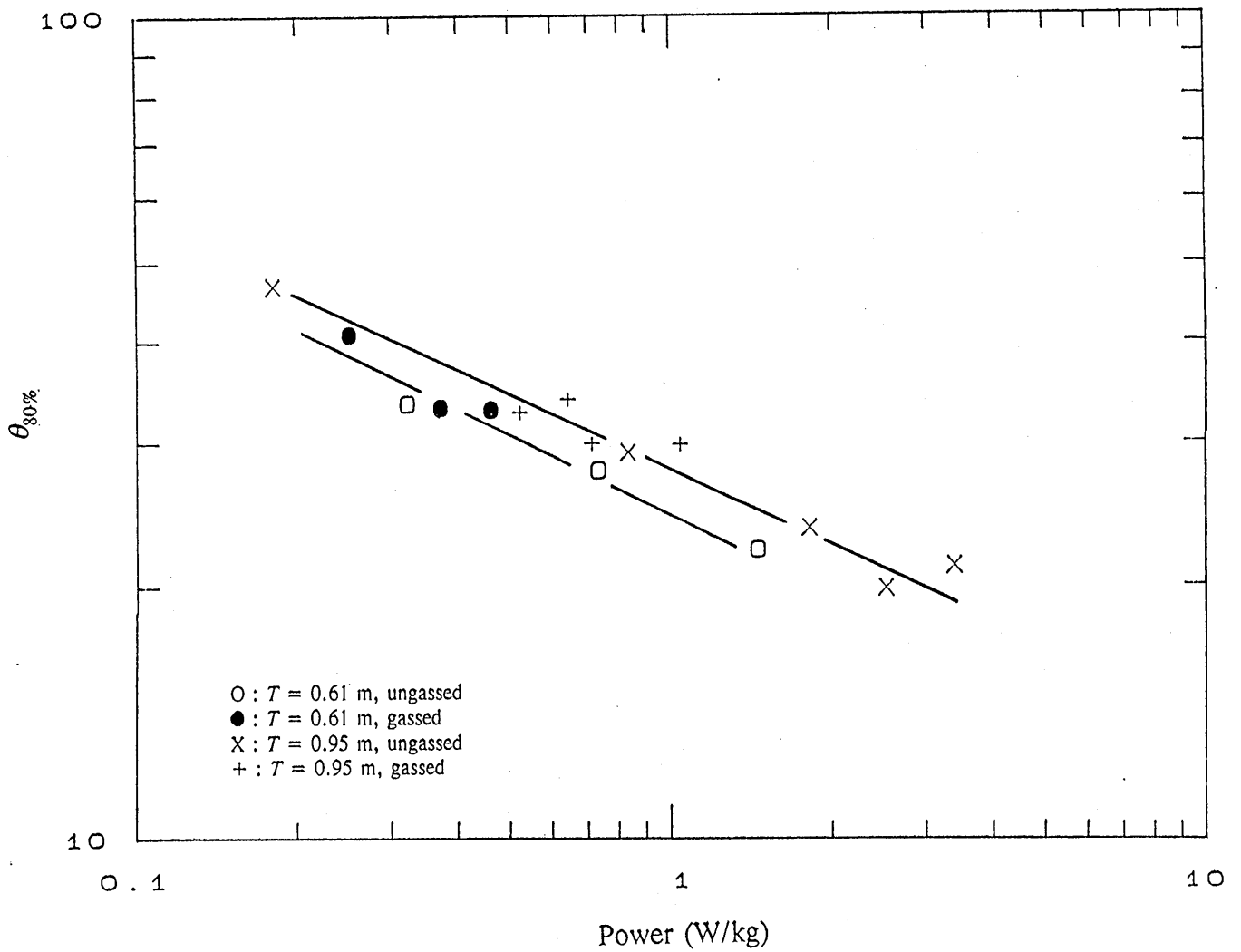


Figure 5.25: Correlation of mixing time data from two scales (3RT combination).

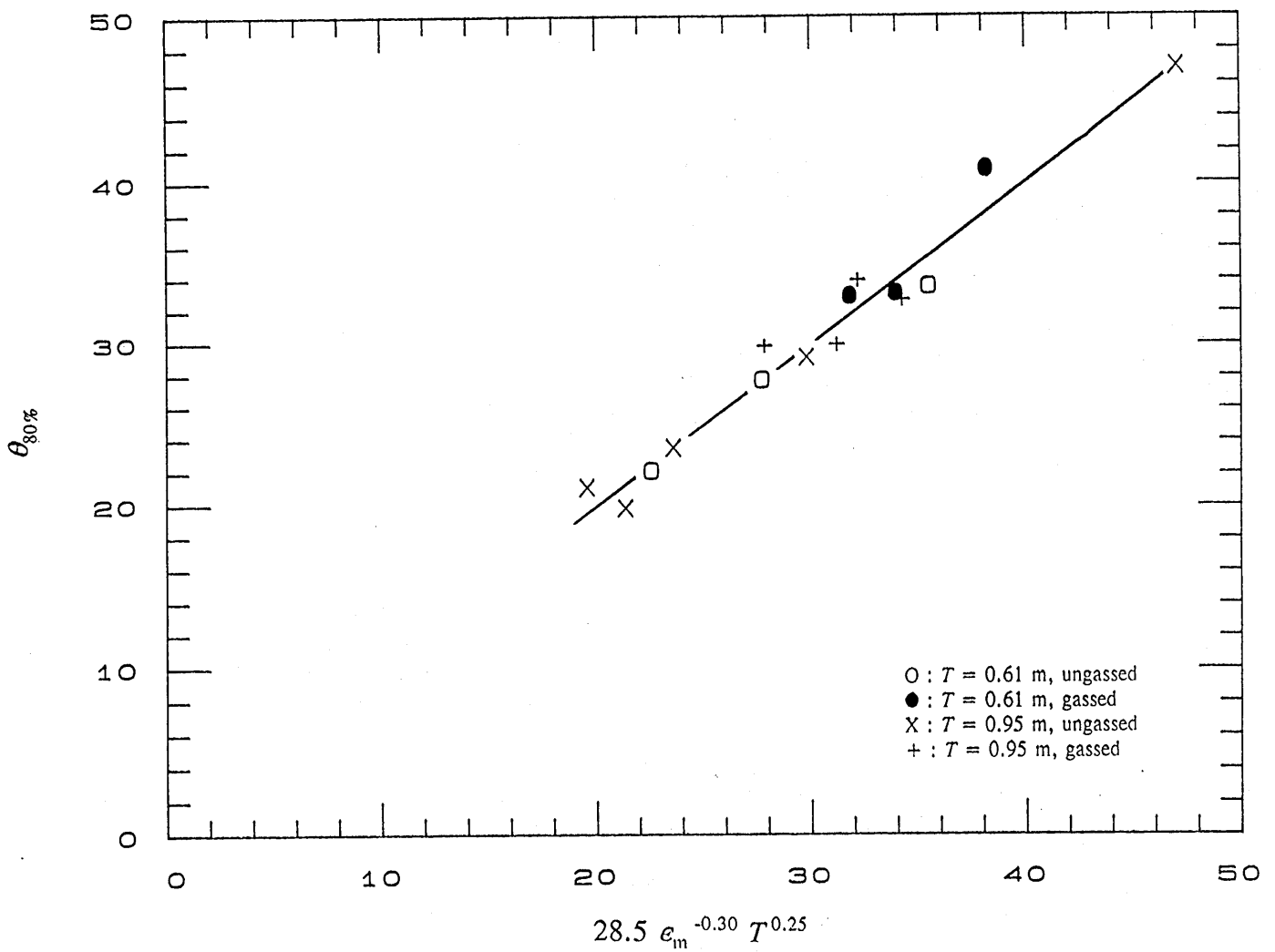


Figure 5.26: Effect of scale on liquid mixing time (RT+2×LE20 combination).

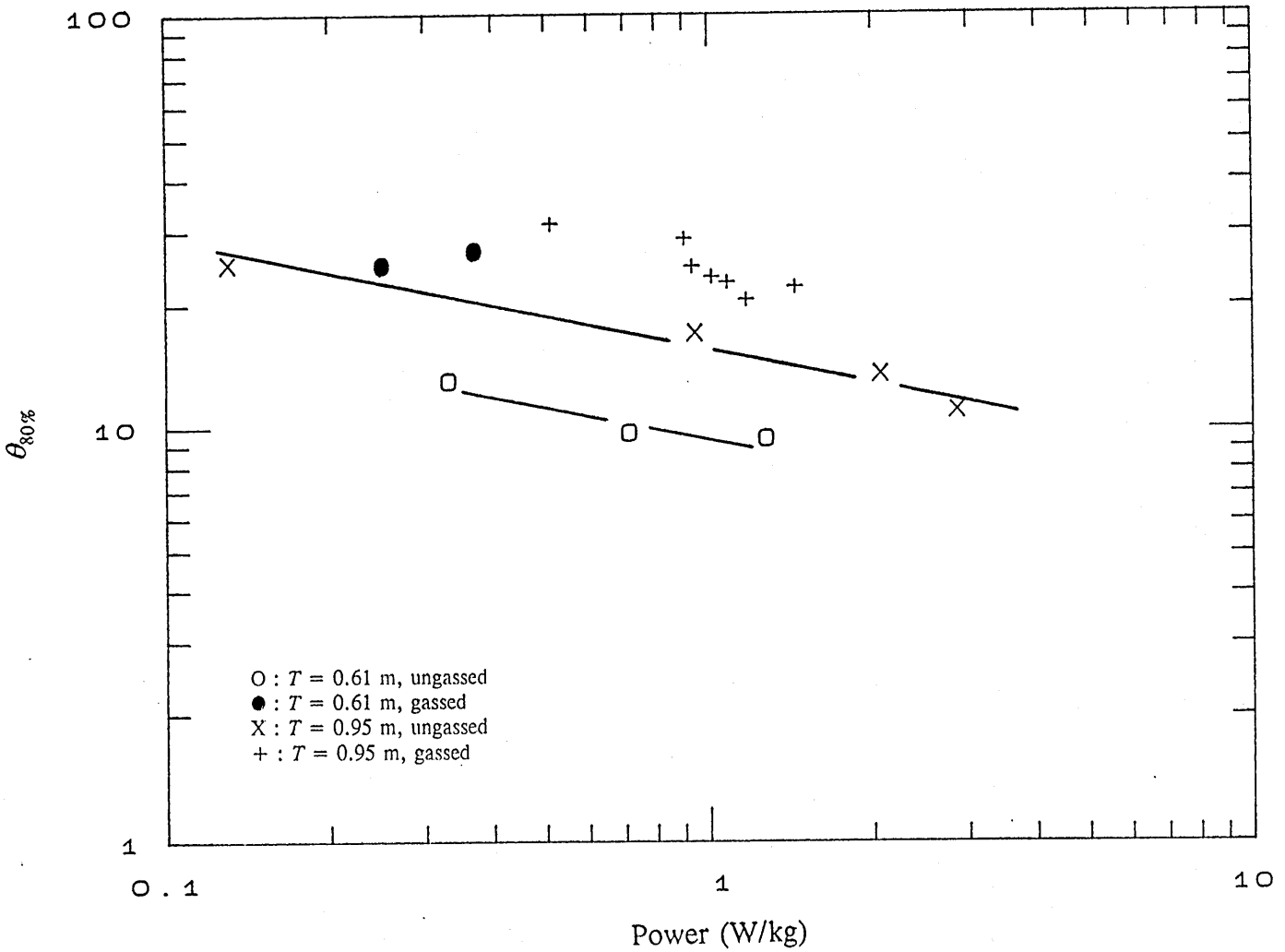
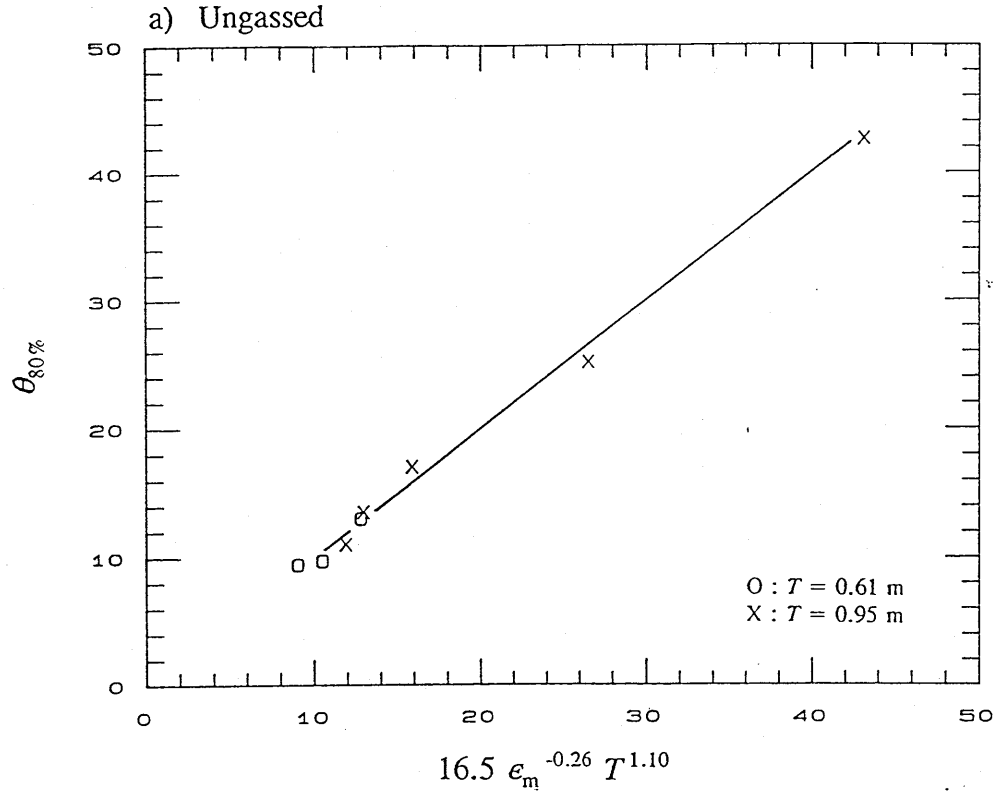
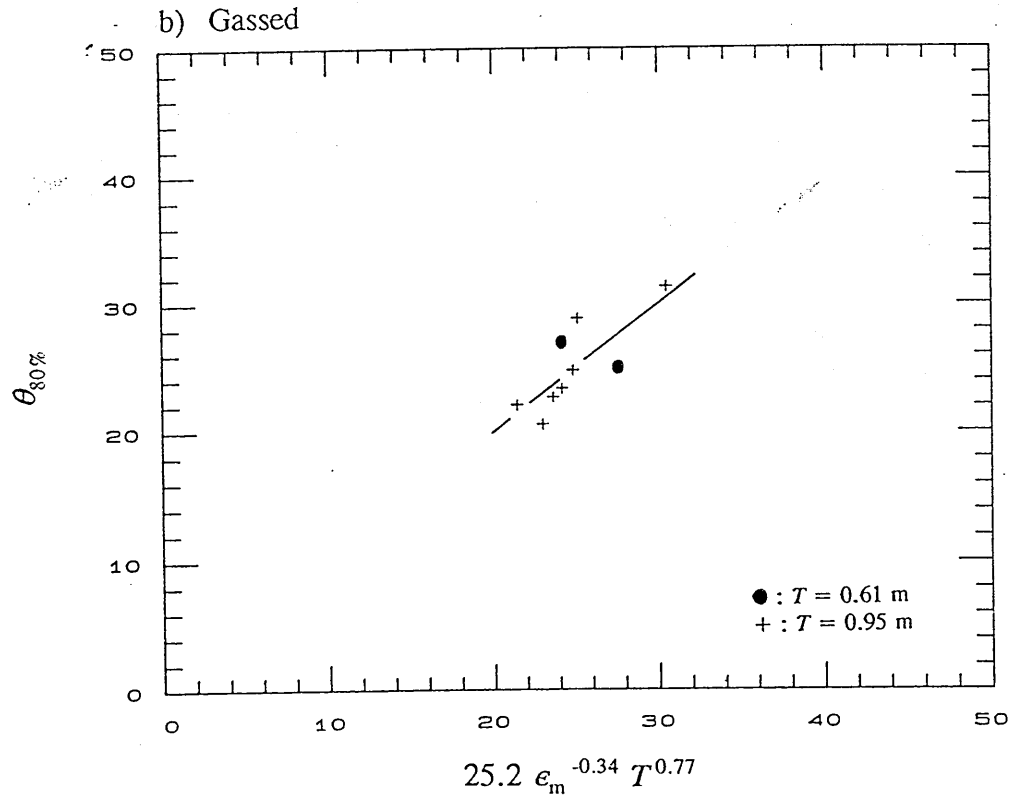


Figure 5.27: Correlation of mixing time data from two scales (RT+2×LE20 combination).





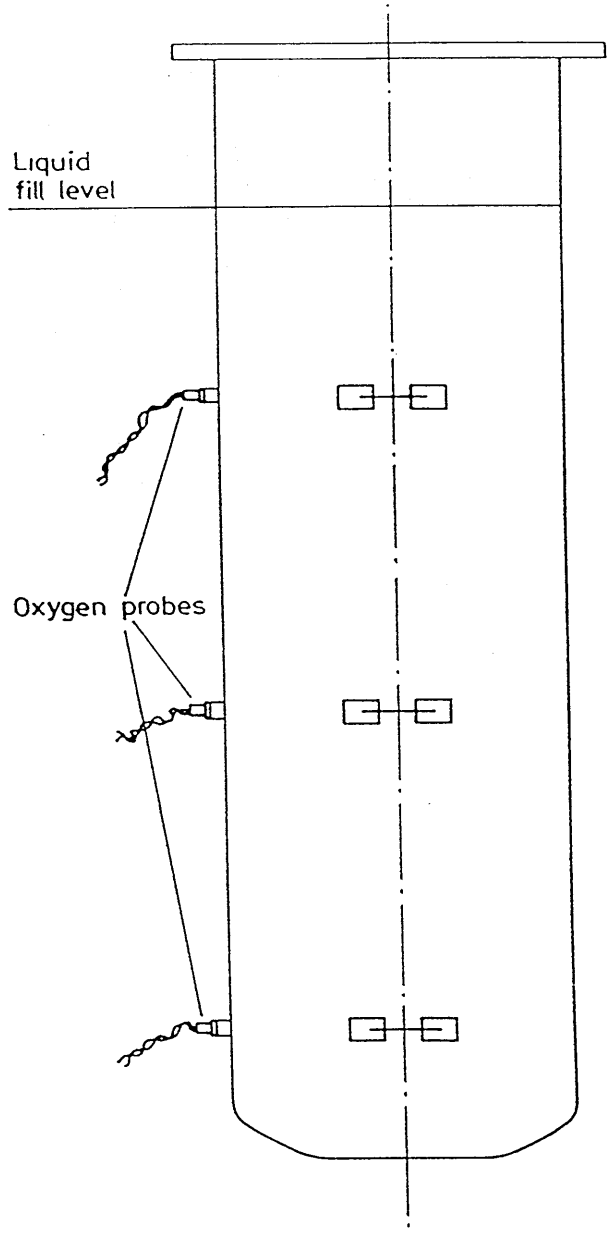


Figure 6.1: Oxygen probe positions, T = 0.95 m.

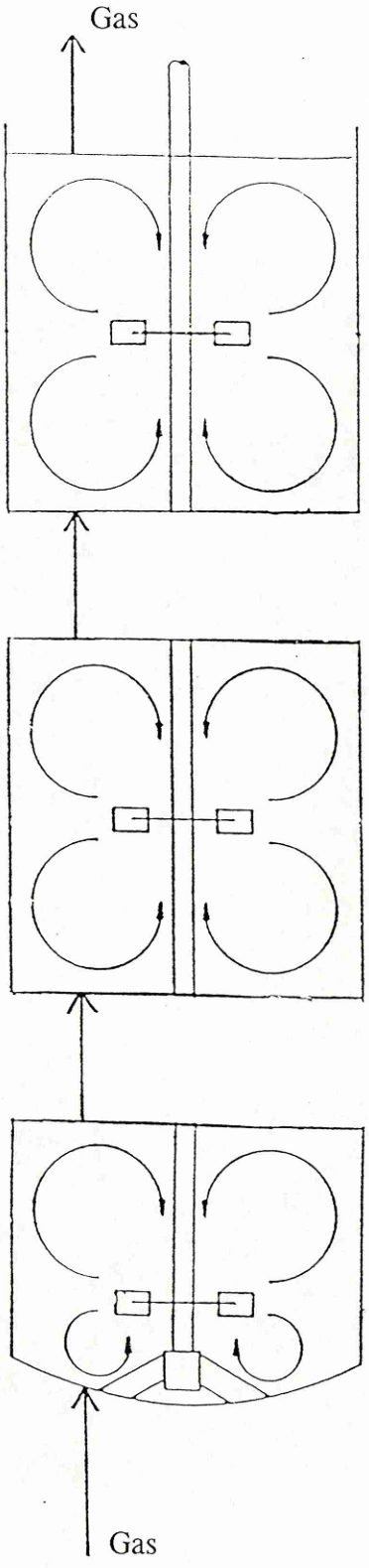


Figure 6.2: Simple mass transfer model. Three separate perfectly mixed liquid cells with gas in plug flow.

Figure 6.3: k_La from simple model.

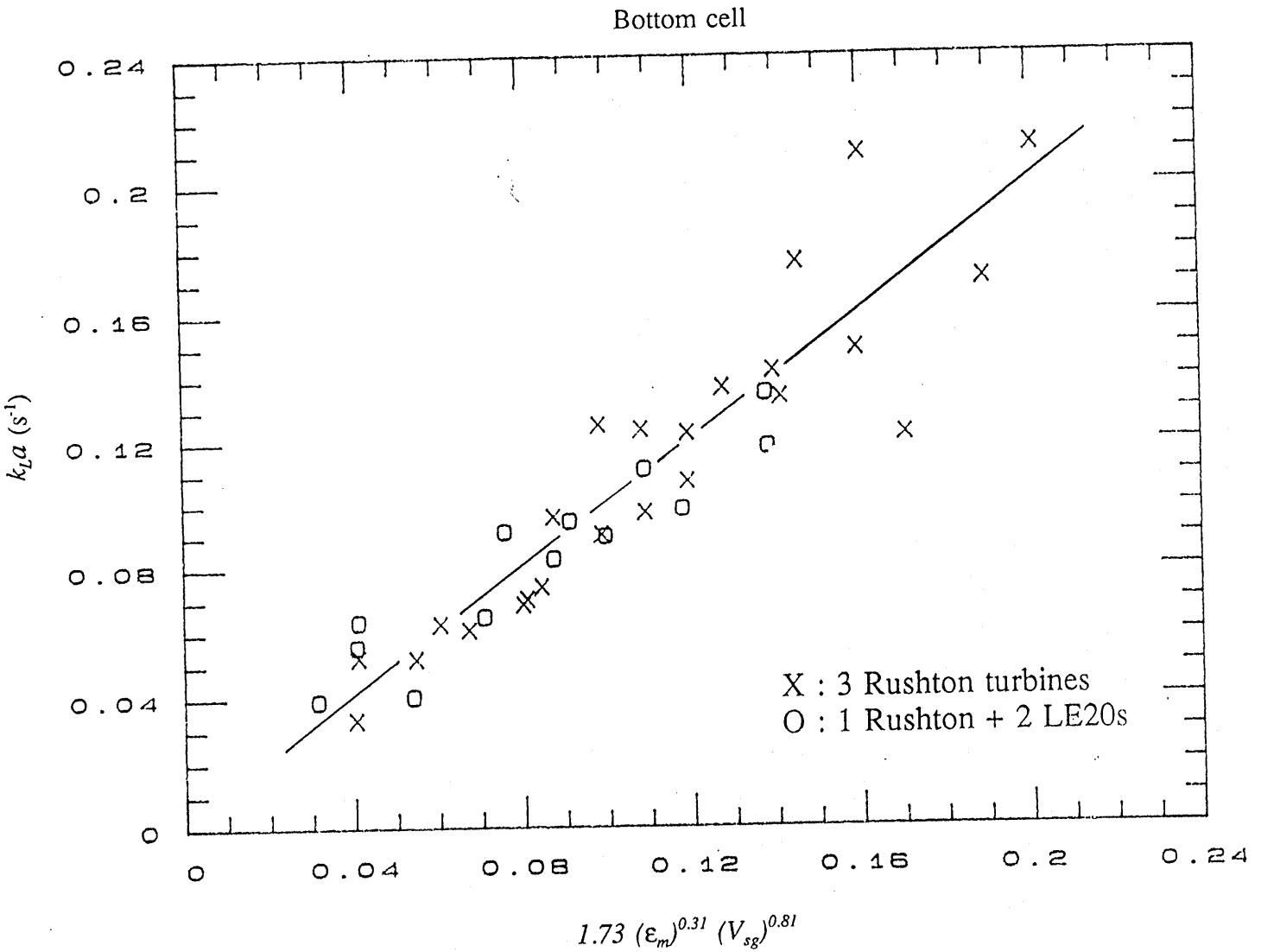


Figure 6.3: k_La from simple model.

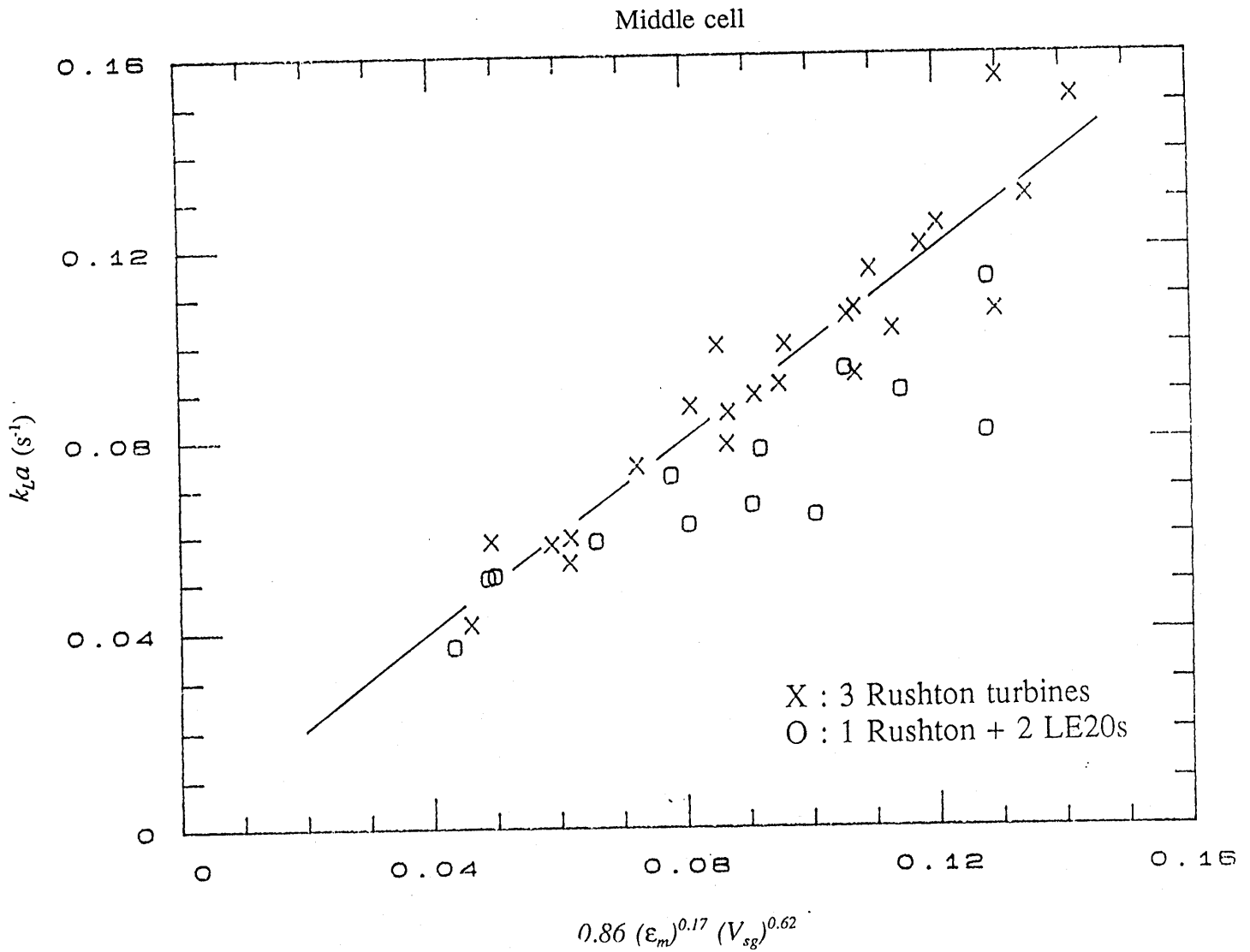
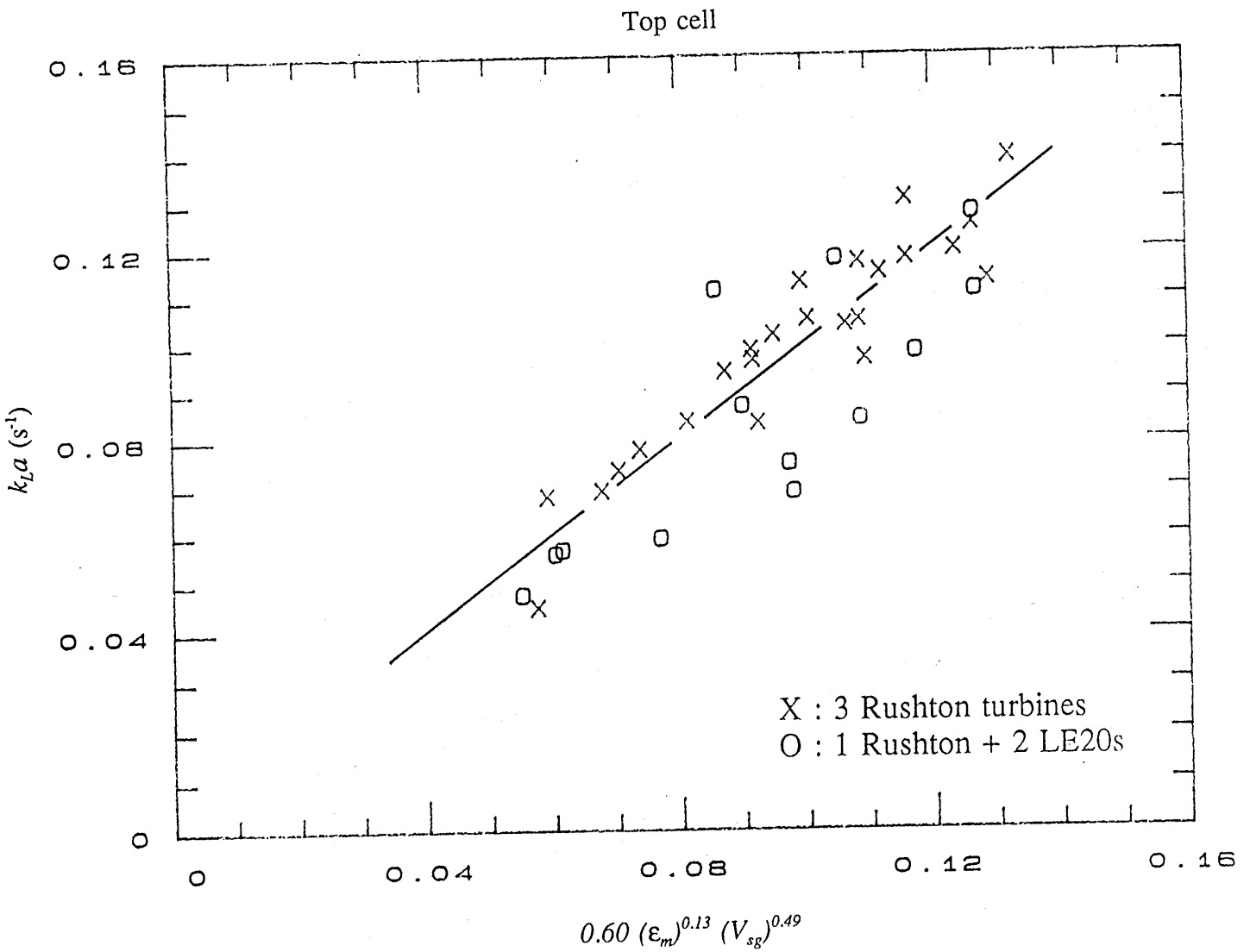


Figure 6.3: k_La from simple model.



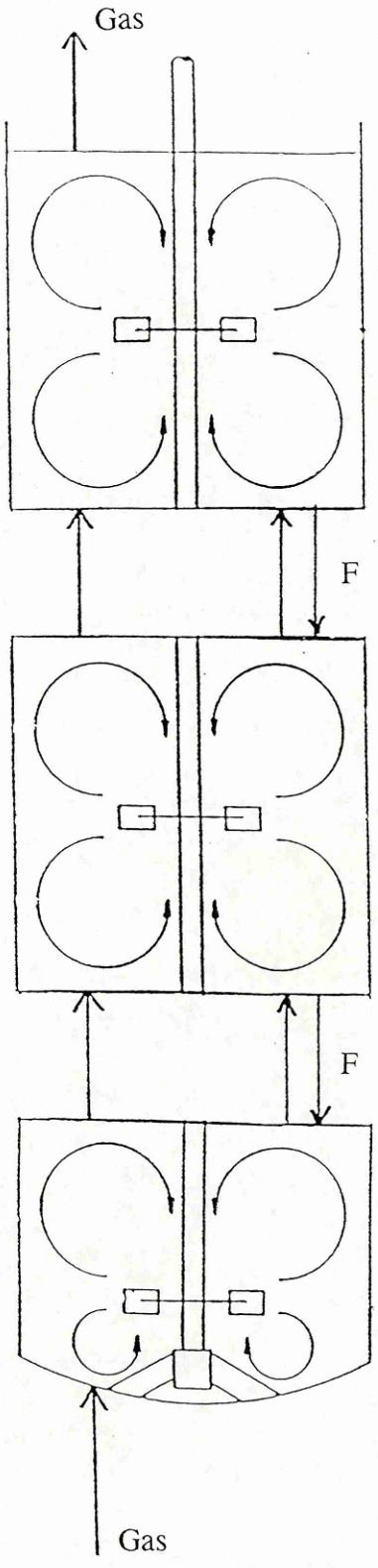


Figure 6.4: Mass transfer model including liquid exchange flows.

Figure 6.5: Effect of exchange flows on calculated $k_L a$ values

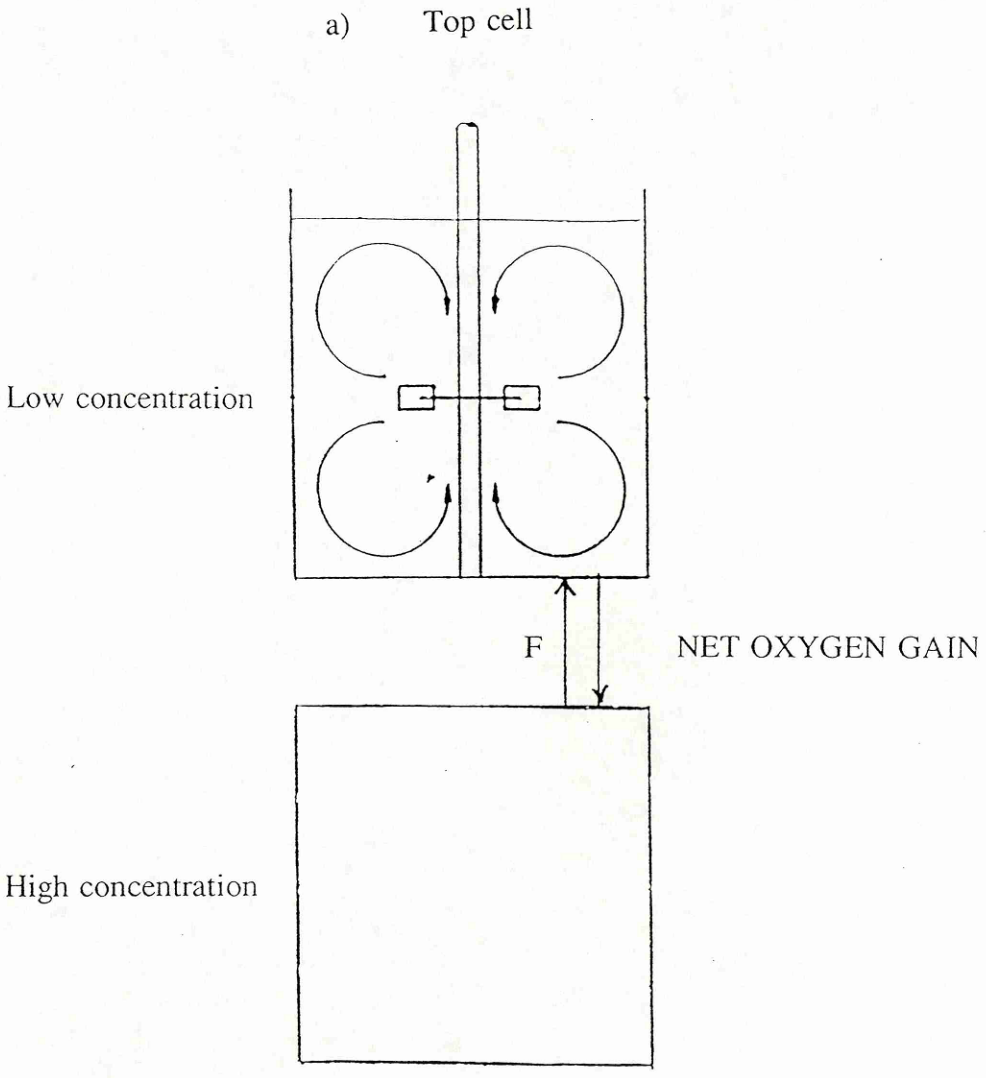


Figure 6.5: Effect of exchange flows on calculated $k_L a$ values

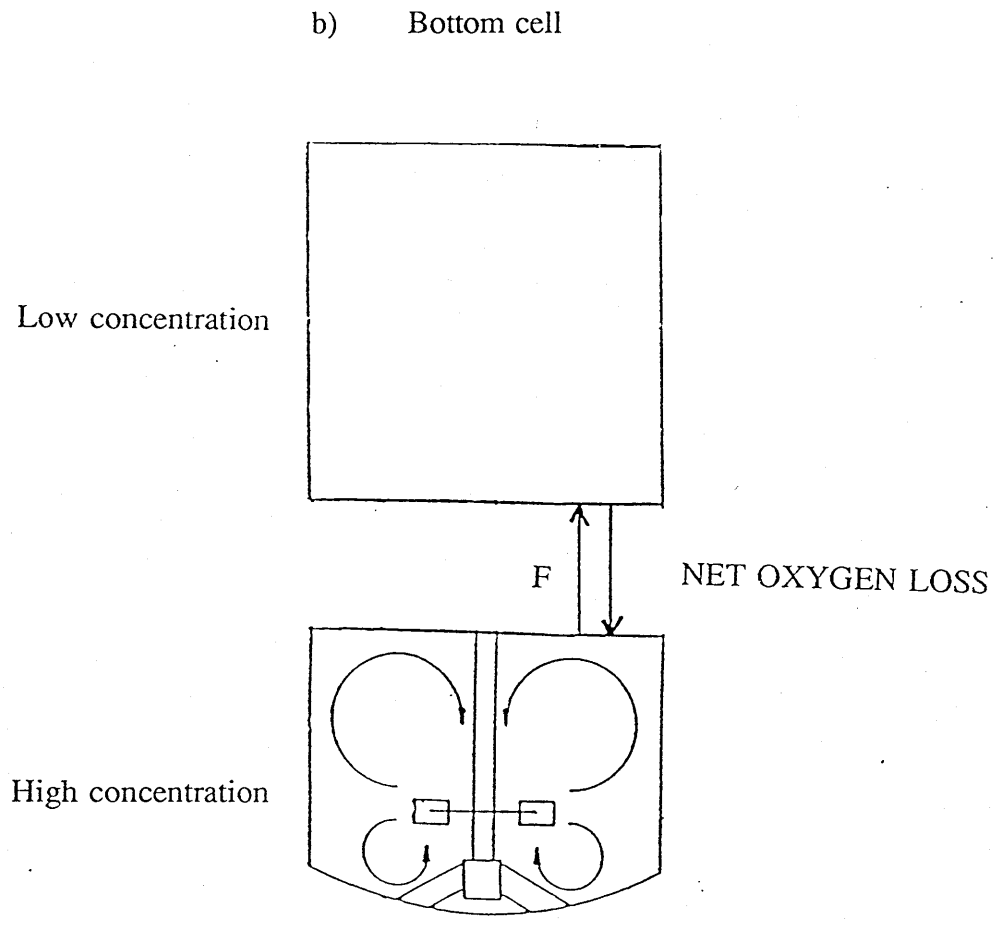


Figure 6.6: Sensitivity of $k_L a$ to exchange flows.

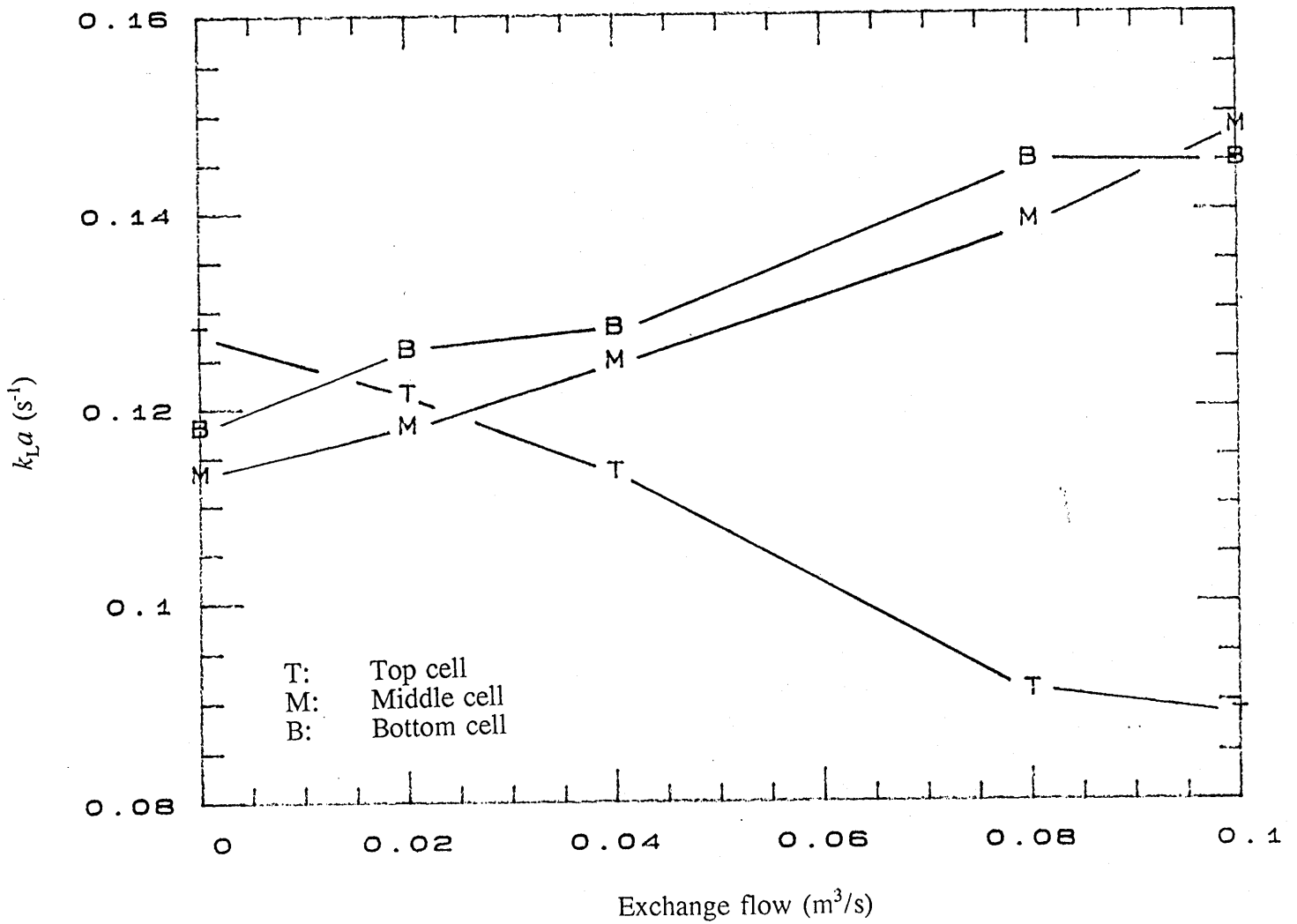


Figure 6.7: $k_L a$ values from exchange flow model (Bottom cell only).

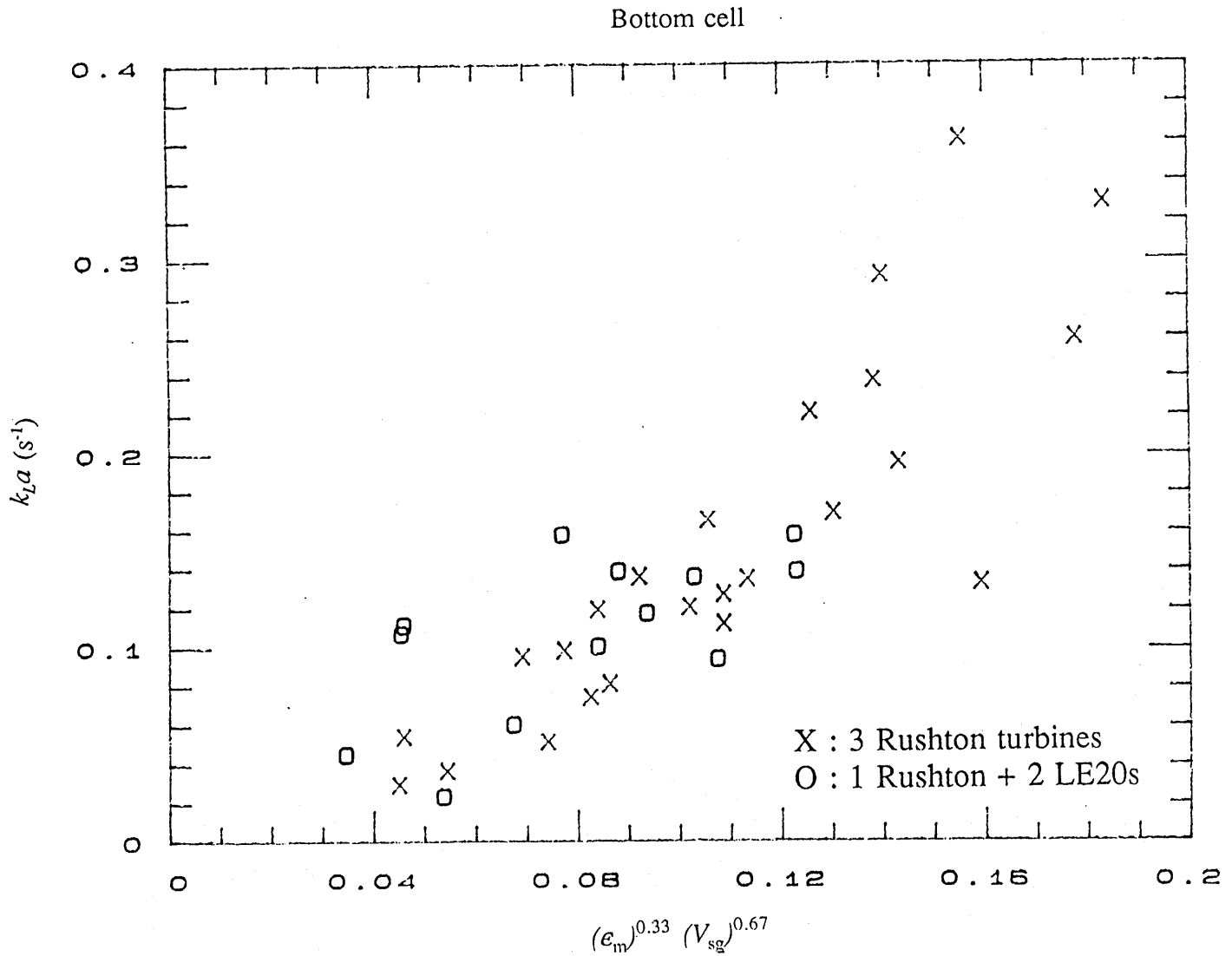


Figure 6.8: $k_L a$ values from exchange flow model.

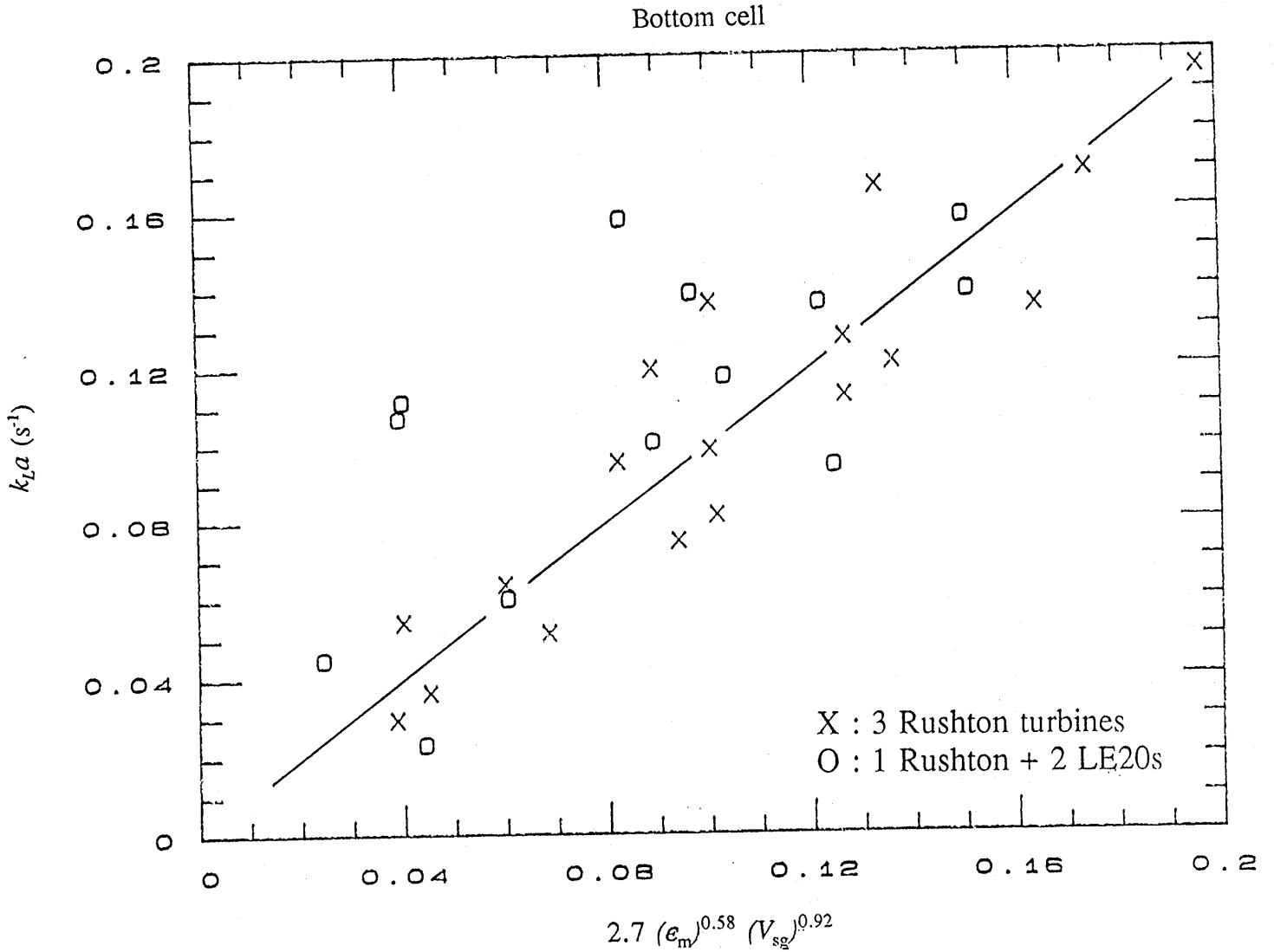


Figure 6.8: $k_L a$ values from exchange flow model.

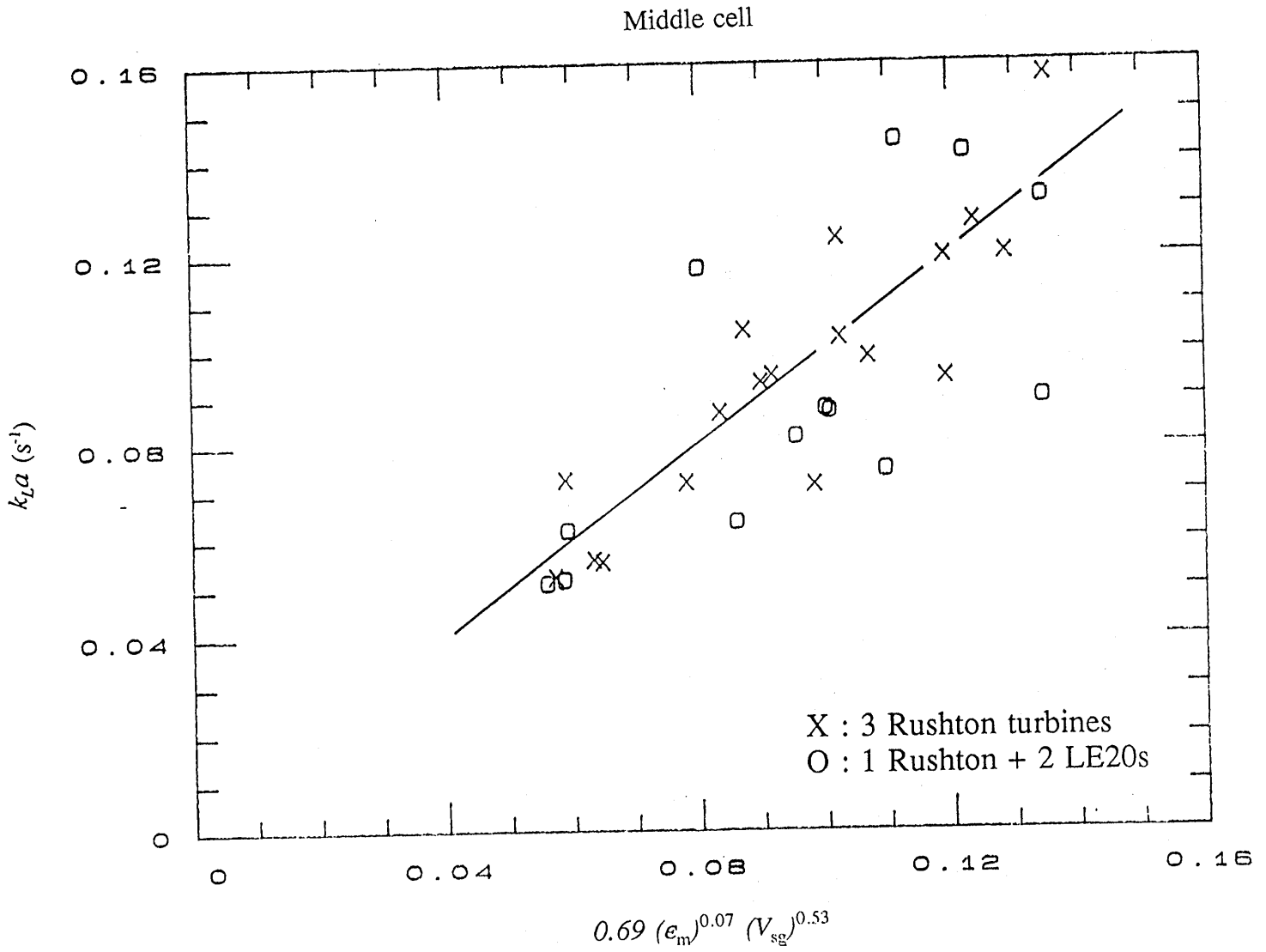


Figure 6.8: $k_L a$ values from exchange flow model.

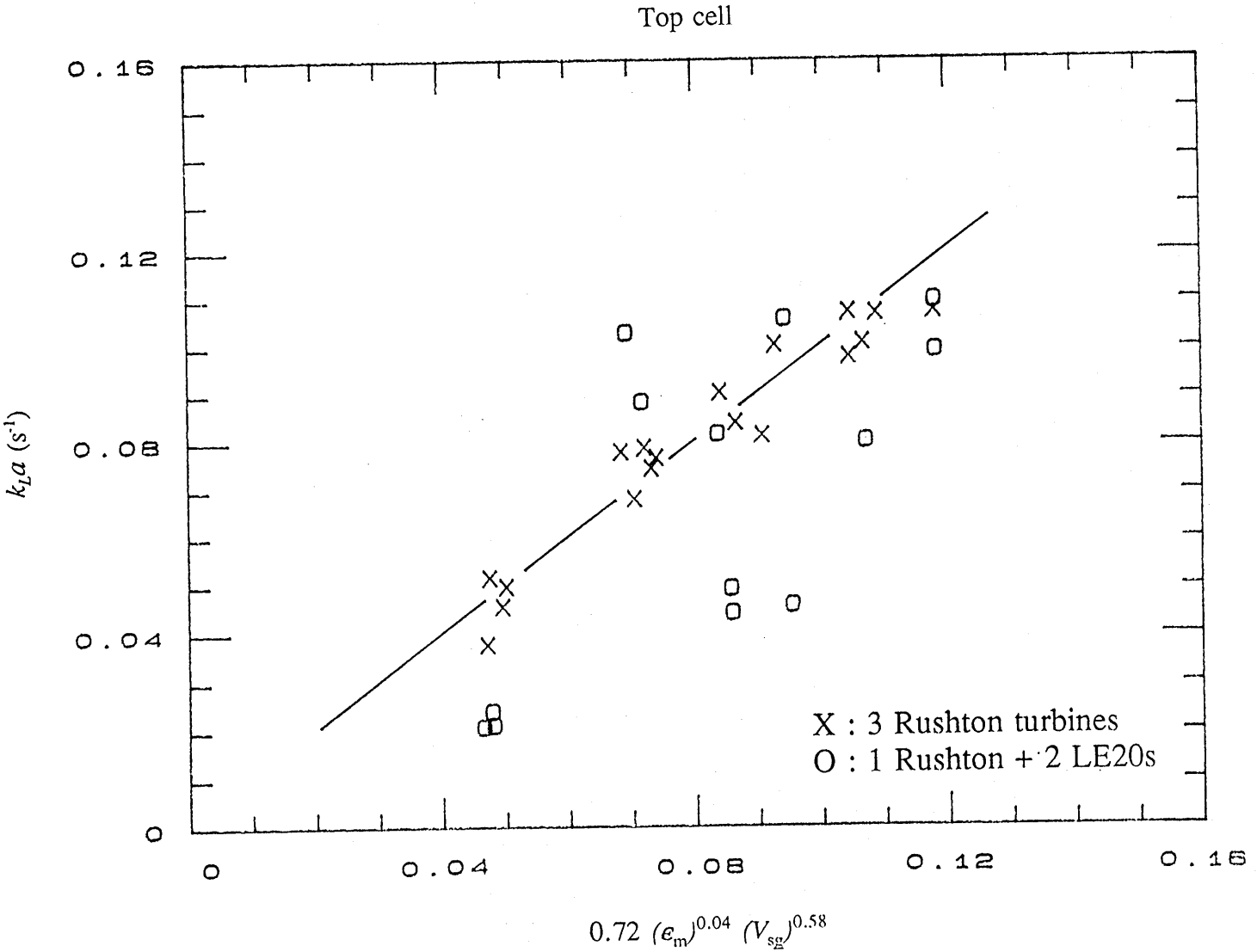


Figure 7.1: Effect of vessel scale on process options

Q_G = 1 vvm, ϵ_m = 2 W/kg, P = 1 bar.

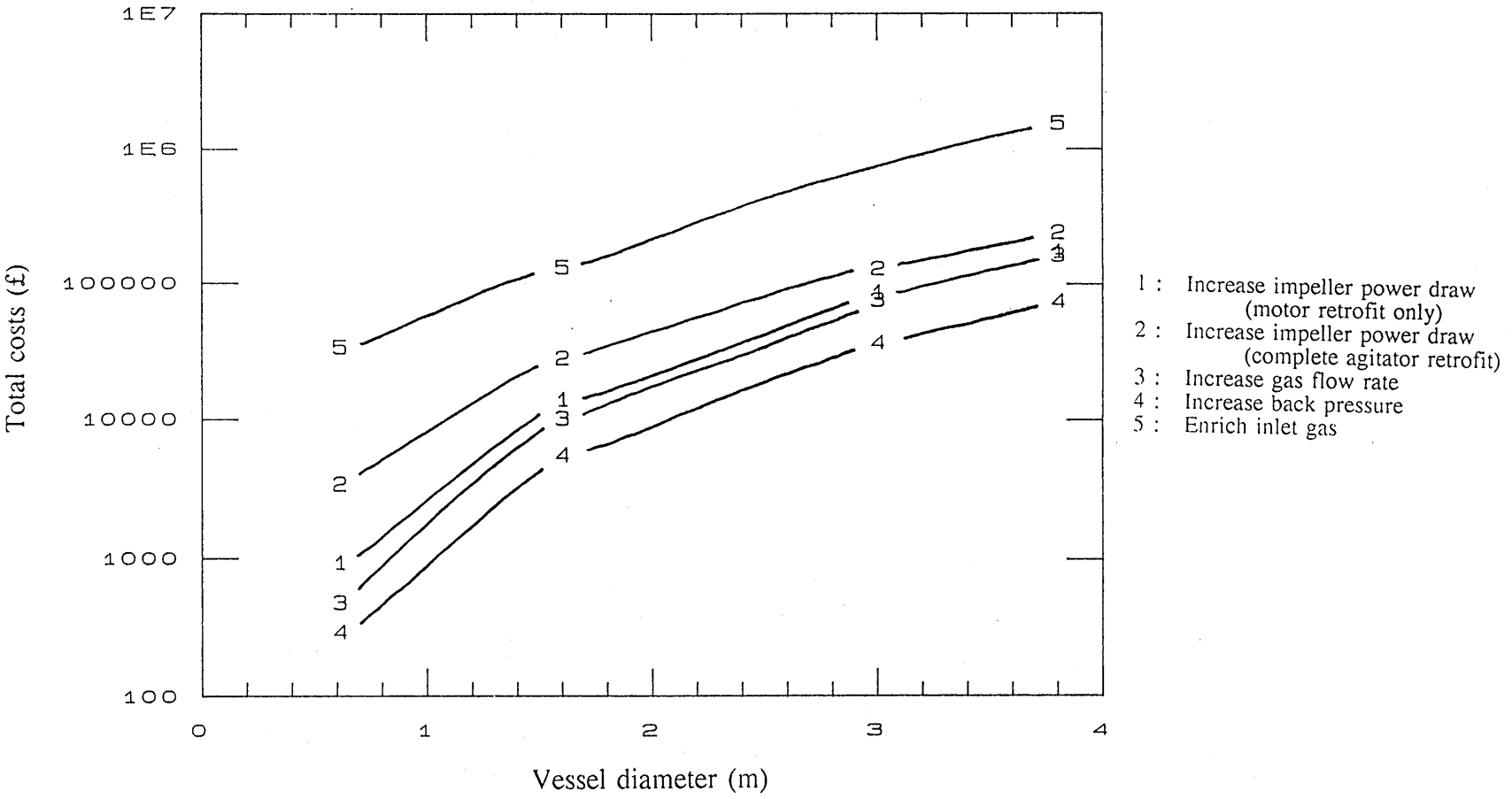


Figure 7.2: Effect of power input on cost of process options at large scale (low gas flow rate, low back pressure)

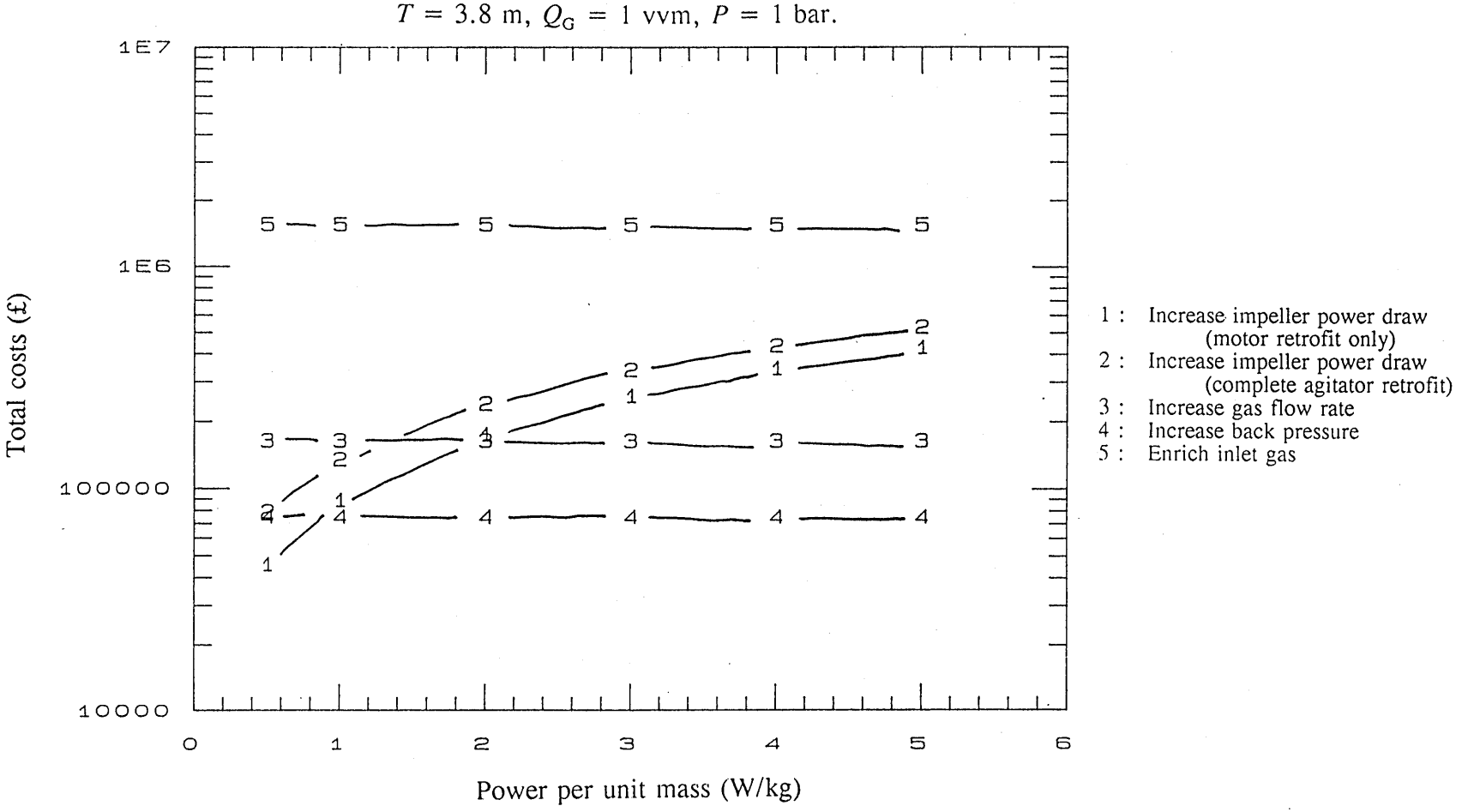


Figure 7.3: Effect of power input on cost of process options at large scale (low gas flow rate, high back pressure)

T = 3.8 m, Q_G = 1 vvm, P = 5 bar.

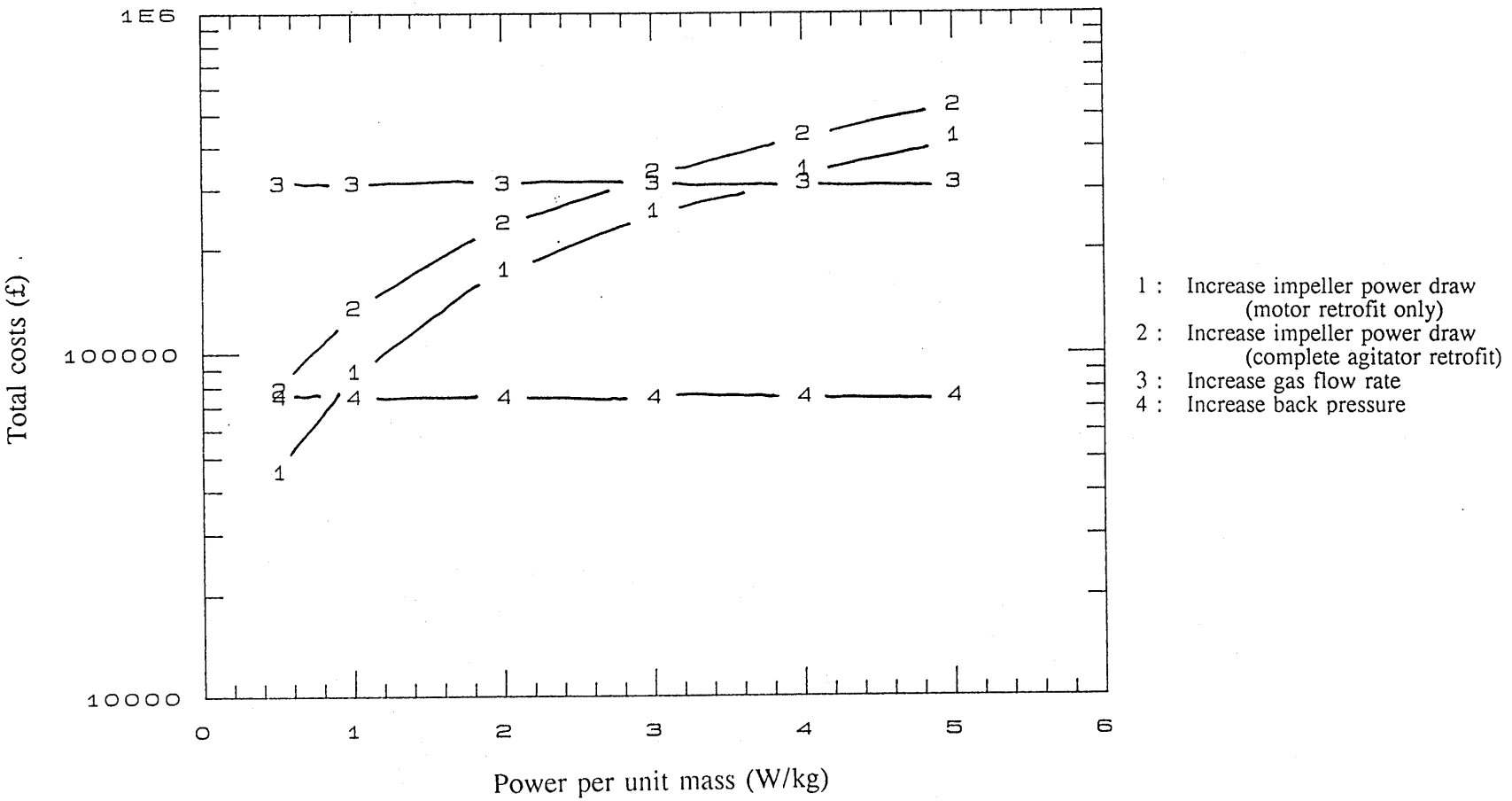


Figure 7.4: Effect of power input on cost of process options at large scale (high gas flow rate, low back pressure)

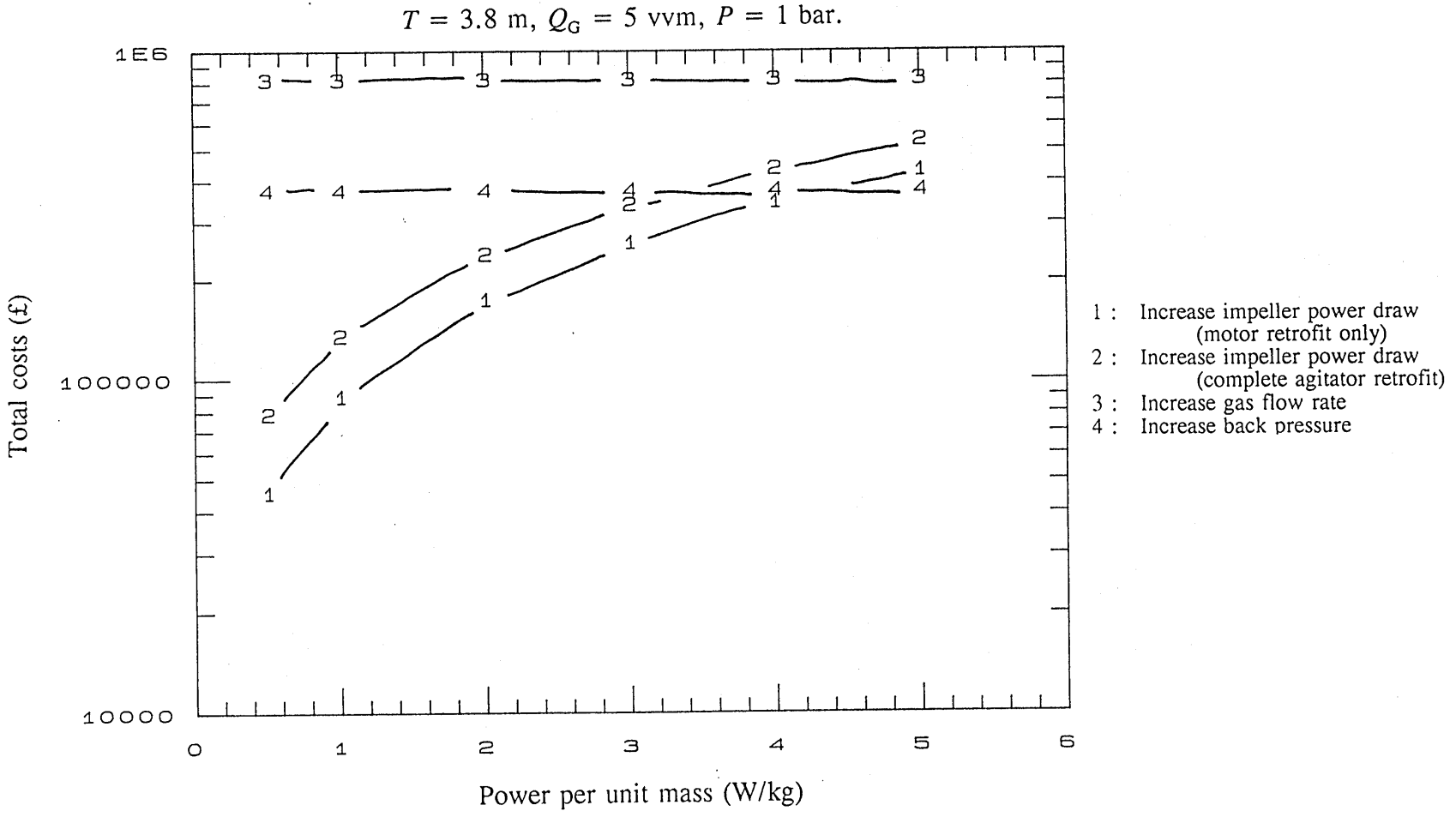


Figure 7.5: Effect of power input on cost of process options at large scale (high gas flow rate, high back pressure)

T = 3.8 m, Q_G = 5 vvm, P = 5 bar.

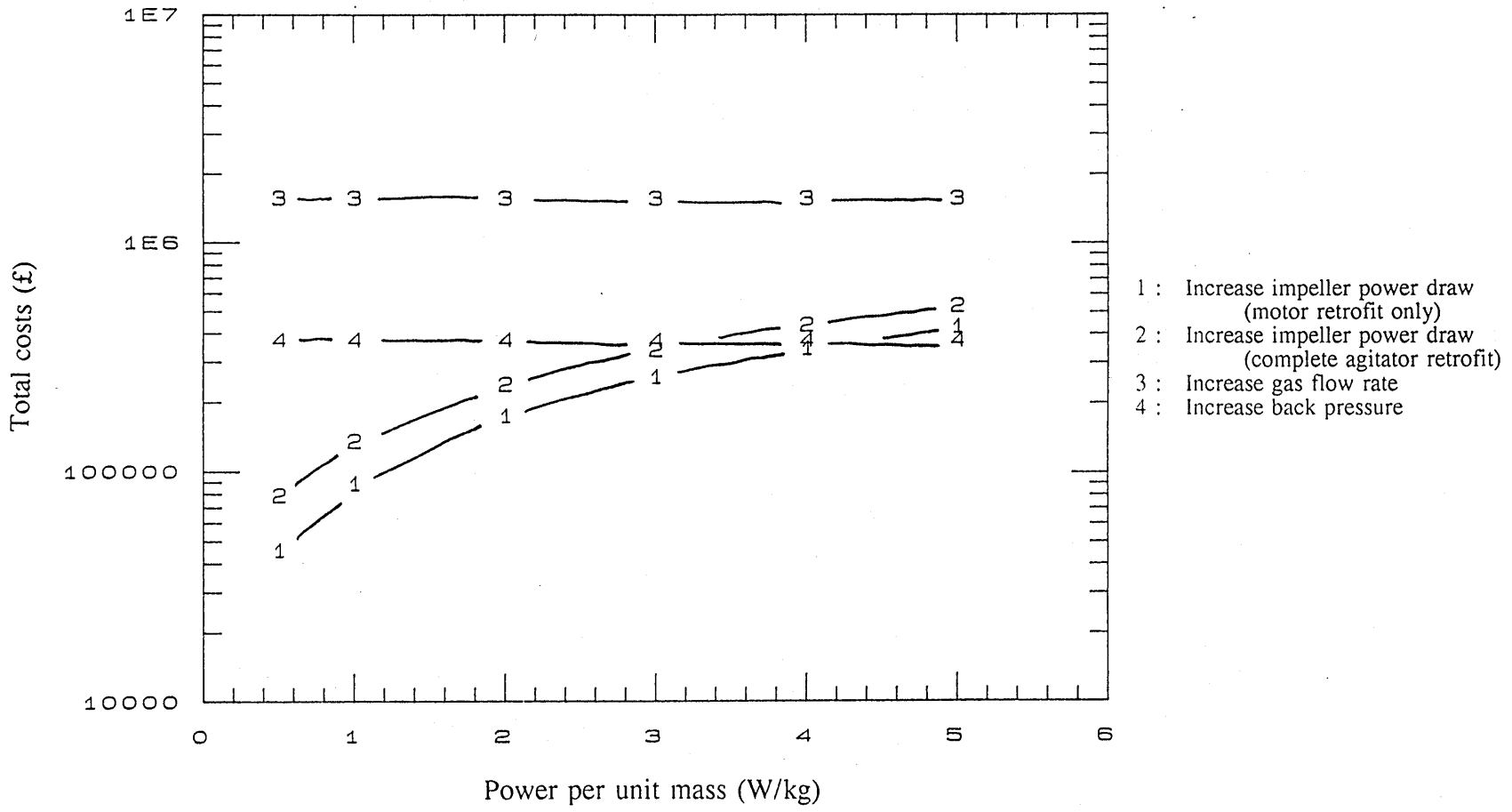


Figure 7.6: Effect of power input on cost of process options at small scale (low gas flow rate, low back pressure)

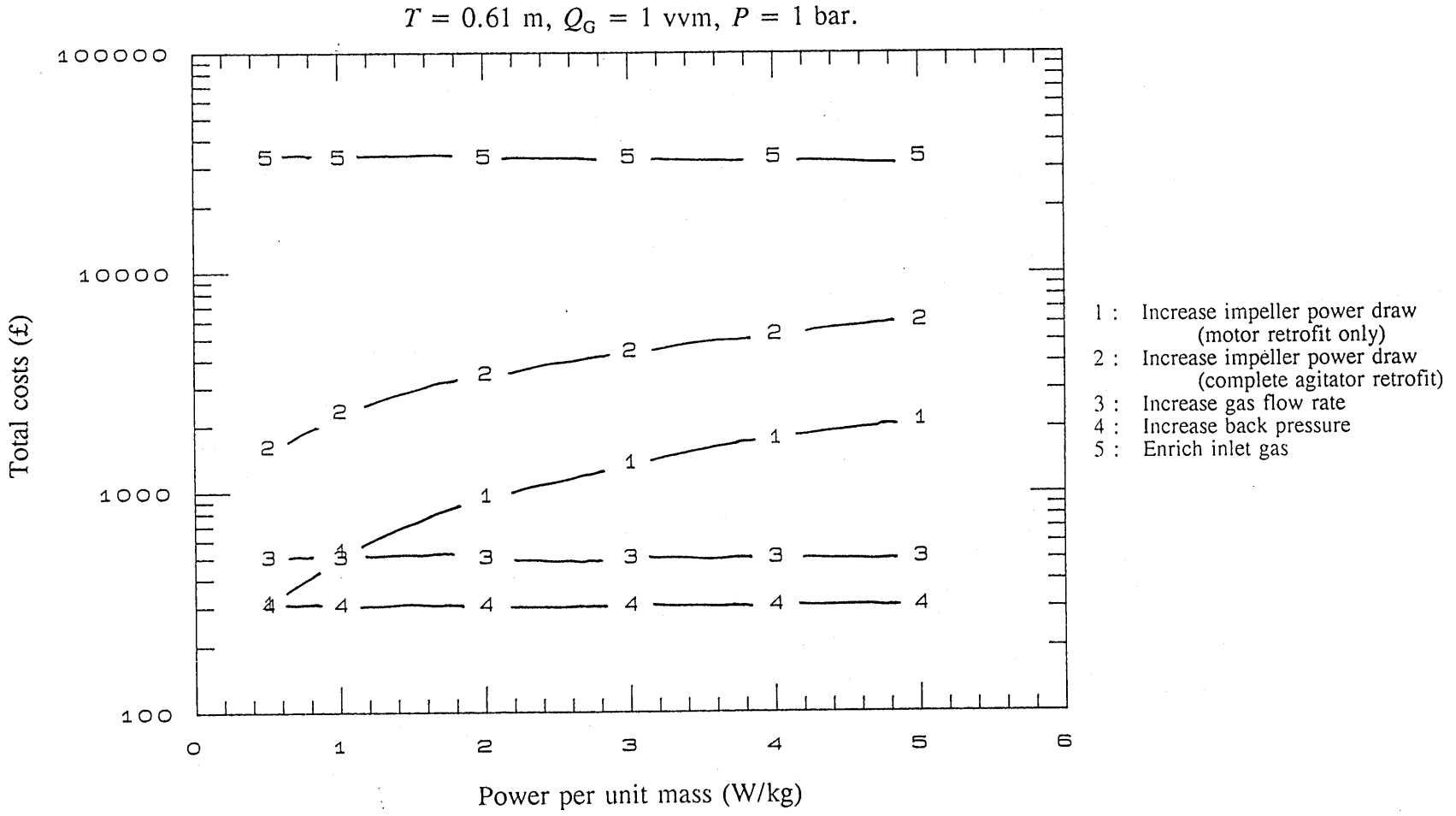


Figure 7.7: Effect of power input on cost of process options at small scale (low gas flow rate, high back pressure)

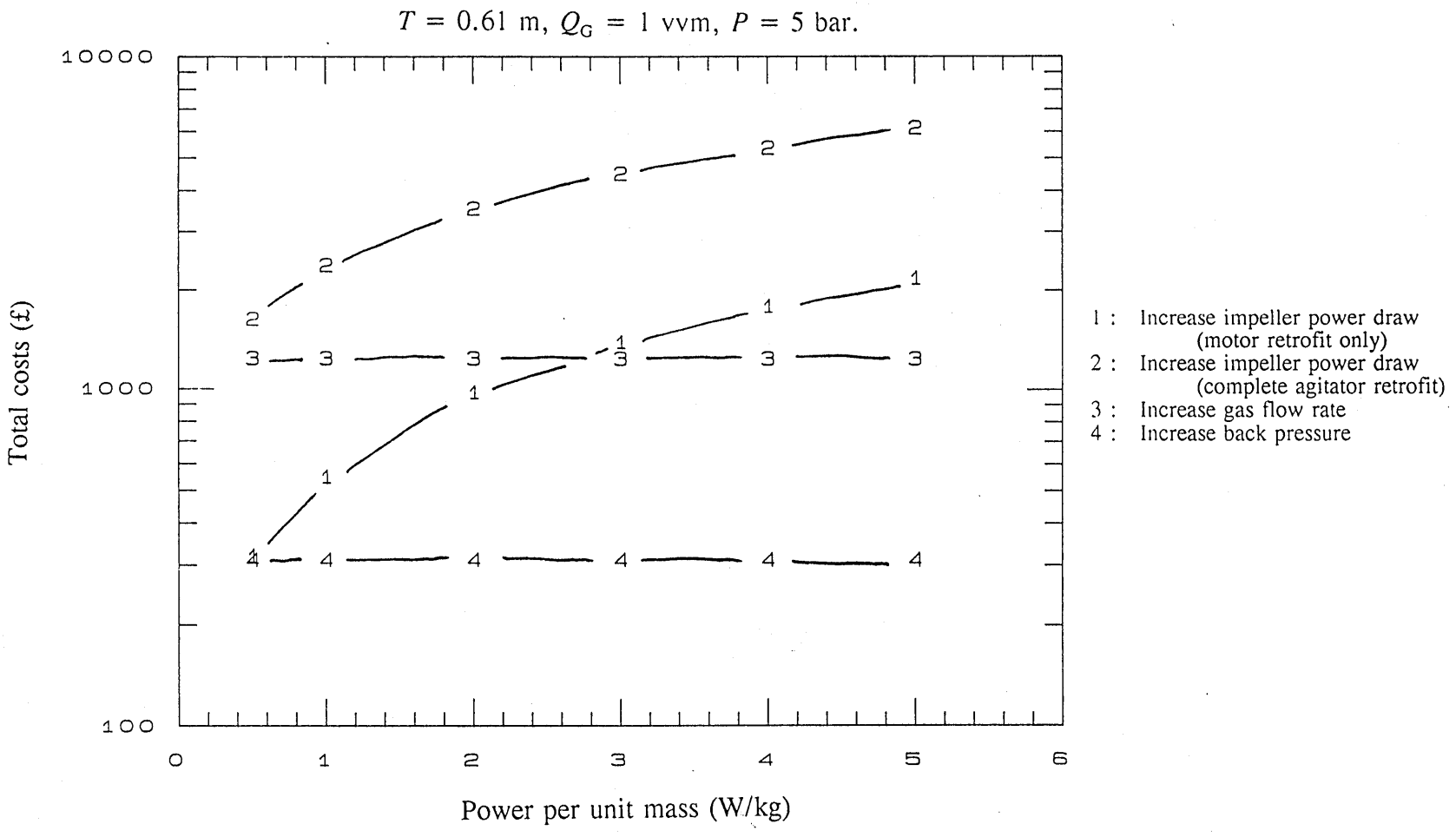


Figure 7.8: Effect of power input on cost of process options at small scale (high gas flow rate, low back pressure)

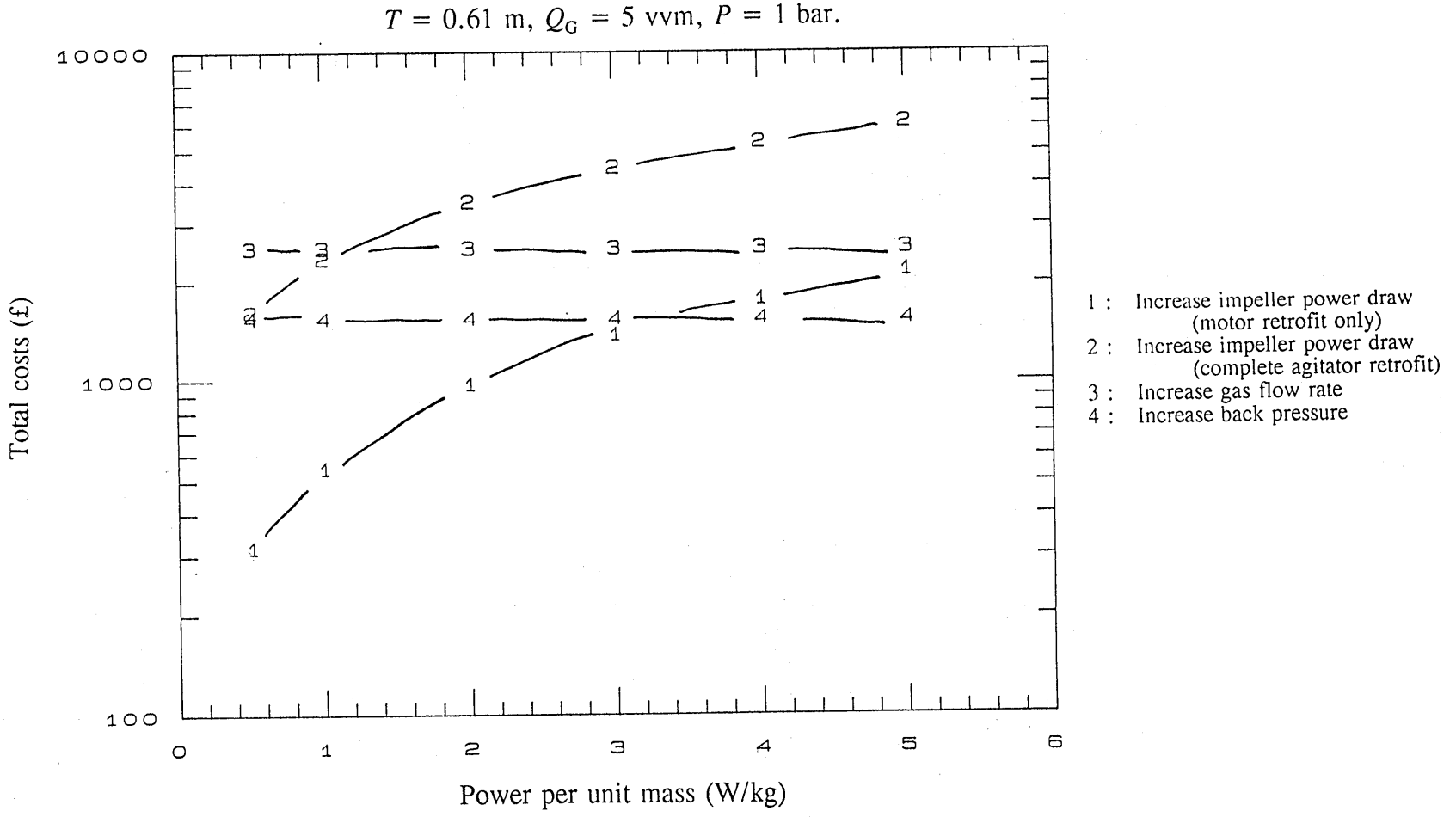


Figure 7.9: Effect of power input on cost of process options at small scale (high gas flow rate, high back pressure)

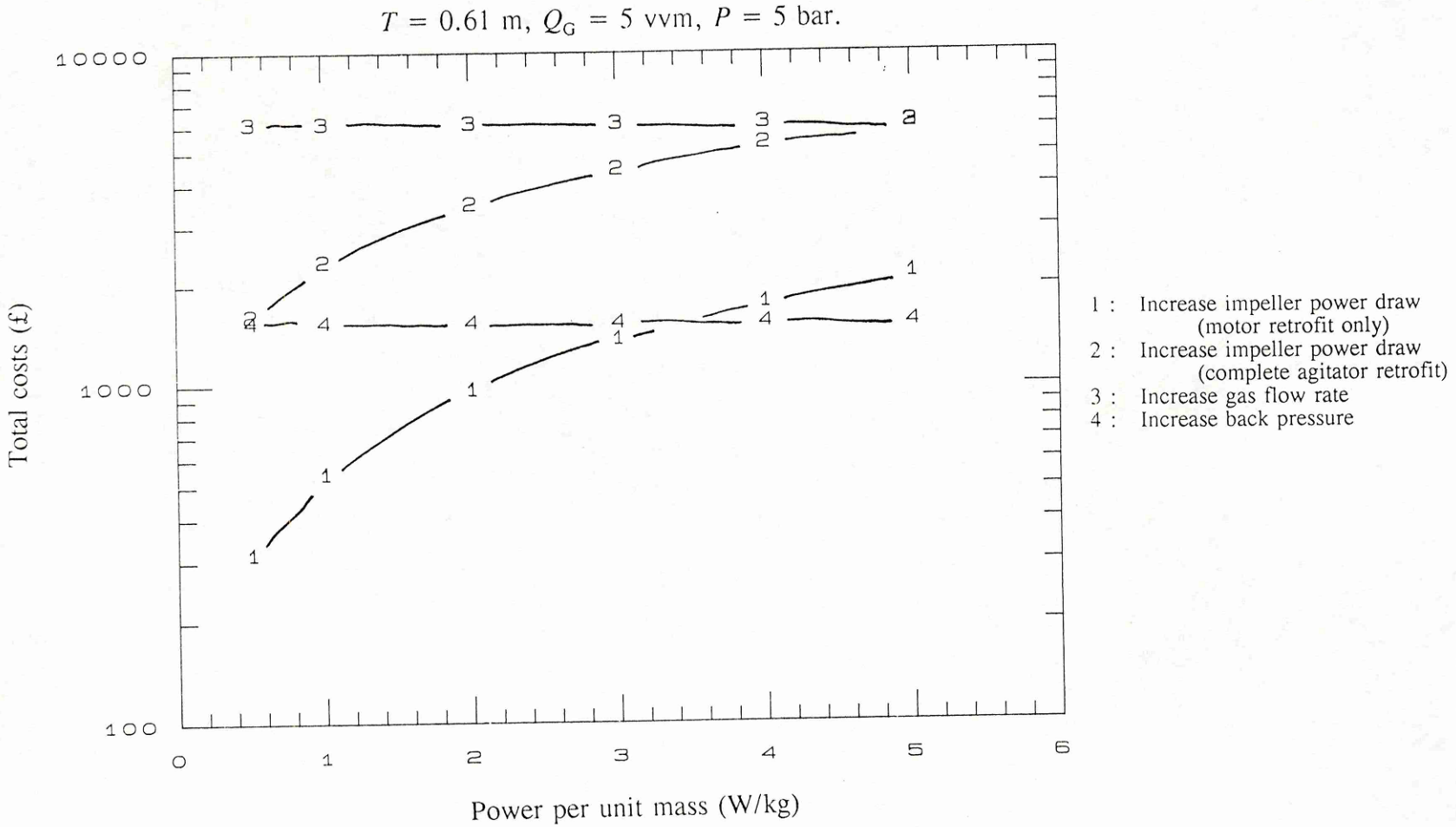


Figure 7.10: Sensitivity of costs to project life.

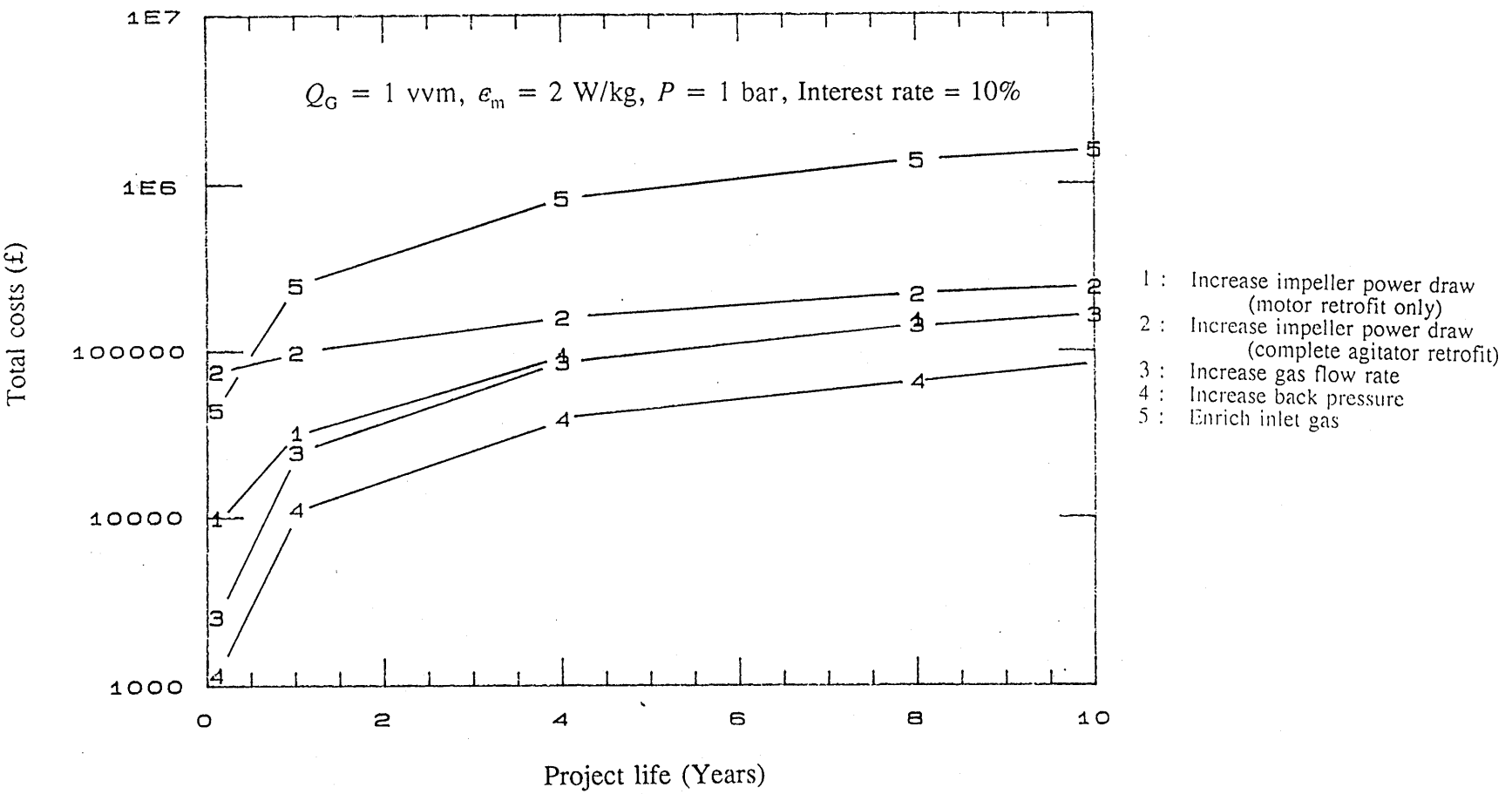


Figure 7.11: Sensitivity of costs to interest rate.

